2nd International Symposium on

Therapeutic Ultrasound

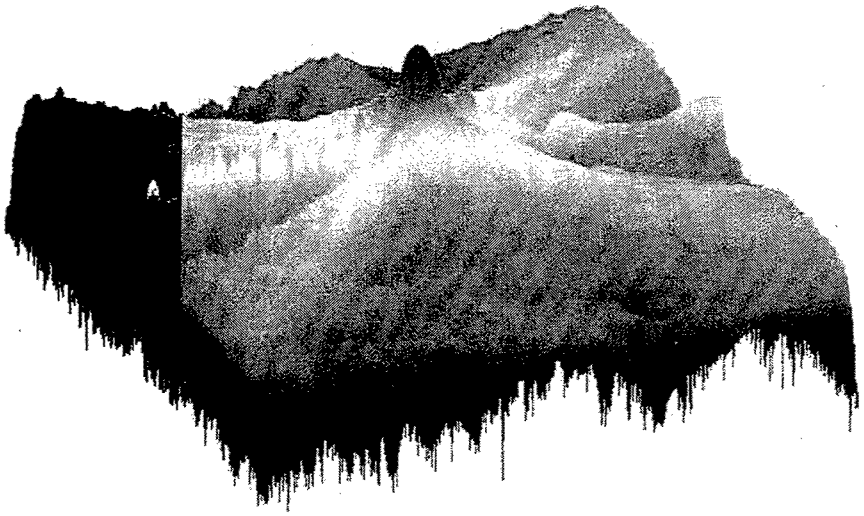

29 July – 1 August, 2002

Seattle, Washington, USA

Conference Proceedings

Editors: M.A. Andrew, L.A. Crum, and S. Vaezy

Center for Industrial & Medical Ultrasound
Applied Physics Laboratory
University of Washington

2nd International Symposium on

Therapeutic Ultrasound

Seattle, Washington, USA

29 July–1 August, 2002

Conference Proceedings

EDITORS

Marilee A. Andrew

Lawrence A. Crum

Shahram Vaezy

Center for Industrial & Medical Ultrasound
Applied Physics Laboratory • University of Washington

Editors:

Marilee A. Andrew
Email: *marilee@apl.washington.edu*

Lawrence A. Crum
Email: *lac@apl.washington.edu*

Shahram Vaezy
Email: *vaezy@apl.washington.edu*

Center for Industrial & Medical Ultrasound
Applied Physics Laboratory, University of Washington
1013 NE 40th Street
Seattle, WA 98105-6698 USA

This publication was made possible through the U.S. Army Medical Research Acquisition Activity under terms of Assistance Award No. DAMD17-01-1-0824. Any opinions, findings, and conclusions or recommendations expressed in this material are those of the author(s) and do not necessarily reflect the views of the U.S. Army Medical Research Acquisition Activity, 820 Chandler Street, Fort Detrick MD 21702.

L.C. Catalog Card No. 2003103129

ISBN 0-7354-0125-X

Printed in the United States of America

Produced for the University of Washington by The American Institute of Physics

AD_____

Award Number: DAMD17-01-1-0824

TITLE: 2nd International Symposium on HIFU Therapy "HIFU Seattle 2002"

PRINCIPAL INVESTIGATOR: Lawrence A. Crum, Ph.D.

CONTRACTING ORGANIZATION: University of Washington
Seattle, Washington 98105

REPORT DATE: December 2002

TYPE OF REPORT: Final Proceedings

PREPARED FOR: U.S. Army Medical Research and Materiel Command
Fort Detrick, Maryland 21702-5012

DISTRIBUTION STATEMENT: Approved for Public Release;
Distribution Unlimited

The views, opinions and/or findings contained in this report are those of the author(s) and should not be construed as an official Department of the Army position, policy or decision unless so designated by other documentation.

REPORT DOCUMENTATION PAGE

Form Approved
OMB No. 074-0188

1. AGENCY USE ONLY (Leave blank)	2. REPORT DATE	3. REPORT TYPE AND DATES COVERED
	December 2002	Final Proceedings (1 Aug 01 - 31 Dec 02)

4. TITLE AND SUBTITLE
2nd International Symposium on HIFU Therapy "HIFU Seattle 2002"

5. FUNDING NUMBERS
DAMD17-01-1-0824

6. AUTHOR(S) :
Lawrence A. Crum, Ph.D.

7. PERFORMING ORGANIZATION NAME(S) AND ADDRESS(ES)
University of Washington
Seattle, Washington 98105

E-mail: lac@apl.washington.edu

8. PERFORMING ORGANIZATION REPORT NUMBER

9. SPONSORING / MONITORING AGENCY NAME(S) AND ADDRESS(ES)
U.S. Army Medical Research and Materiel Command
Fort Detrick, Maryland 21702-5012

10. SPONSORING / MONITORING AGENCY REPORT NUMBER

11. SUPPLEMENTARY NOTES
Original contains color plates: All DTIC reproductions will be in black and white.

12a. DISTRIBUTION / AVAILABILITY STATEMENT
Approved for Public Release; Distribution Unlimited

12b. DISTRIBUTION CODE

13. ABSTRACT ***(Maximum 200 Words)***

none provided

14. SUBJECT TERMS:
therapeutic ultrasound, HIFU therapy

15. NUMBER OF PAGES
586

16. PRICE CODE

17. SECURITY CLASSIFICATION OF REPORT	18. SECURITY CLASSIFICATION OF THIS PAGE	19. SECURITY CLASSIFICATION OF ABSTRACT	20. LIMITATION OF ABSTRACT
Unclassified	Unclassified	Unclassified	Unlimited

To the many pioneers of HIFU,
and especially Frank Fry.

CONTENTS

1. CLINICAL STUDIES

2. LABORATORY STUDIES

3. SIMULATION AND MONITORING

4. DOSIMETRY

5. ENGINEERING

6. LITHOTRIPSY

7. ULTRASOUND-ENHANCED DRUG DELIVERY

8. SONODYNAMIC THERAPY

APPENDIX

Preface

When the Fry brothers introduced the world to HIFU in the 1950's, diagnostic ultrasound was in its infancy. However, the remarkable advances in ultrasound imaging technology over recent years have permitted us now to envision the combined use of ultrasound both for imaging and for therapy. It doesn't take much imagination to picture the tremendous promise of (ultrasound) image-guided (HIFU) therapy (IGT). Just as smaller and smaller diagnostic ultrasound systems will soon replace the stethoscope, so eventually will increasingly precise therapeutic ultrasound systems replace the scalpel. This volume describes in some detail recent advances in IGT, particularly in the treatment of malignant tumors.

This book is a compilation of papers presented at the 2nd International Symposium on Therapeutic Ultrasound, held in Seattle, Washington, July 29–August 1, 2002. The Symposium attracted 200 participants from 14 different countries. A list of the author attendees (without the requisite photograph) is included in these proceedings. Approximately 100 abstracts were accepted for presentation at the conference. Invitations to the authors to submit articles for publication in this proceedings have resulted in this volume, which contains 73 separate articles.

This volume has been divided into a number of topic categories, viz., Clinical Studies, Laboratory Studies, Simulation and Monitoring, Dosimetry, Engineering, Lithotripsy, Ultrasound-Enhanced Drug Delivery, and Sonodynamic Therapy. One can see from this topic coverage that the symposium was largely on HIFU (essentially the first five topics), yet also broad enough to cover most aspects of therapeutic ultrasound.

This Symposium followed a similar one held in Chongqing, PRC in May of 2001. At that conference, a number of us were surprised to learn that, in the P.R. China, medical devices had been approved for the use of High Intensity Focused Ultrasound (HIFU) in the treatment of cancer and other diseases, and that a large number of patients had been treated with excellent results. Since attendance at this meeting by "Western" participants was relatively sparse, a group of us determined that a second meeting should be held soon, not only to publicize the pioneering work of our Chinese colleagues, but also to review the entire field of therapeutic ultrasound.

At the Chongqing meeting, it was also decided that a new Society should be formed to increase and diffuse the knowledge of therapeutic ultrasound more broadly to the scientific and medical community. Accordingly, the International Society of Therapeutic Ultrasound (ISTU) was formed (http://www.istus.org/), and its organization and mission discussed in some detail at the Seattle meeting. It was decided that probably the most important role of ISTU was to organize a regular meeting of the Society; consequently, a procedure was established for the selection of future meeting sites and the activities that should be undertaken by the host organization.

We have featured Clinical Studies as the leading section because it addresses a desired endpoint for the application of therapeutic ultrasound, namely the treatment of disease in human patients. This first section contains reports by a number of groups from China, France, the USA and the UK on the treatment of a variety of tumors, both malignant and benign, in a variety of organs. The successful application of HIFU to tumors of the liver and pancreas is particularly appealing due to the limitations of conventional treatments.

This section is followed by one on Laboratory Studies, in which several papers treat the scientific aspects of therapeutic ultrasound, particularly HIFU. Although the number of patients being treated by HIFU is rapidly growing, a full understanding of the capabilities and limitations of this technology has not yet been achieved. Of particular interest is the developing capability of ultrasound not only to image and target the site of HIFU application, but also to monitor *in real-time* the evolution of the treated volume. This broad capability of ultrasound-guided and *ultrasound-monitored* therapy is practically unique to HIFU and

represents a revolutionary advancement in the treatment of disease. (Of course, we are well aware of the work of MR-guided Focused Ultrasound Surgery and include it in our general grouping of therapeutic ultrasound technologies.)

The next two sections deal with Simulation and Monitoring and Dosimetry. It is well known that for new technologies to gain acceptance within the medical community, and especially the FDA, the level of risk must be as low as possible. This risk reduction is often accomplished by developing validated models that can assess risk without requiring extensive and unnecessary animal trials. Likewise, an important aspect of risk reduction is ensuring that the dose delivered is the intended dose. The papers in these two sections describe significant advances in model development as well as detailed investigations of how to measure the high intensity levels (as high, perhaps, as 20,000 W/cm^2) utilized in focused ultrasound surgery.

One of the most exciting areas of IGT development is in the device engineering being undertaken to perform the tumor-treatment protocols. Accordingly, we invited a number of authors to discuss the Engineering aspects of therapeutic ultrasound, which is the next section in the Proceedings. It is gratifying to note that several commercial ventures are now underway that provide, or will soon provide, government-approved clinical devices for the treatment of patients. Descriptions of a number of these devices are presented in this section.

Arguably the first successful commercial use of therapeutic ultrasound was that of Lithotripsy. Lithotripters use intense shock waves to comminute kidney stones, and more recently, also to treat a variety of orthopedic conditions. These devices produce acoustic pulses that are characterized by a very large acoustic pressure amplitude (as high as 100 Mpa), but extremely low intensities because these pulses are delivered no more often than at 1 or 2 Hz. The bioeffects that are associated with lithotripters were originally thought to be relatively minor; however, recent studies suggest kidney tissue can suffer significant damage during lithotripsy. An interesting sidelight of this research is that shock waves can transiently permeablize membranes, and thus are an excellent mechanism for the induction of gene transfection.

The Symposium closed with two major sessions on the use of ultrasound to enhance drug delivery, viz., Ultrasound-Enhanced Drug Delivery and Sonodynamic Therapy. This technology has exciting promise in that one of the major technological pushes of the new century will probably be to make use of the huge investment made in characterizing the human genome. This characterization has little value if medical science does not find ways to insert material directly into cells. The two final sections of the Proceedings contain papers that provide some important and exciting advances into the use of ultrasound as an alternative to viruses as a gene transfection vector.

This volume contains a relatively complete and certainly broad snapshot of the state-of-the-art of therapeutic ultrasound at the beginning of the 21st Century. It is almost certain that this area of medical science will be one of the most promising areas for research and development as the century progresses. We hope that the articles in this volume stimulate you to explore this promising area of scientific endeavor, and to join the International Society for Therapeutic Ultrasound.

We wish to acknowledge the many authors who submitted articles for these proceedings. Their combined work offers a broad perspective of HIFU at the beginning of the 21st Century. We acknowledge also the generous support of our sponsors, particularly the U.S. Army Medical Research and Material Command, and its representative, Ron Marchessault. Finally, ISTU2 and these proceedings would never have been completed without the indefatigable efforts of Dorothy Lowell. Her remarkable and tireless work ethic, and her insistence that even the most minor detail had to be considered, resulted in a very successful symposium, and tremendously improved the quality of many of these articles; we, the participants, and the authors, owe her a great deal of gratitude.

The Editors

2nd International Symposium on Therapeutic Ultrasound
Seattle, Washington, USA, July 30–August 1, 2002

This symposium was made possible through the generous support of our sponsors:

U.S. Army Medical Research & Materiel Command
Telemedicine & Advanced Technology Research Center
504 Scott Street, Fort Detrick, MD 21702

Ancer Medical
737 Puget Lane
Edmonds, WA 98020
Tel: (425) 778-2362

EDAP Technomed
-6 rue du Dauphine
69120 Vaulx en Velin
France
http://www.edaptechnomed.com/

EKOS Corporation
22030 20th Ave SE, Suite 101
Bothell, WA USA

Focus Surgery, Inc.
3940 Pendleton Way
Indianapolis, IN 46226
http://www.focus-surgery.com/

Chongqing Haifu (HIFU) Technology Co., Ltd.
70-2, 3rd Keyuan Street,
Shiqiaopu, Jiulongpo District,
Chongqing 400041 P. R. China
Tel: 86-23-68623428
E-mail: sales@cnhifu.com
web: http://www.cnhifu.com/

Imasonic
15, rue Alain Savary
25000 Besançon, France
Tel: +33 (0)3 81403130 / 33
http://www.imasonic.com

Johnson & Johnson
http://www.jnj.com/

National Institutes of Health
http://www.nih.gov/

Office of Naval Research
http://www.onr.navy.mil/

The Seattle Foundation
425 Pike Street, Suite 510
Seattle, WA 98101-2334
Tel: (206) 622-2294
http://www.seattlefoundation.org/

Therus Corporation
2401 Fourth Avenue, Suite 200
Seattle, WA 98121 USA
Tel: 206-832-4601
E-mail: info@therus.com
http://www.therus.com/

Ultrasound Therapeutics Ltd.
Ste 2, 1st Flr, New Mansion House
173 /191 Wellington Rd South
Stockport SK1 3UA England
Tel: (44) 161 477 6111
E-mail: sales@utlltd.com
http://www.utlltd.com/

1. CLINICAL STUDIES

HIFU And Localized Prostate Cancer: Efficacy Results From The European Multicentric Study*

Christian Chaussy, Stefan Thüroff

Department of Urology, Staedt. Krankenhaus München-Harlaching

Abstract. Purpose: The safety and the efficacy of High Intensity Focused Ultrasound (HIFU) for the treatment of prostate cancer have been assessed in a phase II-III prospective multicentric clinical trial.
Materials and Methods: Patients presenting with localized prostate cancer and non candidates for radical prostatectomy were included between 1995 and 1999 in 6 European sites. All patients were treated with HIFU under general or spinal anesthesia. During the follow-up, random sextant biopsies and PSA level measurements were performed. Any positive sample in biopsies performed after the last treatment session resulted in a "HIFU failure" classification.
Results: n=402 patients with localized prostate cancer (stage T1-2 N0-x M0) were included and were treated with HIFU as primary care. Main patients baseline characteristics were (mean ± SD): age 69.3 ± 7.1 years, prostate volume 28.0 ± 13.8 cc, PSA 10.9 ± 8.7 ng/ml. 92.2% of the patients were presenting 1 to 4 positive samples at the baseline biopsy. Gleason scores were 2 to 4 for 13.2% of the patients, 5 to 7 for 77.5%, and 8 to 10 for 9.3%. Patients received in mean 1.4 HIFU session. The mean follow-up duration was 407 days (Q1: 135 days, median: 321 days, Q3: 598 days). The negative biopsy rate observed in the T1-T2 primary care population is 87.2%. These results were also stratified according to the usual disease related risk classification, and up to 92.1% negative biopsy rate was observed in low-risk patients. Nadir PSA results were correlated to the prostate size and the clinical procedure.
Conclusion: These short-term efficacy results obtained on a large cohort confirm that HIFU is an option to be considered for the primary treatment of localized prostate cancer.

INTRODUCTION

New non-surgical treatment options for localized prostate cancer are emerging in our daily practice. This trend results from several factors, including the sharp increase in early diagnoses thanks to the PSA screening, and the role of the patient in choosing his treatment. Indeed, patients are more and more concerned with the post-treatment quality of life, i.e. the recovery time and the treatment-related acute and chronic morbidity.

Beside the large experience in the U.S.A. with brachytherapy for localized prostate cancer, using Iodine or Paladium permanent implants, a minimally-invasive option using High Intensity Focused Ultrasound (HIFU) was developed in Europe.

It was first demonstrated that HIFU may destroy prostate cancer by coagulative necrosis of the tissue[1], without damaging the intervening structures passed by HIFU[2], and without increase in metastasis formation[3]. The transrectal approach was validated with an animal model[4], then with the first clinical trials[5, 6].

* Abstract presented at the 2001 AUA congress, Anaheim

In order to evaluate the results of the HIFU treatment in prostate cancer on a larger patient population, the European Multicentric Study was then carried out in 6 investigational sites.

MATERIALS AND METHODS

The European Multicentric Study is a prospective, multicenter, open-labeled, non controlled clinical trial. The study was approved by local Ethics Committees, and all the patients signed an informed consent form for participation prior to their enrollment. From November 1995 to October 2000, 652 patients were included in the clinical study, which is still ongoing in most of the sites for patient follow-up. In November 1999, an interim statistical analysis was performed, including all the patients enrolled and treated at that time. The results of this interim analysis are presented hereafter.

In this 4-year period (Nov. 95-Nov. 99), 559 patients in total were selected and treated with HIFU. All the patients were diagnosed for histology proven prostate cancer, and were not suitable candidates for radical prostatectomy. Of them, n=402 patients were presenting with a localized prostate cancer (T1-2 N0-x M0), and were treated with HIFU as a primary care for prostate cancer. The results are focused on this group. The other sub-populations (patients enrolled but excluded of this analysis) were: 8 patients who underwent previously a radical prostatectomy, 35 patients with a previous external beam radiation therapy, 104 patients with a previous orchiectomy or hormone deprivation, and 10 patients with locally advanced disease or distant metastases (T3-4 and/or N+ and/or M+).

All the patients were treated using the Ablatherm® HIFU device (EDAP Technomed, Lyon, France), generally under spinal anesthesia. Several device prototypes were used during the course of the study, while technical parameters evolved: progressive increase in frequency from 2.25 up to 3 MHz, and progressive increase in the shot duration from 4 to 5 seconds. In parallel, a cooling system and additional safety features were implemented. For the statistical analysis performed, 4 major technical protocols (TP) were identified: TP1 with a 2.25 MHz frequency, and a shot duration $\leq$ 4.5 seconds (no cooling system with TP1), TP2 with a frequency $<$ 3 MHz and a 4.5 seconds shot duration, TP3 with a 3 MHz frequency and a 4.5 seconds shot duration, and TP4 with a 3 MHz frequency and a 5 seconds shot duration.

Patients were systematically treated in 2 HIFU sessions (1 session/lobe) from 1995 to 1998. Then, the prostate was targeted in a single HIFU session. In case of residual positive biopsies or in case of local recurrence during post-treatment follow-up, HIFU retreatment was possibly performed. The patients who were no longer candidates for HIFU were generally managed with external radiotherapy or hormone deprivation, and were therefore considered as HIFU failure patients.

HIFU efficacy was assessed through sextant biopsies and PSA measurements. For each patient, all the biopsies performed 6 weeks or more after the last treatment session were considered, and any positive core, whatever the cancer size, led to the patient classification as "positive biopsy". Nadir PSA was defined as the lowest PSA level measured after the last HIFU session. Only patients with 6 months follow-up or more were considered for PSA nadir determination. Biopsy and PSA results were assessed for the overall localized prostate cancer population (n=402), and were then stratified according to factors which might

influence the results, i.e. patient baseline characteristics and the different technical protocols. For the HIFU safety evaluation, all adverse events were collected.

RESULTS

At inclusion in the study, patients were presenting the following baseline characteristics (Table 1): age 69.3 ± 7.1 years, prostate volume 28.0 ± 13.8 cc, PSA 10.9 ± 8.7 ng/ml, Gleason score 2 to 4 or G1 for 51 patients (13.2%), 5 to 7 or G2 for 300 patients (77.5%), and 8 to 10 or G3 for 36 patients (9.3%). Baseline characteristics were also considered for the patient classification according to the baseline disease-related risk level, using the usual definition with (i) low-risk: T1-T2a and PSA ≤ 10 ng/ml and Gleason score ≤ 6, (ii) intermediate-risk: T2b or 10 < PSA ≤ 20 ng/ml or Gleason score = 7, and (iii) high-risk: T2c or PSA > 20 ng/ml or Gleason score ≥ 8. This resulted in 114 low-risk patients (28.4%), 193 intermediate-risk patients (48.0%) and 95 high-risk patients (23.6%).

TABLE 1: Patient Baseline Characteristics.

	Age (years)	Prostate Volume (cc)	PSA (ng/ml)	Gleason Score
n	**396**	**389**	**397**	**369**
Mean	**69.3**	**28.0**	**10.9**	**6.0**
SD	7.1	12.7	8.7	1.3
Q1	65.0	19.0	5.8	5.0
Median	**70.0**	**25.0**	**8.9**	**6.0**
Q3	75.0	34.0	41.0	7.0
Minimum	51.0	4.2	0.1	2.0
Maximum	88.0	120.0	78.0	9.0

In total, 602 HIFU sessions were performed to 402 patients (1.47 session/patient), with 62.4% of the patient treated with a single session, and 27.9% treated with 2 sessions. The retreatment rate is nevertheless not interpretable due to the change of the clinical procedure during the course of the clinical trial, moving from 1 session/lobe to a single session for the entire prostate. At the first treatment session, 49 patients (12.2%) were treated with TP1, 59 patients (14.7%) with TP2, 184 patients (45.8%) with TP3, and 110 patients (27.4%) with TP4.

For each patient, follow-up time was defined from the first treatment session up to the last histology or PSA measurement available. At the time of the statistical analysis, mean patient follow-up was 407.3 days, ranging from 0 to 1541 days. The quartile distribution (Q1: 135 days, median: 321 days, Q3: 598 days) reflects the patient accrual rate during the course of the study: low inclusion rate during the first year of the study, then progressive increase, and about half of the patients included the last year of the period considered for analysis.

In total, 288 patients were assessable for sextant biopsy results, and a 87.2% negative biopsy rate was observed (Table 2). Biopsy results were stratified according to the prostate size, i.e. for patients with a prostate volume ≤ 40 cc vs > 40 cc: 88.4% and 85.0% negative biopsy rates were observed, respectively (Fisher's exact test: p=0.599, NS). Similarly, biopsy results were stratified according to the antero-posterior (AP) prostate diameter, considering the limitation of the unitary lesion length, for prostate with AP diameter ≤ 25 mm vs AP > 25 mm: 85.4% and 88.1% negative biopsy rates were observed,

respectively (χ^2 test: p=0.622, NS). When stratified according to the disease-related risk level, the following negative biopsy rates were observed: 92.1% in low-risk patients, 86.4% in intermediate-risk patients, and 82.1% in high-risk patients (χ^2 test: p=0.167, NS). When only considering the number of positive cores in pre-treatment sextant biopsies among prognostic factors, the comparison reached the significance level: 88.1% negative biopsy rate in patients presenting with 1 to 4 positive cores, vs 70.8% in patients with more than 4 positive cores (Fisher's exact test: p=0.017). The clinical procedure for HIFU treatment was leading to partial or complete treatment of the gland, due to the treatment strategy or to the prostate size, without statistically significant impact on the negative biopsy rates: 91.7% after complete treatment vs 87.2% after partial treatment (Fisher's exact test: p=0.321, NS). Finally, the biopsy results were stratified according to the technical protocols: 44.4% in TP1, 82.1% in TP2, 91.2% in TP3, and 94.8% in TP4 (χ^2 test: p<0.0001). These results are possibly biased by the time effect, the different technical protocols being successively used during the course of the study, and the first patients treated having more time to reveal a residual or recurrent cancer. In order to reduce this bias, the biopsy results at one year were also calculated in each TP group: 66.7% in TP1, 76.5% in TP2, 91.2% in TP3, and 100.0% in TP4, but with only 9 patients in the TP4 group with one-year biopsy results available (Fisher's exact test: p=0.021).

TABLE 2: Biopsy and Nadir PSA Results.

		Negative Biopsy		Nadir PSA (ng/ml)		
		rate	p	median	mean	p
Overall result		87.2%		0.6	1.8	
Prostate volume	≤ 40 cc	88.4%	NS	0.4	1.5	p=0.000
	> 40 cc	85.0%		2.0	2.9	1
AP diameter	≤ 25 mm	85.4%	NS	0.4	1.4	NS
	> 25 mm	88.1%		0.5	1.3	
Low-risk		92.1%		0.5	1.3	
Intermediate-risk		86.4%	NS	0.7	1.4	NS
High-risk		82.1%		0.5	3.1	
Partial treatment		87.2%	NS	0.6	1.8	p=0.016
Complete treatment		91.7%		0.1	1.4	
TP1		44.4%	p<0.0001	1.2	5.1	p=0.000
TP2		82.1%		2.0	3.3	1
TP3		91.2%		0.5	1.3	
TP4		94.8%		0.3	0.9	

All the patients with at least 6-month follow-up were assessed for PSA nadir. In these n=212 patients, nadir was generally obtained within 3 to 4 months after HIFU treatment (mean: 163.5 days, median: 111.5 days). The quartile distribution of the nadir PSA results was Q1: 0.1 ng/ml, median: 0.6 ng/ml, and Q3: 2.1 ng/ml, while the mean value at 1.8 ng/ml was relatively high due to the non-responders (range: 0-27 ng/ml) (Table 2). As for biopsy results, nadir PSA results were stratified according to the prostate volume (mean=1.5 ng/ml and median=0.4 ng/ml in prostate ≤ 40 cc vs mean=2.9 ng/ml and median=2.0 ng/ml in prostate > 40 cc, Wilcoxon test: p=0.0001); according to the AP diameter (mean=1.4 ng/ml and median=0.4 ng/ml in AP ≤ 25 mm vs mean=1.3 ng/ml and median=0.5 ng/ml in AP > 25 mm, Wilcoxon test: p=0.453, NS); according to the clinical procedure (mean=1.4 ng/ml and median=0.1 ng/ml after complete treatment vs mean=1.8 ng/ml and median=0.6 ng/ml after partial treatment, Kruskal Wallis test: p=0.016); according to the disease-related risk

level (mean=1.3 ng/ml and median=0.5 ng/ml in low-risk patients, mean=1.4 ng/ml and median=0.7 ng/ml in intermediate-risk patients, and mean=3.1 ng/ml and median=0.5 ng/ml in high-risk patients, Kruskal Wallis test: p=0.793, NS); and according to the technical protocols (mean=5.1 ng/ml and median=1.2 ng/ml in patients treated with TP1, mean=3.3 ng/ml and median=2.0 ng/ml in TP2, mean=1.3 ng/ml and median=0.5 ng/ml in TP3, and mean=0.9 ng/ml and median=0.3 ng/ml in TP4, Kruskal Wallis test: p=0.0001). The PSA level stability in further PSA measurements was not assessed due to the high proportion of patients with less than one year follow-up. Indeed, when considering the ASTRO definition, time to nadir plus at least 9 months are needed in order to evidence rising PSA level on 3 successive measurements taken at least 3 months apart. So, after HIFU, patients should have at least one year follow-up to be considered for such an analysis.

The treatment-related morbidity was assessed through the adverse event collection. The most serious adverse event reported was urethro-rectal fistula, which occurred in 5 patients in the following situations: before the implementation of the rectal cooling system (n=2), in patients with a rectal wall thickness over 6 mm which is now considered as a contraindication for the HIFU treatment (n=2), and after a repeated HIFU session with only a 2-month interval in between (n=1). These fistula cases resolved after urinary catheter placement (n=3), after fibrin glue injection (n=1), or after surgery (n=1). Stress incontinence grade I and grade II were observed in 10.6% and 2.5%, respectively. These mild to moderate cases of stress incontinence generally resolved spontaneously or after appropriate management with medication and/or floor muscle training. Grade III stress incontinence was reported in 6 patients and recovered after pelvic floor muscle training (n=1), artificial sphincter placement (n=4) or collagen injection (n=1). Urinary tract infections were reported in 13.8% of the patients, and were easily managed with usual antibiotics. Immediate post-treatment retention was observed in all patients, for 5 days in median when the retention was managed with a trans-urethral catheter Foley type, and for 34 days in median when managed with a supra-pubic tube. Prolonged retention was reported in 8.6% of the cases, mainly due to tissue sloughing, and generally resolved with the evacuation of the necrotic debris. Later during follow-up, 3.6% of the patients presented a urethral stenosis, usually treated with urethrotomy. Thirty five patients spontaneously reported partial or total loss of potency, but the pre-treatment potency status was not systematically recorded in all the sites.

DISCUSSION

The observed short-term efficacy results demonstrate a good local control of the disease after HIFU treatment even considering the high proportion of high-risk patients, better results being observed in patients properly selected as suitable candidates for a local treatment. When considering longer term results as described by Gelet et al.[7, 8], a plateau in the disease free rates survival curves calculated with the Kaplan-Meier method is observed from 20-month follow-up. The time for this plateau occurrence should be confirmed with an updated statistical analysis of the European Multicentric Study cohort.

The prostate size or the clinical procedure does not affect the biopsy results, while it directly impacts the residual PSA level. Moreover, prostate size is not an actual limitation to the HIFU treatment when considering that it may be repeated.

The progressive optimization of the technical parameters led to a better efficiency of the treatment delivered, and the last technical protocol studied (3 MHz frequency, 5 seconds for

the shot duration) was implemented in the standard device. In daily practice, the retreatment rate using these technical parameters does not exceed 10 to 20% according to the first choice treatment strategy, from treatment including the prostate capsula to nerve-sparing treatment excluding 5 mm of tissue near the neurovascular bundle[10, 11, 12].

In our own experience, we are using the standard Ablathem® since 2000. In total, 144 patients staged T1-2 N0-x M0 without any previous prostate cancer treatment were treated with that standard device. From them, n=65 patients had 12 to 18 months follow-up, i.e. were assessable for biopsy results and for PSA stability according to the ASTRO definition. During follow-up, control biopsies were systematically performed (in mean, 2.25 sextant biopsy set/patient), as well as PSA measurements every 3 months. Biopsy assessment evidenced a 85.7% negative biopsy rate. Nadir PSA level was generally obtained within 3 months post-HIFU. Median nadir PSA was 0.1 ng/ml, and 92.6% of the patients were still presenting with a stable PSA level at that short-term follow-up. These results are considering a 9.2% HIFU re-treatment rate.

For the safety aspects, the now standardized clinical procedure for HIFU treatment, as well as the safety features implemented, sharply improved the treatment related morbidity. In patients treated with HIFU as a primary care, and with a safety margin for the treatment of the apex, fistula and grade III stress incontinence disappeared, without increase in apical residual cancer[9, 10, 11, 12]. In order to improve the post-treatment retention, we are now combining a trans-urethral resection of the prostate (TURP) immediately prior to the HIFU treatment, under the same spinal anesthesia, and this procedure leads to a significant reduction in the catheter time, from 2 days with the trans-urethral tube, to 7 days when a supra-pubic tube is placed. The patient management after the combined TURP+HIFU treatment is similar as after a classical TURP.

Following this multicenter experience, HIFU treatments may be efficiently performed with an established procedure, and with a short learning curve (approximately 10 patients for a new user with technical skill in US prostate imaging). As a minimally invasive treatment option, it may be delivered under spinal anesthesia. The HIFU-related morbidity is low, and the post-treatment management is easy. The evening after the HIFU session, the patient returns to normal food, does not need any analgesic medication, and may be discharged the day after with a catheter placed, or a few days later without catheter (according to the country and cultural context). Patients with a TURP history, or presenting with a local recurrence after external radiotherapy or surgery are suitable candidates for HIFU. In case of local recurrence after primary HIFU, the patient may benefit from a further HIFU session, or may still receive external beam radiation.

In our practice, we select for HIFU treatment the patients who are not candidates for surgery due to their age or comorbidities, patients who are poor candidates for surgery due to the local conditions or with a high risk for positive margin, and patients refusing surgery.

REFERENCES

1. Chapelon J.Y., Margonari J., Vernier F., Gorry F., Ecochard R., and Gelet A., "In vivo effects of High Intensity Ultrasound on Prostatic Adenocarcinoma Dunning R3327," *Cancer Research* **52**, 6353-6357 (1992).

2. Chapelon J.Y., Margonari J., Theillère Y., Gorry F., Vernier F., Blanc E., and Gelet A., "Effects of High-Energy Focused Ultrasound on Kidney Tissue in the Rat and the Dog," *Eur. Urol.*, **22**, 147-152 (1992).
3. Oosterhof G.O.N., Cornel E.B., Smits G.A.H.J., Debruyne F.M.J., and Schalken J.A., "Influence of High Intensity Focused Ultrasound on the Development of Metastases," *Eur. Urol.*, **32**, 91-95 (1997).
4. Gelet A., Chapelon J.Y., Margonari J., Theillère Y., Gorry F., Cathignol D., and Blanc E., "Prostatic Tissue destruction by High Intensity Focused Ultrasound: Experimentation on Canine Prostate," *J. Endourol.*, **7**, 3, 249-253 (1993).
5. Gelet A., Chapelon J.Y., Margonari J., Theillère Y., Gorry F., Souchon R., and Bouvier R., "High Intensity Focused Ultrasound Experimentation on Human Benign Prostatic Hypertrophy,". *Eur. Urol.*, **23** (suppl 1): 44-47, (1993).
6. Gelet A., Chapelon J.Y., Bouvier R., Souchon R., Pangaud C., Abdelrahim A.F., Cathignol D., and Dubernard J.M., "Treatment of Prostate Cancer with Transrectal Focused Ultrasound: Early Clinical Experience," *Eur. Urol.*, **29**, 174-183 (1996).
7. Gelet A., Chapelon J.Y., Bouvier R., Rouvière O., Lasne Y., Lyonnet D., and Dubernard J.M, "Transrectal High Intensity Focused Ultrasound: Minimally Invasive Therapy of Localized Prostate Cancer," *J. Endourol.*, **14**, 6: 519-528 (2000).
8. Gelet A., Chapelon J.Y., Bouvier R., Rouvière O., Lyonnet D., and Dubernard J.M., "Transrectal High Intensity Focused Ultrasound for the Treatment of Localized Prostate Cancer: Factors Influencing the Outcome," *Eur. Urol.*, **40**: 124-129 (2001).
9. Thüroff S., and Chaussy C., "High Intensity Focused Ultrasound: Complications and Adverse Events," *Molecular Urol.*, **4**, 3: 183-187 (2000).
10. Chaussy C., and Thüroff S., "Results and Side Effects of High Intensity Focused Ultrasound in Localized Prostate Cancer," *J. Endourol.*, **15**, 4: 437-440 (2001).
11. Chaussy C., and Thüroff S., "High Intensity Focused Ultrasound in Prostate Cancer: Results after 3 Years," *Molecular Urol.*, **4**, 3: 179-182 (2000).
12. Thüroff S., and Chaussy C., "Therapie des lokalen Prostatakarzinoms mit hoch intensivem fokussiertem Ultraschall (HIFU)," *Urologe (A)*, **40**, 3: 191-194 (2001).
13. Chaussy C., and Thüroff S., "PSA Stability after High Intensity Focused Ultrasound (HIFU) in Prostate Cancer," *J. Urol.*,**167**, 4 suppl.: 347 (2002).

Transrectal High Intensity Focused Ultrasound For The Treatment Of Localized Prostate Cancer

T. Uchida[1], N. T. Sanghvi[2], T. Satoh[1], A. Irie[1],
T. Omata[1], S. Baba[1],
M. O. Koch[3], and T. A. Gardner[3]

[1]*Kitasato University, Sagamihara, Japan*
[2]*Focus Surgery, Inc. Indianapolis, IN 46226*
[3]*Indiana University School of Medicine, Indianapolis, IN 46204*

Abstract. High-intensity focused ultrasound (HIFU) delivers ultrasound energy via a transrectal probe to produce rapid thermal necrosis of prostate tissue in the focal region without damaging the surrounding tissue. Since 1992, we have been treating prostate diseases, both benign and malignant, with HIFU. In this study our main objectives were to evaluate efficacy and safety of the HIFU for the treatment of T1b-2N0M0 stage prostate cancer (PCa). We performed over 100 HIFU treatments in 84 patients with biopsy-proven localized prostate cancer using the Sonablate™ HIFU device. We present data on 49 (62 HIFU sessions) patients who underwent six months follow-up and post-operative biopsy. Demographics of these patients are (mean ± SD): age 71.9 ± 6.9 years, prostate volume 27.6 ± 11.6 ml, PSA 17.74 ± 17.9 ng/ml. Gleason scores: 2-4, 5-7 and 8-9 in 14, 30 and 9 patients respectively. 34, 11 and 1 patient received one, two and three HIFU treatment sessions respectively. A mean operating time was 2 hrs 47 min (55-356 min). All patients were treated under epidural anesthesia. Patients were followed with sextant biopsies and serum PSA. The clinical outcome of 49 patients followed for at least 6 months (mean 16.7 ± 16.4 months) is as follows. Complete Response (CR, defined as negative biopsy and PSA velocity of < 0.75 ng / ml of three successive readings) was observed in 95 %, 80%, 40% and 0% for the patients who had pre-operative PSA level (ng/ml) of less then 10, 20, 30 and higher respectively. PSA results were strongly correlated to the completeness of the HIFU treatment. One earlier patient treated with the Sonablate-200 device developed a rectourethral fistula and 10 patients developed a urethral stricture. Our follow-up would suggest that transrectal HIFU therapy can be used safely to ablate localized prostate cancer with minimal adverse events with a relatively high CR rate and the ability to deliver repeated HIFU treatments without added toxicity. This will allow for repeated HIFU therapy for treatment failures. Additional follow-up continues to confirm the long-term durability of treatment.

INTRODUCTION

Prostate cancer is the leading malignancy in men and the second leading cause of death due to cancer in the United States.[1] In recent years, the rate of prostate cancer in Japanese males is also increasing. The death rate of prostate cancer per 100,000 men in 1985 increased from 4.5 to 11.4 in 1999 in Japan.[2] The Surveillance, Epidemiology and End Results program of the National Cancer Institute (NCI) has shown a 52%

decrease in the rate of distant metastatic prostate cancer between 1990 and 1994.[3] With this change in stage distribution, treatments have also changed. Radical prostatectomy rates increased from 17.4/100,000 in 1988 to 54.6/100,000 in 1992.[3] In Japan also, the success of early prostate cancer detection has resulted in an increased number of candidates for radical prostatectomy.[4] Despite excellent 5- to 10-year survival rates after radical prostatectomy for organ-confined disease, surgery is associated with significant morbidity, such as blood loss with transfusion-related complications, impotence in 30% to 70% of cases, and stress incontinence in up to 10% of patients.[3-6] In addition, surgical intervention is not typically considered for patients whose life expectancy is less than 10 years. Although the immediate complication rate is lower with radiation therapy, impotence, incontinence, radiation proctitis, and cystitis are frequent late sequelae.[7-9] Moreover, it has been shown that over 50% of patients have elevated serum levels of prostate-specific antigen (PSA).[7-9]

Recently, a number of alternative minimally invasive treatments have been developed to treat localized prostate cancer. Brachytherapy, cryosurgical ablation, three-dimensional conformal radiotherapy and laparoscopic radical prostatectomy have been applied, but a definitive cure cannot always be achieved, and generally the treatment cannot be repeated in cases of local recurrence.[10,16] Since 1992, we have examined the effect of high-intensity focused ultrasound (HIFU) for canine prostate and kidney, and have been treating benign prostatic hyperplasia with transrectal HIFU.[17,19] HIFU delivers intense ultrasound energy, with consequent heat destruction of tissue at a specific focal distance from the probe without damage to tissue in the path of the ultrasound beam. It has been clinically demonstrated that HIFU can be used to destroy tissue and cure cancer without stimulating metastasis.[20,21] We report herein our clinical experience treating 100 patients with stage T1b-2N0M0 localized prostate cancer by the Sonablate™ HIFU device.

PATIENTS AND METHODS

HIFU Equipment

For this study, we used both modified second- and third-generation HIFU devices, the Sonablate™-200 and the Sonablate™-500 (**Fig. 1**; Focus Surgery, Inc., Indianapolis, IN, USA). These Sonablate™ are computer-controlled devices intended to provide HIFU treatment for both benign prostatic hyperplasia and localized prostate cancer. A treatment module includes the ultrasound power generator, multiple transrectal probes of different focal depth, the probe holding articulated arm, and an active water cooling system. The transrectal HIFU probes use proprietary transducer technology with low-energy ultrasound (4 MHz) for imaging of the prostate and for the delivery of high-energy ablative pulses (site intensity, 1300-2200 W/cm^2). The single piezoelectric crystal alternates between high-energy ablative (1-4 seconds) and low-energy (6-12 seconds) ultrasound for a total cycle of 7 to 16 seconds.

Before the start of the treatment, the operator uses longitudinal and multi-slices of transverse ultrasound images of the prostate and selects the prostate tissue volume to be ablated by a set of cursors on these images. The probe houses a computer-

controlled positioning system that directs sequence of ablative pulses to the targeted region of the prostate. Each discrete high-energy focused ultrasonic pulse ablates a volume of 3x3x10 mm^3 .[22] The individual focal lesion produces almost instantaneous coagulative necrosis of tissue due to a temperature rise of 80° to 95° C in the focal zone.[22,23] Under computer control, the ultrasound beam is steered mechanically to produce consecutive overlapping lesions laterally and longitudinally to ensure necrosis of the entire targeted prostate volume **(Fig. 2).** An active automatic cooling device is used during treatment to maintain a constant baseline temperature of less than 20°C in the transrectal probe that helps to prevent thermal injury of the rectal mucosa.

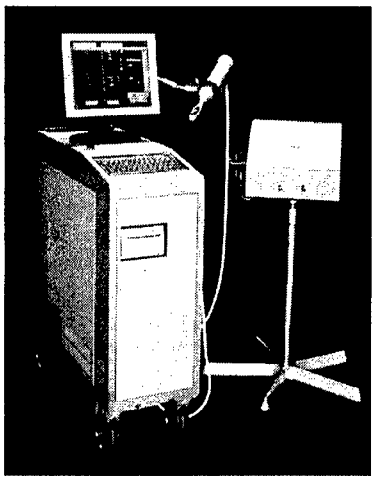

FIGURE 1. The Sonablate™-500 HIFU device with a transrectal probe attached to an articulated arm. The arm is fixed to an operating table and the user adjusts the probe position to optimize both imaging and treatment of the prostate. The active cooling device circulates cold water to keep the rectal temperature at a safe level. The device has both imaging and HIFU capability on the same transducer that ensures absolute coordination of imaging and treatment position to image and monitor tissue changes on each ablative pulse.

HIFU Procedure

Patient preparation included a cleansing enema, and all patients were anesthetized by epidural anesthesia and intravenous sedation. A condom was placed over the probe and degassed water was used to inflate the condom that was covered with ultrasound gel for close coupling of the ultrasound probe to the rectal wall. The patient was placed in the lithotomy position and the probe inserted manually into the rectum. A 16F Foley balloon catheter was inserted into the bladder for identifying the urethra and bladder neck and 100-150 cc saline solution was introduced into the bladder. Probes with focal lengths of 2.5, 3.0, 3.5, 4.0 and 4.5 cm were used according to the size of the prostate as determined by TRUS, with larger glands requiring longer focal lengths. The probe was fixed in position by the articulating arm attached to the operating table and locked in place once imaging of the prostate optimized the position. After selecting the treatment region of the prostate from the verumontanum to the bladder neck, the HIFU treatment was started. The balloon catheter was removed just before the HIFU treatment. The treatment continued layer by layer (10 mm thick) from the apex to the base. Usually, three successive target areas (anterior, mid-part and base) were defined to treat the whole prostate **(Fig. 3)**. The contralateral lobe was then treated using the same procedure. Hyperechoic zones, which correspond to microbubbles induced in the treated area, occasionally, appeared in the targeted area

during the HIFU procedure. When this hyperechoic phenomenon appeared in the targeted area, the power intensity of HIFU was lowered. After disappearance of the hyperechoic phenomenon, power intensity was returned to the normal levels. The thermal effect of transrectal HIFU is extremely precise with a sharp temperature gradient and fall-off characteristics. Therefore, in cases where the cancer is unilateral and preservation of potency is considered mandatory by the patient, the contralateral neurovascular bundle could be excluded from the treatment. After completing treatment, a transurethral balloon catheter, or percutaneous cystostomy using a 16F or 12F Foley balloon catheter was inserted into the bladder.

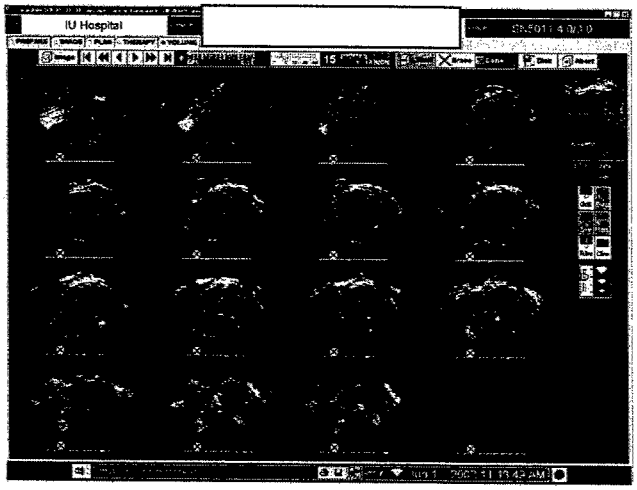

FIGURE 2. The prostate is scanned from the bladder neck to the apex. Each image slice is marked for the treatment using the cursor. The corresponding longitudinal image on the right upper corner shows the extent of treatment in the long axis.

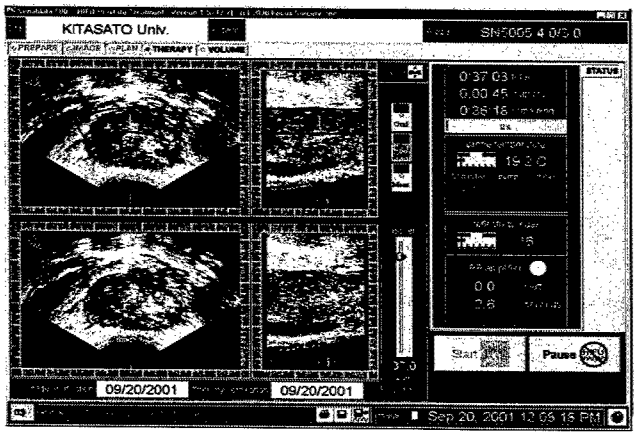

FIGURE 3. In the treatment mode images of the prostate – both pre-treatment (lower panel) and during the treatment (upper panel) – are displayed to observe tissue changes. In addition, temperature and reflectivity index are used for safe operation. The adjustable power level allows the user to decrease and control micro-bubble activity, giving better treatment with increased safety.

PATIENT RECRUITMENT

As per the approved protocol by the local committees, the inclusion criteria for treatment were patients with stage T1b-2N0M0 localized prostate cancer and prostate volumes less than 50 cc. Patients with anal stricture were excluded from the study.

All patients were fully informed of the details of this treatment and provided written consent preoperatively. All patients underwent a digital rectal examination and measurement of serum PSA using an AxSYM PSA assay (Abbott Laboratories, Abbott Park, IL, USA). TRUS, computed tomography (CT) and/or magnetic resonance imaging (MRI) of the pelvic cavity including the prostate were performed to detect evidence of carcinoma and intrapelvic lymph node metastasis. `A chest x-ray, abdominal ultrasound or CT of the liver, and bone scans were performed to detect distant metastasis in all patients. All enrolled patients had negative preoperative metastasis in the lung, liver, bone and intrapelvic lymph nodes. All patients showed evidence of adenocarcinoma by prostate biopsy. The TNM staging system was used for clinical staging.[24]

Follow-Up And Outcome

A total of 49 (62 HIFU treatments) patients with a mean age of 71.9 ± 6.9 years (range, 54-86 years) have been followed over 16.7 months (6-42 months). The mean pre-PSA concentration and prostate volume were 17.74 ± 17.90 ng/mL (range 3.39-89.60 ng/mL) and 27.6 ± 11.6 mL (range 11.4-68.8 mL) respectively. The Gleason sum was 3 to 4 in 14 patients, 5 to 7 in 30 patients, and Gleason sum 8 to 9 in 5 patients.

Patient status and treatment-related complications were followed up by all available means, including periodic patient visits and self-administrated questionnaires dealing with continence and potency. Serum PSA was usually assayed at day 1, 14, 30 and then every 1 to 3 months during follow-up. A randomized sextant control prostatic biopsy was performed at 6 months or when there was any evidence of biochemical failure. Patients with a rising PSA concentration and a negative prostatic biopsy underwent a bone scan and a CT scan to assess for metastatic disease. We defined the complete response (CR) as: No evidence of viable tumor cells by postoperative biopsy, nor three successive elevations of PSA velocity <0.75 ng/year. Based on this definition further data analysis was performed and reported in our results.

RESULTS

The prostate was treated in 1 (n=34 patients), 2 (n=11 patients) or 3 (n=1 patient) HIFU sessions for a total of 62 procedures in 49 patients (1.4 sessions/patient). Reasons for repeat HIFU treatments were: early experiments with On/Off time and large prostate size or partial treatment. The mean operating time was 2 hours 50 minutes (range, 55 minutes to 356 minutes). The mean hospitalization stay and postoperative urinary catheterization time were 6.5 ± 3.5 days (range, 3-20 days) and 9.7 ± 10.7 days (range, 1-55 days), respectively. A gradual reduction in prostate volume occurred in all patients. The gland size decreased from an initial mean volume of 27.6 ± 11.6 cc (range 11.4-68.8 cc) to a final mean volume of 16.1 ± 9.4 cc (range, 4.4-50.3 cc) in average 7.3 (range, 3-23) months interval. The data were analyzed for complete response as a function of pre-treatment level. The results of this analysis are given in Table 1.

TABLE 1. Complete Response Vs Pre-Treatment PSA Range In ng/ml.

Pre-treatment PSA level in ng/ml			
0 – 10 ng/ml	10.1-20 ng/ml	20.1-30 ng/ml	30.1-Higher ng/ml
CR / # Pts.	CR / # Pts.	CR / # Pts.	CR / # Pts.
21 / 22	12 / 15	2 / 5	0 / 7
95%	**80 %**	**40 %**	**0 %**

In addition the data set was subjected to multivariate statistical analysis to define the best correlations to several variables. The best correlation was found between the outcome and pre-treatment PSA. The result of this analysis is given below in Table 2.

TABLE 2. Multivariate Analysis Of Data By Cox Regression Test.

Factor	Hazard Ratio	95% CI	p value
Age	0.976	0.903 – 1.055	0.5425
Stage	0.623	0.279 – 1.392	0.2485
Gleason score	1.716	1.018 – 2.892	0.0428
Neoadjuvant**	1.774	0.333 – 9.435	0.5015
PSA	1.067	1.030 – 1.106	0.0003*

** LH-RH agonist with or without antiandrogen

* PSA has the highest correlation to outcome.

DISCUSSIONS

In 1995, Madersbacher et al. reported the effect of HIFU (using the old Sonablate^{TM}200) in an experimental study of 10 cases of histologically demonstrated, hypoechoic and palpable, localized prostate cancer.[23] In this study, only the focal region of the prostate showing a hypoechoic pattern by TRUS was treated by HIFU. The organs were subsequently removed. In 2 cases, the entire carcinoma had been ablated by the procedure, but in the other 8 cases, a mean of 53% of cancer tissue had been destroyed. However, this study was discontinued primarily as it took 8-9 hours to treat 20 ml volume of the prostate tissue. In January 1999, we began HIFU treatment for localized prostate cancer using a modified Sonablate^{TM}-200 device. Major improvements of our device included: (1) a reduction in HIFU exposure cycle from 16 seconds (4 On/12 Off) to 9 seconds (3 On/6 Off) which reduced treatment time by 40%, and (2) the introduction of a novel transducer and electronics that splits a single ultrasound beam into multiple beams (termed "split beam") to cover a larger tissue volume per exposure. The single beam had a focal region of 2 mm x 2 mm x 10 mm (volume = 40 mm^3) while the split beam focal region is 3 mm x 3 mm x 10 mm (volume = 90 mm^3) that further reduced treatment time about 50%.[15] These developments dramatically shortened the treatment time for a 25 ml prostate gland from 6 hours to 2 hours. Our ideal goal is to be able to treat 1 ml of prostate tissue in 1 minute and finally perform the HIFU treatment in an outpatient clinic under local anesthesia. Like a diagnostic ultrasound phased array, a HIFU array can provide beam steering controlled by electronics in real-time with energy delivery under computer control to make a truly advanced minimally invasive treatment for prostate cancer.

In 1996, Gelet et al. reported a preliminary experience of HIFU using Ablatherm prototype 1.0 (EDAP-Technomed, Lyon, France) for treating localized prostate cancer.[21] They later summarized their clinical outcome in which a complete response was obtained in 56% of the patients with no residual cancer and a PSA less than 4 ng/ml. Biochemical failure (no residual cancer and a PSA greater than 4 ng/ml), biochemical control (residual cancer and a PSA less than 4 ng/ml), and failure (residual cancer and a PSA greater than 4.0 ng/ml) were noted in 6%, 18% and 20% of patients, respectively.[20,22] In 1999, Beerlage et al.[23] reported results of 143 HIFU treatments using the Ablatherm prototype 1.0 and 1.1 in 111 patients with clinical stage T1-3N0M0 prostate cancer, and PSA less than 25 ng/mL. The first 65 treatments in 49 patients were performed selectively (i.e., a unilateral or bilateral treatment in one or two sessions was performed depending on the findings from TRUS and biopsies), and the second 78 treatments in 62 patients that treated the whole prostate. A complete response (defined as a PSA < 4.0 ng/ml and a negative biopsy) was achieved in 60% of the group with whole prostate treatment and in 25% of the selectively treated patients.[23] In our study, one patient who was treated selectively in the right lobe of the prostate for adenocarcinoma identified by a prostate biopsy showed a gradual elevation of PSA as well as viable cancer cells by a postoperative prostate biopsy. A second HIFU treatment was then performed on the whole prostate; the PSA level has remained low and a negative biopsy found. Recently, many imaging analyses have been performed for detecting prostate cancer, including TRUS, CT, endorectal coil MRI and multiple biopsies of the prostate under TRUS. However, prostate cancer is a multi-focal disease and it is not yet possible to determine sites of microscopic focus of cancer cells by imaging analysis alone. Therefore, the whole prostate must be treated, as the results of this HIFU study and other studies corroborate.

The mean hospitalization in our series was 6.5 days. This issue is related to local socio-economics rather than clinical or technical considerations. There is a significant difference in the national insurance systems between Japan and other countries. In Japan, patients older than 70 years of age do not pay for treatments, and only 10-30% of the charges for younger patients are required. Usually, about 30-40 days hospitalization is recommended after a radical prostatectomy in Japan, so the reduction to 6.5 days for the HIFU treatment of localized prostate cancer is a notable improvement. After recently performed HIFU treatments for localized prostate cancer, we were able to release the patient in 3-4 days, and feel that ultimately, an overnight or outpatient stay may be sufficient. One of the most favorable advantages is that HIFU therapy can be repeated in those patients that fail to experience a complete response with the initial treatment or those who may develop a local recurrence. Nine and 1 patients were administered two and three HIFU treatments, respectively, in our series. However, reasons for repeat HIFU treatments were short on or long off interval in 6 patients, large prostate volume in 2 patients, partial treatment of 2 patients, and 1 patient when machine trouble occurred. We have tried a variety of on/off interval times to reduce the total operation time. *Patients who were treated with 3 sec On / 6 sec Off time did not require repeated treatments.*

For many reasons, transrectal HIFU appears highly attractive as a minimally invasive treatment for localized / recurrent prostate cancer. One of the most favorable advantages is that HIFU therapy can be repeated or added even though patients with

local recurrence have already been treated with a radical prostatectomy, cryoablation of the prostate or radiation therapy, including brachytherapy. On the other hand, radical prostatectomy, external beam radiation therapy or brachytherapy cannot be repeated in these patients. A large number of generally younger men who were treated for clinically localized prostate cancer have already had, or are now experiencing, recurrence. If approximately 200,000 patients are diagnosed with prostate cancer per year, of whom two-thirds are treated with surgery or radiation, and up to 40% relapse, up to 50,000 men per year may relapse detected by a PSA increase.[25] Options for these patients include observation, external beam radiotherapy to the prostatic bed and/or hormonal therapy. For radiation cases, the choices are similar except that salvage prostatectomy, cryotherapy and perhaps brachytherapy are options for carefully selected cases. HIFU may be able to treat these patients who diagnosed with local recurrence. The HIFU procedure is very easy and does not require a sterile environment; therefore, it may be possible to perform the HIFU procedure on an outpatient basis.

HIFU treatment is minimally invasive, bloodless (no incision), can be performed on an outpatient basis, has low cost, and avoids systemic side effects. These features, combined with the optional curative effect, provide an ideal treatment for patients with localized prostate cancer. The small number of patients and the relatively short follow-up period in our series limit our ability to draw any definitive conclusions. We believe that the data we present here suggests that HIFU may be a potentially useful treatment option for patients with localized prostate cancer and that it has an acceptable side effect profile to warrant further investigation.

ACKNOWLEDGMENTS

This work was funded in part by the New Energy Development Organization (NEDO), MITI, Tokyo, Japan, and the National Cancer Institute of NIH. Thanks to staff of Focus Surgery, Inc. for their assistance during patient treatment.

REFERENCES

1. Landis, S.H., Murray, T., Bolden, S., et al., "Cancer statistics," *CA Cancer J Clin*, **49**, 8 (1999).
2. Statistics and Information Department, Minister's Secretariat, Ministry of Health and Welfare, Health and Welfare Statistics Association: Statistical Abstract on Health and Welfare in Japan (2000). Tokyo: Health and Welfare Statistics Association, p 55 (2000).
3. Merrill, R.M., and Stephenson, R.A., "Trends in mortality rates in patients with prostate cancer during the era of prostate specific antigen screening," *J Urol*, **16**, 503 (2000).
4. Arai, Y., Egawa, S., Tobisu, K., et al., "Radical retropubic prostatectomy: time trends, morbidity and mortality in Japan," *BJU Int*, **85**, 287 (2000).
5. Han, M., Walsh, P.C., Partin, A.W., et al., "Ability of the 1992-1997 American Joint Committee on Cancer Staging for prostate cancer to predict progression-free survival after radical prostatectomy for stage T2 disease," *J Urol*, **164**, 89 (2000).

6. Amling, C.L., Blute, M.L., Bergstralh, E.J., et al., "Long-term hazard of progression after radical prostatectomy for clinically localized prostate cancer: continued risk of biochemical failure after 5 years," *J Urol*, **164**, 101 (2000).
7. Powell, C.R., Huisman, T.K., Riffenburgh, R.H., et al., "Outcome for surgically staged localized prostate cancer treated by external beam radiation therapy," *J Urol*, **157**, 1754 (1997).
8. Beard, C.J., Lamb, C., Buswell, L., et al., "Radiation-associated morbidity in patients undergoing small-field external beam radiation for prostate cancer," *Int J Radiat Oncol Biol Phys*, 41, 257 (1998).
9. Shipley, W.U., Thames, H.D., Sander, H.M., et al., "Radiation therapy for clinically localized prostate cancer: a multi-institutional pooled analysis," *JAMA*, **281**, 1598 (1999).
10. Vicini, F.A., Kini, V.R., Edmundson, G., et al., "A comprehensive review of prostate cancer brachytherapy: defining an optional technique," *Int J Radiat Oncol Biol Phys*, **44**:, 483 (1999).
11. Sharkey, J., Chovnick, S.D., Behar, R.J., et al., "Outpatient ultrasound-guided palladium 103 brachytherapy for localized adenocarcinoma of the prostate: a preliminary report of 434 patients," *Urology*, **51**, 796 (1998).
12. Ragde, H., Elgamal, A.A., Snow, P.B., et al., "Ten-year disease free survival after transperineal sonography-guided iodine-125 brachytherapy with or without 45-gray external beam irradiation in the treatment of patients with clinically localized, low to high Gleason grade prostate carcinoma," *Cancer*, **83**, 989 (1998).
13. Schmidt, J.D., Doyle, J., Larison, S., "Prostate cryoablation: update 1998," *CA Cancer J Clin*, **48**, 239 (1998).
14. Zelefsky, M.J., Wallner, K.E., Ling, C.C., et al., "Comparison of the 5-year outcome and morbidity of three-dimentional conformal radiotherapy versus transperineal permanent iodine-125 implantation for early stage prostate cancer," *J Clin Oncol*, **17**, 517 (1999).
15. Beerlage, H.P., Thuroff, S., Madersbacher, S., et al., "Current status of minimally invasive treatment options for localized prostate carcinoma," *Eur Urol*, **37**, 2 (2000).
16. Guillonneau, B., Vallancien, G., "Laparoscopic radical prostatectomy: the Montsouris experience," *J Urol*, **163**, 418 (2000).
17. Adachi, K., Ao, T., Uchida, T., "High-intensity focused ultrasound therapy investigated for effect on canine prostate and the efficacy in treating human prostate disease," *Kitastao Med*, **24**, 277 (1994).
18. Igarashi, M., Uchida, T., Ao, T., "Effects of high-intensity focused ultrasound on canine kidney," *Kitasato Med*, **25**, 359 (1995).
19. Uchida, T., Muramoto, M., Kyunou, H., et al., "Clinical outcome of high-intensity focused ultrasound for treating benign prostatic hyperplasia: preliminary report," *Urology*, **52**, 66 (1998).
20. Chapelon, J.Y., Margonari, J., Vernier, F., et al., "In vivo effects of high-intensity ultrasound on prostatic adenocarcinoma Dunning R3327," *Cancer Res*, **52**, 6353 (1992).
21. Oosterhof, G.O., Cornel, E.B., Smith, G.A., et al., "Influence of high-intensity focused ultrasound on the development of metastases," *Eur Urol*, 32, 91 (1997).
22. Wu, J.S.Y., Sanghvi, N.T., Phillips, M.H., et al., "Experimental studies of using of split beam transducer for prostate cancer therapy in comparison to single beam transducer," *IEEE Ultrasonics Symposium Proceedings*, **2**, 1443 (1999).
23. Madersbacher, S., Pedevilla, M., Vingers, L., et al., "Effect of high-intensity focused ultrasound on human prostate cancer in vivo," *Cancer Res*, **55**, 3346 (1995).
24. "International Union Against Cancer," in *TNM classification of malignant tumors, 5th edition*, edited by L.H. Sobin, and C.H, Witterkind, New York: John Wiley and Sons, Inc, 1997, 170–173.
25. Moul, J.W., "Prostate specific antigen only progression of prostate cancer," *J Urol*, **163**, 1632 (2000).

Focused Ultrasound Surgery (FUS): A Non-Invasive Technique For The Thermal Ablation Of Liver Metastases

Mark Allen, Ian Rivens, Andrew Visioli and Gail ter Haar

Joint Department of Physics, Royal Marsden Hospital, Sutton, Surrey, UK

Abstract. There has been great interest in developing minimally invasive techniques for treating liver tumours, but most of these require insertion of needles or probes into the liver, with the risk of seeding tumour along the needle track, as well as requiring anaesthesia and/or sedation. Extra-corporeal focused ultrasound (FUS) avoids these problems and so appears to be ideal for liver tumour ablation.

Three FUS clinical trials are in progress at the Royal Marsden Hospital, UK, using a 15cm focal length curved bowl transducer driven at 1.693 MHz. 52 treatments of liver metastases have been completed. Patients were initially treated at a low in-situ spatial peak intensity to assess tolerability to FUS. This was gradually increased to a value of 1500W/cm^2, and 22 treatments have been given at this level or greater. Patient questionnaires showed 29/52 reports of discomfort during treatment, 15/52 of mild pain, 14/52 of moderate pain and none of severe pain. Histological evidence of tissue damage was seen in 3/6 who proceeded to surgery after FUS. No obvious changes were noted in post-FUS MRI scans in 3/3 patients, although complete resolution of a liver tumour was seen on CT 10 weeks post-FUS in another patient. In 9 patients where a significant proportion of the overall tumour volume could be treated by FUS, reductions in serum tumour marker levels were noted in 6.

FUS is well tolerated, and although there is scope for improvements in technique and equipment, evidence of non-invasive ablation of metastatic liver disease has been seen.

INTRODUCTION

The physiological raison d'être of the hepatic portal venous system is to enable nutrients absorbed from the bowel to be carried directly to the liver for processing before encountering the systemic circulation. When tumours which arise within the bowel (e.g. colorectal cancers) spread to distant organs (metastasize) via the bloodstream, cancer cells usually enter the portal system and deposit within the liver first. Post-mortem studies show that about one-third of patients with metastatic colorectal cancer have secondary tumours within the liver only. For this reason, surgical resection of these liver metastases, where possible and where there is no evidence of tumour spread elsewhere, has become the accepted standard of care. Five-year survival rates from liver surgery are superior to those seen with the use of systemic chemotherapy in this scenario.

The invasiveness of liver surgery, and the fact that a number of cancer patients are not good surgical candidates, has meant there has been a great deal of interest in developing minimally invasive techniques of ablating localized liver tumours. This latter group includes primary hepatocellular carcinomas — a significant health problem in certain parts of the world. Examples of such minimally invasive

therapies include radiofrequency ablation, microwave ablation, laser therapy and percutaneous ethanol injection. The primary requirement of such a technique is that it is effective at causing tumour necrosis, and providing this is the case, an important secondary requirement is to try and make the treatment as convenient to the patient (or 'patient-friendly') as possible. The procedures listed above require insertion of needles or probes into the liver to reach the tumour, which in turn makes necessary the administration of local anaesthetic (at the very least) usually in combination with sedation, and frequently an overnight stay in hospital. By virtue of its non-invasiveness, it has been possible to treat liver tumours in patients with high-intensity focused ultrasound without the need for anaesthesia or sedation, and on an out-patient basis.

Three clinical trials (a phase I and two phase II trials) currently in progress at the Royal Marsden Hospital, UK, are reviewed here. Although patients with a variety of tumour types were eligible for the trials (e.g. prostate cancer, colorectal cancer), treatments of liver metastases only are described here. The principal aim of the phase I trial was to assess the tolerability of FUS treatment. The two phase II trials (histology and radiology) were designed to assess the efficacy of FUS.

PATIENTS AND METHODS

The basic method of treatment was similar in all three trials and is described here. Potentially eligible patients were identified from oncology outpatient clinics, and given information regarding the relevant trial. An initial ultrasound scan was arranged to ensure the tumour to be treated was visible on ultrasound, and that a suitable in-situ spatial-peak intensity (Isp) could be achieved at the tumour site (in practice, this meant the tumour had to lie 4–8 cm from the skin surface, and that there was no intervening bone or gas).

Treatment was given on an outpatient basis, a treatment session usually lasting one morning or one afternoon. A questionnaire asking about pain and discomfort from the tumour to be treated was completed at the start of each session. The tumour to be treated was identified again using a diagnostic transducer and then a waterbag with degassed water was brought into place over the corresponding area of the abdomen, having first applied acoustic gel for coupling purposes. Any trapped air bubbles in the gel were expelled ('debubbling') and the tumour refound with the imaging transducer in the water bag. This transducer was connected to a gantry that had arms in three orthogonal directions, with a graduated scale along each arm. Thus the x, y and z co-ordinates of the volume to be treated could be noted down. When the diagnostic transducer was then replaced with the therapy transducer, the identified volume could be treated. Wherever possible, the transducer was positioned so that it was parallel to the skin and not at an acute angle. Due to the movement of the liver with respiration, its position was noted at end-inspiration and end-expiration, and where the image of the tumour appeared clearer one of these references was chosen to be used as the treatment position. The liver was then observed several times to ensure it returned to the same position on the image screen with each breath. The thickness of the various layers of the abdominal wall and of the liver superficial to the tumour was noted so that attenuation caused by these structures could be taken into account when calculating the appropriate in-situ intensity with which to treat the tumour.

The waterbath-skin interface was debubbled, a pre-treatment scan recorded and the therapy transducer connected to the gantry. The therapy device consisted of a curved bowl transducer with a focal length of 15cm which was driven at its third harmonic of 1.693 MHz. Treatment consisted of brief exposures (1-3 seconds) followed by a 60-second interval (to permit cooling of surrounding tissue). The focus of the transducer was ellipsoid in shape and approximately 20 x 2 x 2mm in size.

After each exposure, the transducer was moved along by 2mm so that an array could be formed. On completion of one array, the transducer was then moved so that an adjacent array could be created and in this way a larger volume of tumour was ablated. The patient was asked if any symptoms (pain or discomfort) had been experienced during the exposure, and these were noted down. If pain was felt, the patient was asked to assign this a score on a scale between 1 and 10. The skin was also checked at regular intervals to ensure no asymptomatic erythema had occurred and that no bubbles were forming within the water bag or acoustic gel.

On completion of treatment, patients were asked to go through the pain questionnaire again noting their overall impression of pain and discomfort. An ultrasound scan was arranged one week after treatment for each patient. Pre- and post-FUS blood samples were taken to measure serum CEA (carcinoembryonic antigen) levels in those patients who had liver metastases from a primary colorectal cancer.

Phase I Trial

Eligible patients had tumours which were no longer responding to standard conventional therapy. They were put into successive cohorts in which both in-situ intensity and exposure duration were gradually increased. It was intended to increase in-situ intensity up to 1500W/cm^2: this value was chosen from in-vivo pre-clinical work as the most reliable to cause coagulative necrosis, and was termed 100% ablative intensity (100% AI). Exposure time started at one second, and went up to three seconds if tolerated by previous cohorts. Treatment cohorts are shown in Table 1.

TABLE 1. Phase I Cohorts.

% Ablative Intensity	Exposure Duration (s)
25	1
50	1
63	1
80	1
100	1
100	2
100	3
125	1
125	2

Data from pre- and post-treatment FUS questionnaires, and from individual pain records after each FUS exposure were collected and analysed.

Phase II Trials

Histology

Eligible patients had liver tumours which were felt to be suitable for resection, and which were in an anatomical position where an ablative intensity of 100% could be achieved. It was also intended that complete FUS ablation of a tumour to be resected would be attempted.

Patients underwent CT (computed tomography) scans within 1 month prior to and 2-3 weeks after FUS, providing the latter fell before the date for surgery. The surgical specimen was examined histologically for evidence of damage caused by FUS, and slides were reviewed by the consultant histopathologist at the Royal Marsden Hospital who specializes in gastro-intestinal cancers.

Radiology

Eligible patients had a liver tumour which could be wholly treated with FUS, but were not suitable for surgical resection. MRI (magnetic resonance imaging) scans of the liver were performed within 2 weeks before FUS and 4-6 weeks after FUS, and examined by a consultant radiologist for evidence of radiological change in the treated region.

RESULTS

Table 2 shows the characteristics of patients with liver tumours treated by FUS. Most had colorectal or breast primaries. Of these 48 patients, 6 were treated in the phase II studies, 40 in the phase I study and 2 patients underwent treatments in both phase I and phase II studies. Two patients were treated twice within the phase I study.

TABLE 2. Patient Characteristics.

No of patients	48
No of treatments	52
(4 patients treated twice)	
Gender (M:F)	22:26
Age, median	62yrs
range	40-79yrs
Tumour type:	
Colorectal	27
Breast	11
Oesophageal	3
Renal cell	2
Melanoma	2
Leiomyosarcoma	2
GI stromal	1

Table 3 shows the number of patients whose tumour it was planned to treat at a specified ablative intensity, and the actual number who underwent treatment at those intensities.

TABLE 3. Planned Vs Actual Intensity.

Intensity	Planned No. Of Patients	Actual No. Of Patients
<60% AI	1	1
60-80% AI	1	6
80-100% AI	4	19
=/>100% AI	42	22

It was occasionally necessary to reduce the intensity level during the course of a patient's treatment if he/she was experiencing pain, hence the discrepancy between the number of patients in whom it was planned to administer an intensity of at least 100% AI and the lower number who actually received that level during treatment. Nevertheless, it should be noted that more than half in whom it was planned to treat at 100% AI were able to tolerate treatment at that level.

Looking at the data from the patient questionnaires, there were 29 reports of discomfort out of 52 treatments, 15/52 reports of mild pain, 14/52 reports of moderate pain and none of severe pain. The issue of pain during treatment, and its possible causes, is dealt with in more detail in Rivens *et al.*, beginning on page 57.

Imaging

It was difficult to identify any significant changes reliably on the routine 1-week post-FUS ultrasound scan, although occasionally changes in echogenecity were noted. In several cases, a bright area was seen in the region exposed to FUS immediately following treatment. This was felt to be due to bubble formation, a theory consistent with the observation that the brightness started to fade as time increased after treatment, and had disappeared by the time of the 1-week post-FUS scan.

MRI scans so far have failed to demonstrate any significant changes post-FUS but a patient in the histology study demonstrated complete resolution of a liver metastasis approximately 10 weeks after treatment. A CT scan just prior to surgery demonstrated two new lung nodules, and so the patient unfortunately did not proceed to surgery. Instead, a course of palliative chemotherapy was recommended. After 8 weeks of treatment, a CT scan showed one liver metastasis to be unchanged in appearance, while the liver metastasis which had undergone FUS was now no longer visible (Figure 1).

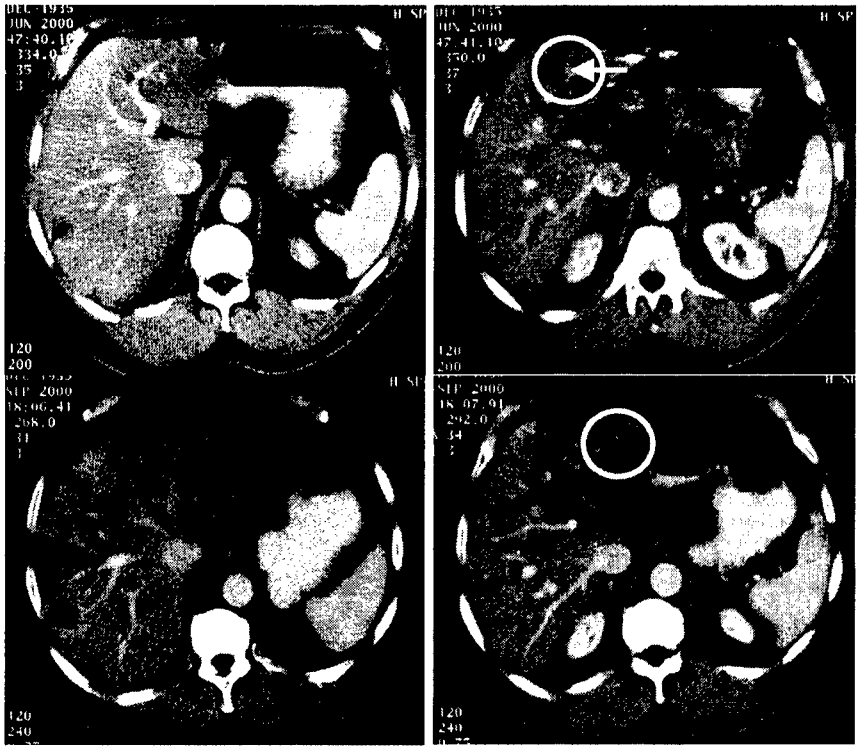

FIGURE 1. CT scans showing resolution of FUS-treated metastasis (right-hand scans; arrow in circle) on bottom scan. Untreated liver metastasis remains stable (left-hand scans)

Histology

Review of the histopathology slides from patients who had undergone liver metastasectomy following FUS with a consultant histopathologist revealed changes to the tumour tissue in 3 out of 6 patients (some patients due to undergo liver resection were treated within the phase I study as the tumour was too large to be treated in its entirety - a requirement for the phase II study). These changes were felt to be cases of non-spontaneous necrosis, caused by FUS. An example is shown in Figure 2.

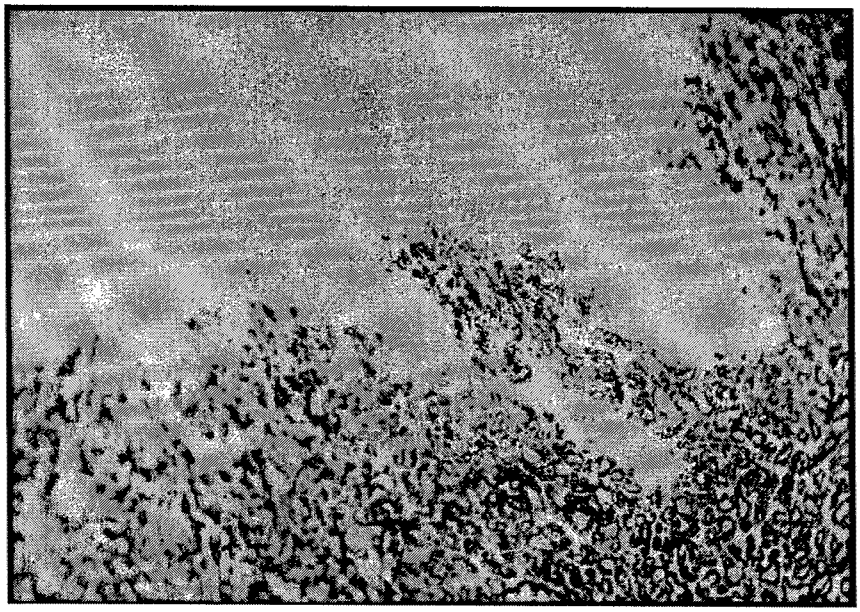

FIGURE 2. Slide showing edge of FUS-induced necrosis of liver metastasis – viable tumour appears bottom right

Tumour Marker Changes

The majority of patients with colorectal cancer will have increased levels of serum carcinoembryonic antigen (CEA). This is a protein secreted by most colorectal cancers, and is used clinically as a marker of tumour activity. Thus, a reduction suggests a reduction in tumour volume, while an increase often reflects an increase in tumour volume. If patients have multiple tumour sites, then there must be an overall reduction in tumour volume to see a fall in CEA level. Occasionally, if a significant volume of the overall tumour burden could be treated with FUS, then a reduction in CEA was noted (Table 4).

TABLE 4. Tumour Marker Changes With FUS.

Tumour Burden	Pre-FUS CEA	Post-FUS CEA
2 liver mets	106	99
Solitary liver met	104	93
Solitary liver met	1536	187
2 liver mets	20	15
Solitary liver met	1829	1783
Solitary liver met	8	10
Solitary liver met	72	67
Solitary liver met	7	8
Liver mets	11	10

DISCUSSION

Data from the phase I trial show that FUS is in general well-tolerated as a thermal ablation technique. The treatment parameters considered necessary to

effect tissue damage (i.e. 100% AI for an exposure duration of 2 seconds) could be achieved successfully in the majority of patients treated. Although more data would be desirable to confirm the efficacy of this FUS system in causing tumour ablation in patients, when examining the radiological, histological and tumour marker data in combination there seems to be sufficient 'proof of principle' that FUS can cause clinical tumour ablation.

An advantage of the method of treatment described here is that there is constant monitoring of side-effects throughout. This means that reductions in intensity can be made if necessary. This is possible because, without sedation or anaesthesia, the patient is able to co-operate throughout the procedure. This could be regarded as a 'safety feature', preventing excess or unwanted tissue damage as the patient informs the operator when pain is felt and appropriate adjustments (e.g. to the intensity setting) can be made. One of the principal advantages of FUS over other localized treatments is its non-invasiveness rather than minimal invasiveness. If the use of anaesthesia becomes necessary, this advantage is lost. The primary requirement of these localized treatments however is that they are effective at causing ablation. If using anaesthesia means that more patients can be treated more effectively, this would seem to take precedence over considerations of non-invasiveness. Nevertheless, ways should be sought of improving treatment effectiveness while maintaining minimal or, if possible, non-invasiveness.

There is scope for improvement in the equipment and techniques described here. A number of patients referred for treatment had to be turned down because of the anatomical position of tumour within the liver, e.g. superiorly behind the ribs with no suitable acoustic window, or too deep to the skin surface so that an ablative intensity could not be achieved within the tumour. More powerful equipment may help and experimental work to assess more accurately the effect of the ribs on the treatment field and intensity may be helpful. The technique of creating arrays of individual lesions is also time-consuming, and the tissue volume ablated per unit time is small. Pre-clinical work is ongoing to see whether creating continuous volumes of damage ('tracks') is feasible, by connecting the transducer to a motor and exposing tissue continuously while the motor moves the transducer across it. As higher intensities are necessary, these treatments may only be possible with the use of anaesthesia.

More general questions are also raised about the best way of assessing the efficacy of new anti-cancer treatments. Radiological imaging has become the standard way of evaluating tumour response to chemotherapy. However, it is conceivable that a treatment may cause tumour damage without producing a significant change in the radiological appearance of the tumour, at least initially. Thus, in these trials the best radiological evidence of FUS effect on tumour was seen some 10 weeks after treatment on CT scan. It is important to decide which form of imaging best demonstrates FUS changes and at what time after treatment it should be performed.

Similar issues arise when considering histological assessment. Changes brought about by FUS were noted in the tumour specimens of 3 of the 6 patients who proceeded to surgery. A possible explanation for the lack of change in the other specimens may be poor targeting, i.e. FUS did not reach the tumour. One disadvantage of this technique is that the tumour to be treated can only be imaged prior to treatment and not during treatment itself. Although efforts were made to ensure patients remained as still as possible while being treated, and that each respiration brought the liver reproducibly to the same point, some small variation

in tumour position was inevitable. Occasionally this may have moved the tumour out of the treatment field. Imaging during treatment (after each exposure) would enable any adjustments in position to be made and avoid this potential downfall. A combined imaging/therapy transducer would seem ideal for this purpose, although real-time CT- or MR-monitoring could be an alternative.

Another explanation for lack of change seen histologically is that cells were killed but did not undergo coagulative necrosis. A phenomenon known as heat fixation may occur, where the tumour cells retain their viable appearance on routine histological examination because they have been instantaneously killed or 'fixed' by high temperatures.

Reductions in colorectal cancer patients' serum CEA levels after FUS provide further evidence of tumour damage caused by FUS. Many of the patients treated, especially in the phase I trial, had very advanced disease and so had large volume metastases at many sites. Treating a small part of the overall tumour burden in these patients would not be expected to produce a reduction in tumour marker levels. Other patients, however, had smaller tumour burdens and in this scenario, a reduction in CEA was often seen. One patient, for example, with two liver metastases, had a CEA of 20 mcg/L (normal <3) pre-treatment and 15 after FUS to one metastasis. It is difficult to explain this reduction other than by a reduction in active tumour volume caused by FUS.

In conclusion, FUS as a non-invasive technique for the thermal ablation of liver metastases is well tolerated, and has also been shown to be effective. Improvements in techniques and equipment should mean that more patients can be treated and with improved efficacy, although these benefits may have to be weighed against the clinically more invasive procedures which they are likely to make necessary.

Tumor Treatment by Interstitial High Intensity Ultrasound

Cyril Lafon*, Dominique Cathignol*, Frédéric Prat•, David Mélo de Lima*, Yves Théillère* and Jean-Yves Chapelon*

** INSERM U556, Lyon, 69003, France*
• Service des Maladies du Foie et de l'Appareil Digestif, CHU Bicêtre, Le Kremlin Bicêtre, 94275, France

Abstract. High Intensity Focused Ultrasound has been proven to be highly effective for the treatment of localized tumors. However certain tumors remain very difficult to reach with an external-to-the-body focused ultrasound applicator. For deep-seated tumors, for example, a miniature applicator following an interstitial route is preferable. The goal of this paper is to present the range of interstitial applicators we developed at INSERM for various applications. The method of treatment consists in positioning the source inside the body in contact to the targeted zone. The sources are rotating plane water-cooled transducers that operate at 5 or 10 MHz depending on the desired therapeutic depth. Specifically, the clinical trials performed on 10 patients for the endoscopic treatment of biliary tumors will be presented. The technique was originally aimed at a palliative treatment for such tumors with a very bad prognosis. But a treated patient was considered to be cured as the bile flow was restored and no trace of cancer was detected 3 and 6 months after ultrasound treatment. For 90% of the patients, negative local biopsies and/or important modifications of the stricture were observed. The success of the treatment appeared to be very dependent on the pre-treatment tumor imaging and localization. These very promising results encouraged us to persevere with this kind of applicator in order to treat other cancers. This work was supported by a grant from the Association pour la Recherche contre le Cancer.

INTRODUCTION

Thermal ablation by high intensity ultrasound is now well accepted as a method for treating localized malignant tumors in a wide variety of applications including neurology, ophthalmology and urology. Most of these applications involve minimally invasive, external and focused transducers designed to intensely heat the focal area while preserving intermediate layers. However, difficulties remain in the treatment by ultrasound of deep-seated volumes. In these cases, an interstitial approach is preferable. The method consists of driving through the body and positioning in contact to the targeted volume a miniature ultrasound applicator. For the last six years, our group at INSERM has developed much experience in this domain, and several applicators were designed and tested clinically for different anatomical sites. The goal of this paper is to present the general features of our applicators. As an example, the pilot study carried out on 10 patients with cholangiocarcinomas of the bile duct is presented.

APPLICATOR FEATURES

The treatment consists in producing rapid heating by delivering high energy to tissues in CW with small transducers. It requires transducers made of a material with low dielectric losses and a good coupling coefficient. Most of our applicators were equipped with Navy III-type plane transducers. The applicators were designed so that the acoustic axis is perpendicular to the applicator axis and the thermal damage extends radially from the applicator surface (Figure 1). Non-divergent plane transducers favor deep heat deposition in comparison to tubular divergent transducers. Using a slightly focused transducer was also envisaged in order to lengthen the therapeutic depth by compensating for the pressure decreases.[1] Thermal ablation with miniature transducers requires higher operating frequencies than HIFU. The goal is to increase absorption and heat deposition as no focusing gain increases the local pressure. The constructed applicators involve transducers operating at frequencies in the range of 5 to 10 MHz. The therapeutic depth is mainly dependent on frequency. Deeper lesions can be obtained by using a lower frequency, provided, of course, that the ultrasound intensity is increased to compensate for lower absorption. The height and width of the lesion are strictly dependent on the transducer dimensions. As the applicator induces collimated lateral damage, rotation around its axis was done to produce cylindrical volumes of coagulation. In most cases, the applicator was rigid and the rotation was transmitted remotely using rigid tubes. But for less accessible applications where the path is not straight, multifilar springs were chosen for the body of the applicator. Specifically for the endoscopic access to the bile ducts, a triplex cable was used: three layers of windings (two clockwise, one anticlockwise) with jointed, stainless steel spirals. Rotation of the external end of this flexible shaft results in rotation of the firing head to an accuracy within 3°. For an application in the esophagus, a cylindrical array was designed to reconstruct a plane wave and rotate it electronically (see Melo de Lima's article beginning on page 364). Our interstitial applicators integrate water cooling of the transducer outer face. The water cooling circuit also ensures acoustic coupling between the transducer and the targeted tissues. Eventually, this cooling favors heat deposition and lesion extent by cooling tissue layers that are in contact with the applicator. An acoustically transparent thin envelope is secured around the active head. Different materials were tested for their mechanical and easy-to-install properties. Latex was selected when a dilatable balloon is desired, and polyethylene for rigid envelopes. Depending on the application and the required water flow, the cooling circuit can be closed or opened.

The treatment must be safe, precise and well controlled. For these objectives, we envisaged a different way of guiding the therapy. An esophageal applicator was designed with a channel where an endo-sonographic probe can slide. Imaging can be done in the esophagus to adjust the position of the therapy transducer with respect to the tumor (Figure 2a). Another esophageal applicator was also constructed to be MRI compatible. Results of compatibility tests are presented in Figure 2b. An advantage of MRI is that this imaging technique offers the possibility to measure the temperature in tissues and observe the thermal damages almost in real time.[2] An additional feature of our applicators designed for endoscopic applications is that the applicator can be driven precisely through the patient's body with a guide wire. For clinical trials, our

applicators are in compliance with all the relevant standards in terms of biocompatibility and electrical security. For example, in some cases we had to cover the applicator body with a biocompatible membrane.

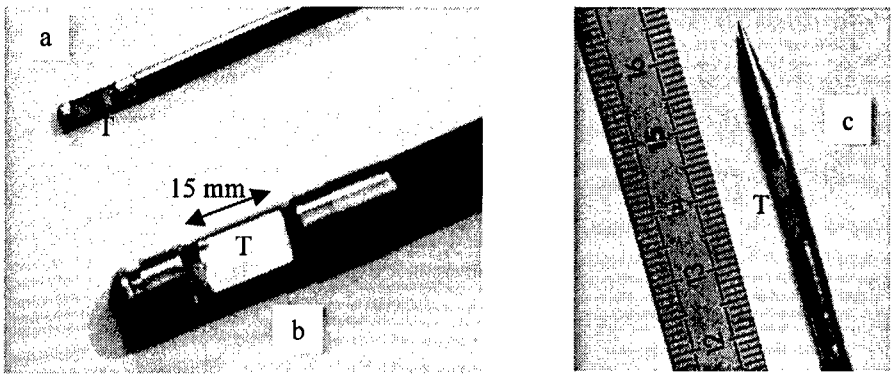

FIGURE 1. Emitting head of applicators for bile duct treatment (a), for esophagus (b), and with a slightly focused transducer (c). The propagation axis of the transducer (T) is radial with respect to the applicator.

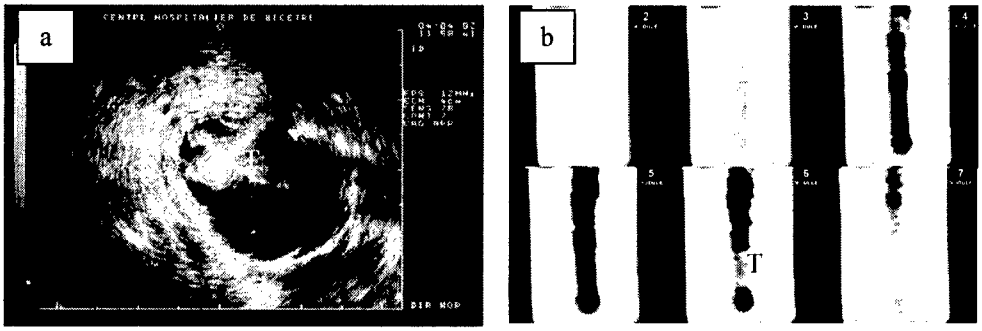

FIGURE 2. (a) Image obtained with an ultrasound miniature probe inserted inside the esophageal applicator in front of the transducer; the esophageal wall and lumen and the therapy transducer (T) can both be seen. (b) Sequence of MR images of a compatible esophageal applicator embedded in agar; the transducer can be easily distinguished (T).

TREATMENT OF BILIARY DUCT TUMORS

To illustrate the description of the interstitial applicators developed at INSERM, the clinical study for the thermal ablation of the cholangiocarcinomas of the bile duct is presented.[3,4]

Patients with cholangiocarcinoma and periampullary carcinoma have a poor prognosis. Despite improvements in surgical management, only a minority can undergo curative resection. Even after radical surgery, long-term survivors are few (5-28% at 5 years in recent series for cholangiocarcinoma). Additionally, these tumors do not respond to chemotherapy and radiotherapy. Most patients are subsequently

candidates for pure palliation, which generally consists in endoscopic or transhepatic biliary stenting to relieve jaundice and pruritus and temporarily improve appetite and comfort. Thermal ablation of these tumors by high intensity ultrasound using an endoscopic minimally invasive approach seems very suitable.

Material and Methods

Criteria for patient inclusion in this study were as follows: presence of a cancer of the ampulla of vater or a cholangiocarcinoma of the common bile duct or the main biliary confluence staged Bismuth's type I or II; positive histologic or cytologic findings; patient considered 1) inoperable for cure on the basis of general condition (age, comorbidities) or tumor extension or 2) patient operable for cure provided the surgical team accepted ultrasound therapy to be performed less than 1 week before surgery; patient classified ASA 3 or less in the American Society of Anaesthesiology's classification and ECOG 0,1 or 2 in the Eastern Cooperative Oncology Group's classification, meaning that the patient had no permanent life-threatening comorbidity and was able to cope with usual daily activities more than 50% of the time; patient's informed consent. Ten patients were included in the pilot study.

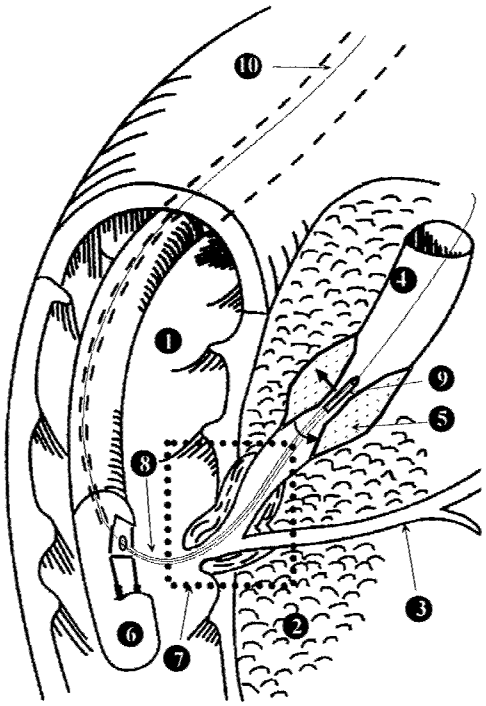

FIGURE 3. 1: The second segment of the duodenum, 2: The head of the pancreas, 3: The pancreatic duct (Wirsung's canal), 4: The common bile duct, 5: Tumoral stenosis of the common bile duct, 6: The Duodenoscope positioned opposite the papilla (side view), 7: The hepatopancreatic ampulla or Oddi's sphincter, 8: The triplex cable, 9: The active part of the interstitial ultrasound applicator, 10: The guidewire.

A customized applicator was constructed for this application. The applicator features include a water-cooled 3 x 8 mm^2 plane transducer operating at 10 MHz, a triplex cable for remote control of the active head rotation and a tube inside the applicator for using a guidewire. The applicator, 3.8 mm OD, fits in the operating channel of an Olympus TJF-20 jumbo fiberduedenoscope (Olympus optical, Tokyo, Japan). An Endoscopic Retrograde Cholangio-Pancreatography (ERCP) session was done under general anesthesia. After removal of the plastic stent (usually in place for palliative reasons), a 0.018'' guidewire was passed through the stricture. Radio opaque contrast agent was injected in the bile duct to evaluate the tumor extent by fluoroscopy. The ultrasound applicator was slid over the wire and positioned under fluoroscopic guidance in the stricture (Figure 3). The intensity was set to 14 W/cm^2. Twenty 10 s-long elementary exposures were performed to treat an entire cylinder around the bile duct lumen. The angular step was set to 18°. If necessary the applicator was moved along the guide wire and several rings of thermal ablation were performed to treat the entire stricture. The applicator was removed when the therapy session was done and a stent was positioned in the stricture. The patients were kept 48 hours after the treatment in the hospital. Follow up sessions were planned 3 and 6 months after ultrasound therapy.

Results

Ten patients have been enrolled in this study. Three patients had an ampullary carcinoma. Control endoscopy after 3 months showed no change in one patient and a regression of the biliary stricture with progression of the tumor in the duodenum in the 2 others.

Three other patients had a cholangiocarcinoma of the common bile duct. Two of the 3 patients had no signs of vascular or lymphatic extension on CT-scan and endosonography and were considered good candidates for surgery. Both underwent ultrasound therapy during the week before operation. In one patient, pre-operative investigations had unerestimated tumor extension, and the tumor was found unresectable at laparotomy. Endoscopic palliation was continued and follow-up showed progression with development of liver metastases. However, on control endoscopy after 3 months, the stricture pattern remained remarkably changed as compared to its initial aspect of neoplastic stricture. In particular, the central portion of the stricture was nibbled, suggesting necrosis in this area while the tumor had progressed at both ends. The second patient operated with cholangiocarcinoma of the common bile duct has been described in a recent case report.[3] The tumor was successfully resected and the pathological analysis revealed circular and homogeneous tumor necrosis up to 10 mm in depth. One session of ultrasound therapy induced complete regression of the stricture at the first control endoscopy of the last patient of the group of three (Figure 4). Bile outflow after stent removal was satisfactory and the patient was discharged without a stent. The common bile duct remained normal at the second endoscopic control 6 months after treatment, with some dysmorphic cells, but no dysplasia on brush cytology. More than 2 years after ultrasound therapy, this patient is still in excellent condition.

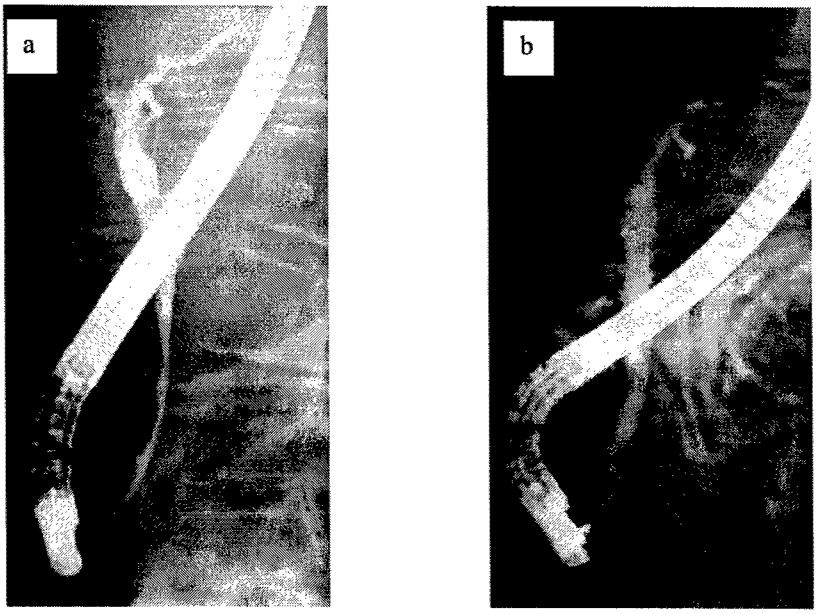

FIGURE 4. Fluoroscopy of the bile duct of one patient before the ultrasound session (a) and 3 months after the treatment (b). The treatment restored the bile flow and no stent was necessary anymore.

Three other patients had a Bismuth's type II Klatskin's tumor (the tumor developed beyond the main biliary confluence). All were considered inoperable as a consequence of local lymphatic extension, age or associated alcoholic and post-hepatitic cirrhosis. In one patient, passage through the stricture failed via the papilla, and a complementary trans-hepatic drainage was required. The ultrasound applicator was therefore introduced by the rendez-vous technique. This patient was the only one in this series to experience abdominal pain during 12 hours post-operatively, probably as a consequence of peritoneal bile leakage. In spite of ultrasound treatment, tumor progression led to the patient's death within 2 months, without control endoscopy being done. Another patient remained in excellent condition during nearly 9 months after ultrasound treatment and presented important changes of the stricture pattern suggesting tumor necrosis at endoscopic controls at 3 and 6 months after treatment. However, distal progression occurred and the stricture was classified Bismuth's type III 6 months after treatment. The third patient with type II stricture is in excellent condition 9 months after ultrasound therapy and control endoscopy at 6 months has shown the persistence of a moderate stricture with no evidence of tumor progression. This patient also underwent 4 courses of chemotherapy associating fluorouracil and cisplatinum.

The last patient had an intra-hepatic cystadenocarcinoma; she had undergone left hepatectomy and presented with tumor recurrence on the remaining lobe 18 months after surgery. She presented recurrent stent obstructions. None of the stents remained patent for more than 4 weeks. Finally, ultrasound therapy was attempted in the intra-hepatic ducts beyond the tip of the stents. After this procedure, jaundice decreased

very slowly, returning to normal values within 4 weeks, but the patient presented no more stent occlusion until her death 5 months after ultrasound therapy.

Discussion

This clinical study showed that using an intra-ductal plane rotating ultrasound transducer is a very suitable approach for the treatment of cholangiocarcinomas of the common bile duct. The treatment was demonstrated to be very precise and effective according to the results obtained on patients operated on a few days after ultrasound application. The complete series is one more step forward in assessing the feasibility and tolerance of the method. The designed applicator worked out very well. The applicator progression through the papilla and inside the bile ducts, and positioning under fluoroscopy guidance were feasible in all cases. The transducer rotation was also easily monitored both endoscopically and fluoroscopically. This treatment requires an additional sedation time of 15 to 45 minutes depending on the extent of tumor to be treated. During this period, the operator's hands are free for treatment monitoring.

The treatment was well tolerated in all but one patient, who experienced transitory abdominal pain that was not clearly related to ultrasound therapy, but rather to a percutaneous drainage. Since the bile duct is stented when the procedure is finished and blood flow in the large surrounding vessels (hepatic artery and mesenteric-portal vein) constitute a natural cooling circuit, the risk of undesirable local damage did not appear to be a matter of major concern. Interesting clinical results have been achieved in this short series, including the permanent remission of a common bile duct carcinoma, allowing for permanent stent removal, and the relatively long-lasting local control of a mucin producing tumor causing repeated stent obstructions. However, weak ultrasound transmission to ampulloma or peri-ampullary carcinoma resulted in insufficient treatment. For two patients, tumor regression was observed for the intra-ductal portion, but the intra-duodenal part of the tumor was not affected. Another limitation in this series was the absence of fine assessment of local tumor extent. Because most cholangiocarcinomas develop longitudinally and intra-ductal tumor extent can be underestimated on the sole basis of ERCP, complementary pre-treatment and control miniprobe endosonography could be helpful. Future studies will have to determine whether this treatment is only a new palliative method, perhaps abolishing the need for stents in some cases, or if it also can be a curative method in selected cases of high-risk patients or locally developed tumors.

CONCLUSIONS

Choosing an interstitial approach for heat deposition is extremely interesting when tumor sites are unattainable by external HIFU. Our original goal was to ablate thermally bile duct cholangiocarcinoma following an endoscopic approach. Our design involved a plane rotating interstitial ultrasound applicator. Very promising results encouraged us to persevere with this kind of applicator in order to treat other cancers. The rotating transducer allows for treating not necessarily the whole

circumference of the organ, but only specific segments of the lumen, which can be of particular interest in some tumor locations such as the esophagus.

ACKNOWLEDGMENTS

This study was supported in part by a grant from ARC (N°4343).

REFERENCES

1. Lafon, C., Melo de Lima, D., Theillère, Y., Prat, F., Chapelon, J.Y. and Cathignol, D., *Medical Physics* **29(3)**, 290-297 (2002).
2. Hynynen, K., Pomeroy, O., Smith, D.N., Huber, P.E., McDannold, N.J., Kettenbach, J., Baum, J., Singer, S. and Jolesz, F.A., *Radiology* **219(1)**, 176-85 (2001).
3. Prat, F., Lafon, C., Theillère, Y., Fritsch, J., Choury, A.D., Lorand, I. and Cathignol, D., *Gastrointestinal Endoscopy* **53 (7)**, 797-800 (2001).
4. Prat, F., Lafon, C., Melo de Lima, D., Théillère, D., Fritsch, J., Pelletier, G., Buffet, C. and Cathignol, D., *submitted to Gastrointestinal Endoscopy* (2002).

High Intensity Focused Ultrasound For Extracorporeal Treatment Of Solid Carcinomas: Four-Year Chinese Clinical Experience

Feng Wu, Zhi-Biao Wang, Wen-Zhi Chen, Jian-Zhong Zou, Jin Bai, Hui Zhu, Ke-Quan Li, Fang-Lin Xie, Cheng-Bing Jin, Hai-Bing Su, Gen-Wu Gao

Clinical Center for Tumor Therapy of 2nd Affiliated Hospital, and Institute of Ultrasonic Engineering in Medicine, Chongqing University of Medical Sciences, Chongqing 400016, China (mfengwu@yahoo.com)

Abstract. The objective of this article is to introduce the early Chinese clinical experience of using extracorporeal high intensity focused ultrasound (HIFU) for the treatment of patients with solid tumors. From December 1997 to October 2001, a total of 1038 patients with solid tumors underwent HIFU ablation in ten Chinese hospitals. The tumors included primary and metastatic liver cancer, malignant bone tumors, breast cancer, soft tissue sarcomas, kidney cancer, pancreatic cancer, abdominal and pelvic malignant tumors, uterine myoma, benign breast tumors, hepatic hemangioma and other solid tumors. In this article, real-time diagnostic US images for targeting, monitoring, and evaluating rapid therapeutic effects during HIFU ablation procedures are presented. Assessments of HIFU treatment by follow-up images, including color Doppler and power US, subtraction angiography (DSA), computed tomography (CT), magnetic resonance (MR), and single photon emission computed tomography (SPECT) are studied. Pathologic changes of tumor cells, vascular vessels, and tumor molecular markers in tumors treated with HIFU are investigated. Early clinical results from various kinds of malignant tumor treatments in our clinical center and complications of the technique are also reported.

INTRODUCTION

Recently, a promising modality for the treatment of localized malignancies, namely the noninvasive, image-guided, *in situ* tumor ablation with focused ultrasound energy, has received increasing interest. Several clinical HIFU projects are underway at various research groups, and significant results indicate that HIFU treatment is safe, effective, and feasible in clinical applications [1 - 6]. In China, the first HIFU treatment was performed on December 10, 1997, on a male patient with tibia osteosarcoma. Up until October 2001, a total of 1038 patients with solid tumors have undergone extracorporeal HIFU ablation, as shown in Table 1. Herein, we review technical development of HIFU, describe some of our own clinical applications in the treatment of human solid tumors with HIFU ablation, and conclude with a discussion of challenges and opportunities for the future.

TABLE 1. Categories of Solid Tumors Treated by HIFU Ablation.

Solid Malignancies	Number of Patients
Primary and Metastatic Liver Cancer	474
Malignant Bone Tumor	153
Breast Cancer	106
Soft Tissue Sarcoma	77
Kidney Cancer	27
Pancreatic Cancer	10
Abdominal Cancer	20
Lung Cancer	4
Others	31
Benign Tumors	
Uterine Myoma	85
Benign Breast Tumor	28
Benign Soft Tissue Tumor	13
Benign Liver Tumor	4
Others	6
Total	1038

HIFU THERAPEUTIC EQUIPMENT

The HIFU system (Model JC Focused Ultrasound Knife) we used in clinical trials is manufactured by Chongqing Haifu (HIFU) Tech Co., Ltd. (Chongqing, China). As described in detail previously [7], it essentially consists of a diagnostic US device, units for computer automatic control, 6-direction movement and therapeutic planning system, an US generator, integrated US therapy transducers, and a degassed water circulation unit. A color Doppler US device is used for real-time imaging of HIFU thermal ablation. The therapeutic US energy is produced by a 12-cm diameter piezoelectric ceramic PZT-4 transducer. The focal lengths used in clinical applications are 90, 130, or 160 cm. The US frequencies used for treatment are 0.8, 1.6 or 3.2 MHz. The focal region is an ellipsoid, which is mapped using a membrane-type hydrophone at focal peak intensities from 200 to 300 Wcm^{-2}. However, the focal region changes little with the different transducers. For example, the focal region is 3.3 mm along the beam axis of and 1.1 mm perpendicular to this axis for the 1.6 MHz transducer with the focal length of 90 mm. In clinical applications, the target tissue is exposed to focal peak intensities from 5,000 to 20,000 Wcm^{-2}, according to the focal depth.

Diagnostic Imaging For HIFU Ablation

Real-time diagnostic US is generally applied for the guidance of ablative procedures because of its extensive availability, real-time visualization capabilities, flexibility, and low cost [8 - 11]. The disadvantages of real-time sonography are occasional poor lesion

detection as a result of a lack of inherent tissue contrast or overlying bone structures such as ribs, and that it is less sensitive than MR imaging in predicting treated-tumor margin. Therefore, in our clinical applications, good-quality MR imaging is an essential imaging examination for determining the number, size of tumor focus, and relationship to surrounding vital structures before HIFU treatment. We observe that this preoperative imaging is helpful in establishing the 3–dimensional co-ordinates of the treated tumor during HIFU procedure and compensate for some of the shortcomings of diagnostic US imaging. In order to establish a HIFU treatment plan (TP) for the complete ablation of a tumor, it is our regular practice to compare the difference between the MR imaging and US imaging before HIFU treatment. Also, during the HIFU procedure, after the TP has been determined, the physicians trained in HIFU ablation compare the real-time US images with the MRI images prior to performing the 3D HIFU conformal treatment.

In order to prevent under- or over-ablation of a lesion, a color Doppler US device is generally used for the guidance of HIFU ablative procedures in our clinical applications. US exposures, comprising line by line scans, and slice by slice scans of focused US beams, induce coagulation necrosis of the targeted tissue. This is frequently seen on the US image. Compared to US imaging before HIFU, obvious differences in tissue gray-scale in the targeted region are immediately detected after HIFU line-ablation. There was a close relationship between the extent of necrosis as measured by gross examination and the hyperechoic extent measured immediately after HIFU on the US image in various pig tissues. In the clinical trial for the treatment of patients with breast cancer, we discovered that this hyperechogenic region in targeted tissue was regular in shape and size, and conformed to the extent of the coagulation necrosis that was induced by HIFU thermal ablation. Therefore, the hyperechogenicity generally seen in the treated areas on real-time US imaging is very helpful in monitoring therapeutic effects, and for controlling the US energy deposition during the ablation procedure. Although the mechanism for tissue gray-scale change in HIFU targeted regions is not clear, US effects on tissue such as heating and cavitation are involved in the formation of coagulation necrosis. In our study we have shown that HIFU can induce circumscribed coagulation necrosis and that gas bubbles mainly arose from the ablated tissue vaporization in the targeted region.

Because postprocedural core biopsy does not provide pathologic results for the whole treated tumor, follow-up with both anatomical and functional imaging techniques, including color and power Doppler US, CT, MRI, DSA, and SPECT, are essential in order to evaluate the short-term efficacy of *in situ* HIFU ablation. These enable evaluation of the effect of HIFU on tumor cells and vasculature, as well as on cellular functions and metabolisms. Among anatomic imaging techniques, MRI can rapidly assess the therapeutic response of a target tumor treated by HIFU thermal ablation 1–4 weeks after HIFU ablation. Altered signals on T2-weighted and T1-weighted images are predictive of coagulation necrosis induced in the targeted tissues. For gadolinium-enhanced images, it is common to observe the absence of contrast enhancement in the treated region and a thin peripheral rim of enhancement surrounding the coagulation necrosis. This often corresponds to an early inflammatory reaction to the thermal ablation. Follow-up at 3 months is necessary to detect residual tumor in untreated regions. Imaging at 6–12 months can show obvious regression of the lesion and the region of induced coagulation necrosis. Most frequently, the nonenhancing treated volume shrinks by less than 20–50% in volume. SPECT is a radionuclide scanning

technique that uses a radioisotope as a tracer to assess abnormal tumor function rather than to provide simple anatomy in the patient with solid malignancies. There is a high extraction rate at the malignant focus in the patients before treatment. After the HIFU ablation no uptake of radioisotope is found in the treated tumor, indicating a positive therapeutic response and an absence of viable tumor.

Pathological Changes Of Carcinoma Treated With HIFU

A total of 48 patients with biopsy-proven breast cancer were randomized into a HIFU-treated group and a control group. For the histopathological study, the 23 patients in the HIFU-treated group underwent initial extracorporeal ablation of their breast cancer with US-guided HIFU 1–2 weeks before modified radical mastectomy. The remaining 25 patients in the control group underwent modified radical mastectomy, without any intervention.

Macroscopic examination indicated that within 1–2 weeks of HIFU treatment, the destroyed area presented clear evidence of cellular destruction with a sharp boundary between the HIFU necrosis and viable tissue. Outside the boundary the tissue was normal. Inside the lesion, the treated tissue appeared completely ablated with pale coagulation necrosis. On the margins of the ablation was a ring of congestion. The boundary between the treated and untreated region was readily visible and the HIFU-induced lesion extent included the breast tumor mass plus a margin of treated normal breast parenchyma about 1.5–2.2cm (mean 1.80±0.58) around the cancer. Microscopic examination showed coagulative necrosis in the treated region with distorted tumor cells, pyknotic nuclei, shrinkage of nuclei, cell debris, and destroyed normal tissue extending 1.5–2.0 cm around the tumor. A clear border between the treated and untreated areas was extremely sharp and comprised only a few cell layers. 7 days after HIFU treatment, a small amount of granulation tissue was visible with the presence of immature fibroblasts, many inflammatory cells, and new capillaries in the boundary region. 10–14 days after the treatment, destroyed tumor cells were disaggregated and had no distinct cytoplasm and nucleus. The boundary area was generally replaced by mature fibrous tissue, while the ultrasound damaged area was only partially absorbed and replaced with new proliferative repair tissue. Also, HE staining showed that small blood vessels less than 2 mm in diameter, (including both arteries and veins) were severely damaged in the treated region of breast cancer. Although not preferentially, this vascular structure displayed cellular discohesion, disruption of the endothelium and tunica media, as well as condensed or non-existed nuclei, indicative of coagulative necrosis. Scattered intravascular thrombi were frequently seen in the destroyed vessels. Elasticity fibrin Victotia and ponceau's histochemical staining revealed that the structure of tumor vessel walls were destroyed, and the vascular elasticity fibrin and collagen fibrin in the treated region collapsed significantly. SP immunohistochemistry staining showed that no ulex-europeus agglutinin-1 (UEA-1) expression at the treated region was observed in the HIFU group, compared to the positive rate of 52.2% in UEA-1 expression in the tumor vascular endothelium of the control group. Furthermore, our studies showed a significant difference between the groups in functions of the cancer cells, including proliferation, invasion, metastasis, and immortalisation. In the control group, the positive rate of

PCNA, CD44v6, MMP-9, C-erbB-2 mRNA expression in the breast cancer cells was 44.0%, 56.0%, 54.6% and 36%, respectively. In the HIFU group, no expression of these molecules in the treated region was observed. In the control group, the telomerase activity of untreated cancer tissue was 1.87 while the telomerase activity was 0.17 at the treated cancer tissue in the HIFU group. The difference was highly significant.

CLINICAL APPLICATIONS

Our first patient was treated with extracorporeal HIFU ablation at the end of 1997, in the second affiliated hospital of Chongqing University of Medical Sciences, China. He was a young patient with femoral osteosarcoma. In October 2001, ten hospitals in Chongqing, Beijing, Chengdu, Guangzhou, Nanjing, Jinan, and Xining joined a clinical study group for HIFU application in China, and 1038 patients with solid tumors have undergone HIFU ablation, as shown in Table 1. Our clinical application can hopefully provide significant data in patients with various stages of solid malignancies. One goal of thermal ablation in patients with early-stage cancer is curative, and HIFU treatment can induce complete necrosis of the targeted tumor. Additional treatments, such as chemotherapy, are essential to patients with breast cancer and osteosarcoma for conservation of the diseased breast or limb. Patients in this group are followed up with diagnostic imaging to detect vital tumor cells within targeted tissue. The goal of HIFU treatment in patients with advanced-stage cancer is palliative, to impede tumor growth and to improve the quality of life. Patients in this second group are frequently those who have unresectable tumors and for whom conventional tumor therapies, including chemotherapy and radiotherapy, has failed to control tumor growth. In our experience, the clinical application of extracorporeal HIFU ablation for solid tumors consists of the following steps: preoperative assessment for each candidate; establishment of the therapeutic plan; anesthesia and medication; HIFU ablation guided by real-time US imaging; and follow-up imaging as discussed in detail above.

HIFU Ablation Of Liver Cancer

A total of 474 patients with liver cancer (including HCC and metastatic liver cancer) have undergone HIFU treatment. Almost all patients had unresectable HCC lesions that were 4–15 cm in diameter. The diagnosis of HCC was determined by means of either US-guided biopsy or, from the combination of diagnostic images which show classic imaging manifestations of this tumor and an abnormal AFP level (> 200 $\mu g\ L^{-1}$). In all patients, routine serum chemistry examination, including electrolytes, liver function, renal function and hematologic evaluation, was performed.

HIFU ablation was performed with the use of extradural or general anesthesia. When a tumor was more than 4.0 cm in diameter or there were multiple tumors, general anesthesia was selected with endotracheal intubation and mechanical ventilation. This had the supplementary benefit of permitting provisional suspension of respiration with controlled pulmonary inflation, as necessary, to ablate the tumor behind the ribs. When a HCC lesion was more than 8.0 cm in diameter, a piece of rib overlying the treated tumor was sometimes resected to provide an "ultrasonic window." In our clinical center we assessed the local therapeutic efficacy of HIFU therapy combined with transcatheter

arterial chemoembolization (TACE) and TACE alone for 50 patients with advanced-stage HCC in a randomized controlled trial. 26 patients underwent TACE alone, and the remaining patients underwent TACE followed within 2–3 weeks by HIFU ablation. The results indicated that the median survival time, 6-month and 12-month survival ratios were significantly higher in the HIFU plus TACE treated patients than in the TACE treated patients ($p<0.01$). 6 patients with resectable HCC underwent surgical removal within 2–3 weeks following only HIFU ablation in our center. Histological examination showed that HIFU induced complete coagulative necrosis of the treated lesion.

HIFU Ablation Of Breast Cancer

A total of 106 patients with biopsy-proven breast cancer have undergone extracorporeal HIFU ablation in China. Of these, 46 patients were treated in our center. For the histological study, a modified radical mastectomy was performed in 24 breast-cancer patients no later than 2 weeks after HIFU treatment. The remaining 22 patients underwent breast conservation treatment with HIFU, in combination with adjuvant chemotherapy, postoperative axillary node dissection or/and postoperative radiation therapy mainly including draining the lymph node region. The HIFU targeted region consisted of the primary focus of breast cancer and a normal tissue margin about 1.5–2.0 cm around the cancer. Preoperative and postoperative clinical assessment included breast color Doppler ultrasonography, histological examination made by US-guided biopsy, CT and/or MR imaging, single photon emission computed tomography (SPECT), and others as required for each case. The mean follow-up time for patients with breast conservation treatment in our center is 22 months (range 10 to 36 months).

Short-term follow-up images, such as SPECT, color Doppler US, and MR imaging revealed a positive therapeutic response when compared to the images before HIFU. Compared to preoperative scintimammography, Tc-99m sestamibi SPECT showed no uptake of radioisotope in the HIFU treated tumor within 1 week after the thermal ablation. This indicates an absence of viable tumor cells. Gadolinium-enhanced MRI revealed an absence of contrast enhancement in the treated region and a thin peripheral rim of enhancement surrounding the coagulation necrosis.

Postoperative US-guided core needle biopsy of the treated tumor was performed in the breast-conserved patients at 1, 3, 6, and 9 months, respectively. Pathologic examination showed that there were significant changes in the center of the treated tumor postoperatively. The treated tumor became coagulated at 1 month, partially fibrotic at 3 months, completely fibrotic at 6 months. However, this fibrous structure vitrified at 9 months. Long term follow-up color and power Doppler US was performed to examine treated tumor regression. This imaging revealed a gradual shrinkage of treated breast cancer with time in all patients. Total resorption of ablated tumor was found in half of them within 1–2 years after HIFU treatment, which mainly correlated with the increase of follow-up time and tumor size. All patients are still alive and disease-free, and only one case presented with local recurrence in the targeted region 18 months after breast conservation treatment with HIFU.

HIFU Treatment Of Human Osteosarcoma

HIFU treatment has been performed in 153 patients with malignant bone tumor, including primary and metastatic malignant neoplasms. In our center we have recently assessed the effectiveness of HIFU ablation in 44 patients with primary malignant bone tumor, for the purpose of conserving the diseased limb, from December 1997 to May 2000. Thirty-four patients in b stage (Enneking classification) underwent HIFU ablation as a noninvasive limb-salvage treatment, in combination with new adjuvant chemotherapy. Ten patients with b stage (9 patients with lung metastasis) were treated with HIFU as a palliative modality. Preoperative and postoperative clinical assessments included serum ALP level, histological examination made by core needle biopsy, CT and /or MR imaging, SPECT, DSA, and others as required for each case. Mean follow-up time was 23 months (range 10 to 39 months).

Short-term follow-up images included anatomical and functional assessment. For evaluating the therapeutic response of thermal ablation, MR imaging was performed as an anatomic examination, and SPECT scanning as a functional examination. When compared to the images before HIFU, MR imaging showed complete coagulation necrosis of treated tumors, including both tumors in bone and in soft tissue. SPECT scanning revealed the complete ablation of tumor after HIFU treatment. DSA indicated that HIFU destroyed the microcirculation, and after HIFU treatment the tumor vascularity disappeared completely. Total survival rate was 85% (38 alive, 6 dead). One case in b stage died of brain metastasis, and 5 patients with lung metastasis in b stage died of lung metastasis after HIFU treatment. Five patients underwent amputation because of local recurrence after HIFU treatment.

HIFU Treatment Of Human Soft Tissue Sarcoma

A total of 77 patients with soft tissue sarcoma (STS) underwent HIFU treatment extracorporeally. Almost all of them were recurrent STS patients following surgery. Among them, 18 patients with recurrent STS were successfully treated with HIFU in our center. Pathological examination showed liposarcoma in 6 cases, synovial sarcoma in 2, fibrosarcoma in 2, malignant peripheral nerve sheath tumor in 2, and other STS. The tumor lesions were 5.5–16 cm in diameter (mean 8.6 cm in diameter). Follow-up time varied from 11 to 39 months (mean 21 months). Contrast-enhanced MR imaging showed the complete ablation of targeted tumor with HIFU. To date, 16 patients with STS are still alive, and 2 cases died of metastasis after HIFU treatment. 3 patients had local recurrence, and then underwent a second HIFU treatment again for the purpose of control.

HIFU Treatment Of Other Human Solid Cancers

A total of 27 patients with advanced renal cell cancer (RCC) have undergone extracorporeal ablation of renal tumor with HIFU. Nine patients (mean age 58 years, range 48 to 76 years) who were diagnosed with advanced RCC were successfully treated with HIFU, including 5 cases with extensive lung metastasis, 3 cases with unresected tumor, and 1 case of synchronous bilateral renal tumor. The RCC lesions were 4–13 cm in diameter. Mean follow-up time was 9 months (range 1 to 22 months). After HIFU

treatment, there was no evidence of postoperative urine extravasation, acute renal failure, tumor bleeding, significant gross hematuria, or urinary obstruction in any case. Follow-up MR imaging showed a positive therapeutic response and gradual shrinkage of the ablated tumor. Both patients with extensive lung metastasis died of cachexia and dyspnea caused by severe lung infection at 1 and 3 months, respectively. The remaining 7 patients are still alive, and more significantly, chest X-ray revealed that the lung metastases seen in the patients preoperatively were stable postoperatively.

Extracorporeal HIFU ablation was successfully performed in 10 patients with unresectable pancreatic cancer. The tumors were 5–8 cm in diameter. The pain was immediately relieved following HIFU treatment. Although the anatomy surrounding the pancreas is very complicated, no local complication was found during or after HIFU treatment.

For the purpose of analgesia, HIFU treatment alone was performed in advanced cancer patients who had severe pain related to their cancer. Most of the patients had been provided with appropriate pain medications, including antineoplastic therapy, and pharmacological approaches preoperatively, but the cancer pain was still not well controlled. The results in our center indicated that HIFU was able to control the pain successfully, without any local complication. After HIFU treatment, severe cancer pain was significantly relieved, and patients' daily activities, quality of life, and psychological status were markedly improved.

COMPLICATIONS OF HIFU ABLATION

Among 1038 patients treated with HIFU, an extremely low major complication rate has been observed. 5–10% patients had low-grade fever up to 38.5° C that persisted for approximately 5–7 days after HIFU ablation. The severity and time of fever seems to be directly related to the amount of destroyed tissue. With large-volume tissue ablations the fever is often observed. Several patients with large HCC had severe fever as high as 39.5° C that lasted for as long as 2–3 weeks. At the present time less than 5% of patients still had HIFU-induced skin burns. Some treated patients (20–30%) experience slight and mild local pain within 1 week after HIFU ablation. But only 5–10% patients were given 3–5 days prescription for oral analgesics. Six of 474 patients with liver cancer had hepatic abscesses within 2–3 weeks of HIFU treatment. Four of 153 patients with malignant bone tumors had local infection within 1–3 months of HIFU treatment. Tumor bleeding or large blood vessel rupture have never been detected following HIFU ablation. Four patients with malignant tumors had bowel perforation because of severe abdominal cohesion induced by previous operations. It caused HIFU mis-targeting, such that the treated region included the tumor and cohesive bowel. Four patients with primary malignant tumor had complete bone fractures in the treated region. Fortunately, 2 of them recovered and new normal bone has grown. Nerve fiber damage has been caused by HIFU in 4 patients with malignant bone tumor. However nerve functions including sensation and motion recovered completely in 2 patients, and the other 2 patients partially recovered function within 1 year after HIFU.

DISCUSSION AND CONCLUSION

Although more than 1000 patients have undergone HIFU treatment in China since 1997, HIFU technology is still in development, and its clinical applications for extracorporeal ablation of solid malignancies are currently in their infancy. Our clinical results are exciting and encouraging, but longer follow-up is necessary to fully determine the true efficacy of this noninvasive therapeutic modality. Much supplementary investigation is necessary to further evaluate the various HIFU treatment plans, the relationship between HIFU dosage and the extent of coagulation necrosis, and factors that can influence focused ultrasound energy deposition, including tissue structure, movement, function and perfusion.

Beyond optimization of technical and physiological parameters, it is obvious that *in situ* HIFU ablation must be performed with exact knowledge of not only the number and location of the lesions but also the biological characteristics and natural history of the tumor being treated. Despite successful destruction of primary lesions, patients with distant metastases in multiple organs are unlikely to be treated with local therapy such as surgical techniques and *in situ* thermal ablation. Therapeutic failure in these patients is mainly because of uncontrolled growth of new and earlier undetected metastases.

The objective of tumor therapy is the complete destruction of all cancer cells within the patient's body. For most individual patients with cancer, the therapeutic plan for disease must be a multiple treatment plan, which includes local and systemic modalities. Combination therapy has been used for some patients who underwent *in situ* HIFU ablation. A similar multi-disciplinary approach including other modalities such as chemotherapy is useful in the treatment of solid malignancies. Therefore, success achieved in the use of *in situ* HIFU ablation is mainly dependent not only on HIFU technique, but also a better understanding of the biological characteristics and natural history of tumors.

ACKNOWLEDGMENTS

This work was supported by the Ministry of Science and Technology of China (grant No. 96-905-02-01), and the National Natural Science Foundation of China (grant No. 39300125, 39630340, 39630340, 39670749, 39770841, 39770712, 30070217, 30171060). We thank the members of national HIFU clinical cooperation group, Dr. Wei Wang at Beijing 307 Hospital, Dr. Guoqiang Zheng at Beijing Tumor Hospital, Dr. Huiyi Ye at Beijing 301 Hospital, Dr. Yongzhong Gui at 4th Affiliated Hospital of West China University of Medical Sciences, Dr. Ming Zhang at Jiangsu Tumor Hospital, Dr. Yongjian Zhou at Guangzhou NO.1 People's Hospital, Dr. Guoliang Xu at Affiliated Tumor Hospital of Zhongshan University of Medical Sciences, Dr. Ming Li at Shandong Tumor Hospital and Dr. Chengwu Zhang at the Affiliated Hospital of Qinghai University of Medical Sciences, for their clinical data in this research. We thank Dr. Gail ter Haar at Royal Marsden Hospital in UK for the help with linguistic revision of the manuscript.

REFERENCES

1. Foster R.S., Bihrle R., Sanghvi N.T., Fry F.J., Donohue J.P., *Eur. Urol.*, **23** (supple. 1), 29–33 (1993).
2. Gelet A., Chapelon J.Y., Margonari J., et al., *Eur. Urol.*, **23** (supple. 1), 44–47 (1993).
3. Hynynen K., Pomeroy O., Smith D.N., et al., *Radiology*, **219**, 176–185 (2001).
4. Vallancien G., Harouni M., Guillonneau B., Veillon B., Bougaran J., *Urology*, **47**, 204–207 (1996).
5. Visioli A.G., Rivens I.H., ter Haar G.R., et al., *Eur. J. Ultrasound*, **9**, 11–18 (1999).
6. Wu F., Chen W.Z., Bai J., et al., *Ultrasound Med. Biol.*, **27**, 1099–1106 (2001).
7. Wu F., Chen W.Z., Bai J., et al., *Ultrasound Med. Biol.*, **28**, 535–542 (2002).
8. Chen L., Rivens I., ter Haar G.R., et al., *Ultrasound Med. Biol.*, **19**, 67–74 (1993).
9. Vallancien G., Chartier-Kastler E., Harouni M., et al., *Semin. Urol.*, **11**, 7–9 (1993).
10. Yang R., Sanghvi N.T., Rescorla F.J., Kopecky K.K., Grosfeld J.L., *Eur. Urol.*, **23** (suppl. 1), 15–22 (1993).
11. Uchida T., Muramoto M., Kyunou H., et al., *Urology*, **52**, 66–71 (1998).

Treatment of Hepatocellular Carcinoma With High-Intensity Focused Ultrasound Combined With Transarterial Oily Chemoembolization: Preliminary Clinical Outcomes

Wang Wei*, Zhou Jieming*, Liu Wenying*, Bai Ling*, Ye Huiyi, Gai Luhua*, Tan Ying*, Yang Tao*

*Clinical Center of Focused Ultrasound Surgery, Affiliated Hospital, Academy of Military Medical Sciences, Beijing 100850, China
Department of Radiology, PLA General Hospital, Beijing, China

Abstract. Objective: To evaluate the effect of transarterial oily chemoembolization (TOCE) combined extracorporeal high-intensity focused ultrasound (HIFU) ablation for treatment of unresectable hepatocellular carcinoma (HCC). Methods: By using Model JC Focused Ultrasound Therapeutic System, 26 unresectable HCC patients were treated by HIFU ablation. One to 4 weeks before HIFU treatment, the patients underwent TOCE. Serum AFP, MRI and survival rate were assessed to evaluate the efficacy of HIFU. Results: A total of 52 HIFU sessions were performed during the follow-up periods (median: 14.2 months, range 6-30 months) for the 26 patients. The elevated AFP levels decreased more than 50% at 1-2-months after HIFU ablation in 87.5% of patients. MR imaging showed that HIFU induced coagulation necrosis at ablated areas in all 26 patients and more extensive and homogeneous necrosis than TOCE induced. Through one or several courses of the combined therapy, compete ablation was achieved in 17 (65.4%) of the 26 patients. Overall survival was 96.2% (25/26), 88.9% (16/18), and 81.8% (9/11) at 6, 12, and 18 months, respectively. Conclusions: The initial outcomes showed that HIFU ablation combined with TOCE on unresectable HCC treatment may increase the possibility of inducing a complete necrosis and may improve long-term survival.

INTRODUCTION

Hepatocellular carcinoma (HCC) is one of the most common cancers in China. Surgical resection represents the only potentially curative therapy. In China, about 80~90% of HCCs are associated with liver cirrhosis. Advanced or decompensated liver cirrhosis and multicentricity make 80~85% of HCCs inoperable at the time of diagnosis. For treating most unresectable HCC patients, transarterial oily chemoembolization (TOCE) has been widely performed [1]. However, histopathologic studies of resected HCC after TOCE have shown a very low complete necrosis occurrence. Despite successful TOCE, the tumor frequently recurs. The survival benefits of TOCE treatment for HCCs has been doubted [2-4].

A newly developed high-intensity focused ultrasound (HIFU) extracorporeal tumor therapeutic system has been authorized to ablate malignant solid tumors in clinical practice in China since April 1999. This system can produce 3-dimensional conformal

tumor ablation and is guided by real-time ultrasonography. Coagulative necrosis has been shown in the resected HCC after ablation by the extracorporeal HIFU device [5]. An experimental study has also shown that iodized oil enhances the thermal effect of HIFU on ablating liver cancer [6]. Hence, we introduced a combination therapy, consisting of iodized oily TACE followed by extracorporeal HIFU ablation, for unresectable HCCs. Dynamic magnetic resonance imaging (MRI) was used to evaluate tumor necrosis treated by this combination therapy. The effect of the combination therapy on survival rates was also studied. This report summarizes the preliminary outcomes.

MATERIALS AND METHODS

Patient Characteristics

Between January 2000 and December 2001, 26 patients with unresectable HCC lesions who were eligible for this study were treated at the affiliated hospital, AMMS. The diagnosis of the neoplasm is ensured by ultrasound guided core needle biopsy and /or by increased alpha-fetoprotein (AFP) levels. The criteria for entry into this study were as follows: 1) HCC lesions were not suitable for surgical resection; 2) HCC lesions were not diffused; 3) the lesions were detectable by ultrasound and could be scanned completely by the HIFU focus; 4) no evidence was found of main portal trunk thrombosis, hepatic vein thrombosis and extrahepatic metastasis by routine imaging techniques (color Doppler ultrasonography, computed tomography and chest x-ray). Those eligible HCC patients who had previously received TOCE treatment could be enrolled into the study. Exclusion criteria were uncontrolled liver disease decompensation (gastrointestinal bleeding, bacterial infection, Child-Pugh's score: C) and /or presence of contraindications to a peripheral artery catheterization. The Investigation and Ethics Committee of the hospital approved this study. Informed consent was obtained from all patients or their relatives.

The entry patients were 26 men and no women, ranging in age from 36 to 78 years (median 58 years). Of the patients, 11 had a solitary lesion, 9 had 2, 6 had 3 or more lesions, 2 had image-verified portal thrombosis in a major branch, 24 had histologically or clinically diagnosed cirrhosis. The mean largest dimensions of lesions were 6.4±2.6 cm (range 3-12 cm). In seventeen (65.4%) patients, the largest dimension of lesion was > 5 cm. The locations of these lesions were in the left lobe in 3 patients, in the right lobe in 16 patients, and in both lobes in 7 patients. According to the HCC TNM stages, there were 8 in II, 9 in III and 9 in IVA. The classifications of liver functions were 18 in Child-Pugh's A, 8 in B. Nineteen patients had an elevated baseline AFP. These patients did not undergo surgical resection because of 1) advanced cirrhosis and/or the location of the lesion (n = 22), 2) coexisting disease (n = 2), or 3) advanced age (n = 2).

Therapeutic Procedures

We performed TOCE by selectively introducing a catheter into the right or left hepatic artery or a segmental branch artery feeding the lesion(s). A solution of doxorubicin (20mg/M^2) was first infused into the artery, then an iodized oil (lipiodol 10~30 ml)/mitomycin (10mg/M^2) mixture was injected into the feeding artery and completed the embolization.

One week after TOCE, for those patients whose lesion(s) were located at the right lobe, a special costectomy was performed to create an acoustic window for ensuring complete HIFU ablation. Usually part of the adjacent 2 or 3 ribs at the right hypochondriac region were resected 8 cm to 12 cm in length. In this study, 21 patients underwent the costectomy.

The HIFU treatment was started at 1 to 4 weeks after TOCE or at 2 weeks after the costectomy. The sonography-guided HIFU extracorporeal tumor therapeutic system (JC Type, Chongqing Haifu Co. Ltd., Chongqing, China) used a 12-cm diameter piezoelectric ceramic transducer and produced a 0.8 MHz frequency ultrasound beam, which was focused using a lens with a focal length of 120 to 160 mm. The focal spatial peak intensities (Isp) of the acoustic field were from 5000 to 20000 W/cm^2 (mapped by a calibrated polyvinylidene difluoride membrane hydrophone with a spot diameter of 0.5 mm). The focal region was ellipsoid in shape, with dimensions less than 10.8 mm along the beam axis and 3.0 mm in the transverse.

Patients received HIFU ablation under epidural anesthesia. Real-time, two-dimensional ultrasonography using a 3.5-MHz diagnostic transducer coaxial with the therapeutic transducer was used to guide the location of the focal region and monitor the ablation procedure. The abdomen of the patient, oriented in a prone or side position, and the therapeutic transducer were submerged in a bath of degassed water. The 3-dimensional movement of the focused transducer was controlled to position the focus in the target volume. The ablation procedure was to sonicate the tumor in multiple parallel cross-slices at 5-10 mm intervals. In each slice, the transducer was moved (speed 3 mm/s) laterally while continuous ultrasound pulse exposure was maintained. This produced a strip-like area caused by the moving focus (i.e. a line scan). The acoustic power outputs of the transducer were between 120 to 220 W. After echo enhancement in the scan area was displayed on the monitoring ultrasonogram, axial movement of the transducer was controlled in depth from deep to shallow. Then another line scan was made. After each focal slice was completely treated, the transducer was moved to next focal slice until the whole target volume was sonicated. The target volume included the tumor and a visible margin of healthy tissue of about 1.0 to 1.5 cm if possible.

Evaluation and Follow-up

For evaluation, static and dynamic gadolinium-enhanced magnetic resonance (MR) imaging was performed 1-4 weeks before and after HIFU ablation. A decreased signal on T2-weighted images in the ablated areas was considered a marker for induced coagulation necrosis [7,8]. The hypointense and unenhanced areas on the gadolinium-enhanced T1-weighted image represented necroses. The enhanced areas in the ablated

target volume represented a residual tumor. Complete HIFU ablation was defined as a lack of residual tumor in the targeted volume in the MR images. In cases in which a residual tumor was identified, another course of combination treatment was performed. If the initial evaluation was satisfied, the patient was seen on an outpatient basis every 3 months. The enhanced MR imaging was also used for long-term follow-up at 3-6 month intervals. For those patients with elevated AFP, serum AFP levels were assessed periodically to evaluate the treatment efficacy. If a recurrence was detected through imaging, HIFU or TOCE combined with HIFU was repeated. Patients were evaluated to determine whether they had a recurrence of a treated lesion (local recurrence) or had developed new lesions. Survival was measured from the date of the first HIFU treatment until death.

RESULTS

As of 30 June 2002, a total of 52 HIFU ablation treatments have been performed with follow-up (median: 14.2 months, range 6-30 months) for 26 patients. Eight patients received a single course of combination treatment, 13 patients received 2 courses, and 5 patients underwent 3 to 5 courses.

Elevated AFP levels were decreased more than 50% according to the baseline level in 17 (89.5%) of 19 patients and became normal in 9 patients at 1-2 months after HIFU ablation.

Enhanced MR imaging obtained before HIFU ablation often showed that the necrosis of TACE treated lesion was not complete. From MR imaging performed 1-3 months after HIFU treatment, a decreased signal on T2-weighted images was found in HIFU ablated areas in all 26 patients, which indicated coagulation necrosis had been induced (Fig.1). The enhanced T1-weighted imaging showed more extensive and homogeneous necrosis in the HIFU ablated areas than those taken prior to HIFU ablation (Fig.2). Surrounding the necrotic area a thin peripheral rim of contrast enhancement corresponded to an early inflammatory response to treatment. A bulky irregular rim at the edge of the treatment site was the most common appearance of an incompletely treated lesion. Through one or several courses of combination therapy, complete ablation was achieved in 17 (65.4%) of 26 patients, including the 2 patients with portal branch thrombosis. At long-term MR imaging follow-up, the completely ablated lesions showed a continuing absence of gadolinium enhancement and regression in different volumes. Local tumor recurrence in the ablated areas was found in 3 (11.5%) patients and new lesions in untreated areas were found in 9 (34.6%) patients. Distant metastases were found in 3 patients (pulmonary or lymph node).

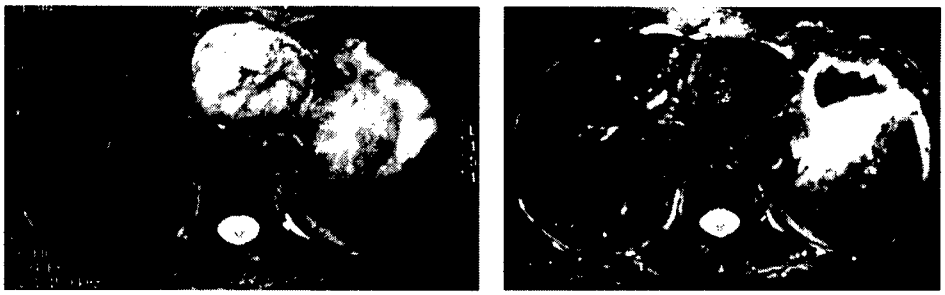

(A) (B)

FIGURE 1. Signal changes on T2-weighted fat-suppressed MR image. 65-year-old-man with biopsy-verified solitary hepatocellular carcinoma and coexisting chronic renal failure undergoing HIFU ablation after TOCE. **(A)** 2 weeks after TOCE and 4 days before HIFU ablation, T2-weighted image shows the lesion as heterogeneous and of high signal intensity. **(B)** 6 weeks after HIFU ablation, T2-weighted image shows markedly decreased signal intensity in the ablated area and the lesion as relatively homogeneous.

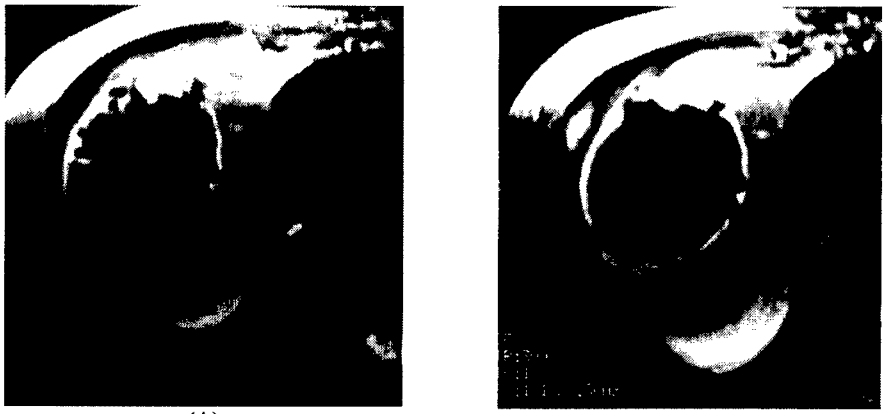

(A) (B)

FIGURE 2. HIFU induced signal changes on gadolinium-enhanced T1-weighted fat-suppressed MR image. 38-year-old-man with a larger solitary hepatocellular carcinoma undergoing HIFU ablation after 2 TOCE treatments. **(A)** 4 weeks after TOCE and 1 week before HIFU ablation, late phase enhanced T1-weighted image shows the lesion as heterogeneous hypointense with irregular enhancing in the central and peripheral area. **(B)** 1 week after HIFU ablation, late phase enhanced T1-weighted image shows lesion as homogeneous hypointense and unenhanced area, no evidence of central enhancement. A thin peripheral rim of contrast enhancement is identified and corresponds to an early inflammatory response to ablation.

As of June 2002, 6 of the 26 treated patients (23.1%) have died. Among them, cancer was the cause of death in 4 patients (66.7%), and 2 patients died of hepatic failure. Survival time of the deceased patients was 5 to 25 months (mean 15.9 months) after HIFU treatment. A total of 26, 18 and 11 patients were observed for a follow-up period of 6, 12 and 18 months, respectively, after HIFU treatment. The survival rates were 96.2% (25/26), 88.9%, and 81.8% at 6, 12, and 18 months, respectively.

The main complications were the 2 - 3 degree skin burns in the acoustic window area, which occurred in 5 patients. No other serious complications were encountered during the HIFU treatment procedure and late follow-up period.

DISCUSSION

TOCE treatment has been widely used for patients with unresectable HCC. However, it is difficult to induce a complete tumor necrosis by this ischemia method. It is believed that the double-blood supply system for the liver is the major cause. Another reason is the toxicity of chemical drugs to the hepatocyte, especially for those patients with cirrhosis. Some of local thermal ablation therapies, such as radiofrequency (RF) and microwave, have received much recent attention for the treatment of focal liver malignancy. But use of these methods often depends on lesion size and shape. Usually, the largest dimension of the lesion should be less than 5 cm. Extracorporeal HIFU treatment provides a possible conformal ablation method for liver cancer. This allows ablation of HCC lesions independent of lesion size, shape and location. This advantage makes HIFU ablation a potentially effective treatment for larger and unresectable HCC lesions.

We introduced the current combination therapy under these hypotheses: 1) Occlusion of the feeding artery of the tumor by TOCE may decrease the undesired loss of HIFU heat energy. 2) TOCE-deposited iodized oil may increase the acoustic impedance of the tissue as well as enhance conversion of HIFU sound energy into thermal energy. 3) TOCE-induced ischemic changes may markedly shorten the time needed for HIFU ablation to produce coagulation necrosis. 4) Combination therapy may lead to a higher rate of complete "thermal resection" for these unresectable patients.

This theory is supported by our initial clinical results. From the MR imaging performed before and after HIFU ablation, a definitive coagulation has been shown and more complete necrosis has been achieved. The low rate of recurrence of the ablated lesions during the follow-up period also supports this hypothesis.

Because the sample is small and the follow-up duration is short, we need to enroll more patients and follow up for a longer period to confirm the hypotheses. Also, the combination procedure and HIFU ablation program is far from perfect. A randomized, multicenter, controlled trial including a larger number of patients is needed to evaluate the effects of HIFU treatment on HCC.

In conclusion, these preliminary clinical outcomes show that extracorporeal HIFU ablation combined with TOCE on unresectable HCC lesions may increase the possibility of inducing a complete tumor necrosis, and that it has a tendency to reduce the tumor recurrence rate and may improve long-term survival for these high-risk patients. Long-term studies assessing clinical outcomes are needed and ongoing. We anticipate further technologic and therapeutic advances to allow more effective HIFU treatment.

ACKNOWLEDGMENTS

We thank Professors Chen Wenzhi, Wu Feng and Wang Zhibiao, who come from Chongqing Medical University, for their technical support and instruction during our HIFU studies.

REFERENCES

1. Takayasu, K., Shima, Y., Muramatsu, Y., et al., "Hepatocellular carcinoma: treatment with intraarterial iodized oil with and without chemotherapeutic agents," *Radiology*; **163**, 345-51 (1987).
2. Bruix J., Llovet J.M., Castells A., et al., "Transarterial embolization versus symptomatic treatment in patients with advanced hepatocellular carcinoma: results of a randomized, controlled trial in a single institution," *Hepatology*; **27** (6), 1578-1583 (1998).
3. Pelletier, G., Ducreux, M., Gay, F., et al., "Treatment of unresectable hepatocellular carcinoma with lipiodol chemoembolization: a multicenter randomized trial," *J Hepatol*, **29** (1), 129-34 (1998).
4. Group d'Etude et de Traitement de Carcinome Hepatocellulaire, "A comparison of lipiodol chemoembolization and conservative treatment for unresectable hepatocellular carcinoma," *N Engl J Med*; **332**, 1256-1261 (1995).
5. Wu, F., Chen, W.Z., Bai, J., et al., "Pathological changes in human malignant carcinoma treated with high-intensity focused ultrasound," *Ultrasound Med Biol*, **27** (8), 1099-106 (2001).
6. Cheng, S.Q., Zhou, X.D., Tang, Z.Y., et al., "Iodized oil enhances the thermal effect of high-intensity focused ultrasound on ablating experimental liver cancer," *J Cancer Res Clin Oncol*; **123** (11-12), 639-44 (1997).
7. Boaz, T.L., Lewin, J.S., Chung, Y.C., "MR monitoring of MR-guided rediofrequency thermal ablation of normal liver in an animal model," *J Magn Reson Imaging*; **8**, 64-69 (1998).
8. Mueller-Lisse, U.G., Thoma, M., Faber, S., et al., "Coagulative interstitial laser-induced thermotherapy of benign prostatic hyperplasia: online imaging with a T2-weighted fast spin-echo MR sequence: experience in six patients," *Radiology*; **210**, 373-379 (1999).

The Noninvasive Treatment Of 251 Cases Of Advanced Pancreatic Cancer With FUS

He Shen Xu[1], Wang Guo Min[2], Niu Shu Gai[3], Yao Bo[4], Wang Xiao Jie[5]

[1]*Applied Research Institute of Lithotrity, Peking University, China*
[2]*Zhong Shan Hospital, Fudan University, China*
[3]*The First Hospital of Shanxi Medical University, China*
[4]*The Central Railway System Hospital of Liuzhou, China*
[5]*Oncosis Hospital, Liaoning Province, China*

Abstract. To evaluate the efficacy and safety of focused ultrasound surgery (FUS) for the treatment of pancreatic cancer. Two hundred fifty-one cases of advanced pancreatic cancer were treated by FEP-BY series equipment in 25 hospitals (including People's Hospital of Peking University) in China. The results show: 54 (21.5%) cases exhibited a remarkable effect, and 161 cases (64%) exhibited a general effect. Survival time of bearing tumor is 12.5 months post treatment by FUS. No complications, such as skin burn, gastrointestinal perforation and pancreatic fistula were observed. We consider FUS to be a new and local method for noninvasive, safe and efficacious treatment of pancreatic cancer.

MATERIALS AND METHODS

Patient Characteristics

Two hundred fifty-one patients from 25 Chinese hospitals were included in the study. Patients age ranged from 39 to 82 years old, with an average of 59. There were 147 men and 104 women in the group. The diameters of the tumors were 3 to 12 cm. TNM grading was: II grade, 18 cases (7%); III grade, 85 cases (34%); IV grade, 148 cases (59%). Of these, 18.7% patients had concurrent jaundice and 68% of patients had concurrent pain. The location of the cancer was as follows: head, 183 cases; body, 53 cases; tail, 14 cases. The tumors were confirmed by CT scan in all patients. The clinical diagnosis for pancreatic cancer was made by more than two hospitals. Patients presenting concurrent jaundice were corrected by surgery. The anticipatory survival times were all more than one month.

Equipment

All patients were treated with FEP-BY0I or 0II type machine (which were development by People's Hospital of Peking University). See Fig 1.

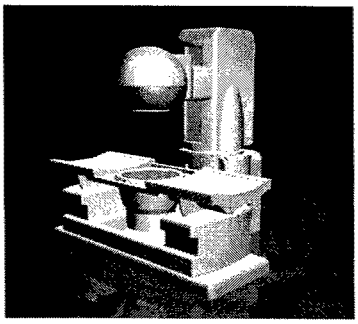

FIGURE 0. FEP-BY0II type machine.

Pre-Treatment Preparation

Patients must have gastrointestinal tract preparation before treatment. The method consisted of fasting on the treatment day, following a low fiber diet before treatment day, and taking Chinese herbs to relieve constipation and evacuate the stomach contents, drinking degassed water if too much gas is found in the stomach by B-mode ultrasound examination.

Selection Of Therapeutic Parameters

1. Selecting the focal intensity (as measured in water) depending on the depth of the target to be treated; the range is 1150 ~ 1500 W/cm^2.
2. Selecting the emission unit depending on the color Doppler arterial flow velocity; the range is 0.12~0.24 s.
3. Selecting the interval period depending on the mean value of B-Mode ultrasound histogram; the range is 0.12~0.24 s.
4. Selecting the unit count depending on the killing time and treatment area; the range is 50~80 times/min.

Selection Standard Of Cases

1. Anomalous mass in the pancreas area as verified by CT.
2. Specific pathological diagnosis or clinical diagnosis by more than two hospitals.
3. No metastases detected in brain, bone and lung.
4. Jaundice has been corrected by surgery.
5. Anticipatory survival time > one month.

Treatment Posture

Prone position on FEP-BY0I. Dorsal position on FEP-BY0II.

Evaluating The Curative Effect

1. To evaluate the long-term effect to a five-year survival time.
2. To evaluate cancer cell metabolic rate with PET post-treatment independence. This is difficult to perform in some patients.
3. To develop a comprehensive evaluation based on the following:
   (1) Evaluating the short-term effect in terms of a reduction of the color Doppler arterial velocity (CDAV): a remarkable effect was defined as a CDAV drop of more than 80% (or disappeared) post treatment; a general effect was defined as a CDAV drop of 50%~80%; no effect was defined as a CDAV drop of < 50%.
   (2) Evaluating the short-term effect by monitoring the rise in the M value of a B-Mode ultrasound histogram (M value): remarkable was defined as an

M value increase of 100%; a general effect was defined as an M value increase > 50%; no effect was defined as an unchanged M value.

(3) Evaluating the short-term effect in terms of the decreasing tumor marker Ca19-9: remarkable was defined as a reduction from high level pretreatment to normal; a general effect was defined as a 20%~50% decrease from pretreatment level; no effect was defined as no change.

(4) Evaluating effect by cytomorphology examination. Puncture biopsy and autopsy were performed to determine the amount of cancer cell death. Typane staining was used to judge the death rate.

(5) Evaluating the effect in terms of increasing quality of life scores. We sum up quality of life in terms of five factors: weight and appetite, activity level, ability to live independently, psychosis, and pain relief. We evaluated every factor and assigned individual scores for averaging: for example we used NRS grading, which consisted of four grades: stage 0 – no pain; stage I – need to take analgesic; stage II – need to inject dolantin; stage III – need to inject morphine. Thus a remarkable effect consisted of pain decreased by more than two grades; a general effect consisted of pain decreased by one grade; no effect was defined as no change in pain. The averaged result was defined as: remarkable – 2.5~3; general – 2.0~2.5; no result - < 2.

RESULTS

Treatment Effect

Nineteen patients in the group received a post-treatment PET examination. In seventeen cases, no cancer foci was found; in 2 cases, a residual foci was found and treatment repeated.

Twenty-one patients received a post-treatment puncture biopsy. Analyses showed denucleus necrosis in most specimens. One patient received an autopsy upon death, 23 months after FUS treatment.

FUS treatment can relieve the pain that accompanies pancreatic cancer.

Sixty-three patients showed changes in color Doppler arterial velocity.

TABLE 1. Statistics Of CDAV Contrast In 63 Patients.

Effect	Cases	Rate
Remarkable Effect (decreased > 80%)	13	20.7%
General Effect (decreased 50% ~ 80%)	44	69.8%
No Effect (no change)	6	9.5%

87 patients contrasted M value between pre and post treatment.

TABLE 2. Statistics Of M Value Change In 87 Patients.

Effect	Cases	Rate
Remarkable Effect (increased 100%)	19	21.8%
General Effect (increased > 50%)	56	64.4%
No Effect (no change)	12	13.8%

The change of tumor marker.

TABLE 3. Contrasted In Ca19-9 Value Of 187 Patients.

Effect	Cases	Rate
Remarkable Effect	39	20.9%
General Effect	114	61.0%
No Effect	34	18.1%

181 patients dropped the pain in different degree.

TABLE 4. Cytomorphology Examination In 21 Patients.

	Result	Cases
Puncture Biopsy	Cancer cells denucleus necrosis death rate 100%	17
	Cancer cells can be seen	3
Autopsy	Cancer cells denucleus necrosis death rate 100%	1

The change of quality scores of life.

TABLE 5. Statistics of Quality of Life Scores For 251 Patients.

Effect	Cases	Rate
Remarkable Effect	53	21.1%
General Effect	158	62.9%
No Effect	40	16.0%

Complications

No patients presented complications such as skin burn, perforation of gastrointestinal tract, or pancreatic fistula.

Follow-up

Two hundred twenty-three patients were followed up. The follow-up time was 8~36 months. The average survival time was 12.5 months and post FUS is 10.4 months. Six patients have survived more than 3 years.

DISCUSSION

1. The key to FUS treatment for pancreatic cancer is to ensure the target tissue reaches 70–100°C in the focal area. Clinical experiments have shown that the gastrointestinal contents have a very high ultrasound absorption coefficient (Table 6). FUS energy losses in the tract are too high unless the tract is cleaned. The gastrointestinal tract will be perforated if one only increases the input power. Animal studies showed that if the gastrointestinal tract were full of normal content, the highest temperature the focal area could reach was 53°C. After cleaning the tract and inputting the degassed water, the temperature could reach 95°C. So we combined a low-fiber diet, fasting, and drinking degassed water to clean the gastrointestinal tract and got good results. Ensuring the lowest attenuation of ultrasound with the gastrointestinal passage is key to ensuring the success of FUS treatment for pancreatic cancer.

TABLE 6. Experimental Determination Of The Acoustic Characteristics Of Gastrointestinal Contents.

	Density (g/cm^3)	Velocity (m/s)	Impedance (10^5rayls)	Attenuation coefficient (dB/cm)
Water	0.997	1433	1.438	0.00025
Costive dejecta	1.14	765	0.874	16.1
Ordinary dejecta	1.07	843	0.903	11.4
Halfliquid dejecta	0.977	958	0.936	4.2
Diarrhea dejecta	0.97	1257	1.222	1.8
Gastric content	1.01	1483	1.498	2.1
Alvine chyle	0.99	1298	1.285	5.6
Air	0.00118	335	0.000395	11.8

2. We selected therapeutic parameters based on the following: (1) Selecting the input power depending on the depth of the treatment area; (2) Selecting the emission unit depending on CDAV; (3) Selecting the interval period depending on B-U-S M value; (4) Selecting the unit count depending on the size and crossing percent of the target area.

3. More metastasis and diffusion easily occur in the early stages of the disease because of no pancreatic capsule. How to enlarge the treatment area is a difficult clinical problem both for surgery and FUS: FUS is only a kind of local treatment for pancreatic cancer. This point must be emphasized.

4. By increasing the convergence angle of ultrasound, using the theory of painful threshold, and applying the interval emission of FEP-BY machines, the treatment didn't cause concurrent pain and burn of skin. Avoiding injury of the gastrointestinal tract through cleaning of the content was important in decreasing the local absorption of ultrasound and to avoid creating a thermoadhesion.

5. Pain is a common symptom of advanced pancreatic cancer. FUS treatment was shown to relieve the pain of pancreatic cancer. One hundred eighty-one patients presented concurrent pain in the group. The rate of pain relief can reach 84%. This demonstrates FUS as a new method to treat cancer that can not only kill the cancer cells, but also control the resulting pain. The method is as follows: (1) Kill the cancer cells to cause atrophy of tumor tissue. Relieve the pressure on the pancreatic duct by relieving the obstruction of duct; (2) Relieve the pressure and dilation on the common bile duct caused by the invasion of the tumor; (3) Relieve the stimulation to the celiac plexus caused by advanced pancreatic cancer.

CONCLUSION

FUS is a new, safe, efficacious, and local therapeutic method for advanced pancreatic cancer. It is the best selection for pancreatic cancer that cannot be resected.

REFERENCES

1. He, S.X., Xiong, L.L., Yu, J.S., et al., "High Intensity Focused Ultrasound for Treatment 14 Cases Malignancy Tumors of Abdomen and Pelvic," Beijing: *Chinese Journal of General Surgery*, **15**, pp 480-482 (2000).
2. He, S.X., Xiong, L.L., Yao, S.S., et al., "The Experiment before Clinical Using of High Intensity Focused Ultrasound," ppl, Beijing: *Peking University Journal*, **31**, pp 573-576 (1999).
3. Jun, R.W., et al., "Effect of Acoustic Streaming on Ultrasonic Heating," *UMB*, **20** (2), pp 195 (1994).
4. Pennes, H.H., "Analysis of tissue and arterial blood temperature in the resting human forearm,"*J Appl Physiol*, **1** (2), pp. 93-222 (1948).
5. Yang, J., Li, J., and He, S.X., "Determination of Gastrointestinal Contents' Acoustical Quality and the Application in HIFU therapy for Tumors in Abdomen," Beijing: *Chinese Journal of Ultrasound in Medicine*, **9** (17), pp 650-652 (2001).
6. Pratt F., Chapelon, J.Y., Abou, E.I., et al., "Focused Liver Ablation by Cavation in the Rabbit, a Potential New Method of Extracorporeal Treatment," *Gut*, **35**, pp 395-400 (1994).
7. Nyborg, W.L., Dunn, F., Carson, R.L., et al., *Biological Effects of Ultrasound*, NCRP Publications, pp 131-133 (1983).
8. Vallancien, G., Chopin, D., Thibauld, P., et al., "Extracorporeal Focalized Piezoelectric Hypothermial Fist Experimentation," *Eur Urol*, **18**, pp 285 (1990).
9. Vaughan, M.G., Ter Haar, G.R., Hill, C.R., et al., "Minimally Invasive Cancer Surgery Using Focused Ultrasound: a Pre-clinical, Normal Tissue Study," *British J Radiology*, **67**, pp 267-274 (1994).
10. Ter Haar, G,, Sinnett, D., and Rivens, I., "High Intensity Focused Ultrasound: A Surgical Technique for the Treatment of Discrete Liver Tumors", *Phys Med Biol*, **34**, pp 1743-1750 (1989).

Ultrasound Guided Clinical FUS: Patient Response To Tumour Treatments In Different Organs

I.H. Rivens[1], M.A. Allen[2], A. Visioli[1,3], D.C. Cunningham[2], A. Horwich[3], R. Huddart[3], G.R. ter Haar[1]

[1]Joint Department of Physics, [2]Department of Medicine, [3]Department of Radiotherapy, Royal Marsden Hospital, Downs Road, Sutton, Surrey. SM2 5PT

Abstract. Ultrasound guided focused ultrasound surgery (FUS) has been used at the Royal Marsden Hospital to treat patients with tumours in a variety of organs since 1996. Patients have been treated in both Phase I (n=63) and Phase II (n=9) trials. Treatment is performed without the need for patient sedation or anaesthesia. Symptoms and sensations experienced by patients have been documented both on an exposure by exposure basis, and by patient questionnaire before and after treatment. Sensations have been characterised as "discomfort" (including tingling, warmth, electric shock type sensations) and "pain". Sensations have been graded as None, Mild, Moderate or Severe. The use of diagnostic ultrasound for treatment planning immediately prior to exposure allows the position of potentially sensitive tissue layers such as the skin, liver and prostate capsules to be accurately determined and thus the ultrasound intensity incident on these layers can be calculated and compared with sensations experienced. Variations in sensation between tumours in different organs and due to ultrasound exposure of different sensitive tissues is analysed and discussed.

METHODS

Patients have been treated according to approved protocols using our prototype focused ultrasound surgery (FUS) device. In the Phase I clinical trial we aimed to treat accessible soft tissue tumours in a dose escalation study of side effects and toxicity (1). In the Phase II study of liver disease we are attempting to treat entire tumours in order to demonstrate efficacy of FUS. In all studies, fully conscious, unsedated patients have been treated in an outpatient setting.

Further details of the patient eligibility, treatment methods, treatment monitoring and follow up used in the clinical trials may be found in the paper by Allen et al (2). Here, only methods relevant to the treatment and to quantifying side effects and/or toxicity are detailed.

Immediately prior to treatment, patients are required to complete a questionnaire asking whether they have suffered any pain or discomfort that they attribute to the tumour we intend to treat. Pain and discomfort levels are described separately as being None, Mild, Moderate or Severe. Whether the pain is internal or superficial is also noted. During treatment, patients lie supine on a couch (for up to 3 hrs). A bag of degassed water is lowered onto the skin surface above the target tumour. The treatment consists of creating an array of single ablative FUS lesions each separated by 2mm at 60 second intervals, to allow tissue cooling. After each exposure patients are asked whether they were aware of any sensations and to classify them as either discomfort or pain. If discomfort was experienced the nature

of the discomfort was noted. If pain was experienced the patient was asked to quantify the pain using the validated Brief Pain Inventory (see for example (3, 4)), a scale from 1 to 10, with 10 defined as the "worse pain imaginable". In order to allow us to compare pain between patients, they are also asked to quantify the pain experienced from a "pin prick to the skin". For each exposure the duration and the focal depth beneath the skin were noted and, post-treatment, the in situ spatial peak intensity (Isp), and the peak and average intensities at the capsule and skin surfaces were calculated.

The clinical trials were primarily designed to study tumour ablation by FUS under diagnostic ultrasound guidance. An "ablative intensity" (AI) has been established from our pre-clinical studies. An in situ intensity of 1500 Wcm-2 was defined as being 100% AI. Patients are treated with exposures between 25 and 125% AI for 1-3 seconds. The actual treatment time used (and in some cases the maximum intensity) was determined by patient tolerance. In the early Phase I trial, if patients experienced pain this was subsequently avoided by reducing the exposure (duration, in situ intensity or both). Later in the Phase I trial and for the Phase II trials, if patients experienced tolerable pain, treatment continued unchanged. If patients experienced severe (intolerable) pain the exposure was reduced to a level which could be tolerated. Immediately after treatment all patients were asked to fill in the next section of the questionnaire which documented pain and other symptoms/sensations experienced during treatment.

Pain could be quantified for a complete treatment using either the patient questionnaire data or the maximum pain reported by a patient during the treatment (max pain). Pain was also analysed on a shot by shot basis. Whichever technique was used, the pain was graded as None (0), Mild (1), Moderate (2), Severe (3). Where pain was initially reported as a score out of 10, this was reduced to the above categories using the ranges: 1 to 3 = Mild, 4 to 6 = Moderate, 7+ = Severe.

The variables investigated were: Patient number (in order of recruitment into the trial), gender, age, and the organ containing tumour (whether it was prostate or liver). In addition to this, for liver tumours it was noted whether patients had received prior surgery involving the tissues overlying the treated tumour, and whether the tumour was located close to a ligament (falciform ligament, ligamentum venosum) as these were thought to be possible factors contributing to pain.

RESULTS & DISCUSSION

As of July 2002, 63 phase I and 9 phase II patients have been treated. 54 treatments have been delivered to tumours in the liver, 12 in the prostate and 6 in other locations (kidney (2), hip, abdomen (2) and nephron bed).

Discomforts experienced by the patients were described as tingling, "mild electric shock", and sensations of warmth. None of these caused patients intolerable discomfort and most were described as being not unpleasant.

The variation of individual's pain perception was investigated by asking patients to ascribe a score to a pin prick to the skin (such as experienced during a blood test). This demonstrated a wide variation in tolerance with scores ranging from 1/10 to 10/10. In the majority of cases, the worst pain experienced during a treatment did not exceed the pain level which individuals associated with a pin

prick. Furthermore, pain was frequently described as a hot pin prick or a hot "needle like" sensation.

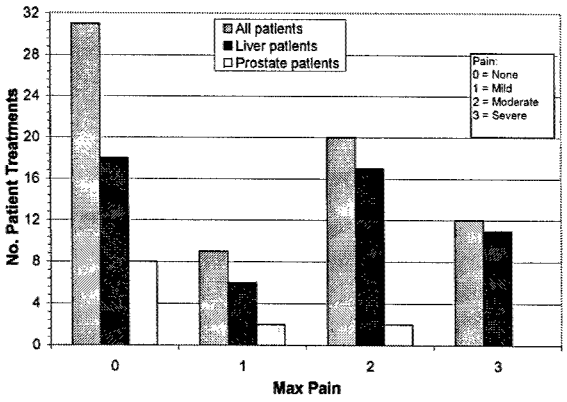

Figure 1. The number of patient treatments (total =74) are shown as a function of the maximum pain reported immediately after an exposure, analysed on the basis of the location of the tumour treated.

Overall, 31/74 patient treatments were completely pain free. A breakdown of maximum pain reported is shown in Figure 1. Table 1 shows the number of exposures at each pain level in the 3 anatomical sites given in Figure 1. 71% of all exposures were completely pain free. Less than 1% of exposures resulted in severe pain, and these were predominantly for patients with liver tumours. From the Phase II trial and latter stages of the Phase I trial we know that most patients can tolerate moderate pain. We believe that this is due to the short duration of the pain, which has generally been reported as lasting no longer than the exposure duration.

TABLE 1. No. of exposures (%) giving pain at each level, grouped according to anatomical site.

Pain level	All	Liver	Prostate	Others
3	41 (1)	38 (1)	0 (0)	3 (2)
2	266 (6)	258 (8)	7 (1)	1 (1)
1	907 (22)	838 (25)	69 (13)	0 (0)
0	2457 (71)	1860 (66)	447 (85)	150 (97)
Total	**3671**	**2404**	**523**	**154**

In general, the volume of tumour treated increased as the trials proceeded, as did both the maximum pain level and the number of painful exposures experienced by patients. The latter is best explained by the fact that the initial aim was to avoid all pain, and so exposure levels were reduced as soon as pain was reported. Later in the trials, and especially after commencement of the Phase II trial, the aim was to avoid intolerable pain (as determined by the patient).

Comparison of pain as recorded on the questionnaire, with the maximum pain recorded at any point during a patient treatment showed that patients tend to "average" pain over the treatment so that the pain recorded in the questionnaire was usually less than the maximum experienced. Because of this the maximum pain has been used in analysis in preference to that recorded on the patient questionnaire.

Analysis of the effects of both age and gender on maximum reported pain (not shown) demonstrated little in the way of trends. In particular, there was no significant evidence to suggest that women have a higher pain threshold than men.

During the trial there was only a single incidence of significant skin toxicity. One patient developed a blister over the treatment site 24 to 48 hours after treatment. The blister had resorbed without treatment within 1 week. The patient concerned reported no pain or discomfort during treatment. Furthermore, all patients who experienced pain believed the pain to be at depth rather than being superficial and related to the skin. Thus, lack of correlation of the average or spatial peak intensity on the skin surface with pain was not unexpected.

Figure 2 shows that as the spatial peak intensity within the prostate was increased, generally so did the pain experienced, although no cases of severe pain were recorded and only 6 cases of moderate pain occurred. The trend with the liver is less clear with higher levels of pain occurring at lower intensities (for a constant exposure time), and the effect of exposure duration is also counterintuitive. Thus, the correlation of pain with *in-situ* spatial peak intensity in the liver is poor. The lack of nerve endings in the liver or prostate and hence within any tumour growing in these organ means that the *in-situ* focal peak intensity should not necessarily be well correlated with pain. The results seem to confirm this lack of pain receptors.

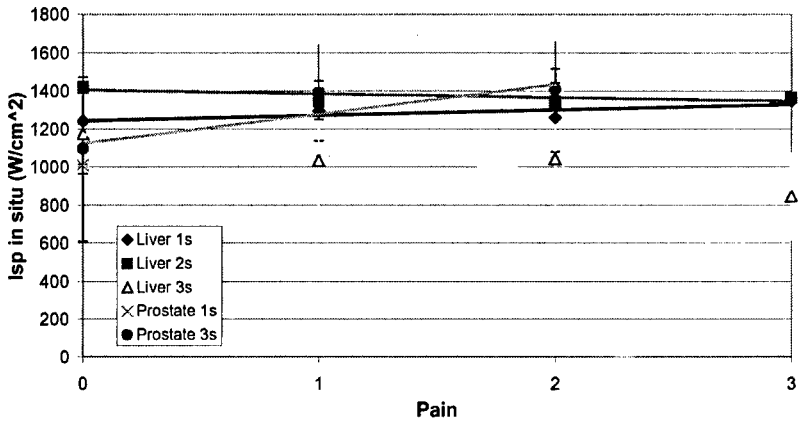

FIGURE 2. The effect of increasing *in-situ* spatial peak intensity at constant exposure duration, on the pain reported immediately after exposure for patients with tumours in the liver and prostate.

The presence of stretch receptors in the capsule of the liver makes this the anatomical structure closest to the focal region which is likely to give rise to pain. Thus, comparison of the spatial peak and average intensities at the liver and prostate capsules was made in order to investigate this. Figure 3a shows that higher intensities (in excess of 1000 Wcm^{-2}), at even the longest exposure duration (3s), appeared to be well tolerated on the prostate capsule. In general, target regions within the liver were further away from the capsule than they were in the prostate. Despite much lower intensity (~100 Wcm^{-2}) being incident on the liver capsule (Figure 3b), higher levels of pain were recorded during treatments to liver tumours.

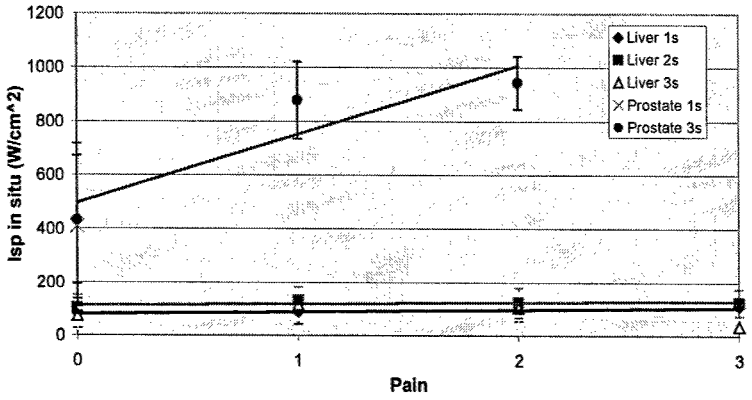

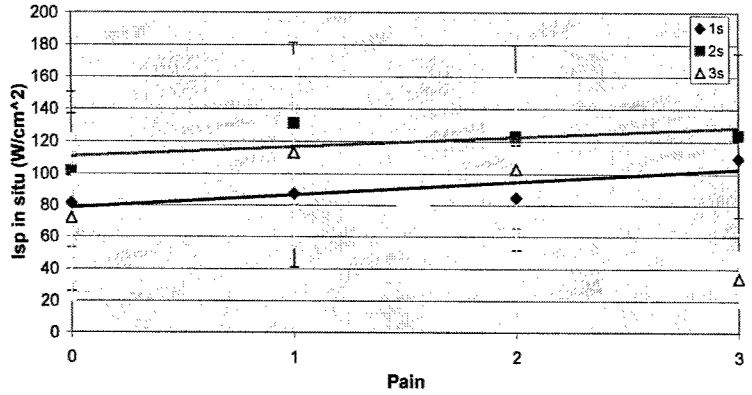

FIGURE 3a (top) and **3b** (bottom) show the effect of increasing the intensity incident on the capsule of the prostate and liver (at constant exposure duration) on the pain recorded after each exposure (NB the different intensity scales used in 3b for the liver capsule alone).

CONCLUSIONS

We have determined that it was possible to treat fully conscious, unsedated patients, and that although tolerance varied from patient to patient, more often than not it was possible to deliver a treatment that was capable of ablating the target tumour.

Assessment of pain was of secondary concern in the clinical trials, but we have sufficient information that we can draw some preliminary conclusions.

1. Treatments to the prostate were associated with less pain than treatments to the liver for a given exposure level. No sensations of severe pain were reported for prostate treatments. Moderate pain was only reported when the capsular Isp exceeded 800 Wcm^{-2}.
2. In the liver capsular Isp as low as 90 Wcm^{-2} caused moderate pain, however more data is required from liver treatments in order to try to identify a treatment limiting threshold intensity (most probably on the liver capsule).
3. Pain appears to be age, gender and prior surgery independent
4. Skin side effects have been almost completely avoided in our study.

From a clinical viewpoint it is more important that the patient is given an effective treatment than a pain free treatment, and we have found that most patients can tolerate moderate pain. Thus, our future strategy would be to continue to treat patients when they experience pain that they describe as tolerable and to assess treatment efficacy under these conditions.

ACKNOWLEDGEMENTS

This work was funded by the Southern and London Regional Health Departments. Dr. Visioli was funded by Dr. J. Glees, and Dr. Allen was funded by Dr. D. Cunningham, of the Royal Marsden NHS Trust.

REFERENCES

1. Visioli A.G., Rivens I.H., ter Haar G.R., Horwich A., Huddart R.A., Moskovic E., Padhani A., Glees J., *European Journal of Ultrasound*, **9**, 11-18 (1999).
2. Allen M., Rivens I.H., Visioli A.G., ter Haar G.R., "Focused Ultrasound Surgery (FUS): A Non-invasive Technique For The Thermal Ablation Of Liver Metastases," *Ibid.*
3. Hawthorn J., Aranda S., Webb P., *Management of Cancer Pain*, Australia, Glaxco Wellcome, (1996).
4. Jensen M.P., Karoly P., Brauer S., *Pain* **27(1)** 117-126 (1986).

Pulsed High-Intensity Focused Ultrasound-Induced Endothelial Cell Injury In Vessels Infused With Ultrasound Contrast Agent

Joo Ha Hwang[1,2,3], Andrew A. Brayman[1], and Shahram Vaezy[1,2]

[1]*Center for Industrial and Medical Ultrasound, Applied Physics Laboratory*
[2]*Department of Bioengineering*
[3]*Department of Medicine, Division of Gastroenterology,*
University of Washington, Seattle, WA 98195

Abstract. Background: The objective of this study was to determine if the endothelial surfaces of blood vessels are damaged when perfused with ultrasound contrast agent (UCA) and exposed to pulsed high-intensity focused ultrasound (HIFU).
Methods: The auricular arteries of New Zealand white rabbits were perfused with either varying concentrations of ultrasound contrast agent (Optison®) in saline or saline alone then exposed to pulsed HIFU (1.1 MHz, 3 MPa peak-negative acoustic pressure, 30 cycles/pulse, 100 Hz pulse repetition frequency) for a duration of 1 minute. After treatment the animals were euthanized and the vessels were removed. Specimens were prepared for observation under light microscopy, and scanning and transmission electron microscopy.
Results: The vessel perfused with ultrasound contrast agent and exposed to HIFU demonstrated structural changes on both light microscopy and electron microscopy suggestive of mechanical forces originating within the vessel lumen causing damage to the vessel wall. The damage included fragmentation and erosion of endothelial cells and subendothelial fibroblasts, and disruptions of the basement membrane.
Conclusions: Damage appears to occur to the endothelial surface of arteries perfused with UCA and exposed to pulsed HIFU. Damaged endothelial cells and exposure of the subendothelial matrix is known to be thrombogenic. This effect could potentially be used to thrombose vessels supplying tumors and occlude angiodysplasias.

INTRODUCTION

High-intensity focused ultrasound (HIFU) is being investigated for a wide variety of clinical applications. Many of these applications utilize the ability of HIFU to produce thermal lesions to obtain the desired bioeffect. This approach is being investigated in humans for the treatment of tumors and benign prostatic hyperplasia [1-3]. Thermocoagulation is also believed to be the primary mechanism involved in HIFU induced hemostasis [4].

Besides thermal mechanisms, HIFU also can induce cavitation, especially in the setting of ultrasound contrast agents (UCA). The therapeutic applications of cavitational effects include drug and gene delivery [5-7], and thrombolysis of blood clots[8-11]. Since UCAs are circulated in the vascular system, the most likely target for cavitation-induced damage are the endothelial cells that line the blood vessels.

Since damage to endothelial cells and exposure of the subendothelial matrix are know to be thrombogenic [12], endothelial damage due to cavitation may potentially be used to thrombose blood vessels. This effect has the potential to occlude the vascular supply to tumors, obliterate angiodysplasias, and occlude actively bleeding vessels or those at high risk of future bleeding.

It has been reported that tissue perfused with UCA and exposed to moderate intensities of ultrasound results in capillary disruptions and petechial hemorrhages [13,14]. There are also studies that demonstrate the erosion of cultured cell monolayers when exposed to ultrasound in the presence of UCA [15,16], and pitting of individual cells [17].

The aim of this study was to examine the mechanical bioeffects of cavitation on *ex vivo* endothelial cells in an intact vessel. To do this, we infused Optison® into a cannulated rabbit auricular artery and exposed it to pulsed HIFU. Light microscopy, transmission electron microscopy, and scanning electron microscopy were used to evaluate the vessel after the exposure. Our results suggest that mechanical damage to endothelial and subendothelial structures occur and are likely to be due to the occurrence of inertial cavitation nucleated by the contrast agent microspheres.

METHODS AND MATERIALS

Rabbit ears were obtained immediately after euthanasia. The auricular artery was cannulated with a 24-gauge angiocatheter to provide vascular access. The vessel was then infused with Dulbecco's phosphate buffered saline to maintain viability of the endothelial cells until the experiment was carried out (within 2 hours of euthanasia). Excised ears were kept at room temperature prior to and during the experiment. The procedures were carried out according to the guidelines of the U. S. National Institutes of Health for the use of laboratory animals.

Five ears were subjected to the experimental protocol. The length of the auricular artery was divided into three segments (Table 1). The segments correspond to the following treatment protocols: 1) no exposure to ultrasound/no contrast agent, 2) exposure to pulsed HIFU/saline infusion, and 3) exposure to pulsed HIFU/UCA infusion (Optison®, Mallinckrodt Inc., St. Louis, MO).

The experimental setup used to treat vessels examined using scanning electron microscopy (Fig. 1) consists of a water tank filled with degassed water with a focused ultrasound transducer fixed to the side of the tank. The ultrasound transducer is custom built and is comprised of an air-backed PZT C-5800 1 inch diameter disk (Channel Industries, Santa Barbara, CA) attached to an aluminum focusing lens

TABLE 1. Ultrasound exposure and infusion protocol.

Vessel segment	Ultrasound exposure (3 MPa P^-)	Infusate
1	no	saline
2	yes	saline
3	yes	0.3% Optison® in saline

with a radius of curvature of 5 cm. The driving electronics consist of a waveform generator (33120A, Agilent Technologies, Palo Alto, CA) and an RF power amplifier (A-300, ENI, Rochester, NY). Prior to performing the experiments, the transducer output was calibrated using a membrane hydrophone (MHA 200A, NTR Systems, Inc. Seattle, WA) to determine the focal dimensions (-6 dB focal width and –3 dB focal length 4.3 mm and 5.25 cm, respectively) and the necessary input voltage to obtain 3 MPa peak negative pressure at the focus.

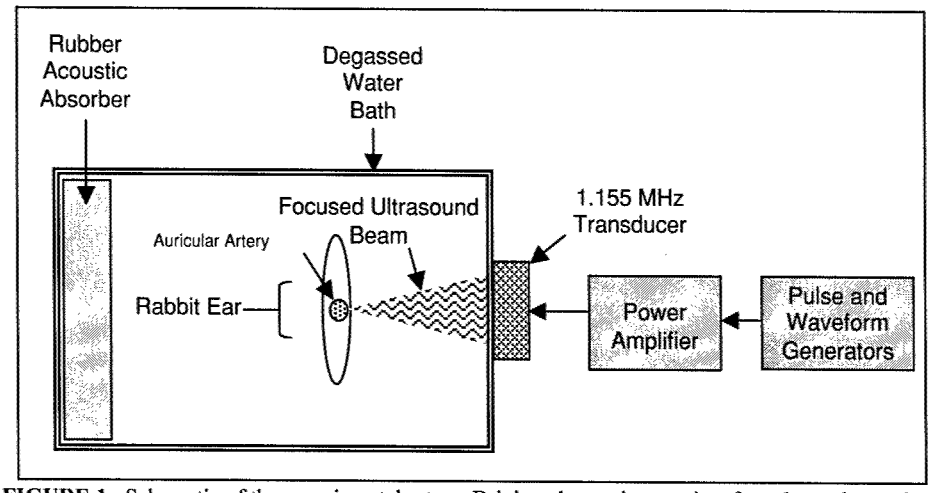

FIGURE 1. Schematic of the experimental setup. Driving electronics consist of a pulse and waveform generator and power amplifier. Ultrasound transducer is attached to the side of a water tank filled with degassed water. A custom fixture that is positioned by an XYZ motion stage holds the rabbit ear in place. A rubber acoustic absorber is used to minimize back reflection of ultrasound waves.

Rabbit ears were placed in a custom-built fixture that was mounted to an XYZ motion stage by which the targeted region of the vessel was placed at the focus of the ultrasound beam. Ultrasound exposure conditions were: f = 1.155 MHz, peak negative acoustic pressure = 3 MPa, pulse length = 30 cycles, pulse repetition frequency = 100 Hz, and total treatment time = 60 s. Saline infusion consisted of 30 ml of non-degassed saline infused *via* syringe over 60 s. Optison® infusion consisted of 30 ml of 0.3% Optison® (by volume) in non-degassed saline infused *via* syringe over 60 s. After treatment of segments 2) and 3), the ear was removed from the holder and half-strength Karnovsky's fixative was infused into the auricular artery for primary fixation. The vessel was infused intermittently with half-strength Karnovsky's fixative over 1 hour. The auricular artery was then dissected from the ear and placed in half-strength Karnovsky's solution overnight prior to preparing the sample for scanning electron microscopy.

A similar experimental setup was used to treat vessels observed using light and transmission electron microscopy. However, a spherically curved PZT transducer operating at 1.1 MHz was used. Unfortunately, the transducer was later damaged and we were unable to characterize its output. Therefore, the peak negative pressure that these vessels were exposed to is not known; however, it is believed to be between 3-5 MPa peak negative.

Light Microscopy And Transmission Electron Microscopy

After fixing in half-strength Karnovsky's solution the vessels were rinsed in phosphate buffer. The vessels were then post-fixed and stained *en-bloc* in 1% osmium tetraoxide. The samples were then rinsed in phosphate buffer and dehydrated with ethanol. The tissue was further dehydrated in propylene oxide and subsequently embedded in epoxy. The samples were then cut using an ultramicrotome. Thick sections (1 μm) were first cut and stained with Richard's stain (methylene blue/ azure II) for observation with a light microscope. Thin sections (90 nm) were then cut using a diamond knife, placed on copper TEM grids, and post-stained with uranyl acetate followed by lead citrate. The samples were observed using a Philips EM 400T transmission electron microscope. The microscope was operated under high-vacuum conditions ($<10^{-7}$ Torr) with an acceleration voltage of 60 kV.

Scanning Electron Microscopy

After fixing in half-strength Karnovsky's solution the vessels were rinsed in phosphate buffer. The vessels were then post-fixed and stained *en-bloc* in 1% osmium tetraoxide. The samples were then rinsed again in phosphate buffer and dehydrated with ethanol. The samples were then critical point dried in a pressure chamber filled with carbon dioxide. The vessels were then orientated on a SEM specimen stub and sputter coated with gold. The specimens were then observed using a JEOL 840A scanning electron microscope operated at 15 kV.

RESULTS

Light Microscopy

Figure 2-A is a light microscopy image of a sham-treated vessel infused with saline (segment 1). The basement membrane is intact without any disruptions. Also, endothelial cells completely cover the basement membrane. Figure 2-B is a light microscopy image of the vessel infused with ultrasound contrast agent and exposed to pulsed high-intensity focused ultrasound. This figure demonstrates damage to the vessel wall; note that several sections of basement membrane have been disrupted. Endothelial cells have lifted off the basement membrane in some areas.

Transmission Electron Microscopy

Transmission electron microscopy further characterized the damaged areas of the vessel wall. Figure 3-A was obtained from the sham-treated vessel infused with saline (segment 1). The endothelial cells are seen to be adherent to the basement membrane, and the basement membrane is continuous; *i.e.*, without major disruptions. Below the basement membrane are perivascular fibroblasts that have normal morphology. Figure 3-B is a TEM image obtained from the vessel infused with ultrasound contrast agent and exposed to pulsed HIFU. Figure 3-B demonstrates damaged endothelial cells,

sections of disrupted basement membrane, and damage to the perivascular fibroblasts. The pattern of the damage suggests that the damaging force originated from the lumen of the vessel and was directed into the wall of the vessel.

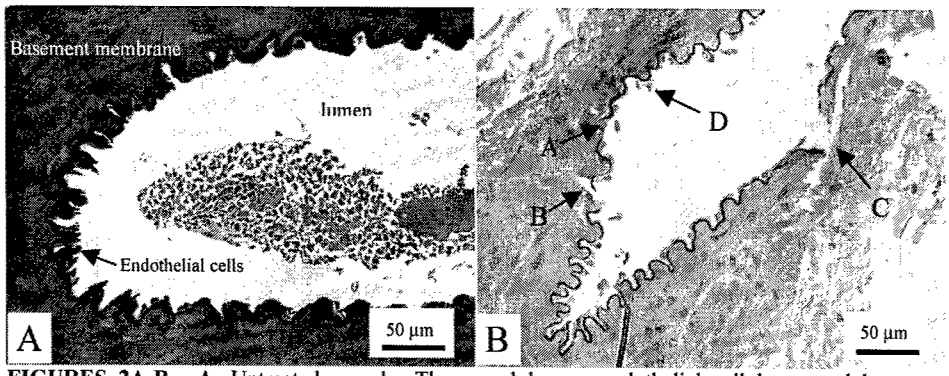

FIGURES 2A-B. **A.** Untreated vessel. The vessel lumen, endothelial cell layer, and basement membrane are identified. (40X). **B.** Vessel infused with ultrasound contrast agent and exposed to pulsed high-intensity focused ultrasound. Arrows labeled A, B, and C demonstrate disruptions in the basement membrane. The arrow labeled D demonstrates endothelial cells that have partially lifted off the basement membrane.

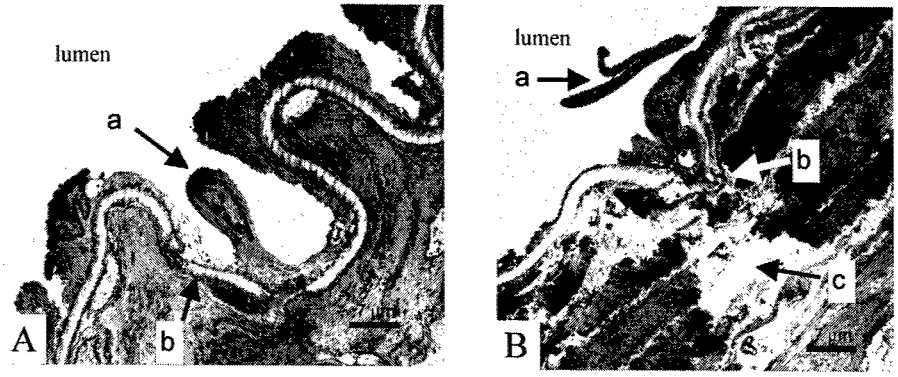

FIGURES 3A-B. **A.** TEM of vessel infused with saline. Arrow (a) points to a normal endothelial cell resting on an intact basement membrane (b). Lumen is labeled. **B.** TEM image of a damaged vessel wall. Vessel was infused with ultrasound contrast agent and exposed to pulsed high-intensity focused ultrasound. Arrow (a) demonstrates a damaged endothelial cell that has lifted off the basement membrane. White arrow (b) demonstrates an area of damaged basement membrane. Arrow (c) demonstrates a damaged region of the subendothelial matrix, including perivascular fibroblasts. (2800X magnification).

Scanning Electron Microscopy

Scanning electron microscopy demonstrates pitting and erosion of the endothelial surface in vessels that were infused with non-degassed saline or UCA and exposed to pulsed ultrasound. Figures 4-A and B are SEM images obtained from a sham-treated vessel (segment 1). There is no evidence of erosion or pitting of the endothelial surface. Figures 4-C and D are SEM images of vessels that were infused with non-

degassed saline and exposed to pulsed HIFU. These figures demonstrate some erosion of the endothelial cells off the basement membrane as well as pitting of the endothelial surface. Figures 4-E and F are SEM images of vessels that were infused with 0.3% Optison® and exposed to pulsed HIFU. There is evidence of greater endothelial cell erosion and pitting of the endothelial surface than in the saline-infused, ultrasound-exposed vessel. Most of the damage to the endothelial surface occurred on the surface of the vessel that faced the ultrasound transducer (*i.e.*, the posterior surface).

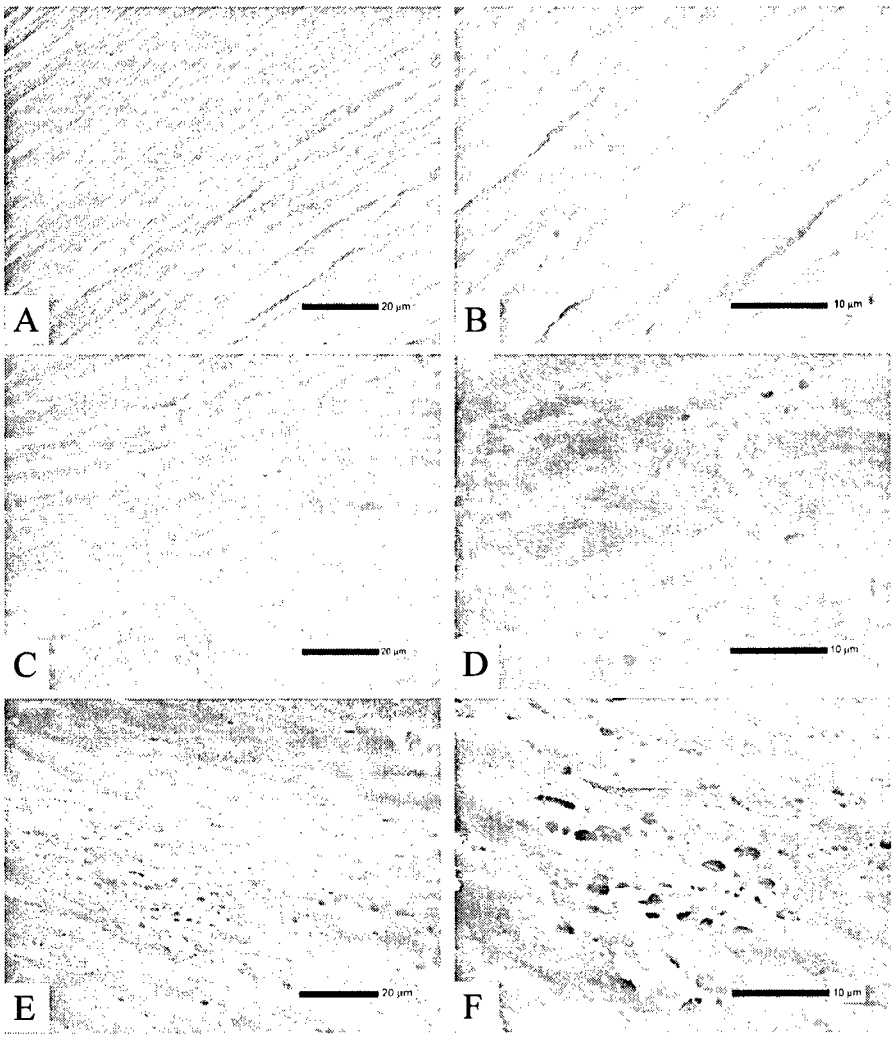

FIGURES 4A-F. A-B. SEM of sham-treated endothelial surfaces. There is no evidence of pitting or erosion of the endothelial surface. **C-D.** SEM of vessels infused with non-degassed saline and exposed to pulsed HIFU. There is evidence of some erosion and pitting of the endothelial surface. **E-F.** SEM of vessels infused with UCA and exposed to pulsed HIFU. There is evidence of a greater degree of erosion and pitting of the endothelial surface compared with the saline infused vessel.

DISCUSSION

Based on these preliminary findings, there appears to be damage to the endothelial surface of vessels that are infused with either non-degassed water or UCA and exposed to pulsed HIFU. The SEM findings of pitting of the cell surface are similar to those of Tachibana et al. [17] and the erosions are consistent with the findings of Brayman et al. [15] and Miller and Bao [16] in their cultured cell monolayer systems. The characterization of the damage using light microscopy, TEM, and SEM suggests a mechanical mechanism. The pattern of damage suggests forces that are acting on the vessel wall originating from the vessel lumen. These findings are consistent with a mechanism involving inertial cavitation [18-20]. Erosion to the endothelial surface may also be a result of microstreaming due to stable cavitation from bubbles on the endothelial surface.

To avoid thermal mechanisms, we used a short duty cycle (0.3%) for the ultrasound exposures. Although we did not employ any methods to detect cavitation in these preliminary studies, previous experiments using the same experimental setup have used passive cavitation detection to confirm the presence of inertial cavitation under similar experimental conditions (peak negative pressure, frequency, pulse length, pulse repetition frequency, and UCA concentration). Therefore, we are confident that inertial cavitation was occurring in the vessels exposed to pulsed HIFU.

Future studies will be directed at improving the experimental setup and obtaining additional data. Improvements that easily can be made include the use of degassed saline in the infusion control experimental group, incorporating passive cavitation detection to confirm the presence of inertial cavitation, and the use of color Doppler ultrasound to image flow and cavitation within the vessel when infused with UCA and exposed to pulsed HIFU. Furthermore, we would like to vary parameters such as the peak negative pressure, concentration of UCA, pulse length, pulse repetition frequency, and exposure time to determine thresholds where damage to the endothelial surface occurs and to see if we can obtain graded degrees of damage. By determining the parameters needed to obtain different degrees of damage to the endothelial surface, one can better identify the parameters needed to obtain desired bioeffects (or minimize undesirable ones). For example, in ultrasound-enhanced gene delivery it is desirable to pierce the surface of the cell membrane without inducing lethal damage to the cell, whereas, it is desirable to damage all endothelial cells when the goal is to occlude the vessel by inducing thrombosis. Also, in our experiments we observed that most of the erosions and pitting of the endothelial surface occurred on the luminal surface of the vessel facing the transducer. It is unclear if this is due to acoustic radiation force leading to aggregation of bubbles on this surface or some other mechanism. Further investigation is required.

CONCLUSIONS

Damage to the endothelial surface in the form of erosions and pitting was observed in vessels infused with both non-degassed saline and UCA and exposed to pulsed HIFU. Cavitation is a likely mechanism for the observed damage. Further studies are

needed to better characterize the mechanisms responsible for cavitation-induced bioeffects in order to harness this property of ultrasound for clinical use.

REFERENCES

1. N.T. Sanghvi, R.S. Foster, R. Bihrle, R. Casey, T. Uchida, M.H. Phillips, J. Syrus, A.V. Zaitsev, K.W. Marich, and F.J. Fry, *Eur J Ultrasound,* **9**, 19-29 (1999).
2. F. Wu, W.Z. Chen, J. Bai, J.Z. Zou, Z.L. Wang, H. Zhu, and Z.B. Wang, *Ultrasound Med Biol,* **27**, 1099-106 (2001).
3. G.R. ter Haar, Echocardiography 18, 317-22 (2001).
4. S. Vaezy, R. Martin, H. Yaziji, P. Kaczkowski, G. Keilman, S. Carter, M. Caps, E.Y. Chi, M. Bailey, and L. Crum, *Ultrasound Med Biol,* **24**, 903-10 (1998).
5. K. Tachibana and S. Tachibana, *Echocardiography,* **18**, 323-8 (2001).
6. Y. Taniyma, K. Tachibana, K. Hiraoka, T. Namba, K. Yamasaki, N. Hashiya, M. Aoki, T. Ogihara, K. Yasufumi, and R. Morishita, *Circulation,* **105**, 1233-1239 (2002).
7. E.C. Unger, E. Hersh, M. Vannan, T.O. Matsunaga, and T. McCreery, *Prog Cardiovasc Dis,* **44**, 45-54. (2001).
8. C.W. Francis and V.N. Suchkova, *Vasc Med,* **6**, 181-7 (2001).
9. Y. Birnbaum, H. Luo, S. Atar, M.C. Fishbein, A.V. Brasch, T. Nagai, D. Pal, T. Nishioka, J.S. Chae, C. Zanelli, T.M. Peterson, and R.J. Siegel, *J Thromb Thrombolysis,* **11**, 229-34. (2001).
10. K. Tachibana and S. Tachibana, *Circulation,* **92**, 1148-1150 (1995).
11. K. Tachibana, *J Vasc Interv Radiol,* **3**, 299-303 (1992).
12. R.W. Colman, J. Hirsh, V.J. Marder, A.W. Clowes, and J.N. George, *Hemostasis and thrombosis : basic principles and clinical practice,* 4th ed. (Lippincott Williams & Wilkins, Philadelphia, 2001).
13. D.L. Miller and J. Quddus, *Proc Natl Acad Sci,* USA **97**, 10179-84. (2000).
14. D.M. Skyba, R. J. Price, A. Z. Linka, T. C. Skalak, and S. Kaul, *Circulation,* **98**, 290-3 (1998).
15. A.A. Brayman, L. Lizotte, and M.W. Miller, *Ultrasound Med Biol,* **25**, 1305-1320 (1999).
16. D.L. Miller and S. Bao, *J Acoust Soc Am,* **102**, 1183-1189 (1998).
17. K. Tachibana, T. Uchida, K. Ogawa, N. Yamashita, and K. Tamura, *Lancet,* **353**, 1409 (1999).
18. Y. Tomita and A. Shima, J *Fluid Mechan,* **164**, 535-564 (1986).
19. L. Crum, *J Phys,* **40,** 131-135 (1979).
20. R. Apfel, *Meth Exptl Phys,* **19**, 355-441 (1981).

Enhancement Of Gene Delivery Of Naked Human Factor IX Plasmid Into Mouse Livers By Ultrasound Exposure

Carol H. Miao [*], Andrew A. Brayman [†], Peiqing Ye [*], Pierre Mourad [†], Lawrence A. Crum [†]

*Departments of Pediatrics and Medicine, University of Washington, Seattle, WA 98195, USA
†Center for Industrial and Medical Ultrasound, Applied Physics Laboratory, University of Washington, Seattle, WA 98195, USA

Abstract. Interaction of ultrasound [US] with tissues and/or gas bodies can alter cell membranes and thus mediate gene transfer. Plasmid DNA delivery efficiency can be greatly increased by appropriate acoustic conditions. Furthermore, US contrast agents (*viz.*, stabilized microbubbles) can be used as cavitation nuclei, and lower the ultrasonic pressure threshold for cavitation occurrence. A liver-specific, high-expressing human factor IX plasmid (pBS-HCRHP-FIXIA, 50 mg in 250 ml solution; [15]) was mixed with contrast agent (Optison®) or PBS, and delivered to mouse livers by intrahepatic injection, with simultaneous exposure to US (1.13 MHz, 0.8 MPa peak negative pressure [P^-], 500 cycle bursts, 1 Hz PRF, 60 s) applied using a solid cone transducer. This P^- was selected on the basis of *in vitro* data indicating that the pressure was sufficient to disrupt Optison microspheres, generate free microbubbles, and to initiate moderate levels of inertial cavitation activity. Furthermore, in terms of bubble dynamics, 500 cycle bursts are essentially CW, while the long quiescent period between bursts allows for new microbubbles and plasmid to enter and accumulate in the tissues before the next burst. In this experiment, up to a 13-fold increment in transgene expression was achieved in plasmid+US+Optison® treated animals (n=6), whereas up to a 3-fold increment was obtained in plasmid+US treated animals (n=6). This increment was not observed in plasmid only, or plasmid+sham US control animals (0/12). These preliminary results demonstrate that therapeutic ultrasound in combination with microbubble contrast agents can be developed to promote safe and efficient nonviral gene transfer.

INTRODUCTION

Non-viral gene therapy has many advantages over viral gene therapy; *e.g.*, ease of production of the plasmid DNA, low toxicity, reduced immunogenicity, and the ability to deliver large genes. However, nonviral gene delivery is usually less efficient than delivery by viral vectors. Ultrasound [US] has been used recently to enhance the transfection of mammalian cells by plasmid DNA *in vitro* and *in vivo*. Interaction of mechanical ultrasonic waves with tissues and/or gas bodies can alter cell membranes and thus mediate the gene transfer. *In vitro* investigations have found that US can permeabilize cell membranes and facilitate transfer of plasmids or liposomes into cells (1,2). US can also alter *in vivo* drug (3) or gene (4-6). In

addition, US-induced cavitation *in vivo* has been shown to produce hemolysis (7,8) extravasation from capillaries (9-11) and opening of the blood-brain barrier (12). Therefore, US can not only facilitate the entry of plasmid DNA into cells, but also enhance extravasation of plasmid-containing solution from capillaries into the extracellular space. Consequently, the delivery efficiency of plasmid DNA or plasmid DNA-carrier complexes should be greatly increased with the aid of appropriate acoustic conditions.

Hemophilia has long been used as a gene therapy model system. Hemophilia B is caused by a deficiency of the blood coagulation factor IX. Although viral gene transfer recently showed promise for gene therapy of hemophilia (13,14), many obstacles remain. The nonviral approach would provide an alternative and safer gene delivery strategy to avoid the potentially harmful effects of viral gene therapy. We have recently demonstrated that injecting naked DNA that contained a liver-specific promoter into the liver resulted in long-term, therapeutic levels of human factor IX [hFIX] (0.5-2 μg/ml) in mouse plasma by a hydrodynamics-based method (15). Our construct with a liver-specific hFIX expression cassette achieved episomal persistence of plasmids and long-term preservation of active promoters. In these studies, we employed a rapid, high-volume infusion method for efficient delivery of naked plasmid DNA into the liver (16,17). This technique induced small liver lesions that were rapidly repaired in the first few days after gene delivery. Neither transgene-specific cytotoxic effects nor long-term toxicity were observed (18). Our results demonstrated for the first time that gene transfer using a non-viral, plasmid-based system can reproducibly achieve persistent and liver-specific expression of a therapeutic protein. Presently, the rapid, high-volume venous injection procedure is not suitable for clinical applications. As a potentially viable clinical alternative, we attempted in the present study to use US to facilitate plasmid DNA transfer as a novel strategy for safe and efficient delivery. If successful, US enhancement of delivery could reduce/eliminate the synthetic delivery vehicles needed for therapeutic effect, thus reducing the associated potential toxicity, immunogenicity, and costs. Once suitable acoustic conditions are established, non-viral gene transfer of plasmid DNA mediated by ultrasound should provide a new avenue for the treatment of hemophilia B patients and other genetic diseases.

Two hypotheses guided this research: (I) *US can facilitate both direct entry of plasmid DNA into cells and extravasation of plasmid into the extrahepatic space, increasing plasmid DNA or plasmid DNA-carrier complex delivery efficiency*; (II) *the effect will arise via a cavitation mechanism* (*i.e.*, involving bubbles).

MATERIALS AND METHODS

Constructs. In our previous work, naked DNA transfer of a high-expressing hFIX plasmid yielded long-term (over one and a half years) and therapeutic-level (0.5-2 μg/ml) gene expression of hFIX from mouse livers (15). Our liver-specific plasmid contains an expression cassette including a hepatic locus control region (HCR) from the ApoE gene locus, an α1-antitrypsin promoter, hFIX cDNA, a

portion of hFIX's first intron, and a polyadenylation signal from bovine growth hormone (Fig. 1). The construction of plasmids pBS-HP-FIXA and pBS-HCRHP-FIXIA is described elsewhere (19). Large scale preparation of the plasmids was done using a Qiagen maxi-prep kit (Valencia, CA). No protein or RNA was detected after purification.

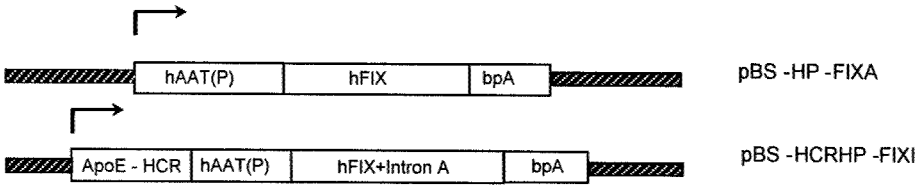

FIGURE 1. The structure of constructs containing different hFIX expression cassettes. ApoE-HCR, hepatic locus control region from ApoE gene locus (771bp); hAAT(P), human α1-antitrypsin promoter (408 bp); hFIX, human factor IX cDNA (1.4 kb); IntA, truncated human factor IX first intron (1.4 kb); bpA, bovine growth hormone polyadenylation signal (265 bp).

Ultrasound. A solid, truncated cone transducer [TD] was designed to produce a modestly focused beam over a flat surface of dimensions comparable to the murine liver, to which the TD was to be applied directly. The driving signal was provided by pulse generator providing 1 V (peak-to-peak) output. This signal was routed through an attenuator pad and thence to a class A power amplifier, which provided 55 dB of gain. The spatial peak, temporal peak negative acoustic pressure was measured using a 0.2 mm aperture membrane hydrophone (NTR Systems, Seattle, WA).

Animal studies. Adult C57/Bl6 mice were purchased from Taconic (Germantown, NY), and housed under SPF conditions at the University of Washington. Animals were treated according to the National Institutes of Health guidelines for animal care and the guidelines of the University of Washington. Plasmid pBS-HCRHP-FIXIA (50 μg/250 μl of 0.9% saline solution) was injected directly into one lobe of the mouse liver. Plasmid suspensions were supplemented with either 10 V% saline solution or 10 V% Optison®. Initial efforts have explored the effects of simultaneous presentation of plasmid containing the gene for Factor IX and either US alone, or in combination with the CA Optison®.

Preliminary experiments involved two acoustic protocols. In both, the acoustic frequency was 1.13 MHz, P^- was 0.8 MPa, the duty factor was 0.01, US exposure duration was 60 s, and Optison® (or saline solution) used. In the first protocol, the livers were exposed or sham-exposed to 20 cycle acoustic pulses at a pulse repetition frequency [PRF] of 500 Hz. In the second protocol, the livers were exposed/sham-exposed to 500 cycle tone bursts at PRF = 1 Hz.

RESULTS AND DISCUSSION

In the first gene transfer protocol, the livers were exposed or sham-exposed to 20 cycle acoustic pulses at 500 Hz PRF and 0.8 MPa P^-, with simultaneous injection of either hFIX plasmid (pBS-HCRHP-FIXIA; 50 μg/250 μl of 0.9% saline solution) +

sham contrast agent, or of plasmid + 10 V% contrast agent. Expression of hFIX was enhanced up to 3-fold by US exposure; however, no further enhancement was associated with the inclusion of Optison® in the plasmid suspension (Table 1). The latter result was contrary to expectation. *Post hoc* consideration of the protocol lead to the hypothesis that the lack of CA effect on US-mediated gene expression was likely due to the use of short pulses at a high (500 Hz) PRF; *viz.*, that this protocol destroyed the contrast agent microbubbles as they exited the injection needle, thereby essentially abolishing the opportunity for the microbubbles to enter the extracellular space and nucleate inertial cavitation. The protocol was therefore revised. In the second protocol, the livers were exposed/sham-exposed to 500 cycle tone bursts at PRF = 1 Hz. These conditions were selected so that there would be a long quiescent period between sequential US bursts, thus allowing new microbubbles and plasmids to enter and accumulate in the tissues before the next burst. With this protocol, up to a 13-fold enhancement in gene expression was achieved by applying US + Optison®, whereas a 3.7-fold increment was achieved with US alone (Table 1). No increment in gene expression levels was observed in animals treated with plasmid only, or with plasmid + sham US (0/18 animals; Table 1). Nevertheless, within each group of animals in which there was apparent enhancement of gene expression, there was great variability in the hFIX expression levels. Additional experiments are being designed to achieve more consistent and reproducible results.

TABLE 1. Enhancement of hFIX gene expression with ultrasound facilitated gene delivery.

Protocol #	Mouse #	US	Optison®	Fold Enhancement of FIX Level Day 1	Day 4
1	208,209,211	-	-	0.85 - 1.26*	1.10 - 1.41
1	223,224,225	-	+	1.01 - 1.22	1.29 - 1.48
1	231,232,233 234,241	+	-	1.12 - 3.14	1.05 - 2.06
1	226,227,228 229,230	+	+	1.03 - 2.25	1.15 - 2.33
2	261,262,264 265,272,274	-	-	0.81 - 1.12	0.82 - 1.15
2	263,267,268 269,270,271	-	+	0.98 - 1.21	1.06 - 1.43
2	296,297,298 299,300,404	+	-	1.05 - 3.72	1.11 - 2.96
2	287,288,290 291,293,294	+	+	1.15 - 13.07	1. 31 - 6.45

* 1.00 is a representative value (Avg.=0.95ng/ml) for a negative control by administration of plasmid DNA into mouse livers without application of ultrasound and contrast agent (Optison®).

SUMMARY

We have developed a low-energy, modestly-focused ultrasound probe and an acoustic protocol that can stimulate naked hFIX plasmid transduction up to 13-fold in mouse livers. We are currently optimizing acoustic protocols to further enhance gene delivery efficiency. We envision the eventual use of relatively low frequency, relatively high output diagnostic US (*e.g.,* harmonic-mode Doppler US) to simultaneously image plasmid/CA mixture presence in the liver and to induce IC in the tissue to facilitate gene transfer. This technique might also be combined with synthetic delivery vehicles to achieve high-level gene transduction for a therapeutic effect.

REFERENCES

1. Manome, Y., Nakamura, M., Ohno, T. & Furuhata, H. *Hum. Gene. Ther.* **11**, 1521-8 (2000).
2. Newman, C.M., Lawrie, A., Brisken, A.F. & Cumberland, D.C.. *Echocardiography* **18**, 339-47 (2001).
3. Mukherjee, D., Wong, J. & Griffin, B. *J. Am. Coll. Cardiol.* **35**, 1678-86 (2000).
4. Greenleaf, W.J., Bolander, M.E., Sarkar, G., Goldring, M.B. & Greenleaf, J.F. *Ultrasound Med. Biol.* **24**, 587-95 (1998).
5. 5Kim, H.J., Greenleaf, J.F., Kinnick, R.R., Bronk, J.T. & Bolander, M.E. *Hum. Gene Ther.* **7**, 1339-1446 (1996).
6. Shohet, R.V., Chen, S. & Zhou, V.T.. *Circulation* **101**, 2554-6 (2000).
7. Brayman, A.A., Coppage, M.L., Vaidya, S. & Miller, M.W. *Ultrasound Med. Biol.* **25**, 999-1008 (1998).
8. Dalecki, D. *et al. Ultrasound Med Biol* **23**, 307-313 (1997).
9. Miller, D.L., Gies, R.A. & Chrisler, W.B. *Ultrasound Med Biol* **23**, 625-33 (1997).
10. Miller, D.L. & Gies, R.A. *Ultrasound Med Biol* **26**, 307-13. (2000).
11. Skyba, D.M., Price, R.J., Linka, A.Z., Skalak, T.C. & Kaul, S. *Circulation* **98**, 290-3 (1998).
12. Hynynen, K., McDannold, N., Vykhodtseva, N. & Jolesz, F.A. *Radiology* **220**, 640-6. (2001).
13. Kay, M.A. *et al.. Nat. Genet.* **24**, 257-61 (2000).
14. High, K. *Ann. N. Y. Acad. Sci.* **961**, 63-4 (2002).
15. Miao, C.H., Thompson, A.R., Loeb, K. & Ye, X. *Mol. Ther.* **3**, 947-57 (2001).
16. Liu, F., Song, Y. & Liu, D. *Gene Ther.* **6**, 1258-1266 (1999).
17. Zhang, G., Budkar, V. & Wolff, J.A. *Human Gene Ther.* **10**, 1735-1737 (1999).
18. Ye, X., Loeb, K.R., Stafford, D., Thompson, A.R. & Miao, C.H. *Thromb. and Haemost.* in press (2002).
19. Miao, C.H. *et al. Mol. Ther.* **1**, 522-532 (2000).

The Application Of High Intensity Focused Ultrasound In The Treatment Of Advanced Pancreatic Cancer: A Preliminary Report Of 13 Cases

Zhang Ming, Li Weibing, and Bai Xiangjun

HIFU Center, Jiangsu Cancer Hospital, Nanjing 210009

Abstract. Objective. To explore the safety and effectiveness of the treatment for advanced pancreatic cancer by high-intensity focused ultrasound system (HIFU). Methods. Thirteen cases of unresectable local advanced pancreatic cancer were treated with extracorporal therapy by HIFU. All of the patients received chemotherapy afterwards. Results. After the treatment, the clinical symptoms improved, the tumors regressed by CT/MR examination, and the color ultrasonography showed that blood supply of the tumors decreased by 75% and greater. Conclusion. The HIFU technique provides a new, safe, effective, and feasible method for the local treatment for pancreas cancer. Key Words: HIFU, Advanced Pancreatic Cancer.

INTRODUCTION

The primary choice for treatment of pancreatic cancer is surgical resection. It is difficult, however, to make an early diagnosis of pancreatic cancer, and because of this, patients are in an advanced stage when a diagnosis is established. Also, the possibility of resection in subsequent surgeries is very low for those with postoperative recurrent pancreatic carcinomas. These are dilemmas in the clinical treatment of pancreatic cancer. Thirteen cases of advanced pancreatic cancer were treated with intra-tumor therapy by high intensity focused ultrasound. The effectiveness and clinical safety of this therapeutic method will be discussed

MATERIALS AND METHODS

Clinical Data

General Data. Thirteen cases of advanced pancreatic carcinoma were diagnosed by radioimmunoassay, B-type ultrasonography, computer tomography, magnetic resonance imaging and surgical operation. Six of these were identified by histopathology, and the diagnoses of pancreatic cancer for the other 7 cases were established according to clinical symptoms and signs, imaging and CA199. There

were five male and eight female patients, and the mean age was 67 years (range, 42 to 80 years). All of the pathological foci were lumps which localized in the head (two cases), neck (two cases), and body and tail (nine cases) of the pancreas. The range of the diameters of the tumors was from 3.5 to 9.7 cm. Most of the patients have celiac lymph node metastasis, and some of them have hepatic metastasis and other distant metastasis. All of the patients consented to HIFU treatment.

Therapeutic Coverage. The masses were completely overlaid in three cases; HIFU therapeutic coverage includes the whole tumor and the normal tissue within one centimeter of the circumference of the tumor. The masses were partially overlaid in 10 cases; HIFU treatment was only confined within the tumors.

JC Type Focused Ultrasound Tumor Therapy System

This apparatus was designed and produced by Chongqing Haifu Technology Co, Ltd. The main parameters are as follows:

- therapeutic frequencies: 0.8MHz, 1.6MHz;
- average diameters of focused fields: 1.1mm, 1.3mm;
- lengths of focused fields: 9.8mm, 10.7mm;
- focus: 100-160 mm;
- sonic intensity of focused fields: 5,000-20,000 Wcm-2;
- therapeutic duration: 2814-8269 seconds.

The Therapeutic Methods And Process Of HIFU

The preparation before operation. The therapeutic formula is designed according to the location, size, and shape of the tumor, and its relationship with the adjacent organs, blood vessels and biliary ducts, which are determined by physical and imaging examinations.

The therapeutic methods and process. After fixing the patient's position, inflating a self-made water cyst lessens the distance between the skin and the tumor. The location and size of the tumor, the amount of therapeutic layers and the therapeutic field of each layer are re-confirmed by diagnostic ultrasound. Afterwards, each layer of tumor tissue is treated from the outside of the body with the therapeutic ultrasound probe by a sequence of layering and in a way of line-to-field and shape orientation, until the whole target region is completely covered. The whole process is under the real-time location and supervision of color Doppler ultrasonography. The three-dimensional target region is completely treated via destruction of every layer of tumor tissue. During the treatment, according to the changes of both the configuration of imaging graphics and the echoic texture of each layer of tissue before and after the operation, the HIFU treatment can be evaluated in real time by the computer image processing system, and the preset doses of ultrasonography in the scheme can be fed back by the alteration of the ultrasonographic imaging.

The Evaluation Of Clinical Effectiveness

- The imaging alteration before and after HIFU treatment (CT, E-CT, MRI & B-type Ultrasound).
- The change in the volume of the lesion and any existence of hemorrhage or disrupture of the tumor.
- Any jaundice or bile leakage.
- The alteration of clinical symptoms and/or local function.
- The change of serum tumor markers.

Surveillance And Evaluation

Twenty-four hours of electrocardiographic surveillance and evaluation of blood biochemical markers before and after the treatment were used to estimate postoperative systemic response of thermal trauma.

RESULTS

The Alteration In Imaging After HIFU Treatment

Color Doppler ultrasonic examination. The difference between the ultrasonic imaging graphics before and after treatment was observed in 13 patients. Of these 13 patients, the blood supply was decreased or disappeared in 5, the tumor regressed in 4, and the echoic texture of the tumor intensified apparently in 2. The cloud-like echoic texture was found in 3 cases.

CT examination. Of the 8 patients who were examined by CT before HIFU treatment, 6 were re-examined after the operation. The results showed that the tumor intensification weakened and the margin became clear in 4, and the tumor regressed in 2 patients.

MRI examination. The results of MRI examination before and after HIFU treatment were compared in 8 patients. These showed that the blood supply within the tumor decreased one month after the operation, and the T2WI of the tumor presented lower signals.

The Alteration Of Clinical Symptoms And Signs

The improvement of local pain. Of the 11 patients who suffered from pain before the treatment, the pain remitted partially or disappeared in 10. Only in 1 patient did the remission of pain last only one week.

The improvement of appetite and body weight. Appetite improved distinctly in 9 patients, and body weight increased in 7 patients.

The alteration of other symptoms. One week after the treatment, jaundice resolved in 2 jaundiced patients. The body temperature rose to about 38° C in the 3 days after the treatment in 3 patients, and then gradually became normal.

The total response rate of complete and partial remission was 60%.

The Change Of Blood Tumor Markers

One month after HIFU treatment, the level of CA199 began to decrease, but it was still slightly higher than normal.

Side-Effects

A II+ skin burn was found in 1 patient and gastric atony was found in another.

DISCUSSION

Surgery is one of the main methods for the local treatment of pancreatic carcinoma. In the last two decades, the incidence of pancreatic cancer has increased year after year, and the magnitude of augmentation is 15% per year. Pancreatic cancer is now one of the relatively common digestive tumors. Because of the wide clinical use of imaging examinations, there has been a great increase in the rate of clinical diagnosis and histopathological finding of pancreatic carcinoma. However, most of the patients are already in a mid-advanced stage when the diagnosis is established, and thus have lost the chance to receive a radical resection, in particular because of the delay of patients' referral to physicians. Nowadays, comprehensive treatments still remain the major measures with which to treat a majority of advanced pancreatic cancer patients. These comprehensive measures are palliative surgical drainage, chemotherapy, radiation therapy, interventional therapy and immunotherapy, etc., but the curative effects are not satisfactory. The clinical difficulty is therefore how to improve the treatment of mid-advanced pancreatic cancer, to relieve pain caused by the malignancy, to enhance the quality of life and to prolong the survival of the patients. HIFU, which was developed in recent years, is one therapeutic technique for the local treatment of tumors. Abiding by the principle of oncological surgery, under the real-time surveillance of a diagnostic ultrasonography, HIFU is able to destroy, from outside of the body, neoplastic lesions of different size and different shape in vivo. It is a "no injury" therapeutic measure and has been applied successfully in the treatment of solid tumors of the intra-abdominal organs such as liver, kidney, prostate, etc. Yet, no report has been found on the application of HIFU in the treatment of pancreatic cancer. In this report, with a total effective rate of 60%, the application of HIFU with postoperative chemotherapy in the treatment of pancreatic carcinoma is believed to be a recommended method.

After local treatment by HIFU, all the patients in the group had a relatively slight systemic stress and only a little disturbance to the function of the vital organs of the body. This indicates that systemic thermal traumatic response is limited. Due to sufficient preoperative preparation and design, real-time surveillance of color ultrasonography during treatment to determine the therapeutic range of the target region and the relationship of adjacent organs, and estimation of therapeutic efficacy by observing the alteration in ultrasonic images before and after treatment, the therapeutic dose can be monitored and adjusted. These measures guarantee a visible and controllable process and the safety of HIFU treatment.

In 1985, Callian, et al. suggested a practical and effective standard to evaluate the quality of life, which included condition of pain, physical status, and body weight, etc. In this article, all of the patients were in an advanced stage of disease and had no chance receive surgery. They had severe clinical symptoms and, especially, pain of different degrees. They were in general lymphatic and blood metastases in advanced pancreatic cancer, and the prognosis was bad. Therefore, the median survival could not be prolonged only by a local treatment of the pancreatic mass. Chemotherapy alone apparently does not remit the clinical symptoms. There were 2 patients in this group; one received a five-cycle chemotherapy of gemcitabine and 5-Fu, and another only three cycles. After the end of the chemotherapy, the tumors grew distinctly larger, and some symptoms appeared. Then, the patients received HIFU treatment. One month after treatment, CT examination showed that the mass had regressed and the pain had disappeared. All 13 patients in this group received HIFU treatment and postoperative chemotherapy. The effectiveness rate was 60%, much higher than that of simple chemotherapy (20%). After treatment, pain in all of the patients was relieved over the short-term, and patient appetite and body-weight increased. In a word, the recent clinical application proves that HIFU is one of the brand-new methods in the treatment of tumors. It is a safe, effective, and feasible local treatment for pancreatic cancer. The major application of this technique in the treatment of advanced pancreatic carcinoma, we believe, is the reduction of the tumor load and the palliative therapy. More clinical observation and research is necessary because of the short duration and limited patients involved in the study.

REFERENCES

1. De Vita, Jr., V.T., Hellman, S., Rosenberg, S.A., *Cancer Principles & Practice of Oncology (5th Edition)*, USA: Lippincott-Raven, 1997, pp. 1089-1116.
2. Burris H.A., Moore M.J., Anderson J., et al., "Improvenments in survival and clinical benefit with gencitabine as first-line therapy for patients with advanced pancreas cancer: a randomized trial," *J Clin Oncol*, **15** (6), 2403-2413 (1997).
3. Rowland I.J., Rivens I., Chen L., et al., "MRI study of hepatic tumors following high intensity focused ultrasound surgery," *Br J Radiol*, **70**, 144-153 (1997).
4. Sanghvi N.T., Foster R.S., Bihrle R., et al., "Noninvasive surgery of prostate tissue by high intensity focused ultrasound: an updated report," *Eur J Ultrasound*, **29**, 19-29 (1999).
5. Wu, F., Chen, W.Z., Bai, J., et al., "Pathological changes in human malignant carcinoma treated with high-intensity focused ultrasound," *Ultrasound in Med &Bio*, **27**, 8-11) 2001).

High Intensity Focused Ultrasound For Treatment Of Patients With Advanced Tumors Located In The Walls Of Chest And Abdomen: A Preliminary Report

Guoqiang Zheng, Feng Guo, Ling Huo, Zheng Li,
Yi Wang, Guangwei Xu

Division of HIFU, Department of Surgery, Peking University School of Oncology
Beijing Institute for Cancer Research, Beijing Cancer Hospital
Beijing 100036 China

Abstract. Objectives: To present our results of high-intensity focused ultrasound (HIFU) treatment in 10 patients with advanced tumors involving the walls of chest and abdomen. Methods: We performed 73 HIFU treatments in 59 patients with malignant tumors using a JC model HIFU device from February 2001 to March 2002. Tumors located in the walls of the chest and abdomen in 10 patients were treated by HIFU. One case was a local recurrence of fibrosarcoma; others were local invasions or metastases of lung cancer, liver cancer, breast cancer, or malignant soft tissue tumors from other sites. Tumor size was between 3 to 5 cm in 4 cases, 5 to 8 cm in 3 cases, and greater than 8 cm in 4 cases. There were multiple tumors in 8 patients. All 10 patients had received anti-cancer treatments before HIFU, surgery in 8 cases, radiotherapy in 7 cases, and chemotherapy in 7 cases. Three patients were complicated with intercostal neuralgia. Results: Partial responses were obtained in 2 patients, a minor response in 1 patient, stable disease in 4, and progressive disease in 2 after HIFU treatments. In 3 patients all the intercostal neuralgia disappeared after HIFU. A bone scan showed that the site of rib metastasis before HIFU became normal after HIFU in one patient. Only one patient in this group died within 5 months after HIFU treatment through June, 2002. Conclusions: Malignant tumors located in the walls of chest and abdomen were a difficult problem in clinical treatment, because most of them had received anti-cancer therapies and were usually in advanced stages before the tumors appeared on the walls of chest and abdomen. Our preliminary results show that HIFU could achieve a good result for patients with malignant tumors located in the walls of chest and abdomen if it is a focal tumor, even if it was complicated by rib metastasis. HIFU would be one good choice for these patients in advanced stage to inhibit tumor enlargement and to achieve better quality of life. Key Words: malignant tumors, HIFU, chest wall, metastasis, intercostal neuralgia.

INTRODUCTION

The incidence of primary tumor of walls of chest and abdomen is limited; most tumors located within the chest and abdomen walls are distance metastases or local invasions of malignant tumors. Usually they occur during or after anti-cancer treatments, and the conditions of the patients is usually complex, with varying local structures near each tumor and differing tumor biological behavior. Tumors in

advanced stages located in the wall of chest and abdomen in 10 patients were treated by HIFU in our hospital; this report reviews the therapeutic effect.

MATERIALS AND METHODS

From February 2001 to March 2002, 59 patients received extracorporeal HIFU treatment for malignant tumors in our hospital. Tumors in the walls of the chest and the abdomen were treated in 10 patients. Six men and 4 women, mean age 52, range 19 to 79 years, were treated. One case was a local recurrence; metastases or local invasions comprised 9 cases. The tumor size was 3 cm–5 cm in 4, 5 cm–8 cm in 3, and above 8 cm in 4. Multiple tumors were present in 8 cases. Patients received surgical resection before HIFU in 8 patients, radiotherapy in 7, and chemotherapy in 7. Seven patients had received two kinds of anti-cancer treatments before HIFU. The diagnoses of all patients were proved by cellular pathology. Three patients were complicated with severe intercostal neuralgia. All patients signed informed consent forms before treatment in accordance with the specification stipulated by the Helsinki Committee.

Preoperative clinical assessment was the same as for surgical patients. Three HIFU treatments were given in 1 case, 3 to 4 weeks apart, two HIFU treatments in 1 case, and only one HIFU treatment in the others. All the patients were given follow-up after HIFU treatment. Because patients were in advanced stages, we evaluated the results of HIFU treatment at 3 to 6 months after HIFU treatment. Five patients continued to receive chemotherapy after HIFU according to individual conditions.

The HIFU therapeutic system was designed by Chongqing Haifu Co. Ltd., China. The ultrasound beam was produced by a 12-cm diameter piezoelectric ceramic transducer PZT-4 with a focal length from 135 mm to 105 mm, operating at a frequency of 0.8 MHz. A 3.5 MHz diagnostic ultrasound scanner was used for guiding the targeting during HIFU treatment. The beams of the therapeutic transducer and diagnostic scanner completely overlaid each other and were moved together under computer control. The output acoustical power was from 8750W/cm2 to 17850W/cm2.

The HIFU treatment was performed as described in (1).

RESULTS

Patient characteristics are shown in Table 1. The entire tumor was treated by HIFU in 5 cases, and partial tumor treatment occurred in 5 cases, because of large tumor size, presence of multiple tumors, or tumor partly located beyond the reach of ultrasound therapy. A partial response was observed in 2 patients (Fig. 1 and Fig. 2), a minor response in 1, stable disease in 4, and progressive disease in 2, at 3 to 6 months after HIFU treatment. The patient with 0.57 FEV1.0/L of lung function smoothly recovered following the HIFU treatment (Fig. 3). Rib metastasis shown by bone scan in one patient before HIFU disappeared after the treatment (Fig.4). All 3 patients with intercostal neuralgia did not need analgesic medicine after HIFU treatment. In 2 patients with progressive disease (tumor sizes were > 8 cm in both), one patient with a

metastatic tumor (8 cm x 10 cm2) near the clavicle from breast cancer, had to receive partial HIFU treatment because of breathing problems during the operation. The other patient with recurrent tumor (12 cm x 8 cm2) of malignant fibrous histiocytoma within the right chest was scheduled to receive 2 HIFU treatments. A skin burn occurred after the first HIFU treatment, and we had to cancel the second HIFU treatment. Although the patient received 3 treatments of radiotherapy after HIFU, he died of respiration impairment 5 months later. All others were alive until June 2002 with follow up of 3 – 15 months.

TABLE 1. The situation of advanced tumors located in the wall of chest and abdomen with HIFU treatment.

No.	Sex	Age	Site	Primary Ca	Multiple	Therapy	T N M	Cover	Follow-up
1	M	45	ab	colon	yes	O	T3N2M1	yes	miss
2	F	19	ch	fibrosarcoma	no	O,R	G1T2N0M0	yes	PR
3	M	33	ch	esophagus	no	O,R,C	T3N1M1	no	SD
4	F	60	ch	lung	yes	C	T4N1M1	no	SD
5	M	70	ch	lung	no	C	T4N0M0	yes	MD
6	F	47	ch	mfh	yes	O,R	GXT2N0M1	yes	PR
7	M	49	ch	mfh	yes	O,R	G3T2N0M1	no	PD
8	F	68	ch	breast	yes	O,R.C	T4N3M1	no	PD
9	M	53	ch	lung	yes	O,R,C	T4N2M1	no	SD
10	F	79	ab	liver	yes	C	T3N0M1	yes	SD

ab=abdomen; ch=chest; cover=entire tumor was treated by HIFU; malignant fibrous histiocytoma
O=surgical operation; R=radiotherapy; C=chemotherapy

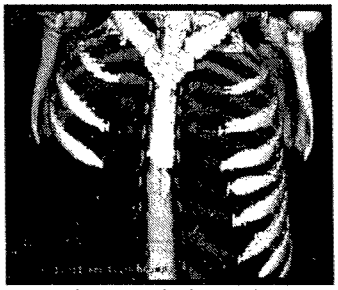

2 times surgical resections

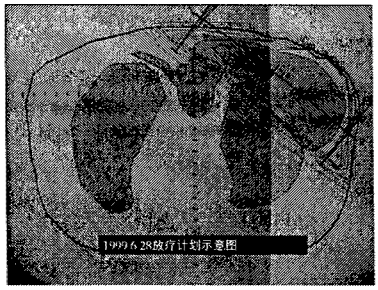

Radiotherapy

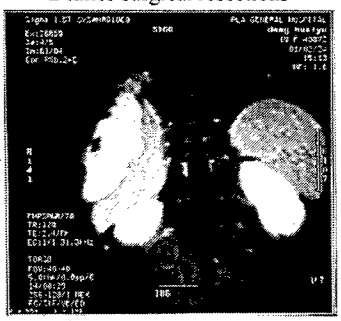

Before the treatment of HIFU

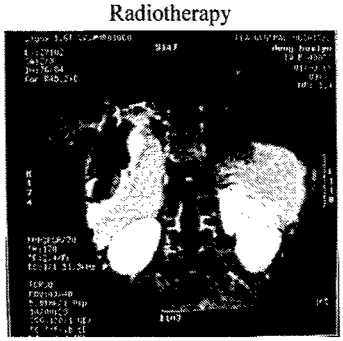

After the treatment of HIFU

FIGURE 1. Case 2, malignant fibrosarcoma recurrence located in the left wall of the chest after 2 surgical resections. After HIFU treatment, an MRI showed tumor site devitalization.

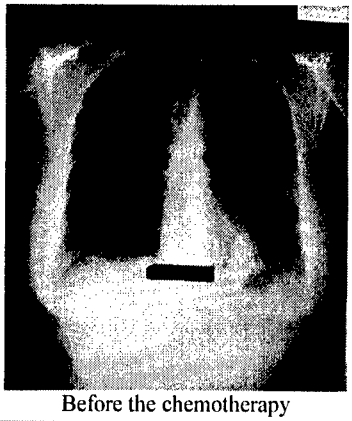

Before the chemotherapy

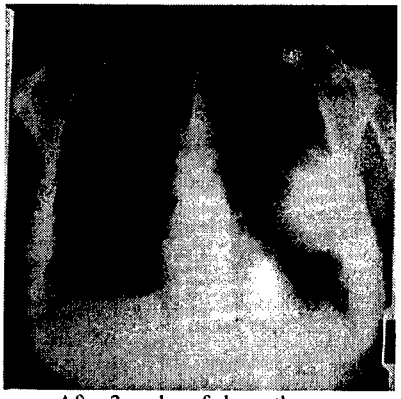

After 2 cycles of chemotherapy

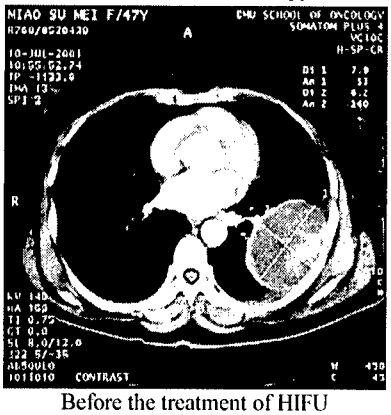

Before the treatment of HIFU

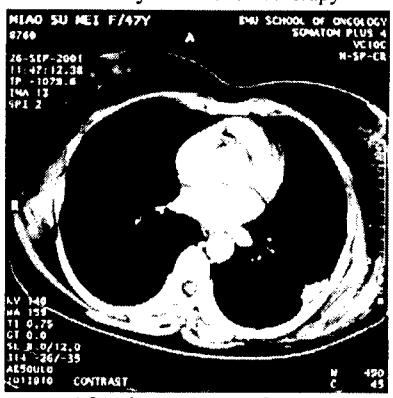

After the treatment of HIFU

FIGURE 2. Case 6, Malignant fibrous histocytoma after 2 cycle chemotherapy, tumor is enlarged before the treatment of HIFU. After HIFU treatment, CT showed that most of the tumor had disappeared.

DISCUSSION

As one form of thermal ablation therapy, HIFU has been reported in the treatment of hepatic, breast, and bone tumors, as well as soft tissue sarcomas (1). Promising results have received much attention for focal malignant tumors (2,3,4). Because the sites and variety of biological behaviors of solid tumors, combination therapy is often used for most cancer patients. Since the mechanism of HIFU to destroy tumor cell by cytotoxic heat is different from surgery, radiation, or chemotherapy (5,6), HIFU should play a special role in anti-cancer treatments (7,8).

It is a difficult to cure malignant tumors located in the wall of the chest and abdomen, especially after surgical or radiological treatments. HIFU has a special effect on such tumors, the reasons may be that more tumor is located near the skin, and more power is focused on the tumor, compared with tumors far from the skin. We know that some ultrasound power is "wasted" before it reaches its target, the site of tumors. Second, lung tissue, which is backed by air and lies against the tumor within the chest wall, can serve as a "rebound plane"—ultrasound will be reflected off the

lung tissue. Rebound ultrasound will be focused on the tumor consequently, and thus we believe one treatment will have "twice" the effect.

Some tumors located in the walls of the chest and abdomen were complicated with intercostal neuralgia, i.e. invasion with the intercostal nerve and/or rib metastases. While HIFU destroyed the tumors, the intercostal nerve and rib metastasis would be "treated" at the same time. All of 3 patients with intercostal neuralgia felt no pain, and none needed analgesic medicine. Rib metastasis was cured effectively if it is focal after HIFU treatment (Fig 4). In case 2, the patients had 2 surgical resections, with many ribs cut off, to "open" a "window" to allow more focused ultrasound to reach the tumor site. In this condition, patients have better results than those with "normal" ribs (Fig 1). In case 5, a patient suffered from chronic bronchitis, severe emphysema and bronchiectasis; the FEV1.0L was only 0.57 (normal 2.0). He could not receive any surgical or radiological treatment because of respiration impairment. However, he recovered smoothly following HIFU treatment, with good results (Fig 3). Compared with routing anti-cancer treatment, HIFU can play an important role in these advanced cancer patients.

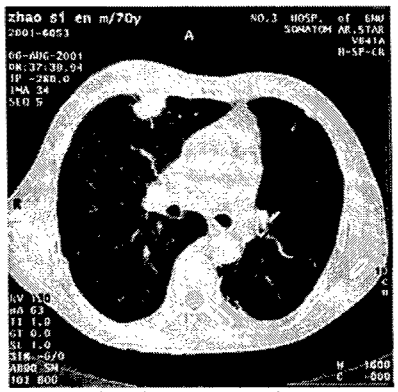

Before the treatment of HIFU

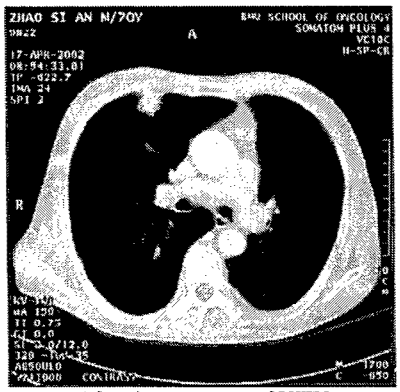

After the treatment of HIFU

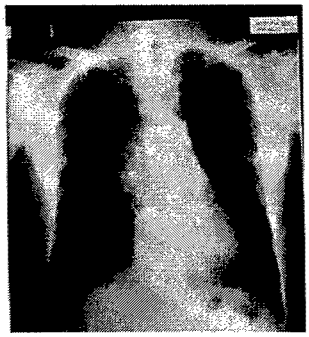

Before the HIFU treatment
Severe pulmonary emphysema

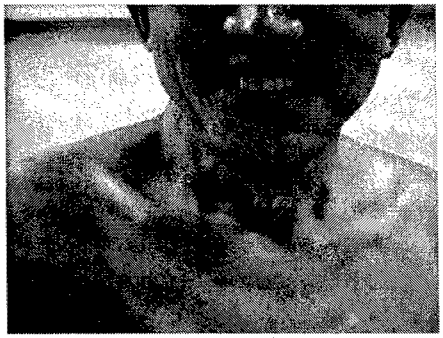

The first day after the HIFU
labored breathing

FIGURE 3. Case 5, lung adenocarcinoma with severe pulmonary emphysema and abnormal lung function. He could not receive surgical or radiological treatments. Patient recovered smoothly and CT showed tumor minor response after HIFU treatment

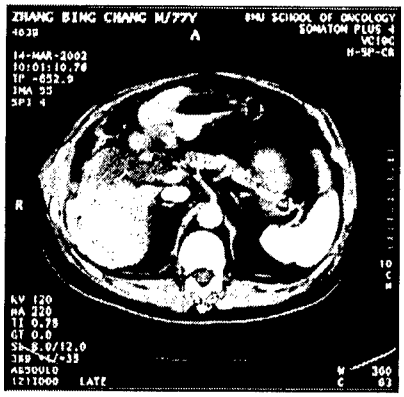

Liver cancer, right lobe of liver. After 8 times of intraarterial embolization. local abdomen wall was invasive with rib metastasis by liver cancer.

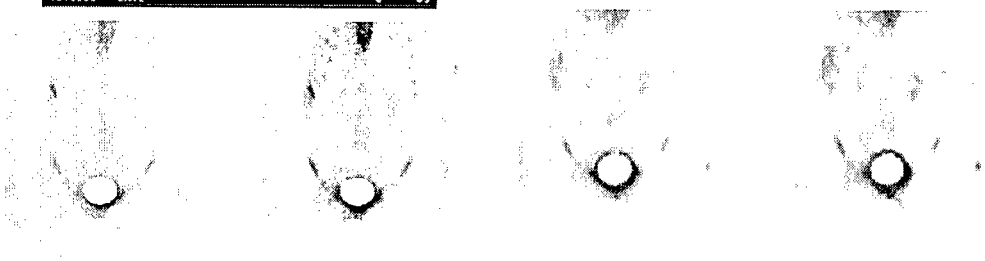

Bone scan before the HIFU

Six days after the HIFU treatment
Local signal noise since its swelling

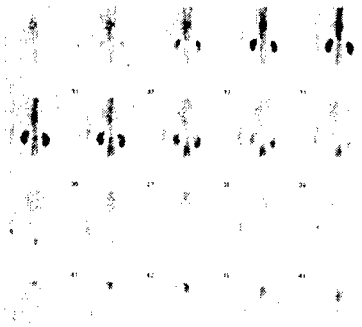

The section bone scan showed no sign of bone metastasis.

FIGURE 4. Case 10, liver cancer with local abdomen wall invasion and rib metastasis.

HIFU treatment results in this group were not impressive. Because most patients were in advanced stages, more than half of them received other therapies before the HIFU treatment, had multiple tumors, had biological behavior of recurrent or metastases tumors, complex conditions, or big tumor volume. However, some did get hopeful results and better life qualities.

It is suggested that HIFU could achieve good results for patients with malignant tumors located in the walls of chest and abdomen if they have a focal tumor, and even

if it is complicated by rib metastasis. HIFU would be a good choice to inhibit tumor growth in these advanced stage patients.

REFERENCES

1. Wu, F., Chen, W.Z., Bai, J., et al., "Pathological changes in human malignant carcinoma treated with high-intensity focused ultrasound," *Ultrasound in Med. & Biol.*, **27** (8), 1099-1106 (2001).
2. Goldberg, S.N., Gazelle, G.S., Mueller, P.R., "Thermal ablation therapy for focal malignancy: a unified approach to underlying principles, techniques, and diagnostic imaging guidance, *AJR*, **174**, 322-331 (2000).
3. Haaga, J. "Imaging-guided microsurgery and the future of radiology," *AJR*, **17**, 303-304 (2000).
4. Thuroff, S., Chaussy, C., "High-intensity focused ultrasound: complications and adverse events," *Mol Urol*, **4**, 183-187 (2000).
5. ter Haar, G., "High intensity focused ultrasound for the treatment of tumors," *Echocardiography*, **18**, 317-322 (2001).
6. Uchida, T., Sanghvi, N.T., Gardner, T.A., et al., "Transrectal high-intensity focused ultrasound for treatment of patients with stage T1b-2n0m0 localized prostate cancer: a preliminary report," *Urology*, **59**, 394-398 (2002).
7. Harvey, C.J., Pilcher, J.M., Eckersley, R.J., et al., "Advances in ultrasound." *Clin Radiol*, **57**, 157-177 (2002).
8. Kallel F, Stafford RJ, Price RE, et al., "The feasibility of elastographic visualization of HIFU-induced thermal lesions in soft tissues," *Ultrasound Med Biol*, **25**, 641-647 (1999).

Clinical Study On The Extracorporeal Ablation Of Breast Cancer With High Intensity Focused Ultrasound

Zhu Hui[1], Wu Feng[1], Chen Wenzhi[1], Cao Youde[2],
Yu Yongkang[1], Bai Jin[2], Wang Zhibiao[2]

[1]Clinical Center for Tumor Therapy, 2nd Affiliated Hospital of Chongqing University of Medical Sciences, Chongqing 400010, China
[2]Institute of Ultrasonic Engineering in Medicine of Chongqing University of Medical Sciences, Chongqing 400016, China
Correspondence to: Dr. Zhu Hui, Clinical Center for Tumor Therapy, 2nd Affiliated Hospital of Chongqing University of Medical Sciences, 76 Linjiang Rd., Yuzhong Dist. Chongqing 400010, P. R. China (clinical@haifu.com.cn)

Abstract. Objective The aim of this paper is to explore the possible role of High Intensity Focused Ultrasound (HIFU) plays in conservative treatment of breast cancer, and to select prospective evaluation means for HIFU ablation in clinical practice. Methods HIFU treatment was performed in 16 patients with breast cancer. ^{99m}Tc-MIBI ECT and MRI examinations were performed before and after HIFU treatment. All the patients underwent follow-up (mean time 30 months). Results During the period of follow-up, significant shrinkage of treated tumor was observed in 15 patients. Local recurrence was found in 1 patient 18 months after HIFU ablation. The external appearance of sick breast in 15 patients was kept well during follow-up period. Among them, a complete disappearance of treated-tumor was found in 3 patients, more than 75% shrinkage of treated tumor was observed in 11 patients. Only one patient had less than 50% shrinkage of treated-tumor. ^{99m}Tc-MIBI ECT and MRI examination showed no radioisotope uptake and no blood supply within treated tissue. Conclusion HIFU is safe and effecitive in the treatment of patients with breast cancer. It can provide a local non-invasive therapy in breast-conservative treatment. Key Words High intensity focused ultrasound (HIFU), breast cancer, and conservative treatment

INTRODUCTION

From August 1997 to February 2000, our center carried on clinical practice and research work on extracorporeal ablation of breast cancer with High Intensity Focused Ultrasound (HIFU). The purpose was to explore the possible role of HIFU in conservative treatment of breast cancer.

MATERIALS AND METHODS

Sixteen female patients, aged 36-62 (mean 46.5) years old, were all diagnosed suffering with breast cancer by pathological examination. The tumor masses were

2 cm to 4.8 cm in diameter with an average of 3.1 cm. In six cases, there was tumefaction of homogeneous axillary lymphatic nodes. One of these was accompanied by tumefaction of homogeneous clavicle superior lymphatic nodes. In 6 cases, 3 underwent simple lymphadenectomy after HIFU treatment; the other 3 patients refused surgery and received only radiotherapy of regional lymph nodes. In all 16 patients, 4 were in stage I, 8 were in stage II_A, 3 were in stage II_B, and 1 was in stage IV.

A model JC focused ultrasound tumor therapeutic system, developed by Chongqing Haifu (HIFU) Technology Co., Ltd. and the Institute of Ultrasonic Engineering in Medicine of Chongqing University of Medical Sciences, was used. This system comprises a combined treatment head, a localizing and monitoring system, a 4-dimension motion device, and two water treatment systems. The whole HIFU system is under computer control. It can perform the following functions: localizing tumor focus, ablating targeted tumor focus with 3D focused scanning beam, monitoring and analyzing therapeutic effects in real time, and controlling therapeutic dosage according to the feedback data. The therapeutic parameters are physical focal length of 2 mm × 2 mm × 8 mm, focal peak intensity (sound power) of 10,054 W/cm^2, and frequency of 0.8 MHz. Each tumor and the marginal tissue 2 cm around it ablated extracorporeally by successive scanning of focused ultrasound beams, with an average treatment time of 3,600 seconds.

CDFI examination was used in all patients before and after HIFU treatment. Large-core needle biopsy was also performed on all patients at 1 month, 3 months, a half year, and 1 year after HIFU treatment. Examinations of chest X-ray, abdominal B-ultrasound and total body ^{99m}Tc-MDP ECT were made regularly. In the 16 patients, 4 had ^{99m}Tc-MIBI ECT examinations before and after HIFU treatment, 1 had MRI examination before and after HIFU treatment, and 1 had two PET examinations after HIFU treatment.

RESULTS

After HIFU treatment, the skin of the treated breasts remained health and only had an appearance of soft tissue tumefaction in treated area. The vital signs were steady during and after HIFU treatment. Six patients with a low temperature (<38°C) within a short time after HIFU treatment gradually became normal without any special management. Of 3 patients receiving simple axillary lymphadenectomy, 2 were found to have metastatic tumors by pathological examination (4/12,1/14); 1 had reactive hyperplasia in the lymph nodes (0/8).

All the patients had follow-up after HIFU treatment, with a different period ranging from 18-40 months and an average of 28 months. Physical examination and B-mode Ultrasound imaging changes verified that the treated mass gradually shrank and became thinner. Disappearance of tumor lesion was found in 3 patients. Large-core needle biopsy at different times after HIFU treatment showed the targeted tissue with coagulated necrosis had been gradually replaced by hyperplasia of fiber connective tissue, that then grew to mature fiber connective tissue (Fig.1). The function of the upper limb in the sick side was normal in 3 patients after simple axillary

lymphadenectomy. Three patients receiving radiotherapy of local lymph node had a follow-up lasting 24-30 months, which showed that axillary lymph nodes had been in a stable state. Compared with normal breast, the sick breast after HIFU treatment remained healthy in appearance and elasticity.

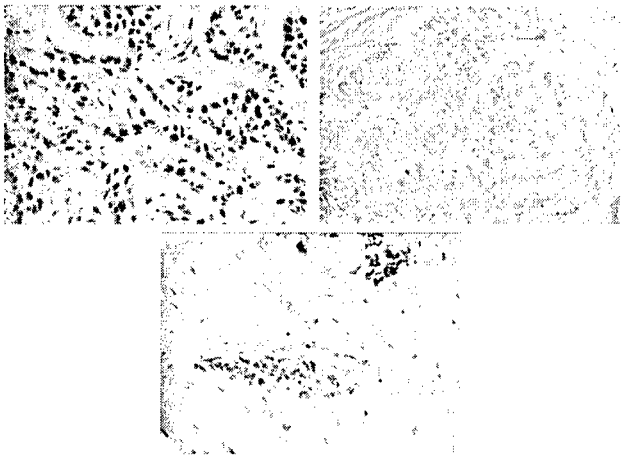

FIGURE 1. Pathological changes of breast cancer after HIFU treatment (× 100).

^{99m}Tc-MIBI ECT examinations on 4 patients before HIFU treatment showed abnormal radioactivity uptake at the tumor site. After HIFU treatment, it disappeared. Enhanced MRI showed there was no blood supply in targeted region. After HIFU treatment, the treated region covered tumor site and a margin (Fig. 2). Two PET examinations on 1 patient showed that there was no tumor stain.

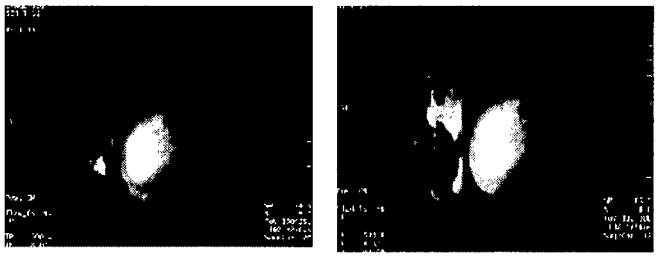

Figure 2. T-enhanced MRI of breast cancer before and after HIFU treatment 2.

One patient was found to have gradual shrinkage of the tumor mass within a period of time after HIFU treatment. However, eighteen months after HIFU treatment, the tumor mass enlarged and had possible local recurrence. Modified radical mastectomy was performed. Pathological examination on excised tissue indicated local recurrence.

DISCUSSION

Surgical operation is the major means for breast cancer treatment. Halsted established the radical mastectomy in 1894, and it has been considered the standard operation for breast cancer from then on. Since the 1960's, with a developing understanding of the biological features of tumors, physicians have realized that breast cancer is a kind of systemic disease and all kinds of surgical operations with different styles are only a means of local treatment. Breast conservative treatment thus became the trend of treatment for early stage breast cancer (Veronesi, 1995).

High intensity focused ultrasound (HIFU) is a newly developed technique for extracorporeal tumor treatment (Hill, 1995). Because ultrasound beams can be focused and transmitted in solid biological tissues, this makes it possible to use an external therapeutic source of ultrasound to induce a high-energy volume within the body. Temperature at the targeted volume is instantaneously elevated to 65° C or more. However, there are no significant temperature changes outside the targeted region (Clarke, 1997). Thus, tissue at the target region is destroyed by heat and cavitation, and coagulative necrosis results. Numerous animal trials and preliminary clinical studies have proven that HIFU can extracorporeally ablate transplanted liver carcinoma (Van Leenders, 2000), bladder cancer (Holland, 1985), and breast cancer effectively and safely.

Multi-focus breast cancer was believed the absolute contraindication of conservative treatment for breast cancer (Fisher, 1985). It was considered that the morbidity of multi-focus was more common than that of central-focus in breast cancer from the research done by Holland. When the tumor size is not more than 4 cm, the focus was usually concentrated in a 2 cm region at the center. The key point to decreasing the recurrence rate was to keep the incisal margin negative. However, to patients receiving radiotherapy after surgery while still having a small quantity of viable tumor foci at the incisal margin, there still was a low local recurrence rate. Among 16 patients treated in this study, 1 had a local recurrence after HIFU treatment. This was possibly related to the difficulty in identifying large-ranged focus with B-Ultrasound, or the treated region not covering the tumor focus completely.

Conservative treatment for breast cancer is composed of treatments for two parts: breast and axilla. Fisher and his colleagues (1985) thought that axillary lymphadenectomy could be performed with breast conservative therapy simultaneously, and could be also performed when tumefaction of lymph nodes were found in the follow-up period. The two kinds of treatments mentioned above had the same therapeutic effects without any difference of survival rate.

Evaluation of the therapeutic effects was very important after HIFU treatment. Currently it is believed that using Magnetic Resonance Imaging (MRI) and Positron Emission Tomography (PET) are more beneficial to observe the differences of blood-supply, signals and isotope uptake, and to judge the survival of the tissue in targeted area. This is supported by the cases and the follow-up results of the study presented in this paper. However, more cases and longer follow-up are needed for verification.

CONCLUSION

It was concluded from our research that HIFU could extracorporeally ablate breast cancer of different sizes and shapes completely under a real-time monitoring with diagnostic ultrasound according to surgical principle. In the follow-up period, we found HIFU can effectively damage the tumor focus, which was absorbed gradually after HIFU treatment. There were no significant differences between normal breast and HIFU-treated breast in appearance and elasticity. It was demonstrated that HIFU has an extensive prospect in breast conservative treatment.

REFERENCES

1. Clarke, R.L., ter Haar, G.R., "Temperature rise recorded during lesion formation by high-intensity focused ultrasound," *Ultrasound Med Biol*, **23** (2), 299-306 (1997).
2. Fisher, B., Redmond, C., Fisher, E., et al., "Ten year results of a randomized clinical trial comparing radical mastectomy and total mastectomy with or without radiation," *N Engl J Med*, **312** (1), 674-681 (1985).
3. Hill,, C.R., ter Haar, G.R., "High intensity focused ultrasound potential for cancer teatment," *Br J Radio*, **68** (816), 1296-1303 (1995), *J Clin Pathol*, **53** (5), 391-394 (2000).
4. Holland, R., Veling, S., Mravunac, M., et al., "Histologic multifocality of Tis, T1-2 breast carcinoma. Implications for clinical trials of breast-conservation surgery," *Cancer*, **56** (5), 979-990 (1985).
5. Kambiz, D., Ming, F., et al., "Stereotactically guided laser therapy of occult breast tumor," *Arch Surg*, **135**, 1345-1352 (2000).
6. Mumtaz, H., Hall-Craggs, M.A., Wotherspoon, A., et al., "Laser therapy for breast cancer: MR imaging and histopathological correlation," *Radiology*, **200** (3), 651-658 (1996).
7. Schnitt, S., Connolly, J., Knettry, U., et al., "Pathologic findings on re-excision of the primary site in breast cancer patients considered for treatment by primary radiation therapy," *Cancer*, **59** (4), 675-681 (1987).
8. Van Leenders, G.J., Beerlage, H.P., Ruijter, E.T., et al., "Histopathological changes associated with high intensity focused ultrasound (HIFU) treatment for localised adenocarcinoma of the prostate," *J Clin Pathology*, **53** (5), 391-394 (2000).
9. Veronesi, U., Salvador, B., Luini, A., et al., "Breast conservation is a safe method in patients with small cancer of the breast. Long-term results of three randomised trials on 1973 patients, *Eur J Cancer*, **31A** (10), 1574-1579 (1995).

Experimental Study Of Injury To Rabbit Stomach Wall With High Intensity Focused Ultrasound

Zou Jianzhong[1], Lu Min[2], He Xuemei[1], Bai Jin[1], Wu Feng[1], Wang Zhibiao[1]

[2]*Sonographic Imaging Department and* [1]*Clinical Center for Tumor Therapy of 2nd Affiliated Hospital, Chongqing University of Medical Sciences, Chongqing 400010, P R China*
Correspondence to Dr. Zou Jianzhong, Box 153, 1 Yixueyuan Rd., Yuzhong District, Chongqing 400016, P. R. China

Abstract. Purpose In this study, we irradiated the rabbit stomach wall with ultrasound beams of the same intensities and exposing methods used in clinics. The subject of this paper is to investigate the safety of routine HIFU treatment by studying possible injury of rabbit stomach wall after HIFU. Materials and Methods Twenty New Zealand rabbits were randomly divided into ten groups with two rabbits in each. Both rabbits in each group received the same radiation. After each experiment, one rabbit was euthanized for pathological examination and the other retained for survival follow-up. During the experiment, ultrasound images were used to monitor the progress. Results Experimental rabbits showed their unease during treatment and became feckless after HIFU. The control rabbits for survival follow-up died 1-7 days after HIFU. Pathological and imaging changes showed that the stomach wall tissue became acutely necrotic. The tissue structure and blood vessels were destroyed irrevocably. The stomach wall of experiment rabbits was easy to injure. Conclusion This study showed that the acoustic intensity used in routine HIFU treatment can cause injury to the stomach wall, which generally leads to necrosis or perforation of stomach. It could be a serious complication occurring during the treatment to malignant tumors located in the liver, pancreas, kidney, and peritoneal or celiac organs. Therefore, it is important for us to learn about the possible injuries to the surrounding structures and organs during treatment of tumors with HIFU, and how to avoid such injuries.
Keywords: high intensity focused ultrasound, HIFU, rabbit, stomach

INTRODUCTION

As an emerging modality for noninvasive tumor treatment, high intensity focused ultrasound (HIFU) has been gradually applied in clinical use in recent years. For example, it can be utilized to treat either benign or malignant tumors and its effectiveness has been widely recognized. Nevertheless, safety and efficacy are of the same significance to any medical approach. To avoid accidents and to minimize clinical complications, it is valuable to learn more about the degree, extent and characteristics of coagulative necrosis induced by HIFU (Wu et al, 2002) in a routine HIFU procedure. The incidence rate of injury to gastrointestinal ducts seems greater than that of any other accident or complication. In this study, we duplicated the exposure modes and focal peak intensities used in the clinic to irradiate targeted rabbit

stomach wall. During treatment, real-time ultrasound image changes were monitored, and pathological examination after treatment was performed to study the induced lesions. This was done in the hope that we could assess the characteristics and degree of possible injury to the stomach wall caused with routine HIFU, and further study the clinical safety of HIFU.

MATERIALS AND METHODS

Research Objects

Twenty New Zealand rabbits, with mean weight of 2.2 kg and provided by the Experimental Animal Center of Chongqing University of Medical Sciences, were divided into ten groups with two rabbits in each. For each group, rabbits received the same radiation; one was euthanized to obtain a stomach wall sample for pathological examination and the other retained for survival follow-up study. The latter was not fed 8 hours after the operation.

Instrument And Methods

A model-JC focused ultrasound tumor therapeutic system was used, which was developed and manufactured by Chongqing Haifu (HIFU) Technology Co. Ltd. based in Chongqing, China. This system, composed of a 3D conformal scanning device and a real-time ultrasound image monitoring device, is able to predetermine the target region, outline a treatment bound, conduct a 3D conformal treatment, monitor and evaluate therapeutic effects in real time, and provide feedback to and control of the therapeutic effects.

In this study, a 1.6 MHz transducer, 150 mm in diameter, 120 mm focal length, was used. Its mean focal volume was 2 mm in diameter and 6 mm in length. Its focal surface was 79 mm in height. The focal peak intensity of this transducer was 309.8 ± 136.5W. The exposure mode adopted in this study was linear scanning, for which the line was 2 cm in length, scanning speed was 3 mm/s and mean tissue depth was 3 cm.

HIFU Procedures

Experimental rabbits were inhibited from feeding 12 hours before HIFU procedures and denuded at the chest and abdominal parts including breastbone, xiphoid and lower abdominal skin. We degreased and dewatered this region with ethanol. Two to three milliliters 10% animal anesthetic vein injection were given.

After placing the rabbit in a prone position, we set the θ-motion device at a 90° angle and obtained a longitudinal ultrasound image, trying to display the left lobe of the liver and stomach wall in one image. An experiment was performed using a clear image with stomach wall and liver as the treatment slice. Linear scanning mode was adopted to irradiate the stomach wall and liver, covering 1 cm for each (see Fig. 1).

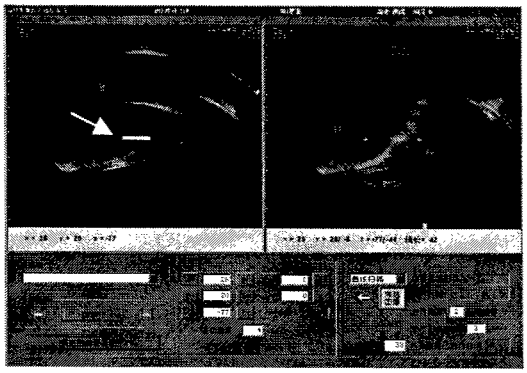

FIGURE 1. The line (see arrow) on image indicates the scanning position and scope. The left image shows the line lies between liver and stomach before exposure. The right one shows there was a hyperechoic region after exposure.

During ultrasound exposure, B mode ultrasound images were used to monitor injury caused at the target, and to feedback and control the exposure dose according to the image changes. The ultrasound images acquired before, during and after exposure were analyzed for gray scale changes and saved (see Fig. 2).

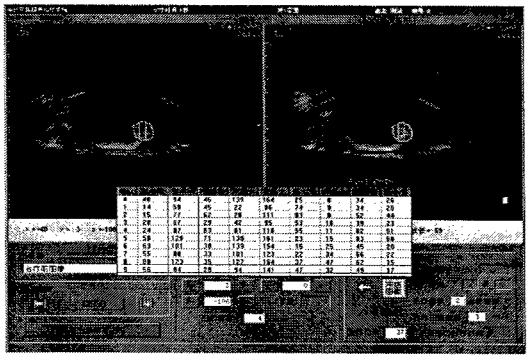

FIGURE 2. The gray scale changes before and after exposure. The left were values before and right were after. Gray scale values contrast before and after the procedure were listed in the form.

Follow-Up After Procedures

We observed general conditions of experimental rabbits after procedures. One rabbit was autopsied for visual inspection, and the stomach tissue sample was excised for pathological examination. The other rabbit in same group survived and died spontaneously. We also autopsied it for visual inspection and pathological examination after its death.

RESULTS

General Behavior Of Experimental Rabbits

Generally, the rabbits showed their unease during HIFU procedures and became feckless and weak after that. The surviving rabbits died spontaneously 1-7 days after HIFU.

Ultrasound Imaging Monitoring

Distinct echo enhancement in the exposed stomach wall and liver tissue was observed on an ultrasound image immediately after HIFU. The appearance of the stomach wall changed obviously and the tissue was destroyed continuously. The margin between stomach wall and liver turned unclear and irregular (see Fig. 3).

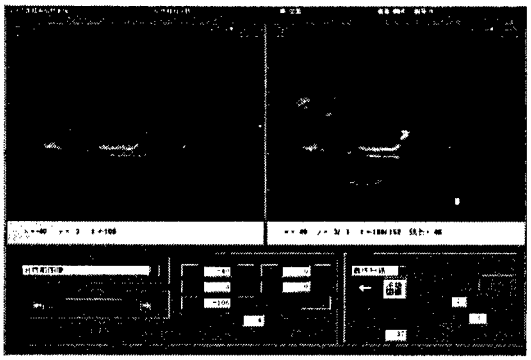

FIGURE 3. Distinct echo enhancement was observed immediately after HIFU exposure on target stomach wall and liver.

The gray scale differences before and after HIFU were 25.4 ± 8 (see Fig. 4).

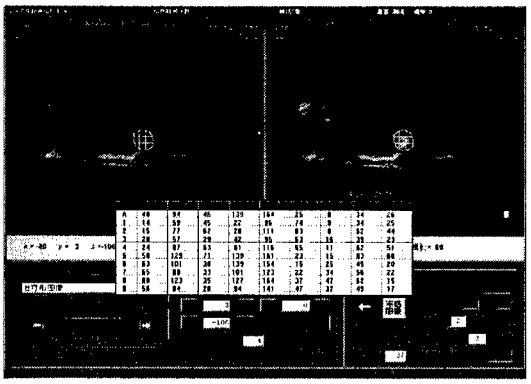

FIGURE 4. The quantitative analysis of echo intensity changes after HIFU exposure at target.

Pathological Examination Of Autopsied Sample

We autopsied the rabbit immediately after exposure and found obvious injury to the targeted stomach wall and liver tissue. The stomach wall lesion appeared a gray-white color with a clear hematose boundary. Blood vessels of stomach wall serosa distention was observed with a wine or brown color. The exposed liver tissue revealed coagulative necrosis with a clear hematose boundary as well (see Fig. 5). The stomach wall tissue became tough and the seroca surface touched concavo-convex; the mucosa surface appeared black in color and was likely to become necrotic and perforated (see Fig. 6 and 7).

Rabbits in the survival group suffered from stomach perforation within 1 to 6 days after HIFU and subsequently died (see Fig. 8).

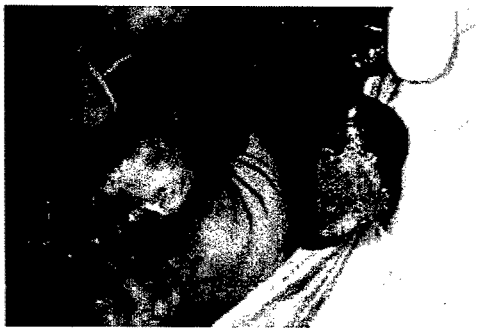

FIGURE 5. Stomach wall and liver tissue at target.

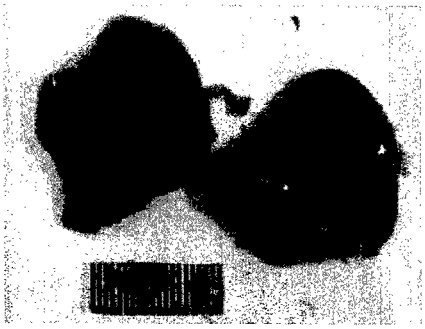

FIGURE 6 Stomach wall tissue at target, the left showed mucosa surface and the right serosa, surface.

FIGURE 7. The mucosa surface was likely to become necrotic and perforated.

FIGURE 8. The stomach perforation after HIFU.

Under light microscope, we observed that the stomach wall was destroyed completely from the mucosa, mucosa lower layer, muscle layer and serosa; mucosa epithelial cells and gastric gland cells fell into disorder and cells vacuolized obviously (see Fig. 9). The nuclei of stomach cells became pyknotic, lytic and resolved, and the nucleolus turned unclear or disappeared (see Fig. 10). The smooth muscle cells fell into disorder, the endothelial cells of blood vessels were destroyed and the vascular wall collapsed (see Fig. 11).

FIGURE 9. The mucosa of stomach wall vacuolized and fell into disorder.

FIGURE 10. Under light microscope, tissue vacuolization and cell granulation was found. The cell nuclei became pyknotic and lystic with an unclear nucleolus.

FIGURE 11. The normal structure of stomach wall serosa and blood vessels were destroyed and tissue vacuolization was found.

DISCUSSION

At Megahertz frequencies, ultrasound can penetrate deep into biological tissues. Beam focusing and energy deposition in tissue can easily be controlled. Therefore, low energy ultrasound can be focused at a target in vivo to form a high-energy region, where hyperthermia due to ultrasound energy deposition induces coagulative necrosis. As a novel option for the treatment of tumors, HIFU gradually has been introduced to clinics. Doctors and scientists are also exploring its applications step by step; in the meantime, to its every specific use, the clinical effects and safety should be deeply and cautiously studied in order to avoid accidents and to minimize complications (Feng, 1999).

When treating malignant tumors located in the liver, pancreas, kidney, abdominal cavity and peritoneum with HIFU, injury to and even perforation of the stomach is one of the most severe clinical complications that has occurred. Some factors are possibly relevant to this, such as identification of target tissue to be treated, accuracy of intraoperative ultrasound monitoring, control and feedback of the therapeutic dose and choice of therapeutic plan. The failure to deal with these factors properly will cause stomach injury in HIFU treatment.

In this study, exposure methods and intensities simulating a clinical application have been used to irradiate the rabbit stomach wall. Intraoperative ultrasound monitoring and pathological examination after HIFU verified that the dose of routine HIFU treatment is able to cause injury to the stomach wall, and even perforation. This is because, as a larger structure in the human body, the stomach lies very close to the target region and is easily injured by direct sound beams or sound reflections.

One experimental rabbit in this study suffered from paragastric wall and adjacent intestinal wall injury besides stomach wall injury after HIFU, and finally died from intestine and stomach perforation. This may be caused by ultrasound refraction or reflection from the stomach wall or other effective interfaces, which leads to injury of paragastric wall and adjacent intestinal wall. It implies that a doctor, before starting to treat a patient with HIFU, should attach much attention and awareness of the surrounding tissues and structures of the target.

Therefore, to avoid the stomach injury, a doctor must identify the tumor focus and its boundary accurately, be familiar with its correlation with surrounding organs and structures, and prepare a sufficient and effective therapeutic plan. Moreover, the ultrasound monitoring images should be precisely analyzed.

We found that the injury to the stomach wall was ellipsoidal. The long axis of the lesion was perpendicular to the direction of linear scanning, *i.e.*, the diameter of the lesion parallel to the scanning direction was less than that in the direction perpendicular to the scan. The mechanisms by which this result arose are not yet clear.

REFERENCES

1. Wu, F., Wang, Z.B., Chen, W.Z., et al., "Clinical Safety Study of Extracorporeal Treatment of Malignant Tumors with High Intensity Focused Ultrasound," *China Journal of Ultrasound in Medicine*, **10**, 213-215 (2002).
2. Feng, R., "Uprising of Noninvasive High Intensity Focused Ultrasound Surgery," *Journal of Clinical Ultrasound in Medicine*, **1** (2), 65-67 (1999).

The Ultrasound Treatment Of Dystrophy Of Vulva: A Clinical Pathological Report Of Forty-One Cases

Li Chengzhi, Wang Zhibiao, Ruan Xiangyan, Chen Wenzhi

Institute of Ultrasound Engineering in Medicine, Chongqing University of Medical Sciences
Correspondence to Li Chengzhi, Institute of Ultrasound Engineering in Medicine, Chongqing University of Medical Sciences 1Yixueyuan Rd., Yuzhong District, Chongqing 400016, P. R. China,

Abstract. Objective: This study was undertaken to investigate the clinical pathological changes of the dystrophy of vulva after Ultrasound Treatment. Methods: Forty-one women patients, who had the pathological diagnosis of dystrophy of vulva, were study objects. They were divided into two groups randomly. Twenty-one received ultrasound treatment, and the others were treated with Spectrum. Results: The patients in the ultrasound treatment group recovered. In a follow-up of two years, the symptom of vulva pruritus of patients was resolved. The pathological changes indicated that the stratified squamous epithelium of the vulva had recovered normal stratification and thickness. And the basal layer had deposited pigment cells. The patients in the Spectrum group quickly developed recurrences after treatment. Conclusions: This study demonstrates that as a new noninvasive treatment technology, Ultrasound Treatment provides a new method for clinical treatment of dystrophy of vulva. Key words: Ultrasound treatment, dystrophy of vulva, pathological change.

INTRODUCTION

Vulva dystrophy is one of the most common gynecologic diseases in elderly women. It is a chronic cutaneous mucosa disease of the female external genitalia, which leads to the disorder in the growth of epidermis tissues and degeneration of dermis. The clinical features of vulva dystrophy are refractory pruritus vulva and hypopigmentation of local skin. The pathological alteration mainly exists in the epidermis and dermis layers. Because of the particularity of vulva dissection site and tissue structure, the treatment of vulva dystrophy is the most troublesome problem in gynecological disease. Local medication with hormones is still the main treatment method, but the recurrence rate is high. The pruritus seriously affects patient's quality of life. So it is very necessary to develop new and effective treatment techniques.

Ultrasound treatment has developed a new noninvasive treatment technology in recent years. It has been adopted in the treatment of liver cancer, breast cancer and bone tumor, and has demonstrated good curative effects (Cao 2001; Chen 2001). The physical properties of ultrasound enable it to be focused on a certain target region inside tissues. Thus, a series of physical, chemical and biochemical effect are produced, which transform the circulation of the constitution of target region, and improve the nutrition and function of blood capillaries and nerve endings (ter Haar,

1995). After investigating the effects of ultrasound treatment on 200 New Zealand white rabbits with vulva transplanted VX^2 cancer, and 5 mini-sweet-pigs with vulva injuries, we have studied the relation between energy and efficacy (Ruan 2000). On the basis of demonstration from specialists and sufficient preliminary studies, we applied therapeutic ultrasound to treat vulva dystrophy in patient trials that began in 1999. This paper reports the clinical and pathological changes of the dystrophy of vulva after ultrasound treatment.

PATIENTS AND METHODS

Forty-one women patients with pathologically diagnosed vulva dystrophy were selected for the study. The oldest was 70 years old and the youngest was 22 (average age of 43.45). These patients had refractory vulva pruritus for many years; all of them had received various drug treatments and physical therapy, but received no effect. Among them, 25 cases presented squamous cell hyperplasia, and the other 16 cases lichen sclerosis of the vulva. Two in the 25 also were diagnosed with atypical hyperplasia of slight and medium degrees. Patients were divided into two groups randomly. Twenty-one in the ultrasound group received ultrasound therapy; the others (20) were treated with Spectrum.

The therapy device was a small-sized portable ultrasound treatment machine developed by the Chongqing Haifu (HIFU) Technology Co., Ltd. Scanner frequencies used were 8.98-9.06 MHz, and the average focusing sound intensity was 50 W/cm^2. Continuous scanning mode was adopted. The relation of scanning time and scanning volume was 50 sec/cm^3. The treatment lasted 20 minutes and only one treatment was needed.

The power of the Spectrum treatment was 20 W. The treatment lasted 20 minutes, and one treatment period was seven days.

After ultrasound treatment, the following targets were observed and followed up: the symptoms of vulva pruritus of patients, the changes of local epidermis tissues, characteristics as assessed by microscope and electronic microscope, and quality of life of the patients.

The following pruritus evaluation scores were defined for evaluation: 0 points for no pruritus, 1 point for momentary pruritus, 2 points for pruritus, and 3 points for serious pruritus.

Curative effectiveness was evaluated as follows: (1) Cure: the symptoms and physical signs resolved. Pathological changes indicated that the stratified squamous epithelium of vulva recovered normal stratification and thickness. (2) Significantly effective: the symptoms of vulva pruritus resolved. The color and resilience of local skin improved. (3) Validity: the vulva pruritus and the size of the vulva depigmentation area decreased. (4) Ineffective: the symptoms and physical signs indicated no change.

RESULTS

First, after treatment, the pruritus evaluation score for the Spectrum group was 3 points (15 cases); those in the ultrasound group were 0-1 point (18 cases) respectively ($P < 0.05$). Comparison before and after ultrasound treatment showed that the treated region changed visually and grew toward a normal appearance (See Figs. 1 and 2).

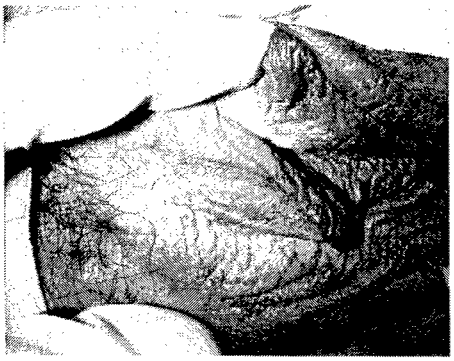

FIGURE 1. Before ultrasound treatment, the skin was found rough, patchy, and of lichenification and depigmentation. The diagnosis was dystrophy of vulva with atypical hyperplasia of slight and medium degrees.

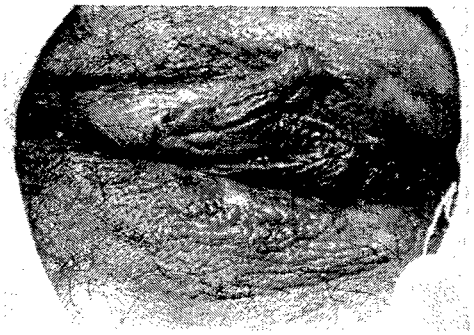

FIGURE 2. After ultrasound treatment, the appearance of vulva skin was normal, and the pigmentation was normal without rough and patchy areas.

Second, after ultrasound treatment, pathological changes indicated that the stratified squamous epithelium of the vulva recovered normal stratification and thickness. And the basal layer had deposited pigment cells (See Figs. 3 and 4).

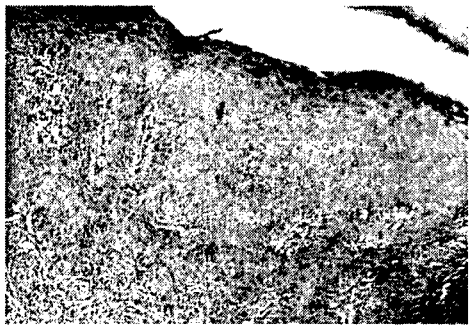

FIGURE 3. Before ultrasound treatment, there were spine cell hyperplasiaed pigment cells in the basal layer, and slight-degree infiltrations of leukocytes and lymphocytes in the dermis layer. The pathological diagnosis was hyperplastic dystrophy of vulva with atypical hyperplasia of slight and medium degrees.

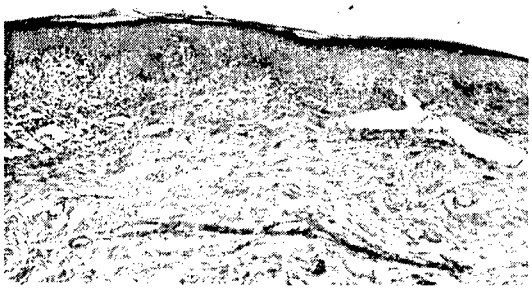

FIGURE 4. In the sixth month after ultrasound treatment, pathological diagnosis indicated that stratified squamous epithelium of vulva had recovered normal stratification and thickness, and the basal layer had deposited pigment cells.

Third, we made the following curative effect evaluation: validity rate for the Spectrum group and Ultrasound group were 70% and 100% respectively ($P < 0.05$).

Fourth, the patients' quality of life in the ultrasound group was better than that of the Spectrum group ($P < 0.05$). The patients in the Spectrum group quickly developed recurrences after treatment.

CONCLUSION

Ultrasound treatment causes little harm to the vulva and may improve quality of life. After ultrasound treatment, the local vulva pruritus disappeared completely. At the same time, the local skin recovered well. The shape of the vulva remained unchanged. Because of the adjustable depth and scope of ultrasound beams, no harm was done to the urethra, rectum and blood vessels of patients in the ultrasound group.

It is effective and safe to treat vulva dystrophy with therapeutic ultrasound. It provides a new method to treat vulva dystrophy in the clinic.

REFERENCES

1. Cao Youde, Zhu Hui, Chen WenZhi, et al., "The pathological changes of breast cancer after HIFU treatment," *J Practical Tumor*, **16** (3), 161-163 (2001).
2. Chen WenZhi, Wu Feng, Zhu Hui, et al., "High Intensity Focused Ultrasound in treatment of experimental malignant bone tumor," *Chin J Ultrasonogr.*, **10** (5), 313-315 (2001).
3. ter Haar, G., "Ultrasound focal beam surgery," *Ultrasound Med. Biol.*, **21** (9), 1089-1100 (1995).
4. Ruan XiangYan, Gu MeiLi, Wang ZhiBiao, "Study of injure of vulva of sweet-pig with High intensity ultrasound," *Chin Ultrasonogr.*, **9** (9),569-571 (2000).

2. LABORATORY STUDIES

MRI-Guided Focused Ultrasound Techniques for Application in the Brain

G. Clement, S. Sokka, N. McDannold, N. Sheikov, F. Jolesz, N. Vykhodtseva, K. Hynynen

Brigham & Women's Hospital, Harvard Medical School, Boston, MA

Abstract. A noninvasive technique for focusing ultrasound through the human skull is performed using MR guidance. The approach is based on a layered wavevector-frequency domain model, which propagates ultrasound from a hemisphere-shaped transducer through the skull using input from CT scans of the head. This approach is tested on *ex vivo* human skulls using a 0.75 MHz, 500-element ultrasound array. Using MRI targeting and temperature measurement, the technique is used to produce thermal lesions in a rabbit brain *in vivo* after propagating through an *ex vivo* human skull. In addition, a cavitation enhanced heating method was investigated as means to lower the total energy requirements for transcranial brain treatment. MRI imaging techniques were used to monitor and evaluate this cavitation-enhanced heating generated by focused ultrasound (FUS). FUS exposures were designed to induce and then sustain gas bubbles during heating. These ultrasound protocols as well equivalent acoustical power control FUS exposures deigned not to cavitate, were administered in seven New Zealand white Rabbits. MRI thermometry was used to monitor temperature during the treatment and T2-enhanced imaging was used to evaluate the resulting lesions. MRI thermometry showed higher temperatures and thermal dose in the cavitation-enhanced heating exposures. In addition, the follow-up T2 images showed the cavitation-enhanced heating resulted in lesions 2-3 times larger than equivalent acoustical power control treatments.

INTRODUCTION

Recently a technique was developed for focusing ultrasound through the human skull by using bone data from CT scans of the head (1). With precise monitoring, this technique could potentially provide a completely noninvasive method for treating tumors and other brain disorders (2). The present study uses MRI to monitor the temperature change induced when ultrasound is focused through ex vivo human skulls. The temperature is monitored in a tissue mimicking brain phantom placed inside the skull and a skin phantom formed around the skull's surface. MRI-monitored transskull surgery is demonstrated by focusing through an ex vivo human skull and into a rabbit brain in vivo, resulting in tissue damage.

Traditionally, FUS ablation is performed with constant levels of high intensity ultrasound for durations of 10-30 seconds, ensuring that temperature rise at the focus is linear. Theoretical models, ex vivo and phantom experimental work have shown that higher temperatures can be obtained if cavitation is induced at the focus during the

ultrasound exposure (3-5). However, cavitation has been difficult to monitor and control, and therefore it has not been employed in FUS surgery. In this portion of the study, we propose an ultrasound protocol that uses cavitation to produce higher temperatures and potentially larger lesions in vivo. We show that this cavitation-enhanced heating can be reliably monitored by MRI thermometry and then evaluated post-exposure with MRI T2-enhaced imaging.

METHODS

Focusing Ultrasound through Human Skull

The algorithm for focusing through the skull was operated by numerically projecting an ultrasound field in wave vector-frequency space (6) to the intended focus. The algorithm then selected the ultrasound transducer driving phases necessary to produce a focus. Data for the algorithm was obtained from a digitized human skull profile obtained using CT images. Each skull was imaged with a Siemens SOMATOM CT Scanner (FOV = 20 cm, slice thickness = 1 mm). A bone reconstruction kernel (AH82) was used to acquire image intensities proportional to the bone density.

Experiments were performed in a water-filled tank using a stereotaxic reference frame to affix a skull to a 500-element hemispherical ultrasound transducer designed for transskull therapy (f = 0.74 MHz, diameter = 30 cm). CW sonications were performed for 20-30 s at electrical powers ranging from 300-1200W. Low power sonications (<800W) were applied to the brain phantoms to measure reversible heating. To demonstrate the ability to produce tissue damage in vivo, high power sonications (>800W) were focused through a human skull and into a rabbit brain. The upper portion of the rabbit's skull was removed to create an acoustic window. The imaging was performed in a 1.5 T clinical MRI unit (LX, GEMS). Temperature images were acquired in one plane from phase-difference images of a fast spoiled gradient echo sequence (7) (TR/TE = 51.7/25.6 ms, flip angle = 30°, bandwidth = 3.1 kHz, FOV = 12 cm, slice thickness = 3 mm, matrix size = 256x128, scan time = 6.8 s). A temperature sensitivity of –0.011 ppm/°C was used (8). A time series of temperature maps were produced.

Cavitation Enhanced Heating

All experiments were performed under MRI guidance with one of two standard eight-sector, spherically curved piezoelectric transducers (100-mm diameter, 80-mm radius of curvature). The two transducers, one with 1.1 MHz resonance and the other a 1.7 MHz transducer were driven by our in-house multi-channel, computer controlled, ultrasound-driving system. FUS exposures were delivered to the thighs (15-20 locations per thigh) of seven New Zealand white rabbits. Cavitation-enhanced heating exposures consisted of 280 acoustic watts for 0.5 seconds followed by either 10 W, 20 W, or 30 W for 19.5 seconds. The equivalent power control sonications were 20-second exposures of 20.5 W, 30.25 W, and 40 W respectively.

The transducer was mounted in an MRI-compatible manual positioning system (9), and the rabbit was placed on top of system with a surface coil (diameter = 12.5 cm, GEMS) adjacent to the thigh to improve signal to noise. An ultrasound detector ring was fixed with the therapy transducer to monitor cavitation activity during treatment.

The imaging was performed in a 1.5 T clinical MRI unit (LX, GEMS). Fast spin echo (FSE) T2, proton density (PD), and T1-weighted imaging was used to target the rabbit thigh and to image after the sonications. Temperature images were acquired as described above. In addition, thermal dose was calculated from these images and used to predicate lesion size and shape (8).

RESULTS

Focusing Ultrasound Through Human Skull

Temperature rises were recorded inside five skulls both with, and without using the model correction. To evaluate the correction method, an additional focus was obtained using ultrasound feedback from a hydrophone placed at the point of focus. Figure 1 shows the temperature changes in a brain phantom due to a 20 s, 320 W sonication without phase correction, with the correction, algorithm, and using the hydrophone feedback. The model is observed to correct for aberration caused by the skull and increase the overall peak temperature change (no correction = 12.2° C, model = 17.0° C, hydrophone = 25.1° C). Figure 2 shows two thermally-induced lesions produced in a rabbit brain *in vivo*.

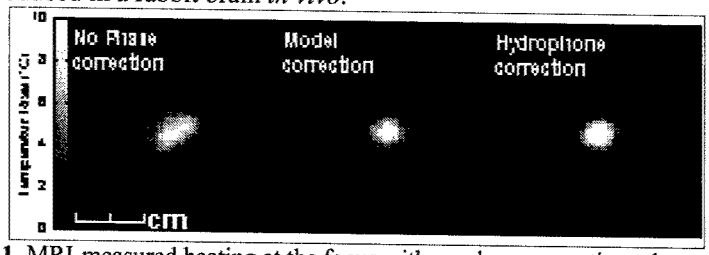

FIGURE 1. MRI-measured heating at the focus with no phase correction, phase correction with the acoustic model, and correction with a hydrophone.

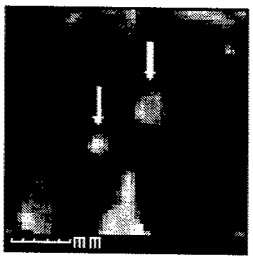

FIGURE 2. Contrast-enhanced T2-weighted FSE images of thermal lesions created through a human skull in a rabbit brain in vivo.

Cavitation Enhanced Heating

Figure 3 shows the temperature profiles at the focus in thigh muscle during the control and pulsed sonications with the 1.7 MHz transducer. The graphs on the left, the control group exposures, show the expected exponential rise in temperature at the focus during continuous wave exposures. The graphs in the right column, the results from the experimental protocol, show a sharp temperature rise within the first 4 seconds. Figure 4 shows a T2-weighted image of two lesions, one generated by the control and the other by the cavitation-induced heating protocol. This image highlights the trend seen in similar images: lesions from the experimental protocol are more spherical and generally located closer to the transducer than the control sonications. Figure 5 shows a T2-weighted image with the thermal dose from the thermometry contours overlaid. The image shows that the dose contours match well with the actual lesions. Lesion size measurements conducted from these T2-weighted images show a 2-3 times increase in lesion size with cavitation-enhanced heating.

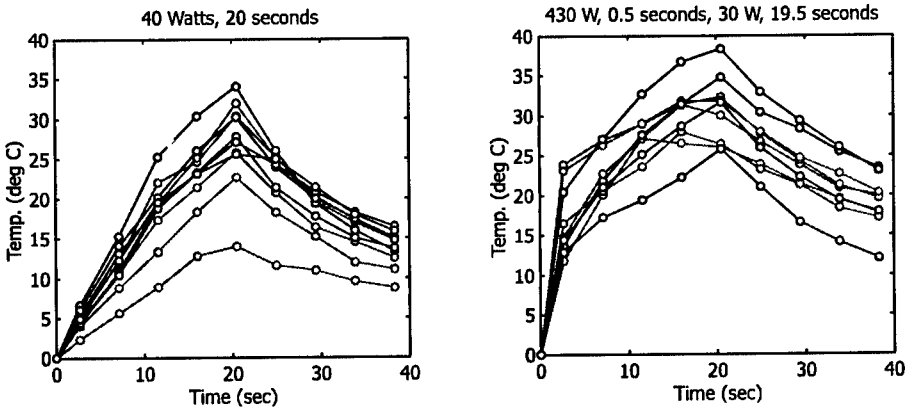

Figure 3

Figure 4

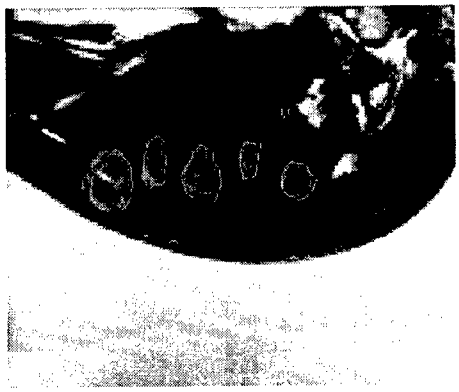

Figure 5

DISCUSSION

This preliminary study also demonstrates the feasibility of combining MR thermal targeting and monitoring with a CT-derived acoustic projection model for focusing through the intact skull. Results indicate that this MR-guided technique can produce intensities sufficiently high to destroy brain tissue *in vivo* without excessive heating of the surrounding tissue.

The results also demonstrate that MRI can be used to monitor cavitation-enhanced heating. MRI thermometry captures the fast temperature rise characteristic of cavitation-enhanced heating. The thermal dose contours calculated from these thermal images accurately predict the lesion size, location, and shape. The T2-weighted images acquired post-exposure show that cavitation-enhanced heating produce larger lesions at the same acoustic power. With MRI established as a reliable and effective monitoring and quantifying tool, cavitation-enhanced heating can become a valuable FUS surgery technique.

ACKNOWLEDGMENTS

This work was supported by grant CA76550 from the National Institutes of Health and by InSightec-TxSonics.

REFERENCES

1. Clement, et. al., Proc. 17th. Int. Cong. on Acoust. (2001).
2. Hynynen , et al., *Ultrasound Med.Biol.*, **24**, 275-283 (1998).
3. Hynynen, et al., *Ultrasound Med Biol*, **17**, 157-69 (1991).
4. Holt, et al., *Ultrasound Med Biol,* **27**, 1399-1412 (2001).
5. Tran, et al., IEEE Ultrasonics Symposium, 1425 (2000).
6. Stepanishen, et al., *J Acoust. Soc. Am.*, **71**, 803-812 (1982).
7. Ishihara, et al., *Magn Reson Med,* **34**, 814-23 (1995).
8. Chung, et al., *Phys Med Phys.*, **26** (9), 2017-26 (1999).
9. Cline, et al., *Radiology,* **194**, 731-7 (1995).

Study On Energy Efficiency Factor Of Ultrasound Therapy

Zhibiao Wang, Faqi Li, Jin Bai, Feng Wu, Jianzhong Zou, Yonghong Du, Wenzhi Chen

Institute of Ultrasound Engineering in Medicine, Chongqing University of Medical Sciences, Chongqing 400016, PR China

Abstract. A difficult problem in HIFU therapeutic dosimetry is how to use a BFR to ablate tissue mass and to determine the energy-efficiency relation, that is, the qualification of biological effects of HIFU. A mass ablation was realized in this study according to a treatment principle of damaging tissue from BFRs to row lesions, slice lesions and a mass. A 1.6 MHz transducer, 150 mm in diameter and with a focal length of 120 mm. was used. The focal peak intensities (I_{SATA}) were 0-27000Wcm^{-2} and the scanning speeds were 1 mm/s to 4 mm/s. The distance between every row was from 5 mm to 10 mm and that between every slice was from 10 mm to 20 mm. Row and slice lesions at different treatment depths and a mass lesion were observed after HIFU procedures in this study. We name the energy in joules required for producing coagulative necrosis per cubic millimeter in biological tissue the energy efficiency factor (EEF) of ultrasound therapy. Results showed that the EEF needed for producing row lesions increased with increasing treatment depth. EEFs required to induce a row lesion, a slice lesion and a mass lesion in biological tissue were different. Generally, it followed the law: $EEF_{solid}<EEF_{slice}<EEF_{row}$. EEF for slice lesion was not simply a summation of EEFs for row lesions at different depths, although the slice lesion was assembled with row lesions at different depths in the same treatment slice. In the same way, EEF for a mass lesion was not simple summation of EEFs for slice lesions at different layers. Factors influencing EEF of HIFU include acoustic power, exposure time, radiation depth, tissue structure, and tissue functional status. Besides, another important factor is how the acoustic environment changes during the HIFU procedure. Keywords: high intensity focused ultrasound, ablation, ox liver tissue, solid lesion, energy efficiency factor and acoustic environment

INTRODUCTION

As a noninvasive extracorporeal approach to tumor ablation, high intensity focused ultrasound (HIFU) can selectively destroy normal and tumor tissues in liver, kidney, muscle and prostate [1,2,3]. However, for a long time, such bottlenecks as the biological effects of HIFU have seriously hindered the development of this technology, especially the focusing of the ultrasound beam inside various tissues, the law of energy deposition and its expression and the quantification of the biological effects [4,5]. The region bounded by the pressure contour lying 3 dB (decibel) below the peak pressure is defined as the Acoustic Focal Region (AFR). Correspondingly, the dot-shaped volume of the coagulated necrosis produced by energy deposition of a single HIFU exposure inside the tissues is named the Biological Focal Region (BFR). Based on AFR, BFR is correlative to the acoustic intensity, exposure time, radiation

depth, tissue structure and its functional status [6]. Although HIFU can induce a BFR precisely and controllably inside tissues at depth, it does not mean that a tumor could be completely ablated with HIFU. It is a difficult problem in HIFU therapeutic dosimetry how to use a BFR to ablate tissue mass and to determine the energy-efficiency relation, that is, the qualification of biological effects of HIFU. After a long-term study, a therapeutic principle for mass ablation through a BFR, row lesions and slice lesions under B-mode ultrasound monitoring have been proposed. Under this principle, EEF is able to quantify the biological effects produced by acoustic energy, and this principle has provided a new idea for studying the quantification of biological effects (i.e. the HIFU therapeutic dosimetry).

MATERIALS AND METHODS

In Vitro Tissue Samples

Fresh ox liver tissues were resected from the ox within six hours after it was slaughtered. Tissue samples were immersed in 0.9% physiological saline. Tissues with few blood vessels and connective tissues were selected and cut into 100 mm×100 mm×100 mm slices, heated to 20° C and degassed under –0.05 to –0.1 MPa for 30 minutes, as stand-bys.

Machine For Experiments

A Model JC-A Haifu Focused Ultrasound Tumor Therapeutic System (shown in Fig. 1), developed and manufactured by Chongqing Haifu (HIFU) Technology Co., Ltd., was used. This machine includes a circulating water degassing device, a high frequency generator, a combined treatment head, a six-dimentional motion device, a computer control system and a B-mode ultrasound monitoring system. Ultrasound beams are generated with a piezoelectric ceramic disk PZT-4 that operates at a frequency of 1.6 MHz and has a focus of 120 mm. A diagnostic ultrasound probe with a frequency of 3.5/5.0 MHz is mounted at the center of the combined treatment head to guide the localization of target tissue and to monitor the therapeutic effects in real time. The combined treatment head is placed within a rubber water reservoir that is filled with circulating degassed water. The water used for treatment has an air-containing ratio of less than 3 ppm and is at a constant temperature of 20° C. A standard PVDF hydrophone with a 0.5 mm diameter, provided by Shanghai Jiaotong University, was used to calibrate the distribution of the acoustic focal region of ultrasound beams in the water reservoir. The AFR is calibrated as an ellipse with an axial diameter of 6 mm and a transverse diameter of 0.6 mm. Free field focal peak intensities from 7000 to 27700 W/cm2 were used, which is determined by calibration of the radiated pressure.

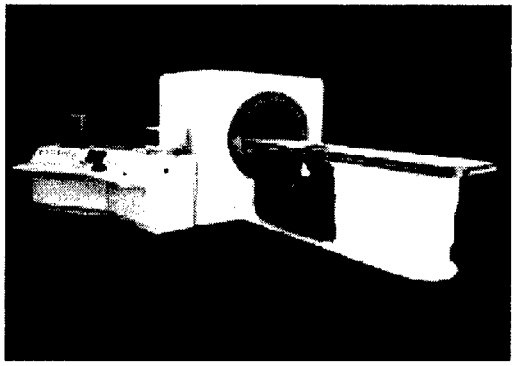

FIGURE 1. Model JC-A Focused Ultrasound Tumor Therapeutic System

Methods

A plastic cylinder container full of degassed water was used. It had an inner diameter of 150 mm and a height of 150 mm and at its bottom, a 0.1 mm thick Mylar® membrane was spread. The sample tissues were put into the container at a room temperature of 20° C. The therapeutic principle of using HIFU to ablate the tissue mass is to be realized according to the protocol of BFR to row, to slice and to mass at last (shown as Fig. 2).

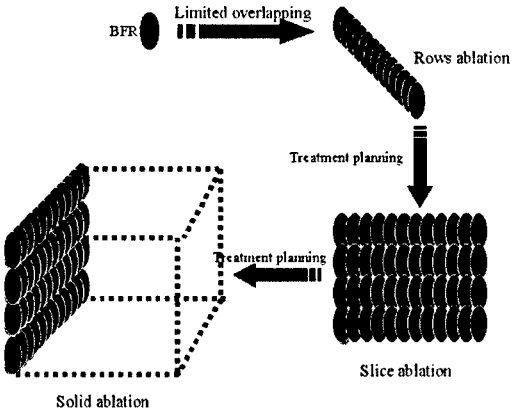

FIGURE 2. A sketch of the therapeutic principle using HIFU to ablate a tumor mass.

BFR to Row: Adopting line-scanning mode, that is, continuous single exposures overlapping, to move the BFR to induce a row-shaped lesion. A 2D treatment slice was selected under B-mode ultrasound monitoring. The focus of the transducer was put at certain depths of the slice, say 20 mm, 30 mm and 40 mm. The scanning length was 30 mm and scanning speeds are from 1 mm/s to 4 mm/s. When a hyperechoic region was found at the targeted area, it was considered to be effective.

Row to Slice: A 2D treatment slice was selected under B-mode ultrasound monitoring. The focus of the transducer was put at 40 mm from the slice. Row lesions

at different depths were added from the deepest to the closest, and a slice lesion was finally induced. The scanning length was 30 mm in length and there was a 5 mm to 10 mm distance between one row and another. The exposure intervals were between 2 and 5 minutes. B-mode ultrasound images at different layers were overlapped with each other.

Slice to Mass: A 2D treatment slice was selected under B-mode ultrasound monitoring. A slice lesion was produced according to the procedures above. Then the combined treatment head was moved to select next exposure slice. There was a 10 to 20 mm distance between each slice and the exposure interval was above 5 minutes. Slice lesions induced at different layers assembled into the mass lesion.

Determination of the boundary of the coagulative necrosis region: Immediately after the procedures, we incised the BFR and row lesion along its maximum section, and resected slice and mass into 5 mm thick pieces. We put the specimens into 1% TTC (Triphenyl tetrazoLium chloride, TTC) suspension at 37° C and stirred. We took the specimens out of the suspension 10 to 15 minutes later or when the boundaries of coagulative necrosis were clear to see. Phosphoric acid buffer was used to wash the tissue surface and then put the tissues samples on a tray for visual observation.

Calculation of EEF: A standard caliper was used to measure the length, width and thickness of the row, slice and mass, and we calculated the lesion volume according to the formula V=Length×Width×Height. Energy efficiency factor (EEF), the basic dose unit of HIFU therapeutic dosimetry, was defined as the energy in joules required for producing coagulative necrosis per cube millimeter in tissue, that is,

$$EEF = TD/V = \eta \frac{pt}{v} \left(J/mm^3 \right),$$

where, η is the focusing coefficient of HIFU transducer, representing the energy converging ability of a ultrasound transducer. In our study, η=0.7. P (w) is the gross acoustic power of HIFU generator. t (s) is the total exposure time and V (mm^3) is the lesion volume.

Data Processing: All data obtained were figured as $\overline{X} \pm SD$.

RESULTS

According to the principle of inducing coagulative necrosis from BFRs to rows, slices and finally mass, HIFU can be used to completely ablate a tissue mass. Most important is to induce row lesions through the scanning of BFR and observe the obvious ultrasound hyperechoic region in various rows produced at different treatment slices and depths. This was also the essence of real-time monitoring during the whole treatment procedure. Fig. 3 shows the BFR, row lesion, slice lesion, and mass lesion induced in ox liver *in vitro*. The gray coagulative necrosis region could be observed with the naked eye. There were clear boundaries between BFR, row lesion, slice lesion and normal tissues, while no residual normal tissues were found inside the mass lesion.

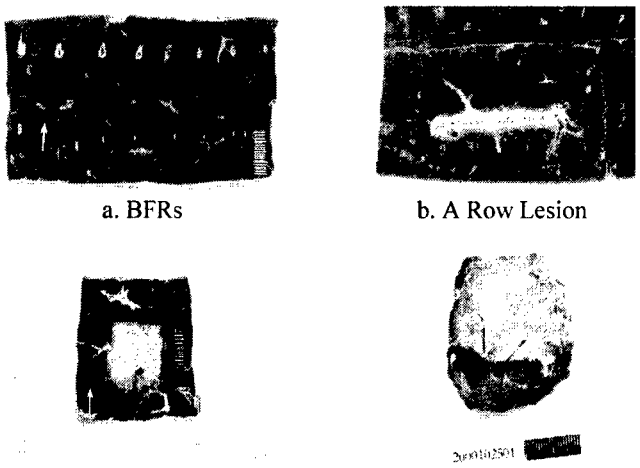

a. BFRs b. A Row Lesion

c. A Slice Lesion d. A Mass Lesion

FIGURE 3. BFRs, row lesion, slice lesion and mass lesion produced in ox liver *in vitro* with HIFU

From Table 1 it can be observed that the EEF needed for inducing row lesions at different depths varied, and EEF increased with the increase of exposure depth. That is, when the scanning length was constant, the ultrasound energy needed for inducing a unit volume of row lesion in deep tissue was greater than that needed for a shallower layer. In other words, when the acoustic output intensity was constant, the exposure time required for producing a certain length row lesion would be greater, and the scanning speed decreased or scanning circles increased. Compared with the EEF required for inducing a slice or a mass lesion, that for generating a single row lesion at different depths was greater; likewise, EEF for inducing a slice lesion was greater than that for a mass. These indicated that EEF for a slice lesion was not simply a summation of EEFs for row lesions at different depths, although the slice lesion was assembled with row lesions at different depths in the same treatment slice. In the same way, EEF for a mass lesion was not a simple summation of EEFs for slice lesions at different layers.

TABLE 1. EEFs For Generating Row, Slice And Mass Lesions Inside Ox Liver *in vitro*.

	EEF (J/mm^3)	
Row lesion	Exposure depths (mm)	
	20 mm	8.41 ± 4.77
	30 mm	10.83 ± 5.85
	40 mm	11.96 ± 5.17
Slice lesion	2.71 ± 0.85	
Mass lesion	1.73 ± 0.39	

DISCUSSION

The mechanisms of HIFU for producing coagulative necrosis inside biological tissues include hyperthermia, and cavitation and other mechanical effects (7,8,9). HIFU can be used to generate precise tissue destruction inside tissues at depth. However, this does not mean a tumor mass at depth can be completely ablated with HIFU. The crucial point for successful application of the HIFU technique is to ablate a tumor mass thoroughly. The lesion formed inside biological tissues by a single HIFU exposure is of an ellipse shape. Chen et al [10] placed one lesion adjacent to another to form arrays and to remove a tumor finally. The most important point for this technique was to choose appropriate intervals, including the time delay between every two exposures and the distance between every two lesions, to completely overlay the region to be treated without residual normal tissues remaining. However, no remarkable protocol for thorough ablation of a tumor mass was obtained. It was reported that when attempting to ablate a tumor mass continuously, the cavitation of ultrasound would be in superposition, leading to the disappearance of a lesion or transference of lesion to the superficial tissue, and finally to the failure to destroy the targeted region. That is, an existing lesion was likely to affect the formation of the next lesion. Ter Haar et al [4] named this phenomenon lesion-lesion interference effect. Compared with applying lesion arrays to cover the tumor mass, we proposed the principle for tumor ablation by moving the BFR. After long-term study and research, we found that, applying the principle of ablating a tumor mass from BFRs to rows, to slices, and finally to a mass, the tumor mass could be removed completely. The row and slice lesions had clear margins with normal tissues and tissues within the target region became coagulative necrotic, with no residual normal tissue.

Studying the therapeutic dosimetry of HIFU seems to be tough work at all times. The attempt to quantify the biological effects and to reflect the energy deposition of HIFU inside the tissue through theoretical analysis or simply the value of ultrasound energy (i.e. acoustic power and exposure time) will fail in vain. Studies have shown that HIFU can produce a BFR within biological tissues. To a fixed ultrasound transducer, BFR value is closely related not only to acoustic power and exposure time, but to radiation depth, tissue structure and tissue functional status [6]. That is to say, besides known sound source parameters such as the physical parameters of the transducer, acoustic power and exposure time, factors affecting energy deposition inside biological tissues also include the unknown factors such as radiation depth, tissue structure and tissue functional status. Nevertheless, the coagulative necrosis region produced in tissue exists, and can be identified and evaluated by means of B-mode ultrasound imaging, CT imaging, MR imaging and light microscope inspection [8,9,11,12]. Therefore, to a fixed transducer, we correlate the acoustic energy with the correspondingly induced coagulative necrosis. And EEF, the value of a unit coagulative necrosis volume in the tumor mass divided by the energy needed, is used to quantify the biological effects and to carry on the study of therapeutic dosimetry of HIFU. The authors find that EEF is relevant to acoustic power and exposure time, and reflects the influence of radiation, tissue structure and tissue functional status on the formation of a coagulative necrosis volume.

The authors also find the EEF for inducing a row lesion is relevant to radiation depth due to the sound attenuation along the propagation path. For a plane wave, the acoustic power decreases exponentially with distance. Therefore, the acoustic power or exposure time for inducing a row lesion at depth is greater than that needed for inducing a row lesion in a shallower layer. When acoustic power is constant, the scanning speed should be reduced or more scanning sessions should be added.

The EEF required for inducing slice lesions and mass lesions is far less than that needed for forming row lesions at various depths; likewise the EEF for mass lesions is less than that for a slice lesion. EEF for a mass lesion is not simply the summation of EEFs for slice lesions at various depths, although the slice lesion is fit together with row lesions at different depths. In the same way, EEF for a mass lesion does not seem to be the summation of EEFs for various slices at different treatment layers. This is because an existing row lesion in deep tissue has altered the tissue structure, changing the acoustic properties of the tissue: the sound attenuation coefficient of lesion tissue is two times greater than that of normal tissue [13]. During a treatment procedure, row lesions at different depths are continuously assembling a slice lesion, from the deep layer to shallower layers, and finally a mass lesion is produced. With the progress of this procedure, the apparent tissue structure alteration is ongoing, that is, the acoustic environment is immediately being changed, and thus the acoustic properties change in real time. In the meantime, the radiation depth becomes shallower and shallower, such that an existing row lesion will influence the sound energy needed for the next row lesion: sound energy needed for the next row lesion will reduce greatly. These indicate that changing the tissue acoustic environment (i.e. changing the tissue sound coefficient) and altering the tissue of high sound absorption into that of low absorption, the EEF could be decreased according to the requirements. Results of this study have proved this.

By moving BFR with HIFU, a tumor mass can be ablated without residual tissues according to the principle of BFRs to rows, to slices, and to a mass. The whole procedure is under real-time monitoring of B-mode ultrasound. Factors influencing EEF of HIFU include acoustic power, exposure time, radiation depth, tissue structure, and tissue functional status. Besides, another important factor is how the acoustic environment changes during the HIFU procedure. The authors agree that a great deal of experiments should be done to establish the EEF database for ablating all kinds of tissue masses. This will no doubt improve the application and popularity of HIFU technology.

ACKNOWLEDGEMENT

Authors thank the national Ninth Five Key Scientific Project of China (grant No. 96-905-02-01), and Key Project (grant No. 39630340) and subject project (grant No. 30070217) of National Nature and Science Foundation of China for their support to this study.

REFERENCES

1. Sibille, A., Prat, F., Chapelon, J.Y., et al., "Characterization of extracorporeal ablation of normal and tumor-bearing liver tissue by high intensity focused ultrasound," *Ultrasound Med Biol*, **19** (8), 803-813 (1993).
2. Bihrle, R., Foster, R.S., Sanghvin, N.T., et al., "High intensity focused ultrasound for treatment of benign prostatic hyperplasia: Early United States clinical experience," *J Urol*, **151**, 1271-1275, (1994).
3. Adams, J.B., Moore, R.G., Anderson, J.H., et al., "High-intensity focused ultrasound ablation of rabbit kidney tumors," *J Endourol*, **110**, 71-75 (1996).
4. ter Haar, G.R., Robertson, D., "Tissue destruction with focused ultrasound in vivo," *Eur Urol*, **23** (Suppl. 1), 8-11 (1993).
5. Malcolm, A.L., ter Haar, G.R., "Ablation of tissue volumes using high intensity focused ultrasound," *Ultrasound Med Biol.*, **22** (5), 659-669 (1996).
6. Wang, Z.B., et al., "Concept of biological focal field and its importance in tissue resection with high intensity focused ultrasound," *J Acoust Soc Am*, **103** (5), 2869 (1998).
7. Chapelon, J.Y., Margonari, J., Theillère, Y., et al., "Effects of high-intensity focused ultrasound on kidney tissue in the rat and the dog," *Eur Urol*, **22**, 147-152 (1992).
8. Yang, R., Kopecky, K.K., Rescorla, F.J., et al., "Sonographic and CT charateristics of liver ablation induced by high-intensity focused ultrasound," *Invest Radiol*, **28** (9), 796-801 (1993).
9. Yang, R., Sanghvi, N.T., Rescorla, F.J., et al., "Liver cancer ablation with extracorporeal high-intensity focused ultrasound," *Eur Urol*, **23** (Suppl. 1), 17-22 (1993).
10. Chen L., ter Haar G., Hill C.R., "Influence of ablated tissue on the formation of high-intensity focused ultrasound lesions," *Ultrasound Med Biol*, **23** (6), 921-931 (1997).
11. Susani, M., Madersbacher, S., Kratzik, C., et al., "Morphology of tissue destruction induced by focused ultrasound," *Eur Urol.*, **23** (Suppl. 1), 34-38 (1993).
12. Rowland, I.J., Rivens, I., Chen, L., et al., "MRI study of hepatic tumors following high intensity focused ultrasound surgery," *Br J Radiol*, **70**, 144-153 (1997).
13. Bush, N.L., Rivens, I., ter Haar, G.R., et al., "Acoustic properties of lesions generated with an ultrasound therapy system," *Ultrasound Med Biol*, **19** (9), 789-801 (1993).
14. Chen, L., Rivens, I., ter Haar, G.R., et al., "Histological change in rat liver tumor treated with intensity focused ultrasound," *Ultrasound Med Biol.*, **19**, 67-74 (1993).

Bubbles And HIFU: The Good, The Bad, And The Ugly

R. Glynn Holt, Ronald A. Roy, Patrick A. Edson, Xinmai Yang

Boston University, Department of Aerospace and Mechanical Engineering
Boston, MA 02215

Abstract. Rapid hyperthermia resulting in tissue necrosis has proven to be a useful therapeutic modality for clinical application of high-intensity focused ultrasound. At therapeutic intensities, the hyperthermia is often accompanied by bubble activity. In vitro and in vivo experiments alike have shown that under certain conditions bubble activity can give rise to a doubling of the heating rate. With a view towards harnessing the energy-concentrating effects of bubbles to do useful clinical work, we report the results of experiments and modeling for the dynamic and thermal behavior of bubbles subjected to 1-megahertz ultrasound at megapascal pressures. The dominant heating mechanism depends on bubble size, medium shear viscosity number and frequency-dependent acoustic attenuation. The bubble size distribution, in turn, depends on insonation control parameters (acoustic pressure, pulse duration), medium properties (notably dissolved gas concentration) and bubble-destroying shape instabilities. The evidence obtained so far points to a range of control parameters for which bubble-enhanced heating can be assured.
[Work supported by DARPA and the U.S. Army]

BUBBLES AND HIFU: BACKGROUND AND MOTIVATION

Acoustic cavitation (the acoustically induced nucleation and subsequent oscillatory activity of bubbles) is often the result of the application of ultrasound in a biomedical context. There are sound reasons, both experimental and theoretical, for defining therapeutic and diagnostic operating conditions in order to minimize bubble activity (Williams et al. 1991; Carstensen et al. 1993; Penney et al. 1993; Everbach et al. 1997). Most of the arguments boil down to the fact that bubbles perform a very efficient and highly nonlinear conversion of acoustical energy to mechanical motion. In diagnostic ultrasound, the Mechanical Index (MI) was conceived and implemented because of the perceived risk of mechanical bioeffects from the violent inertial collapses of bubbles (Apfel and Holland 1991). In therapeutic ultrasound, bubbles formed in the propagation path inhibit deposition of acoustic energy because they scatter and absorb much of the energy before it can reach the target area, a process often referred to as 'screening' or 'shielding'.

Conversely, there are often diagnostic situations in which the use of bubble-based contrast agents make cavitation activity unavoidable (Fowlkes and Holland 2000), and therapeutic situations in which it is desirable to excite cavitation. Such is the case in the field of ultrasound surgery using high-intensity focused ultrasound (HIFU), where the goal is to produce irreversible necrosis deep into the tissue with

minimal damage in the intervening path (as reviewed in ter Haar 1995, and highlighted in the special issue of IEEE UFFC, November 1996). The fact that bubbles enhance ultrasound imaging via their high backscatter cross section makes them useful in targeting applications. If gross mechanical damage and tissue ablation is desired, then excitation of cavitation bubbles is the most efficacious (if also unavoidable) method at high insonation pressures and long insonation durations (for example, Fry et al. 1950; Lehmann and Herrick 1953; Fry et al. 1970; ter Haar et al. 1982; Fry et al. 1996; Tavakkoli 1997; Arefiev et al. 1998, Smith and Hynynen 1998).

However, if controlled, highly localized hyperthermia is the desired outcome, then most investigators have argued that cavitation is to be avoided, since it has typically led to unpredictable thermal results. Several authors observe irregular lesions and collateral damage outside the focal zone when uncontrolled cavitation occurs during insonation (Fry et al. 1970; Lele 1987; Hynynen 1991; Chapelon et al. 1991; Sibille et al. 1993; Chapelon et al. 1996; Clarke and ter Haar 1997; Chapelon et al. 2000). These studies all contain unambiguous statements recommending actively *avoiding* cavitation when the therapeutic goal is controlled localized heating.

In the preceding list of authors, Lele (1987), Hynynen (1991) and Clarke and ter Haar (1997), as well as Sanghvi et al. (1996), observe cavitation-related enhanced heating – the heating rate measured via single thermocouple during insonation increased dramatically above some threshold insonation pressure, with (in the Lele and Hynynen studies) concomitant dramatic increase in measured acoustic emission. In the Hynynen and Sanghvi studies, regions of enhanced echogenicity in ultrasound images of the focal region were observed. Sanghvi et al. report 'cloud-like' regions of echogenicity that started at the focus and gradually migrated toward the therapy transducer. They were unable to effectively propagate the ultrasound beyond the cloud, a clear indication of bubble activity.

Thus we see that bubbles are important in HIFU applications, and in particular that a bubble-mediated heating effect has been demonstrated in the literature in vivo. It is one aim of the current work to provide a basis for using bubbles to enhance controlled localized heating. It is precisely the fact that bubbles are so efficient at transducing acoustic energy into mechanical energy that motivates the present work.

THE GOOD: ENHANCING RAPID HYPERTHERMIA

We have undertaken a series of laboratory experiments on tissue-mimicking phantoms insonated by 1 MHz focused pulsed ultrasound at MPa pressure amplitudes. The need for independently and simultaneously measured pressures and temperatures, (as opposed to using a derating process to infer the pressure), as well as the ease of instrumentation afforded by cast test samples, motivated the use of a phantom rather than animal tissue. Equally important in our choice of phantoms was the desire to quantitatively model (albeit with Newtonian assumptions) both the acoustic absorption and the bubble dynamics in order to compare to our experiments without employing adjustable parameters – our phantoms allowed us to independently measure both acoustic and thermal material properties to facilitate the partial achievement of this aim.

Experiments

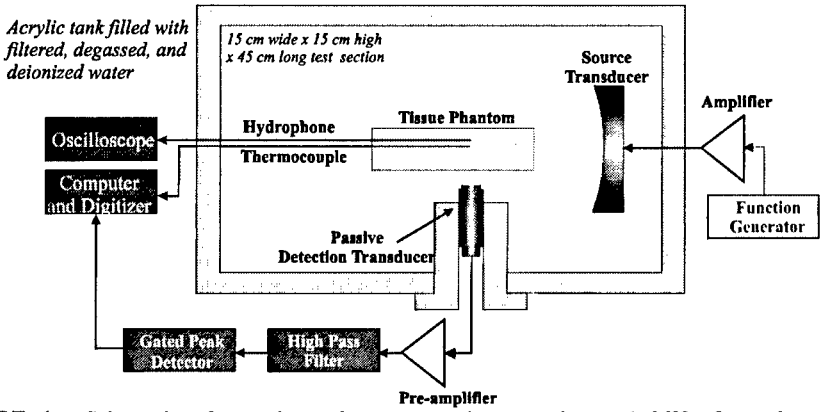

FIGURE 1. Schematic of experimental apparatus, incorporating a 1 MHz focused source, a thermocouple array, a needle hydrophone, and a 15 MHz focused detection transducer

The details of the apparatus and phantoms used in these studies are published elsewhere (Holt and Roy, 2001; Edson 2001; Huang 2002). Figure 1 (from Edson, 2001) depicts the major elements of the insonation geometry and the diagnostic schemes, and is representative of similar setups used in Yang (2002), Holt et al (1998) and Holt and Roy (2001), though the latter 2 did not employ a passive cavitation detector.

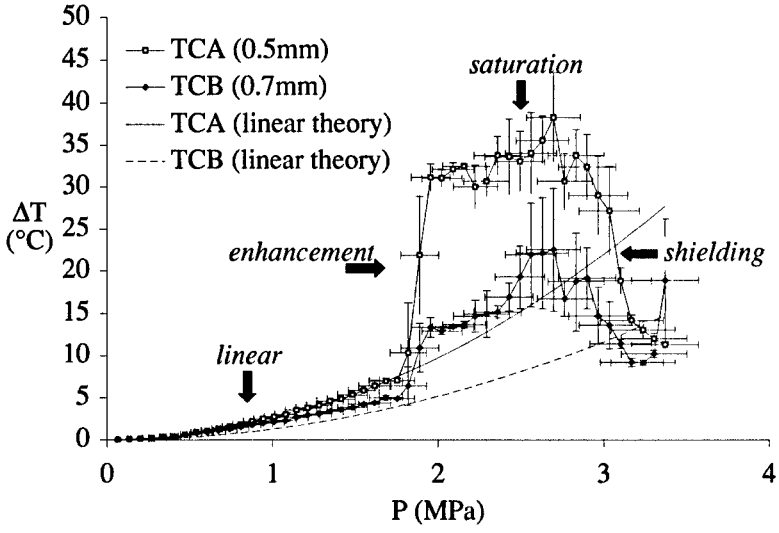

FIGURE 2. Peak temperature increase from ambient vs peak-positive acoustic pressure for an Agar phantom subjected to 0.7 sec 1MHz tonebursts. The thermocouple locations are measured relative to the acoustic axis. The theoretical curves are fit to the data below 1.5 MPa by adjusting the material absorption. Each data point is the mean of 5 runs at that pressure, with 100 sec cooling between runs.

Figure 2 illustrates the typical phenomena associated with the onset of cavitation. For low pressures (*"linear"* in the figure), the temperature rise is governed by linear absorption of the primary 1MHz field, and is linearly proportional to the acoustic intensity, or the square of the acoustic amplitude (Parker 1983; Nyborg 1988; Clarke and ter Haar 1997). Above some critical threshold pressure, the heating increases dramatically *("enhancement")* and becomes rather erratic as indicated by the vertical error bars, which represent the sample standard deviation of 5 runs at each pressure. Upon further increase of the pressure, a *saturation* is often encountered, which may be followed by an actual decrease *("shielding")* in the peak temperature in the focal region where the thermocouples are located.

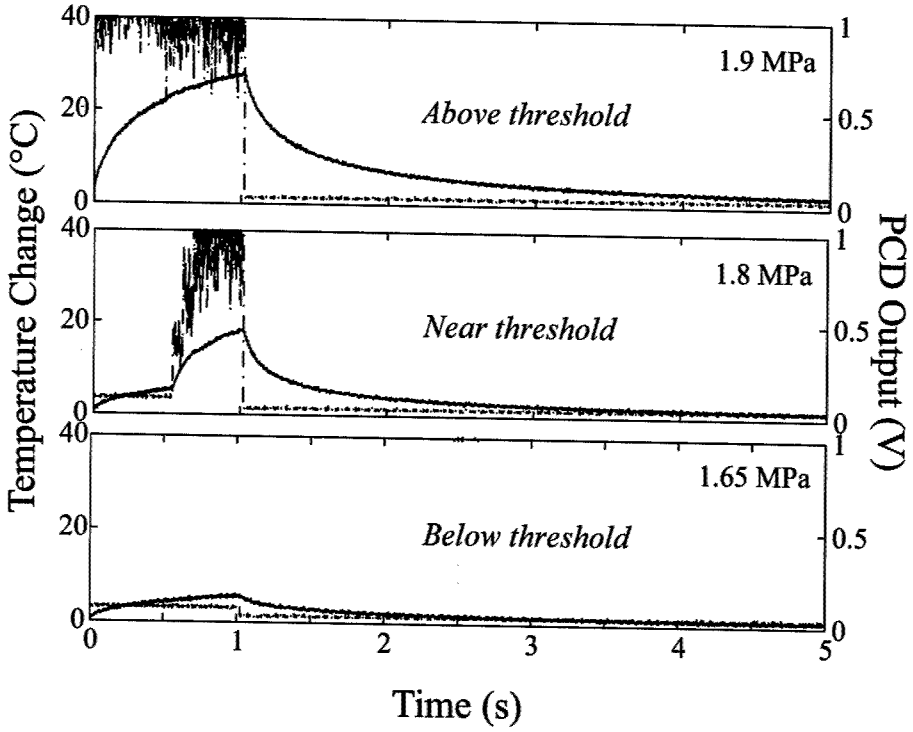

FIGURE 3. Temperature (solid line) and passive cavitation transducer output (dotted line) as a function of time for three 1 sec insonations spanning the threshold pressure for enhanced heating.

Figure 3 illustrates the correlation of broadband noise due to cavitation activity with temperature rise. In all cases, the onset of cavitation activity coincides with the onset of enhanced heating. Not only is this further corroboration of the hypothesis that bubbles are responsible for the enhanced heating seen in Figure 2, but the nature of this mode of detection indicates that at least inertial cavitation (characterized by large expansions followed by violent collapses, see Leighton 1994) is present. This clue is key to our investigation of the bubble size distribution, see below.

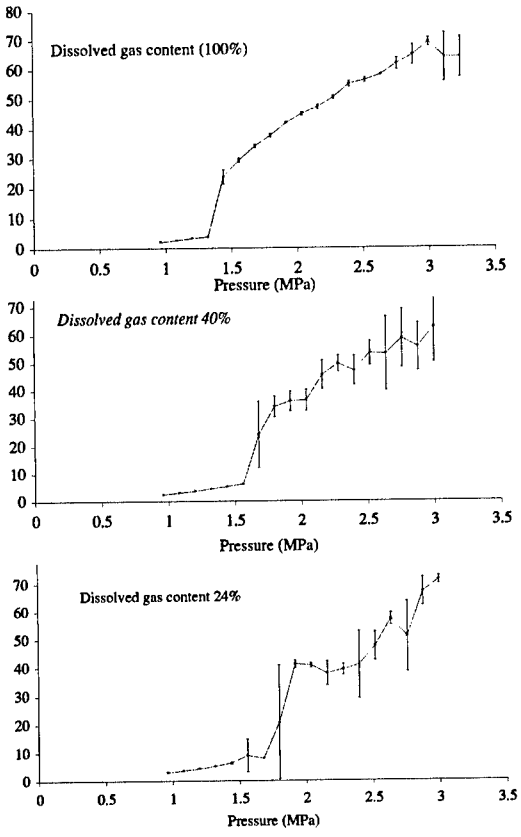

FIGURE 4. Peak temperature rise vs acoustic pressure for different dissolved gas concentrations

Figure 4 illustrates the effect of dissolved gas concentration on bubble-enhanced heating.

Modeling

In an effort to understand the dominant mechanisms responsible for the enhanced heating, we assume, based on the foregoing evidence, that bubbles are responsible for the extra heating. We proceed to build a model for heat deposition in the medium which incorporates contributions from the primary (nonlinear) field, and any bubble sources.

Thermal Sources: Primary Acoustic Absorption, Bubble Viscous Dissipation And Bubble Secondary Acoustic Absorption

The heat conduction equation is solved numerically, with thermal sources due to the primary heating and due to bubble terms (Edson, 2001). Since we are working at 1 MHz, and we infer that most of our bubbles will be less than 50 microns in radius, and also assuming that bubbles remain spherical for most of their lifetime, the 2 dominant bubble terms will come from viscous heating of the external medium, and secondary acoustic heating due to the absorption of the sound actively radiated by the bubble (Holt and Roy, 2001). The heat conduction equation is written in the following form:

$$\rho C \frac{\partial T}{\partial t} = \overbrace{K\nabla^2 T}^{\text{Conduction}} + \overbrace{q_{us} + q^*_{vis} + q^*_{rad}}^{\text{Source/Sink Terms}} \qquad (1)$$

where T is the temperature, ρ the density, C the specific heat, and K the thermal conductivity of the tissue phantom material that we determine independently (Huang, 2002). The source terms are defined as

$$q_{us} = \frac{2\alpha}{\omega^2 \rho c} \left\langle \left(\frac{\partial p}{\partial t} \right)^2 \right\rangle_t ; \qquad (2)$$

q_{us} is the primary acoustic absorption heating term, where a is the absorption, w the frequency of the primary acoustic field, c is the speed of sound, and p is the local

acoustic pressure, and the bracket denotes a time average. The pressure is obtained from the Westerveldt equation (Hamilton and Morfey, 1998) which is solved via a Finite-Difference Time-Domain (FDTD) technique (Hallaj and Cleveland, 1999):

$$\nabla^2 p - \frac{1}{c^2}\frac{\partial^2 p}{\partial t^2} + \underbrace{\frac{2\alpha}{c\omega^2}\frac{\partial^3 p}{\partial t^3}}_{\text{Loss Terms}} + \underbrace{\frac{\beta}{\rho c^4}\frac{\partial^2 p}{\partial t^2}}_{\text{Nonlinear Terms}} = 0, \tag{3}$$

where $\beta = 1\text{-}B/2A$ is the medium nonlinearity coefficient. The bubble viscous heating source term q^*_{vis} is obtained from the viscous dissipation density for a single bubble q_{vis}, given by the following time average (Prosperetti, 1977):

$$q_{vis} = {W_{vis}}/{V_{eff}}\,; W_{vis} = 16\pi\mu\left\langle R\dot{R}^2\right\rangle_t, \tag{4}$$

where μ is the phantom shear dynamic viscosity, V_{eff} is an effective volume for the viscous dissipation (approximately $\langle R\rangle_t$), and the time average of the bubble radius $R(t)$ is computed by solving a version of the Rayleigh-Plesset equation (Keller and Kolodner 1956; Keller and Miksis 1980):

$$\left(1-\frac{\dot{R}}{c}\right)R\ddot{R} + \frac{3}{2}\dot{R}^2\left(1-\frac{\dot{R}}{3c}\right) = \left(1+\frac{\dot{R}}{c}\right)\frac{P\left(R,\dot{R},t\right)}{\rho} + \frac{R}{\rho c}\frac{\partial P\left(R,\dot{R},t\right)}{\partial t} \tag{5}$$

$$P\left(R,\dot{R},t\right) = P_l\left(\frac{R_0}{R}\right)^{3\kappa} + P_v - P_0 - \frac{2\sigma}{R} - \frac{4\mu\dot{R}}{R} - P_a\sin(\omega t) \tag{6}$$

$$P_l = P_0 - P_v - \frac{2\sigma}{R_0}, \tag{7}$$

where κ is the polytropic exponent, σ is the surface tension, P_l is the pressure in the phantom medium, R_0 is the equilibrium radius of a bubble, P_0 is the ambient pressure, P_v is the vapor pressure, and P_a is the acoustic pressure, obtained from Eq. (3). Finally, the bubble secondary acoustic heating source term q^*_{rad} is obtained from the secondary acoustic heating estimate for a single bubble q_{rad}:

$$q_{rad} = \frac{\rho\alpha}{c}\left\langle R\left(2\dot{R}^2 + R\ddot{R}\right)\right\rangle_t, \tag{8}$$

where the absorption coefficient α may be considered as frequency-dependent (Hilgenfeldt et al., 2000; Edson, 2001) to more accurately account for the absorption of the outgoing shock waves emitted by inertially-collapsing bubbles.

Results: Heating From Single Bubbles In The Parameter Space

Equations (1-8) may be integrated to obtain numerical estimates for bubble-induced heating. Before presenting those results, it is of interest to present the underlying bubble response. Figure 5 presents the response of a bubble driven by a 1 MPa, 1 MHz sine wave in the parameter space of bubble size and medium viscosity. Both the absolute maximum radius (5a) and the normalized expansion ratio (5b) are plotted. The nonlinear resonances typical of bubbles are easily identified in (5a), while in (5b) the location of inertially-collapsing bubbles is concident with the single large peak. In both depictions, at low viscosities and near 100 nm bubble sizes, a critical radius

(corresponding to a quasi-static Blake threshold) below which the bubble response is negligible due to the effect of surface tension.

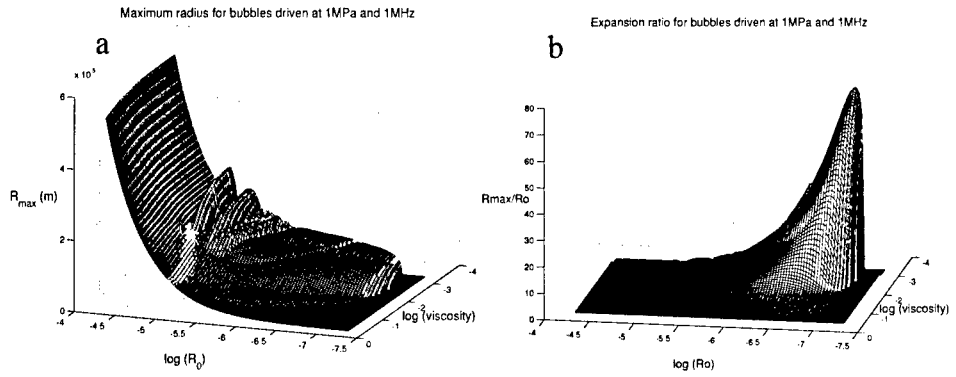

FIGURE 5. Maximum radius (a) and expansion ratio R_{max}/R_0 (b) for bubbles driven at 1 MPa and 1 MHz vs bubble equilibrium size R_0 and host medium shear dynamic viscosity μ.

Figure 6 plots the calculated contributions of viscous heating (Eq. (4)) and secondary acoustic heating (Eq. (8)) for the same parameter space (but slightly higher pressures) as in Figure 5. Fig. 6a shows a global maximum for the viscous source power for large viscosity and intermediate bubble size, corresponding to a noninertial response in Fig. 5; Fig. 6b indicates that the maximum power developed by the secondary acoustic emission mechanism is due to inertially-collapsing bubbles, corresponding to the peak in Fig. 5b (shifted to smaller bubble sizes in 6b due to the higher pressure used).

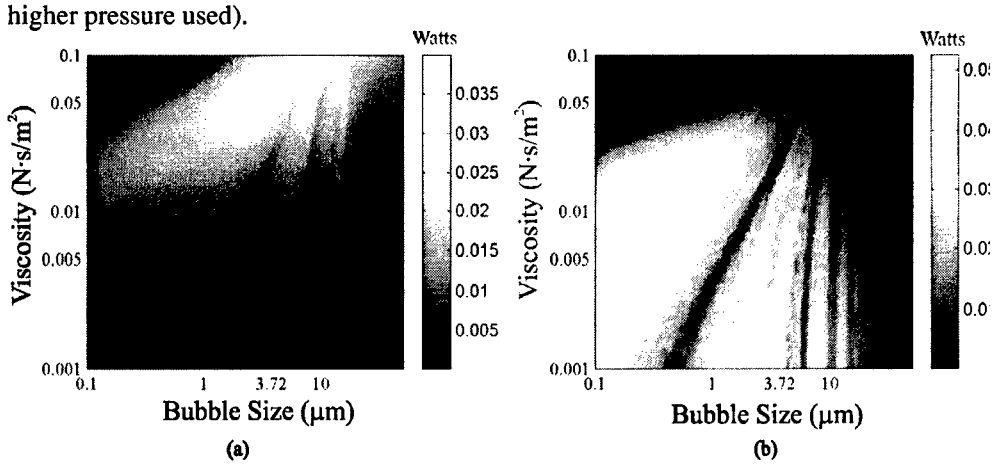

FIGURE 6. Single bubble heating contributions for a 1MHz, 2.8 MPa acoustic pressure. Viscous power (a) and secondary acoustic absorption power (b) are plotted vs bubble size and phantom viscosity.

If we choose 'optimal' bubble sizes for each type of contribution, then the optimal viscous source bubble would be roughly 4 μm at 0.07 Pa-s viscosity. The optimal secondary acoustic or inertial bubble would be say 200 nm at 0.003 Pa-s. We can then

define the source strengths $q^*_{vis,rad}$ in Eq. (1) as $Nq_{vis,rad}$, where N is the number of bubbles in the focal region required to make up the difference between the primary acoustic heating and the bubble-enhanced heating observed in a situation as depicted in Fig. 2. Table 1 illustrates the results of such a calculation for a typical run:

TABLE 1. Number of bubbles required to achieve experimentally observed ΔT.

Acoustic Pressure (MPa)	ΔT (°C)	Number of optimal viscous bubbles	Number of optimal inertial bubbles
2.06	6.8	10	10
2.18	8	12	12
2.30	10	16	15
2.41	12	17	16
2.53	15	22	22
2.64	21	27	28
2.76	24	35	35

It is rather striking that no more than 35 'optimal' bubbles would be required to generate an extra 24°C temperature rise. Certainly 35 is not to be taken exactly, but the order of magnitude is correct.

THE BAD: WHAT WE DON'T KNOW

Bubble Size Distribution

Our working hypothesis is that sufficient nuclei (hydrophobic inclusions, or possibly even stabilized microbubbles) exist in our phantoms such that, above a threshold pressure amplitude, acoustic cavitation occurs. The distribution of bubble sizes is, however, unknown. The nuclei most susceptible to inertial cavitation at 1 MHz will possess an equilibrium radius R_0 of order 0.1 μm (Apfel and Holland 1991; Allen et al. 1997), and one might guess at an initial distribution centered on this size. But over the course of a typically 1-sec long insonation, the size distribution will evolve, eventually resulting in an asymptotic bubble size distribution. Imaging these bubbles via ultrasound or optics is not feasible, at least in these phantoms. Below we discuss a method to narrow down the possible bubble size distributions.

Tissue And Tissue-Mimicking-Phantom Viscosity

The Agar phantoms we use (as well as most biological fluids and tissues) exhibit viscoelastic properties, and we should properly be using a model of the host medium which possesses such features. We can reasonably assume that at the extremely high strain rates typical of nonlinear bubble oscillations at MHz frequencies we will reside in the high-frequency asymptote for the shear viscosity number. This is important because the asymptotic value of the shear viscosity number is determined by shear thinning, and will in general be orders of magnitude below the static or low-strain-rate value. This still leaves us with some uncertainty regarding the shear viscosity of our Agar phantoms. We can invert the well-known expression relating the

measured acoustic absorption (18 Np/m/MHz) to the shear dynamic viscosity to obtain a value of 3.15 Pa-s (water is 10^{-3} Pa-s, and whole blood at body temperature has a measured value of ~5 x 10^{-3} Pa-s.). In light of the above discussion of the viscoelastic nature of our phantom 3.15 Pa-s should be considered an extreme upper bound, while water (0.001 Pa-s) should be considered a lower bound. We note that, in light of the results from our passive cavitation detector in Fig. 3, we expect that we indeed have bubble sizes near 1 micron, and a viscosity value on the order of 0.005 Pa-s.

THE UGLY (BUT USEFUL): HOW WE DETERMINE WHAT WE DON'T KNOW

Growth by rectified diffusion (Eller and Flynn 1965; Crum and Hansen, 1982; Church 1988)) will shift the mean of the bubble size distribution to larger radii over a long time scale of hundreds to thousands of acoustic cycles. Bubble growth will be interrupted by: (1) the onset of shape instabilities leading to breakup of the bubble (Eller and Crum 1970; Brenner et al. 1995; Gaitan and Holt 1999; Hao and Prosperetti 1999) or, (2) the diminution of bubble response as the mean bubble size increases well past the regime of resonant behavior such that bubble growth by rectified diffusion is halted.

By coupling Eqs. (5-7) with the equations for shape and diffusive stability, we may then place further bounds on bubble sizes and medium viscosities. Without reproducing the equations here (for details see the above references, as well as Yang, 2002), we present results for shape instabilities and rectified diffusion equilibria in our parameter space. Figure 7 shows the mass diffusion equilibrium (threshold for growth by rectified diffusion) and the shape instability boundary in the parameter space. Bubbles to the left of the diffusion equilibrium will grow, bubbles to the right will dissolve. Bubbles above the shape instability boundary are stable with respect to perturbations from sphericity, while below the boundary they are unstable, and will rapidly exhibit large amplitude shape oscillations and subsequent breakup. Thus, the allowed region for bubbles is the shaded wedge shape, with asymptotic bubble size distributions to be expected near the rightmost boundary of the wedge.

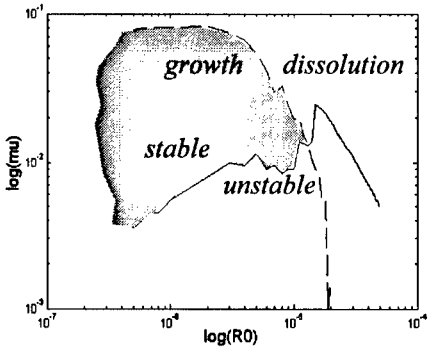

FIGURE 7. Thresholds for growth by rectified diffusion (dotted line) and onset of shape instability (solid line) for the most unstable modes. Calculations are for 1 MHz and 2.0 MPa, and a dissolved gas content of 10% of saturation.

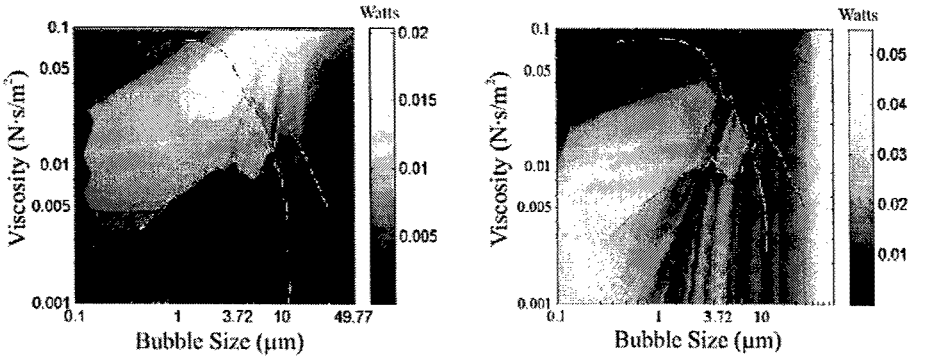

FIGURE 8. Stability thresholds from Fig. 7 overlaid on the heating power plots from Fig. 6, for 1 MHz, 2.0 MPa, and 10% saturation. Plot (a) is the viscous heating, plot (b) the acoustic heating. The allowed region for bubbles is shaded.

Figure 8 combines the stability thresholds with the bubble heating calculations. It can be seen that the allowed region of stable growing bubbles significantly narrows the possible bubble sizes, and thus also the possible heating contributions, notably excluding the viscous peak heating, while allowing the secondary acoustic emission heating from inertial bubbles. If we further restrict ourselves to a single viscosity value consistent with our passive cavitation experiment results, we conclude that our likely bubble size distribution ranges from 0.1 to 1 micron, and our effective viscosity is most likely near 0.005.

OUTLOOK AND FUTURE WORK

The above results indicate that we can expect to quantitatively model bubble-enhanced heating in a predictive way. We need further experiments to verify the predictions of our instability models for bubble-size distributions. With such a validated model, it may be possible in the future to ensure that HIFU parameters are chosen in order to maximize the efficiency benefit of bubble-enhanced heating; conversely, such a model (perhaps also combined with a passive cavitation monitoring capability) could ensure the avoidance of cavitation which would go undetected using conventional ultrasound imaging.

ACKNOWLEDGMENTS

We gratefully acknowledge the support of DARPA (via a subcontract to the University of Washington) and the U.S. Army (via a subcontract to the National Center for Physical Acoustics). X. Yang was partially supported by NASA.

REFERENCES

1. Allen, J.S/, Roy, R.A., Church, C.C., *IEEE UFFC*, **44**, 743-751(1997).
2. Apfel, R.E., Holland, C.K., *Ultrasound Med. Biol.*, **17**, 179-181 (1991).
3. Arefiev, A., Prat, F., Chapelon, J-Y., Tavakkoli, J., Cathignol, D., *Ultrasound Med. and Biol.*, **24**, 1033-1043 (1991).
4. Bacon, D.R., Carstensen, E.L., *J. Acoust. Soc. Am.*, **88**, 26-34 (1990).
5. Brenner, M.P., Lohse, D., Dupont, T.F., *Phys. Rev. Lett;*, **75**, 954-957 (1995).
6. Bush, N.L., Rivens, I., ter Haar, G.R., Bamber, J.C., *Ultrasound Med. Biol.*, **19**, 789-801 (1993).
7. Carstensen, E.L., Kelly, P., Church, C.C., et al., *Ultrasound Med. and Biol.*, **19**, 147-165 (1993).
8. Chapelon, J-Y., Cathignol, D., Cain, C., Ebbini, E., Kluiwstra, J-U., Sapozhnikov, O.A., Fleury, G., Berriet, R., Chupin, L., Guey, J-L., *Ultrasound Med. and Biol.*, **26**, 153-159 (2000).
9. Chapelon, J-Y., Dupenloup, F., Cohen, H., Lenz, P., *IEEE UFFC*, **43**, 623-625 (1996).
10. Chapelon, J-Y., Prat, F., Delon, C., Margonari, J., Gelet, A., Blanc, E., *Proc. IEEE Ultrason. Symp.*, 1357-1360 (1991).
11. Chavrier, F., Chapelon, J-Y., Gelet, A., Cathignol, D.J., *J. Acoust. Soc. Am.*, **108**, 432-440 (2000).
12. Christopher, T., Carstensen, E.L., *Ultrasound Med. Biol.*, **22**, 1103-1116 (1996).
13. Church ,C.C., *J. Acoust. Soc. Am.*, **83**, 2210-2217 (1988).
14. Clarke, R.L., ter Haar, G.R., *Ultrasound Med. Biol.*, **23**, 299-306 (1997).
15. Crum, L.A., Hansen, G.M., *Phys. Med. Biol.*, **27**, 413-417 (1982).
16. Damianou, C.A., Sanghvi, N.T., Fry, F.J., Maass-Moreno, R.. *J. Acoust. Soc. Am.*, **102**, 628-634 (1997).
17. Dalecki, D., Carstensen, E.L., Parker, K.J., *J. Acoust. Soc. Am.*, **89**, 2435-2447 (1991).
18. Ebbini, E.S., ed., Special issue on therapeutic ultrasound. *IEEE Trans UFFC*, 43, 989-1129 (1996).
19. Edson, P.L., "The role of acoustic cavitation in enhanced ultrasound-induced heating in a tissue-mimicking phantom," Ph.D. dissertation, Boston University, Boston, MA (2001).
20. Eller, A., Flynn, H.G., *J. Acoust. Soc. Am.*, **37**, 493-503 (1965).
21. Eller, A., Crum, L.A., *J. Acoust. Soc. Am.*, **47**, 762-767 (1970).
22. Everbach ,E.C., Makin, I.R.S., Azadniv, M., Meltzer, R.S., *Ultrasound Med. and Biol.*, **23**, 619-624 (1997).
23. Fowlkes, J.B., Holland, C,K., "Mechanical Bioeffects from Diagnostic Ultrasound: AIUM Consensus Statements," *J. Ultrasound Med.*, **19** (2), 69-72 (2000).
24. Fry , F.J., Kossoff, G., Eggleton, R.C., Dunn, F., *J. Acoust. Soc. Am.*, **48**, 1413-1417 (1970).
25. Fry, F.J., Sanghvi, T., Foster, R.S., et al., *Ultrasound Med. and Biol.*, 21, 1227-1237 (1996).
26. Fry, W.J., Wulff, V.J., Tucker, D., *J. Acoust. Soc. Am.*, 22, 867-876 (1950).
27. Gaitan, D.F., Holt, R.G., *Phys. Rev. E*, **59**, 5495-5502 (1999).
28. Goss, S.A., Johnson, R.L. and Dunn, F., *J Acoust. Soc. Am.*, **64**, 423-457 (1978).
29. Goss, S.A., Johnson, R.L. and Dunn, F., *J. Acoust. Soc. Am.*, **68**, 93-108 (1980).
30. Hallaj, I.M., Cleveland, R.O., *J. Acoust. Soc. Am.*,**105** (5), L7-L12 (1999).
31. Hamilton, M.F., Morfey, C.L., "Model equations" in *Nonlinear Acoustics*, edited by M.F. Hamilton and D.T. Blackstock, New York: Academic Press 1998.
32. Hao, Y., Prosperetti, A., *Phys. Fluids*; **11**, 1309-1317 (1999).
33. Hilgenfeldt, S., Lohse, D., Zomack, M., *J. Acoust. Soc. Am.*, **107**, 3530-3539 (2000).
34. Holt, R.G., Cleveland, R.O., Roy, R.A., "Proc. of the 16th ICA/135th Meeting of the ASA, Seattle, WA," edited by P. Kuhl and L. Crum, New York: ASA, 1998, pp. 1057-1059.
35. Holt, R.G., Roy, R.A., *Ultrasound Med. Biol.*, **27**, 1399-1412 (2001).
36. Huang, J., "Heating in vascular tissue and flow-through tissue phantoms induced by focused ultrasound," Ph.D. dissertation, Boston University, Boston, Massachusetts, 2002.
37. Hynynen, K., *Ultrasound Med. Biol.*, **17**, 157-169 (1991).
38. Hynynen, K., Jolesz, F., *Ultrasound Med. Biol.*, **24**, 275-283 (1998).
39. Kamath, V., Oguz, H.N., Prosperetti, A.. *J. Acoust. Soc. Am.*, **92**, 2016-2023 (1992).
40. Keller, J.B., Kolodner, I.I., *J. Appl. Phys.*, 27, 1152-1161 (1956).
41. Keller, J.B., Miksis, M.J., *J. Acoust. Soc. Am.*, **68**, 628-633 (1980).
42. Lehmann, J.F., Herrick, J.F., *Arch. Phys. Med. Rehab.*, **34**, 86-98 (1953).

43. Leighton, T.G., *The acoustic bubble*, Academic Press, London, 1994, 291-298.
44. Lele, P.P., "Effects of ultrasound on solid mammalian tissues and tumors in vivo" in *Ultrasound: Medical applications, biological effects and hazard potential*, edited by M.H. Repacholi, M. Grandolfo, and A. Rindi, New York: Plenum, 1987, 275-306.
45. Nyborg, W.L., *Phys. Med. Biol.*, **33**,785-792 (1988).
46. Parker, K.J., *J. Acoust. Soc. Am.*, **74**, 1356-1361 (1983).
47. Penney, D.P., Schenk, E.A., Maltby, K., et al., *Ultrasound Med. and Biol.*, **19**, 127-135 (1993).
48. Prosperetti, A., *J. Acoust. Soc. Am.*, **61**, 17-27 (1977).
49. Prosperetti, A., *J. Fluid Mech.*, **222**, 587-616 (1991).
50. Sanghvi, N.T., Fry, F.J., Bihrle, R., Foster, R.S., Phillips, M.H., Syrus, J., Zaitsev, A.V., Hennige, C.W., *IEEE Trans UFFC*, **43**, 1099-1109 (1996).
51. Sibille, A., Prat, F., Chapelon, J-Y., El Fadil, F.A., Henry, L., Theilliere, Y., Ponchon, T., Cathignol, D.. *Ultrasound Med. and Biol.*,**19**, 803-813 (1993).
52. Smith, N.B., Hynynen, K., *Ultrasound Med. and Biol.*, **24**, 1045-1054 (1998).
53. Tavakkoli, J., Birer, A., Arefiev, A., Prat, F., Chapelon, J-Y., Cathignol, D., *Ultrasound Med. and Biol.*, **23**, 107-115 (1997).
54. ter Haar, G.R., *Ultrasound Med. and Biol.*, **21**, 1089-1100 (1995).
55. ter Haar, G.R., Daniels, S., Eastaugh, K.C., Hill, C.R., *Br. J. Cancer*, **45** (Suppl. V), 151-155 (1982).
56. Vaezy, S., Martin, R., Schmiedl, U., et al., *Ultrasound Med. and Biol.*, **23**, 1413-1420 (1997).
57. Vaezy, S., Martin, R., Yaziji, H., et al., *Ultrasound Med. and Biol.*, **24**, 903-910 (1998).
58. Williams, A.R., Kubowicz, G., Cramer, E., et al., *Echocardiography*, **8**, 423-433 (1991).
59. Yang, X., "Investigation of bubble dynamics and heating during focused ultrasound insonation in tissue mimicking materials," Ph.D. dissertation prospectus, Boston University, Boston, MA, 2002.

Ultrasonic Ablation Of Renal Tissues *In Vitro*

Christakis Damianou

Frederick Institute of Technology (FIT)
18, Mariou Agathangelou, 3080, Limassol, Cyprus

Abstract. The aim of this paper is to present issues regarding the ablation of excised porcine renal tissues *in vitro* using High Intensity Focused Ultrasound (HIFU). Renewed interest in evaluating kidney ablation is justified because of the advancement in information and ultrasonic technology.

A spherically focused transducer of 4 cm diameter having 10 cm radius of curvature and operating at 4 MHz was used. The intensity used was between 2000-4000 W/cm^2 and the pulse duration between 1 and 10 s.

Production of lesions in the cortex is consistent, whereas lesions in the medulla *in vitro* are created whenever there are no air spaces in the medulla. Typically the lesion length at 2000 W/cm^2 and 5 s pulse duration is around 20 mm and the corresponding width around 3 mm. A thermal simulation model that was developed previously for other applications was proven to be a useful tool for incorporating new treatment protocols in renal tissues.

Lesioning of a large volume was achieved by moving the transducer in a grid formation. Lesioning through a fat layer is possible provided there are no air spaces between fat and kidney. Several experiments were performed in a muscle-fat-kidney tissue arrangement, demonstrating that modern HIFU technology could be a very efficient modality for the treatment of deep-seated tumours in the kidney.

INTRODUCTION

HIFU is a non-invasive procedure for heating tumours without affecting the normal tissue surrounding the tumour. Therefore HIFU is being investigated as alternative to standard surgical techniques. Although, the idea of using of HIFU was proposed in the middle of this century [1], its maximum potential for clinical use is being established recently due to the developments of sophisticated systems (for example, [2,3,4]). HIFU has been proven though the research of nearly 60 years to be an effective and efficient method for ablating soft tissue.

HIFU was explored almost in every tissue that is accessible by ultrasound. The following literature represents some examples of some applications explored: eye [5], prostate [6, 7], liver [8], brain [9,10,11], and Kidney [12,13].

Recently, the technology of HIFU is becoming stronger because now therapy can be guided by imaging. Ultrasonic imaging is the simplest and most inexpensive method, however it has poor contrast between soft tissues. On the other hand Magnetic Resonance (MR) imaging offers superior contrast. Several studies have been published in the area of ultrasonic imaging (for example [14,15]) and in the area of MR imaging (for example [16,17]), enhancing the potential of HIFU.

The main goal of HIFU is to maintain a temperature between 50-100^o C for a few seconds (typically <10 s), in order to cause tissue necrosis. Typically a focal peak intensity between 1,000-10,000 W/cm^2 is used with a pulse duration between 1-10 s and a frequency of 1 -5 MHz.

Experiments were performed using a generic HIFU system, which includes a signal generator, a RF amplifier, a 3-D robotic system, a transducer and a PC that controls the entire system. Pulse duration smaller than 10 s was used in all the experiments in order to minimise effects of blood perfusion. In this work methods suggested by [18] were used in order to produce complete, reliable and consistent ablation of clinically useful renal tissues.

Results of HIFU ablation of kidney *in vitro* are presented. Single lesions in the cortex and medulla, were created with/or without a fat layer. The ultimate goal was to create large lesions, which was accomplished by moving the transducer in patterned schemes. The experimental results are compared with the results of a simulation model, which includes the effect of rapid increase of attenuation during the transition of a tissue from normal to necrotic.

MATERIALS AND METHODS

Ultrasonic System

Figure 1 shows an illustrated block diagram of the system with photos of the actual instruments. The system consists of a signal generator (HP 33120A Hewlett Packard, now Agilent technologies), an RF amplifier (LA 100-CE, Kalmus, Bothell, Washinghton), a three dimensional positioning system (MD-2, Arrick Robotics, Hurst, Texas), and a 10 cm spherically shaped bowl transducer made from piezoelectric ceramic PZT4 (Etalon, Lebanon, Indiana). The transducer operates at 4 MHz, has focal length of 10 cm and diameter of 4 cm. The transducer was rigidly mounted on the three-dimensional positioning system.

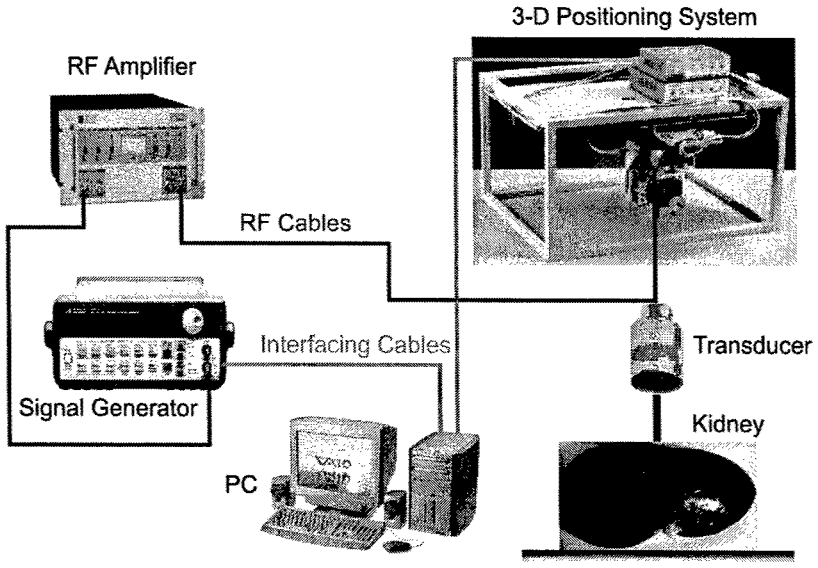

FIGURE 1. Block diagram of the High Intensity Focused Ultrasound.

The signal generator was controlled using the serial port whereas the 3-D robotic system was controlled using the parallel port. A user-friendly program written in Visual Basic has been developed in order to control the system.

Acoustical Power

The total power delivered by the transducer was measured before the beginning of each experiment with an ultrasound power meter (Precision advanced, Model UPM-DT-10). The spatial average intensity (I_{SAL}) at the center of the focal region could be determined from the total power (P) and the –6 dB radial dimension (D) by using the following equation

$$I_{SAL}=0.87P/D^2. \quad (1)$$

In all the experiments the intensity used is the spatial average intensity.

In Vitro Experiments

The tissue under ablation was placed in a water tank. Boiling the water to 100° C degassed the water. The tissue was placed on top of an absorbing material in order to shield adjacent tissue form stray radiation from the bottom of the plastic water tank. The transducer was placed on the arm of the 3-D robotic arm and was immersed in the water tank, thus providing good acoustical coupling between tissue and transducer. Any bubbles that may have collected under the face of the transducer face were removed in order to eliminate any reflections. The sample size was typically 60 mm x 40 mm with thickness of around 30 mm. The sample was gently massaged after thawing to remove any trapped air bubbles, and the experiment was initiated 10-20 min after placing the sample in the tank. While it is difficult to assess whether this procedure was sufficient to remove very small air bubbles, in several samples where this procedure was not followed the presence of air bubbles was easily detected from the resulting lesion appearance.

The intensity used during the experiments was kept to a level that does cause boiling of tissue water that leads to the formation of vapour bubbles, which prevent the production of pure thermal lesions, whose size can be controlled.

Simulation Model

The lesion size was predicted using a model that uses the thermal dose concept described in [19], and [20]. It is known that the thermal dose threshold referenced at 43° C for kidney is 50 min [21]. For thermal dose below 50 min at 43° C the attenuation at room temperature of 4 Np/m/MHz was used based on [22]. For thermal dose higher then 50 min at 43° C the kidney tissue is necrosed and then the attenuation of necrotic tissue was used (8 Np/m-MHz) [22].

Basically attenuation α (attributed mostly to absorption in homogeneous tissue) affects the power density Q which is given by the following equation:

$$Q=2\alpha I e^{-2\alpha x}, \quad (2)$$

where I is the intensity, and x is the depth in tissue. For short pulses the power density is the main factor elevating the tissue temperature.

RESULTS

Figure 2 shows the length of a lesion created in excised porcine kidney using the intensity of 2000 W/cm^2 for 5 s (focal depth=15 mm). The lesion produced is placed entirely in the cortex of the kidney. The length is measured along the transducer central axis, whereas width is measured perpendicularly to the transducer central axis. The lesion length is about 20 mm, and the width is about 3 mm. In a certain row of lesions only one dimension of the lesion (length or width) was possible to be measured, since the sample was sliced along one dimension. Figure 3 shows lesions that propagated inside the medulla region. Thus, in the case that there are no bubbles inside the medulla, ablation is feasible.

FIGURE 2. Thermal lesion placed in the cortex of pig kidney *in vitro*.

FIGURE 3. Lesions propagating in the medulla of pig kidney *in vitro*.

Table 1 shows the simulated length and width using the pure thermal model and using the model that accounts for the increased attenuation of necrotic tissue. The transducer parameters used are: frequency = 4 MHz, Radius of curvature =10 cm, and Transducer diameter = 4 cm. The focal intensity of 2000 W/cm^2 was applied for 5 in a focal depth of 15 mm. Note that the zero perfusion represents the case of in-vitro kidney, whereas the case of in-vivo is modeled by using the perfusion of 70 Kg/m^3-s.

TABLE 1. Simulated length and width for the pure thermal model and the model of varying attenuation of necrotic tissue. The transducer parameters used are: frequency = 4 MHz, Radius of curvature =10 cm, and Transducer diameter = 4 cm. The focal intensity of 2000 W/cm^2 was applied for 5 s in a focal depth of 15 mm.

Quantity	Pure thermal model		Varying attenuation model	
	Perfusion (Kg/m^3-s)		Perfusion (Kg/m^3-s)	
	0	70	0	70
Length	22.5	19.1	20.2	17.2
Width	3.9	2.9	3.1	2.2

Creation of lesions through fat layer is possible if there are no bubbles between the fat-kidney interface. Figure 4 shows lesion length through fat layer with a 2000 W/cm^2 ablation for 5 s. Note that compared to a similar ablation in kidney tissue the lesion length is smaller than with the presence of a fat layer. This is attributed to the fact that fat has much higher attenuation (7-8 Np/m/MHz) than kidney tissue, and therefore acts as an acoustical barrier. Figure 5 shows the corresponding figure showing the lesion width (matrix of 3 x 3 lesions). Lesions appeared to be light brown inside the white fat tissue.

Figure 6 shows a lesion created by moving the transducer in a patterned movement (square grid of 12x12 with 2 mm step) in both directions (red pattern indicates the intended target). The power used was 2000 W/cm^2 for 5 s. A delay of 10 s was used between the pulses in order to eliminate the near field heating [19]. Based on the width obtained in Figure 2, a 2 mm step will secure overlapping lesions. Although a bigger step can be proposed after extensive optimisation studies, for simplicity the 2 mm is used which is a very safe choice at this point. Figure 7 shows the corresponding length of the large lesion. The lesion was extended up to the medulla. Figure 8 shows a large lesion created though fat using transducer movement in a grid pattern. Presumably there were no air spaces between fat and kidney interface and therefore the intended target was completely covered with necrosis.

The presence of cavitation was verified by using a wide band receiver placed perpendicular to the insonation beam. For the given transducer and for a pulse duration of 5 s it was observed that cavitation took place for intensity levels greater than 3200 W/cm2. Figure 9 shows lesion length using 5 s pulse and 4000 W/cm2 intensity in kidney tissue in vitro. Note that at this acoustic level cavitational effect occurred which was verified by the cavitational receiver. Tissue examination revealed gross tissue disruption verifying the event of acoustic cavitation.

DISCUSSION

The lesion length and width of Figure 2 which is produced in a tissue *in vitro* (i.e. perfusion rate is 0) is best estimated using the varying attenuation model. Note that at perfusion of 70 Kg/m^3-s (i.e. *in vivo* case) the simulated lesion length and width is decreased compared to the *in vitro* case. The lesion length and width is generally smaller in the varying attenuation model because the increased attenuation lowers the power density in the tissue and thus the lesion size is decreased.

Lesions were created all the way to the medulla, provided that there were no air spaces in the medulla. Air spaces are created because of the absence of blood that normally flows in this region. However, ablation of cortex tissue is of primary concern since the renal carcinoma (most important renal cancer) grows inside the cortex and then extends to the peritoneal fat.

Lesions can be created though fat layers provided that there are no air spaces between the fat and kidney interface. The lesion size when the beam goes through a fat layer is decreased because of the high attenuation of fat which acts likes an acoustic barrier. With a 4 MHz transducer, 5 s pulses and intensity levels below about 3200 W/cm2 the lesions created are based solely on thermal effects.

FIGURE 4. Lesions created in pig kidney *in vitro* through fat layer.

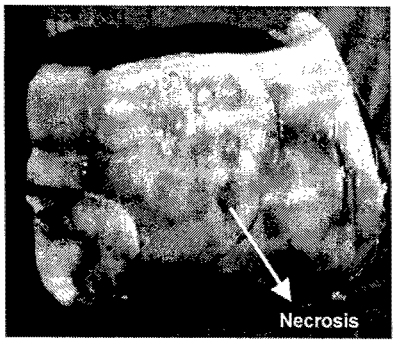

FIGURE 5. Lesions in peritoneal fat.

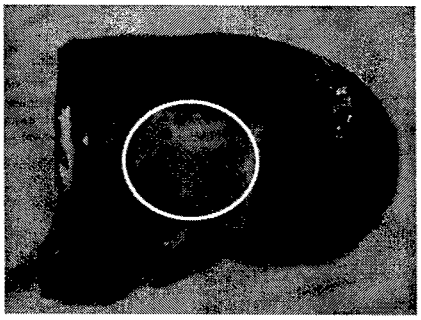

FIGURE 6. Large lesion in pig kidney *in vitro* by moving the transducer in a grid formation (12 x12) (top view).

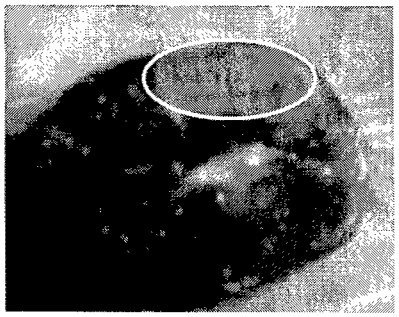

FIGURE 7. Large lesion in pig kidney *in vitro* by moving the transducer in a grid pattern (12 x12) (side view).

FIGURE 8. Large lesion in pig kidney *in vitro* through fat layer using a grid pattern (side view).

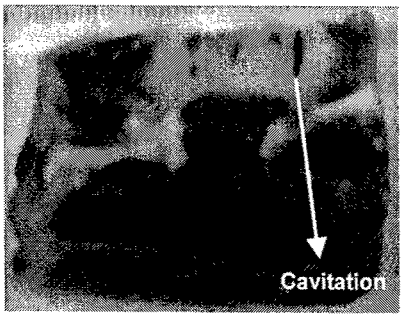

FIGURE 9. Large lesion in pig kidney *in vivo* by moving the transducer in grid pattern showing cavitational activity.

Data from Hynynen (1991) [23] suggests that the threshold spatial peak intensity at 4 MHz is about 6000 W/cm^2 (extrapolated) or 3333 W/cm^2 (average intensity). Thus, with the average intensity of 4000 W/cm^2 used in the *in-vivo* experiments, cavitation was not avoided.

During cavitation, lesions have irregular boundaries, as opposed to the case of operating below cavitation, where the lesions have smooth boundaries, exhibit less mechanical damage to the tissues, and always occur at the center of the focal region.

ACKNOWLEDGEMENTS

This work was supported by the Research Promotion Foundation (RPF) of Cyprus, under the contract 25/99.

REFERENCES

1. Lynn, J.G., Zwemer, R.L., Chick, A.J., Miller, A.E., *J Gen Phyciology*, **26**, 179-93 (1942).
2. Chapelon, J-Y., Margonari, J., Vernier, F., Gorry, F., Ecochard, R., Gelet, A., "*In vivo* effects of high-intensity ultrasound on prostatic adenocarcinoma", *Dunning R3327, Cancer Res.*, **52** (22), 6353-7 (1992).
3. Hynynen, K., Damianou, C., Darkazanli, A., Unger, E., Schenck, J.F., *Ultrasound in Med. & Biol.*, **19(1),** 91-2, (1993).
4. Bihrle, R., Foster, R.S., Sanghvi, N.T., Donohue, J.P., Hood, P.J., *Journal of Urology*, **151 (5),** 1271-5 (1994).
5. Lizzi, F., Coleman, J., Driller, J., Franzen, L., Jakobiec, F, *Invest. Ophthalmol. Visual Sci.*, **5**, 350-360, (1977).
6. Sanghvi, N., Fry, F., Foster, R., Chua, R., Chua, G., Griffith, S., Birhle, R., Yang, R., Zink, J., Hennige, L., *Med Biol Eng Comp*, **29**, 748 (1991).
7. Chapelon, J-Y., Ribault, M., Vernier, F., Souchon, R., et al., *Eur J Ultrasound Mar* , **9** (1), 31 8, (1999).
8. ter Haar, G., Sinnett, D., Rivens, I., *Phy Med Biol.*, **34 (11),** 1743-50 (1989).
9. Fry, W., Mosberg, W., Barnard, J., Fry, F., *J Neurosurg*, **11**, 471-9 (1954).
10. Lele, P.P., J. *Physiol.*, **160**, 494-512 (1962).
11. Vykhodtsev, N.I., Hynynen, K., Damianou, C., *Ultrasound Med Biol.*, **20 (9),** 987-1000 (1994).
12. Chapelon, J-Y., Margonari, J., Theillere, Y., Gorry, F., Vernier, F., Blanc, E., Gelet, A., *Eur Urol.*, **22 (2)**, 147-52 (1992).
13. Hynynen, K., Damianou, C.A., Colucci, V., Unger, E., Cline, H.H., Jolesz, F.A., *Journal of Magnetic Resonance Imaging*, **5 (3),** 259-66 (1995).
14. Seip, R., and Ebbini, E., *IEEE Trans. Biomed Eng.*, **42 (8),** 828-839 (1995).
15. Maass-Moreno, R., Damianou, C.A., Sanghvi, N.T., *J. Acoust. Soc. Am.*, **100** (4 Pt 1), 2522-30 (1996).
16. Cline, H.E., Schenck, J.F., Hynynen, K., Watkins, R.D., Souza, S.P., Jolesz, F.A., *J Comput. Assist. Tomogr.*, **16**, 956-65 (1992).
17. Hynynen, K., Darkazanli, A., Unger, E., Schenck, J.F., *Med. Phys.*, **20(1),** 107-15 (1993).
18. Malcolm, A.L., ter Haar, G.R., *Ultrasound Med Biol.*, **22 5)**, 659-69 (1996).
19. Damianou, C., Hynynen, K., *Ultrasound in Med. Biol.*, **19 (9)**, 777-87 (1993).
20. Damianou, C., Hynynen, K., *J. Acoust. Soc. Am.*, **95 3),** 1641-9 (1994).
21. Borrelli, M., Thompson, L., Cain, C., Dewey, W., *J. Radiation Oncology Biol. Phys.*, **19**, 389-399 (1990).
22. Damianou, C., Sanghvi, N., Fry, F., Maass, R., J. *Acoust. Soc. Am.* **102 (2),** 628-634 (1997).
23. Hynynen, K., *Ultrasound in Med. Biol.*, **17 (2),** 157-69 (1991).

Experimental Study Of Tumor Cells Apoptosis Induced By Ultrasonic Thermal Therapy Combined With Chemotherapy

Jingfeng Bai[1], Yuhong Guo[1] , Yazhu Chen[1], Yifei Yang[2], Hong Zhao[3]

[1]*Department of Biomedical Engineering, Shanghai JiaoTong University, Shanghai, China 200030*
[2]*Shanghai Ninth People Hospital, Shanghai Second Medical University, Shanghai, China 200025*
[3]*Shanghai Huashan Hospital, Fudan University, Shanghai, China 200010*

Abstract. In this paper, the tumor cells of the oral cavity were selected as experimental objects, and the cooperative effects of ultrasonic thermal therapy combined with chemotherapy to induce tumor cell death were studied. Combined with special chemotherapy, the optimal parameters of ultrasonic therapy, such as frequency, dose, sound field, treatment time and temperature, were found by the animal trials in which the human tumor cells were inoculated into the body of nude mice. Experimental results show that the optimized thermal treatment technology of ultrasonic combined with chemotherapy can produce obvious inhibitory effects to limit the tumor's growth. The reason is that the cooperative effects of the two treatment methods can induce tumor cell apoptosis, and the optimized therapy plan is the main factor to affect the cooperative effects. Additionally a result has been found that the heat-drug interaction can produce the inhibitory action with respect to tumor weight, and the tumor inhibitory ratio is 97.86% in our experiment.

INTRODUCTION

In recent years, malignant tumor has become one of the most common diseases and one of the main causes of human death. Its incidence shows an increasing tendency. According to the prediction of WTO, tumors will become the number one killer in the 21st century. It is well known that most patients with malignant tumors are diagnosed while in the middle to late stages, and any kind of traditional or conventional treatment method, such as resection, chemotherapy, or radiotherapy, cannot be completely effective in healing such a disease alone [1-3]. So a combined treatment method must be adopted. Thermotherapy has been demonstrated to be effective in killing tumor cells and inducing cancer cell apoptosis. As an effective adjuvant therapeutic method, localized thermotherapy has been used in clinical tumor treatment combined with chemotherapy or radiotherapy [4,5]. The degree of thermal enhancement of these therapies has been strongly dependent on the ability to localize and maintain therapeutic temperature elevations, and the effectiveness of thermotherapy has been shown to be strongly dependent upon the temperature uniformity delivered [6].

With the rapid development of the past 10 years, an ultrasonic thermal therapy system has been considered an effective approach to heating tumors [7]. This method takes advantage of ultrasound's greater penetration, satisfactory efficacy of temperature control and acute temperature measurement. Ultrasound technology has

significant characteristics that allow for a higher degree of spatial and dynamic control of heating compared to other common heating methods [8,9]. It has also shown the superiority of thermal therapy over other approaches and has begun to receive much attention in the tumor thermotherapy field. So ultrasound is regarded as the most promising thermotherapy technique. But the exact mechanisms responsible for its antitumor effect are still not yet fully understood and need further experimental investigation [10].

In this paper, the antitumor effects of ultrasonic thermal therapy, chemotherapy and their combined methods will be studied and a pilot study result also will be given.

METHODS OF CELL APOPTOTIC INDUCEMENT

Ultrasonic Thermal Therapy Equipment

The ultrasound field was generated by four single square PZT transducers. Each was of dimensions 32 mm×32 mm, and the system had two resonant frequencies for different treatment objects, 1 MHz and 3.5 MHz, respectively. The power signal feeding the transducers was generated by a frequency generator and amplified by an LC amplifier. The electrical impedance of the transducer was matched to the output impedance of the amplifier by the LC matching network. An Acerate temperature sensor was used to measure the actual temperature of the treatment target for accurate power control of the PZT transducers.

Movement of the treatment head in the x, y or z direction was performed by the use of a 3D Movement Machine-compatible mechanical positioning system. A plastic membrane covered the treatment head so that the water could be infused into the head. The entire setup was placed in the whole frame of the system. The treatment plan, composed of target location, ultrasound dose, frequency, and temperature control, was proposed by the supporting software with the participation of the doctors. The whole schematic diagram was shown in Figure 1.

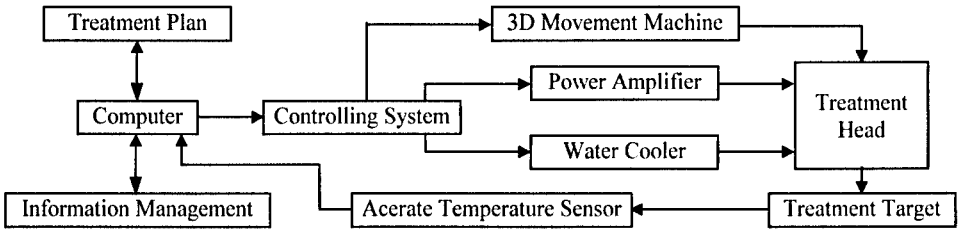

FIGURE 1. Schematic Diagram of Ultrasonic Thermal Therapy System.

Experimental Method

The therapy plan for this study is shown in Table 1. The experimental nude mice, which had been inoculated with Tca8113 tumor cells, were divided into five groups. The CDDP was used as the chemotherapy medicine. The mice in the CDDP group were injected with 0.1ml CDDP (0.6mg/ml) into their abdomens, the treatment interval was two days and total trials were five in number. In the thermal group, the mice were anesthetized, and the ultrasound was localized on the tumor with a dose of 3.5 MHz, 42° C, 40 min. The two acerate sensors were used to control the thermal temperature. The third group of the carcinomatous mice was treated by ultrasound therapy combined with the CDDP method as used on mice of the first group. In the fourth group, the mice were selected as the contrast objects, and none of the above treatments were adopted. In the other two experimental groups, the treatment interval and times were the same as those in the CDDP group.

TABLE 1. Treatment Method of Each Experimental Group.

Name of Group	Number of Nude Mice	CDDP (0.6mg/ml)	Ultrasonic Thermal Dose
Contrast	13	0	0
CDDP	10	0.1 ml×5	0
Thermal	10	0	3.5MHz, 42° C, 40 min×5
Thermal+CDDP	10	0.1 ml×5	3.5MHz, 42° C, 40 min×5

In order to obtain the study results, some parameters were used to describe and evaluate the changes of tumors in each experimental group. The tumor volume was the most important parameter, and showed an obvious treatment effect. Equation (1) can be used to calculate the tumor volume. A is the longest diameter of the tumor, and B is the shortest one in the vertical direction [11].

$$V = AB^2\pi / 6 \tag{1}$$

Tumor inhibitory ratio was another important parameter with which to evaluate the therapy method. There were two different ways to compute the result, according to the tumor volume (R_V) or tumor weight (R_W).

$$R_V(\%) = (1 - \frac{\bar{V}_E}{\bar{V}_C}) \times 100\% \tag{2}$$

$$R_W(\%) = (1 - \frac{\bar{W}_E}{\bar{W}_C}) \times 100\% \tag{3}$$

where $\bar{V}_E$ and $\bar{W}_E$ are the average values of experimental groups, while $\bar{V}_C$ and $\bar{W}_C$ are the average values belonging to the contrast group.

RESULTS AND DISCUSSION

Experimental results for the 3 treatment methods are detailed below. In the thermal group, some obvious dropsy occured in the skin of tumors at the beginning of the trial. But over three to five weeks, the dropsy disappeared step by step, and the color of the skin changed from purple to purple-black. Then the tumors died and became covered with scabs. At last, the scabs fell off. However, if the therapy effect was not so significant, the tumor grew after treatment, maybe after seven to ten days.

The tumor average volume in each group was recorded, as shown in Table 2.

TABLE 2. Dynamic Inspection of Tumor Average Volume in Each Experimental Group (mm^3).

Name of Group	Time (Week)					
	0	1	2	3	4	5
Contrast	197.1	439.8	784.5	1099.2	1555.1	1847.8
CDDP	192.2	307.6	398.8	564.6	1007.7	1315.9
Thermal	183.8	145.9	34.5	114.6	261.4	510.3
Thermal+CDDP	210.9	136.7	5.5	0.98	5.98	27.9

With careful inspection and research, the change in tendency of the tumor volume in the experimental groups can be found. From the first week, the tumors of the contrast group grew very fast, and the average volume was up to 1847.8 mm^3 at the end of the experiment. At three weeks, the tumors of the CDDP group grew very slowly. But in the fourth week, the growth rate increased, and the average volume was up to 1315.9 mm^3 at the end. After thermal therapy, the tumors of the third group decreased in volume. However, after the third week, these tumors began to grow slowly. At last, the average volume was 510.3 mm^3. Contrasting with the thermal group, the tumor growth of the fourth group was clearly inhibited, and the inhibition time was much longer than in the thermal group. And at the end of inspection, the tumor average volume was 27.9 mm^3. The ultrasonic thermal treatment combined with the CDDP method was the main reason.

For another parameter, Tumor Inhibitory Ratio (TIR), the calculation and experimental analysis also has been finished. The results are shown in Table 3 and Table 4.

TABLE 3. Changes of Average Tumor Inhibitory Ratio in Each Experimental Group.

Name of Group	Time (Week)				
	1	2	3	4	5
Contrast	0	0	0	0	0
CDDP	30.1	49.2	48.6	35.2	28.8
Thermal	66.8	95.6	89.6	83.2	72.4
Thermal+CDDP	68.9	99.3	99.9	99.6	98.5

TABLE 4. Inhibitory Ratio of Tumor Weight in Each Experimental Group.

Name of Group	Tumor Average Weight (g)	Tumor Inhibitory Ratio
Contrast	1.26±0.16	
CDDP	1.03±0.11	18.25
Thermal	0.33±0.17	73.81
Thermal+CDDP	0.03±0.02	97.86

The TIR had a high value at the start of treatment in the CDDP group, but decreased quickly with time. The ultrasonic thermal therapy combined with the CDDP method had a higher TIR and was much more effective during the whole treatment period. From the experimental results, the ultrasonic thermal therapy method combined with chemotherapy could improve the ability to kill the tumor tissue. The tumor inhibitory ratio of heat-drug interaction was 97.86%. So the conclusion is drawn that combined therapy can produce a cooperating effect.

After inspection of the this tumor research, another four groups of carcinomatous nude mice were prepared for further study. The reason that the ultrasonic thermal therapy method combined with the chemotherapy was more effective in killing tumor cells should be explained. From inspection of the experimental data, tumor cell apoptosis was found to be strongly induced by ultrasonic thermal therapy, combined with CDDP.

Apoptotic Index (AI) was a better value by which to assess the cooperating domino effect of the combined methods. At the appointed time, the mice were euthanized, and tumor tissue was selected and slices cut for an inspection. A statistical method was used to compute the AI according to the numbers of apoptotic cells and total cells in the inspection field. Some results are shown in the following two tables.

TABLE 5. Tca8113 Tumor Cell Apoptosis Induced by Ultrasonic Thermal Therapy+CDDP.

Name of Group	Apoptosis Cells
Contrast	3.17±1.78
CDDP	4.12±2.06
Thermal	7.74±1.26
Thermal+CDDP	12.03±1.42

TABLE 6. Dynamic Inspection of Tumor Cell Apoptotic Index (%).

Name of Group	Time (Hour)				
	0	6	12	24	48
Contrast	3.56±0.78	2.68±0.34	2.72±0.63	3.76±1.88	3.30±0.65
CDDP	2.94±0.61	4.23±2.06	6.12±0.82	3.68±1.24	3.58±1.22
Thermal	6.41±1.96	11.82±2.87	5.71±1.69	4.22±0.54	3.27±0.91
Thermal+CDDP	6.84±1.91	13.58±1.51	15.88±1.33	7.34±0.76	6.36±1.05

In Figure 2 to Figure 5, the apoptotic process of experimental tumor cells is shown on a microscopic level. The method of ultrasonic thermal therapy combined with CDDP can be seen to be more effective. In Figure 5, the number of apoptotic cells increases with ongoing treatment time, and the treatment resulted in the formation of apoptotic cell lumps as shown in Figure 4.

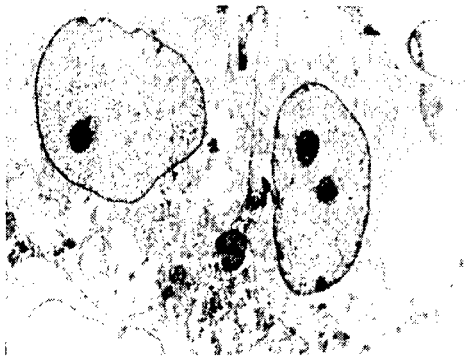

FIGURE 2. Normal Tca8113 Tumor Cells under the Electron Microscope.

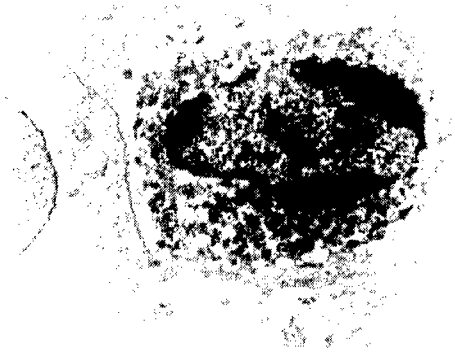

FIGURE 3. Tendency of Tumor Cell Apoptosis in Thermal +CDDP Group.

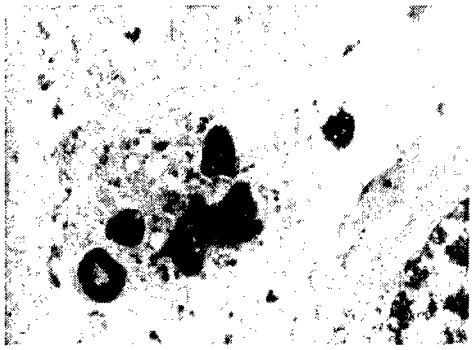

FIGURE 4. Occurrence of Apoptotic Cell Lumps after Thermal Therapy Combined with CDDP.

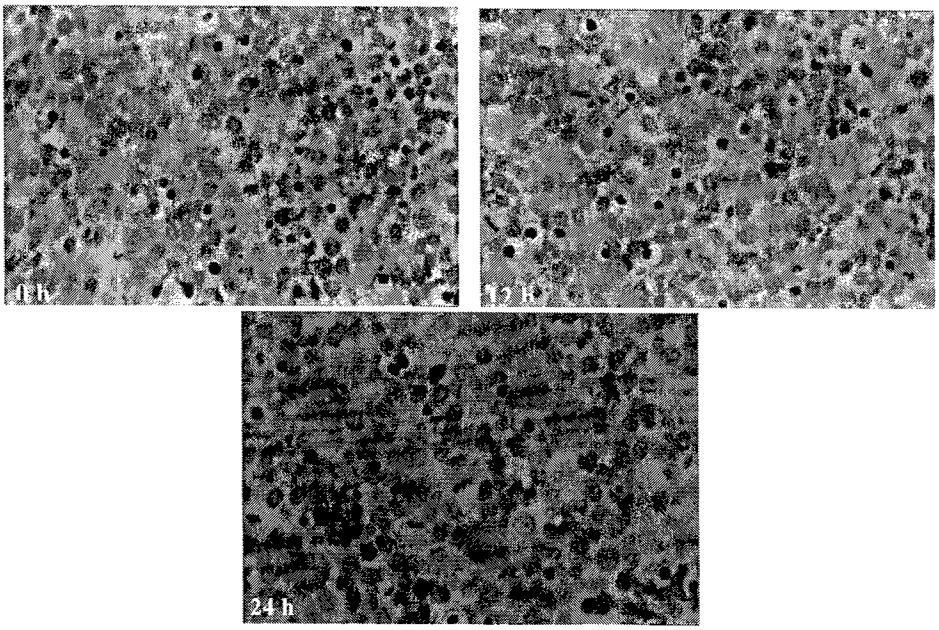

FIGURE 5. The Therapy Process of Tumor Cell Apoptosis in Thermal +CDDP Group (hours after treatment).

The putrescence and apoptosis were the two main factors to cause tumor cell death. Our experimental results showed that the combined method of ultrasonic thermal therapy plus CDDP could induce tumor cell death.

Another result was found, namely, that any single method (Ultrasonic Thermal Therapy or CDDP Chemotherapy) had equal ability of inducement, but the efficacy of combined methods was much larger. The compatible parameters of ultrasound, such as frequency, dose, sound field, treatment time and temperature, were more effective to accomplish the thermal therapy. And other antitumor effects of ultrasound therapy need further study.

ACKNOWLEDGMENTS

This research was funded by the grants 994419072 of Shanghai Technological Development Foundation. The authors also express the deep thanks to Shanghai Ninth People Hospital and Shanghai Huashan Hospital of Fudan University for experimental support.

REFERENCES

1. Hynynen, K., *1997 IEEE Ultrasonics Symposium*, 1305-1313 (1997).
2. Diederich, C.J., and Hynynen, K., *Ultrasound in Med. & Biol.*, **25** (6), 871-887 (1999).

3. Sanghvi, N.T., Hynynen, K., and Lizzi, F.L., *IEEE Engineering in Medicine and Biology*, 83-92 (1996).
4. Daum DR, Smith NB, King R, Hynynen K., *Ultrasound in Medicine and Biology*, **25** (7), 1087-1098 (1999).
5. Hynynen K., *Ultrasound Med. Biol.*, **17** (2), 157-169 (1991).
6. McGough, R.J., Kessler, M.L., Ebbini, E.S. and Cain, C.A., *IEEE Transactions on Ultrasonics, Ferroelectrics, and Frequency Control*, **43** (6), 1074-1084 (1996).
7. Hong Wan, Aarsvold, J., O'Donnell, M., and Cain, C., *IEEE Transactions on Ultrasonics, Ferroelectrics, and Frequency Control*, **46** (4), 913-928 (1999).
8. Damianou, C., and Hynynen, K., *Acoustical Society of America*, **95** (3), 1641-1649 (1994).
9. Rong, Y., and Mack, P., *Int J Hyperthermia*, **16** (1), 19-27 (2000).
10. Diederich, C. and Hynynen, K., *Ultrasound in Med Biol.*, **25**, 871-887 (1999).
11. Wiedemann, G.J., Siemens, H.J., et al, *Cancer Res.*, **53** (18), 4268-4272 (1993).

Can Heat Treatment By High Intensity Focused Ultrasound (HIFU) Enhance Anticancer Immunity In Human Prostate Cancer?

Gero Kramer, Georg E. Steiner and Michael Marberger

Department of Urology, University of Vienna, Austria

Abstract. Introduction and objectives: Defective antigen presentation in cancer may be overcome by induction of heat shock protein (HSP) expression. Thus the impact of heat treatment by high intensity focused ultrasound (HIFU) on promotion of anticancer immunity in human prostate cancer was analyzed. Methods: 10 human prostates were treated by thermoablation with transrectal HIFU 3 hours and 6 days before surgical removal and analyzed immunohistologically for HSP and cytokine expression. *In vitro*, regulation of HSP and cytokine mRNA and protein expression after sublethal heating was determined in BPH epithelial cells (EC), LNCaP and DU145 cells using cDNA expression array, RT-PCR and Western blotting. Effect of heat on T-cell immune response was investigated by analysis of T-cell receptor Vß-chain usage of peripheral blood T-lymphocytes after coculture with autologous of heat-treated prostate EC. Results: At the HIFU-border and -necrosis zone significantly enhanced expression of HSP72, HSP73, glucose regulated protein-78 and tumor necrosis factor-alpha of both benign and malignant EC was found. *In vitro*, LNCaP cells respond to heat by upregulation of HSPs on the mRNA and protein level. Further, more than 60 genes were upregulated, including those stimulating growth and communication of immunocompetent cells (ICAM-1, CSF). Stimulation of autologous peripheral blood T-lymphocytes by heat treated EC induced disproportional outgrowth of certain T-cell subsets with a defined T-cell receptor repertoire (Vß2, Vß 5.1). Conclusions: Heat response after HIFU may enhance anticancer immunity by increasing antigenicity of EC.

INTRODUCTION

Most of prostate cancer (CaP) specimens show lymphocytic infiltration to some extent and the theoretical capacity of the immune system to kill CaP cells has been demonstrated *in vivo* and *in vitro* (1). However, defective or insufficient tumor antigen presentation prevents an effective anticancer immune response. This is based on the fact that malignant transformation is frequently associated with a marked loss of major histocompatibility complex class I antigens. Cytotoxic T-lymphocytes require co-recognition of HLA class I epitopes and by their loss tumor cells escape T-cell recognition. Another reason is the spatial immune barrier built up by tumor cells which consists of tumor cell matrix and connective tissue cells and prevents contact between infiltrating lymphocytes and CaP cells. HSPs are major players in the immune response to cancer as they carry the antigenic fingerprint of a tumor cell. When one immunizes a mouse with a purified HSP-antigenic peptide preparation, the

HSPs interact with the antigen presenting cells (APC) present at the site of immunization. The same thing may happen naturally when HSP-peptide complexes are released from cells as a result of cell lysis due to cell necrosis. HSP upregulation on prostate cancer cells following heat stress may provide the danger signals required for a more effective immune response (2). Recent studies have indicated that tumor immunogenicity is associated with upregulation of the highly inducible HSP70 isoform, HSP72 (3). HSP72 can activate monocytes and up-regulate the expression of proinflammatory cytokines. Finally, HSPs may even prime cytotoxic T-lymphocytes in instances where tumor cells do not express sufficient cell surface MHC class I antigens (4). Consequently, we reasoned that upregulation of HSPs (5) in association with extensive coagulative necrosis of CaP tissue by means of transrectal high-intensity focused ultrasound (HIFU) (6-9) may elicit a very effective anticancer immune response.

To test this hypothesis, we analyzed whether (1) immunogenic HSPs and proinflammatory cytokines are upregulated after heat shock *in vivo* and *in vitro*, (2) heat treatment of prostate EC increase the antigenicity of epithelial cells *in vitro* and (3) heat treatment upregulates mRNA expression of genes, which are involved in immune defense and cell communication.

MATERIALS AND METHODS

Patients

Six patients with clinically localized CaP were treated with transrectal HIFU and underwent radical prostatectomy under the same anesthesia 3 hours later. The prostates of 4 patients with invasive bladder cancer were treated with a HIFU marker lesion at the time of staging transurethral resection of the bladder 6 days prior to radical cystoprostatectomy.

Transrectal High Intensity Focused Ultrasound (HIFU) For Prostatic Tissue Ablation

Transrectal HIFU treatment for prostatic tissue ablation was performed as described in detail elsewhere (9,10).

Immunoperoxidase Staining

For immunoperoxidase staining the following monoclonal antibodies were used: anti-HSP72 (clone C92F3A-5), anti-HSP72/73 (clone N27F3-4), anti-GRP-75(clone 30A5), anti-GRP-78 (clone 10C3) and anti-tumor necrosis factor-alpha. Tissue expression of HSPs was scored in a semiquantitative manner (minimum score: 0; maximum score: 3,5).

Western Blotting

LNCaP and prostatic stromal cells were prepared as described elsewhere (5). A chemoluminescence detection system was used for visualization and computer analysis.

Atlas Array

Primary prostate EC and LNCaP cells were incubated for 1 hour at 43° C. mRNA was prepared from heated and non-heated cells and 1μg of RNA was transcribed into cDNA using [a-^{32}P] dATP. Labeled, complex cDNA probes were separately hybridized overnight to the Atlas Arrays and double spotted with 588 different 200-500bp cDNA fragments. The signals were analyzed quantitatively using GS 250 molecular imager and the amount of reactivity was adjusted by the amount of reactivity with the blotted house keeping genes.

Reverse Transcriptase-Polymerase Chain Reaction (RT-PCR)

RT-PCR using primers specific for tumor necrosis factor-alpha (TNF-alpha) and granulocyte macrophage-colony stimulating factor (GM-CSF) was used as described elsewhere (10).

Autologous Prostate Epithelial Cell - T-Lymphocyte Reaction

To test the effect of sublethal heat treatment on T-cell immune response sublethally heated prostate EC were cocultured with autologous peripheral blood T-lymphocytes in the presence or absence of interleukin-2 (IL-2R) for 4 weeks. The quality of immune response was analyzed by implementation of an antibody panel directed against 14 individual Vß T-cell receptor chains and the IL-2R (anti-CD25).

Flow Cytometry Analysis

Two/three color analyses were performed using FACS and are described in detail elsewhere (11).

Statistical Analysis

For statistical analysis, a nonparametric Wilcoxon test was performed. A p value of <0.05 was statistically significant.

RESULTS

Effect Of Sublethal Heat Treatment On The Expression Of Heat Shock Proteins Of Primary BPH-Derived Prostate Epithelial Cells And LNCaP Prostate Carcinoma Cells

To investigate the heat response of BPH epithelial cells (EC) and CaP cells to sublethal temperatures cells were subjected to a 1-hour long 43° C heat shock. Identical amounts of radioactively labeled mRNA derived from both experimental groups were subsequently used for hybridization of the Atlas Array membranes (Fig.1). In contrast to the equally intense hybridization signals of BPH-EC obtained before and after heat shock when probed for the housekeeping gene, HSP72 mRNA expression in BPH EC was only found after heat shock. In contrast, untreated LNCaP cells constitutively expressed low levels of HSP72 mRNA. The heat response of LNCaP cells was characterized by a considerable upregulation of HSP72 mRNA considering the fact that the hybridization product of the housekeeping gene was by far less intense in the group of heated-treated LNCaP cells when compared with untreated LNCaP cells. Also HSP27 and HSP86 mRNA expression was considerably upregulated after heat exposure in both cell types. Following cell heating in the range of 43-49° C, HSPs were also upregulated on the protein level, but showed different, temperature dependent expression pattern. The maximum expression of HSP60 was after 46° C, while the maximum expression of GRP-75 was at 43° C.

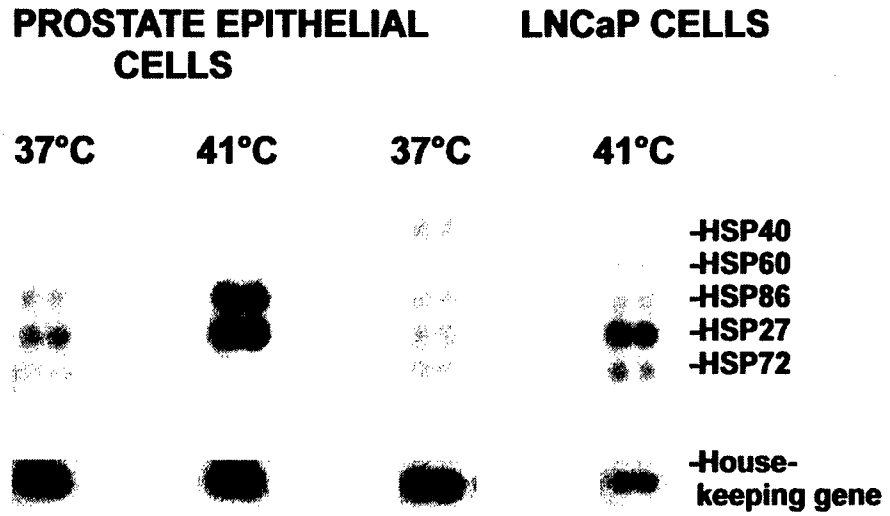

Figure 1. Kramer ,et al.

Effect Of Sublethal Heat Treatment On The Expression Of Cytokines Of DU145 Prostate Carcinoma Cells

Reverse transcriptase-polymerase chain reaction using primers for the proinflammatory cytokine tumor necrosis factor alpha confirmed that heat treatment of DU145 prostate carcinoma cells increased the production of mRNA of tumor necrosis factor alpha. TNF-a is known to induce proliferation and maturation of antigen presenting cells.

Upregulation Of Representative Genes By Heat On The Atlas Human cDNA Expression Array

However, the response to sublethal heat exposure is far more complex than only a simple upregulation of a small number of heat shock proteins. It involves a panel of more than 60 other important genes of various functional classes, including those which also stimulate anticancer immune response. For example, growth factors such as CSF-1 (=Macrophage-specific colony-stimulating F1m factor), which stimulate the growth of antigen presenting cells or costimulatory adhesion molecules such as ICAM-1 (Intercellular adhesion molecule-1), which enhance the contact between APC and cytotoxic T-cells. Further, cell cycle regulators, DNA synthesis, repair and recombination proteins or apoptosis-related proteins such as DAD-1 (Defender against cell death) or growth arrest and DNA-damage inducable protein GADD153 were significantly upregulated.

Effect Of HIFU Treatment On Heat Shock Protein And Cytokine Expression *In Vivo*

Specimens (n=10) were divided into three distinct compartments (see Table 1): (1) Tissue far distant from the treatment zone without histologic signs of treatment (untreated area); (2) tissue next to the treatment zone (border zone) and (3) tissue from the HIFU treatment zone itself demonstrating all typical histologic features of HIFU-induced necrosis (necrotic area).

In untreated areas, HSPs were differentially expressed. For example, BPH-basal EC stained moderately or strongly for HSP72, while BPH-secretory EC were either completely HSP72 negative or showed only a weak reactivity. Tumor EC in untreated areas were either completely negative or exhibited only a weak anti-HSP72 reactivity. In contrast, staining with anti-HSP73 was moderate to strong in most of the areas and types of cells. Compared with HSP72, the differences were significant for all cell types and areas ($p<0.05$) except for basal EC in the necrotic area.

Screening for alterations of HSP expression in the border zone of the HIFU beam focus revealed significant upregulation of HSPs in most of benign and malignant EC (Table 1). Also in the necrotic area HSPs were upregulated, although to a lesser extent than in the border zone.

As with HSPs, cytokines such as tumor necrosis factor alpha were upregulated both in the HIFU-border and -necrotic zone, too.

Table 1. Heat Shock Protein Upregulation After Heat Treatment By Transrectal HIFU Analyzed By Immunohistology (n=10).

	Untreated Zone			**HIFU-Border Zone**			**HIFU-Necrosis Zone**		
	Basal EC	Secretory EC	Tumor EC	Basal EC	Secretory EC	Tumor EC	Basal EC	Secretory EC	Tumor EC
GRP - 75	1,5 ± 1,1	1,4 ± 1,1	1,7 ± 1,1	1,5 ± 1	1,8 ± 0,9	2,2 ± 1	1,3 ± 0,9	1,7 ± 0,9	2,2 ± 1,1
GRP - 78	2,8 ± 0,8	2,8 ± 0,6	3,2 ± 0,6	3,3 ± 0,4	3,3 ± 0,4	3,5 ± 0	3,4 ± 0,4	3,3 ± 0,4	3,5 ± 0
HSP - 72	2,7 ± 0,8	0,7 ± 0,6	0,4 ± 0,6	3,2 ± 0,5	0,7 ± 0,7	0,7 ± 0,7	2,9 ± 1,3	0,8 ± 1	0,3 ± 0,6
HSP - 73	3,3 ± 0,3	2,5 ± 0,7	2,5 ± 0,9	3,5 ± 0	3,1 ± 1,1	2,8 ± 1	3,1 ± 0,9	2,9 ± 1	2,3 ± 1

Effect Of Heat Treatment Of Prostate Epithelial Cells On Antigen-Specific T-Lymphocyte Response

BPH-EC were sublethally heated and cocultured with autologous peripheral blood T-lymphocytes. The following immune response was analyzed by determination of the Vß T-cell receptor chains usage. For control, T-lymphocytes were cocultured with non-heated epithelial cells or cultured alone. After coculture with heated EC, FACS analysis showed the disproportional outgrowth of certain T-cell subsets with expression of defined T-cell receptor Vß chains, first of all Vß2 and Vß5.1, in half of the patients (n=6). For example, if peripheral blood T-lymphocytes were cultured alone, 5% expressed the TCR Vß2 chain. If peripheral blood T-lymphocytes were cocultured with non-heated prostate epithelial cells from the same BPH patient, the number of outgrowing T-lymphocytes expressing the TCR Vß2 chain inclined to 8%, indicating recognition of epithelial antigens. However, if peripheral blood T-lymphocytes were co-cultured with heated epithelial cells, the number of outgrowing T-cells with TCR Vß2 usage was more than doubled when compared to baseline values, indicating increased antigenicity of epithelial cells after heat treatment.

CONCLUSION

Here we report for the first time on the differential expression of HSP70s and of the GRPs 75 and -78 in untreated prostate tissue and its selective upregulation in response to heat treatment *in vivo* and *in vitro*. Overexpression of HSP70 is probably most clinically relevant, since HSP70s are the most temperature sensitive HSPs, playing a key role in the induction of thermotolerance within the cell. Another fact that makes heat induced overexpression of HSP70 more essential than that of HSP27 is their essential role in antigen presentation (12). The release of HSP70s *in vivo*, as a result of cell injury, e.g. after HIFU-induced necrosis, can promote (13, 14) a very strong tumor specific T-cell response. Further, heat led to increased antigenicity of EC and caused a response of T-cell subsets with a defined T-cell receptor repertoire. Finally, upregulation of proinflammatory cytokines such as TNF-alpha may activate the APC system. However, heat response of CaP cells is far more complex than the upregulation of some HSPs. It involves upregulation of more than 60 genes, which control cell growth, cell survival and, most importantly, provide crucial prerequisites for an effective antitumor response. Taken together, heat treatment by transrectal HIFU may indeed enhance immunity against prostate cancer.

REFERENCES

1. Kramer, G., Steiner, G.E., Sokol, P., Handisurya, A., Klingler, H.C., Maier, U., Földy, M., and Marberger, M., "Local intratumoral tumor necrosis factor-alpha and systemic IFN-alpha 2b in patients with locally advanced prostate cancer," *J Interferon and Cytokine Res*, **21**, 475-484 (2001).
2. Todryk, S.M., Melcher, A.A., Dalgleish, A.G., and Vile, R.G, "Heat shock proteins refine the danger theory," *Immunology*, **99**, 334-337 (2000).
3. Todryk, S., Melcher, A.A., and Hardwick, N., "Heat shock protein 70 induced during tumor cell killing induces Th1 cytokines and targets immature dendritic cell precursors to enhance antigen uptake," *J Immunol*, **163**, 1398-1408 (1999).
4. Srivastava, P.K., Udono, H., Blachere, N.E., and Zihai, L., "Heat shock proteins transfer peptides during antigen processing and CTL priming," *Immunogenetics*, **39**, 93-98, (1994).
5. Madersbacher, S., Gröbl, M., Kramer, Dirnhofer, G., Steiner, G.E., and Marberger, M., "Regulation of heat shock protein 27 expression of prostatic cells in response to heat treatment," *Prostate*, **37**, 174-181 (1998).
6. Madersbacher S., Kratzik C. Susani M., and Marberger M., "Tissue ablation in benign prostatic hyperplasia with high intensity focused ultrasound," *J Urol*, **152**, 1956-1961 (1994).
7. Madersbacher, S., Pedevilla, M. Vingers, L. Susani, M., and Marberger, M., "Effect of high intensity focused ultrasound on human prostate cancer *in vivo*," *Cancer Res*, **55**, 3346-3351 (1995).
8. Beerlage, H.P., Thuroff, S., Debruyne, F.M., Chaussy, C., and de La Rosette, J.J., "Transrectal high-intensity focused ultrasound using the Ablatherm device in the treatment of localized prostate carcinoma," *Urol*, **54**, 273-277 (1999).
9. Van Lenders, G.J., Beerlage, H.P., Ruijter, E.T., de La Rosette, J.J., and van de Kaa, C.A, "Histopathological changes associated with high intensity focused ultrasound (HIFU) treatment for localised adenocarcinoma of the prostate," *J Clin Pathol*, **53**, 391-394 (2000).
10. Kramer, G., Steiner, G.E., Handisurya, A., Stix, U., Haitel, A. Knerer, B., Gessl, A., Lee, C., and Marberger, M., "Increased expression of lymphocyte-derived cytokines in benign hyperplastic prostate tissue, identification of the producing cell types, and effect of differentially expressed cytokines on stromal cell proliferation," *The Prostate*, **52**, 43-58 (2002).
11. Steiner, G.E., Gessl, A., Kramer, G., Schöllhammer, A. Förster, O., and Marberger, M., "Phenotype and function of peripheral and prostatic lymphocytes in patients with benign prostatic hyperplasia, *J. Urol*, 151, 480-484 (1994).
12. Udono, H., and Srivastava, K., "Comparison of tumor-specific immunogenicities of stress-induced proteins gp96, hsp90, and hsp70," *J Immunol*, **152**, 5398 (1994).
13. Melcher, A., Todryk, S., Hardwick, N., Ford, M., Jacobson, M., and Vile, R.G., "Tumor immunogenicity is determined by the mechanism of cell death via induction of heat shock protein expression," *Nat Med*, **4**, 581-587 (1998).
14. Somersan, S., Larsson, M., Fonteneau, J.F., Basu, S., Srivastava, P., and Bhardwaj, N., "Primary tumor tissue lysates are enriched in heat shock proteins and induce the maturation of human dendritic cells," *J Immunol*, **167**, 4844-4852 (2001).

Comparison Of The Vas Deferens And Epididymis As Targets For Noninvasive Male Sterilization Using Focused Ultrasound

Nathaniel M. Fried[1], William W. Roberts[1], Yegor D. Sinelnikov[3], E. James Wright[1], and Stephen B. Solomon[1,2]

[1]Department of Urology, [2]Department of Radiology, Johns Hopkins Medical School, Baltimore, MD 21224, USA
[3]Transurgical, Inc., Setauket, NY 11733, USA

Abstract. A simple, incision-less method of male sterilization may reduce the incidence of infection, bleeding, and scrotal pain associated with conventional surgical vasectomy, and provide a less skill-intensive method of male sterilization capable of being performed in a nonsterile environment. This study compares the vas deferens and epididymis as two potential anatomical targets for noninvasive male sterilization using therapeutic focused ultrasound. A two-radian ultrasound transducer mounted on a plastic clip delivered 4 MHz ultrasound energy to the target located between the clip jaws. Active skin cooling was provided by circulating chilled degassed water through a latex balloon attached to the front of the clip. Thermocouples placed at the skin, intradermally, and at the epididymis, recorded tissue temperatures during ablation. The left and right canine epididymis were ablated in a total of 4 dogs using similar transducer acoustic powers and sonication times (Control, 3W/120s, 5W/90s, 7W/60s) to previous vas ablation experiments. Successful thermal occlusion of the epididymis may be achieved over a large therapeutic window (Power = 3-7 W, SI = 0.8 – 1.9 W/cm^2, Time = 20-120 s) without adverse effects. The epididymis provides a larger and easier target than the vas, eliminating problems with co-location of the ultrasound focus within the target and skin burn complications. Long-term azoospermia ejaculation studies in animals will be necessary to definitively confirm permanent sterilization without recanalization after focused ultrasound ablation of the vas and epididymis.

INTRODUCTION

Surgical sterilization is the most common form of contraception in the United States [1]. Although male sterilization (vasectomy) is more successful, has less complications, is less expensive, and easier to perform than female sterilization (tubal ligation), tubal ligation remains twice as common as vasectomy [1,2]. Couples choose tubal ligation over vasectomy due to several factors, including cultural and societal pressures, ignorance of vasectomy, and fear of complications [1-3]. These concerns may be alleviated by developing a rapid, noninvasive, and safe method of vasectomy which eliminates incision, bleeding, infection, and scrotal pain.

Preliminary work in our laboratory has indicated that thermal coagulation of the vas deferens using therapeutic focused ultrasound may lead to a completely noninvasive or incisionless method of male sterilization [4,5]. However, several limitations with our

technique were encountered during preliminary studies, including concerns with the vas deferens slipping out of the ultrasound clip jaws, which were co-located with the focus of the ultrasound transducer. Problems were also encountered with skin burns, a commonly reported complication of focused ultrasound applications [6-8].

The purpose of this study is to use thermocouple temperature measurements to compare two different anatomical targets for male sterilization: the vas deferens and the epididymis. The vas deferens is a single, muscular tube, with an approximately 2-mm-diameter [9]. Proper co-location of the clip jaws and ultrasound focus inside the vas is necessary to insure proper targeting and thermal occlusion of the vas. The epididymis, on the contrary, is composed of a bundle of much smaller ducts (200-μm-diameter) wrapped into an approximately 2-cm-diameter sphere at the head of the epididymis (Figure 1a). A large thermal lesion placed within the epididymal head would presumably occlude the same duct at several locations. Targeting the epididymis could potentially eliminate problems with co-location, which would no longer be necessary, and skin burns, which may be eliminated through the use of lower acoustic intensities to thermally occlude the smaller and more delicate epididymal ducts.

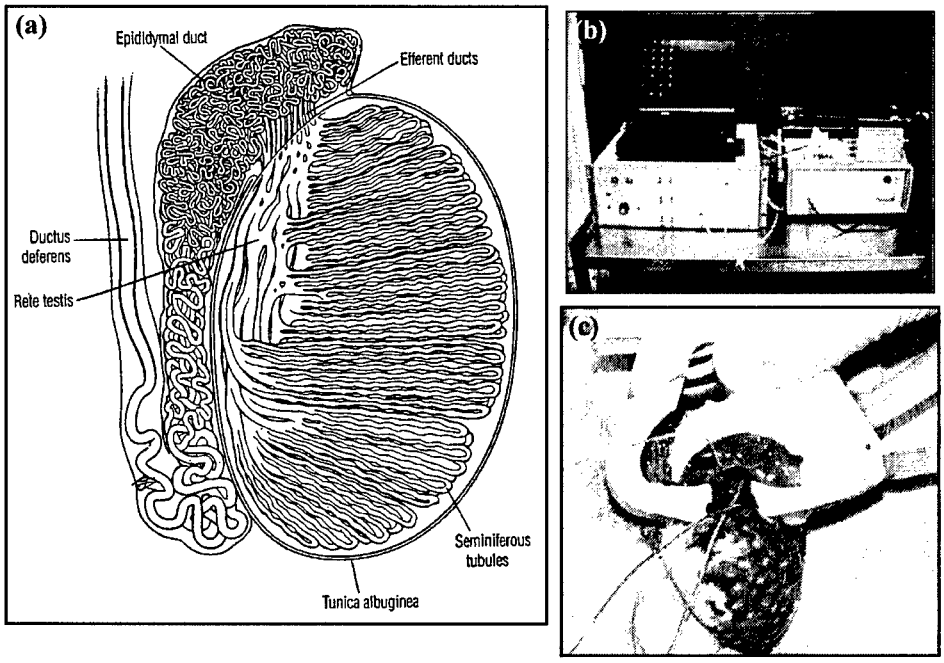

Figure 1. (a) Detailed anatomy of the vas deferens and epididymis. Diagram reproduced with permission from Harcourt Health Sciences [10]. (b) Diagram of experimental setup (laptop PC, cooling system, RF power supply, and vasectomy clip). (c) Photograph of the ultrasound clip placed on the epididymis with thermocouples inserted.

MATERIALS AND METHODS

The ultrasound vasectomy system consisted of a 100 W radiofrequency power supply interfaced with a laptop PC and operated with Labview software (Figure 1b). The two-radian transducer had dimensions of 1 x 4 cm (width x length), with a 2-cm-radius, and was made of an inexpensive and disposable proprietary polymer material (Transurgical, Inc., Setauket, NY). The transducer was designed to focus 4 MHz ultrasound energy at a 3-mm-depth below the skin surface, creating a FWHM intensity profile of 0.3 x 1 x 8 mm (width x depth x length) at the focus (Figure 2a). The transducer was mounted into a disposable plastic clip with movable jaws for grasping the vas deferens (Figure 1c). A heat exchanger flowed chilled (10 $\pm$ 2° C), degassed water through a latex balloon attached to the clip on the front side of the transducer. An acoustic power meter was used to calibrate the transducers. Electrical to acoustic energy conversion was not optimized, and measured only 10-15% with chilled water flowing across the front surface of the transducer (Figure 2b).

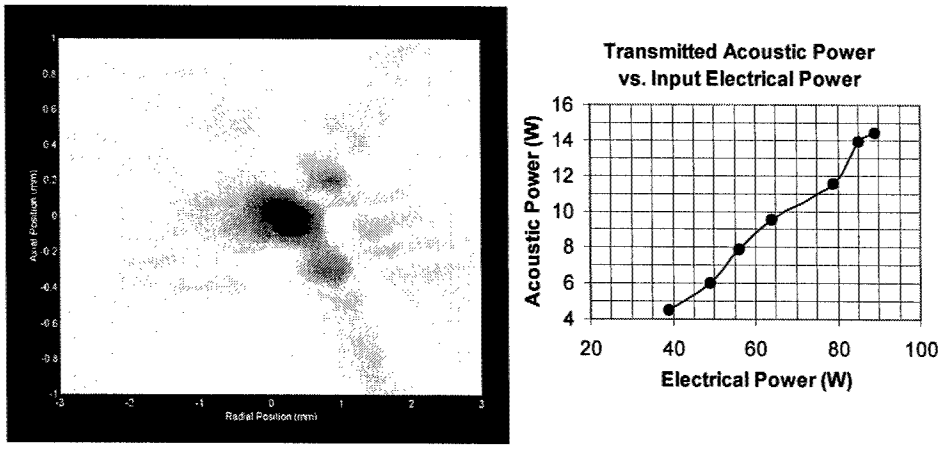

(a) (b)

Figure 2. (a) 2D intensity profile taken along the focus of the ultrasound transducer using a needle hydrophone. The horizontal axis measures depth of focus and the vertical axis measures width of focus (the center of the focus is shown here). The FWHM of the ultrasound focus measured 0.3 × 1.0 × 8.0 mm (width x depth x length). (b) Transmitted acoustic power plotted as a function of input electrical power. Typical efficiencies ranged from 10-15% with chilled water flowing across the front surface of the transducer.

All animal work was approved by the Animal Care and Use Committee at Johns Hopkins University. Mongrel dogs (40-50 lbs.) were premedicated with an intramuscular injection of acepromazine (0.75 mg/kg). An endotracheal tube was then inserted and the dog placed on respiratory support with maintenance anesthesia of 1-2% isofluorane in oxygen. The epididymal head was placed between the jaws of the ultrasound clip. Ultrasound gel was then applied to the skin and the balloon inflated to insure good skin contact and acoustic coupling. Microthermocouples were guided to the epididymis, intradermal (subsurface skin), and skin surface (at the skin-balloon

interface) through 16 gauge syringe needles. A PC with data acquisition software recorded temperatures every 33 msec with an accuracy of $\pm$ 1° C. This approach was similar to that of previous experiments on the vas deferens [4,5].

Pre-ablation cooling experiments were conducted to determine the length of time necessary to cool the skin surface to the chilled water temperature (10 $\pm$ 2° C). A pre-ablation cooling period of 60 sec. was used during all of the ablation experiments. The first 10 sec. recorded the baseline temperatures in the tissue, followed by 60 sec. of pre-ablation cooling. At t = 70 sec., sonication was initiated and ran for varying times between 60 - 120 sec. After sonication, the ultrasound system was turned off, and post-ablation skin cooling began. Experiments were performed in a total of four dogs for the epididymis (n=8) with a single set of ablation parameters (control, 3W/120s, 5W/90s, or 7W/60s) being used for the left and right side (n=2) on each dog. The transducer surface intensities were 0.8, 1.4, and 1.9 W/cm^2, respectively, for these parameters. Representative thermocouple temperature curves were then plotted for each set of ablation parameters.

During the animal recovery period, the ablation sites were examined grossly for evidence of skin burns. After 21 days, the testicles were excised and the epididymis processed using standard histologic procedures and H & E staining.

RESULTS

Representative temperature-time data was taken for the epididymis using identical ablation parameters as that used for previous vas deferens ablation experiments (Control, 3W/120s, 5W/90s, 7W/60s). Pre-ablation cooling studies were performed in which chilled water was rapidly circulated through the balloon to help determine the optimal pre-ablation cooling times (Figure 3a). The temperatures at the skin-balloon interface and intradermally decreased rapidly, producing a large thermal gradient between the target epididymis or vas deferens and intervening skin layers within 60-120 s. Pre-cooling times longer than 120 s provided decreasing benefit at the expense of increased operative times.

Temperature-time curves for epididymal ablation at intermediate transducer acoustic powers (5W/90s) are shown in Figure 3b. Peak temperatures at the epididymis reached 64° C, while intradermal skin temperatures continued to rise, reaching the coagulation threshold of ~ 52° C just as sonication was stopped. The therapeutic window is defined as the difference between the time necessary to bring the skin and epididymis temperatures above 52° C. These temperature trends indicate that a large therapeutic window of approximately 60 s exists, corresponding to a sonication time of 90 s before skin burns should start to appear.

Vas ablation temperature-time curves (5W/90s) are shown in Figure 3c for comparison. Peak vas and intradermal temperatures reached 90° C and 53° C, respectively. The therapeutic window is only approximately 35 s corresponding to an ablation time of 45 s without skin burns.

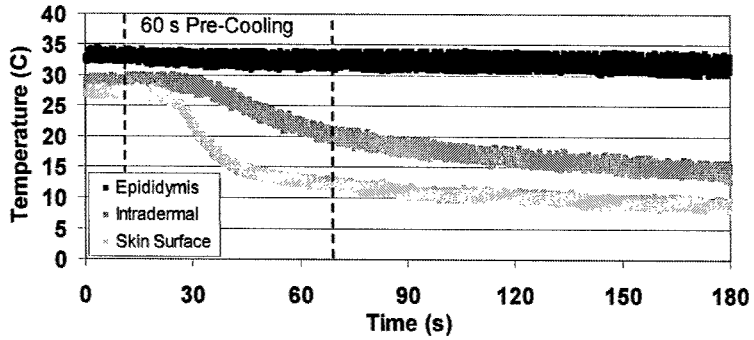

(a)

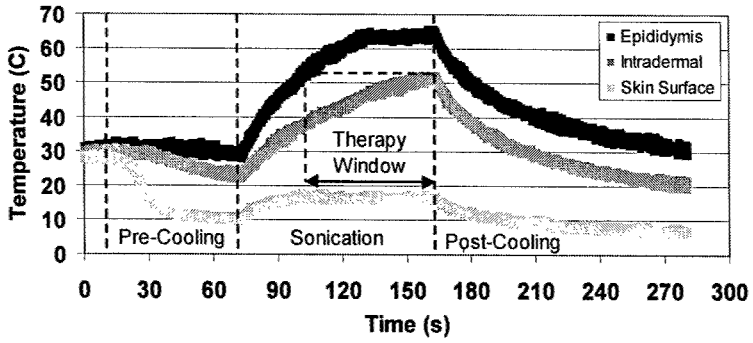

(b)

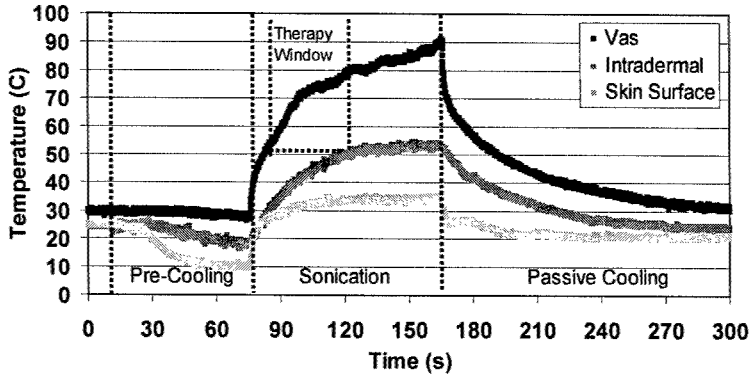

(c)

Figure 3. (a) Pre-ablation cooling study of the skin and epididymis. (b) Epididymis ablation (P = 5 W, t = 90 s). (c) Vas deferens ablation (P = 5 W, t = 90 s). Note the large difference in peak temperatures between the epididymis (T = 64° C) and vas deferens (T = 90° C) using identical ablation parameters. Large differences in the therapeutic window also exist between the epididymis (TW = 60 s) and vas deferens (TW = 30 s).

There was no evidence of skin burns at the ablation sites during gross observation of the scrotum immediately after epididymal ablation. There were also no observable

signs of pain by the dogs either during the procedure or during postoperative monitoring. Successful creation of a thermal lesion in the epididymal head was confirmed by the presence of a hard nodule beneath the skin during manual examination. A histologic cross section of the ablated epididymis and adjacent testicular tissue at 21 days is shown in Figure 4. A large area of the epididymis was thermally occluded, as demonstrated by the presence of a dense region of scar tissue.

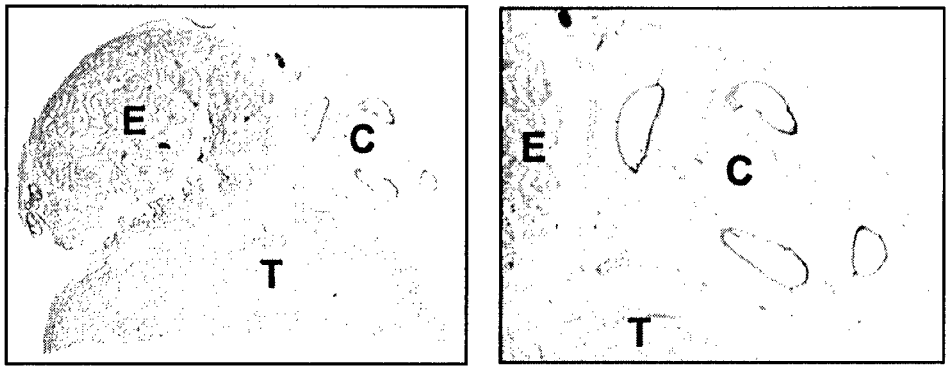

Figure 4. (a) Representative H&E stained histologic photograph of the testicle and epididymis. (b) Close-up image of the epididymal head ablated with a power of 5 W for 60 s, shown here 21 days after ablation. (T = Testicle; E = Epididymis; C = Coagulated area resulting in scar tissue). There is no apparent damage to the testicle.

Table 1 summarizes the best results obtained during optimization of the ultrasound ablation parameters for both epididymis and vas deferens ablation. Higher occlusion rates and lower skin burn complications were encountered for epididymal ablation.

TABLE 1. Best preliminary results for thermal occlusion rates and skin burn complications.

Target	Power, Time	Occlusion Rates	Skin Burns	Reference
Vas Deferens	7 W: 30, 60 s	4/6 (67%)	2/6 (33%)	Roberts, et al.[a]
Epididymis	5 W: 45, 60, 75 s	10/12 (83%)	0/12 (0%)	Roberts, et al.[b]

[a] Roberts, W.W., Chan, D.Y., Fried, N.M., Wright, E.J., Nicol, T., Jarrett, T.W., Kavoussi, L.R., and Solomon, S.B., *J. Urol.* **167**, 2613-2617 (2002).
[b] Roberts, W.W., Wright, E.J., Fried, N.M., Nicol, T.M., Jarrett, T.W., Kavoussi, L.R., Solomon, S.B., *J. Endourol.* **15**:A64 (2001).

DISCUSSION

Previous studies using focused ultrasound ablation of the vas deferens resulted in two major problems: skin burns and inconsistent vas occlusion [4,5]. Burns were due to high ultrasound absorption in the skin, and the low occlusion rates were due to difficulty in targeting the vas and delivering sufficient thermal energy for occlusion. Our more successful results with focused ultrasound ablation of the epididymis may be attributed to significant anatomical differences between the two targets.

The epididymis represents an easier target than the vas deferens for several reasons. First, the epididymal head is larger than the vas (2-cm-diameter vs. 2-mm-diameter), not only eliminating co-location issues, but also allowing deeper targeting and less probability of skin burns. No skin burns were observed during epididymal ablation due to our ability to grasp more tissue between the jaws of the clip, thus providing a "thermal buffer" between the target epididymis and the skin surface. These differences in anatomy explain the large differences observed in the peak target temperatures during sonication. For example, at acoustic powers (5W/90s), peak epididymis and vas temperatures reached 65° C and 90° C, respectively.

Second, the individual epididymal ducts are much easier to occlude than the vas. The ducts have a smaller lumen than the vas and are more delicate than the thick, muscular, and insulating wall of the vas. A lesion placed in the epididymis should theoretically occlude the same duct at several different locations, leading to a higher probability of successful occlusion. On the contrary, problems with co-locating the focus of the ultrasound transducer with the single 2-mm-diameter vas deferens resulted in frequent misses of the target. These differences may help explain why occlusion rates with the best sets of ablation parameters measured approximately 83% (10/12) when targeting the epididymis, and only 67% (4/6) when targeting the vas deferens during previous studies [5,11]. Skin burn rates using these parameters measured 33% for the vas deferens and 0% for the epididymis [5,11].

There are several limitations to our preliminary studies. First, optimization of the treatment parameters and histologic evidence supporting thermal occlusion of the epididymis represent significant advances towards development of a noninvasive vasectomy procedure. However, definitive evidence of permanent male sterilization without recanalization will ultimately need to be confirmed through ejaculation studies in animals with sperm count measurements.

Second, it should be noted that an epididymal approach to male sterilization may limit the reversibility of the procedure. However, the importance of developing a reversible method of male sterilization may be exaggerated. Only a small percentage (2-6%) of couples choose to reverse the vasectomy procedure [12,13]. This small percentage is due to a combination of the high cost of vasectomy reversal and the lack of interest. Furthermore, only a fraction (40-60%) of the couples choosing vasectomy reversal have success [12-14]. These statistics suggest that only 1-3% of couples would be adversely impacted by a nonreversible male sterilization method.

Finally, the canine animal model used in these studies has significant limitations. We have observed that canine skin is considerably thicker than human skin on average. This difference may exaggerate the problem encountered with skin burns when transitioning to clinical studies. It should also be noted that the results in this preliminary study are only valid for direct comparison between the canine epididymis and vas deferens, and cannot be generalized to humans, or even other dog types. Nevertheless, this study demonstrates that epididymal ablation is easier, more successful, and has less adverse effects than vas ablation under comparable conditions.

CONCLUSIONS

This study has demonstrated that the epididymis may be an easier target than the vas deferens for thermal occlusion using focused ultrasound. A larger therapeutic window was observed with the epididymis than with the vas using similar ablation parameters. The larger anatomical target, absence of skin burns, and elimination of co-location issues make the epididymis a more desirable target for noninvasive male sterilization than the vas deferens. Long term, azoospermia ejaculation studies in animals will be necessary to confirm permanent sterilization after focused ultrasound ablation of the epididymis and vas deferens.

ACKNOWLEDGMENTS

The authors thank Pat Lopath, Todd Fjield, Paul Harhen, and David Acker of Transurgical, Inc., who developed the ultrasound transducer and clip used in these experiments. We also thank Dr. Louis Kavoussi of the Johns Hopkins Department of Urology for his clinical expertise and assistance. Nathaniel Fried and Stephen Solomon serve as consultants to and have a financial interest in Transurgical, Inc.

REFERENCES

1. Chandra, A., *Vital Health Stat,* **23**, 1-41 (1998).
2. Miller, W.B., Shain, R.N., and Pasta, D.J., *Fertility Sterility,* **56**, 278-284 (1991).
3. Shain, R.N., Miller W.B., and Holden, A.E., *Fertility Sterility,* **43**, 234-244 (1985).
4. Fried, N.M., Sinelnikov, Y.D., Pant, B.B., Roberts W.W., and Solomon S.B., *IEEE Trans. Biomed. Eng.,* **48**, 1453-1459 (2001).
5. Roberts, W.W., Chan, D.Y., Fried, N.M., Wright, E.J., Nicol, T., Jarrett, T.W., Kavoussi, L.R., and Solomon, S.B., *J. Urol.,* **167**, 2613-2617 (2002).
6. Gelet, A., Chapelon, J.Y., Bouvier, R., Souchon, R., Panguard, C., Abdelrahim, A.F., Cathignol, D., and Dubernard, J.M., *Eur. Urol.,* **29**, 174-183 (1996).
7. Adams, J.B., Moore, R.G., Anderson, J.H., Strandberg, J.D., Marshall, F.F. and Kavoussi, L.R., *J. Endourol.*, **10**, 71-75 (1996).
8. Watkin N.A., Morris, S.B., Rivens, I.H., and ter Haar, G.R., *J. Endourol.,* **11**, 191-196 (1997).
9. Goldstein, M., "Surgical management of male infertility and other scrotal disorders," in Campbell's Urology, edited by P.C. Walsh, et al., W.B. Saunders, Philadelphia, 1998, pp. 1338-1358.
10. Schlegel, P.N. and Chang, T.S.K. "Physiology of male reproduction: the testis, epididymis, and ductus deferens," in Campbell's Urology, edited by P.C. Walsh, et al., W.B. Saunders, Philadelphia,1998, p. 1256.
11. Roberts, W.W., Wright, E.J., Fried, N.M., Nicol, T.M., Jarrett, T.W., Kavoussi, L.R., Solomon, S.B., *J. Endourol.*, **15**:A64 (2001).
12. Potts, J.M., Pasqualotto F.F., Nelson, D., Thomas, A.J., Agarwal, A., *J. Urol.*, **161**, 1835-1839 (1999).
13. Heidenreich, A., Altmann, P., Neubauer, S., and Engelmann, U.H., *Urologie, A* **39**, 240-245 (2000).
14. Holman, C.D., Wisniewski, Z.S., Semmens, J.B., Rouse, I.L., and Bass, A.J. *B.J.U. Int.*, **86**, 1043-1049 (2000).

Hemostasis And Sealing Air Leaks In Lung Using High Intensity Focused Ultrasound

Shahram Vaezy, Carol Cornejo*, Roy Martin, and Lawrence Crum

*Center for Industrial and Medical Ultrasound, Applied Physics Laboratory, and *Department of Surgery, University of Washington, Seattle, WA 98195*

Abstract. In thoracic surgery, bleeding and air leaks from the lungs can be difficult to control. We have investigated the use of High Intensity Focused Ultrasound (HIFU) for control of lung bleeding and air leaks in operative situations. An intra-operative HIFU device, equipped with a Titanium coupler, was used. The HIFU transducer was a PZT-8 concave element, with a focal length of 5 cm, and a diameter of 2.5 cm. The transducer was operated at 5.7 MHz and intensity of 5000 W/cm^2. The coupler length was 4 cm, placing the focal volume, defined by Full Width Half Maximum at approximately 1 cm from the tip of the coupler. A pig animal model was used. Incisions in the lung were made, having lengths of 2-5 cm, and depths of 3-10 mm, which created both parenchymal hemorrhage and air leakage from the lung. HIFU was applied within 10 seconds of inducing the injury. The average hemostasis time was 60 seconds. All incisions were completely sealed, and no blood or air leaked from the incisions. Intra-operative HIFU may provide an effective method in various pulmonary surgery indications including bleb resections for pneumothorax, resection of pulmonary nodules, lung biopsies, decortication for empyema, and hemostasis and control of air leaks from lacerations due to trauma.

INTRODUCTION

Bleeding and air leaks are major problems when lung tissue is disturbed either due to trauma or during thoracic surgery. Prolonged air leak is a major contributor of postoperative morbidity, and prolonged hospital stay after pulmonary surgery. Moreover, bleeding is difficult to control in certain conditions such as coagulopathy and anticoagulant use. Current methods of hemostasis (arrest of bleeding) and pneumostasis (arrest of air leaks) include the use of sutures and staples, biological and synthetic sealants, electrocautery, lasers, and ultrasonic harmonic scalpel [1-5]. While each method offers some advantages, they all have some shortcomings, including persistent air leak, anaphylactic reaction and consideration of blood born diseases, low tolerance to

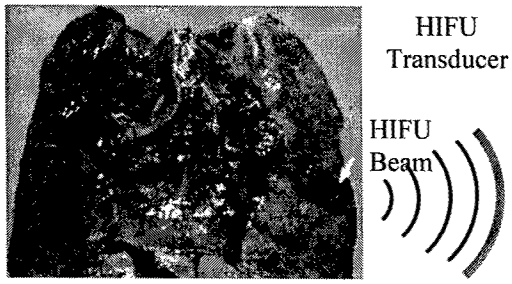

FIGURE 1. The concept of treating a lung injury using High Intensity Focused Ultrasound. The white arrow is pointing to a gun-shot wound. HIFU application will cause hemostasis and pneumostasis at the injury site.

increased pressure, damage to healthy lung tissue, and additional procedures. Our previous results have shown that High Intensity Focused Ultrasound (HIFU) was effective and safe in achieving hemostasis in blood vessels, liver and spleen [6]. In this report we present our preliminary results on applying HIFU intraoperatively for treatment of bleeding and air leaks in the lung (Fig.1).

MATERIALS AND METHODS

Nine domestic pigs were used. All procedures were carried out according to the guidelines of the National Institutes of Health (NIH) for use of laboratory animals, and with the approval of the Institute of Animal Care and Use Committee (IACUC) of the University of Washington. The animals were anesthetized using Isoflurane. EKG, heart rate, blood pressure, and pedal reflex were monitored to evaluate anesthesia level. At the end of the study, the pigs were euthanized via injection of pentosol, 6 grains/ml at 1 ml/lb animal weight, followed by a 20cc injection of concentrated KCl.

A total of 70 incisions were produced in the lungs using a number 20 scalpel blade. The incisions were on average 2.5 cm long, as measured by the operator. The length of the incision was measured after treatment. The depth was measured from the depth of the scalpel blade in the tissue. Moderate bleeding and air leak (bubble formation at the incision site) started immediately.

HIFU treatment started within 10 seconds of making the incision. The HIFU applicator was scanned at a rate of approximately 2 mm/s over the incision. The applicator was held at a 45° angle to the plane of the incision. Several passes over the incision were made if needed. HIFU application continued until hemostasis and pneumostasis was achieved, and confirmed visually. Hemostasis was defined as the complete arrest of bleeding, and pneumostasis was defined as the complete sealing of air leaks, determined from the lack of bubble formation at the incision site. HIFU was administered to all the bleeding sites using a 5.7 MHz transducer (f-number of 1.7), water-cooled titanium coupled applicator, operating at 100% duty cycle [7]. The acoustic intensity at the focus was approximately 3000 W/cm^2. Figure 2 shows a schematic drawing of HIFU application for the treatment of lung.

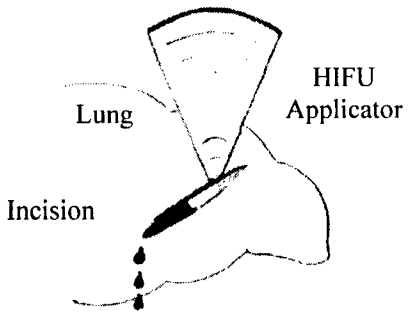

FIGURE 2. The method of applying HIFU for treatment of a lung injury.

The lung tissue was harvested for histological analysis after the animal was euthanized. The tissue was fixed in 10% formalin, and after approximately a month, selected regions were excised and embedded in paraffin, and stained with hematoxylin and eosin (H & E) for general cellular structure visualization.

RESULTS

Figure 3 shows the procedure and result of a representative lung incision, and HIFU treatment. The scalpel blade (Fig. 3A) made an incision that resulted in moderate bleeding and air leaks. While bleeding was observed visually, air leaks were detected by their bubbling action over the incision. Figure 3B shows bubbles on an incision during the treatment. HIFU treatment, requiring several passes over the incision frequently, resulted in production of brown color homogenate that is thought to be of blood and lung tissue (Fig. 3B). The homogenate was fluid-like, but viscous, and spread over the entire incision when formed. The effect of the homogenate for achieving hemostasis and pneumostasis was quite dramatic. Within 1-2 seconds of production of the homogenate, bleeding and air leaks were stopped, wherever the homogenate was deposited on the incision. The result was a hemostatic incision (Fig. 3C) that was dry with no air leaks.

All 70 incisions were completely hemostatic and pneumostatic after the HIFU treatment. No rebleeding or air leaks occurred up to approximately 30 minutes of observation period after the completion of the treatment. The average (± standard deviation) of HIFU duration time was 57 (± 37) seconds. This result indicates that on average approximately 22.3 seconds of HIFU application was required for a centimeter of incision with a depth of 5 mm. Figure 4 shows the distribution of hemostasis times for all 70 incisions. Over 95% of all incisions were hemostatic within 2 minutes of HIFU application.

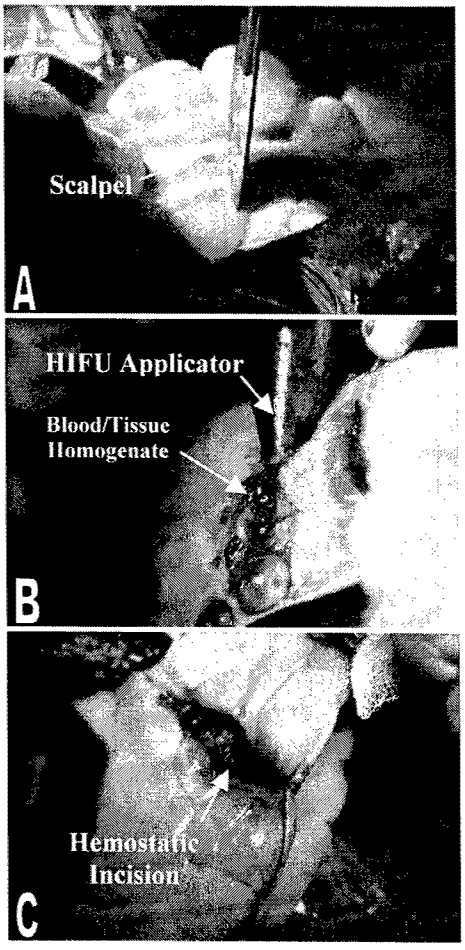

FIGURE 3. Procedure and result of HIFU application for treatment of lung incision. A) making the incision, B) HIFU treatment, and C) hemostatic incision.

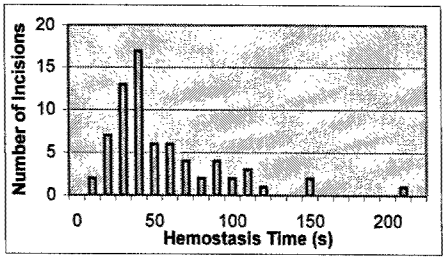

FIGURE 4. Distribution of hemostasis times.

Figure 5 shows a plot of HIFU treatment time as a function of volume of injury, which was calculated assuming a half ellipsoidal shape for all incisions. The incision length and depth were considered as long and short axes. The plot shows approximately linear relationship between the treatment time and the injury volume. A longer treatment time was required for larger incisions.

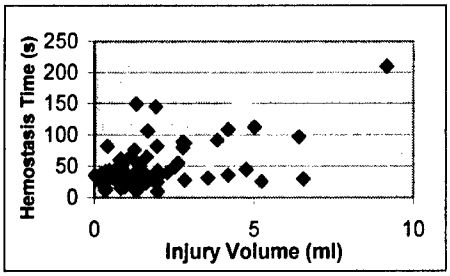

FIGURE 5. Relationship between hemostasis time and volume of injury.

Figure 6 shows the results of hisotological analysis of the lung tissue. Normal lung tissue is shown in Fig. 6A for reference, where patent, viable blood vessel (arrow), and open alveoli (arrowhead) are observed. Figure 6B shows HIFU-treated lung where a thrombosed blood vessel (arrow), and collapsed alveoli (arrowhead) are observed. Figure 6C also shows HIFU-treated lung where a collapsed airway (arrow), and the surrounding cartilage plate (arrowhead) are observed. Figure 6D is a high magnification light micrograph of a HIFU-treated incision showing fibrin deposition on the surface of the incision (arrow), and ruptured alveoli (arrowhead).

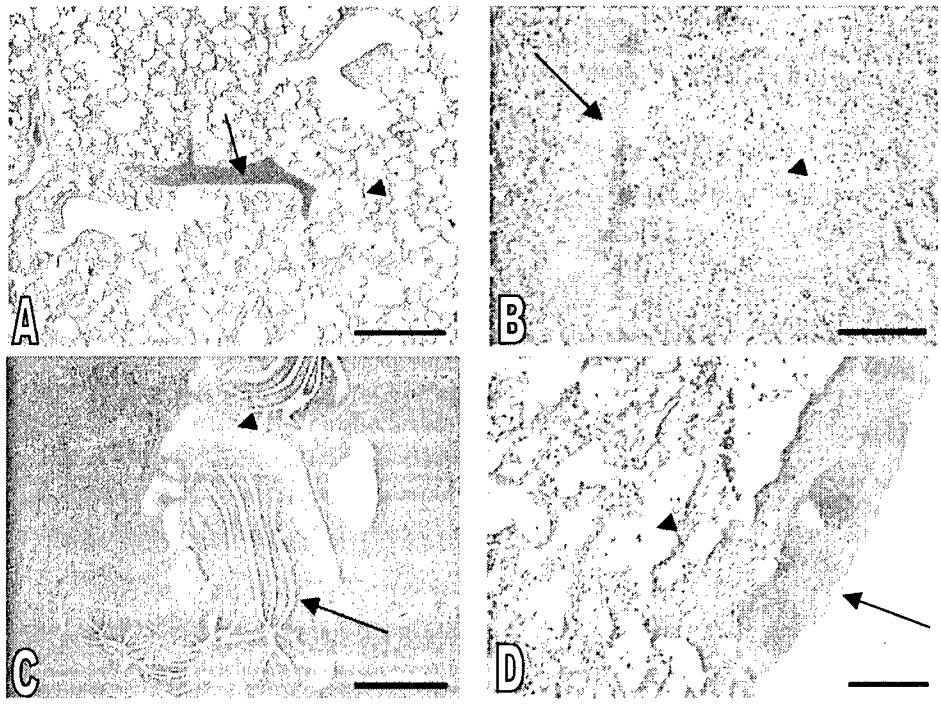

FIGURE 6. Histological Analysis of HIFU-Treated Lung Tissue. A) Normal lung tissue showing patent, viable blood vessel (arrow), and open alveoli (arrowhead). B) HIFU-treated lung showing a thrombosed blood vessel (arrow), and collapsed alveoli (arrowhead). C) HIFU-treated lung showing a collapsed airway (arrow), and the surrounding cartilage plate (arrowhead). D) High magnification micrograph of a HIFU-treated incision showing fibrin deposition on the surface of the incision (arrow), and ruptured alveoli (arrowhead). All magnification bars are 500 μm, except in "D" which is 100 μm.

DISCUSSION

The results show that intra-operative HIFU was effective for hemostasis and pneumostasis of lung incisions in pigs. The treatment was in a reasonable time of approximately 23 seconds for a centimeter of incision length. Thermal effects of HIFU, due to absorption of high intensity ultrasound by the lung tissue, are believed to play an important role in hemostasis and pneumostasis. Alveoli and airway collapse may be a direct of result of thermally-induced coagulative necrosis. High collagen content of bronchi is favorable for this mechanism, due to the high absorption coefficient of collagen. Mechanical effects of HIFU include acoustic cavitation and bulk fluid streaming. Acoustic cavitation may be responsible for tissue disruption, resulting in the release of tissue factors that enhance the coagulation. Streaming was observed to push the blood away from the incision, providing a relatively dry field that is favorable for high energy deposition and absorption. Boiling of tissue and blood may also be involved, especially in the production of blood/tissue homogenate that was observed to be effective in achieving hemostasis and pneumostasis. Future studies will further investigate the biological and physical mechanisms responsible for the observed effect, as well as the long term safety and healing of HIFU treatment of the lung.

Intra-operative HIFU may provide an effective method in various pulmonary surgery indications including bleb resections for pneumothorax, resection of pulmonary nodules, lung biopsies, decortication for empyema, and hemostasis and control of air leaks from lacerations due to trauma.

ACKNOWLEDGMENTS

This research was supported by grants from the National Institutes of Health grant number NIH 8 R01 EB00292-03 and Department of Defense DAMD 17-002-0063.

REFERENCES

1. Eichfeld, U., et al., "Evaluation of ultracision in lung metastatic surgery," *Ann Thorac Surg*, **70** (4): p. 1181-4 (2000).
2. Kjaergard, H.K., et al., "Autologous fibrin glue--preparation and clinical use in thoracic surgery," *Eur J Cardiothorac Surg*, **6** (1): p. 52-4 (1992).
3. LoCicero, J., 3rd, et al., "New applications of the laser in pulmonary surgery: hemostasis and sealing of air leaks," *Ann Thorac Surg*,. **40** (6): p. 546-50 (1985).
4. Ono, K., et al., "Experimental evaluation of photocrosslinkable chitosan as a biologic adhesive with surgical applications," *Surgery*, **130** (5): p. 844-50 (2001).
5. Ranger, W.R., et al., "Pneumostasis of experimental air leaks with a new photopolymerized synthetic tissue sealant," *Am Surg*, **63** (9): p. 788-95 (1997).
6. Vaezy, S., et al., "Hemostasis using high intensity focused ultrasound," *Eur J Ultrasound*, **9** (1): p. 79-87 (1999).
7. Martin, R., et al., "Water-Cooled Intraoperative HIFU Applicators with Frequency Tracking," in 2nd International Symposium on Therapeutic Ultrasound, Seattle, WA (2002).

Real-Time Detection Of Multiple Lesions During High Intensity Focused Ultrasound (HIFU) Treatments

Ralf Seip[1], Jahangir Tavakkoli[1], Adam Wunderlich[1], Narendra T. Sanghvi[1], Kris A. Dines[2], and Lawrence A. Crum[3]

[1]*Focus Surgery, Inc., Indianapolis, IN 46226, USA*
[2]*XDATA Corp., Indianapolis, IN 46220, USA*
[3]*APL, University of Washington, Seattle, WA 98105, USA*

Abstract. This work describes the development of a non-invasive real-time technique to detect changes in tissue caused by the production of multiple lesions during a HIFU treatment sequence. It is based on estimation of relative changes in tissue properties derived from backscattered RF data, such as speed of sound, density, absorption coefficient, backscattering power, etc., as a function of HIFU exposure. The HIFU-induced changes were studied using a modified Sonablate® HIFU device. It makes use of a confocal 4 MHz pulse-echo ultrasound imaging transducer coupled with a HIFU delivery source on the same crystal. During the HIFU exposure period, every 0.5s the dosage delivery was interrupted for a short time (<80ms) and RF echo signals were acquired using the confocal imaging transducer. Using thermocouples, the temperatures at several locations in tissue were measured to correlate with the changes in tissue parameters. The RF data were digitized using a 50 MHz, 12-bit A/D converter and used for real-time as well as off-line processing and analysis. Several time- and frequency-domain echo RF processing algorithms were developed and tested through *in vitro* chicken breast and *in vivo* canine prostate experiments to estimate changes in tissue parameters in real time. Among these, the time-domain algorithms showed better correlation to gross pathology of HIFU-induced lesions in tissue. Work is in progress to implement the algorithm-of-choice in the Sonablate® device for clinical applications in human prostate cancer treatments.

INTRODUCTION

Lesion detection enables users to monitor HIFU treatments non-invasively and in real-time. It also enables them to obtain treatment feedback to determine whether the desired tissue location (e.g. a tumor) is being ablated sufficiently, and to make appropriate corrections if it is not (treatment control). Finally, lesion detection provides a quantitative tool to evaluate HIFU treatments after their completion.

All ultrasound lesion detection techniques are based on the hypothesis that the backscattered RF ultrasound signal acquired from the focal zone of the HIFU transducer during treatment contains information which can be extracted using signal processing techniques to monitor and image (either directly or indirectly) the HIFU-induced lesion. Previous work in this area demonstrates that the backscattered RF signal does indeed contain information that potentially can be used for lesion detection, treatment control, and evaluation [1, 2, 3, 4, 5, 6].

Most of this work has focused on detecting or imaging a single lesion. Clinically, however, the detection of multiple lesions is required, since all current clinical HIFU treatments treat large tissue volumes via the consecutive placement of multiple elementary lesions [7, 8, 9]. Extending single-lesion detection algorithms to multiple-lesion detection imposes new challenges: tissue properties change from one HIFU shot to the next, requiring adaptive or dynamic algorithms. The verification of the accuracy of such algorithms is also challenging, since individual lesions can merge to form a single contiguous lesion, some HIFU shots may not create the expected lesion, and ambiguities exist that are associated with detecting lesions created in locations where a lesion has already been created.

Imaging ultrasound-based lesion detection as a *visual* treatment feedback (based on B-mode images) is already being used with some success in clinical applications of the Sonablate® system for the non-invasive treatment of benign prostatic hyperplasia (BPH) and localized prostate cancer (PC) [8]. Not all HIFU-created lesions are seen in B-mode images, however. A different approach for multiple lesion detection and visualization is required. This paper describes the development of non-invasive techniques to detect the relative changes in tissue caused by the production of multiple HIFU lesions during a prostate treatment sequence for *automated* treatment feedback, control and evaluation (based on the analysis of RF backscattered data), and their real-time implementation and *in vivo* testing in the Sonablate®500 HIFU system.

MATERIALS AND METHODS

To support the development of the multiple lesion detection algorithms, RF backscattered data was acquired with the imaging transducer of the Sonablate®500 system, and stored for off-line processing. The imaging transducer (4MHz, 35% FBW Transmit/Receive Mode) is confocally aligned with the HIFU therapy transducer enabling accurate imaging of the HIFU-generated lesions in the prostate, as shown in Figure 1.

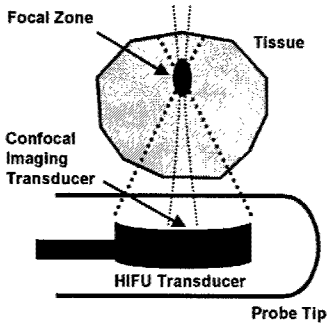

FIGURE 1. Confocal arrangement of the imaging transducer with the therapy transducer inside the transrectal probe tip enables accurate collection of RF ultrasound backscattered data lines (1D) which include the therapy transducer focal zone before, during, and after the HIFU lesion creation in the prostate.

RF backscattered data is sampled at 50 MHz (4096 points total, corresponding to an imaging depth of 61 mm), and always images a region containing the focal zone of the therapy transducer, located at 25, 30, 35, 40 or 45 mm for various focal-depth probes. 1D signals from the tissue containing the focal zone are collected before, during, and after the creation of each HIFU lesion for each HIFU lesion (300 to 600 elementary lesions are required to ablate an entire prostate for typical HIFU prostate cancer treatments). To acquire interference-free RF backscattered data during the HIFU "ON" time, HIFU delivery is briefly interrupted for <80 ms. 32 individual RF signals are acquired and averaged to generate a single RF echo signal every 500 ms. Reference data is acquired for each lesion site once at the beginning of the treatment before any HIFU energy has been delivered to the tissue (Pre-Treatment Reference Line, at T=-∞), and then again before the particular site is treated (Pre-Lesion Reference Line, at T=0s). The data acquisition methodology followed for each lesion site is shown in Figure 2.

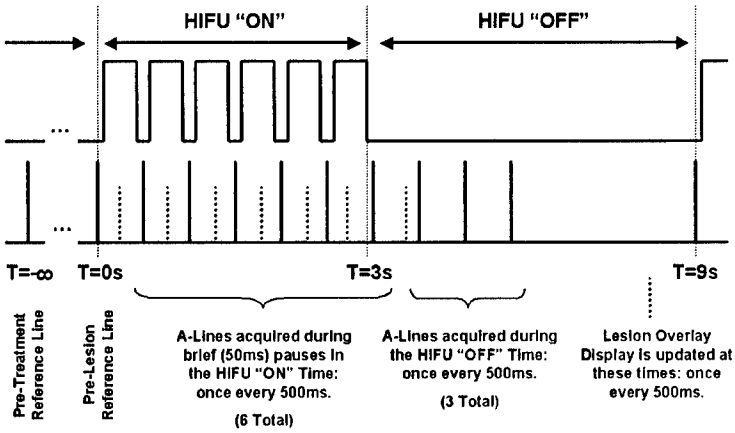

FIGURE 2. Acquisition methodology followed to acquire RF backscattered data for each lesion site before, during, and after the lesion creation. Note: the RF backscattered data contains pre-focal, focal, and post-focal imaging data. The top trace shows the brief HIFU interruptions that enable the acquisition of interference-free imaging data (1D), indicated by the vertical solid bars on the bottom trace.

Data was collected from *in vitro* turkey tissue to verify the data acquisition methodology and implementation in the Sonablate®500 HIFU system. Canine whole prostate HIFU ablation experiments (N=4) were performed to collect *in vivo* data. This data was processed both in real-time on the Sonablate®500 during the HIFU treatment to evaluate the lesion detection algorithm in a clinical setting, and stored for additional off-line analysis. During the *in vivo* evaluation, detection algorithm results were displayed as real-time color overlays on the B-mode images of the current treatment site acquired pre-treatment (see Figure 3), to indicate the estimated size and location of each lesion, both during and after the HIFU exposure. The dashed vertical bar in Figure 2 indicates when this lesion overlay update occurs. This allows the user to follow the actual lesion formation process.

LESION DETECTION ALGORITHMS

Several multiple-lesion detection algorithms have been examined as part of this research, and are briefly described below. New candidates are constantly being evaluated against the stored *in vivo* data for their ability to detect HIFU-induced multiple lesions and image tissue changes (either directly or indirectly), including wavelet approaches, adaptive filtering approaches (linear and/or non-linear), and template matching approaches. All algorithms use pre-lesion reference lines for calibration and/or normalization purposes.

In all approaches, $p(n,T)$ is the parameter indicative of the lesion displayed as a color overlay during the HIFU treatment, n is the index into the echo data (in depth, or "fast time"), and T is the index selecting the RF signal data lines (in treatment time, or "slow time"). $Echo(n,T_0)$ refers to the pre-lesion reference line, and $echo(n,T)$ refers to the RF backscattered data acquired at time T (every 500 ms) for the current lesion site. For analysis and display, $p(n,T)$ is computed for pre-focal, focal, and post-focal regions to localize the lesion in depth n, using windowed signal echo data (Blackman window, 1.5 to 3.5 mm long). $T - \Delta T$ references the previously acquired echo.

Signal Energy

This algorithm detects changes in echo amplitude caused by treated tissue, vapor bubbles, or cavitation bubbles induced by the HIFU energy delivery. It is normalized by the pre-lesion reference line to detect changes resulting only from the HIFU delivery to the current site.

$$p(n,T) = \frac{E_{signal} - E_{reference}}{E_{reference}} \tag{1}$$

$$E_{signal} = \sum_{window(n)} echo(n,T)^2 \qquad E_{reference} = \sum_{window(n)} echo(n,T_0)^2 \tag{2,3}$$

Tissue Displacement

This algorithm detects changes in the displacement of the tissue due to the temperature-dependent speed of sound changes and the coefficient of thermal expansion of tissue due to the elevated tissue temperature induced by the HIFU energy delivery [4]. It is normalized by detecting differential displacements only with respect to the previous echo line.

$$p(n,T) = displacement[echo(n,T-\Delta T), echo(n,T)] \tag{4}$$

Signal Entropy

This algorithm detects changes in the shape of the overall RF backscattered data caused by treated tissue, vapor bubbles, or cavitation bubbles induced by the HIFU energy delivery. It is normalized by the pre-lesion reference line to detect changes resulting only from the HIFU delivery to the current site.

$$p(n,T) = H_{signal} - H_{reference} \quad (5)$$

$$H_{signal} = \sum_{k=0}^{N-1} p_{k(signal)} \cdot \log_2(p_{k(signal)}) \qquad H_{reference} = \sum_{k=0}^{N-1} p_{k(reference)} \cdot \log_2(p_{k(reference)}) \quad (6,7)$$

In equations 6 and 7, p_k indicates the probability that the symbol k is present in the echo window signal, and $N = 2b - 1$, where b is the number of quantization bits [10].

Attenuation Slope

This algorithm detects changes in the attenuation coefficient (slope) of the tissue due to the tissue temperature increases and the delivered HIFU dose [2,11]. It is normalized by the pre-lesion reference line to detect changes resulting only from the HIFU delivery to the current site:

$$p(n,T) = slope\ at\ f_c\ of\ best\ line\ fit\ to\ \Delta S \quad (8)$$

$$\Delta S = S_{signal} - S_{reference} \quad (9)$$

$$S_{signal} = 20\log_{10}[|\ fft(echo(n,T))\ |] \qquad S_{reference} = 20\log_{10}[|\ fft(echo(n,T_0))\ |] \quad (10,11)$$

where f_c is the center frequency of the imaging transducer.

Attenuation Intercept

This algorithm detects changes in the attenuation of the tissue due to the tissue temperature increases and the delivered HIFU dose [2,11]. It is normalized by the pre-lesion reference line to detect changes resulting only from the HIFU delivery to the current site:

$$p(n,T) = intercept\ at\ f_c\ of\ best\ line\ fit\ to\ \Delta S \quad (12)$$

where fc is the center frequency of the imaging transducer, and ΔS, S_{signal}, and $S_{reference}$ are as defined in equations 9, 10, and 11.

RESULTS

All algorithms were evaluated against the *in vivo* data. Thermometry data collected during the *in vivo* experiments recorded temperatures above 85°C at the exposure sites, indicating that thermal lesions were created with the selected treatment parameters (3s HIFU "ON", 6s HIFU "OFF" for each site, at 30-37W Total Acoustic Power typical). Histology and gross pathology examination of the treated prostates confirmed the creation of thermal lesions. It was not possible to determine from the histological samples if every HIFU shot created a lesion, since over time elementary lesions merged into a large contiguous lesion due to heat conduction.

It was found (assuming a lesion was created for every HIFU exposure) that signal energy-based algorithms consistently outperformed all other algorithms investigated.

When properly calibrated, these algorithms track the lesion formation from the onset of the HIFU delivery and update the color screen overlay every 500 ms for real-time lesion formation visualization. Figure 3 shows the result of the signal energy-based detection algorithm overlaid on the B-mode image of the current treatment site (acquired as part of the HIFU treatment procedure at T=5s after each HIFU shot delivery for conventional *visual* treatment feedback) for a sequence of 6 multiple lesions created linearly one after the next in a dog prostate.

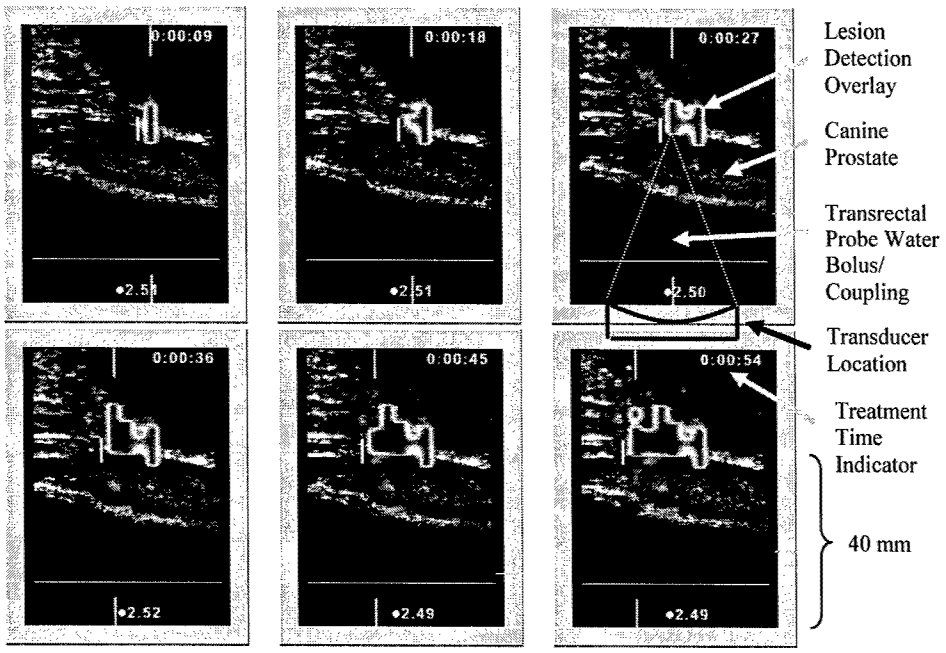

FIGURE 3. Real-time output of signal energy detection algorithm overlaid on the B-mode images of the current treatment site during a HIFU treatment of a dog prostate. 6 consecutive lesions are created with a 40 mm focal length HIFU transducer, from the prostate mid-section (top left image) to the bladder neck region (bottom right image).

DISCUSSION AND CONCLUSIONS

The results presented in this paper show that it is possible to implement a real-time detection algorithm that produces clinically useful results for HIFU treatment monitoring. Overlaying treatment feedback data on the conventional B-mode ultrasound images is an effective and intuitive way to present such information to the user. Accurate and consistent acquiring, computing, and displaying this information is the first step for implementing automated HIFU treatment control.

The results presented in this paper also show that developing and verifying algorithms to detect and image multiple lesions (such as those needed to ablate large tissue volumes via their superposition) give rise to additional problems and challenges not encountered in single-lesion imaging: (i) tissue properties change from one HIFU

shot to the next, (ii) individual lesions can merge to form a contiguous lesion, and (iii) ambiguities are created when one lesion is placed in a site already containing a lesion.

In order to address (i) and (ii) above, all of the developed algorithms have focused on measuring a relative change in tissue properties, using pre-HIFU reference lines (acquired pre-treatment at T=-∞ and pre-lesion at T=0s) for parameter normalization and calibration. It was found that for *in vivo* implementations, the pre-treatment reference echo line is not well suited for calibration purposes of the detection algorithm: it de-correlates with respect to the pre-lesion echo within several minutes into the treatment due to HIFU-induced tissue changes and small probe/patient motion. The pre-lesion reference echo line, on the other hand, is extremely useful (and possibly even required) for the normalization of the detection algorithm. Using it as a reference ensures that only tissue changes induced by the current HIFU shot are detected.

Currently, out of all detection algorithms examined, the simple signal energy based detection algorithm has proven to be the most effective algorithm for non-invasively detecting (directly or indirectly) HIFU-induced lesions.

Even though these results are encouraging, it is believed that none of the algorithms developed thus far directly image the complete production of the lesion, but detect indirect indications that a lesion has been created, such as the presence of cavitation or vapor bubbles, or temperature rises. For any algorithm to be considered a direct (single or multiple) lesion imaging algorithm, we believe that it must meet the following criteria:

1. It must be able to localize the lesion in the tissue.
2. It must be able to follow the lesion creation process (i.e. be able to accurately track lesion size changes during HIFU delivery).
3. Its lesion size and shape estimates must agree with histo-pathological lesion size and shape estimates to a given tolerance.

For any algorithm to be considered a direct multiple lesion imaging algorithm, we believe that it must meet all of the criteria defined above, and:

4. Its lesion estimation methodology must be independent of the treatment time-history.

The signal energy-based multiple lesion detection algorithm is effective for point 1, relatively effective for point 2, but not very effective for point 3 (see irregular estimates of lesion shapes in Figure 3). Normalization has allowed the algorithm to be somewhat effective for point 4, but current clinical results still show a reduction in the magnitude of the parameter $p(n,T)$ as a function of treatment time T. For these reasons, the signal energy algorithm (as well as the others examined so far) currently fall into the category of indirect multiple lesion detection algorithms.

It is believed that the signal energy lesion detection algorithm is (at least partially) sensitive to cavitation and/or vapor bubbles. These are indirect lesion indicators, since their presence would indicate high intensities and temperatures that also create HIFU lesions, but do not necessarily outline the thermal lesion itself. Experiments are currently planned to test this hypothesis by suppressing cavitation and vapor bubble formation during HIFU using overpressure.

The pre-focal zone of the *in vivo* data was also analyzed to try to image purely thermal tissue changes not subject to possible cavitation or vapor bubbles, but still

subject to elevated temperatures as indirect indicators of thermal HIFU lesions. The results of this analysis are as of yet inconclusive. It is believed, however, that a pre-focal data analysis can provide useful lesion information, and work continues in this area.

Finally, the results also indicate that both direct and indirect lesion detection or lesion imaging methods can be clinically useful tools for the evaluation and control of HIFU treatments. Work continues on algorithm development, data acquisition methodologies, calibration, and implementation into the Sonablate® device for clinical applications in human prostate cancer treatments using HIFU.

ACKNOWLEDGMENTS

We would like to thank Dr. T.A. Gardner, MD., Dr. M.O. Koch, MD., and the staff of The Indiana University School Of Medicine at LARC for their help with the *in vivo* canine experiments. This work was partially funded by NIH SBIR Grant: 2 R44 CA83244-02.

REFERENCES

1. Wear, K., Wagner, R., Insana, M., Hall, T., "Application of Autoregressive Spectral Analysis to Cepstral Estimation of Mean Scatterer Spacing," *IEEE Transactions on Ultrasonics, Ferroelectrics, and Frequency Control*, **40**, pp. 50-58 (1993).
2. Greenleaf, J.F., *Tissue Characterization with Ultrasound*, Boca Raton: CRC Press, 1986.
3. Ribault, M., Chapelon, J.Y., Cathignol, D., and Gelet, A., "Differential Attenuation Imaging for the Characterization of High Intensity Focused Ultrasound Lesions." *Ultrasound Imaging*, **20**, pp. 160-177 (1998).
4. Seip, R., Feedback for Ultrasound Thermotherapy, Ph.D. Disseration, The University of Michigan, 1996.
5. Fry, F.J., Sanghvi, N.T., Morris, R.F., Smithson, S., Atkinson, L., Dines, K., Franklin, T., and Hastings, J., "A Focused Ultrasound System for Tissue Volume Ablation in Deep Seated Brain Sites," *Ultrasonics Symposium Proceedings*, **1**, 1001-1004 (1986).
6. Bevan, P.D., and Sherar, M.D., "B-Scan Ultrasound Imaging of Thermal Coagulation in Bovine Liver: Frequency Shift Attenuation Mapping," *Ultrasound in Medicine and Biology*, **27** (6), pp. 809-817 (2001).
7. Muschter, R., Bohlen, D., Thuroff, S., Ebert, T., and Madersbacher, S., "High Intensity Focused Ultrasound in Urology: Consensus Report" in *High Energy Shock Waves in Medicine: Clinical Application in Urology, Gastroenterology, and Orthopedics*, Georg Thieme Verlag, Stuttgart - New York, 1997, pp. 140-146.
8. Sanghvi, N.T., Fry, F.J., Bihrle, R., Foster, R.S., Phillips, M.H., Syrus, J., Zaitsev, A.V., and Hennige, C.W., "Non-Invasive Surgery of Prostate Tissue by High Intensity Focused Ultrasound," *IEEE Transactions on Ultrasonics, Ferroelectrics, and Frequency Control*, **43**, pp. 1099-1110 (1996).
9. Madersbacher, S. and Marberger, M., "High-Intensity Focused Ultrasound in Urology," *J. of Endourology*, **9** (1), pp. 5-15 (1996).
10. Hughes, M.S., "Analysis of Ultrasonic Waveforms using Shannon Entropy," *Ultrasonics Symposium Proceedings*, **2**, 1205-1208 (1992).
11. Damianou, C.A., Sanghvi, N.T., Fry, F.J., and Maass-Moreno, R., "Dependence of Ultrasonic Attenuation and Absorption in Dog Soft Tissues on Temperature and Thermal Dose," *J. Acoust. Soc. Am.*, **102** (1), 628-634 (1997).

In-Vitro Imaging Of Thermal Lesions Using Three Dimensional Vibration Sonoelastography

L.S. Taylor*, M. Zhang† , J.G. Strang**, D.J. Rubens* and K.J. Parker*

*University of Rochester, ECE Department, Rochester NY
†University of Rochester, BME Department, Rochester NY
**University of Rochester, Radiology Department, Rochester NY

Abstract. HIFU and radio frequency (RF) ablation are methods for treatment of cancerous lesions which create a coagulation necrosis killing the undesirable cells. A technique for real time monitoring of HIFU lesions would be a useful adjunct to this therapy. Sonoelastography is being investigated as a real time monitoring method. Fresh bovine liver was degassed and RF ablation was used to induce a coagulation necrosis in the liver. Three dimensional sonoelastography images were acquired. After imaging, lesions were dissected to document their size, shape and volume.

Upon dissection the induced lesions were all found to be palpably hard, ellipsoidal in shape and of differing texture and color than the untreated tissue. The mean volume of the five lesions determined by fluid displacement was 4.7 cc. In the sonoelastography images each lesion appeared as a dark region surrounded by a field of bright green. The precise edge of each sonoelastography lesion was somewhat ambiguous, +/- a few mm. The mean sonoelastography volume for the five lesions was found to be 87% of the volume determined by fluid displacement when only the lowest vibration amplitude region was taken to represent the lesion. Real time monitoring of thermal lesions can be accomplished *in-vitro* by making the sonoelastography lesion equal to the desired treatment zone.

INTRODUCTION

High intensity focused ultrasound (HIFU) and radio frequency (RF) ablation are both used for non-invasive tissue ablation treatments. Often the objective is to create a coagulation necrosis lesion at the site of an existing and known malignant lesion. Real time monitoring of these lesions is a major challenge for the application of these methods in a clinical setting. Ultrasound B-mode imaging is often used for probe placement but the hyperechoic zones seen during treatment correspond only weakly with the extant of the tissue necrosis [1]. Computed tomography (CT) and magnetic resonance (MR) imaging can be used but their size, cost and relative immobility limit their usefulness [1].

Several approaches to this problem are under active investigation and capitalize either on the fact that tissue temperatures rise during the treatment process or that coagulation necrosis lesions have an elevated Young's modulus relative to the untreated tissue. Stafford et al. [2] used elastography to visualize thermally induced lesions *in-vitro*. A surgical laser was used to create thermal lesions in ovine kidney. Elastography images of the treated kidneys revealed reduced strain levels in the lesion area as confirmed later by histology. In a subsequent study at the same institution Righetti et al. [3] used high intensity focused ultrasound to induce thermal lesions in canine livers. The strain

images showing the lesion location were validated by photographs of the dissected livers. Konofagou et al. [4] have proposed using ultrasound stimulated vibroacoustography [5] to monitoring tissue ablation. Since the ultrasound stimulated acoustic emission depends on the temperature it can be used for localized temperature detection.

Sonoelastography has been previously proposed as a method of imaging the relative elastic properties of soft tissues [6]. In this technique, low frequency shear waves (0 - 1000 Hz) are propagated through tissue while Doppler vibration detection methods [7] are used to image the resulting vibration field. Under the correct boundary conditions [8, 9], regions in the image with an elevated elastic (shear or Young's) modulus, will appear as regions of decreased vibration indicating the location of the stiffer tissue. We have demonstrated this technique in phantoms containing hard lesions [10, 11].

In this paper we propose sonoelastography imaging as a method for the real-time imaging of coagulation necrosis lesions. RF ablation lesions are used as a model for coagulation necrosis lesions. We show that real-time sonoelastography images can accurately detect the location and size of these lesions. Details on how to implement this technique are provided.

MATERIALS AND METHODS

In this section details on the various materials used to validate real-time imaging of thermal lesions will be presented, including the liver specimens, embedding materials, RF ablation equipment, vibration sources and ultrasonic scanner. After this the experimental set-up will be described along with methods used for specimen embedding, lesion creation, application of the vibration, three-dimensional 3D image acquisition, lesion dissection and lesion volume calculation from the sonoelastography images.

Materials

Whole fresh bovine liver was purchased from a local butcher (Wegmans Food Market, Pittsford, NY). The liver was immersed in a degassed 0.9% NaCl solution and stored at approximately 4^o C for 24-36 hours. Tissue samples ($\approx$ 10 x 10 x 6 cm) were cut and soaked in the degassed saline solution before sonoelastography imaging. This process avoided large bubbles in the tissue which would have an ill effect on image display.

DIFCO^{TM} Technical Agar (Becton Dickinson, Sparks, MD) was used to create 2.25% agar molds embedding bovine liver samples. The mechanical characteristics of 2.25% agar molds were similar to the liver tissue at the vibration frequencies used, which was verified by prior research.

Thermal lesions were induced in liver tissue samples using (RF) ablation. Figure 1 shows a *LeVeen*^{TM} needle (RadioTherapeutics Corporation, Mountain View, California, USA) of 15 cm in length along with a centimeter scale. The umbrella-shaped tines are extended and a RF current which is generated by a RF ablation machine (RadioTherapeutics Corporation, Mountain View, California, USA) passes through the needle tip to the target tissue. The current is returned by means of four attached grounding pads

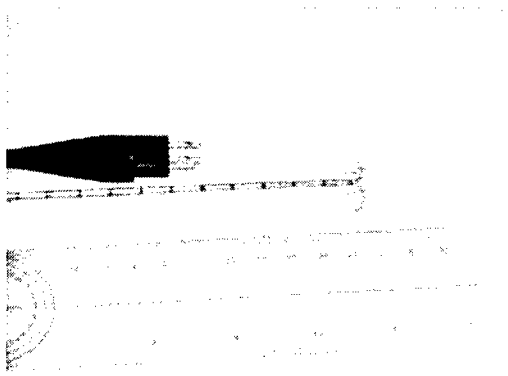

FIGURE 1. Needle used for the RF ablation process.

connected back to the machine through electric cables. This equipment is used clinically in liver cancer therapy at our institution.

A GE Logiq 700 (General Electric Medical Systems, Milwaukee, WI) ultrasound scanner was used to perform sonoelastography imaging. The scanner was specially modified so that the Doppler spectral variance of the vibrating tissue is mapped to the screen in color mode when the appropriate color map is selected. Huang et al. [7] have shown that the standard deviation of the power spectrum depends directly on the vibration amplitude of the tissue. In order to acquire three-dimensional images, a 7-MHz linear array transducer (739L GE Medical) was mounted and aligned in the holder of a motorized linear track.

In preparation for imaging, the embedded specimens were placed on two thin parallel bars which were separated by 5 cm on center. The purpose of using the two parallel bars as a vibration source was twofold, to produce a uniform vibration and to focus and concentrate the shear wave production into a region of interest [12]. The twin bar assembly was in turn mounted on a 100 lb. (force) piston shaker (VTS Aurora, OH) which provided the low frequency vibration field required for the vibration imaging. The shaker was driven by an audio amplifier whose voltage output waveform could be precisely controlled by a frequency generator. A harmonic waveform generator (3511A, Pragmatic Instruments, San Diego, CA) was used to provide multi-tone vibrations.

Methods

Figure 2 shows the experimental setup used for imaging RF ablation lesions. Two parallel bars were applied at the center of the bottom surface of the agar embedded specimen and low frequency multi-tone vibration was used to drive the shaker. The transducer was used to locate the lesions of interest in the phantom. The color Doppler mode of the modified GE Logiq 700 ultrasound system was used for image display.

The proper mass of agar powder was weighed and added to the near boiling degassed H_2O (2.5 liters), which was stirred when adding the agar until most of agar was dis-

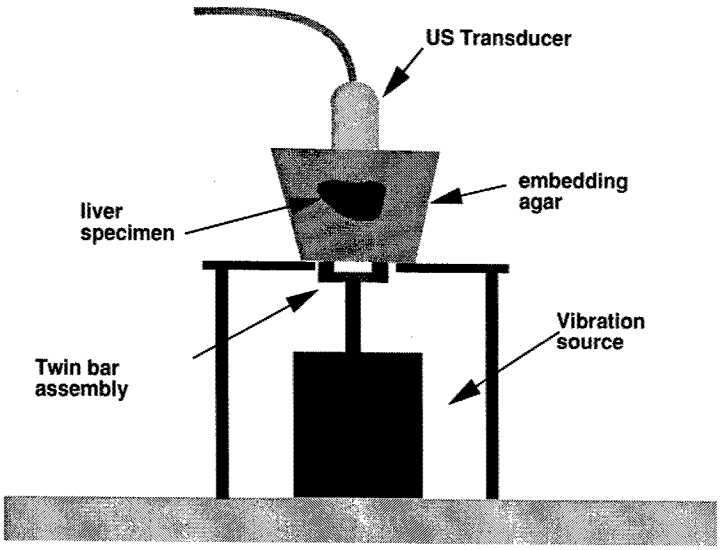

FIGURE 2. Experimental Set-up.

solved. Then this solution was boiled again in a microwave. Deviation from this procedure sometimes resulted in an agar mixture which did not gel properly. The solution was allowed to cool to $\approx 70^oC$. Then 1.7 liters of the solution was poured into a 2.5-liter $Ziploc^{TM}$ bowl-shaped container. Another smaller cylindrical container ($\approx$ 10 cm in diameter) was inserted into the solution to create a cavity 8 cm in depth in the center.

After 2 hours in the refrigerator, the agar shell was created and the liver sample was put into the cavity. The remaining 0.8 liter agar gel was remelted and boiled. It was allowed to cool but not harden, and poured into the cavity to embed the liver sample completely. In this step, bubbles should be removed from the agar solution carefully. The whole mold was allowed to harden for an hour before the insertion of the $LeVeen^{TM}$ needle.

From the screen of the ultrasound scanner, we could control and adjust the depth and direction of the needle. The optimal insertion direction would be 45^o between the needle and the mold surface. The insertion depth was about 5-6 cm beneath the mold surface. This RF ablation process heated the tissue, successfully making a lesion centered at the needle tip. The process required about 150 seconds for completion.

In order to image the lesions using sonoelastography, the scanner was placed into color Doppler mode and the multi-tone vibration source was activated to drive the double bar assembly. Multi-tone signals were used to reduced the modal artifacts which occur during *in-vitro* imaging because of specular reflection of the shear waves off of the specimen holder boundaries [13]. On this scanner the estimated vibration field is mapped to a gray scale where high vibration is bright and lower vibrations are dark. By observing the location of the dark pixels, it was possible to located the stiffer tissue, which vibrates at a lower amplitude. The location of the lesions was also possible using the B-scan image which showed the needle track and gas bubbles from the ablation process. In

order to acquire 3D sonoelastography images, the linear track holding the transducer was activated so that the velocity of the motor was synchronized to the frame rate of the scanner so that images were acquired at a fixed spatial interval of 1 mm. The sequence of images was saved as a cine-loop of co-registered B-mode and sonoelastography images.

After image capture the files were transferred from the scanner's hard drive to an image processing laboratory via a network connection. Both the two-dimensional (2D) and 3D sonoelastography images display areas of decreased vibration as dark gray or black. The sonoelastography images of the lesions were manually segmented using the ImageJ software package from NIH to calculate lesion area in each slice. The vibration deficit in each image was outlined and ImageJ was used to calculate the area . After outlining, the lesion was filled in and the sonoelastography image was converted to a binary image where the lesion was white and the background was black. The sequence of binary 2D renderings of the lesion was imported into IRIS Explorer, a 3D visualization package to create a 3D rendering of the lesion. Since images were acquired at 1 mm intervals the volume was estimated using a cylindrical approximation multiplying the thickness of the slice by the area of the lesion in each slice.

After imaging, the lesion sizes were verified by removing them from the embedding agar and cutting away the soft untreated tissue from the hard thermal lesions. Their volumes were then measured by two methods. The typical shape of a thermal lesion was ellipsoidal and the texture and color of it are different from the surrounding normal tissue, which facilitated accurate determination of the thermal necrosis. Caliper measurements were applied to measure the three maximum axes of a dissected lesion, using an ellipsoidal geometrical model. The volume, V, of each lesion was calculated by the formula:

$$V = \frac{4}{3}\pi xyz, \tag{1}$$

where x, y and z are the half lengths of the three axes.

The volume of each lesion was also determined by fluid displacement. In this method, a dissected lesion was placed into a water filled vessel whose displacement indicated the volume of the lesion.

The vibration deficit in each (sonoelastography) image was an ellipsoidal-shaped dark area. The longest two axes were measured from the slices in which the dark area was largest compared to the others in the sequence. The third axis was determined by counting how many slices contained a deficit in vibration. This established the tumor size in the out of plane direction. The volume could then be estimated from the total thickness of all slices containing lesions and the lengths of the two principal in plane axes described above using equation 1.

RESULTS

Figure 3 shows a typical RF ablation lesion after it has been dissected. Measurements of five lesions are given in Table 1. The volume of each dissected lesion was determined by caliper measurements and fluid displacement. The lesion dimensions and image volumes of the same lesion were observed and calculated from the sonoelastography images.

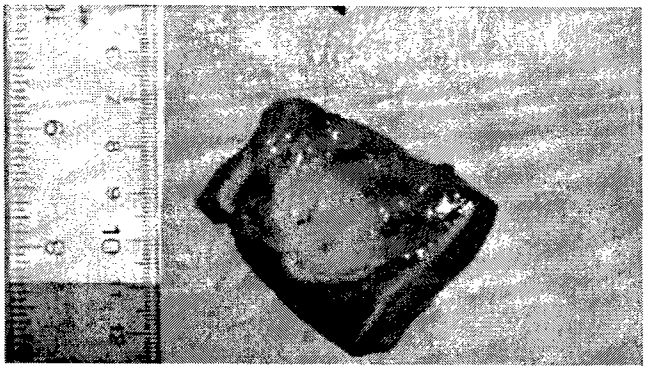

FIGURE 3. Dissected RF lesion.

In the sonoelastography images each lesion appeared as a dark region surrounded by a bright field. In our experiments, only the darkest pixels were taken to represent the lesion. However, the exact edge of each sonoelastography lesion was somewhat unclear. If the largest possible regions were used in measurements, the dimensions and image volumes of the five lesions would be much larger than those of the dissected lesions. We found that the volume of each dissected lesion was between the sonoelastography volume with only the darkest pixels taken into account and that with the largest possible region. The sonoelastography volumes for the five lesions were smaller than the volumes determined by fluid displacement. The mean percentage was 87% . In Table 1 the column marked *Caliper Volume* refers to the volume estimated from the caliper measurements using Equation 1, *Caliper Msr* , refers to caliper measurements on the dissected lesion, *Fluid Vol* gives the true volume determined by fluid displacement, *Sono Axes* are the lesion dimensions from the 3D sonoelastography images, *Sono Volume Axes* refers to the volume calculated using the axes measured in the sonoelastography images and *Sono Volume* refers to the lesion volume estimated by segmenting the 3D sonoelastography image set.

Figure 4 shows three lesions imaged using sonoelastography. Shown from left to right are lesions 1, 2 and 3. The arrows mark the location of the thermal lesion in the image.

TABLE 1. Measurements on Five Lesions.

	Caliper Volume cm	**Caliper Msr cc**	**Fluid Vol cc**	**Sono Axes cm**	**Sono Volume Axes cc**	**Sono Volume cc**
1	4.8	3.0 x 1.9 x 1.6	4.8	2.6 x 2.1 x 1.6	4.5	4.4
2	4.2	2.5 x 2.0 x 1.6	4.2	2.3 x 2.2 x 1.5	4.0	3.8
3	4.9	2.8 x 2.1 x 1.6	4.6	2.6 x 2.2 x 1.3	3.9	3.6
4	4.6	2.6 x 2.1 x 1.6	4.4	2.5 x 2.1 x 1.5	4.1	3.9
5	5.4	3.0 x 2.3 x 1.5	5.4	2.9 x 2.4 x 1.5	5.5	4.6

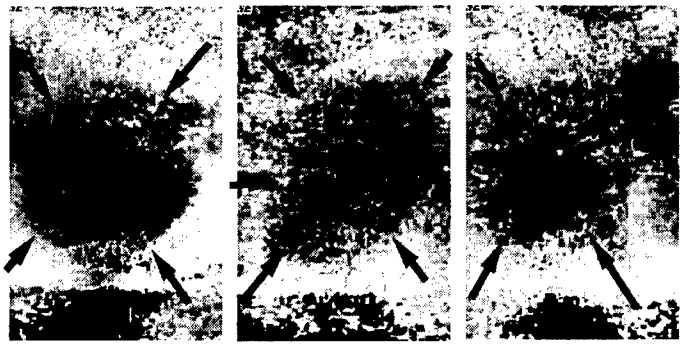

FIGURE 4. Three RF Lesions imaged using sonoelastography.

Each of these images were taken in the plane of the ablating needle. It was from these images that the first and third numbers in column *Sono Axes* of Table 1 were measured. The second number in that column is the out of plane thickness of the lesion.

Figure 5 shows co-registered B-mode and sonoelastography images of lesion 4, taken in the plane of the ablating needle. The needle is visible in the B-mode image (A) entering the image in the middle left hand side and ending at the lesion. In the sonoelastography image the lesion is clearly visible as a dark region. The lesion boundary determined by the sonoelastography image has been superimposed on the B-mode image.

Figure 6 shows a 3D sonoelastography rendering of lesion 3. Each image in the sequence of 2D sonoelastography images was segmented into tumor and background, then imported into IRIS Explorer and rendered as a 3D object. The field of view shown is contained with a bounding box of 2.8 x 2.1 x 1.6 cm.

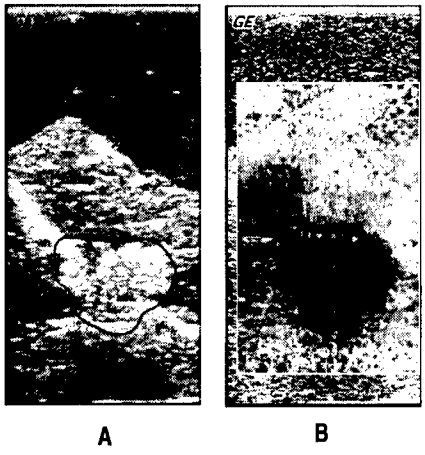

FIGURE 5. Lesion 4 B-mode image (A) and sonoelastography image (B).

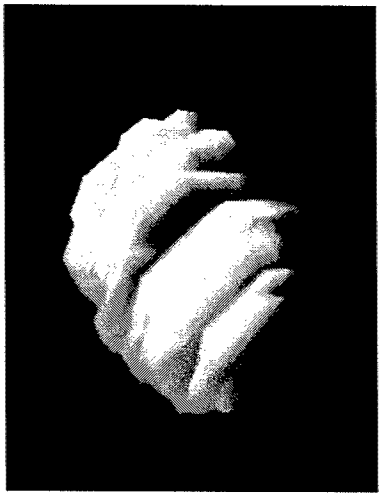

FIGURE 6. 3D Rendering of Lesion 3.

DISCUSSION

We have used RF ablation of healthy bovine calf liver as a model for coagulation necrosis lesions in general, and have shown that such lesions appear very clearly in sonoelastography lesions. In the clinic the goal of RF ablation is to generate an coagulation lesion whose diameter is equal to or greater than that of the tumor. Since sonoelastography images the relative elastic properties of tissue, when imaging a tumor which is itself stiff the contrast between the thermal lesion and the tumor may not be as high as suggested in Figure 4.

Our observation that the lesion boundaries in the sonoelastography images were somewhat ambiguous suggests two alternative explanations. First, it might be that the boundary between the normal tissue and thermal lesion is quite sharp and the ambiguity is a result of the vibration field at the boundary. Second, it might be that the variation in the tissue elastic modulus across the boundary itself varies slowly in the spatial dimension and the sonoelastography image is reflecting that variation in modulus. It seems reasonable to assume that the ablation in the tissue depends on the local density of RF current during the ablation process. Since current originates at the needle's tines and spreads out more or less spherically, it is safe to assume that the current flux density falls off with the radius, r, from the needle point as $1/r^2$. If the increase in local elastic modulus is proportional to the square of the current (i.e. energy flux) and the overall temperature-time history produced at a point, leading to heat denaturing of proteins, it could be that the boundaries themselves are more ambiguous than suggested by the photograph of a dissected lesion shown in Figure 3. Based on our prior work on imaging hard lesions in phantoms cited in the introduction, we find support for the second explanation, as phantom lesions show sharp boundaries whenever vibration artifacts were properly controlled.

SUMMARY AND CONCLUSIONS

Sonoelastography imaging of thermal induced lesions in liver tissue has been verified. Two-dimensional sonoelastography images through the plane of the ablating needle showed deficits of vibration centered at the end of the needle track. From this it is concluded that sonoelastography effectively detects thermal lesions in soft tissue. Dissection of the thermal lesions verified that they were palpably harder than the surrounding tissue. The true size of the lesion can be accurately estimated from the 3D images. Sonoelastography may be useful as a means of real-time monitoring of thermal lesion formation.

ACKNOWLEDGMENTS

This work was supported in part by the University of Rochester Departments of Radiology and Electrical Engineering, the General Electric Company (GE) and NIH grant 2 RO1 AG16317-01A1. The authors thank GE Medical Systems Division for the loan of the scanner used in the imaging experiments. The authors thank Clark Zhe Wu for his suggestions on using the needle axis as a basis for the lesion measurement coordinate system.

REFERENCES

1. Gazelle, G., Goldberg, S., Solbiati, L., and Livraghi, T., *Radiology*, **217**, 633–646 (2000).
2. Stafford, R., Kallel, F., Hazle, D., J Cromeens, Price, R., and Ophir, J., *Ultrasound in Med. & Biol.*, **24**, 1449–1458 (1998).
3. Righetti, R., Kallel, F., Stafford, R., Price, R., Krouskop, T., Hazle, J., and Ophir, J., *Ultrasound in Med. & Biol.*, **25**, 1099–1113 (1999).
4. Konofagou, E., Thierman, J., Karjalainen, T., and Hynynen, K., *Ultrasound in Medicine and Biology*, **28**, 331–338 (2002).
5. Fatemi, M., and JF, G., *Science*, **280**, 82–85 (1998).
6. Parker, K., Huang, S., Musulin, R., and Lerner, R., *Ultrasound in Med. & Biol.*, **16**, 241–246 (1989).
7. Huang, S., Lerner, R., and Parker, K., *J Acoust Soc Am*, **88**, 310–317 (1990).
8. Gao, L., Alam, S., Lerner, R., and Parker, K., *J Acoust Soc Am*, **97**, 3875–3886 (1995).
9. Parker, K., Fu, D., Gracewski, S., Yeung, F., and Levinson, S., *Ultrasound in Med. & Biol.*, **24**, 1437–1447 (1998).
10. Taylor, L., Porter, B., Rubens, D., and Parker, K., "3D sonoelastography for prostate tumor imaging," in *Proceedings of the International ICSC Congress on Computational Intelligence: Methods and Applications*, ICSC Academic Press, 1999, pp. 468–472.
11. Taylor, L., Porter, B., Rubens, D., and Parker, K., *Physics in Medicine and Biology*, **45**, 1477–1494 (2000).
12. Wu, Z., Taylor, L., Rubens, D., and Parker, K., *Journal of the Acoustical Society of America*, **109**, 439–446 (2002).
13. Taylor, L., Rubens, D., and Parker, K., "Artifacts and artifact reduction in sonoelastography," in *2000 IEEE Ultrasonics Symposium Proceedings*, IEEE, 2000, pp. 1849–1852.

The Effects Of Absorbers Such As Ribs In The HIFUS Beam-Path On The Focal Profile

James E. Kennedy*¶, Robert L. Clarke†, Gail R. ter Haar¶

*Dept. of Urology, Churchill Hospital, Oxford, OX3 7LJ, England. jekennedy@doctors.org.uk
†Dept. of Physics, Carleton University, Ottawa, Canada
¶Joint Dept. of Physics, Royal Marsden Hospital, Institute of Cancer Research, Downs Road, Sutton, Surrey, SM2 5PT

Abstract. There are no published data on the effects of ribs on the high-intensity focused ultrasound (HIFUS) focal profile. Many targets lie in the ribcage's acoustic shadow. To ensure safe and effective treatment, it is important to know detail both of field changes and of local effects on overlying ribs. A series of hydrophone measurements were performed to map experimentally the focal profile of a 1.7 MHz focused bowl transducer, with absorbers or ribs in the HIFUS beampath. Results were compared with a theoretical model. Lesions were created *ex vivo* to correspond with these plots, and rib surface temperature rises estimated.

Experimental and modeled focal profiles agreed closely. Focal position was maintained, but profile and peak intensity varied markedly. Absorber and rib experiments both indicated that by directing the beam axis through an intercostal space, it should be possible to target a tumour lying beneath the ribcage. However, if the beam axis is directed at the rib itself at lesioning HIFUS doses, even though it remains possible to create targeted tissue damage behind the rib, the temperature rise on the rib surface becomes unacceptably high as the rib position approaches the focal plane. These experiments also indicate that sensitive areas on the skin surface could be shielded by acoustic absorbers while maintaining the ability to create lesions. The theoretical model should allow prediction of the dose adjustments necessary in these circumstances.

INTRODUCTION

High-intensity focused ultrasound (HIFUS) is now in clinical use in many centres, where tumours are often being treated in target organs such as the liver or kidneys [1]. The anatomical positions of these organs necessitate that the HIFUS beam passes either close to the costal margin, or even between ribs. The published literature reflects work that is currently ongoing on the complex issues involved to compensate for major obstacles such as the intact skull [2], but there are no publications relating to the impact that more commonly encountered obstructions such as ribs have on the size, shape or position of the HIFUS focus. It is also important to quantify the local effects that the HIFUS beam would have on the ribs themselves in order to ensure adequate treatment and to minimise inadvertent thermal damage.

In some circumstances ribs are surgically removed prior to HIFUS treatment in order to provide an acoustic window, but this can give rise to problems when the scar

lies in the incident beampath, and skin burns may be encountered in subsequent treatment episodes. If the impact of absorbing obstructions can be reliably predicted, it should be possible to shield sensitive areas, thereby averting the risk of skin damage, without compromising treatment efficacy.

AIMS

The aims of these experiments were to assess the effects of HIFUS treatment when directed across the ribcage. The effects on the focal region and the local effects on the rib surface were evaluated. A theoretical model was developed to predict the focal profile in the presence of various configurations of absorbers or ribs, and the predictive value of the model was assessed.

MATERIALS AND METHODS

A 1.7 MHz focused bowl transducer, of 84 mm aperture and 150 mm focal length was used in all experiments, details of the system can be found elsewhere [3]. The focal profile was mapped using a PVDF membrane hydrophone at low exposure intensities. All lesioning experiments were conducted using core cylinders of fresh ox liver *ex vivo*, in a degassed water tank.

Preliminary experiments were conducted using absorbing 'rib phantoms' made from sheets of Perspex-backed corrugated rubber matting. These absorbers were placed against the face of the transducer in symmetrical configurations designed to mimic ribs in the beam-path. Hydrophone plots were recorded using these configurations and any reduction in focal peak intensities noted. See Fig. 1. Subsequently, corresponding lesions were created in ox liver *ex vivo*, adjustments in exposure parameters having been made to compensate for the energy absorbed by the obstructions.

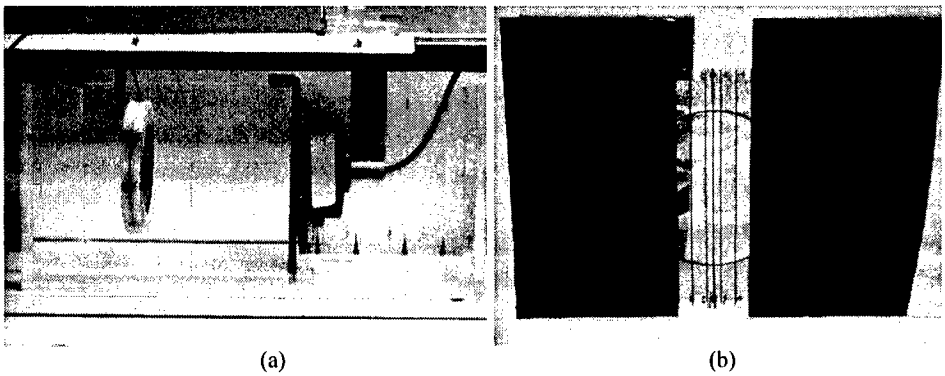

(a) (b)

FIGURE 1. (a) Photograph of experimental set-up for membrane hydrophone plots with absorbers against transducer face in degassed water tank. (b) Photograph of position of absorbers relative to beam profile when 50% of beam area is obscured.

For the purposes of modelling, these absorbers were also placed at various distances from the focal plane, with a central aperture of 1.5 cm, and hydrophone plots were compared with theoretical values.

In a second set of experiments, stripped *ex vivo* porcine ribs were held using a purpose-built rib-holder in a degassed water bath, and placed in the HIFUS beam-path as shown in Fig. 2. Porcine ribs were placed with intercostal spaces of 1.5 cm in order to approximate the clinical scenario. In the series of rib experiments, the beam axis was centred either on the intercostal space, the rib edge, or the centre of the middle rib of three. For each of these axial arrangements, the plane of the front surface of the ribs was placed 4 cm, 7 cm, or 10 cm in front of the focus and hydrophone plots were made.

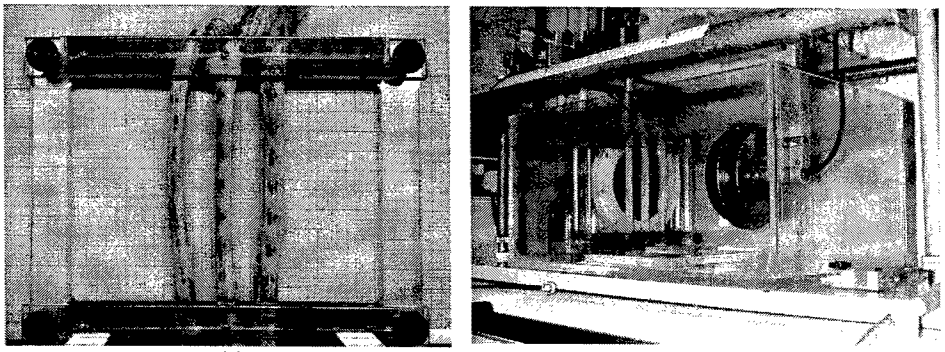

(a) (b)

FIGURE 2. (a) Photograph of porcine ribs in rib-holder. (b) Photograph of experimental set-up with for membrane hydrophone plots with rib holder in HIFUS beam-path in degassed water tank.

Lesioning experiments were repeated using these ribs, and once suitable parameters for the creation of lesions had been deduced from the hydrophone plots, the temperature on the rib surface was determined under these exposure conditions. In order to measure the temperature rise on the rib surface, a fine wire thermocouple was attached to the front surface of the rib, and slices of ox liver (of 1 cm thickness) were placed both in front of, and behind the rib. The transducer was then moved so that the position of the rib relative to the beam axis corresponded to each of the previous experiments in turn.

In all experiments, the positions of the absorbers and of the ribs relative to one another and to the transducer were noted. A theoretical model was designed and these relationships were entered into the model. In this way, theoretical predictions of the focal profile were compared with experimental findings.

RESULTS

When the sheet absorbers were placed in the beampath, the hydrophone plots of the focal profile demonstrated that the position of the focus remained constant in spite

of increasing obstruction of the incident HIFUS beam. The relationship between the reduction in focal peak pressure amplitude, and the percentage of the beam area that was blocked by the absorbers, was approximately linear. The width of the focus increased as the peripheral absorption increased from 0 to 75% of the beam area as shown in Fig. 3.

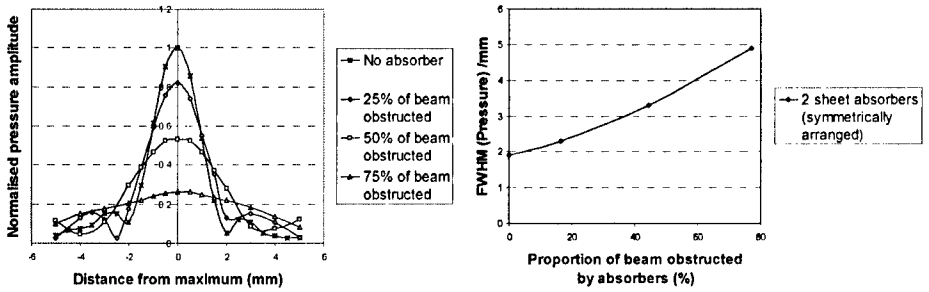

(a) (b)

FIGURE 3. (a) Low intensity trans-axial membrane hydrophone plots of focal region. Sheet absorbers were used to create varying degrees of beam obstruction as shown in Fig. 1(b). (b) Variation of FWHM (pressure) with beam obstruction.

The plots of the focal peak from the absorber experiments were similar in profile to those seen when using ribs. Theoretical modeling also matched experimental results closely for the central peaks and the first side peaks. See Fig. 4 for sample plots.

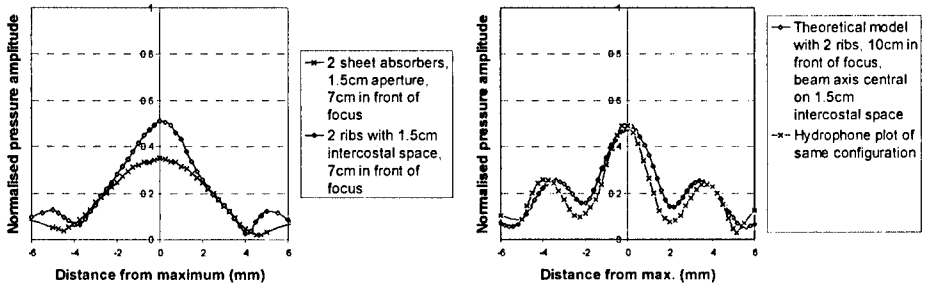

(a) (b)

FIGURE 4. (a) Comparison of hydrophone plots using 2 sheet absorbers or 2 ribs placed at 7 cm in front of focus. (b) Comparison of hydrophone plot and theoretical model using two ribs, placed at 10 cm in front of focus. In both (a) and (b) beam axis lies along the centre of the 1.5 cm 'intercostal space'.

The hydrophone plots from the series of rib experiments demonstrated that, when directing the beam axis at the intercostal space, the 6dB focal width varied between 2.5 mm and 4 mm, but that the position of the central peak was constant, and its amplitude remained constant until the ribs approached the focal plane. With the ribs at 4 cm from the focal plane, the beam-width approximately equaled the intercostal dimensions, and so the peak pressure value approached the free field value. See Fig. 5(a).

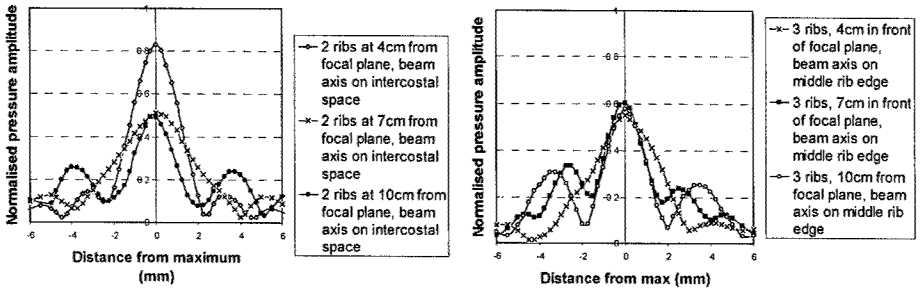

(a) (b)

FIGURE 5. (a) Membrane hydrophone plot with 2 ribs in beam-path at various distances from focal plane. Beam axis on centre of 1.5 cm intercostal space. (b) Similar plot with 3 ribs (1.5 cm intercostal spaces, beam axis on rib edge.

When the beam axis was directed at the rib edge, the focal profiles, shown in Fig 5(b), were very similar to those when the axis was on the intercostal space except when the ribs approached the focal plane. When the ribs were positioned at 4 cm in front of the focal plane, the focal peak pressure amplitude remained similar to the rest of the plots, while the 6dB focal width had increased from 2.0 mm to 3.5 mm.

Hydrophone plots were made when the axis of HIFUS beam was directed at the centre of the rib, the rib positions mapped carefully, and these configurations entered into the theoretical model. The experimental and theoretical results agreed closely in all cases as demonstrated in Fig. 6. When the plane of the ribs was at a distance of 7 cm or 10 cm from the focal plane, the focal profiles were similar to those when the beam axis fell on the rib edge or intercostal space, but at 4 cm in front of the focal plane, the central peak amplitude was markedly reduced, and its value approached that of the first side peaks.

These plots were analysed, and in each case, the proportional reduction in peak focal intensity (as compared to the free field value) was calculated. A corresponding increase was made in the transducer output for each set of experimental conditions, and lesions were created in ox liver *ex vivo*. It was possible to create lesions for all experimental configurations, but these lesions did not always conform to the familiar 'cigar shape'. When the ribs were positioned at distances of 7 cm and 10 cm from the focal plane, it was possible to create ellipsoidal lesions predictably, of approximate dimensions 2 mm x 20 mm, at a depth of 2 cm in the liver. This was the case whatever the relationship between the rib and the beam axis. For these configurations, using 'lesioning' exposure parameters, the temperature rise on the rib surface did not exceed 17° C. When the ribs were placed closer to the focal plane, at a distance of 4 cm, the appearance of the lesions was more interesting.

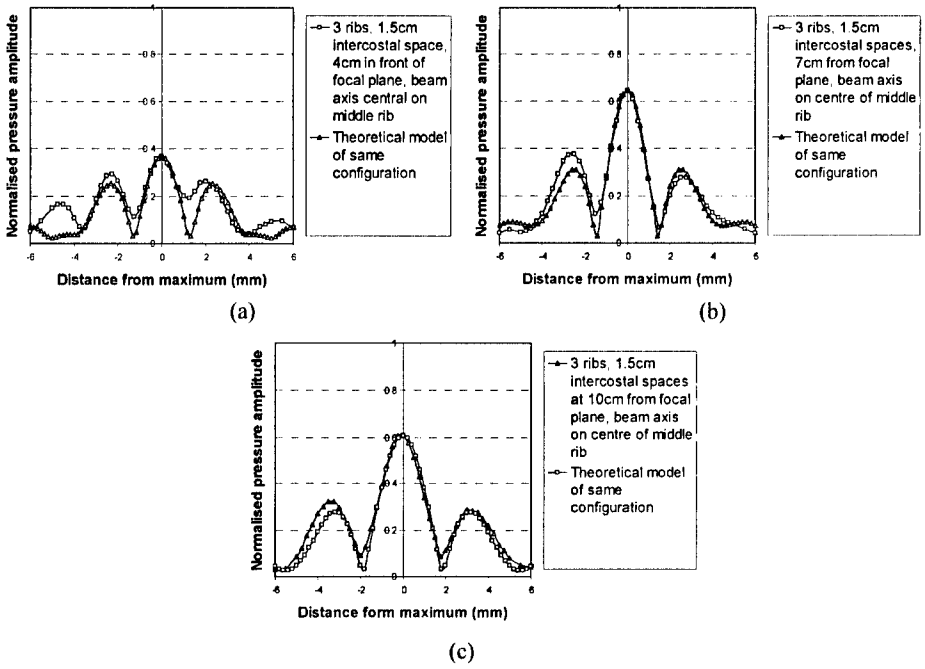

FIGURE 6. Membrane hydrophone plots compared to results from the theoretical model when 3 ribs, with intercostal spaces of 1.5 cm, were placed in the HIFUS beam-path at (a) 4 cm, (b) 7 cm and (c) 10 cm from the focal plane, with the beam axis directed at the centre of the middle rib.

With the ribs placed at 4 cm in front of the focal plane, when the beam axis was directed at the centre of the intercostal space, a 'standard' 2 mm x 20 mm lesion could be created. See Fig. 7(a). If the beam axis fell on the rib edge, a lesion could be created after a single 2 second exposure (equivalent free field I_{sp}=4.7kWcm^{-2}), but at an angle to the beam axis. See Fig. 7(b). When a rib was positioned centrally on the beam axis, a single 5 second exposure (I_{sp}=5.5 kWcm^{-2}) led to the creation of a Y-shaped lesion. If the exposure time was reduced, it could be seen that the individual components of this 'Y' were created simultaneously, rather than through the lesion advancing towards the transducer. See Figs. 7(c) and (d).

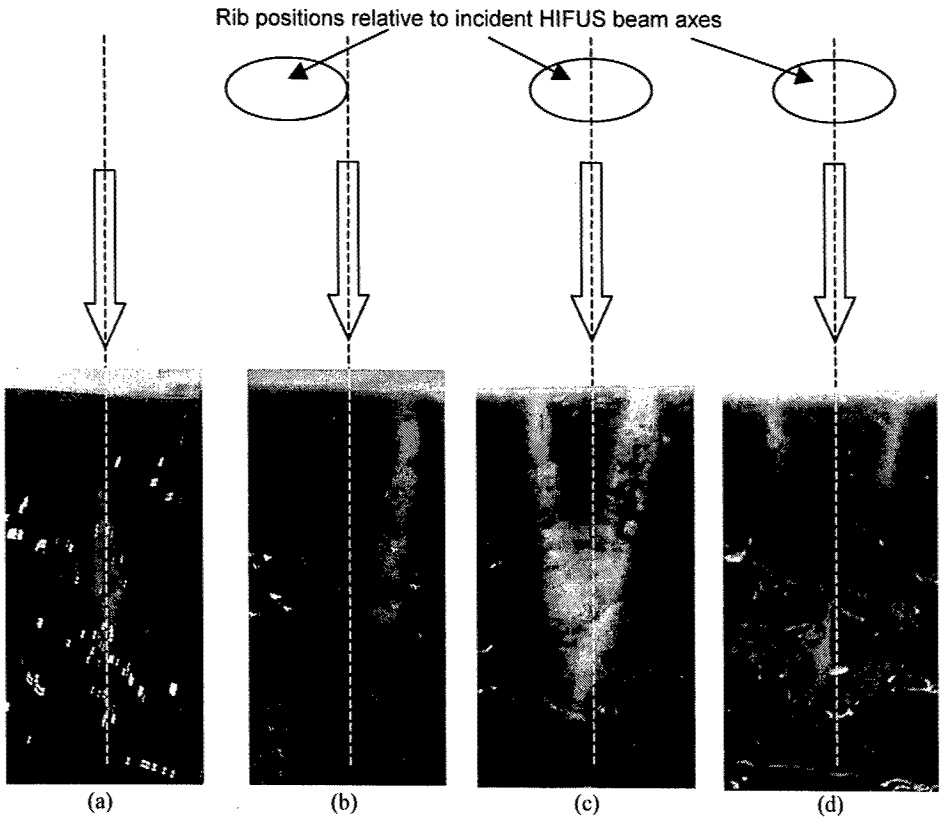

FIGURE 6. Photographs of individual lesions created in ox liver *ex vivo*. In all cases, ribs were placed at 4 cm from focal plane, and focal depth was at 2 cm from liver surface. (a) Beam axis central on 1.5 cm intercostal space, I_{sp}=2.1KW cm^{-2}, 2 second exposure. (b) Beam axis on rib edge, I_{sp}=4.7KWcm^{-2}, 2 second exposure. (c) Beam axis on centre of rib, I_{sp}=5.5KWcm^{-2}, 4 second exposure. (d) Beam axis on centre of rib, I_{sp}=5.5KWcm^{-2}, 5 second exposure.

When the axis was on the intercostal space, the temperature rise on the rib surface was only 2(±0.2)° C, but when directed at the rib edge, the corresponding rib surface temperature rise was 34(±3)° C. This rose again to 47(±5)° C when the beam axis fell on the rib itself.

DISCUSSION

The hydrophone plots demonstrate that using a focused bowl transducer, a discrete focal region can still be mapped despite the presence of a variety of configurations of absorbers and ribs in the beampath. Furthermore, it has been shown that the position and profile of these focal regions can be predicted reliably using a theoretical model.

When the exposure parameters are adjusted to compensate for absorption by such obstructions, it is possible to create lesions in ox liver *ex vivo*. If ribs are placed in the

incident beampath at a distance from the focal plane, it is again possible to achieve targeted tissue damage regardless of the relative positions of the ribs to the beam axis, and without causing unacceptable temperature rises on the rib surface. However, when these ribs approach the focal plane, more care must be taken to ensure predictable targeted lesions. If the beam axis is directed at the rib, unacceptable temperature rises are encountered on the rib surface, and tissue damage occurs simultaneously at the focus, and in a 'Y' shape in front of the focus. If the beam is centred on the rib edge, rib temperatures are again likely to cause local injury, and the pattern of tissue damage is asymmetrical about the beam axis. Only if the beam is directed at the intercostal space can predictable lesions be created at the focus, without causing damage to the adjacent ribs.

The earlier experiments using absorbers show the possibility of creating targeted tissue damage even in the presence of obstructions in the beampath. This infers that it should be possible to use such absorbers in clinical application, to shield sensitive areas on the skin surface from the HIFUS beam. The necessary alterations in dose could then be calculated from the theoretical model.

Many potential sources of experimental error are recognised in this series of experiments, most notably in the exact positioning of the ribs relative to the HIFUS beam axis, and in the estimation of any necessary dose modification. In clinical application, it is therefore clear that real time imaging is of prime importance. The two forms of real-time imaging in current clinical use are ultrasound and MRI [1,4]. Of these, only ultrasound can accurately predict the relationship between the beam axis and the ribs, and prevent injury from excessive HIFUS irradiation of those ribs. Further investigation is warranted in this field.

ACKNOWLEDGEMENTS

This research was supported by funding through a grant from Ultrasound Therapeutics Limited. We would also like to thank Ian Rivens and the Therapeutic Ultrasound team at the Institute of Cancer Research for their technical support.

REFERENCES

1. Wu, F., Chen, W.Z., Bai, J., Zou, J.Z., Wang, Z.L., Zhu, H., Wang, Z.B., *Ultrasound Med. Biol.*, **27** (8), 1099-1106 (2001).
2. Clement, G.T., White, J., Hynynen, K., *Phys. Med. Biol.*, **45**, 1071-1083 (2000).
3. Watkin, N.A., ter Haar, G.R., Rivens, I., *Ultrasound Med. Biol.*, **22** (4), 483-491 (1996).
4. Hynynen, K., Pomeroy, O., Smith, D.N., Huber, P.E., McDannold, N.J., Kettenbach, J., Baum, J., Singer, S., Jolesz, F.A., *Radiology*, **219**, 176-185 (2001).

Shear-Like Response Of Endothelial Cells To Therapeutic Ultrasound

Monica Dines[1], Eitan Kimmel[1,2], David Elad[2], Shmuel Einav[2], Dalit Raz[2] and Nitzan Reznick[3]

[1]*Faculty of Agricultural Engineering, Technion IIT, Haifa 32000, Israel.*
[2]*Department of Biomedical Engineering, Tel-Aviv University, Tel-Aviv 69978, Israel*
[3]*Faculty of Medicine, Technion IIT, Haifa 32000, Israel*

Abstract. Mechanical forces in general and shear stress in particular are known to affect endothelial cell (EC) functioning and play a role in the formation of mature, muscular arterioles and arteries (arteriogenesis). Recent studies shows that shear stress regulate angiogenic receptors such as vascular endothelial growth factor receptors (VEGFR-1 and VEGRF-2) and angiopoietin receptors (Tie-1 and Tie-2). We study the *in-vitro* influence of low intensity therapeutic ultrasound (TUS, intensity 1W/cm^2 and frequency 1.5 MHz) on Bovine Aortic Endothelial Cells (BAEC). VEGFR-2 expression increases after 30 and 60 min of irradiation; VEGFR-1 level decreases after 30 min of irradiation; Tie-1 shows a transient response to TUS - decreases at first and increases later; and Tie-2 starts increasing only after 60 min of irradiation. The regulating effect of TUS on the above receptors is similar to the effect that steady shear stress order 10 dynes/cm^2 has on BAEC when exposed *in-vitro* to laminar flow. The viability of the ultrasound treated EC is not reduced and no preferred orientation has been observed. There is no indication for unstable cavitational damage of jet formation. The results point to the possibility that random shear stresses are involved when TUS is applied to BAEC *in-vitro*. This may be attributed to stable cavitation and micro streaming that are induced by pulsating micro bubbles near the EC surface. The described influence of TUS on angiogenic mechanisms in BAEC *in-vitro* might have therapeutic effect on the cardiovascular system *in-vivo* and be used as a controlled, non-invasive stimulus for vascular regeneration.

INTRODUCTION

Our long-term goal is to utilize therapeutic ultrasound (TUS) as a stimulus for vascular regeneration. Cardiovascular disease is the major cause of morbidity and premature death in industrialized societies. Stimulation of new blood vessel growth under ischemic conditions is crucial in preventing large damage following major events such as acute infarction, and kidney or liver dysfunction. Endothelium – mediated formation of blood vessels is a multi-step process, occurring via one or more of several alternative pathways, among them: *Vasculogenesis* is the development *in situ* of vessels from angioblasts that happens in embryos forming a primitive tubular network. This network evolves into main blood vessels including aorta and major veins. *Angiogenesis* is the sprouting of new capillaries from existing network. *Arteriogenesis* is the formation of mature muscular large vessels (arterioles and proliferation of preexisting collateral arteries [1]. While blood vessel formation through angiogenesis occurs mainly in ischemic tissues, hemodynamic changes in the

vessel itself and biomechanical induced changes in the surrounding tissue govern arteriogenesis (e.g. Clark's observation in 1918 of preferred capillary sprouting from capillary with high flow [1]).

Among the angiogenic factors that control formation and remodeling of blood vessels are protein ligands that modulate the activity of transmembrane tyrosine kinase receptors. Worth noting are Vascular Endothelial Growth Factors (VEGFs) and their receptor families (VEGFRs), Angiopeitins and their receptors, Basic Fibroblast Growth Factors (bFGF), Platelet Derived Growth Factor (PDGF), and Transforming Growth Factor β (TGF-β).

VEGF Receptors

The family of VEGF receptors is formed from three receptors of tyrosine kinases: VEGFR-1 (Flt-1), VEGFR-2 (Flk-2), and VEGFR-3 (Flt-4). VEGFR-1 and VEGFR-2 are specific to vascular endothelium in their expression while VEGFR-3 is specific to lymphatic endothelium [2]. The receptor VEGFR-2 is involved in the induction of endothelial cells proliferation, migration, and in sprouting activity. It helps in promoting endothelial cells to form tubule-like structures. VEGFR-2 is critical for the earliest stages of vasculogenesis *in vivo*. Embryos lacking one or two alleles of VEGFR-2 died in early phases of development because vessels fail to develop [3]. Analysis of embryos with heterozygous gene disruption show that VEGFR-2 is involved not only in the very initial phases of vasculogenesis, but also in the later stages, in sprouting, and in other phases of angiogenesis, as well as in vessel survival [4,5]. Studies in mice lacking VEGFR-1 show that this receptor is antagonist to VEGFR-2 and those mice have excess formation of endothelial cells, which abnormally coalesce into disorganized tubules [6]. Mice engineered to express only a truncated form of VEGFR-1, without its kinase domain, appear normal, and this is consistent with the notion that the primary role of VEGFR-1 may be that of a decoy receptor [7].

Angiopoietin Receptors

Similar to VEGF receptors, the angiopoietin receptors, Tie-1 and Tie-2, are specific for endothelial cells and are tyrosine kinase receptors. The entire four known angiopoietins bind to Tie-2, yet it is still unclear what binds to Tie-1.

More understanding of the roles of Tie-2 came from the analysis of mice engineered to lack the relevant gene products [8, 9]. Unlike mouse embryos lacking VEGFR-2, embryos lacking Tie-2 develop a rather normal primary vasculature, but this vasculature fails in the normal future remodeling [10]. The most serious defects are in the heart, with problems in the association between the endocardium and underlying myocardium, in trabeculae formation, and also in the remodeling of vascular beds into large and small vessels [10]. In the ultrastructural analysis of these vascular beds and hearts it was observed that endothelial cells fail to associate with underlying support cells, [8]. This led to the conclusion that Tie-2 maybe involved in the integration process of endothelial cells with supporting cells.

The important roles of Tie-1 receptor came from studies done on mice that suffer target disruption on Tie-1 gene. Those mice died immediately after birth by extensive hemorrhage and defective microvessel integrity [11, 9]. This suggests that Tie-1 have an important role in maintenance of blood vessel integrity. The phenotypic analyses of the Tie-1 and Tie-2 null mutants suggest that these receptors have distinct roles in blood vessel development, with Tie-2 required at an earlier stage than Tie-1 [12]. The cellular functions of Tie-1 are still unknown, yet recently it was found that Tie-1 physically interacts with Tie-2 in endothelial cells. This suggests that Tie-1 might participate in some aspects of Tie-2 signaling [13].

MATERIAL AND METHODS

Primary bovine aortic endothelial cells (BAECs) were cultured at 37°C, 5% CO_2 in a humidified incubator in a DME medium containing 10% CS, 2mM L-Glutamine, 20 U/ml Penicillin, 20 μg/ml Streptomycin, 0.25 μg/ml Amphotericin B, and 50 μg/ml Gentamycin.

Ultrasound Treatment

A sleeve guide filled with water was placed on a 1.5 MHz transducer with intensity of 1 Wcm^{-2}, continuous wave, and burst time of 2 msec. Its length was set to 12cm to avoid near field irregular conditions. A 60 mm diameter cell culture dish with cells was placed on top of the water column, allowing no air gap between the water and the bottom of the dish. Calibration of the ultrasonic intensity in the dish was done using a needle hydrophone. In our experiments the BAE cells were seeded in dishes and were grown to confluence. Prior to the experiments the cell culture medium was changed. The confluent BAE cells were irradiated for 5, 15, 30, and 60 min. During the irradiation period all the system was stored at 37° C, 5% CO_2 in a humidified incubator. The temperature was tested with an 80TK Thermocouple module with sensor (Fluke) connected to 77 Multimeter (Fluke).

Cell Testing

Cells Extracts

Immediately after the cells were exposed to TUS, they were washed two times. The cells at the boundaries of the dish, away from the center, were scraped and removed from the dishes. The rest of the cells were placed into a 15 ml washing buffer and were centrifuged for 10 min/ 2500 rpm, resuspended in a 1 ml washing buffer and centrifuged again for 1 min/13000 rpm. After this the cells were lysed in 10-30 μl lyses buffer and centrifuged for 15 min/13000 rpm. The supernatant obtained was stored immediately at –70° C.

Western Blot Analysis And Immunoblotting

Some 50-100 μg of the cell extract protein were mixed with sample buffer, boiled for 5 min, centrifuged and stored on ice. The cell extract protein with the sample buffer was electrophoresed in SDS-8% polyacrylamide with running buffer (0.1% SDS, 25 mM Tris pH 8.3, 192 mM glycine) for 120 min at 80 mA. After this the gel was immersed in Towbin buffer and also the nitro-cellulose membrane. The Blotting was done with Towbin buffer for 120 to 150 min at 200 mA.

The membranes were incubated for 60 min with a blocking solution (TBS ,5% Non-Fat Dry Milk 0.05% Tween 20) at room temperature. Then, the membranes were incubated for 120 min with VEGFR-1 or VEGFR-2 (Santa Cruz Biotechnology) antibodies (0.8 μg/ml) at room temperature or overnight at 4°C, and for 1h at room temperature with Tie-1 and Tie-2 (0.8 μg/ml) antibodies (Santa Cruz Biotechnology). After the incubation with the first antibody the membranes were washed three times for 10 min with TBS 0.05% Tween 20 and incubated again with the second antibody (A/G - Pierce, HRP- Protein, IL, USA) for 60 min. The membranes were washed 2 times for 10 min with TBS 0.05% Tween 20 and once with TBS. The immune complexes were detected with a chemiluminescence detection system (LumiGlu, Cell Signaling, Harahan, LA, USA). After this the membranes were immediately exposed to autoradiographic films (Kodak) for different period of times.

A CCD camera was used for the gel pictures. Band intensity was determined by a densitometer with the program Bio-Profile Imaging (Vilber Lourmant, France). All results were presented as mean (of at least three repeated experiments) ± SD. The results were checked by ANOVA two-tailed t-test. Significance was determined for $p<0.05$.

Viability Tests

For the viability tests we used a commercial XTT kit (Biological Industries, Kibutz Beit Haemek, Israel). The XTT kit is a colorimetric assay. The cells are incubated for 4 h and absorbance was measured with a spectrophotometer at a wavelength of 500 nm. In order to measure reference absorbance we used a wavelength of 650 nm. The results were expressed as OD (optical density). The negative control was the sham-radiated cells and cells stored in the incubator.

Apoptotic cells were marked immediately after TUS irradiation and 24 h later by staining with fluorescent Hoechst 33258 dye in a final concentration of 1 μg/ml. The condensed chromatin of apoptotic (or dead) cells stained by this dye appears brighter than the chromatin of normal cells. The counting was performed using a Plan Fluor 10× objective and a UV filter for Hoechst 33258. The images where taken by CCD camera connected to an Olympus microscope. Each experiment was performed in duplicate. Data are expressed as percent of total cells/field ± SD.

RESULTS

No significant changes were observed in BAECs viability after TUS irradiation (see Fig. 1). The results in Fig. 1 are expressed in units of optical density (O.D.) and *percentage of total cells/field ± SD.*

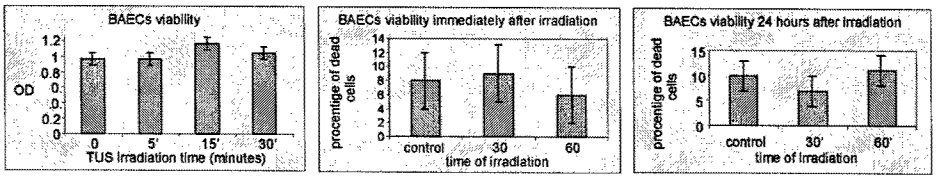

FIGURE 1. BAECs viability in response to TUS irradiation.

The Response Of Angiogenic Receptors To TUS

The four angiogenic receptors: VEGFR-1, VEGRF-2, Tie-1 and Tie-2 are important receptor in the formation process of new blood vessels and in blood vessel remodeling. In order to determine their response to TUS, confluent cultures of BAECs were exposed to various times intervals (5-60 min) of TUS irradiation and were compared with BAECs grown under static conditions (control). The effect of TUS was compared with laminar shear stress (LSS) of 10 dynes/cm^2 (as obtained from reference [14] and other unpublished results from the group of Dr. N. Resnick).

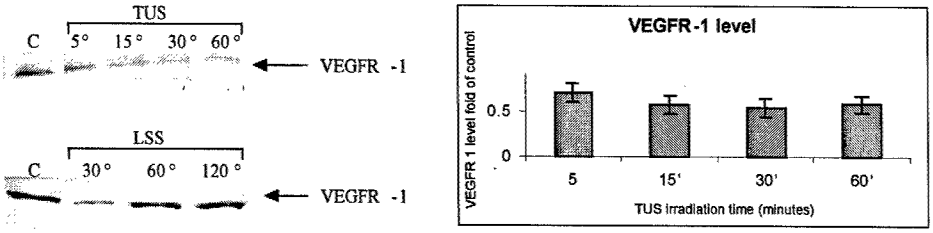

FIGURE 2. The response of VEGFR-1 in BAEC to TUS, compared with the response to LSS.

TUS, similar to LSS, down regulate the VEGFR-1 level (Fig. 2). This down regulation is better observed after a 30 min of ultrasound irradiation. TUS is similar to LSS in the way it up regulates the level of VEGFR-2 (Fig. 3). Relatively short intervals of TUS irradiation (15-30 min) are sufficient to increase the level of VEGFR-2. TUS has a complex influence on Tie-1 level (Fig. 4), similar to LSS. It first down regulates the Tie-1 level and later, only after about 60 min of TUS exposure it up regulates the Tie-1 level. Relatively short intervals of TUS irradiation (5-30 min) are sufficient to decrease the level of Tie-1 and longer intervals are needed to increase the Tie-1 level. It seems that the up regulation of the TUS is to a lower level than the initial value of Tie-1 level. In difference, LSS is capable of causing a net increase of Tie-1 level relative to the initial value after 60 min of exposure. As shown in Fig. 5 TUS, similar to LSS, up regulates the VEGFR-2 level. The increase in the level of Tie-2 is observed only after long exposure time to TUS of 60 min.

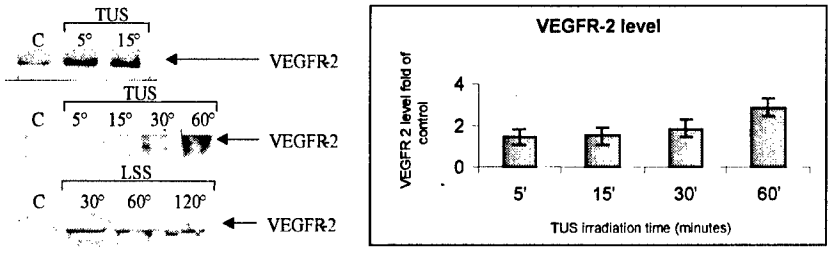

FIGURE 3. The response of VEGFR-2 in BAEC to TUS, compared with the response to LSS.

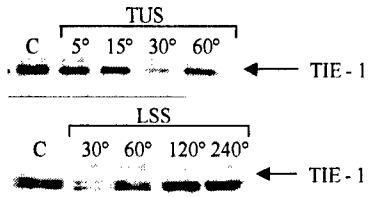

FIGURE 4. The response of Tie-1 in BAEC to TUS, compared with the response to LSS.

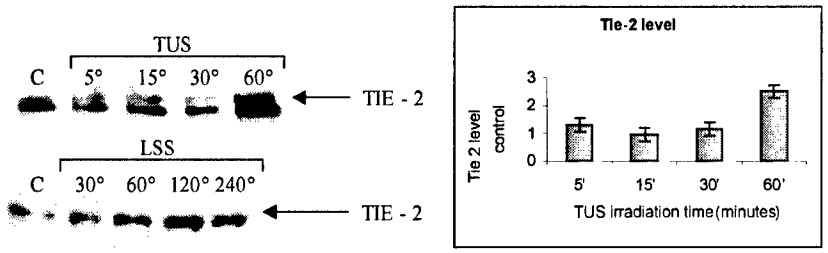

FIGURE 5. The response of Tie-2 in BAEC to TUS, compared with the response to LSS.

DISCUSSION

Mechanical forces (mainly shear stress), acting through the endothelium, have a role in initiating new blood vessel formation through a process of arteriogenesis [15]. Nevertheless, until now biomechanical forces were not considered as a vascular therapeutic tool. This study checks the possibility to use TUS as a modality to produce local, well controlled shear stress. The results are encouraging first because of the similarity between the *in-vitro* response of BAEC to TUS and LSS, and second because of the no changes in the viability of endothelial cells after exposure to TUS. It seems that low intensity TUS does not cause damage to the endothelial cells and does not affect their basic functioning. This type of non-destructive mechanical-like loading of cells was observed before when TUS induced in fish epidermis widened intercellular spaces between cells while the cells seemed intact [16]. Those

intercellular spaces might have generated by localized shear stresses that act on the surface of the epidermis.

The major question is what is the mechanism that works like a mild shear stress generator. This mechanism does not cause damage to the endothelial cells and still is capable of affecting angiogenic receptors. Endothelial cells need a certain shear for normal functioning, while increased levels of shear make the endothelial cells more involved in vascular genesis mechanisms. If TUS was fierce enough to cause membrane rupture, it would have reduced both viability and migration performance. One can assume that not too large values of shear were able to regulate molecular levels of receptors without causing any changes in the viability.

Standing waves or wave interference cannot be correlated with the results obtained because their wavelength (about 500 μm, for 1.5 MHz and the velocity of 1500 m/s) is much higher than the typical dimension of a cell (about 10 μm). Because of such relatively high wavelength pressure amplitude variations are negligible over a distance of few micrometers and, therefore, no relative displacements and subsequent strains are expected between neighboring cells or even between cell and base.

Some evidence appears to point to formation of transverse (shear) waves in the upper layers of the fish epidermis [16] as the mechanism responsible for similar shear stress on BAEC after TUS irradiation. Longitudinal waves can be transformed by mode changing into transverse waves when striking a plane interface obliquely. Transverse waves are likely to develop from longitudinal waves on transition between two media with different impedances, provided the incidence angle is not 0°. Impedance difference of few percent only, such as between blood and endothelial cells, is enough that significant amplitudes of transverse waves may be found at the interface between the two media. In our setup transverse waves at the endothelial cell layer maybe either transmitted through the plastic dish, or reflected from the dish walls and propagate as longitudinal waves until refracting at the cell surfaces.

The shear stress like response of endothelial cells to TUS stimulation can be also attributed to steady oscillations of gas bubbles in liquid, very close to a rigid surface. The bubble oscillations induce on the surface oscillating shear stress together with a steady shear stress and micro streaming [17]. Mathematical simulations show that significant shear stresses develop on the surface when the distance between the bubble and the surface is comparable in size to the bubble radius. In this case pressure amplitude of 20 kPa generate maximal steady shear stress of about 1000 Pa (10000 dyne/cm^2) and maximal oscillatory shear stress of about 10 kPa (for comparison physiological shear acting on blood vessels walls is about 1000 times smaller). The effect of the shear stress is limited to a typical surface area comparable to the bubble size [17]. Both mechanisms, the "pulsating bubble near a rigid wall" and "the transverse waves at impedance transition" is very localized.

CONCLUSIONS

The described influence of TUS on angiogenic mechanisms in BAEC *in-vitro* might have therapeutic application in the cardiovascular system *in-vivo* and be used as a controlled, non-invasive stimulus for vascular regeneration.

ACKNOWLEDGEMENTS

This work was supported by a grant from the Israeli Ministry of Science. The contribution of Dr. Boris Krasovitski and Dr. Uri Zaretsky is highly appreciated.

REFERENCES

1. Buchman, I., and Schaper, W., "Arteriogenesis versus angiogenesis: two mechanisms of vessel growth," *News Physiol. Sci.*, **14**, 121-125 (1999).
2. Kukk, E., Lymboussaki, A., Taira, S., Kaipainen, A., Jeltsch, M., Joukov, V., and Alitalo, K., "VEGF-C receptor binding and pattern of expression with VEGFR-3 suggests a role in lymphatic vascular development," *Development – Supplement*, **122**, 3829-37 (1996).
3. Gale, N.W., and Yancopoulos, G.D., "Growth factors acting via endothelial cell-specific receptor tyrosine kinases: VEGFs, angiopoietins, and ephrins in vascular development," *Genes & Development*, **13**, 1055-66 (1999).
4. Carmeliet, P., Ferreira, V., Breier, G., Pollefeyt, S., Kieckens, L., Gertsenstein, M., Fahrig, M., Vandenhoeck, A., Harpal, K., Eberhardt, C., Declercq, C., Pawling, J., Moons, L., Collen, D., Risau, W., Nagy, A., "Abnormal blood vessel development and lethality in embryos lacking a single VEGF allele," *Nature*, **380**, 439 – 439 (1996).
5. Ferrara, N., Bunting, S., "Vascular endothelial growth factor, a specific regulator of angiogenesis," *Current Opinion in Nephrology & Hypertension*, **5**, 35-44 (1996).
6. Fong, G.H., Rossant, J., Gertsenstein, M., Breitman, M.L., "Role of the Flt-1 receptor tyrosine kinase in regulating the assembly of vascular endothelium," *Nature*, **376**, 66 – 70 (1995).
7. Hiratsuka, S., Minowa, O., Kuno, J., Noda, T., Shibuya, M., "Flt-1 lacking the tyrosine kinase domain is sufficient for normal development and angiogenesis in mice," *Proceedings of the National Academy of Sciences of the United States of America*, **95**, 9349-54 (1998).
8. Suri, C., Jones, P.F., Patan, S., Bartunkova, S., Maisonpierre, P.C., Davis, S., Sato, T.N., Yancopoulos, G.D., "Requisite role of angiopoietin-1, a ligand for the TIE2 receptor, during embryonic angiogenesis," *Cell*, **87**, 1171-80 (1996).
9. Sato, T.N., Tozawa, Y., Deutsch, U., Wolburg-Buchholz, K., Fujiwara, Y., Gendron-Maguire, M., Gridley,T., Wolburg, H., Risau, W., Qin, Y., "Distinct roles of the receptor tyrosine kinases Tie-1 and Tie-2 in blood vessel formation," *Nature*, **376**, 70-76 (1995).
10. Gale, N.W., Yancopoulos, G.D., "Growth factors acting via endothelial cell-specific receptor tyrosine kinases: VEGFs, angiopoietins, and ephrins in vascular development," *Genes & Development*, **13**, 1055-66 (1999).
11. Puri M. C., Rossant J., Alitalo K., Bernstein A., Partanen J. The receptor tyrosine kinase TIE is required for integrity and survival of vascular endothelial cells. *EMBO Journal*. **14**, 5884-9 (1995).
12. Loughna, S., Sato, T.N., "Angiopoietin and Tie signaling pathways in vascular development," *Matrix Biology*, **20**, 319-25 (2001).
13. Hughes, D.P., Edge, M.D., Marron, M.B., Forder, C.L., Brindle, N.P., "Evidence for heterotypic interaction between the receptor tyrosine kinases TIE-1 and TIE-2," *Journal of Biological Chemistry*, **275**, 39741-6 (2000).
14. Shay-Salit, A., Shushy, M., Wolfovitz, E., Yahav, H., Breviario, F., Dejana, E., and Resnick, N., "VEGF receptor 2 and the edherens junction as a mechanical transducer in vascular endothelial cells," *Proc. Natl. Acad. Sci., USA*. **99**(14), 9462-9467 (2002).

15. Buschmann, I., Schaper, W., "The pathophysiology of the collateral circulation (arteriogenesis)," *Journal of Pathology*, **190,** 338-42 (2000)
16. Frenkel, V., Kimmel, E., "Ultrasound-induced intercellular space widening in fish epidermis," *Ultrasound in Med. & Biol.*, **26,** 473-480 (2000)
17. Krasoviski, B. and Kimmel, E., "Flow regimes induced by pulsating gas bubbles in living tissues," *In the Proceedings of the* 16th *International Symposium on Nonlinear Acoustics*, Moscow (2002).

Laparoscopic High Intensity Focused Ultrasound: Application To Kidney Ablation

Jahangir Tavakkoli[1], Victor V. Rao[1], Ralf Seip[1], Ryan F. Paterson[2], Eric Barret[3], Liang Cheng[4], Arieh L. Shalhav[3], and Narendra T. Sanghvi[1]

[1] *Focus Surgery Inc., Indianapolis, IN*
[2] *Methodist Hospital Institute for Kidney Stone Disease, Indianapolis, IN*
[3] *Dept. of Urology, Indiana University School of Medicine, Indianapolis, IN*
[4] *Dept. of Pathology, Indiana University School of Medicine, Indianapolis, IN*

Abstract. This work demonstrates the feasibility of using high intensity focused ultrasound (HIFU) for selective ablation of renal tissue through laparoscopic procedures. Two laparoscopic HIFU probe prototypes were developed and tested.

Probe 1: It is a hand-held probe with no integrated ultrasound imaging capability. It consists of two focused rectangular HIFU piezoceramic crystals mounted on a stainless steel tube for side and front firing configurations working at 4 and 5MHz respectively. During laparoscopic operation a separate video camera imaging channel is used for treatment monitoring.

Probe 2: It is a computer-controlled probe with an integrated ultrasound imaging working in conjunction with the Sonablate® HIFU system. It consists of a 4MHz focused rectangular HIFU piezoceramic transducer confocally coupled with a circular central element used for real-time pulse-echo imaging. Precise bi-plane mechanical movements of the transducer enable it to treat targeted tissue volumes under ultrasound imaging guidance.

Both prototypes were fully characterized for electrical impedances, acoustic fields, and total acoustic power outputs. They were then tested in an *in vivo* animal experimental study in which 20 pigs were treated through both open and sterile laparoscopic HIFU surgery procedures. Gross pathology and histology results demonstrated the feasibility of the laparoscopic HIFU to generate selective homogenous well-delineated necrotic lesions in a lobe of the kidney. Specifically, when treating under real-time ultrasound imaging guidance (probe 2) the ablated tissue region agrees with the planed lesion size and position within ± 1mm. Moreover, it can be used as a hemostasis tool during standard partial nephrectomy to significantly reduce bleeding associate to these procedures.

INTRODUCTION

Nowadays, there is an increasing interest in laparoscopic techniques for performing different kinds of surgeries with significantly less morbidity and mortality [1,2]. Among others, the urology surgery community is also investigating several laparoscopic surgery techniques. Notable examples are cryoablation using extreme cold, radiofrequency ablation, and HIFU (high intensity focused ultrasound) ablation [3-5]. HIFU technology has demonstrated promising results in treating benign and malignant diseases in different organs including prostate, liver, kidney, breast, etc. [6-9]. Moreover, several recent studies have been demonstrated the ability of the

HIFU to control bleeding and to generate hemostasis (partial or total) in different tissues and vessels [10,11].

Renal cell carcinoma is the third most common cancer in urology and is by far the most common malignant tumor of the kidney. After detection of the tumor, if the features are suggestive of malignancy or if it is growing rapidly, the patient is treated surgically with either partial or total nephrectomy depending on the size and location of the lesion and the preference of the physician. Since kidney is a highly vascularized organ, nephrectomy, as an invasive procedure, is usually associated with significant bleeding and high morbidity.

In the current feasibility study, we extended the application of the HIFU technology to laparoscopic surgery. To this end, two laparoscopic HIFU probe prototypes were developed and tested in porcine renal tissue treatments [12,13]. Results of the *in vivo* porcine studies demonstrated the feasibly of HIFU in selective ablation of renal carcinoma through well-delineated contiguous necrosed lesion extending from the kidney's pelvic system to the capsule. It was also demonstrated that laparoscopic HIFU could induce a circumferential disk-shaped necrotic tissue volume confined in a lobe of the kidney. This may be served as a hemostasis barrier prior to partial nephrectomy that leads to much less bleeding and lower morbidity.

MATERIALS AND METHODS

Probe 1: Hand-held Laparoscopic HIFU Probe

A hand-held HIFU probe was developed to meet the main features required for sterile laparoscopic operations. The probe was built from a stainless steel tube with 11 mm outer diameter and 38 cm length (Figure 1). The probe consists of two focused rectangular HIFU piezoelectric crystals for side and front firing configurations. The crystals were made from a special high-power piezoceramic material (KEZITE NOVA 3B) capable of providing high acoustic powers required in HIFU applications (KERAMOS Inc., Indianapolis, IN). The parameters of the crystals are:

Side firing crystal: Geometry = Truncated spherical concave, Radius of curvature = 30 mm, Aperture dimensions = 30×8 mm, Center frequency = 4.0 MHz.

Front firing crystal: Geometry = Truncated spherical concave, Radius of curvature = 10 mm, Aperture dimensions = 10×7 mm, Center frequency=5.0 MHz.

During HIFU procedure, the transducers are covered by a latex sheath filled with circulating water and supported by a backing sleeve. The backing support sleeve (Fig. 1-b), made from brass, has two functions: (1) protection of the coupling latex sheath, and (2) providing acoustic windows to allow the latex sheath to distend in the desired planes only in front of the crystals, i.e. in direction of the HIFU beam propagation for both the side and front firing crystals.

The laparoscopic HIFU probe was fully characterized by measuring its electrical impedance, acoustic field, and total acoustic power output. The probe was able to generate total acoustic power (TAP) levels of up to 35 W and 10 W for the side and front transducers respectively. These, in turn, correspond to maximum tissue focal

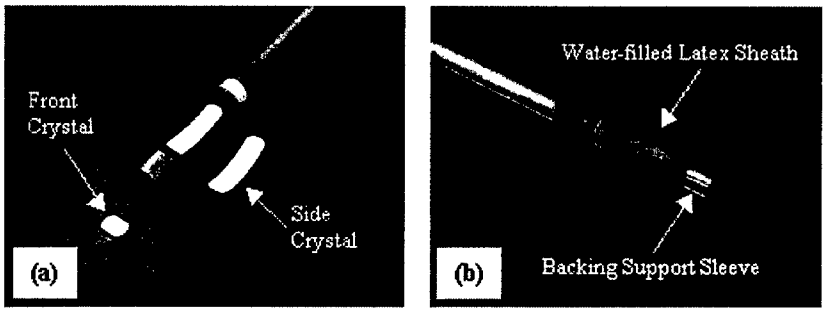

FIGURE 1. (a) The hand-held laparoscopic HIFU probe and the piezoceramic crystals shown separately. (b) A close-up of the probe tip covered by the coupling latex sheath.

intensities over 2000 W/cm^2 and 4000 W/cm^2 for the side and front transducers respectively. These intensity levels would be sufficient for tissue ablation through coagulation necrosis by rapid temperature rise (>90° C) and bubble activities initiated by superheating mechanisms.

Figure 2 shows the temperature response simulations of the front and side transducers in the kidney tissue. The temperature maps are shown at the end of a 3-s HIFU exposure time at the typical TAP values given in the figures. A full 3D solution to the linear acoustic field coupled to the bioheat transfer equation (BHTE) was used to calculate the temperature response [14]. However, since the HIFU fields are highly nonlinear, these simulations may give an underestimation in the peak focal intensities and an overestimation in the focus dimensions.

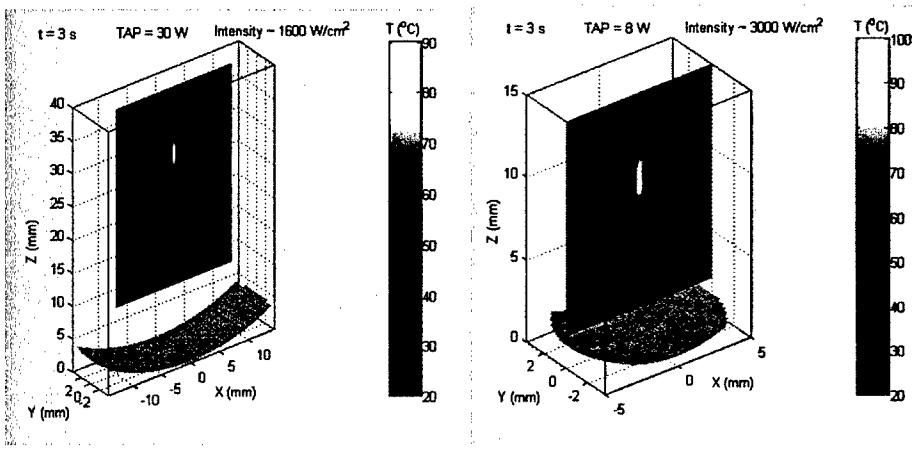

FIGURE 2. Computer simulations of the temperature response in the kidney tissue for the side and front transducers. Exposure parameters are given in the figures.

Experimental Setup

Figure 3 shows the block diagram of the experimental setup to control the HIFU exposure from the hand-held laparoscopic probe. The overall operation is controlled

by a laptop computer. The control programs were written in Matlab and C. The operator controls the HIFU shots using a foot switch. Each time the foot switch was pressed, 5 HIFU shots were fired each of 2 s on time followed by 2 s off time.

An active pump/chiller unit (SonaChill™, Focus Surgery Inc., Indianapolis, IN) was used in conjunction with the laparoscopic probe to ensure continuos circulation of cold water (~20° C) around the HIFU transducers. This allowed the application of high powers by increasing the efficiency of the transducer and reducing the risk of transducer overheating.

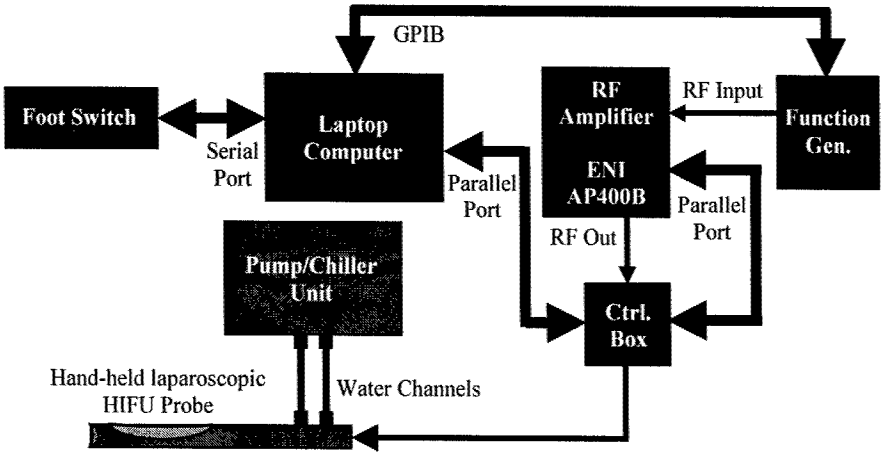

FIGURE 3. Experimental setup used for the hand-held laparoscopic probe.

Probe 2: Computer-controlled Laparoscopic HIFU Probe

The computer-controlled laparoscopic HIFU probe assembly (Figure 4-a) was designed based on modifications to the standard Sonablate® transrectal probe (Focus Surgery Inc., Indianapolis, IN). While the electrical and mechanical components of the probe left unchanged, two major modifications were implemented into it.

- The probe tip was redesigned and built from stainless steel to make it adaptable to laparoscopic surgery requirements by making it narrower and longer.
- A new dual-element piezoelectric transducer (4.0 MHz center frequency for both therapy and imaging, and 30-mm focal length) was built with a geometry that was adaptable to the new tip. In the new design, therefore, the therapy element of the transducer was made narrower while the imaging element remained unchanged.

A supporting sleeve made from stainless steel is used to cover the probe tip (Figure 4-b). Similar to the hand-held probe, the sleeve is used for protection of the latex sheath, and to provide a window to allow the latex sheath to distend in the desired plane only in front of the crystal.

The probe should be used in conjunction with the Sonablate® HIFU device and the SonaChill™ active pump/chiller unit. The Sonablate® device was originally developed for computer-controlled image-guided HIFU treatment of prostate diseases including BPH (benign prostatic hyperplasia) and localized prostate cancer (Figures 4-c and

4-d). Precise biplane mechanical movements of the transducer controlled by the Sonablate® device along with real-time ultrasound imaging during HIFU treatment and advanced treatment planning, make it a reliable and safe system for selective tissue ablation in order to treat solid tumors. Please refer to [15] for a more detailed description of the device.

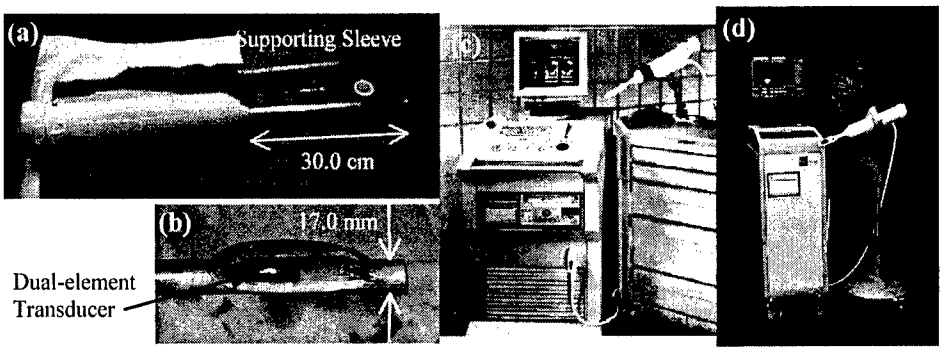

FIGURE 4. (a) The computer-controlled laparoscopic HIFU probe and the supporting sleeve, (b) a close-up of the probe tip covered with the supporting sleeve and the water-filled latex sheath, (c) Sonablate® 200 HIFU device, and (d) Sonablate® 500 HIFU device.

Figure 5 shows the specifications of the dual-element transducer used in the laparoscopic probe for image-guided HIFU therapy. The transducer consists of two confocal elements (piezoelectric crystals). The central circular element is used for real-time ultrasound imaging of the target zone in the pulse-echo mode and the outer element is used to deliver HIFU energy to generate coagulation necrosis in the focal region.

The probe was fully characterized through a set of simulations and measurements similar to those performed for the hand-held laparoscopic probe.

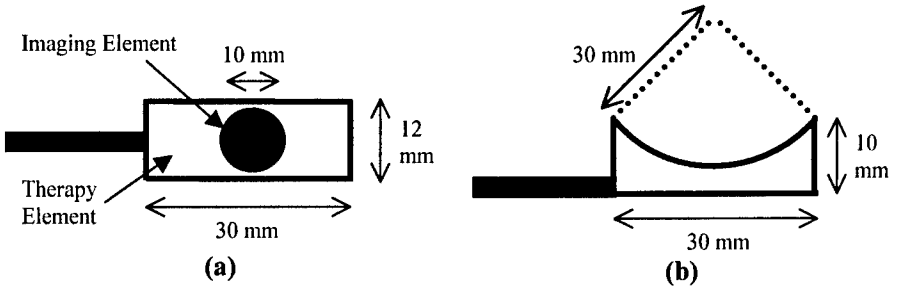

FIGURE 5. Dual-element laparoscopic transducer. (a) Top view, and (b) side view.

IN VIVO ANIMAL STUDY

Twenty female Yucatan pigs with weights ranging from 40 to 55 kg were used in this study. The right kidney was treated in all the pigs under protocols approved by the

"Animal Experimental Usage Committee", Indiana University School of Medicine, Indianapolis, IN. The animals were divided into 3 groups:

- Group 1 included 5 pigs, which were treated with the probe 1 (hand-held). The animals in this group were treated through sterile open and laparoscopic surgery procedures under a subacute 3-day survival study.
- Group 2 included 10 pigs, which were treated with the probe 2 (computer-controlled). The animals in this group were treated through sterile laparoscopic procedures under a subacute 3-day survival study.
- Group 3 included 5 pigs, which were treated with the probe 2. These animals were treated through sterile laparoscopic surgery procedures under a chronic 15-day survival study.

Table 1 below gives a summary of the protocols used for each group of animals.

TABLE 1. Summary of the protocols used for the *in vivo* porcine kidney experiments.

Group	No. of Animals	Probe Type	HIFU Exposure Parameters	Surgery Procedure	Applications
1	5	Hand-Held (Probe 1)	• TAP = 30 W • ON/OFF Times = 2/2 s • No. of Shots/Site = 5	• 3 open surgery • 2 lap. surgery • Sterile • Subacute (3-day survival)	• Feasibility • Hemostasis prior to partial nephrectomy
2	10	Computer-controlled (Probe 2)	• TAP = 28 W • ON/OFF Times = 5/6 s • No. of Shots/Site = 1	• Lap. surgery • Sterile • Subacute (3-day survival)	• Selective ablation of renal tissue
3	5	Computer-controlled (Probe 2)	• TAP = 28 W • ON/OFF Times = 5/6 s • No. of Shots/Site = 1	• Lap. surgery • Sterile • Chronic (15-day survival)	• Selective ablation of renal tissue

All animals were treated under general anesthesia. Prior to surgery the animal received 1 g intravenous Cefazolin to prevent infection. Then it was anaesthetized with IM injection of Ketamine (100 mg/ml) and Xylazine (20 mg/ml) for induction followed by Sodium Pentothal (2.5% solution, 0.5 ml/lb) intubated and placed on isoflurane gas anesthesia throughout the procedure. For laparoscopic procedures, two laparoscopic trochars were inserted into the abdominal cavity to provide portals to introduce the HIFU probe as well as a separate video camera. The probe tip was then advanced under video camera guidance to the desired area close to the lower pole of the right kidney. Once the treatment was finished, the cannulas were removed and the openings in the abdominal wall were then closed with sutures and the animal returned to the cage when it recovered from anesthesia.

RESULTS

Hand-held Laparoscopic HIFU Probe

The hand-held laparoscopic probe was used to induce a cross-sectional disk-shaped necrotic lesion in the lower pole of the right kidney in the group 1 animals (n=5) through open and laparoscopic surgery procedures. During laparoscopic procedures, a separate laparoscopic video camera was used to guide the operator in positioning the probe. On autopsy (3-day post treatment) a coagulated area appeared as a whitish circumferential rim about 1 cm wide on the surface of the kidney (Figure 6-a). A drastic change in color of the lower pole was also observed within the circumferential HIFU lesion. This is believed to be due to the depletion of arterial blood supply resulting in gangrene of the lower pole. This indeed supports the hypothesis that the HIFU-induced lesion may act as hemostasis barrier which significantly blocks the blood flow to the lobe of the kidney. Both gross pathology and histology results revealed contiguous well-delineated necrotic disk-shape lesion extending from the kidney's pelvic system to the capsule (Figures 6-b and c). The average treatment time for a circumferencial lesion of about 30cc was approximately 45 minutes.

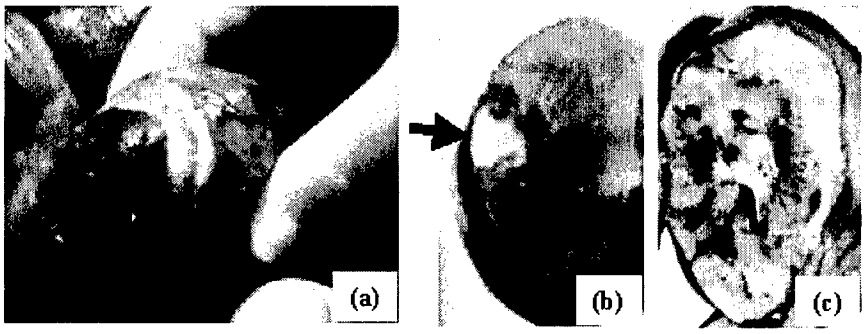

FIGURE 6. (a) 3-day post treatment view of the circumferential HIFU lesion created in the kidney's lower pole. (b) Cut section of the kidney through a single lesion. The arrow shows direction of the HIFU beam. (c) Cut section of the kidney through a complete circumferential lesion to show the uniformity of the lesion extending from the pelvic system to the capsule.

Computer-controlled Laparoscopic HIFU Probe

Fifteen pigs, divided in two groups (subacute and chronic), were treated using the computer-controlled laparascopic HIFU probe. The entire operation was controlled by the Sonablate® 200 HIFU system. To obtain an adequate positioning, the kidney was imaged in the transverse and longitudinal planes under the Sonablate® 200 imaging. Then, through the Sonablate® 200 treatment planning, a target zone of dimensions $2.0\times1.6\times1.5$ cm^3 were planned in the lower pole of the kidney. The overall treatment time to create a contiguous lesion of about 5cc was around 30 minutes. Gross pathology (Figure 7) and histology (Figure 8) examinations revealed well-delineated contiguous necrosed lesions with excellent agreement in location and size (within

± 1 mm) with the planned treatment zone. Moreover, Figure 8-b clearly demonstrates a very sharp demarcation of only a few cells wide (<20 cells) between the treated and the intact kidney tissue.

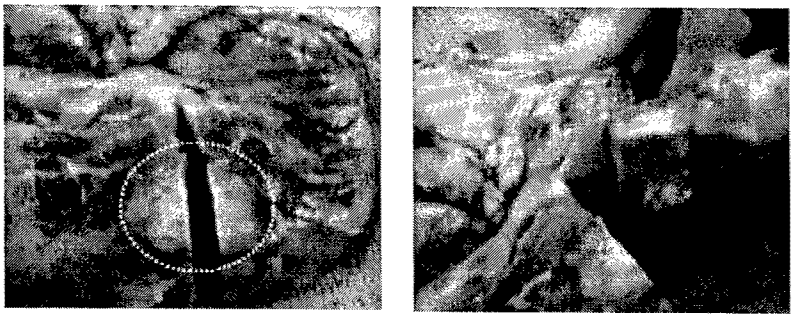

FIGURE 7. Cut sections of the kidney through the necrotic lesions show the accuracy and uniformity of the selective lesioning achieved by the computer-controlled laparoscopic HIFU probe.

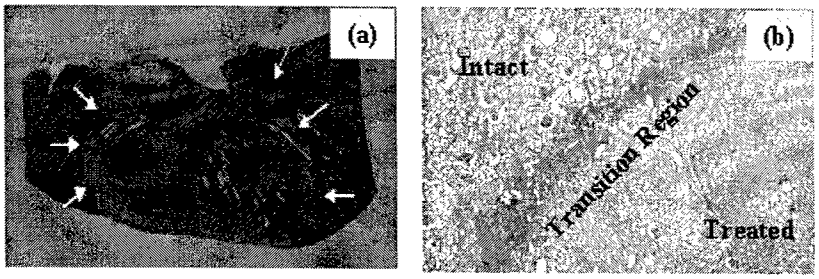

FIGURE 8. Histology slices of the necrotic lesions. (a) H&E stained slice. (b) A magnified slice to show the boundary between the treated and intact regions of the kidney tissue.

DISCUSSION AND CONCLUSIONS

This study shows the feasibility of laparoscopic HIFU to create repeatable well-delineated selective necrotic lesions in a highly vascular organ such as kidney. In this technique the HIFU applicator comes in direct contact to the organ which leads to a more efficient delivery of the HIFU dosage. Specifically, it was shown that the delivery of the HIFU dosage under real-time ultrasound imaging guidance (probe 2) led to an accurate selective tissue ablation with an accuracy of ± 1 mm in lesion size and position. Moreover, when applied properly, the laparoscopic HIFU can be used as a hemostasis tool during standard partial nephrectomy to significantly reduce bleeding associate to these procedures.

Acoustic field and temperature response measurements and simulations in the kidney tissue as well as the histo-pathologic examination of the lesions suggest that the tissue ablation was obtained through both thermal (coagulation necrosis) and non-thermal (bubble-related activities) mechanisms. Indeed, within the range of powers (TAP) we used in this study the temperature at the focal point may rise to above 90°C in less than a second. Moreover, the appearance of a hyperechoic region (usually

observed in the real-time ultrasound B-mode images during treatment) around the focus supports that cavitation/bubble activities may have a significant role in this mode of tissue ablation.

Work is under progress to develop the next generation of the laparoscopic HIFU probe. This new design combines a HIFU source and a confocal phased array imaging transducer into a flexible hand-held laparoscopic probe. The phased array imaging allows for real-time monitoring of the target zone during HIFU treatment. Besides, a manually-controlled hinge design gives the flexibility in movement and positioning which is required during laparoscopic operations.

ACKNOWLEDGMENTS

This work was funded in part by the New Energy Development Organization (NEDO), MITI, Tokyo, Japan. Thanks to Drs. A. P. Evan, D. Savatta and T. Siqueira from the Indiana University School of Medicine, Indianapolis, IN, for their support in animal study.

REFERENCES

1. Wolf, J.S. Jr., Seifman, B.D., and Montie, J.E., "Nephron sparing surgery for suspected malignancy: open surgery compared to laparoscopy with selective use of hand assistance", *J. Urol.*, **163**, 1659 (2000).
2. Kozlowski, P.M., and Winfield, H.N., "Laparoscopic partial nephrectomy and wedge resection for the treatment of renal malignancy", *J. Endourol.*, **15**, 369 (2001).
3. Gill, I.S., Novick, A.C., Soble, J.J., et al., "Laparoscopic renal cryoablation: initial clinical series", *Urology*, **52**, 543 (1998).
4. Gill, I.S., Hsu T.H.S., Fox, R.L., et al., "Laparoscopic and percutaneous radiofrequency ablation of the kidney: acute and chronic porcine study", *Urology*, **56**, 197-200 (2000).
5. Patel, V.R., Leveillee, R.J., Hoey, M.F., et al., "Radiofrequency ablation of rabbit kidney using liquid electrode: acute and chronic observations", *J. Endourol.*, **14**, 155 (2000).
6. ter Haar, G., "Acoustic Surgery", *Physics Today*, **54**, 29-34 (2001).
7. ter Haar, G., "Ultrasound focal beam surgery", *Ultrasound Med. Biol.*, **21**, 1089-1100. (1995).
8. Sanghvi, N.T., Foster, R.S., Bihrle, R., et al., "Noninvasive surgery of prostate tissue by high intensity focused ultrasound: an updated report", *European J. Ultrasound.* **9**, 19-29 (1999).
9. Gelet, A., Chapelon, J.Y., Bouvier, R., et al., "Transrectal high-intensity focused ultrasound: minimally invasive therapy of localized prostate cancer", *J. Endourology*, **14**, 519-528 (2000).
10. Vaezy, S., Martin, R.W., et al., "Hemostasis using high intensity focused ultrasound", *European J. Ultrasound*, **9**, 79-87 (1999).
11. Vaezy, S., Martin, R.W., et al., "Use of high-intensity focused ultrasound to control bleeding", *J. Vascular Surgery*, **29**, 533-542 (1999).
12. Tavakkoli, J., Seip, R., Rao, V.V., et al., "A laparoscopic HIFU probe for kidney ablation prior to partial nephrectomy", *2001 IEEE Int. Ultrasonics Symp.: Proceedings*, October 7-10, 2001, Atlanta, GA, 1369-1372.
13. Sanghvi, N.T., Tavakkoli, J., Rao V.V., et al., "Laparoscopically delivered HIFU for partial renal ablation", *17th Int. Congress on Acoustics: CD-ROM Proceedings, Volume IV (Biomedicine)*, September 2-7, 2001, Rome, Italy.
14. Pennes, H.H., analysis of tissue and arterial blood temperature in the resting human forearm", *J. Appl. Physiol.*, **2**, 93-122 (1948).
15. Sanghvi, N.T., Fry, F.J., Bihrle, R., et al., "Non-invasive surgery of prostate tissue by high intensity focused ultrasound", *IEEE Trans. Ultrason. Ferroelec. Freq. Contr.*, **43**, 1099-1110 (1996).

The Effect Of Unequal Countercurrent Vessels On 3-D Temperature Fluctuations During Simulated High Intensity Focused Ultrasound

Qi Chen*, Jingfeng Bai, and Yazhu Chen

Department of Biomedical Engineering, Shanghai JiaoTong University, Shanghai, China

Abstract. In this paper a 3-D bioheat transfer model based on three heat balance equations is applied to study the effects of the presence of unequal countercurrent vessels during high intensity focused ultrasound therapy. The simulations of this model using finite element methods were carried out with 50-300 μm diameter vessels in the tissue. Contribution from the vessel diameter, blood flow rate and blood perfusion rate were compared, and the influence on temperature distribution was estimated. The results show that it is possible to obtain therapeutic temperature values in the tissue with unequal blood vessels. Moreover, the model is able to give more precise information about the lesion volume of heated tissue.

INTRODUCTION

High intensity focused ultrasound (HIFU) has been used to cause tissue ablation for the local control of cancer and other diseases [1]. Successful HIFU treatment of tumors requires understanding the attendant thermal processes in both tissue and blood vessels. Accordingly, it is essential for developers of HIFU to predict and measure the tissue thermal and vascular response to heating, especially in the vicinity of the 100-500 μm diameter countercurrent vessels of microcirculation [2]. So when the heat source is small and intense, as in the case of HIFU heating, the temperature nonuniformities near blood vessels are expected to be particularly significant.

Most of the existing theoretical analyses of heat transfer in tissue have been based on the Penns bioheat transfer model [3]. Several different heat transfer models have been further developed to simulate the behavior in the tissue. The analytical models [4,5] for a single vessel have been developed, in which the effect of large vessels has been studied. In addition, other investigators [6-9] have performed numerical and experimental studies of single vessels and countercurrent vessel pairs. However, there is little information concerning thermal effects of the unequal countercurrent vessels under HIFU conditions, especially for transient and 3-D calculations. Such unequally paired vessels exist in tumors, and their thermal effects should be studied in particular.

In this paper, a bioheat transfer model is applied to develop and depict the transient 3-D temperature distribution within the heated tissue. Two cases were studied, one

* Corresponding author.
E-mail: qw_chen727@hotmail.com

corresponding to a primary artery and vein (100-300 μm diameter), and the other corresponding to a small artery and vein (50-100 μm diameter). Moreover, the thermal dose is predicted in tissue with countercurrent vessels during HIFU treatment.

3-D BIOHEAT TRANSFER MODEL

The dimensions of the overall tissue region for the 3-D bioheat transfer and unequal countercurrent vessel model are shown in Figure 1. The tissue dimensions are formed by a 2 mm diameter by 3 mm height cylinder, and the length of vessels in the tissue is $L = 3$ mm.

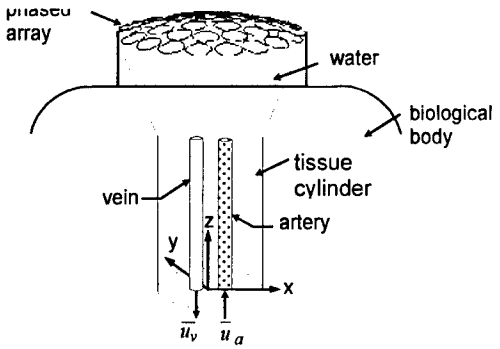

FIGURE 1. Schematic of an artery-vein pair and tissue configuration for HIFU treatment.

The 3-D bioheat transfer corresponding to a clinical HIFU thermal treatment is modeled by three equations. Tissue and blood temperature are calculated using the following three coupled heat balance equations that comprise this 3-D system:

artery:

$$\rho_b c_b \frac{\partial T_a}{\partial t} = \rho_b c_b \bar{u}_a \cdot (\frac{\partial T_a}{\partial x} + \frac{\partial T_a}{\partial y} + \frac{\partial T_a}{\partial z}) - q_{av} + q_{ta} + q_{hif,a} \quad (1)$$

vein:

$$\rho_b c_b \frac{\partial T_v}{\partial t} = \rho_b c_b \bar{u}_v \cdot (\frac{\partial T_v}{\partial x} + \frac{\partial T_v}{\partial y} + \frac{\partial T_v}{\partial z}) + q_{av} + q_{tv} - \omega \rho_b c_b (T_v - T_t) + q_{hif,v} \quad (2)$$

tissue:

$$\rho_t c_t \frac{\partial T_t}{\partial t} = k_t (\frac{\partial^2 T_t}{\partial x^2} + \frac{\partial^2 T_t}{\partial y^2} + \frac{\partial^2 T_t}{\partial z^2}) - q_{ta} - q_{tv} - \omega \rho_b c_b (T_t - T_a) + q_{met} + q_{hif,t} \quad (3)$$

where ρ, c, and k are the density, specific heat, and thermal conductivity, with the subscripts b and t referring respectively to blood and tissue domains; ω is the blood perfusion rate; and $\bar{u}$ is blood velocity, with the subscripts a and v referring respectively to artery and vein. The heat source q_{hif} generated through HIFU is several hundred times larger than the metabolic heat source q_{met}, so the q_{met} term is ignored in the calculations.

The term q_{av} represents the heat conduction between the countercurrent artery and vein; the term q_{ta} represents the heat flow between the artery and the tissue. The term q_{tv} represents the heat flow between the vein and the tissue.

The heat flows between the countercurrent vessels and tissue are given by

$$q_{av} = k_b \sigma_b (T_a - T_v), \tag{4}$$

$$q_{ta} = k_t \sigma_a (T_t - T_a), \tag{5}$$

$$q_{tv} = k_t \sigma_v (T_t - T_v), \tag{6}$$

where the parameters σ_b, σ_a and σ_v are functions of the spacing between the vessels, the radii of vessels, and the Nusselt number used to describe the heat transfer between blood and surrounding tissue.

For isolated blood vessels, the shape factor σ_a and σ_v are defined

$$\sigma_a = \frac{2\pi L}{In(r_0 / r_a) + 2k_t / k_b \mathrm{Nu} - 1/2}, \text{ for } L >> r_a; \tag{7}$$

$$\sigma_v = \frac{2\pi L}{In(r_0 / r_v) + 2k_t / k_b \mathrm{Nu} - 1/2}, \text{ for } L >> r_v, \tag{8}$$

where r_0, r_a and r_v are the radii of the tissue cylinder, artery and vein vessels as shown in Figure 2, and Nu is the Nusselt number.

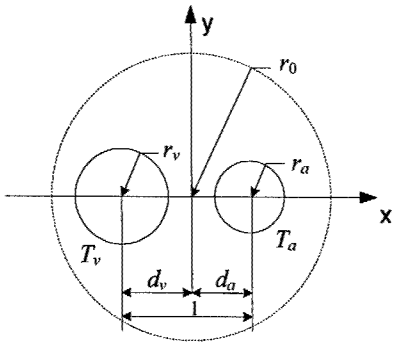

FIGURE 2. Unequal countercurrent vessel configuration considered in this study.

For two parallel vessels, the shape factor σ_b [10] is defined

$$\sigma_b = \frac{2\pi L}{\cosh^{-1}((4l^2 - r_a^2 - r_v^2)/2r_a r_v)}, \text{ for } L >> l. \tag{9}$$

where l is distance between artery and vein. The blood vessel parameters [11] used in this study are shown in Table 1.

TABLE 1. Vascular parameters in the neighborhood of a single artery-vein pair.

Blood vessels	Diameter $2r$(μm)	Blood velocity u(cm/s)	Vessel eccentricity d(μm)
Primary artery	200	5	250
Primary vein	300	6	200
Small artery	50	2	150
Small vein	100	3	100

The term q_{hif} in Equations (1) - (3) is the rate of heat production per unit volume due to the ultrasonic field. It is assumed that the acoustic beam attenuation in tissue is primarily due to absorption $q_{hif,t}$=48.3W/cm^3, and these losses reduce the amount of heat deposited in blood flow. During the simulation, the ultrasound power was uniformly deposited within the desired heating volume, and the absorption of ultrasound power by the blood is assumed to be 1/10 that of tissue [12]. The media thermal properties [13,14] used in the simulations are given in Table 2.

TABLE 2. Properties in the thermal model.

Medium	Thermal conductivity k [W /m °C]	Density ρ [kg/ m^3]	Specific heat c [J/ kg °C]	Perfusion rate ω [kg /m^3 s]
tissue	0.56	1060	3600	0.5 - 10
blood	0.49	1055	4032	0

Five boundary conditions are required to solve the system of equations given in (1)-(3). In the model, the boundary conditions for the artery and vein equations are

$$T_a(t) = T_{a0}(t), \quad \text{at z =0,} \tag{10}$$

$$T_v(t) = T_t(t), \quad \text{at z = L,} \tag{11}$$

and the transient thermal tissue boundary conditions are

$$-k_t \frac{\partial T_t}{\partial z} = q'', \quad \text{at z = 0, and z = L,} \tag{12}$$

where k_t is the conductivity of the tissue and q'' is the heat flow.

The boundary conditions at the vessel walls are Robin conditions, written as

$$-k \frac{\partial T}{\partial n} = h_i (T_b - T), \tag{13}$$

where n is a unit normal vector, h_i = Nu$k_b/(2r_i)$, T_b is the bulk temperature of the blood in the vessel, and T is the local temperature of the tissue.

THERMAL DOSE

A method of thermal dose estimation in cancer therapy has been developed to provide a quantitative relationship between temperature and time for the heating of tissue [15], and has been suggested for use in thermal ablation therapy [16]. For temperatures achieved in HIFU (generally above 43° C), the expression for thermal dose (T_{FU}) can be written as:

$$T_{FU} = \sum_{t=0}^{t_{end}} 2^{(T(t)-43)} \Delta t, \tag{15}$$

where T(t) is the time-dependent temperature for an arbitrary tissue coordinate. The thermal collection of temperature maps and the Sapareto-Dewey method were used to

compute the thermal dose to the tissue. Using this information, heating tissue to 43° C for 120 min is roughly equivalent to heating to 56° C for 1s. In this work, this thermal dose is considered as the threshold for lesion formation.

RESULTS AND DISCUSSION

Figures 3 and 4 show the transient temperature at ω = 0.2 or 10 kg/m^{3}s in the case of the primary vessels. Figures 5 and 6 show the same information, but for the case of the small vessels. Figures 4 to 7 illustrate how the temperature increases during the 2 seconds of heating and then decays after power is turned off. The blood vessels act as a thermal sink, removing heat from the neighboring tissue. Heat conduction for the direction of flow into the blood tends to spatially shift the region of highest temperature in the direction of the flow.

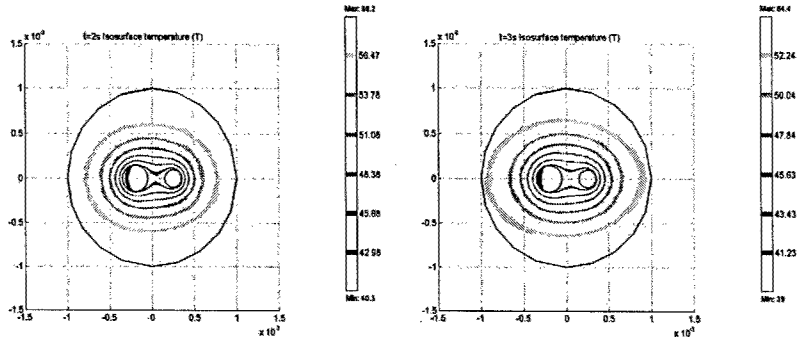

FIGURE 3. Spatial temperature profiles at ω = 0.2 kg/m^3 s for 2 seconds of heating in the case of the primary vessels.

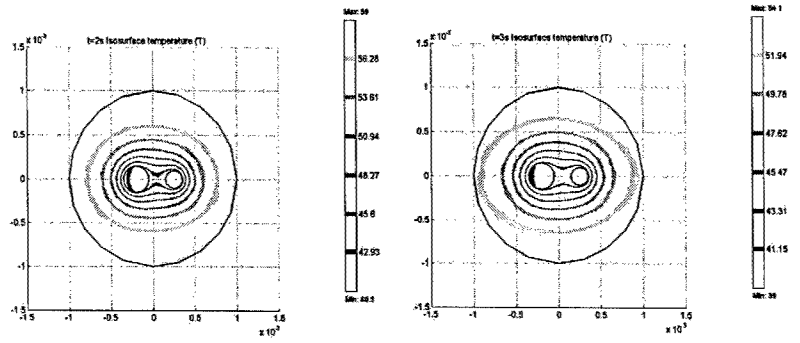

FIGURE 4. Spatial temperature profiles at ω = 10 kg/m^3 s for 2 seconds of heating in the case of the primary vessels.

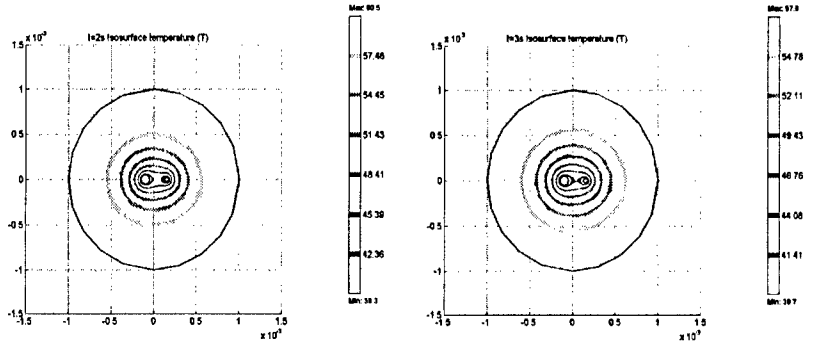

FIGURE 5. Spatial temperature profiles at ω = 0.2 kg/m^3 s for 2 seconds of heating in the case of the small vessels.

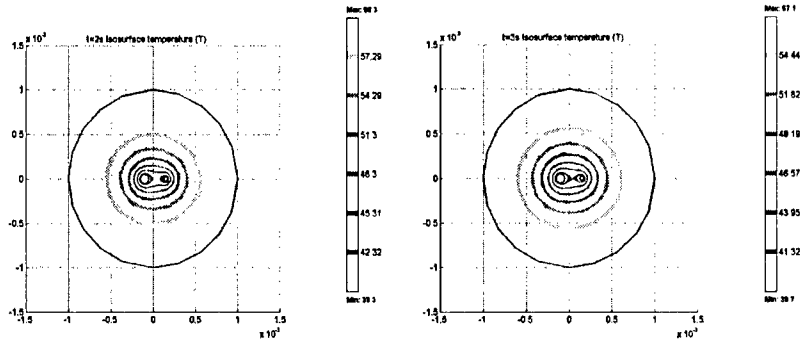

FIGURE 6. Spatial temperature profiles at ω = 10 kg/m^3 s for 2 seconds of heating in the case of the small vessels.

The maximum temperature of the blood reaches only about 67% of the maximum temperature of the tissue within the heated region. And the average blood temperatures in the artery and vein vessels are similar. During the heating simulation the maximum temperature rise of ΔT_{av} = 2.3° C in the 50-100 μm vessels is less than the rise of 3.3° C in the 100-300 μm vessels. Significant temperature fluctuations appear in the tissue near the artery and vein.

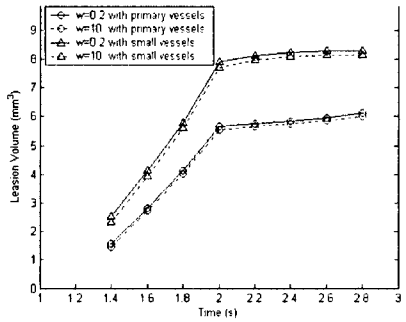

FIGURE 7. Illustration of lesion volumes for simulated 2 seconds heating.

Comparing Figures 3 and 5 with Figures 4 and 6, rapid heating (2 seconds) induces almost the same peak temperature values, even when the perfusion rate was changed from 0.2 to 10 kg/m^{3}s. The volume of thermal lesion is still effectively constant, as shown in Figure 7. And the maximum lesion volume in the tissue with primary vessels is a quarter greater than in the tissue with small vessels. Our results suggest that the rapid heating is effective in delivering the power energy to the desired treatment volume during HIFU treatment.

This study also shows that it is necessary to use more flexible, higher resolution power deposition patterns to obtain desirable temperature distributions for HIFU and to obtain good treatments. Thus, careful treatment planning with optimized heating parameters is needed to obtain optimal power deposition patterns for different blood vessel patterns.

ACKNOWLEDGMENTS

This work was supported by the grant number 994419072 from the Shanghai Technological Development Foundation.

REFERENCES

1. Daum, D.R., and Hynynen, K., *IEEE Trans. Ferrolect. Freq. Contr.*, **46**, 1254-1268 (1999).
2. Lemons, D.E., Weinbaum, S., and Jiji, L.M., *Am. J. Physiol.*, **253**, 128-135 (1987).
3. Penns, H.H., *J. Applied Physiology*, **1**, 93-122 (1948).
4. Chato, J.C., *ASME J. Biomech. Eng.*, **102**, 110-118 (1980).
5. Huang, H.W., Chan, C.L., and Roemer, R.B., *ASME J. Biomech. Eng.*, **116**, 208-212 (1994).
6. Weinbaum, S., and Jiji, L.M., *ASME J. Biomech. Eng.*, **107**, 131-139 (1985).
7. Baish, J.W., *ASME J. Biomech. Eng.*, **112**, 207-211 (1990).
8. Wissler, E.H., *ASME J. Biomech. Eng.*, **109**, 226-233 (1987).
9. Charny, C.K., and Levin, R.L., *ASME J. Biomech. Eng.*, **111**, 263-270 (1989).
10. Incropera, F.P., and De Witt, D.P., *Fundamentals of heat and mass transfer*, Second edition, Wiley & Sons, New York, 1985, pp. 387-404.
11. Weinbaum, S., Jiji, L.M., and Lemons, D.E., *ASME J. Biomech. Eng.*, **106**, 321-330 (1984).
12. Duck, F.A., *Physical properties of tissue*, A Comprehensive Reference Book, London: Academic Press, 1990, pp. 13-37.
13. Crezee, J., and Lagendijk, J.J.W., *Phys. Med. Biol.*, **37**, 1321-1337 (1992).
14. Goss, S.A., Frizzell, L.A., and Dunn, F., *Ultrasound Med. Biol.*, **5**, 181-186 (1979).
15. Sapareto, S.A., and Dewey, W.C., *Int J Radiat Oncol Biol. Phys.*, **10**, 787-800 (1984).
16. Vykhodtseva, N.I., Hynynen, K., and Damianou, C., *Ultrasound Med. Biol.*, **20**, 987-1000 (1994).

Rate Of Temperature Increase In Human Muscle During Ultrasound Treatments At Various Intensities And Frequencies

[1]David O. Draper, EdD, ATC; [2]Chris & Dawn Castel

[1]Professor, Coordinator of Graduate Athletic Training/Sports Medicine; Brigham Young University, RB 120-C, Provo, UT, 84602 USA
[2]Accelerated Care Plus, 958 Spice Islands Dr., Sparks, NV 89431 USA

Abstract To achieve the thermal effects of ultrasound, the tissue temperature must be raised from 1 to ≥4° C depending on the desired outcome of the treatment. Prior to this research, there have been few in vivo studies that have measured rate of change in temperature during 1-MHz ultrasound treatments, and none have ever been performed with the 3-MHz frequency. Thus, much speculation exists regarding how long to administer an ultrasound treatment. We performed this study to plot the rate of temperature increase during ultrasound treatments delivered at various intensities and frequencies. We inserted two 23-gauge thermistors into each subjects' medial triceps surae at the following depths: 1 MHz at depths of 2.5 and 5.0 cm (12 subjects) and 3 MHz at depths of .8 and 1.6 cm (12 subjects). Each subject received a total of four 10-minute treatments, one each at .5, 1.0, 1.5, and 2.0 W/cm^2, and temperature was measured every 30 seconds. No significant difference was found in the rate of heating at the two depths ($p = .987$) within the same frequency and dose levels. The 3-MHz frequency heated on average 3 times faster than the 1-MHz frequency at all doses tested ($p < .001$). On average, the rate of temperature increase per minute at the two depths of the 1-MHz frequency was: .04° C at .5 W/cm^2; .16° C at 1.0 W/cm^2; .33° C at 1.5 W/cm^2; and .38° C at 2.0 W/cm^2. The rate of temperature increase per minute at the two depths of the 3-MHz frequency was: .3° C at .5 W/cm^2; .58° C at 1.0 W/cm^2; .89° C at 1.5 W/cm^2; and 1.4° C at 2.0 W/cm^2. This research should enable clinicians to choose the correct parameters when using thermal ultrasound.

INTRODUCTION

In general, the effects of ultrasound are either thermal, nonthermal or a combination of both. Typically, the thermal effects [5,21,30] are performed for the treatment of pain [22,29,35,38,39], reduction of sub-acute and chronic inflammation and muscle spasm [3-6,19-21,30, and stretching of collagenous tissue in joint and connective tissue contracture [7,19,27]. The low dose nonthermal ultrasound is used for stimulation of tissue repair [11-15], reduction of edema [21,31], and treatment of trigger points for pain management [31].

Apparently, specific temperature increases are required to achieve beneficial effects in tissue. Based on previous studies by Lehman [24] and Lehman et al [25,26], where the baseline muscle temperature was 36-37° C, an increase of 1° C (mild heating) accelerates metabolic rate in tissue. An increase of 2-3° C (moderate heating) reduces muscle spasm, pain, and chronic inflammation, and increases blood flow. Vigorous

heat (≥4°C) affects visco elastic properties of collagen and inhibits sympathetic activity.

Prior to this investigation, there had been no human in vivo studies that compared heating rates of 1 MHz and 3 MHz continuous ultrasound. Thus, clinicians not only resorted to trial and error regarding how long to administer an ultrasound treatment, but they often used the same treatment time for both frequencies. We initiated this study to plot the rate of temperature increase in human muscle during ultrasound treatments at various intensities and frequencies in an attempt to take the guesswork out of ultrasound treatment dosage.

METHODS

Subjects

Prior to any data collection, this study was approved by the Institutional Review Board at Brigham Young University. Twenty-four college students, with a mean age of 22 ± 1.4 years, volunteered to participate and gave informed consent. Twelve subjects were used for the 1 MHz data collection and 12 subjects participated in the 3 MHz data collection. The left triceps surae muscle of each subject was free from ecchymosis, infection, swelling, or injury during the previous 6 months. Although adipose tissue does not appear to prevent ultrasound from being absorbed [10], we selected subjects with little adipose tissue in the lower leg.

Instruments

The ultrasound unit we employed was the Omnisound 3000™ (formerly, Physio Technology Inc., Topeka, KS; now Accelerated Care Plus, Sparks, NV). The transducer surface area was 5 cm^2 and housed a lead zirconate titanate crystal. The effective radiating area of the crystal was 4.1 cm^2 with a beam nonuniformity ratio (BNR) of 1.8:1. The ultrasound device was new, and we calibrated it prior to our study with a digital power meter (Model DT-10, Ohmic Instruments Inc., St. Micheals, MD) in 25° C degassed water. Both frequencies of the applicator were scanned for beam nonuniformity ratio and effective radiating area using a computerized scanning acoustic hydrophone.

To record the temperature of the muscle, we used 23-gauge thermistor needles (Phystek MT-23/5, Physitemp Instruments, Clifton, NJ). We affixed the thermistors to a monitor (Bailey Instruments BAT-10, Physitemp Instruments, Clifton, NJ) that displayed the temperature in degrees Celsius. We used Ultra Phonic™ (Pharmaceutical Innovations, Inc., Newark, NJ) ultrasound transmission gel at room temperature (25° C) in order to replicate the clinical setting.

Procedures

We shaved and thoroughly cleansed a 10-cm diameter area on the left medial triceps surae muscle. While the subject was lying prone, the examiner used a caliper to

plot the depth that each thermistor was to be inserted. For the 3-MHz application, two 1-cc injections of 1% lidocaine© (Xylocaine) were administered subcutaneously to anesthetize the area.

The thermistors were inserted into the center of the left medial triceps surae muscle belly, one at a depth of .8 cm and the other 1.6 cm deep. We placed a template, cut at precisely two times the size of the effective radiating area (ERA) of the ultrasound applicator, onto the skin overlying the muscle belly. This served to restrict all treatments to the same size surface area. We gas sterilized the thermistors in an autoclave for 30 minutes prior to the study and after each use.

FIGURE 1. Ultrasound application.

The procedures for the 1-MHz application were identical to the 3-MHz procedure except that the thermistors for the lower frequency were inserted at depths of 2.5 and 5 cm. After we implanted the thermistors and connected them to the monitor, we waited for the tissue temperature to stabilize and then recorded this as the tissue temperature baseline (average time to baseline approximately 3 minutes). The subjects were lying prone for all of the treatments and ultrasound gel was applied to the treatment area. We then applied continuous ultrasound to the posterior aspect of the triceps surae muscle perpendicular to the tips of the thermistor needles (Fig. 1). In all, each subject received four ultrasound applications given in random order at .5, 1.0, 1.5, and 2.0 W/cm^2. During this procedure, the sound applicator was moved back and forth within the template at approximately 4 cm/sec as proposed by other researchers [5,34]. During each application, we recorded temperature every 30 seconds. The treatments lasted for 10 minutes or until the rate of heating was uncomfortable. At the end of each ultrasound application, we waited for the temperature to return to its original baseline before starting the next application. At the completion of four applications for each subject, we removed the thermistors, cleansed the area with 70% isopropyl alcohol, and applied a bandage to the injection sites. A three-factor ANOVA (2 X 4 X 2) was used to test for a difference in mean temperatures obtained. This was compared with each depth (two levels), dose (four levels), and frequency (two levels) over time. Alpha was set at the .01 level.

Results

The Table shows the mean muscle temperature increase per minute at all doses tested. At the 3-MHz frequency, at doses of 1.5 W/cm^2 and 2.0 W/cm^2, the rate of temperature increase was so rapid that some subjects were not able to complete the full 10-minute treatment due to discomfort. For the 1.5 and 2.0 intensities, an average rate of temperature increase at 6 minutes and 3 minutes, respectively, was used to compute means and standard deviations.

TABLE 1.

MHz	W/cm^2	Depth (cm)	X	SD
1	.5	2.5	.04	.054
3	.5	.8	.30	.135
1	.5	5.0	.06	.035
3	.5	1.6	.31	.132
1	1.0	2.5	.16	.072
3	1.0	.8	.58	.242
1	1.0	5.0	.16	.059
3	1.0	1.6	.58	.229
1	1.5	2.5	.34	.007
3	1.5	.8	.82	.276
1	1.5	5.0	.31	.115
3	1.5	1.6	.96	.242
1	2.0	2.5	.40	.084
3	2.0	.8	1.5	.354
1	2.0	5.0	.34	.018
3	2.0	1.6	1.3	.602

Tissue Temperature Rise Compared At The Two Depths Among Same Dosage And Frequency

No significant difference was found in the maximum temperature increase at 3MHz between the two depths at all intensities tested [$F(1,11) = 3.60$, $p = .084$]. Average temperatures reached at the two tissue depths of each dose at the end of the 1-MHz treatment were also recorded. No significant difference was found in the maximum temperature increase at 1MHz between the two depths [$F(1,11) = .00$, $p = .987$]. The temperatures at the deep layer for both frequencies were compared and 3 MHz heated about three times greater than 1 MHz at all doses ($p < .001$).

Rate Of Heating During 1-MHz Ultrasound

We evaluated ultrasound doses of .5, 1.0, 1.5, and 2.0 W/cm^2. The rate of heating of the four intensities was compared, and a significant difference was found between each [$F(3, 33) = 131.57$, $p < .001$]. No interaction between intensity and depth was found [$F(3,33) = 1.04$, $p = .389$]. On average, the tissue temperature rate and rise of each subject, recorded at 30-second intervals, was somewhat consistent at dose levels of 1.0, 1.5, and 2.0 W/cm^2. The rate of temperature rise at .5 W/cm^2 heated at only 25% of the rate that 1.0 W/cm^2 heated; therefore, for significant thermal effects, we feel that the .5 W/cm^2 dose is insufficient.

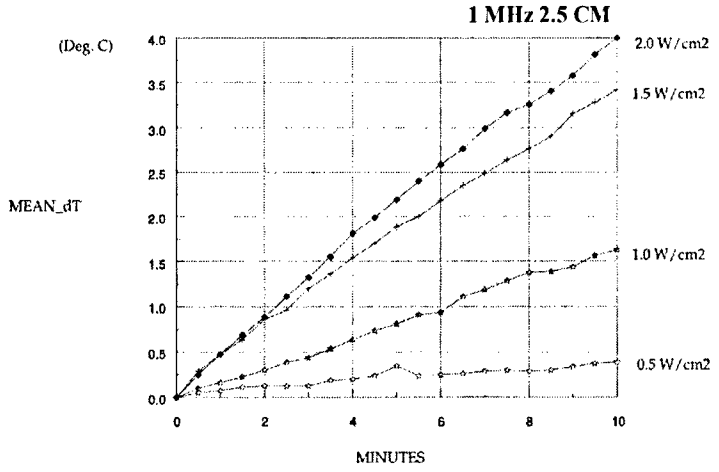

FIGURE 2. Rate of heating of 1 MHz (shallow probe).

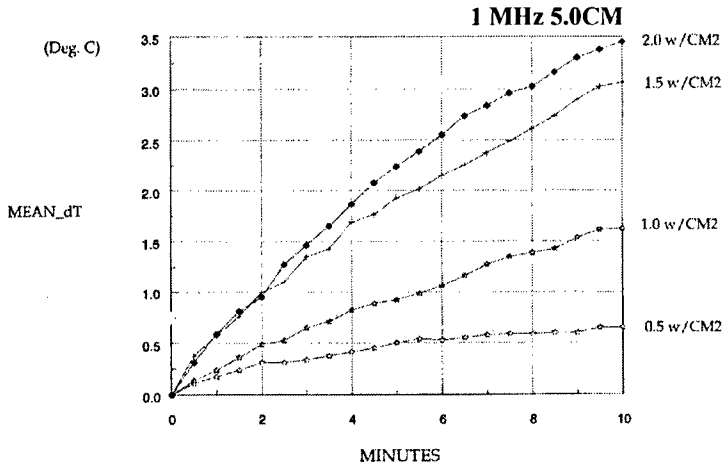

FIGURE 3. Rate of heating of 1 MHz (deep probe).

Rate of Heating During 3-MHz Ultrasound

We evaluated doses of .5, 1.0, 1.5, and 2.0 W/cm^2. The rate of heating of the four intensities was compared, and a significant difference was found between each [F(3,33) _ 41.59, p < .001]. No interaction between intensity and depth was found [F(3,33) = .53, p = .662]. The rate of increase per minute at each dosage was: .3° C at .5 W/cm^2; .58° C at 1.0 W/cm^2; .89° C at 1.5 W/cm^2; and 1.4° C at 2.0 W/cm^2. Basically, the rate of temperature rise at .5 W/cm^2 should be half that of 1.0 W/cm^2; it was very close (51%). The 1.5 W/cm^2 dose should be 50% faster than 1.0 W/cm^2; it also came within 1% (51%). Finally, 2.0 W/cm^2 should heat twice as fast as 1.0 W/cm^2

and 25% faster than 1.5 W/cm^2. In our study, 2.0 W/cm^2 heated tissues 2.4 times faster than 1.0 W/cm^2 and 43% faster than 1.5 W/cm^2. Therefore, on the average, the tissue temperature rate and rise of each subject, recorded at 30-second intervals, was fairly consistent and predictable at all dose levels measured. Note that it took slightly less than 3 minutes at 2.0 W/cm^2 to reach a temperature of 4° C for a surface area of 2 ERA, regardless of tissue depth.

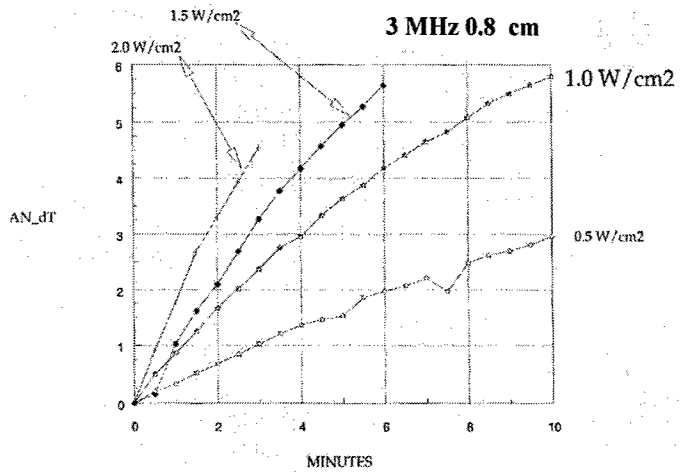

FIGURE 4. Rate of heating of 3 MHz (shallow probe).

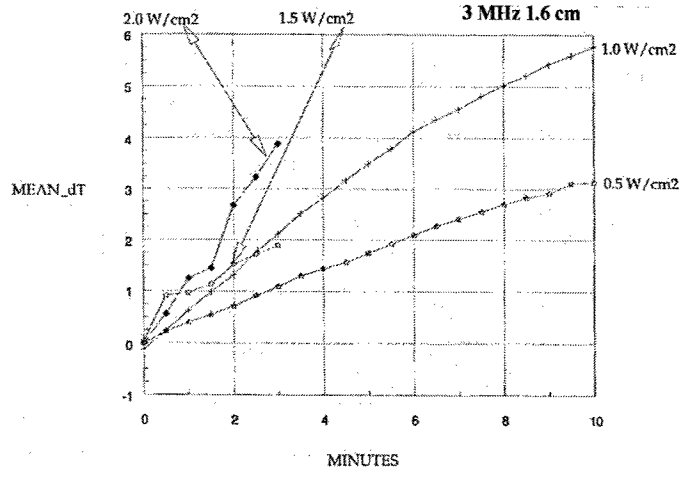

FIGURE 5. Rate of heating of 3 MHz (deep probe).

DISCUSSION

If the treatment goal with therapeutic ultrasound is to raise tissue temperature, failure to achieve the desired temperature will affect the outcome of therapy since the effects are specific to the tissue temperature elevation [16,23]. Thus, the technique of applying ultrasound should be taken more seriously than is currently practiced. In order to increase tissue temperature and to achieve repeatable thermal effects in tissue, careful attention to specific parameters is mandatory. Unfortunately, in current clinical practice, little attention is given to factors such as: 1) the size of the treatment area; 2) the depth of the target tissue; 3) desired temperature increase; and 4) output intensity over time. Each of these factors is critical to achieving a repeatable temperature increase in the tissue. This study was designed to control for the above factors and evaluated the specific temperature increases which can be achieved at various dosage levels and frequencies.

Size Of The Treatment Area

The literature contains little information regarding the appropriate treatment size. We have frequently observed clinicians treating an entire low back with ultrasound. We believe that ultrasound should not be used to heat large areas. We base this on the fact that our experiment used 2 ERA and, according to our results, treating a large area will dilute the dose so that the thermal effects will be minimal. Therefore, the thermal goal of the treatment is negated. The application technique should be limited to an area twice the size of the ERA of the transducer [34]. If a slightly larger area than this needs treatment, a possible solution is to break the total area into sections that are twice the ERA of the transducer and treat one area at a time or use short-wave diathermy [8,9,18,32].

Appropriate Frequency

Another misconception regarding therapeutic ultrasound has to do with the depth of the target tissue. Some feel that the higher the intensity, the deeper the penetration; therefore, they advocate dosages >1.5 W/cm^2 for deep tissues and <1.0 W/cm^2 for superficial treatments [33]. It is, however, the frequency of the ultrasound beam that determines the depth of penetration [17,33]. Typically, 1-MHz ultrasound in the continuous mode is used for heating tissues 2.5-5 cm deep, whereas 3 MHz is used to heat tissues <2.5 cm deep. We have observed several clinicians treating the patellar, Achilles, and peroneal tendons and medial and lateral epicondylitis with the 1-MHz mode. At this depth, much of the sound reflects off of bone, causing periosteal pain, so the clinician often responds by turning down the intensity. If the 3-MHz frequency was used, more of the sound energy would be absorbed in these superficial tendons with little energy reaching the bone [14,30]. Hence, a higher intensity can be used in the 3-MHz mode to bring about the desired temperature increase.

The depth of ultrasound penetration is described in terms of the half-value layer or the depth by which 50% of the ultrasound beam is absorbed in tissue [36]. In the muscle tissue model used for this study, this was deemed to be 2.5 cm for the triceps

surae muscle at 1 MHz and .8 cm for the same muscle at 3 MHz. Temperature effects would be expected to be highest at the half-value layer and less at greater depths. Theoretical predictions would suggest that at twice the half-value layer depth, the thermal effect would be significantly attenuated.

An interesting aspect of our investigation was the small differences in the heating effects at the half-value and two times the half-value layers. At 1 MHz, Lehman et al [26] indicate that the thermal effect of ultrasound peaks in the human thigh at approximately 1 cm above the bone due to reflection of the ultrasound beam from the bone summating with the incoming ultrasound beam. In this respect, our data were consistent with prior investigations as the 5-cm depth in the triceps surae muscle was generally within 1 cm from the bone for the subjects investigated. Therefore, this relative closeness of our deep probe to the reflection point may explain why the temperature was not significantly reduced compared with the shallow probe, which theoretically should be the optimal heating region.

At 3 MHz, the reason for the lack of differentiation of temperature effect at the two measured levels may be described by the likely heat conduction of the tissue at the close proximity of the two depths studied. It is possible that if we were to place a probe even deeper than 1.6 cm, the temperature rate would still not decline. The depth limit at which 3 MHz will effectively heat tissue has not been studied. A future investigation could address this issue by inserting probes at a 2-, 3-, or 4-cm depth and measure heating via 3-MHz ultrasound.

Desired Tissue Temperature Increase

The frequency at which ultrasound is delivered to the tissue has a distinct effect on the rate of temperature increase. At 3 MHz, the heating rate is predicted to be three times faster, since the energy is absorbed at three times the rate of 1 MHz. Our study supports this premise from measurements taken by the deep probes. However, at the half-value layer, the rate of heating at each 3 MHz intensity was over three times that of the respective 1 MHz intensity. This might be why clinicians report faster thermal effects or an apparent heating of the applicator with 3-MHz ultrasound. In actual fact, the surface tissue is heated, but the patient may perceive that the ultrasound transducer is getting hot.

Output Intensity Over Time

We have shown from this study that tissue temperature increase is also dependent upon the intensity and time of sonation. The longer the treatment lasted, the higher the resultant temperature, and the higher the intensity, the greater the temperature increase. However, our rate of heating was less than that predicted by other researchers [37]. Why did our results not track the predicted models? These theoretical calculations do not take into account the effects of blood flow-induced cooling and tissue thermal conduction that would further reduce thermal efficacy. Baker and Bell [2] and Ter Harr [37] acknowledged that the effects of blood flow and thermal conduction on tissue cooling are not well characterized. From our data, it is clear that a base threshold ultrasound intensity is required to overcome cool-down, based on tissue

heat conduction and vascular heat dissipation. These factors act to reduce the heating effects of the ultrasound dosage and may also prevent a linear relationship of intensity to treatment time at low dosage levels. In fact, from our data regarding delivery of 1 MHz at an intensity of 1.0 W/cm^2, the variance was greater than a 65% reduction of heating effect based on the theoretically predicted heat transfer function. This requires a marked increase in dosage intensity and treatment time required to achieve specific thermal effects in tissue. Therefore, the prescribed treatment times to reach predicted heating rates as suggested in the literature are incorrect.

From this study, we have been able to predict tissue temperature rise at 1 and 3 MHz at doses of .5, 1.0, 1.5, and 2.0 W/cm^2. However, when we compared the data from subject to subject, the tissue temperature rise was more predictable at some doses and not as predictable at others. This might be due to our method of collecting the data. Typically, each subject received all four ultrasound applications in one experimental session. For example, a subject would receive a 10-minute application at .5 W/cm^2, wait until the temperature returned to baseline (around 20-30 minutes), and then receive a 10-minute treatment at 1 W/cm^2 and so on until all four applications were randomly administered. These fluctuations in tissue temperature may have affected subsequent treatments, so that the tissue temperature rise was not as predictable as the first treatment. For future study, we suggest that each subject only be given one or two random applications on a given day. This may eliminate any effects, positive or negative, of the preceding application, thus, establishing more predictable and reproducible data.

All Ultrasound Machines Are Not The Same

It is important to note that these heating rates may not be possible with all ultrasound units. We have tested several different machines that do not produce as high of temperatures as the Omnisound 3000C. Our results, therefore, are limited to the Omnisound 3000C. Also, since this original study was performed, we have collected data on nearly 100 other subjects. ***Based upon these data we have developed the following formulae for muscle heating via continuous ultrasound: 1 MHz heats at a rate of .2° C/min/W/cm^2; 3 MHz heats at a rate of .6° C/min/W/cm^2.*** Thus, if 1 MHz were delivered at 1.0W/cm^2 (2 ERA) it would raise deep tissue temperature (2-5 cm) 2° C in 10 mins (3° C at 1.5W/cm^2). If 3 MHz were delivered at 1.0W/cm^2 (2 ERA) it would heat superficial muscle temperature (<2 cm) 6° C in 10 mins (9° C at 1.5W/cm^2).

CONCLUSION

Prior investigations indicate that the therapeutic effect of thermally applied ultrasound relies on specific temperature elevations in the tissue. It is clear that the empirical approach of using 1.5 W/cm^2 of ultrasound output over a non-defined area for a 5-minute treatment is not acceptable if consistent thermal results are to be obtained [2,28]. Our data question many aspects of ultrasound efficacy based on current practice techniques. If the average treatment goal is not thermal, based on

dosage and application technique, we can only speculate that the results obtained with the modality are primarily obtained through the nonthermal effects of ultrasound, such as acoustic streaming, cavitation, and micro massage [15]. If thermal effects are to be achieved and are intended, then careful attention must be given to dosage. Treatment time should be based on results from this study, which will provide more predictable increases in tissue temperature.

In summary, therapeutic ultrasound in the continuous mode increases tissue temperature when properly applied with specific dosage guidelines. Appropriate attention to treatment time, intensity, area, and ultrasound frequency is critical if specific thermal effects are to be predictably obtained in tissue.

Reprinted from [Draper, D.O., Castel, J.C., Castel, D., "Rate of temperature increase in human muscle during 1 MHZ and 3 MHZ continuous ultrasound," *J Orthop Sports Phys Ther.*, **22**, 142-150 (1995).], with permission of the Orthopaedic and Sports Sections of the American Physical Therapy Association.

REFERENCES

1. Aldes, J.H., and Jadeson, W.I., "Ultrasonic Therapy In The Treatment Of Hypertrophic Arthritis In Elderly Patient," *Ann W Med Surg*, **6**, 545-550, (1952).
2. Baker, R.J., and Bell, G.W., "The Effect Of Therapeutic Modalities On Blood Flow In The Human Calf," *J Orthop Sports Phys Ther*, **13** (1), 23-27, (1991).
3. Binder, A., "Is Therapeutic Ultrasound Effective In Treating Soft Tissue Lesions?" *Br Med J*, **290**, 512-514, (1985).
4. Bundt, F.B., "Ultrasound Therapy In Supraspinatus Bursitis," *Phys Ther Rev*, **38**, 826-827, (1958).
5. Byl, N.N., McKenzie,A., Wong, T., West, J., Hunt, T.K., "Incisional Wound Healing: A Controlled Study Of Low And High Dose Ultrasound," *J Orthop Sports Phys Ther*, **18** (5), 619-628, (1993).
6. DePreux, T., "Ultrasonic Wave Therapy In Osteoarthritis Of The Hip Joint," *Br J Phys Med*, **15**, 14-19, 1952.
7. Draper, D.O., Anderson, C., Schulthies, S.S., Ricard, M.D., "Immediate And Residual Changes In Dorsiflexion Range Of Motion Using An Ultrasound Heat And Stretch Routine." *J Ath Train*, **33**, 141-144 (1998).
8. Draper, D.O., Knight, K., Fukiwara, T., Castel, J.C., "Temperature Change In Human Muscle During And After Pulsed Short Wave Diathermy," *J Ortho Sports Phys Ther*, **29** (1), 13-22 (1999).
9. Draper, D.O., Miner, L., Knight, K.L., Ricard, M.D., "The Carry-Over Effects Of Diathermy And Stretching In Developing Hamstring Flexibility, *J Athl Train*, **37** (1):37-42 (2002).
10. Draper, D.O., Sunderland, S., "Examination Of The Law Of Grotthus-Draper: Does Ultrasound Penetrate Subcutaneous Fat In Humans?" *J Athl Train*, **28** (3), 246-250, (1993).
11. Dyson, M., "Mechanisms Involved In Therapeutic Ultrasound," *Physiother*, **73**, 116-120 (1987).
12. Dyson, M., "Therapeutic Applications Of Ultrasound," in *Biological Effects of Ultrasound (Clinics in Diagnostic Ultrasound)*, edited by Nyberg W.L., Ziskin M.C. New York, NY: Churchill Livingstone, Inc., 1985, pp 121-133.
13. Dyson, M., "Role Of Ultrasound In Wound Healing," in *Wound Healing: Alternatives in Management*, edited by Moth, L.C., McCulloch, J.M., Feeder, J.A., Philadelphia: F.A. Davis Compan, J.B,." The Effect Of Pulsed Ultrasound On Tissue Regeneration," *Physiother*, **64**, 105-108 (1970).

15. Dyson, M., Suckling, J., "Stimulation Of Tissue Repair By Ultrasound: A Survey Of The Mechanism Involved," *Physiother,* **64**, 105-108 (1978).
16. Forest, G., Rosen, C., "Ultrasound: Effectiveness Of Treatments Given Under Water," *Arch Phys Med Rehabil,* **70**, 28-29 (1989).
17. Gann, N., "Ultrasound: Current Concept,". *Clin Manag,* **11** (4), 64-69 (1991).
18. Garrett, C., Draper, D.O., Knight, K.L., Durrant, E., "Heat Distribution In The Lower Leg From Pulsed Short-Wave Diathermy And Ultrasound Treatments," *J Athl Train,* **35** (1), 50-55 (2000).
19. Gersten, J.W., "Effect Of Ultrasound On Tendon Extensibility," *Am J Phys Med,* **34**, 362-369 (1955).
20. Gorkiewicz, R., "Ultrasound For Subacromial Bursitis," *Phys Ther,* **64** (1), 46-47, (1984).
21. Kramer, J.F., "Ultrasound: Evaluation Of Its Mechanical And Thermal Effects," *Arch Phys Med Rehabil,* **65**, 223-227 (1984).
22. Kuitert, J.H., "Ultrasonic Energy As An Adjunct In The Management Of Radiculitis And Similar Referred Pain," *Am J Phys Med,* **33**, 61-65 (1954).
23. Lehman, J.F., "The Biophysical Basis Of Biologic Ultrasonic Reactions With Special Reference To Ultrasonic Therapy," *Arch Phys Med Rehabil,* **34** (3), 139-152 (1953).
24. Lehman, J.F., *Therapeutic Heat and Cold (4th Ed),* Baltimore: Williams & Wilkins, 1990. pp 437-442.
25. Lehman. J.F., DeLateur, B.J., Stonebridg.e J.B., Warren, G., "Therapeutic Temperature Distribution Produced By Ultrasound As Modified By Dosage And Volume Of Tissue Exposed," *Arch Phys Med Rehabil,* **48**, 662-666 (1967).
26. Lehman, J.F., DeLateur, B.J., Warren, G., Stonebridge, J.B., "Bone And Soft Tissue Heating Produced By Ultrasound," *Arch Phys Med Rehabil,* **48**, 397-401 (1967).
27. Markham, D.E., Wood, M.R., "Ultrasound For Dupuytrens Contracture," *Physiother,* **66** (2), 55-58 (1980).
28. McDiarmid, T., Burns, P.N., "Clinical Applications Of Therapeutic Ultrasound." *Physiother,* **73**, 155-162 (1987).
29. Nwuga, V.C.B., "Ultrasound In Treatment Of Back Pain Resulting From Prolapsed Intervertebral Disc," *Arch Phys Med Rehabil.*, 88-89 (1983).
30. Oakley, E.M., "Application Of Continuous Beam Ultrasound At Therapeutic Levels," *Physiother,* **64** (6), 169-172 (1978).
31. Patrick, P., "Applications Of Therapeutic Pulsed Ultrasound," *Physiother,* **64** (4), 103104 (1978).
32. Peres, S., Draper, D.O., Knight, K.L., Ricard, M.D., "Pulsed Shortwave Diathermy And Prolonged Stretch Increases Dorsiflexion Range Of Motion More Than Prolonged Stretch Alone," *J Athl Train,* **37** (1), 43-50 (2002).
33. Prentice, W.E., "Therapeutic Modalities For Sports Medicine And Athletic Training," New York; McGraw-Hill, 2003, pp. 102-103.
34. Reid, D.C., Cummings, G.E., "Factors In Selecting The Dosage Of Ultrasound." *Physiother* Can, **25**, 5-9 (1973).
35. Soren, A., "Evaluation Of Ultrasound Treatment In Musculoskeletal Disorders," *Physiother,* **51**, 214-217 (1965).
36. Stewart, H., "Ultrasound Therapy," in *Essentials of Medical Ultrasound* edited by Repacholi, M.H., Benwell, D.A., Clifton, N.J:, Humana Press, 1982, p 196.
37. ter Harr, G., "Basic Physics Of Therapeutic Ultrasound," *Physiother,* **73**, 110-113 (1987).
38. Williams, A.R., "Production And Transmission Of Ultrasound," *Physiother,* **73**, 113116 (1987).
39. Young, R.R., Hennemon, E., "Reversible Block Of Nerve Conduction By Ultrasound." *Arch Neurol,* **4**, 83-89 (1961).

Influence Of Acoustic Intensity On Skin Damage During Extra-Corporeal Hifu

F. Lacoste**, J. Schlosser*, G. Vallancien*

*Department of Urology and Research (CERA) Institut Montsouris,75013 Paris. France
** Edap,69120 Vaulx-en-Velin. France

Abstract. Objectives: In extracorporal HIFU treatment skin burns may occur depending on the acoustic intensity and the duration of the pulses. This study aims at establishing an experimental relationship between the occurrence of skin burns and the acoustic intensity at the skin level.
Methods: The pig model was used for this study because its skin is similar to human's. Single HIFU pulses were applied through 19 pig skin sites (10 pigs) allowing enough time between the pulses for the skin to cool. The duration of the pulses was gradually increased until a first occurrence of skin damage was observed. The experiment was repeated for several values of acoustic intensities ranging from 9 to 177 W/cm2.
Results: At the skin level, the maximum tolerable energy density level of single HIFU pulses decreases with the square root of the acoustic intensity. The skin tolerance may vary by a factor of 3 among animals.
Conclusion: The maximum energy and intensity that skin can support without damage was experimentally determined. At lower intensity more acoustic energy can be applied through the skin than at higher intensities.
Key Words: High intensity focused ultrasound, Skin burns.

INTRODUCTION

In clinical practice, the destruction of the target tissue by High Intensity Focused Ultrasound (HIFU) must occur in rapidly [1]. Unfortunately part of the acoustic energy is absorbed by the tissue interface, e.g. the skin. To avoid undesirable burns, resting pauses must be allowed between the pulses and those have an unfavorable effect on the duration of the treatment. The aim of this study was to estimate the maximum amount of energy that the skin can support without burning so as to maximize ultrasound exposure.

MATERIAL AND METHOD

The HIFU Device (Edap, France)

The treatment head (Edap, France) contained 160 flat round ceramics. The ultrasonic frequency was 1 MHz and the acoustic power, measured with an acoustic force balance, was adjustable between 50 and 6000 Watts. The treatment head was

mobile with a millimeter precision. In the treatment head, the coupling liquid was maintained at a constant 15° C temperature. The target volume was imaged with an ultrasound probe located in the center of the treatment head.

The ultrasound was coupled to the skin via a flexible, non extensible bag filled with coupling liquid.

The Animal Model

Female Large White x Land Race pigs (body weight between 50 to 70 kg) were used for this study. During HIFU treatments, the pigs were anaesthetized. The premedication associated a carazol (0.15 mg) and an atropine (0.5 mg) intramuscular injection. After catheterism of an ear vein, the anesthesia was induced with intravenous thiopental (10 mg/kg) and vecuronium bromide (12 mg). The animals were intubated under direct vision with an endotracheal tube. Anesthesia was maintained with intravenous thiopental.

The pigs were fixed to the table and placed on the right side to treat the left kidney or on their back to treat the bladder (Figure 1). Prior to locating, the skin over the target was cleaned and shaved. The acoustic coupling between the treatment head and the skin was ensured by an acoustic gel (KY Lubrificating Jelly / Johnson & Johnson).

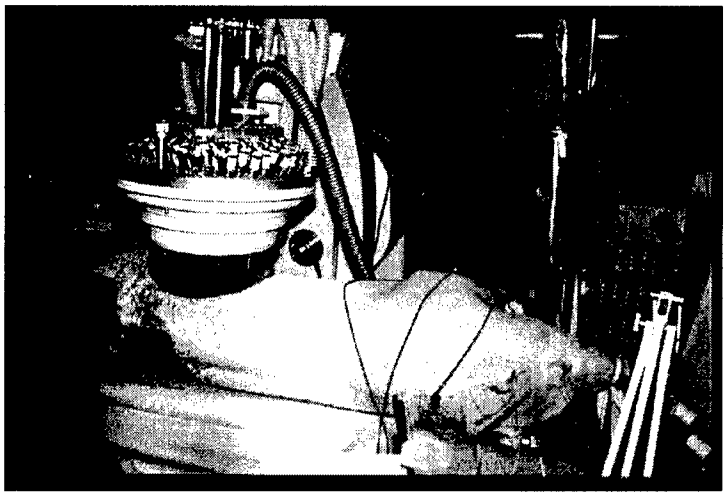

FIGURE 1. Experimental set-up.

Ultrasonic Application

In a first trial (*single pulse study)*, single HIFU pulses were applied through 19 pig skin sites (10 pigs) facing the left kidney, the liver or the bladder. The duration of the pulses, and consequently their energy, was gradually increased in 20% steps until a first occurrence of a white burning spot was observed (Figure 2). This aspect corresponds to an irreversible skin lesion, which would still be present at 3 days post treatment. The energy corresponding to the first burn was considered maximum.

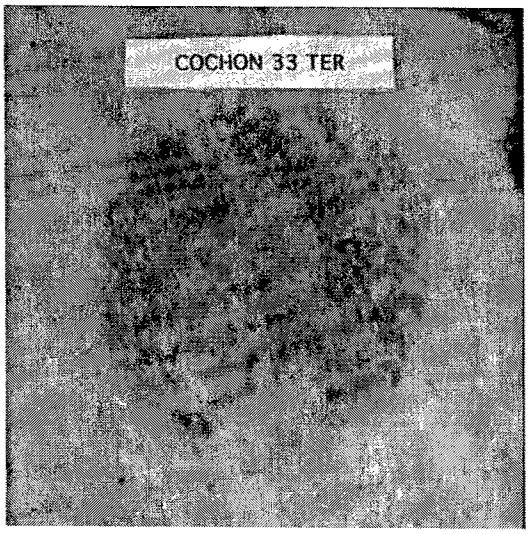

FIGURE 2. Remaining erythema at Day 3, 16 shots @ .9s duration, 50s waiting, 2kJ/shot, 55J/cm²/shot. Site facing left kidney.

The experiment was repeated for several values of acoustic intensities ranging from 9 to 177 W/cm2. Waiting time between the pulses (30 sec to 5 min) was sufficient for the skin to cool.

In another development (*multiple pulse studies*), the state of the skin (i.e. burned or not) was recorded after 166 extracorporal HIFU experimental treatments, where the primary aim was to obtain lesions at the focus. In those treatments, repeated pulses were applied in a wide variety of power and time regimes.

RESULTS

Single Pulse Study

Figure 3 represents the maximum energy Emax tolerated by the skin during a single exposure vs. the acoustic intensity at the skin level Icut. The energy is lower when the acoustic intensity is higher. Below 9 W/cm², no skin burn was observed.

For a same value of acoustic intensity, the maximum tolerable energy varied by as much as 58% from one animal to the other.

Using a best fit algorithm, it appeared that the relationship between the acoustic intensity at the skin level and the maximum pulse energy may be approximated by the experimental relationship: $Emax = 900/\sqrt{Icut}$ where Emax is in J/cm² and Icut in W/cm²

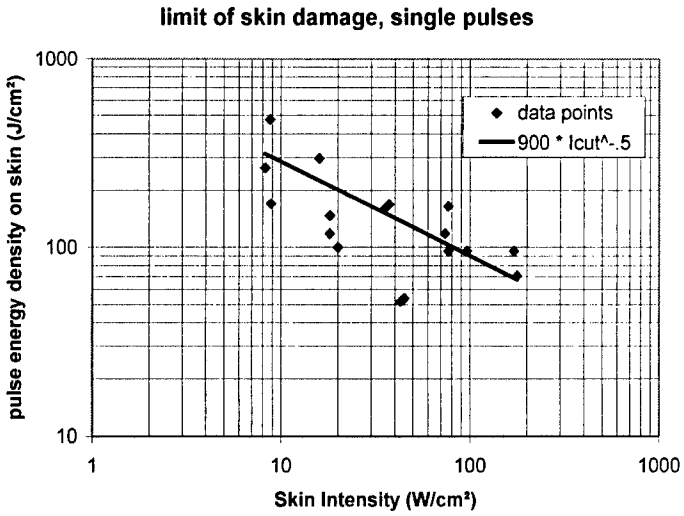

FIGURE 3. Limit of skin damage, single pulses.

Multiple Pulse Studies

The mean skin intensity <Imax> averages the instantaneous skin intensity over the pulse duration and the waiting time between the pulses. When pulses are repeated, as in the case with most HIFU treatment, <Imax> also decreases with the square root of the skin intensity, as shown in Figure 4. The experimental relationship becomes: <Imax> = 6/ √Icut where <Imax> and Icut are in W/cm²

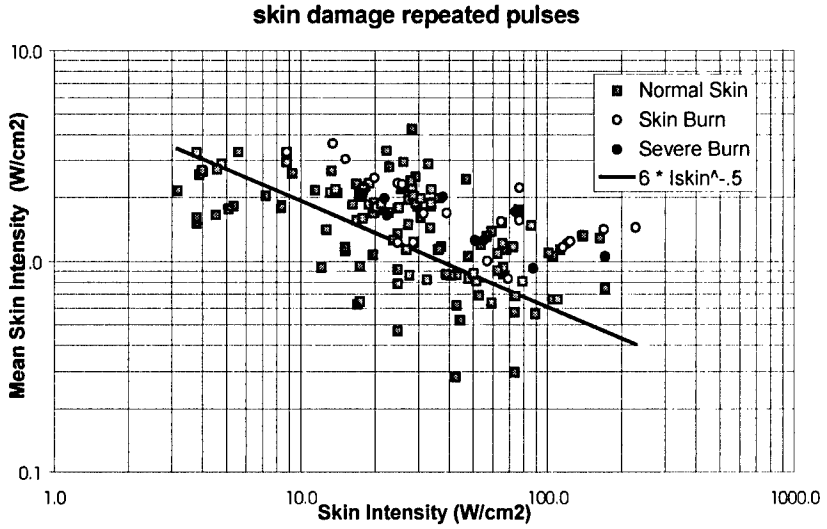

FIGURE 4. Limit of skin damage, multiple pulses.

CONCLUSION

The maximum energy and intensity that skin can support without damage was determined experimentally. At lower intensities more acoustic energy can be applied through the skin than at higher intensities.

ACKNOWLEDGMENTS

The authors want to thank Dr F. Laborde, and all members of the CERA - Fondation de l'Avenir research laboratory for their technical assistance in this research.

Evaluation Of Bone Fraction And Visualization Of Trabecular Architecture Using Ultrasound Signals

Fumio Nogata*, Hirohisa Tamagawa*, and Yasuo Ikeda**

*Department of Human and Information Systems, Faculty of Engineering, Gifu University, 1-1 Yanagido Gifu-city, 501-1193,Japan (nogata@cc.gifu-u.ac.jp)
**Department of Research and Development, Japan Fine Ceramics Center 2-4-1 Rokuno Atsuta-ku, Nagoya-city, 456-8587,Japan

Abstract. Methods for evaluating mechanical integrity of *in vivo* bone were proposed; 1) an evaluation technique of 2-D bone area fraction (S, bone area fraction between bone and bone marrow) using the transit velocity of ultrasound through bone, and 2) a visualization technique of trabecular architecture of spongy bone using ultrasound A-mode signals. The evaluation technique of 2-D bone area fraction is based on the bone length fraction calculated from the difference in the sound speed traveling through cancellous bone. The results showed that there is a good relationship between the BMD (bone mineral density) by DXA (dual energy x-ray absorptiometry) and the bone area fraction by the ultrasound testing. The 2-D visualization technique is capable to create the image size of ~10 mm depths from the surface of cortical bone. We believe that those results are informative to diagnose osteoporosis.

INTRODUCTION

With more people than ever reaching greater age, clinicians, as well as scientists and family doctors, have developed an increasing interest in osteoporosis, which is defined as the clinical manifestation of the atrophy of bone. Bone atrophy is defined as a reduction of the bone mass per space unit of bone tissue. In most cases, a fracture of a vertebral body is found, which would result in long-term bed care. Both compact and cancellous bone mass are decreased in the postmenopausal decade, but the reduction of trabecular bone is more pronounced than compact bone. One of the biggest difficulties facing the medical profession today in the area of osteoporosis is the absence of any accurate way of diagnosing bone loss before the bone actually breaks, so that preventive strategies can be adopted. As the bone becomes less dense, its mechanical properties alter [1] and it is more likely to fracture. Expensive machines called DXA (Dual Energy X-ray Absorptiometry) densitometers can scan bones to give an accurate reading of bone density, but this is harmful due to X-ray exposure and is not available to assess mechanical integrity of bone.

Because osteoporotic changes appear initially in the cancellous bone and it is only at an advanced stage that cortical thinning is detected [2], we must develop methods to inexpensively and non-invasively assess the mechanical integrity of *in vivo* bone tissue of an individual as well as understand bone density which can directly relate to

fracture incidence trabecular density and orientation, and architecture-related strength of cancellous bone [3-5]. Ultrasound methods have long been considered to have potential value for the assessment of bone fragility on the theoretical basis that its propagation velocity is influenced both by bone density and by material elasticity along the travel path [6-10].

In the present report, we propose two methods for evaluating mechanical integrity of *in vivo* bone, 1) an evaluation technique of 2-D bone area fraction (S, bone area fraction between bone and bone marrow) using the transit velocity in bone, and 2) a visualization technique of trabecular architecture using A-mode signals from conventional ultrasound instrument for soft tissue, which permits to diagnose osteoporosis.

EXPERIMENTAL METHOD

Estimation Of Bone Area Fraction And Bone Mineral Density (BMD) For *In Vivo* Heel Bone

Heel bone shows almost spongy shaped structure; we consider its bone material consists of bone substance (solid) and bone marrow (liquid paste). Ultrasound wave propagates at a faster rate in a solid than in a liquid. Thus, wave velocity reflects bone density and its architecture. If the wave frequency is ignored, this can be easily understood that the total distance (b) propagated through bone substances can be calculated by the following equation (Figure 1),

$$b=(t_2-t_1)/[(1/V_2) - (1/V_1)] , \qquad (1)$$

where V_1 is the propagation velocity in bone marrow; 1530m/s, V_2 is the velocity in bone substance; 2986 m/s, t_2 is the time of travel for an ultrasound pulse through the bone specimen with length L, and t_1 is the time propagated through the specimen (length L) which consists of bone marrow;

$$t_1=L/V_1=L/1530 . \qquad (2)$$

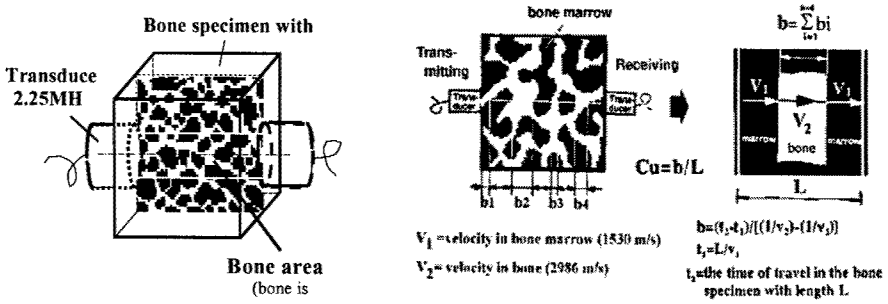

FIGURE 1. a) Measurement of bone area fraction. b) A solid-liquid model for spongy bone.

Therefore, the bone substance length ratio (C) can be calculated by the equation C=b/L. By measuring two directions (x and y; Cx, Cy, respectively) of the specimen,

the bone area fraction (S) can be estimated from their product, i.e., S=CxCy. For isotropic architecture, it is Cx =Cy, i.e., $S=(Cx)^2$.

To validate the bone area fraction measurement technique using Eq. (1), eight cubic bone specimens (18x15x20 mm, approximately) were prepared from some fresh bovine bones (tibia). The cubic specimens contained bone marrow. The size of the specimen was determined considering orientation of structure, and bone density to have equivalent morphological parameters in the specimen. The shape of trabecular bone was obtained for pattern analysis (bone length ratio and cross sectional area) by stamping the specimen (without marrow) after ultrasound testing. The pattern was fed into a computer using an image processor. A pair of 2.25 MHz transducers, 12 mm diameter, was used. Although the wavelength corresponding to a frequency of 2.25 MHz ($\lambda/2$=0.42~0.55 mm when V=1800~2500 m/s: average speed in the heel bone) is longer than the size of the trabecula (~3 mm), the frequency was at a higher limit for measuring *in vivo* properties of human bones including the kneecap and heel bone. The relationship between the bone area fractions by an image processor and by the ultrasonic technique was then examined, since the total bone size (b) calculating from Eq. (1) is dependent on the frequency of the transducer used. This is the method proposed here for estimating *in vivo* bone mass using the empirical relationship based on the laboratory specimens. The transit time was measured from the first wave front of the input pulse to that of the output signal because the transmitted wave is generally distorted due to the complicated architecture of the trabeculae. Five measurement trials were carried out and averaged for each testing.

Since BMD is the most widely used to diagnose osteoporosis, we also examined the relationship between BMD and the bone area fraction S. Furthermore, forty Japanese females aged 21 to 75 years were measured by DXA (Dual X-ray Absorptiometry, Hologic QDR-2000) and the ultrasound testing for heel (*calcaneus*), and spine antero posterior (vertebrae lumbar, L2-4-AP). In the *in vivo* test, the width of the bone and soft tissue and the 2-D bone area fraction were measured using the reflected and transmitted signals, respectively.

Visualization Of Spongy Architecture

To develop a new visualization technique for micro architecture of the cancellous bone, a traditional ultrasound instrument is altered so that A-mode signal, which is utilized as a scan line for the creation of an image, can be extracted from it. The scan line interval of this extracted A-mode signal is 0.2mm, and this signal is sent to the oscilloscope and digitalized by the software, WaveStar, which was converted into a new image. In this experiment, a medical ultrasound instrument with a probe of 7.5 MHz frequency (Medison, SA-600) was used. Two kinds of specimens were used, ceramic foam specimen which is similar to spongy architecture and bone specimen machined from fresh bovine tibia. The experiment was performed in the water environment to ensure the transmission and receiving of ultrasound between the specimen and a probe. Figure 2 shows the visualizing system used in this study. The shape visualized is average 2-D architecture because the size of a transducer element was 0.4 x 5.0 mm. We make a new artificial signal between the elements by

interpolation process, thus the signal of 0.2 mm interval can be used for creating shape of the bone.

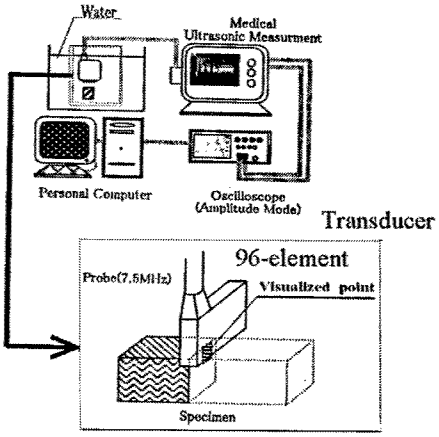

FIGURE 2. Visualizing system for spongy architecture.

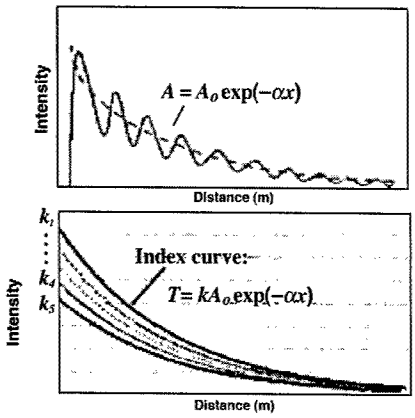

FIGURE 3. Curve fitting to the reflected signal (upper), and threshold curve to distinguish bone or not.

Data processing Of A-Mode Signal To Structure

Ultrasound A-mode signal is utilized for visualizing trabecular architecture. This visualizing procedure can be established by finding a method to distinguish between bone and bone marrow. In this study, we performed A-mode signal data processing by the following procedure.

1) The data of convex point in the A-mode signal is extracted, and these are regarded as pixels constituting a spongy image. Yet, sometimes some of pixels not corresponding to bone is extracted by this method.

2) These extracted data is approximated for the bone specimen by a decay index curve expressed by equation (3), where A, A_0, α, and x represent echo intensity, initial value of echo, attenuation factor, and distance, respectively.

$$A = A_0 \exp(-\alpha x) . \quad (3)$$

3) Assuming the curve T given by the equation (3) and the threshold value k,

$$T = kA_0 \exp(-\alpha x) , \quad (4)$$

if the data of A-mode signal obtained in procedure 1) is larger than this threshold value (T), it is regarded as a pixel of bone image, and the rests are the pixels of bone marrow including the result of procedure 1).

Determination Of Threshold Value, k

To distinguish between bone and bone marrow, fifty of A-mode signals were arrayed and converted into an image. It corresponds to an image with the size of 10 mm width. And the depth of ~10 mm from the bone surface is visualized due to

avoid the influence of reflected signals. The shape of structure and the density of bone vary according to the threshold value. The threshold value is determined through the comparison of it with the bone area fraction of the specimen created, where the threshold value fluctuates according to A_0 in equation (3). Since the ultrasound speed traveling through bone is ~3000 m/s, which is twice as fast as that in bone marrow, 1500 m/s, the size of pixel of created bone image is twice as large as that of bone marrow in the ultrasound direction. That is, the pixel size for creating architecture was 0.2 (width) x 0.15 (depth) mm for bone marrow and 0.2x0.3mm for bone substance due to the difference of wave speeds.

RESULTS AND DISCUSSION

Estimation Of Bone Area Fraction And BMD For *In Vivo* Heel Bone

Figure 4 shows the relationship between the bone length ratios by ultrasound inspection (Cu) and the image processor (Ci), which suggests that a nonlinear relation probably exists due to the complicated architecture (shape of trabecular) in the bone. Therefore, the real bone length ratio (Ci; Ci-x or Ci-y), can be calculated using the empirical relationship of the following equation,

$$Ci = 0.0784\tan(162\,Cu - 80.6) + 0.474\,, \qquad (5)$$

where Cu is calculated from the Eq. (1).

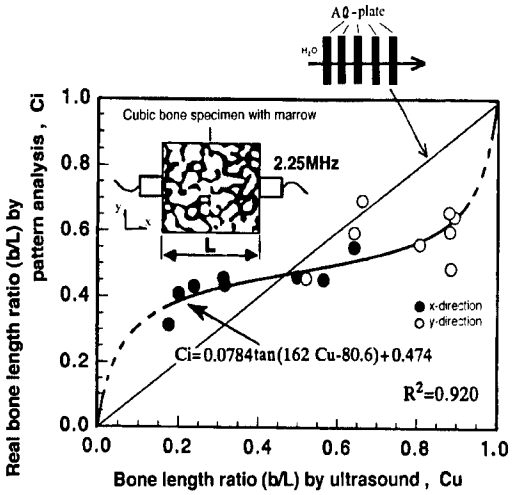

FIGURE 4. Relationship between Cu and Ci for bone.

Figure 5 shows the relationship between BMD by DXA and the area fraction by the present ultrasound testing. This relation allows estimating BMD of the spine and the result can be directly used to diagnose osteoporosis, that is the following equations:

$$\text{BMD (g/cm}^2\text{)} = 0.0167S \quad \text{for heel bone} \quad (r = 0.83) \quad (6a)$$

$$\text{BMD (g/cm}^2\text{)} = 0.0254S + 0.12 \quad \text{for the spine} \quad (r = 0.77) \quad (6b)$$

where S is bone area fraction (percent). On the basis of these results, we have developed a new commercial instrument to measure bone area fraction.

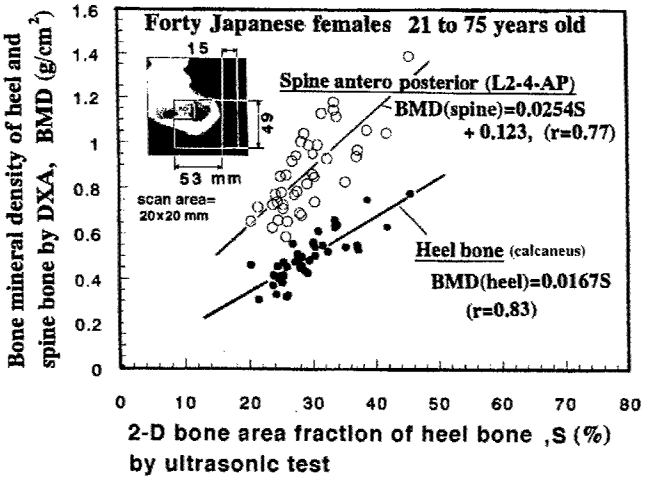

FIGURE 5. Relationship between BMD by DXA and area fraction of heel bone.

Visualization Of Trabecular Architecture Of Ceramic And Bone Specimens

Figure 6 shows the images of ceramic foam specimen, which is structured similar to cancellous bone, created by varying the threshold value. Since the ultrasound speed in the ceramics is 4000 ~ 5000 m/s, which is 3-fold faster than that in water, the pixel of bone material is extended in the direction of ultrasound by 3-fold. Comparing the fraction areas, the specimen and some created images, the threshold value k is suitable as k = 1.16. Through the same manner described above, the image of a bovine cancellous bone specimen is created as shown in Figure 7, the threshold value k is suitable as k = 0.94 ~ 0.96. Four kinds of bone specimens were visualized and some coefficients in Eq. (4) for creating spongy architecture are summarized in Table 1. Through the results, it appears that smaller size of the pixel for creating the architecture of bone should be used by applying higher frequency transducer revised because the real size of trabecular is about 0.1 ~ 0.8 mm.

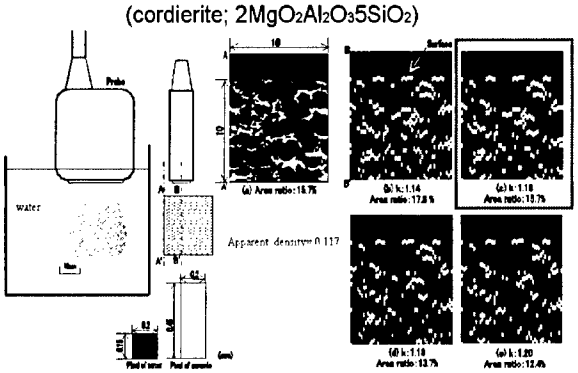

FIGURE 6. Visualized images with some k values for bone specimen.

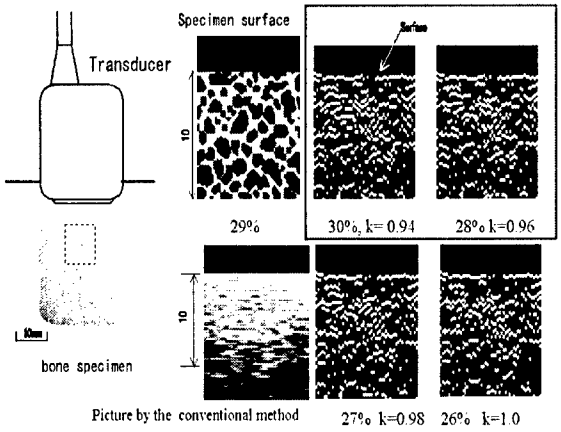

FIGURE 7. Visualized images with some k values for ceramic specimen.

TABLE 1. Summary of coefficients in Eq. (4) for creating spongy architecture.

	Bone Specimen	**Ceramic Foam**
k	~0.96	~1.16
Ao	4~7	3~5
α	0.15~0.4	0.02~0.06

CONCLUSIONS

In this report, two methods for evaluating mechanical integrity of *in vivo* bone were proposed: 1) an estimation technique of 2-D bone area fraction (S, bone area fraction between bone and bone marrow) using transit velocity of ultrasound through bone, and 2) a visualization technique of trabecular architecture using ultrasound A-mode signals. The former is focused on a screening inspection of bone using a pair of the

single transducer of 2.25 MHz. and the latter is focused on a thorough inspection using a linear-arrayed transducer. The results showed that there is a good relationship between the BMD (bone mineral density) by DXA (dual energy x-ray absorptiometry) and the bone area fraction by ultrasound testing. And the 2-D micro architecture is visualized using ultrasound A-mode signals. The pixel size for creating architecture was 0.2 (width) x 0.15 (depth) mm for bone marrow and 0.2x0.3 mm for bone substance due to the difference of wave speeds. The 2-D visualization technique is capable to create the image size of ~10 mm depths from the surface of cortical bone. We believe that those results are informative to diagnose osteoporosis The results indicated that smaller size of the pixel for creating bone architecture should be used by applying higher frequency transducer revised because the real size of trabecular is about 0.1~0.8 mm.

ACKNOWLEDGEMENTS

This work was partially supported by the Grand-in-Aid for Scientific Research from the Ministry of Education, Science and Culture (No. 13680930).

REFERENCES

1. Carter, D.R. and Hayes, W.C., "The compressive behavior of bone as a two-phase porous structure," *J. Bone and Joint Surgery*, **59-A** (7), pp. 954-962 (1977).
2. Nordin, B.E.C., Peacock, M., Crelly, R.G., Heyburn, P.J., Jorrsman, A., and Remagen, W., 1988,"Osteoporosis," Basle, pp.3-42 (1990).
3. Lee, S., Ahern, J.M., and Leonard, M., "Parameters influencing the sonic velocity in compact calcified tissues of various species," *J.Acoust. Soc. Am.*, **74**, pp.28-33 (1983).
4. Gibson, L.J., "The mechanical behaviour of cancellous bone," *J. Biomech.*, **18** (5), pp.317-328 (1985).
5. Rice, J.C., Cowin, S.C., and Bowman, J.A., "On the dependence of the elasticity and strength of cancellous bone on apparent density," *J. Biomech.*, **21** (2), pp.155-168 (1988).
6. Hodgskinson, R. and Currey, J.D., "Effects of Structural Variation of Young's Modulus of Non-human Cancellous Bone," *Proc. Ins. Mech. Engrs.*, **206**, pp.43-52 (1990).
7. Langton, C.M., "The measurement of broadband ultrasonic attenuation in cancellous bone," *Eng. in Medicine*, **13** (2), pp.89-91 (1984).
8. Lippmann, R.K., "The use of auscultatory percussion for the examination of fractures," *J. Bone Joint Surgery*, **14**, pp118-126 (1932).
9. Singh, V.R., Yadav, S., and Adya, V.P., "Role of natural frequency of bone as a guide for detection of bone fracture healing," J. *Biomed. Eng.*, **11**, pp.457-461 (1989).
10. Nogata, F.,et. al. ,"Method and apparatus for evaluating the progress of osteoporosis by ultrasonic signals," United States Patent No.5535750 (1996).

HIFU-Induced Heating In Vascularized Phantoms: A Quantitative Comparison Of Theory And Experiment

Ronald A. Roy, Jinlan Huang and R. Glynn Holt

Boston University, Department of Aerospace and Mechanical Engineering, Boston, MA 02215

Abstract. High intensity focused ultrasound (HIFU) can be used to control bleeding, both from individual blood vessels as well as from gross damage to the capillary bed. The presence of vascularity can limit one's ability to elevate the temperature of blood vessels owing to convective heat transport. In an effort to better understand the heating process in tissues with vascular structure we have developed a numerical simulation that couples models for ultrasound propagation, acoustic streaming, ultrasound heating and blood cooling in Newtonian viscous media. The 3-D simulation allows for the study of complicated biological structures and insonation geometries. We have also undertaken a series of *in vitro* experiments employing non-uniform flow-through tissue phantoms and designed to provide a ground truth verification of the model predictions. The calculated and measured results were compared over a range of values for insonation pressure, insonation time, and flow rate; we show excellent agreement between predictions and measurements. [Work supported by DARPA and the U.S. Army.]

INTRODUCTION

The use of high intensity focused ultrasound to effect medical therapy is a relatively new treatment modality that is flush with possibility and promise. The manner in which one applies the acoustic energy determines, to a large extent, the nature and spatial extent of the biological effect. A broad spectrum of therapy is achievable, ranging from gentle heating of tumors to violent tissue ablation, from drug delivery through sonoporation to kidney stone comminution. A barrier to safe and efficacious HIFU therapy involves targeting and treatment planning: is the sound energy going to the right spot and in the correct dosage? To address this, one needs an accurate model that, in the context of HIFU therapy, includes multiple physical effects: nonlinear sound propagation, arbitrary media inhomogeneity, thermal transport phenomena, convective transport phenomena (i.e. blood flow) and other second order effects as needed (acoustic streaming, acoustic radiation stress, cavitation, etc.).

The years have seen numerous studies devoted to modeling tissue heating from ultrasound exposure, starting with the pioneering works of Frey [1], Lele [2], and Parker [3,4], the latter of whom derived approximate analytical expressions for the temperature rise in a 3D conducting medium. Most published methods are limited to simple situations for which analytical solutions exist and the use of cylindrical geometries suffice. Pond [5] broke down the heating volume into a series of cylinders that he used as elemental heat sources. Robinson and Lele [6] assumed cylindrical

heat deposition pattern and produced analytical expressions for the temperature distributions as a function of time. Muir and Carstensen [7] modeled both focused and unfocused ultrasound heat deposition yielding analytical expressions that incorporated nonlinear effects. Several investigators [8-11] addressed the proper computation of heat generation during ultrasound exposure. Lizzi *et al.* [12,13] developed both analytical and numerical solutions to the Pennes bioheat transfer equation [14] in the context of glaucoma treatment. Hill *et al.* [15] and later Wu and Du [16] developed general analytical models based on a Gaussian approximation to the beam shape.

Owing to the complexity of the propagation medium, accurate predictions of HIFU-induced temperature rise require numerical modeling. Kolios *et al.* [17] employed a finite difference method to model perfused tissues in 2-D cylindrical coordinates. Curra *et al.* [18] used a 2-D finite difference implementation to investigate the importance of nonlinear effects on wave propagation and heat generation in perfused liver models. Fan and Hynynen [19] investigated focused ultrasound surgery (FUS) by phased arrays using a 3-D finite difference model. Wan *et al.* [20] used a matrix relaxation method to investigate critical parameters governing the performance of their phased-array system and Meaney *et al.* [21] computed 3-D heat deposition patterns assuming a linear propagation model. Most recently, Krasovitski and Kimmel [22] presented a 3-D simulation of the temperature field in and around a blood vessel for a simplified geometry. The literature on modeling of ultrasound-induced tissue heating is extensive and this brief summary neglects several important contributions. Readers are directed to the review by Huang [23] for a comprehensive survey.

In this paper, we describe a finite difference time domain implementation of the basic governing equations for sound propagation and bioheat transfer in the presence of blood flow and acoustic streaming. (Other second-order effects will be incorporated in future work.) The simulation is 2-D in pressure and 3-D in all thermal and flow quantities. Performance is assessed through a quantitative comparison with experiments run in uniform and vascularized gel phantoms. These phantoms are characterized *a priori* and instrumented to facilitate measurement of acoustic pressure and temperature in space and time. The comparison with model predictions proceeds without reliance on fitting parameters. Below we describe in brief the theoretical model, numerical implementation and subsequent experimental validation. Additional details describing all facets of the work are presented in [23].

GOVERNING EQUATIONS & NUMERICAL MODEL

We model nonlinear sound propagation in a non-uniform viscothermal medium with the Westervelt equation, modified by the addition of a loss term, which accounts for the effects of diffraction, absorption, inhomogeneity, and nonlinearity [24]:

$$\left(\nabla^2 - \frac{1}{c^2}\frac{\partial^2}{\partial t^2}\right)p - \frac{1}{\rho}\nabla p\cdot\nabla\rho + \frac{\delta}{c^4}\frac{\partial^3 p}{\partial t^3} + \frac{\beta}{\rho c^4}\frac{\partial^2 p^2}{\partial t^2} = 0. \qquad (1)$$

Here c is the sound speed, ρ is the density, δ is the acoustic diffusivity, and $\beta = 1+B/2A$ is the coefficient of nonlinearity with B/A being the nonlinear parameter of the

medium. Our time domain simulation assumes a classical thermoviscous medium in which the absorption increases as the frequency squared, though for tissues the power law for absorption is closer to $f^{1.1}$. This might introduce error in the case of strongly nonlinear waves. However, the current model allows for detailed investigation of spatial and temporal characteristics of the energy deposition and heating in an arbitrary medium using either pulsed or continuous ultrasound.

Since heating is approximately second order in the pressure field, we invoke a Born approximation and assume *a priori* that the sound beam generated by our axis-symmetric HIFU transducer will be unaffected by inhomogeneities in the propagation path. A 2-D cylindrical representation is thus adequate to compute the acoustic pressure and intensity fields, a fact that greatly reduces the computation time required for each simulation. This assumption is motivated by practical considerations and recognizes the fact that the acoustic contrast of various structures in tissue is small (bone and lung being notable exceptions). See Huang [23] for a detailed discussion.

Finally, in order to couple the pressure field model to the temperature field model (described below) we need to quantify the thermal energy deposition associated with the absorption of the ultrasonic wave. To do this we employ the following expression from Pierce [25] for the spatially-dependent ultrasonic power deposition per unit volume:

$$q = 2\alpha_{ABS} I = \frac{2\alpha_{ABS}}{\omega^2 \rho c} \left\langle \left(\frac{\partial p}{\partial t} \right)^2 \right\rangle, \qquad (2)$$

where α_{ABS} refers to the local absorption coefficient of the medium, I is the local acoustic intensity, and the brackets denote time average over one acoustic cycle.

We seek to model thermal transport in perfused tissue containing one or more larger blood vessels. The widely used Pennes bioheat transfer equation, BHTE [14], is a relatively simple modification of the heat conduction equation. The temperature field in the perfused tissue and flowing blood domains can be expressed as

$$\rho_t C_t \frac{\partial T}{\partial t} = \mathrm{K}_t \nabla^2 T - w_b C_b (T - T_\infty) + q \qquad (\textit{tissue domain}), \qquad (3)$$

$$\rho_b C_b \frac{\partial T}{\partial t} = \mathrm{K}_b \nabla^2 T - \rho_b C_b (\vec{u} \cdot \nabla T) + q \qquad (\textit{blood domain}), \qquad (4)$$

where ρ, C, and K are the density, specific heat and thermal conductivity with the subscripts t and b referring to tissue and blood domain, T_∞ refers to the temperature at large distances from the focus, w_b is the perfusion rate (zero for our experiments) and $\vec{u}$ is the blood flow velocity. The blood flow field has two components: a fully developed parabolic flow plus an acoustic streaming flow. Thus, the total blood flow velocity field is written as

$$\vec{u} = \vec{u}_{ext} + \vec{u}_{str} = 2U_0 \left[1 - \left(\frac{r}{r_0} \right)^2 \right] + \vec{u}_{str}, \qquad (5)$$

where $\vec{u}_{ext}$ represents parabolic Pouiseille flow and $\vec{u}_{str}$ is acoustic streaming, U_0 is the average velocity of the Pouiseille flow, r is the distance to the flow axis, and r_0 is the radius of the vessel.

There is a considerable body of literature that develops the theoretical basis of acoustic streaming. The fluid motion is described by the continuity and Navier-Stokes equations applied to a viscous incompressible fluid [26]. The driving force of the streaming derives from the acoustic field and is manifested as a momentum transfer from sound waves to fluid motion that is spatially distributed in the beam. Much of the early work (Eckart [27] and others) assumed continuous plane waves and a second-order approximation, which is unsuitable for HIFU beams. We employ a model that follows from the work of Kamakura *et al.* [28,29] in which we begin with the continuity equation and the Navier-Stokes equation for a viscous incompressible fluid. The representation for the acoustic stress is accurate to second order and the formulation includes full hydrodynamic nonlinearity. We consider only the axial component of the acoustic particle velocity field, which we obtain from the pressure solution (Eq. 1) using a linear impedance relationship. The details of the model are not presented here. Rather, the reader is referred to Huang [23] for more information.

Unlike the pressure field, 3-D solutions for the BHTE and streaming equations are readily obtained for the time step required for the latter is considerably larger than the former. Coding is thus fully 3-D, a feature which allows us to consider a host on insonation geometries in media with arbitrary variability, subject to the Born approximation alluded to above.

Numerical Implementation

Determining the temperature rise due to acoustic absorption proceeds as a three-step process

1. Solve for the 2-D axisymmetric, steady-state pressure in the medium (Eq. 1) based on the known parameters for the acoustic source, the propagation geometry, and material properties. The rate of ultrasonic energy deposition per unit volume q (Eq. 2) and the driving force for acoustic streaming $\vec{F}$ (see Ref. 23) are calculated.
2. Incorporate the driving force $\vec{F}$ in the flow equations [23] and solve for $\vec{u}_{str}$, the 3-D time-dependent acoustic streaming field in blood domain.
3. The specified blood flow characteristics, the energy deposition term, and the streaming velocity field are then fed into the BHTE model, Eqs. 3-5, yielding the 3-D time-dependent temperature field computation. The model supports a time-varying blood flow velocity.

A finite-difference-time-domain (FDTD) simulation is used to calculate the acoustic pressure, the acoustic streaming and the temperature. The FDTD method relies on discrete differences in place of partial derivatives in the model equations by dividing the spatial and time domains into discrete spatial grid points and discrete time steps [30]. We employ an explicit method where only known values from past time steps are required. The initial condition is the pressure at the surface of the focused bowl sound source and absorbing boundary conditions are employed at the edges of the computational domain. The time step for the acoustic and the BHTE/streaming

calculations are 0.01 microseconds and (typically) 0.5 milliseconds respectively. (The time step in the BHTE calculations was adaptive.) Grid point spacing was typically 0.1 mm. Additional details regarding the coding and implementation of the model is provided in Huang [23].

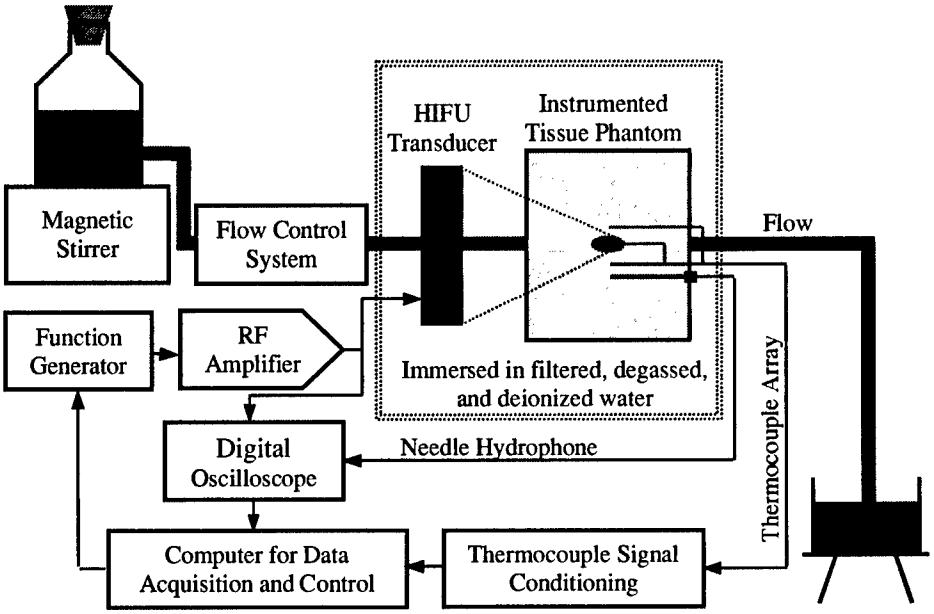

FIGURE 1. Schematic diagram of the apparatus. The HIFU transducer has a hole in the center through which we feed the simulated vascular flow

VALIDATION BY COMPARISON WITH EXPERIMENTS

A schematic of the measurement apparatus is shown in Fig. 1. The acoustic source and tissue phantom are immersed in filtered, deionized, and degassed water contained in a 58-cm long, 43-cm wide and 46-cm high acrylic tank, which is open to the atmosphere. A three-dimensional computer-controlled positioning system (not shown) is used to move the transducer along the beam axis and in both orthogonal directions. We employ an axially symmetric tissue phantom (10.72-cm dia., and 8-cm length) in which the flow is in a straight "vessel" which is aligned collinearly with the acoustic axis or radially displaced from the axis of the beam of sound. "Blood" flow is created by gravity feed, and a flow control and monitor system is used to vary and stabilize the flow rate. Imbedded thermocouples (type E, bare junction, 125 μm diameter, response time less than 40 ms, Omega Engineering Inc., Stamford, CT) monitor the temperature in the flow (central focus, upstream and downstream, and near wall) and in the outer "tissue" (near wall and further away). A calibrated needle hydrophone is embedded in the phantom for *in situ* pressure measurements and position calibration. The hydrophone voltage is sampled using a digital oscilloscope. The function generator, the oscilloscope and the processed thermocouple output are fed into to a computer so

that we can control the source level, capture the *in situ* pressure, and monitor the temperature field. Temperature values are digitized (AT-MIO-16E-1, 12-bit resolution, 1.25 MS/s maximum sampling rate, National Instruments, Austin, TX) at 1 msec intervals and displayed as a 20-point moving average.

Our acoustic source is a single-element, spherically focused, piezoceramic transducer (Sonic Concepts, Woodinville, WA), with a 20 mm-dia. hole in the center, a focal length of 62.64 mm, an aperture of 70.0 mm and a center frequency of 1 MHz. It was calibrated in water using a PVDF membrane hydrophone.

TABLE 1. Measured Material Properties for the Phantom & the Blood Simulant

Physical Property	Agar Tissue Phantom	Blood Simulant
Density (kg/m^3)	1045 (1000-1100)	1108 (1052-1064)
Soundspeed (m/sec)	1551 (1450-1640)	1704 (1540-1590)
Attenuation (Np/m-MHz)	10.17 (4.03-17.27)	1.32 (1.32-1.84)
Specific Heat (J/kg-•C)	3710 (3600-3890)	3450 (3600-3840)
Thermal Conductivity (W/m-•C)	0.59 (0.45-0.56)	0.45 (0.48-0.53)
Viscosity (kg/s-m)		0.0037 (.0035-.0045)

The agar-based phantom material is a mixture of water, agar, graphite powder (acts as a scatterer), methyl paraben (acts as a preservative), and 1-propanol (acts as sound speed tuning). (See Ref. 23 for a detailed recipe.). The most appealing feature of the agar-based phantoms is that the sound speed and attenuation can be varied by altering the phantom recipe. The sound speed can be changed by varying the percentage of 1-propanol, the attenuation can be reduced by using less graphite powder, and both have a nearly linear dependence on the weight percentage [31]. Our blood mimicking fluid employs a suspension of cellulose powder (MN301, Matherey and Nagel, Duren, Germany) in a glycerin/water mixture. This cellulose powder has particle sizes of 2-20 μm. A suspension containing 0.8 g/L in a glycerin/water mixture of ratio 9:10 at room temperature has the same dynamic viscosity (4 cP) as whole blood at body temperature [32]. The advantage of this suspension is that cellulose powder is water wettable, and no surfactant is thus needed. Therefore, this suspension is easy to prepare and degas. The measured [see Ref. 23] acoustical and thermal properties of the phantom and blood simulant are provided in Table 1. The quantities in parenthesis correspond to "typical" literature values for human tissue and blood [33].

Computed And Measured Pressure Fields In Water And Phantom

Figure 2 shows pressure profiles along acoustic axis, and as a function of the radial distance from the acoustic axis (in the focal plane); solid lines and open circles correspond to predictions and measurements respectively. These results were obtained in water at 30•C using a PVDF membrane hydrophone. The pressures shown are all peak negative quantities normalized to the focal pressure, 0.40 MPa. Except maybe for the peripheral regions of the field (where the measurement signal to noise ratio is poor) we see that our model is able to predict all the detail structure and good agreement is found in the focal region and along the side lobes in the focal plane. Since power deposition is quadratic in the pressure, it is in the high-pressure regions in

and near the focus where all the significant heating will take place and the low-signal deviations between measurement and model are not deemed significant.

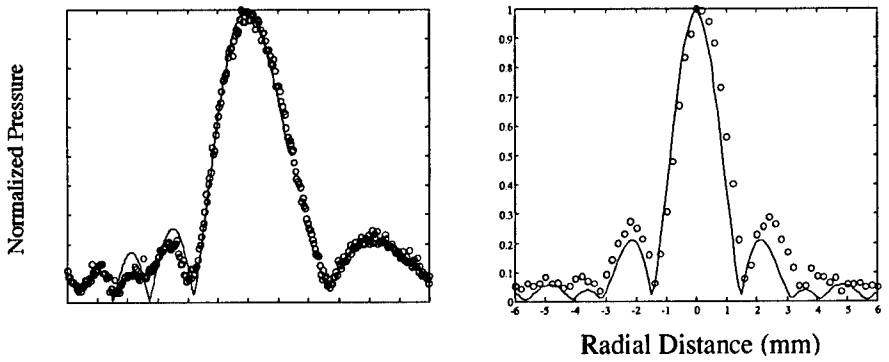

FIGURE 2. Measured and computed pressure profiles in water at 1 MHz and 0.4 MPa peak negative focal pressure.

Although a whole field pressure field measurement cannot be done in the phantom, we can nevertheless compare predicted and measured (*in situ*) focal pressures. Figure 3 shows the measured (circles) and computed (solid line) peak negative pressure at the focus as a function of source pressure (peak negative pressure at the face of the transducer). The source pressure was obtained from the acoustic pressure calibration method described in Ref. [23] and the measurements were obtained with a calibrated needle hydrophone. We show good agreement between the measured and predicted values; all deviations are less than 5% (0.4 dB).

FIGURE 3. A comparison of the measured (circles) and predicted (solid line) peak negative pressure at the focus in phantom as a function of source the pressure. The measurement precision is estimated to be better than 1.5% and is too small to display on this scale

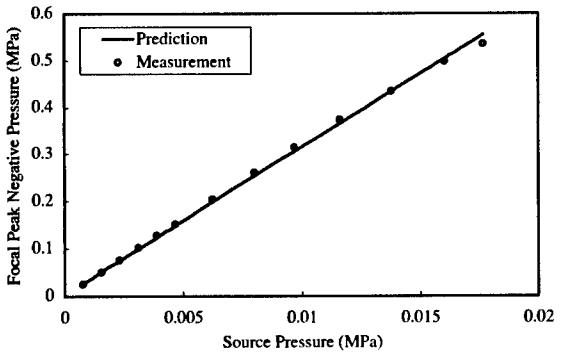

Computed And Measured Temperature Fields In A Uniform Phantom

As an initial test of the BHTE model, experiment we constructed a phantom with no vascularity and measured the focal temperature as a function of time. Results are given in Fig. 4; note the characteristic heating and cooling curves, however, there is a Psignificant difference between the measured (a) and calculated (c) responses. This is

due to the well-know thermocouple artifact effect, which is caused by enhanced heating in the viscous boundary layer adjacent to the thermocouple surface [34]. We are able to independently measure this effect in a low-absorbing material in the absence of streaming using a procedure described in [23]. The measured thermocouple artifact is given by (d), and when one corrects the calculation to account for this artifactual heating (b), the agreement between model and measurement is quite good. We stress that the art-factual heating was measured independently – we do not employ any fitting parameters.

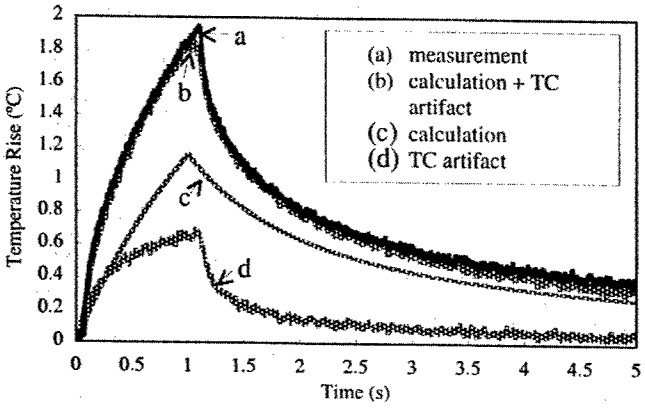

FIGURE 4. A comparison of the measured and simulated focal temperature in a uniform phantom. The TC artifact was independently measured in a separate experiment. The frequency, focal pressure, and exposure time was 1 MHz, 1.11 MPa and 1 second.

Next we equip the tissue phantom with a 2.6-mm diameter vessel positioned parallel to the acoustic axis (Fig. 1). A thermocouple is imbedded in the phantom material, 0.4 mm from the vessel wall and in the focal plane of the transducer. The acoustic focus is entrained on the vessel wall, immediately adjacent to the thermocouple. The objective is to assess the contributions of convective cooling as well as to validate the code when used to model non-axisymmetric configurations.

Figure 5 shows the computed and measured temperature response for insonation times of 1, 3 and 5 seconds and for imposed mean flow velocities of 0 cm/sec and 1.87 cm/sec. The frequency and pean negative focal pressure are 1 MHz and 1.45 MPa respectively. Note the increase in peak temperature with insonation time, and the slight decrease in peak temperature with imposed flow. It appears that convective heat transfer has minimal impact on the temperature elevation in the phantom for these time scales. Note also the excellent agreement between the measured and computed temperature profiles. (The usual thermocouple artifact correction was applied to the calculation.) These results offer strong evidence of both the accuracy and precision of the model, even when applied to no-axisymmetric insonation arrangements.

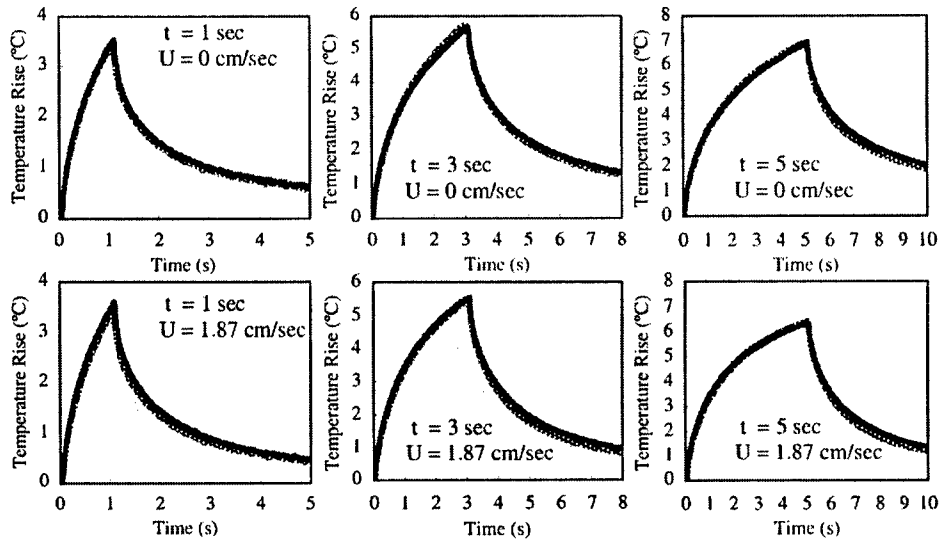

FIGURE 5. Measured and predicted temperature rise versus time 0.4 mm from the focus for differing insonation times and imposed flow velocities. Dark line – data; light line – prediction.

SUMMARY AND CONCLUSIONS

A finite difference time domain code was developed to predict HIFU-induced pressure and temperature fields in absorbing media with arbitrary variability. The pressure model is 2-D axisymmetric and the temperature field model is 3-D. 3-D acoustic streaming is included in the simulation as needed (shown to be important for larger vessels, see Ref. [23]). Simulation performance was demonstrated by a quantitative comparison with experimental results obtained using an instrumented agar & graphite phantom equipped with a linear wall-less flow channel designed to simulate the convective cooling effects of a large blood vessel. Good agreement was demonstrated between simulations and measurements once the thermocouple artifact is accounted for. Additional simulation results that focus on the role of acoustic streaming are not shown due to space limitations.

Ongoing work is focusing on the application of the model to biologically relevant scenarios. The primary advantage of the model is that it supports relatively fast 3-D temperature simulations and, for that reason, can handle complex insonation geometries. Limitations include the Born approximation in the forward propagated pressure field (no high-contrast interfaces allowed) and viscothermal absorption. This latter assumption is not deemed critical, for highly shocked waveforms will likely require peak rarefaction pressures that exceed the cavitation nucleation threshold, at which point most any simulation of the BHTE is going to fail unless bubble enhanced heating in included as a source terms in Eqs. 3 and 4 [35].

ACKNOWLEDGMENTS

The authors gratefully acknowledge the assistance of Dr. Ibrahim Hallaj and Prof. Robin Cleveland in setting up the numerical model, help from Dr. Patrick Edson in the initial stages of experimentation, and helpful comments from Profs. Lawrence Crum and Kullervo Hynynen. We also acknowledge the financial support of DARPA (subcontract through the University of Washington) and the U.S. Army (subcontract from the National Center for Physical Acoustics).

REFERENCES

1. W.J. Fry and R.B. Fry. *J. Acoust. Soc. Am.*, **26**(3): 311-317 (1950).
2. P.P. Lele. *The Journal of Physiology*, **160**: 494-512 (1962).
3. K.J. Parker. *J. Acoust. Soc. Am.*, **74**(5): 1356-1361 (1983).
4. K.J. Parker. *J. Acoust. Soc. Am.*, **77**(2): 719-725 (1985).
5. J.B. Pond. *J. Acoust. Soc. Am.*, **47**: 1607-1611 (1970).
6. T.C. Robinson, and P.P. Lele. *J. Acoust. Soc. Am.*, **51**(2): 1333-1351 (1972)
7. T.G. Muir, and E.L. Carstensen. *Ultrasound in Med. and Biol.*, **6**(4): 345-357 (1980).
8. W.L. Nyborg. *J. Acoust. Soc. Am.*, **70**: 310-312 (1981)
9. K. Beissner. *J. Acoust. Soc. Am.*, **71**(6): 1406-1411 (1982).
10. T.J. Cavicchi, and W.D. O'Brien Jr., *J. Acoust. Soc. Am.*, **76**: 1244-1245 (1984).
11. H.D. Mair, D.A. Hutchins, and P.A. Puhach. *J. Acoust. Soc. Am.*, **81** (2): 328-334 (1987).
12. F.L. Lizzi, J. Driller, and M. Ostromogilsky. *Ultrasound in Med. and Biol.*, **10**(3): 289-298 (1984).
13. F.L. Lizzi, J. Driller, B. Lunzer, A. Kalisz, and D.J. Coleman, *Ultrasound in Med. and Biol.*, **18** (1): 59-73 (1992).
14. H.H. Pennes. *Journal of Applied Physiology*, **2**: 93-122 (1948).
15. C.R. Hill, I.H. Rivens, M.G. Vaughan, and G. ter Haar. *Ultrasound in Med. and Biol.*, **20** (3): 259-269 (1994).
16. J. Wu, and G. Du. *Ultrasound in Med. and Biol.*, **16**(5): 489-498 (1990).
17. M.C. Kolios, M.D. Sherar and J.W. Hunt. *Medical Physics*, **23**, 1287-1298 (1996).
18. F.P. Curra, P.D. Mourad, V.A. Khokhlova, R.O. Cleveland, and L.A. Crum, *IEEE UFFC*, **47** (4), 1077-1088 (2000).
19. X. Fan, and K. Hynynen. *Physics in Medicine and Biology*, **41**(4): 591-608 (1996).
20. H. Wan, P. VanBaren, E.S. Ebbini, and C.A. Cain. *IEEE UFFC*, **43**(6): 1085-1098 (1996).
21. P.M. Meaney, R.L. Clarke, G.R. ter Haar, and I.H. Rivens. *Ultrasound in Med. and Biol.*, **24**(9): 1489-1499 (1998).
22. B. Krasovitski, and E. Kimmel. *J. Acoust. Soc. Am.*, **111**(3): 1454-1459 (2002).
23. J. Huang, *Heating in Vascular and Flow-Through Tissue Phantoms Induced by Focused Ultrasound*, Ph.D. Dissertation, Boston University (2002).
24. M.F. Hamilton, and C.L. Morfey. Model equations. In: M. F. Hamilton, and D. T. Blackstock, editors, *Nonlinear Acoustics*, Chapter 3, Academic Press (1998).
25. A.D. Pierce. *Acoustics, An introduction to its physical principles and applications*, Chap 10, McGraw-Hill Book Company (1981).
26. O.V. Rudenko, and S.I. Soluyan. *Theoretical Foundations of Nonlinear Acoustics*, Chap 8, Plenum, New York (1977).
27. C. Eckart. *Physical Review*, **73**:68-76 (1948).
28. T. Kamakura, M. Matsuda, Y. Kumamoto, and M.A. Breazeale. *J. Acoust. Soc. Am.*, **97**: 2740-2746, 1995.
29. K. Matsuda, T. Kamakura, and Y. Kumamoto. *Ultrasonics*, **34**: 763-765 (1996).
30. C.A.J. Fletcher. *Computational Techniques for Fluid Dynamics*, Vol. 1 of Springer series in computational physics, Spring-Verlag, Berlin, 2nd edition (1991).
31. M.M. Burlew, E.L. Madsen, J.A. Zagzebski, R.A. Banjavic, and S.W. Sum. *Radiation Physics*, **134**, 517-520 (1980).
32. J. Petrick, M. Zomack, and R. Schlief. *Investigative Radiology*, **32**(4): 225-235 (1997).
33. F.A. Duck, *Physical properties of tissue*, Academic Press (1990).
34. K. Hynynen, C.J. Martin, D.J. Watmough, and J.R. Mallard, *British Journal of Radiology*, **56**, 968 (1983).
35. P.L. Edson. *The Role of Acoustic Cavitation in Enhanced Ultrasound-Induced Heating in a Tissue-Mimicking Phantom*, PH.D. dissertation, Boston University (2001).

Visual Anatomic Guidance For Medical Ultrasound Image Acquisition

Florence H. Sheehan MD, Jennifer Dorosz MD, Edward L. Bolson MS

Cardiovascular Research and Training Center, University of Washington, Seattle, WA 98195-6422, USA

Abstract. We developed a visual display to assist minimally trained persons acquire medical ultrasound images by displaying the spatial location and orientation of the current image relative to previously acquired scout images in real time. Using visual guidance yielded more accurate measurements of heart volume. This visual guidance system uses 3D echo technology to improve the accuracy of quantitative ultrasound imaging.

INTRODUCTION

Ultrasound is the ideal imaging modality for the battlefield and for rural communities because it is portable, battery-powered, risk-free, inexpensive, and therapeutic as well as diagnostic. However the training of the medical personnel may be limited, thus greatly reducing the effectiveness with which ultrasound can be deployed. Even experienced diagnostic sonographers commit substantial errors in obtaining complete visualization of a targeted organ and/or in acquiring images in the anatomically correct plane. This is because imaging is performed in a semi-blinded manner: the sonographer's only clue to the position of the current image plane is the target organ's appearance in the current image.

Visual anatomic guidance is a method to give the examiner additional information concerning the location and orientation of the image currently being recorded relative to the anatomy of the target organ. This anatomic information is provided in a real-time graphic display that the examiner can monitor in addition to the ultrasound screen while manipulating the ultrasound transducer. Visual guidance can reduce error in positioning and orienting the transducer while imaging. This paper reports a visual guidance system that we recently completed for NASA to assist flight personnel acquire ultrasound images on each other aboard the International Space Station. In this system, we implemented three methods for visual guidance and tested their efficacy in assisting a medicine resident image the right ventricle of the heart.

METHODS

Visual guidance uses technology developed for three dimensional (3D) echo. This technology includes hardware to track the position and orientation of the ultrasound

transducer in space during scanning, and software for integrating the tracking data with the images and for quantitative analysis of the images.

Method For 3D Echo Imaging And Image Analysis

Image Acquisition

Imaging can be performed using any commercial ultrasound machine. Four to six scans are acquired freehand in 6-10 sec periods of held end-expiration. The duration and number of scans are adjusted for each patient's breath holding ability and image quality. The patient is instructed not to move during imaging or between scans, and to suspend respiration at the same level of expiration during each scan.

Magnetic Field Tracking System

A magnetic field system (Flock of Birds, Ascension Technology Corp., Burlington, VT) is used to track the ultrasound scanhead. The system consists of a magnetic field transmitter, a receiver, and electronic circuitry that interfaces with a computer. The transmitter sequentially generates three orthogonal magnetic fields that are sensed by the receiver and used to compute the receiver's position (x, y, z) and orientation (azimuth, elevation, roll) in space with respect to the origin of the transmitter[1]. Images are digitized directly using a framegrabber (Mutech, Billerica, MA) under the control of a personal computer running custom software. Images are registered with position data, hemodynamic parameters, and scanning parameters such as image depth[2]. The use of a magnetic field system permits freehand scanning from whatever combination of acoustic windows provides optimal image quality. However the sensitivity of the Flock of Birds to ferromagnetic interference necessitated imaging all patients on special beds. More recently we have used an immune tracking system (Internav Inc., Essex Junction, VT) that permits 3D echo can imaging on a hospital bed.

Image Analysis

The images at end diastole and end systole are selected and the median systolic interval is applied to all imaging planes. The borders of the right ventricle and of anatomic features are manually traced in multiple planes and views, fitted using spline curves, and converted to x, y, z coordinates using probe position and orientation data. 3D visualization allows each border to be compared immediately with previously traced borders to verify image plane registration and border tracing consistency[3]. To reconstruct the right ventricular endocardium, a piecewise smooth subdivision surface is fit to 3D points sampled from the traced borders[4]. Right ventricular volume is calculated at end diastole and end systole by summing the volumes of tetrahedra formed from a point to each triangular tile on the reconstructed surface[5]. The volumes determined from this procedure were considered to be the patients' true volumes.

Method for Visual Anatomic Guidance

Line of Intersection

The first method is visualization of the current image's location as a line of intersection on a scout image (Fig. 1). The goal is to store a "scout image" in an initial view and use it to guide the imaging of the next scout image in a view orthogonal to the scout. Then, as the user continues to manipulate the transducer, the position of the current image is displayed as a line of intersection on each scout image[6].

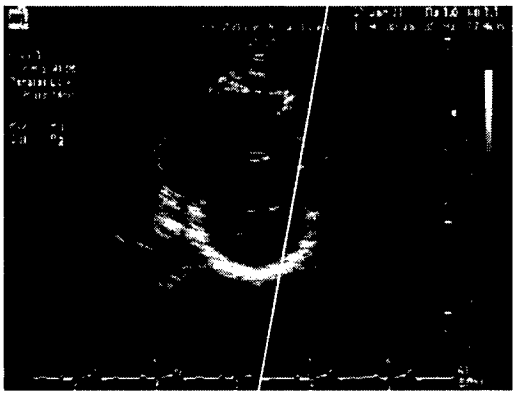

FIGURE 1. Scout image with line indicating intersection with current image plane.

Intersecting Planes

The second method for visual guidance displays the current image plane relative to the scout images in 3D space (Fig. 2). It provides more anatomic assistance in image

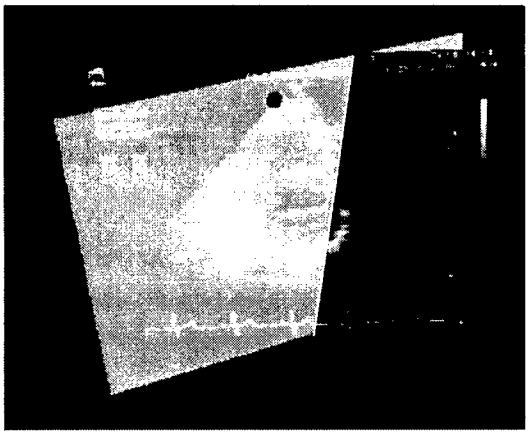

FIGURE 2. Displaying the current image plane as a pale translucent plane facilitates appreciation of its position and orientation relative to the scout image.

plane positioning because the 3D presentation makes it possible to verify not only the position but also the orientation of the current image in the 3rd or out-of-plane dimension relative to the target organ.

3D Surface

To provide even more anatomic guidance we developed a method for displaying where the current image plane intersects a 3D reconstruction of the surface of the target organ (Fig. 3). The advantage of this approach is that the current image does not compete with the scout image for visibility. Instead its position and orientation relative to the heart are clearly visible.

The 3D surface can be rapidly estimated using a catalog-based method[7]. This method provides assistance if the user has acquired several images, but wishes to optimize the position of the views. To obtain the surface, the user traces 5-15 points on the images at anatomic landmarks such as at valve orifices, the apex of the right ventricle, and along the endocardial surface. The traced points are used to estimate the patient's right ventricle by computing a weighted sum of 3D surfaces from a catalog. The weights are determined by an optimization routine, which minimizes the distance from the user points to the surface[8,9]. The catalog contains reconstructions of the same organ that were generated using the piecewise smooth subdivision method, and that were derived from both normal subjects and patients with a variety of diagnoses. At the time of the present study, however, the catalog contained only 12 right ventricular surfaces.

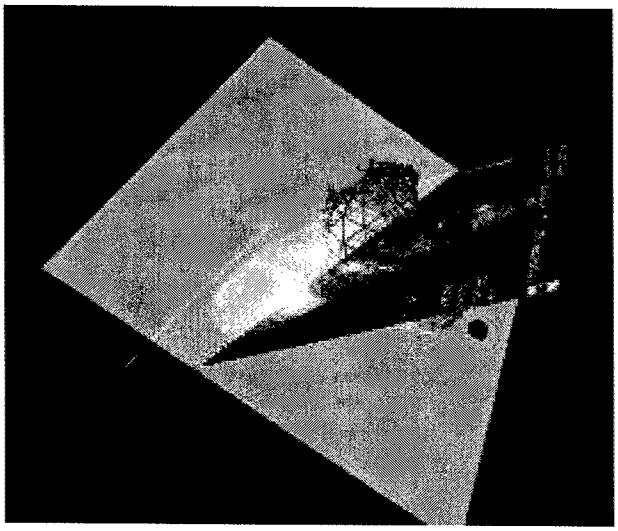

FIGURE 3. A 3D reconstruction of the ventricle is displayed as a triangulated mesh. Here the scout image intersects the mesh in a short axis cut, but the current image plane is so far posterior that it does not appear to be touching the heart.

Evaluation of Visual Guidance

Study Protocol

To test the effectiveness of visual guidance in assisting imaging of the heart, we compared the accuracy of right ventricular volume determined with and without guidance by both untrained and trained users. Since anatomically correct image plane positioning should affect this analysis from 2D methods more than 3D, the test involved identification of the apical four chamber view. Right ventricular area and long axis length were then computed from this view for use in determining volume by the pyramidal method [10].

A medicine resident who had received no prior training in ultrasound imaging, and a registered diagnostic medical sonographer served as the untrained and trained users of visual guidance. They each imaged the right ventricle in five normal subjects with and without guidance. To determine its true volume the sonographer also acquired a full 3D echo study.

Patient Population

The study comprised normal volunteers and patients with heart failure, invited to participate if they had image quality adequate for quantitative analysis, no history of valvular heart disease, sinus rhythm, and no implanted cardiac devices. All subjects gave informed consent. The protocol was approved by the Human Subjects Review Committee at the University of Washington.

RESULTS

Imaging Interface

The guidance system accelerated the rate at which the medicine resident learned to perform scanning by helping her to relate the image to the anatomy. The heart has a complex 3D structure; learning how to manipulate the transducer, to interpret what one is seeing on the images, and where the desired image planes for standard views are located and oriented can be very confusing to the novice. The ability to visualize the current image plane's location relative to the mesh reconstruction proved most useful early on to the untrained user. Surprisingly the line of intersection display was consistently used and indeed was never turned off. We added a new feature – computation of the angle between the current plane and each scout to help the users find orthogonal views.

Another difficulty in cardiac imaging is that the parasternal and apical acoustic windows limit the freedom of the sonographer to search for optimal image quality. Our experienced sonographer found that the guidance system forced her to move the transducer more laterally than expected for the apical views; when displayed relative to the scout images it was obvious that her unguided views tended to be foreshortened.

Volume Accuracy

With calculation of right ventricular volume using a monoplane pyramidal method, the guidance gave our inexperienced physician an error comparable to the results achieved by our experienced, trained sonographer (Table), and comparable to the 16.3% error previously reported using the best 2D method, a biplane pyramidal approach[10].

Table. Error in Determining Right Ventricular End Diastolic Volume* in 5 Subjects.

	Inexperienced		Sonographer	
Method of Determining Right Ventricular Volume	**Unguided**	**Guided**	**Unguided**	**Guided**
Monoplane Pyramidal	33.1	17.0	17.7	18.8

* The mean error is presented as a percent of true volume for comparison with the published study[10] because the latter was performed in pediatric patients and the present study was in adults

DISCUSSION

King et al reported a decade ago that a simple guidance system displaying the current image plane's position as a line-of-intersection with a previously acquired image improved the success with which experienced sonographers achieved optimal image plane position from 32% to 88%. The success at obtaining optimal image plane angle was also improved, from 48% of studies to 92%[6]. The results of the present study suggest that visual guidance can assist not only experienced sonographers but also inexperienced users in diagnostic medical ultrasound imaging. The fact that this assistance was obtained with the right ventricle is particularly pertinent, because imaging the right ventricle is difficult due to its position behind the sternum, providing limited acoustic access.

There are many potential applications of visual anatomic guidance. The first is assisting personnel with limited training and/or experience in acquiring medical ultrasound images of diagnostic quality. The system was initially developed for NASA, but other regions remote from health care such as the battlespace and rural communities may also benefit. We recommend enhancing the capability of visual guidance by enabling experts in a telemedicine facility to review the images live as they are acquired, and to provide directions to the examiner via the visual interface. Such expert guidance would increase the range of application of medical ultrasound while simultaneously improving the quality of health care in underserved populations. The visual interface that we have designed provides the ideal means of communicating expert instructions on transducer manipulation to obtain any additional views that may be desired. Indeed because the interface is visual and non-verbal means that assistance may be rendered even where language differences would pose difficulty under normal circumstances.

Ultrasound is not just for diagnosis; it also has therapeutic applications. The visual guidance tools that have facilitated image acquisition could also be applied to guide the administration of HIFU for hemostasis in casualties and other trauma victims.

Doppler guidance has been shown to increase the speed of hemostasis using HIFU by directing the beam to its most effective orientation[11].

We envision that visual anatomic guidance can also form the technology for an educational tool to assist in the training of ultrasound technicians, physicians, military medical personnel, and rural healthcare providers. Indeed the guidance system could be applied to mimic scanning on a dummy, to display cut planes through stored 3D image data sets as if the trainee were studying a live subject. This type of educational module could be applied to improve the uniformity of medical training as well as provide standardized test sets that enable objective evaluation of skills and proficiency.

In summary, we have developed a software system to provide visual anatomic guidance in acquiring medical ultrasound images. The system has assisted an untrained observer to acquire images of the right ventricle in anatomically well positioned planes, as evidenced by the accuracy of volume determination. The system has many potential applications in health care and medical education.

REFERENCES

1. P.R. Detmer, G. Bashein, T. Hodges, K.W. Beach, E.P. Filer, D.H. Burns, and D.E. Strandness, *Ultrasound Med Biol,* **20**, 923-936 (1994).
2. E.P. Filer, University of Washington: Master's Thesis (1994).
3. F.H. Sheehan, E.L. Bolson, J.A. McDonald, G. Bashein, M.L. Zeppa, and R.W. Martin, *IEEE Computers in Cardiology,* **25**, 649-652 (1998).
4. M.E. Legget, D.F. Leotta, E.L. Bolson, J.A. McDonald, R.W. Martin, X.-N. Li, C.M. Otto, and F.H. Sheehan, *IEEE Trans Biomed Eng*, **45**, 494-504 (1998).
5. M. Hubka, E.L. Bolson, J.A. McDonald, R.W. Martin, B. Munt, and F.H. Sheehan, *Intl J Card Imag* (in press) (2002).
6. D.L. King, M.R. Harrison, D.L. King, Jr, A.S. Gopal, O.L. Kwan, and A.N. DeMaria, *J Am Soc Echocardiogr*, **5**, 569-576 (1992).
7. S.P. Wong, R.K. Johnson, and F.H. Sheehan, *Int J Card Imaging* (in press) (2002).
8. M. Fleute and S. Lavalle, Medical Image Computing and Computer-Assisted Intervention — MICCAI'98 Proceedings, **1496**, 879-887 (1998).
9. T.F. Cootes, University of Manchester (1999).
10. W.A. Helbing, H.G. Bosch, C. Maliepaard, S.A. Rebergen, R.J. van der Geest, B. Hansen, J. Ottenkamp, J.H.C. Reiber, and A. de Roos, *Am J Cardiol,* **76**, 589-594 (1995).
11. R.W. Martin, S. Vaezy, P. Kackowski, G. Keilman, S. Carter, M. Caps, K. Beach, M. Plett, and L. Crum, *Ultrasound Med Biol,* **25**, 985-990 (1999).

Improvement Of Ultrasound Based Temperature Estimation By Compound Imaging

M. Pernot, K. R.Waters, J. Bercoff, M. Tanter and M. Fink

Laboratoire Ondes et Acoustique, ESPCI, C.N.R.S UMR 7587, University Paris VII, Paris 75005, France

Abstract. The feasibility of real-time 2D temperature estimation from pulse-echo diagnostic ultrasound data has been demonstrated by Simon et al (*IEEE Trans Ultrason Ferroelec Freq Contr*, 45, 1998) [1]. This method is based upon the measure of change in backscattered RF-echo due to thermally local changes in the speed of sound and thermal expansion. However it has been shown that ripple artifacts due to the thermo-acoustic lens effect severely corrupts the temperature estimates behind the heated region. We propose a new technique of imaging to improve the temperature estimation behind the heated region. We replace the classical beamforming in the transmit mode by a set of N compounded plane wave illuminations on several subapertures. After estimation of the axial displacement between emissions of identically tilted plane waves, the N two-dimensional temperature maps are averaged, improving the temperature estimation behind the heated region. Experiments have been conducted in a tissue-mimicking, gelatin-based phantom.

INTRODUCTION

In order that high intensity focused ultrasound (HIFU) may be used clinically, it is important to improve monitoring methods of the treatment. A number of thermal imaging techniques have been suggested and investigated such as magnetic resonance imaging [2,3], or impedance tomography, but an ultrasonic system would be of great interest, because of its ability to provide real-time temperature estimates, its portability and its low costs. Several ultrasonic methods have been proposed to estimate the temperature changes in tissue, including changes in the backscattered power [4], frequency dependent attenuation [5], or the combination of the change in speed of sound and thermal expansion [1]. Simon et al proposed a 2D temperature estimation based on tracking the echo shift in the time domain and differentiating the time shifts estimates on the axial direction to obtain a temperature profile. However this method has not been successfully used to measure temperature changes larger than a few degrees. Due to the thermo-acoustic effect [1,6,7], sharp lateral gradients in the temperature distribution introduce ripple on the estimates of the echo shifts, which corrupts severely the temperature estimates behind the heated region. C. Simon et al suggested to introduce spatial filters to get rid of these artifacts. However, the spatial frequency dependence of the ripples and of the temperature focus are of the same kind and are almost impossible to discriminate. We propose here a new technique allowing

to improve the temperature estimates. This method is based on compounding principles. The application of these compounding principles to real-time ultrasound imaging is not new [8,9] and according to the substantial increasing of computational power on modern devices, real time compounding was even recently implemented with success on commercial Philips ultrasound systems [10]. We propose here to apply this compounding technique to the ultrasound based temperature estimation process.

TEMPERATURE ESTIMATION

The time-shifts in the RF echo signals are caused primarily by changes in the speed of sound due to the ultrasonic heating that introduce apparent shifts in the scatterer positions. Physical shifts are also introduced by the thermal expansion of tissue when heating. Simon et al. [1] have derived an expression for the change of temperature $\Delta T(z)$ along the beam axis, taking into account the speed of sound variations and thermal expansion of tissue :

$$\Delta T(z) = \frac{c_0 k}{2} \frac{\partial t(z)}{\partial z} \qquad (1)$$

where t(z) is the time-shift estimated at depth z, c_0 the initial speed of sound in the medium. $k = 1/(\alpha - \beta)$ is a material dependent parameter that can be experimentally determined, α is the linear coefficient of thermal expansion and β the coefficient related to the change in the speed of sound with temperature. In soft tissues typical values are $\beta \sim 1.10^{-3\circ}\ C^{-1}$ and $\alpha \sim 1.10^{-4\circ}\ C^{-1}$.

The time-shifts are estimated by calculating 1D cross-correlation between successive speckles images. In this imaging process time-shifts are accumulated along the beam axis. Therefore the term $\partial t(z)/\partial z$ in (1) corresponds to an apparent stretching in the echo signal due to the thermal effect.

Sharp temperature gradients appear during heating, and the heated region acts like an aberrator [6][7], due to the thermo-acoutic lens effect. As the receiver beamforming algorithm of the imaging system assumes the speed of sound to be constant, it does not compensate for the aberration. Then, when estimating the time-shift, it leads to a decorrelation effect, and ripple artifacts appear in temperature estimates.

COMPOUND IMAGING

In order to improve the temperature estimation behind the heated region, we propose to illuminate successively the medium with ultrasonic plane waves transmitted at different angles. We used a set of N compounded plane wave illuminations with overlapping transmitting subapertures, instead of a conventional beamforming in the transmit mode. Thus, there is no focusing in the transmit mode. This choice was initially made due primarily to the memory limitations of our laboratory imaging system. However, using classical compounding with transmit and receive focusing would also be conceivable.

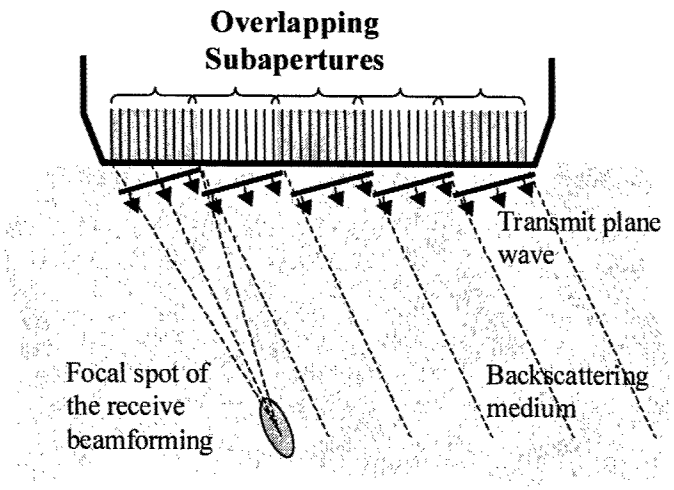

FIGURE 1. Spatial compound image formation.

We are currently limited to a maximum of 31 compound angles. The use of limited transmitting subapertures reduces the region which can contribute to the received ultrasonic echo (Fig 1.). This approach offers significant benefit when transmitting plane waves. As our current system is not able to achieve the receive beamforming in real time, all backscattered echoes are stored in memory during the complete heating process and the beamformation on receive is achieved only in a post-treatment step after the experiment. Thus, the RF data acquisition is real time but the image processing is achieved off-line. While real-time imaging is a future goal, the primary goal of these current investigations however, is to demonstrate the usefulness of compound imaging for temperature estimation. Though the real time implementation of such a technique is fully conceivable, it was not achieved by our system.

In the off-line receive beamforming process, the focal spot is titled with the same angle than the emission angle. We then capture N speckle images corresponding to the same temperature map, but for each compound angle the time-shifts are accumulated in a different direction. The temperature estimates are deduced by correlating and spatially differentiating along the axial direction. An angle correction is included by multiplying by a $\cos(6)$ factor. Once the temperature has been estimated after derivation of the time shift estimates for each compound angle, the temperature estimates are averaged by a correlation-value weighting:

$$< T(x,z) >= \frac{1}{\sum_{n=1}^{N} c_n(x,z)} \sum_{n=1}^{N} c_n T_n(x,z) \qquad (2)$$

where $T_n(x,z)$ is the temperature estimate from the n illumination, $c_n(x,z)$ its corresponding correlation value, and $< T(x,z) >$ is the averaged temperature estimate.

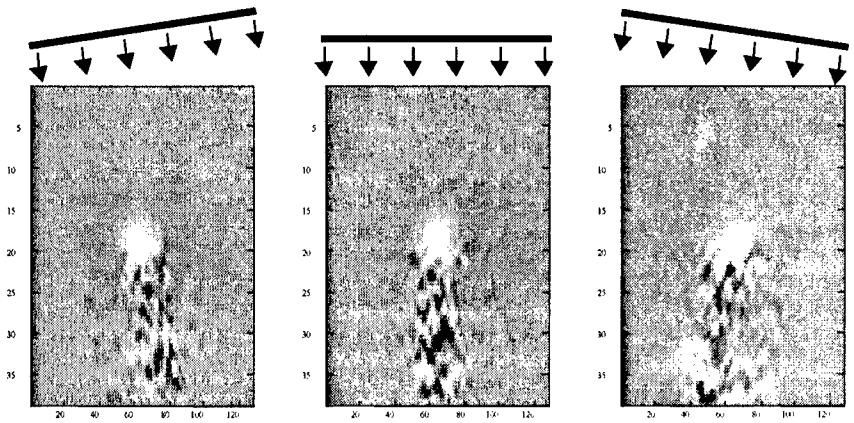

FIGURE 2. Sequence of successive compounded plane waves illuminations (N=3). The imaging array is located at the image top and the heating beam is crossing the image plane according to the setup presented in Fig.3. Transmitted plane waves and temperature estimates for these three different emission angles are shown.

REAL-TIME ACQUISITIONS

The therapeutic system is a 56 elements piezocomposite spherical annular array (1.5 MHz, 100mm diameter, 70 mm focus, 14 annuli). The –6 dB dimension of the therapeutic focus is 1.2 × 1.2 × 7.5 mm^3. The intensity applied at focus in these experiments was varied between 45 and 200 $W.cm^{-2}$. The tissue-mimicking phantom consists of an 8% gelatin gel solution containing 2% agar powder to serve as ultrasonic scatterers. Its thermal and acoustical properties are very similar to those of soft tissues. We determined experimentally the material dependent parameter k = -980° C. Several thermocouples sensors are placed within the phantom to obtain a reference temperature.

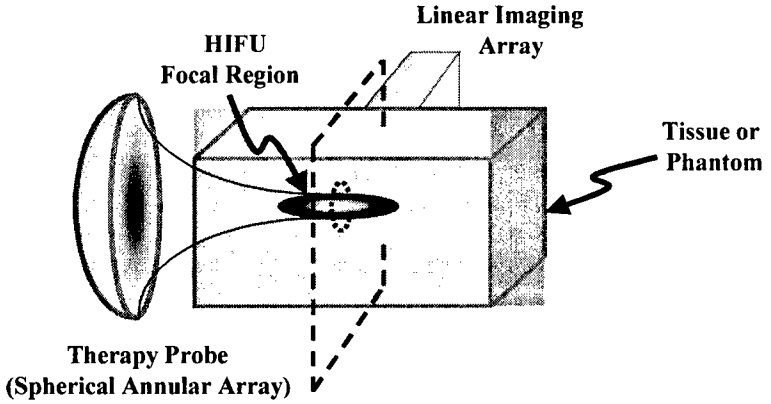

FIGURE 3. Combined imaging/therapy ultrasound system.

In order to compare the compound technique with the results that should be obtained with a classical scanner, we used an HDI 1000 imaging system (Philips ATL, Bothell, WA) that allowed us to record classical beamformed data during the heating process. We achieved the same experiment with our imaging system for compound imaging as we can fully program its transmit emission sequence (the specifications of this system are given in reference [11]). For comparison purposes, the same linear phased array 4-7 MHz could be used with the two imaging systems. Figure 4 presents the temperature estimates performed with the conventional imaging system, and the compound imaging system. One can clearly see the improvement of the temperature estimates behind the focus.

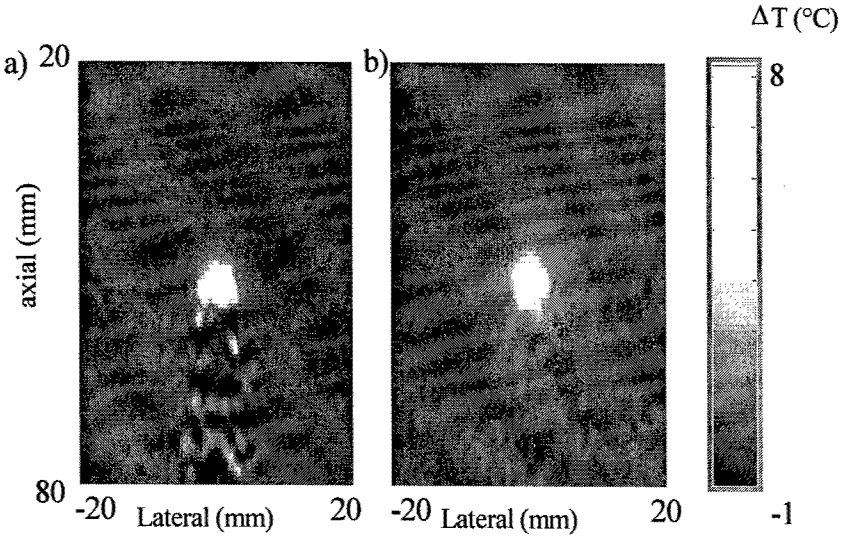

FIGURE 4. 2D Temperature estimates. a) Conventional imaging. b) Compound imaging with N=16 compounded plane wave (-15°<θ<15°, 2° step). Note that 20mm for axial direction corresponds to distance from face of linear array. The intensity applied at focus is 150 W.cm^2.

We have also investigated the dependence of the ripple artifact behind the heated region as the number of compounded plane wave angles and subapertures size are varied. Figure 5. shows how the variance of the ripple artifacts behind the heated region decreases as the number of plane wave increases. The step of the plane wave angles is 1°, and the range of the whole set of 31 angles is [-15°;15°]. A low variance represents a good estimate as the region behind the heated spot should have a relatively uniform distribution. We have also determined that there is a little improvement in the reduction of ripple artifact using more than 5 subapertures (approximately 25 transducer elements).

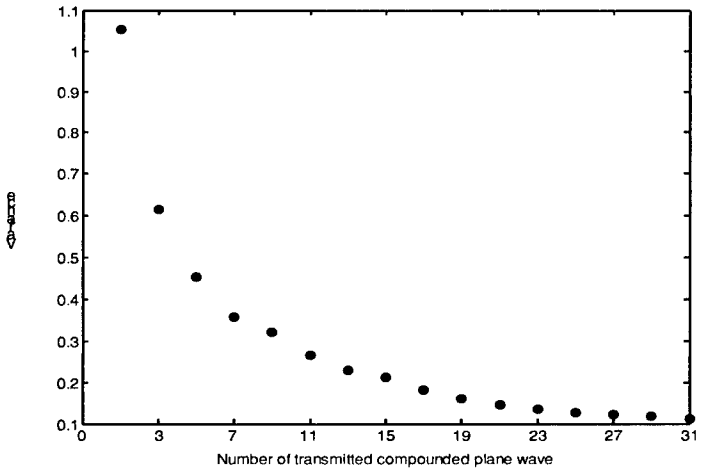

FIGURE 5. Variance of temperature estimation in the ripple artifact as a function of the number of angles with 1° step. Total angle range of the whole set of 31 angles is [–15°;15°]. The variance was determined from a rectangular region-of-interest of 15mm by 15mm directed behind the heated region.

SUMMARY AND CONCLUSION

The use of spatially-compounded plane waves with transmitting subapertures permits significant improvement in the accuracy of the temperature estimation, reducing the ripple artifacts due to the thermo-acoustic lens effect. It was shown that a small number of emitting waves (relative to conventional imaging) is sufficient to reduce significantly the variance of the ripple artifacts in the temperature estimates. The plane waves are recursively emitted every 0.2 ms, which allows to reach very high frame rates. Furthermore, the same compound technique could also be achieved in real time with both transmit and receive focusing. The cross-correlation algorithm used to estimate the time-shifts could be rapidly computed, allowing to perform real-time corrected temperature estimation. However motion artifacts during *in vivo* measurements, especially those related to respiration, have to be considered. Several techniques have been proposed to correct these decorrelation effects [12] that could be combined with this compounding process.

REFERENCES

1. Simon, C., VanBaren, P., and Ebbini, E., "Two-dimensional temperature estimation using diagnostic ultrasound," *IEEE Trans Ultrason. Ferroelec. Freq. Contr.*, **45**, 1088-1099, (1998).
2. De Zwart, JA, Van Gelderen, P, Kelly, DJ, Moonen, CT, "Visualization of MR-Compatible Catheters by Electrically Induced Local Field Inhomogeneities: Fast Magnetic-Resonance Temperature Imaging, " *J Magn Reson,* **112**, 86-90 (1996).
3. Hynynen, K., Chung, A., Fjield, T., Buchanan, M., Daum, D., Colucci, V., Lopath. P., and Jolesz, F., "Feasibility of using ultrasound phased arrays for MRI monitored noninvasive surgery," *IEEE Trans Ultrason. Ferroelec. Freq. Contr.*, **43**, 1043-1053, (1996).

4. Straube, W., and Arthur, R., "Theoretical estimation of the temperature dependence of backscattered ultrasonic power for noninvasive thermometry," *Ultrasound Med. Biol.*, **20**, 915-922 (1994).
5. Ueno, S., Hashimoto, M., Fukukita, H., Yano, T., "Ultrasound thermometry in hyperthermia," *IEEE Ultrason. Symp.*, (1990).
6. Floch, C., and Fink, M., "Ultrasonic mapping of temperature distribution in hyperthermia : the thermal lens effect," *IEEE Ultrason. Symp.*, (Oct 1997).
7. Le Floch C., Tanter, M., Fink, M., "Self defocusing in Hyperthermia: Experiments and simulation," *Appl. Phys. Lett.*, **74** (20), 3062-3064 (1999).
8. Berson, M., Roncin, A., Pourcelot, L., "Compound Scanning with an Electrically Steered Beam", *Ultrasonic Imaging*, **3**, 303-308 (1981).
9. Jespersen, S.K., Wilhjelm, J.E., Sillesen, H., "Multi-angle Compound Imaging," *Ultrasonic Imaging*, **20**, 81-102 (1998).
10. Entrekin, R., Jackson, P., Jago, J.R., and Porter, B.A., "Real Time Spatial Compound Imaging in breast ultrasound: technology and early clinical experienc," *MedicaMundi*, **43**, 3 (Sept. 1999).
11. Sandrin, L., Tanter, M., Catheline, S., Fink, M., "Shear Modulus Imaging using 2D transient elastography," *IEEE Trans. Ultrason., Ferroelec., Freq. Contr.* **49** (4), 426-435 (2002).
12. Simon, C., VanBaren, P., and Ebbini, E., "Motion compensation algorithm for non-invasive two-dimensional temperature estimation diagnostic pulse-echo ultrasound," *SPIE Bios*, (1998).

3. SIMULATION AND MONITORING

Radiation-Force Motion Technique For Monitoring HIFU Exposures

Frederic L. Lizzi, Cheri X. Deng, Robert Muratore, Jeffrey A. Ketterling, S. Kaisar Alam, and Samuel Mikaelian

Riverside Research Institute
156 William Street, New York, NY 10038

Abstract. Motion induced by acoustic radiation force is being investigated for aiming high-intensity focused ultrasound (HIFU) beams and evaluating thermal lesion production. Radiation force is exerted by a 1-5 ms exposure from the HIFU therapy transducer (4.5 MHz). The duration and intensity of this "push" pulse are selected to induce local tissue motion without producing damage. A co-linear diagnostic transducer (7.5 MHz) is used to digitally acquire pre-push M-mode data that documents the initial positions of tissue constituents. M-mode data are also acquired immediately following the push pulse, and cross-correlation algorithms are used to quantify the magnitude and time-course of tissue displacement. The HIFU transducer then delivers a high-intensity pulse designed to produce a focal thermal lesion. M-mode observations and push-pulse procedures are then repeated to detect alterations in tissue motion that occur because of the altered elastic properties in lesioned tissue. A laboratory system with digital control and data acquisition has been implemented to evaluate this technique. Measurable local displacements (e.g., 50 μm) were readily produced in *in-vitro* liver specimens without tissue damage, and results indicate a potential for detecting lesions that may not be evident with B-mode examinations. Acoustical, mechanical, and signal-processing simulation studies have been conducted to evaluate several important topics for the design of a system to be used in *in-vivo* experiments. These topics include exposure parameters, HIFU and diagnostic beam widths, and signal-processing algorithms. Supported in part by CA84588 awarded by the National Cancer Institute and the National Heart, Lung and Blood Institute.

INTRODUCTION

The past few years have witnessed a resurgence of interest in employing intense focused ultrasound beams for non-invasive treatment of disease. Many applications involve the induction of thermal necrosis to treat tumors in, for example, the liver and breast [1,2]. A sequence of treatment sites is employed to rapidly elevate temperatures to tumoricidal levels, before uncertainties are introduced by blood flow cooling.

In these applications, monitoring of induced effects is of primary importance. At very large exposure levels, severe lesions are produced with the formation of small gas bodies, due to vaporization, degassing, or cavitation [3]. Such lesions are readily detected with conventional ultrasonic imaging. However, severe lesions are not desired in most applications, because they interfere with propagation of the therapy beam, limiting areas that can be treated at distal sites in the tumor.

Milder lesions, involving thermal necrosis, can be produced at smaller exposure levels. These are preferred for most applications but, unfortunately, they are not well

visualized with conventional ultrasound. A variety of techniques have been explored to detect these lesions. For example, ultrasonic techniques have been designed to detect the increased acoustic attenuation that has been in such lesions. [4] Off-line elastography has been used to detect stiffness increases associated with thermal lesions [5]. A dual-beam technique has also been investigated to detect the increased stiffness of such lesions by evaluating stimulated acoustic emission [6].

As part of a larger program, our laboratories have been examining a non-invasive method to detect lesions by comparing evaluations of tissue stiffness before and after therapy exposures. As in the diagnostic-ultrasound method described by Nightingale *et al*, [7] we employ radiation pressure to induce internal tissue motion, and characterize induced displacements with pulse-echo correlation algorithms. However, our system is designed specifically for therapy applications: it uses the therapy transducer to generate displacement, and it measures displacement with a separate diagnostic transducer, usually employed for aiming the therapy beam.

This report briefly describes the principle of operation of our technique, presents initial simulation and experimental results, and identifies several issues that must be clarified for reliable, practical use of the method to monitor lesion production.

PRINCIPLES OF OPERATION

The principle-of-operation of our technique is illustrated in Fig. 1. The current transducer assembly comprises a PZT spherical-cap therapeutic transducer with a focal length of 90 mm and an outer diameter of either 40 or 80 mm. This high-intensity transducer is usually operated at its third harmonic, 4.5 MHz. As in our previous reports [8], the therapy transducer has a central 20-mm aperture that houses a colinear focused diagnostic transducer (7.5 MHz center frequency). This broadband transducer has a 60-mm focal length and a 12.5-mm diameter; in previous applications, it was used to position the focus of the therapy transducer within the target tissue.

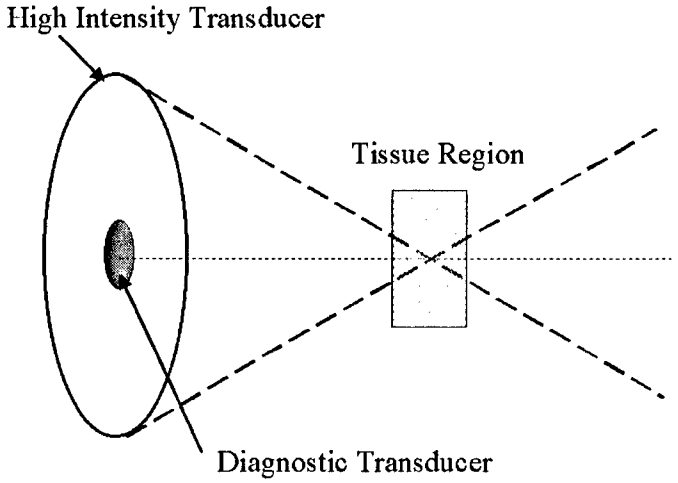

FIGURE 1. Schematic of transducer configuration.

In the current radiation-force techniques, a sequence of produces is used to assess tissue stiffness. First, radio-frequency (RF) echo signals from the target tissue are digitally acquired with the diagnostic transducer. This A-mode signal is digitally stored to effectively document the initial position of tissue scatterers along the transducer's propagation axis.

Then, the therapy transducer delivers a relatively short (e.g., 1 ms) "push" pulse, which produces a corresponding radiation force in the tissue. The force induces tissue displacements that depend on the spatial intensity distribution of the beam, tissue elastic properties (Young's modulus and Poisson's ratio), and exposure time.

Immediately after this pulse, the diagnostic transducer is again excited to acquire a temporal sequence of RF data used to evaluate tissue displacement and return to initial positions. These evaluations are based on cross-correlation algorithms that compare the initial pre-push RF echoes to corresponding post-push RF data [9].

In monitoring lesion production, the above sequence of procedures is executed immediately prior to therapy in order to establish the properties of untreated tissue. The therapy transducer then delivers a high-intensity pulse with a longer duration (1-5 s), designed to produce a thermal lesion. The sequence of radiation-force steps is then repeated to characterize stiffness changes induced by the therapy exposures; the size and location of these changes are used for monitoring induced lesions.

EXPERIMENTAL SYSTEM AND ILLUSTRATIVE RESULTS

The procedures described above have been implemented by interfacing the transducer assembly of Fig. 1 with an initial laboratory control and exposure system. The system computer controls and synchronizes all operations using custom LabVIEW software. It triggers a Panametrics 5400 pulser/receiver to obtain diagnostic echo signals and an Acquiris DP-11D board to digitize RF echo data. Typically, 8-bit digitization is performed at a sampling rate of 500 MHz. The computer also controls push and therapy exposures by means of a programmed signal generator (Agilent 33250A) connected to the therapy transducer via an ENI power amplifier. Acquired RF data are currently processed off-line using cross-correlation algorithms.

This system has been calibrated and employed in initial *in-vitro* experiments to determine whether it provides the required sensitivity and reliability to induce and measure motion in normal tissue and to detect alterations induced by thermal-necrosis lesions.

The results in Fig. 2 show preliminary data obtained in *in-vitro* liver. To generate the push pulse, the therapy transducer (40-mm diameter) was operated at 4.5 MHz with a free-field focal-point intensity of 3.7 kW/cm^2; a 5-ms push pulse, focused 1-cm below the tissue surface, was employed. The subsequent treatment exposure was generated with the same transducer using a 1-s exposure. In both untreated and treated cases, RF data were acquired immediately before and after the push pulse.

The results of Fig. 2 show displacement estimates at the focal point of the therapy transducer; motion was successfully produced and measured in both untreated (no lesion) and treated cases. The peak motion in the untreated case was near 15 μm, and

motion returned to its initial position within about 2 ms. After lesion production, the induced peak motion was decreased by 6 μm to 60% of its pretreatment value; as discussed below, this is consistent with increased lesion stiffness.

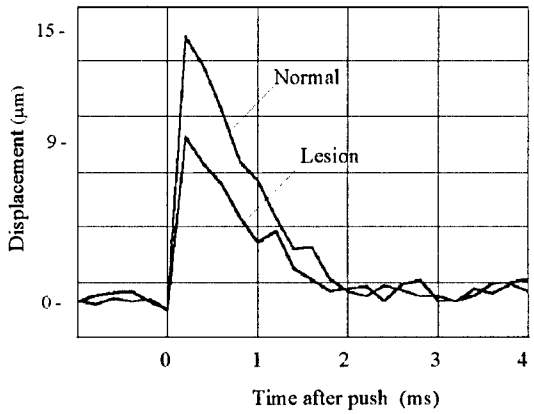

FIGURE 2. Measured focal-point displacements in *in-vitro* liver specimens following 5-ms push pulse (not indicated) prior to 0 on time axis.

DESIGN TOPICS AND APPROACHES

The preceding sections summarized the principles and feasibility of the radiation-force technique for monitoring thermal-necrosis lesions. However, a number of key design issues must be addressed if the full potential of this method is to be realized. The parameters selected for the push exposure are of primary importance; these pulses must induce motion without producing collateral thermal changes. Key design issues relate to the role of the push beamwidth in determining the spatial extent and time course of tissue motion. The properties of the diagnostic transducer are also of central importance; in particular, it is important to understand how the bandwidth and the beamwidth of the diagnostic transducer influence the ability to obtain precise estimates of small displacements that are confined to narrow spatial regions.

To address these and other issues, we have implemented a comprehensive array of simulation algorithms that emulate all of the key exposure and estimation procedures involved in the radiation-force technique. The following sections provide a summary overview of these simulations and present illustrations of initial results that are relevant for system design.

Synopsis Of Simulations

The simulations we employ are schematically diagrammed in Fig. 3. The free-field beam patterns of therapy and push beams are calculated using numerical integration procedures to evaluate the Rayleigh-Sommerfield diffraction equation. These beams are then "aimed" at target tissues using relevant attenuation coefficients to calculate

in-situ intensity fields. A pair of custom simulation packages is then employed to calculate the heat and mechanical effects of these *in-situ* beams. Temperature is calculated by determining absorbed doses and numerically evaluating the bioheat equation; these thermal simulations follow methods described in [10] except that we now evaluate the bioheat equation using flexible finite-difference algorithms. Induced tissue motion is calculated from *in-situ* intensities $I(\underline{x})$ by computing the mechanical force function $\alpha I(\underline{x})/c$ where α is the local absorption coefficient and c is the velocity of propagation; finite-difference methods are then used to evaluate the equations of motion in elastic media using the above force function. Currently, we treat only beams and tissues that exhibit radial symmetry about the beam's central axis.

Motion sensing is simulated using Field II. Tissues are modeled as randomly situated point scatterers. The diagnostic beam is then modeled using transducer parameters with pulse characteristics (7.5-MHz center frequency; 3-MHz bandwidth) representative of those measured for our experimental system. First, pre-push A-mode RF signals are calculated. Then, the point scatterers are effectively repositioned according to the axial and lateral displacements computed in our radiation-force simulations, and the corresponding post-push RF echoes are recomputed. Displacement estimates are then simulated by analyzing these RF echo signals with the same cross-correlation procedures used with our experimental system.

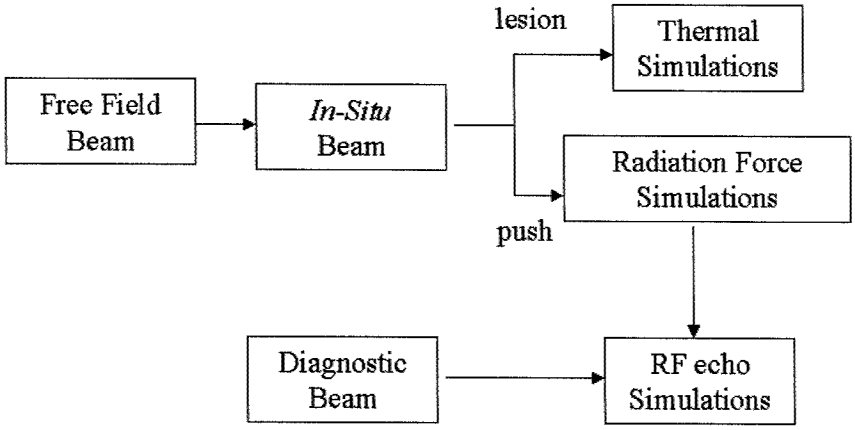

FIGURE 3. Overview of simulations for radiation-force displacement technique.

Illustrative Simulation Results

Figure 4 shows simulation results for the axial displacement induced by the 80-mm diameter therapy transducer using a 5-ms pulse and a free-field focal-point intensity of 1 kW/cm^2. The central displacements (along the beam's center line) are shown for two cases. The solid curve represents results for a 3-cm liver specimen with a Young's modulus of 1.2 kPa, an attenuation coefficient of 0.5 dB/cm-MHz, and an absorption coefficient of 0.375 dB/cm-MHz. As in all cases, the distal surface of the specimen was treated as a fixed surface. The transducer was focused on the center of

the specimen and the plot shows displacement at the end of the 5-ms pulse. The dashed curve in Fig. 4 are results when a simulated ellipsoidal lesion was included in the center of the above liver specimen; the lesion's axial length was 8 mm and its diameter was 2 mm. The lesion's acoustic properties were set to equal those of liver, but its Young's modulus was increased to 6 kPa. In both cases Poisson's ratio was equal to 0.495 and the transducer was focused at the center of the specimen.

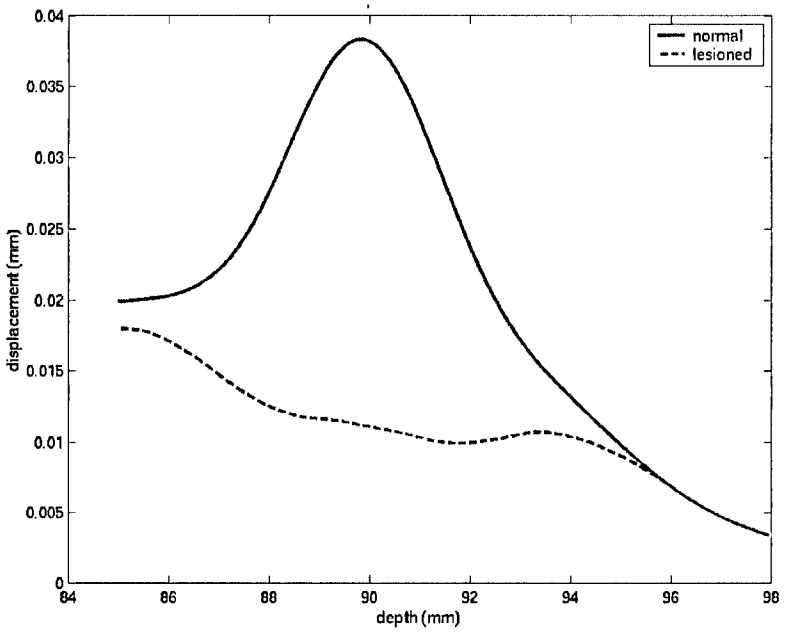

FIGURE 4. Simulation results for displacements along axis of 80-mm transducer focused at 90-mm depth.

The axial displacement in the normal case is seen to exhibit a maximum near 37.5 μm at the focal point (90-mm) of the push beam. The second case shows lowered displacement in the lesion. At the focal point, the displacement is lowered to about 10 μm.

Figure 5 plots results corresponding to those of Fig. 4 but pertain to a 5-ms push exposure generated by the 40-mm diameter therapy transducer at a free-field focal-point intensity of 345 W/cm^2. Again, motion in the normal tissue (solid curve) is larger than that observed for the lesion case (dashed curve).

Figure 6 plots the time course of displacement at the center of the specimen (focal point of the push beam) for the normal (solid) and lesion (dashed) cases using the 40-mm transducer (as in Fig. 5). During the push pulse, these are seen to be quasi linear. The corresponding temperature rise is plotted in Fig. 6b. It also shows a linear rise with a peak that is less than 0.1° C. A very slow recovery towards ambient temperature occurs following the pulse.

Simulations of RF data and cross-correlation displacement estimates were conducted for the above cases. For the narrow-beam 80-mm transducer, the estimated

focal-point displacement in normal liver was 20% lower than the results of Fig. 4. The lesion results were within 10% of the focal point displacement shown in Fig. 4.

For the broad-beam 40-mm transducer, the displacement estimates were within 5% for both normal and lesion cases shown in Fig. 5.

Further theoretical analysis has shown that the disparity in displacement estimates is due to the beamwidth B of the diagnostic transducer compared to the lateral width W of the induced displacement (assumed to be a Gaussian function of off-axis distance). For example, when the ratio W/B is two, the estimated displacement is only about 20% of its axial value.

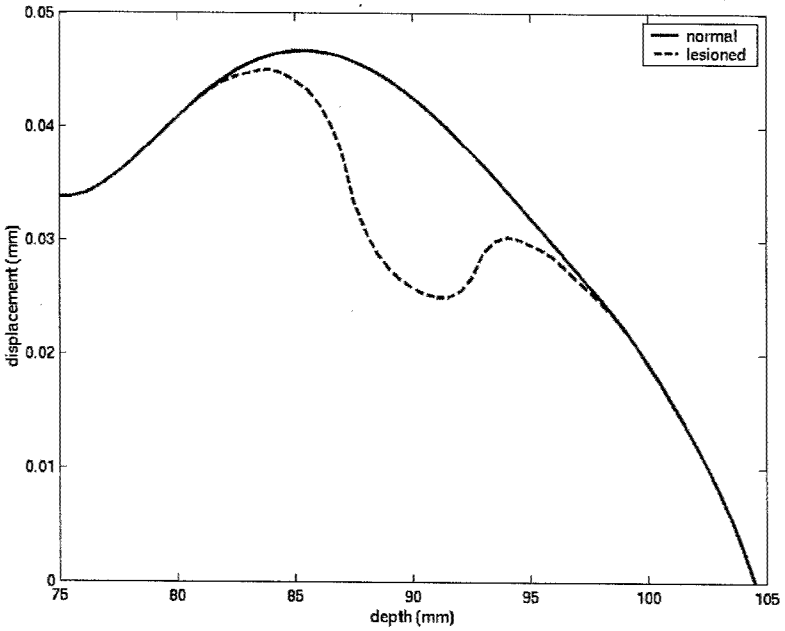

FIGURE 5. Simulation results for displacements along central axis of 40-mm transducer focused at 90-mm depth.

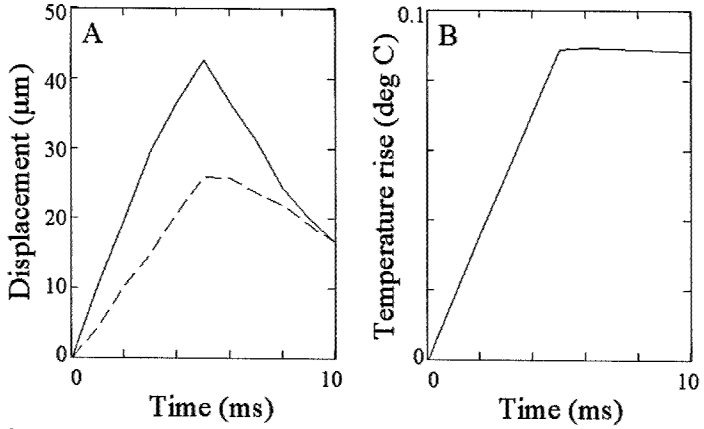

FIGURE 6. Computed displacements (left) and temperature rise (right) at focal point of 40-mm transducer. (Dashed curve is for lesion case.)

DISCUSSION

Our initial experimental and simulation results support the feasibility of using the radiation-force displacement method for monitoring thermal lesions produced by intense ultrasound.

The results in this report illustrate several conclusions consistent with our broader on-going studies. They indicate detectable motion can be produced with short (ms) pulses at intensities that produce low temperature rises. They also show that while temperature rises are small, their slow recovery times may limit the repetition of push pulses that can be tolerated without significant thermal changes in propagation speeds.

Other of our results indicate that the width of the push beam exerts an influence on the rise-times of induced displacements. Narrow beams produce short displacement rise-times compared to broad beams. This beamwidth also affects the accuracy of displacement estimates made with the diagnostic transducer. If the push beam is much narrower than the diagnostic beam, the narrow displacement pattern can lead to significant underestimation of peak displacement values.

We are currently pursuing these studies to develop a system specifically designed to incorporate this lesion-monitoring concept. Towards this goal, we are expanding our simulations and experimental studies and have initiated *in-vivo* liver experiments.

ACKNOWLEDGMENTS

Supported in part by grant CA84588 awarded by the National Cancer Institute and the National Heart, Lung, and Blood Institute. The authors wish to thank A. Kalisz and R. Raskin for their diligent assistance in preparing this manuscript.

REFERENCES

1. Hill, C.R., and ter Haar, G.R., *Br. J. Radiol.*, **68**, 1296-1303 (1995).
2. Hynynen, K. et al., *Med. Phys.*, **20**, 107-115 (1993).
3. Lizzi, F.L., *European Urology*, **23**, 23-28 (1993).
4. Damianou, C.A., Sanghvi, N.T., Fry, F.J., and Maass-Moreno, R., *J. Acoust. Soc. Am.*, **102**, 628-634 (1997).
5. Righetti, R., Kallel, F., Stafford, R.J., Price, R.E., Krouskop, T.A., Hazle, J.D., and Ophir, J., *Ultrasound Med. Biol.*, **25**, 1099-1113 (1999).
6. Fatemi, M., and Greenleaf, J.F., *Science* **280**, 82-85 (1998).
7. Nightingale, K.R., Palmer, M.L., Nightingale, R.W., and Trahey, G.E., *J. Acoust. Soc. Am.*, **110**, 625-634 (2001).
8. Burgess, S.E.P., Silverman, R.H., Coleman, D.J., Yablonski, M.E., Lizzi, F.L., Driller, J., Rosado, A., and Dennis, P.H., Jr., *Ophthalmology*, **93**, 831-838 (1986).
9. Walker, W.F., and Trahey, G.E., *IEEE Trans. Ultrason. Ferroel. Freq. Contr.*, **42**, 301-308 (1995).
10. Lizzi, F.L., Driller, J., Lunzer, B., Kalisz, A., and Coleman, D.J. *Ultrasound Med. Biol.*, **18**, 59-73 (1992).

Parameter Space Investigation For Optimal Thermal Lesion Generation in Noninvasive HIFU Applications

Francesco P. Curra, Steven G. Kargl, and Lawrence A. Crum

Center for Industrial and Medical Ultrasound, Applied Physics Laboratory, University of Washington, 1013 NE 40th St., Seattle, WA 98105

Abstract. Ultrasound can safely penetrate deeply into soft tissue. Several programs are currently underway to exploit this ability for purposes of noninvasive therapies and surgery. In this work, we describe the effects of high intensity focused ultrasound (HIFU) transducers in producing necrotic regions in tissue as predicted by a comprehensive acoustic and thermal numerical model. We focus our attention to optimize lesion generation as correlated to three main parameters: 1) total acoustic power applied per unit time (or total treatment time), 2) transducer's f-number, and 3) transducer's operational center frequency. These parameters are directly correlated to the amount of acoustic nonlinearity and generation of higher harmonics in the signal, as well as with augmented power absorption by the medium; both of which are fundamental parameters in determining the shape and size outcome of the HIFU-generated lesion. Optimization is ranked in terms of greatest treated volume per minimum treatment time by well-controlled, noninteracting adjacent lesions. Results are reported in the form of a three-dimensional parameter space whose points coordinates indicate the best possible treatment protocol for the specified parameters.

INTRODUCTION

Since the pioneering work of Fry [1], numerous *in vitro* and *in vivo* experimental studies have investigated the effects of high intensity focused ultrasound (HIFU) on soft tissues (see [2] and the citations therein). Conceptually, soft tissue absorbs a portion of the acoustic energy, which results in a heating of the tissue. The rate of heating and the temperature in the tissue are largest in the vicinity of steep gradients in the acoustic intensity. Hence, the heating is localized near and at the focus of a focused acoustic source. Under certain conditions, this heating causes coagulative necrosis of the tissue, and the volume of necrotic tissue is often referred to as a "thermal lesion."

Many researchers have previously discussed theoretical and numerical simulations of nonlinear wave propagation in a biological medium and the formation of thermal lesions [3, 4, 5]. Within the last few years computational facilities have permitted the simulation of HIFU in a heterogeneous biological media. Curra has developed a theoretical model linking a full-wave nonlinear acoustic wave model with a bio-heat transfer equation (BHTE) [6]. This model is briefly described below.

MODEL EQUATION AND NUMERICAL METHOD

The equations that describe nonlinear acoustics are a full-wave model, which includes quadratic nonlinearity and relaxation processes. The model equations were derived by Curra [6] and may be written as

$$\frac{\partial \mathbf{v}}{\partial t} = -\frac{1}{\rho_0}\nabla p, \tag{1}$$

$$\frac{\partial p}{\partial t} = -\frac{1}{K_\infty}\left[1+2\beta\left(K_\infty p+\sum_{i=1}^{N} S_i\right)\right]\nabla\cdot\mathbf{v} - \frac{\mathbf{v}\cdot\nabla\rho_0}{\rho_0 K_\infty} - \frac{1}{K_\infty}\sum_{i=1}^{N}\left(\frac{K_i}{\tau_i}p - \frac{1}{\tau_i}S_i\right), \tag{2}$$

$$\frac{\partial S_i}{\partial t} = \frac{K_i}{\tau_i}p - \frac{1}{\tau_i}S_i. \tag{3}$$

Equation (1) is Euler's equation for an ideal inviscid fluid where p and $\mathbf{v}$ are the fluctuations of the pressure and particle velocity about their equilibrium values. The ambient density is ρ_0 and it may have spatial dependence. The viscous terms for a Newtonian fluid that usually appear in a momentum equation have been dropped because attention in biological media does not exhibit the frequency-squared power law. Equation (2) combines the continuity of mass and a Taylor series expansion of the equation of state for the medium. In the derivation leading to Eq. (2), the product of the compressibility of the fluid, K, and acoustic pressure, p, has been replaced by a time convolution operation [7], i.e., $Kp \rightarrow K \star p$. The time convolution operation can be numerically expensive, so the model is further reduced by the introduction of N independent state variables [8]. The evolution equation for the ith state variable, S_i, is given in Eq. (3). Attenuation is described by relaxation processes such that τ_i and K_i are the relaxation time and compressibility for the ith process. Finally, K_∞ and $\beta = 1 + B/2A$ are the frozen compressibility of the fluid and the coefficient of nonlinearity (B/A is the parameter of nonlinearity).

The formation of a thermal lesion is modeled by the bio-heat transfer equation, originally developed by Pennes [9], and the thermal dose [10]. Expressions for the BHTE and thermal dose are

$$\rho_0 C_p \frac{\partial T}{\partial t} = \nabla\cdot(K_T\nabla T) - wC_p(T-T_\infty) - \rho_0 C_p \mathbf{v}_b\cdot\nabla T + Q + Q_m, \tag{4}$$

$$TD_{43} = \int_0^t C^{[43-T(t)]}dt, \tag{5}$$

where ρ_0 is again the ambient density of the tissue and T is the temperature. The thermal conductivity and specific heat at constant pressure are K_T and C_p. The second term on the right-hand side of Eq. (4) accounts for the loss of heat via perfusion of the tissue. The perfusion constant for a given tissue is w and T_∞ is the background temperature. Physically, the blood-filled capillary bed and surrounding tissue are assumed to instantaneously equilibrate. The third term accounts for advection in large blood vessel (if present) where the blood is moving with a velocity of $\mathbf{v}_b$. The final two terms are sources of heat due to the acoustic field, Q, and metabolic processes, Q_m. Metabolic heat sources are usually negligible in comparison to the HIFU induced source and hence

Q_m is dropped from Eq. (4). The HIFU source is

$$Q = -\nabla \cdot \mathbf{I} \tag{6}$$

where $\mathbf{I} = \langle p\mathbf{v} \rangle$ is the time-averaged acoustic intensity vector. Once the temperature has been obtained from Eq. (4), the thermal dose is computed via Eq. (5), where $C = 0.25$ for $T < 43°$ C and $C = 0.5$ for $T \geq 43°$ C. Equation (5) provides a measure of the temperature exposure of the tissue, and necrosis occurs at a thermal dose exceeding 120 minutes at 43° C.

The numerical solution of Eqs. (1)–(3) implements three algorithms. First, the spatial derivatives are computed via a FFT-based pseudospectral method (PSM) [11]. Standard radix-2 or prime number FFT algorithms provide rapid computation and the spatial derivatives are approximated with a very high order of accuracy. One disadvantage of the PSM is a signal leaving one edge of a computational domain re-enters the domain at the other edge. The perfectly matched layer (PML) algorithm [12, 13] is a generalized absorbing boundary condition, which virtually eliminates the wrap around of a signal at any angle of incidence with the boundary. Our PML algorithm is based on the recent work of Chew *et al.* [14]. The final algorithm involves the computation of the temporal partial derivatives on the left-hand sides of Eqs. (1)–(3) via a fourth-order Adam-Bashford (AB4) method on a staggered time grid [15]. The algorithm proposed by Ghist *et al.* yields a domain of stability domain 3 time larger and a error estimate nine times smaller than a standard AB4 method.

The characteristic time and length scales of thermal diffusion are much larger than those of the nonlinear acoustic process, which suggests standard numerical methods are applicable. A second-order explicit finite difference (FD) algorithm was implemented for the spatial derivatives in Eq. (4). This FD algorithm was much faster than the FFT-based derivatives of the PSM. The partial time derivative is computed via a third-order Adam-Bashford algorithm.

A final detail of the numerical implementation involves the relaxation time and compressibility for the ith relaxation process. The available data on absorption of ultrasound in biological media are typically expressed as frequency-power law attenuation coefficients, $\alpha = a(f/f_0)^b$ where f_0 is a convenient reference frequency. Table 4.16 in Duck [16] lists the a and b coefficients for several tissue types over specified frequency ranges. Nachman *et al.* [17] have obtained expressions for the frequency-dependent phase velocity and attenuation coefficient within a relaxing medium, which can be written as

$$c^2(\omega) = \frac{(2/\rho_0)}{[f_1^2(\omega) + f_2^2(\omega)]^{1/2} + f_1(\omega)}, \tag{7}$$

$$\alpha^2(\omega) = (2/\rho_0)\omega^2\{[f_1^2(\omega) + f_2^2(\omega)]^{1/2} - f_1(\omega)\}, \tag{8}$$

where

$$f_1(\omega) = K_\infty + \sum_{i=1}^{N} \frac{K_i}{1+\tau_i^2\omega^2}, \quad f_2(\omega) = \sum_{i=1}^{N} \frac{K_i\tau_i\omega}{1+\tau_i^2\omega^2}. \tag{9}$$

Two relaxation processes were sufficient for the frequency range of our study. Equation (8) was introduced into a constrained nonlinear least squares algorithm to determine the τ_i and K_i. The constraints were $c(\omega) = c_0$, $a(\omega) = \alpha_0$, and $\mathbf{x} \geq 0$ such that c_0 and α_0 are the phase velocity and attenuation at f_0 and $\mathbf{x}$ is a $2N$-dimensional vector of the τ_i and K_i coefficients.

RESULTS

The parameter space investigation of the formation of thermal lesions in noninvasive HIFU applications requires a selection of a set parameters. In our study, we concentrated on the frequency, exposure rate (acoustic power applied per unit time), and the f-number of the transducer because these parameters can be precisely controlled in an experimental or clinical setting. Variations in the material parameters were not considered in this study because we were interested in design criteria for a HIFU device. Once the parameters for a HIFU device have been selected, then a parameter space study in variations of the tissue parameters would be appropriate. That is, for a given HIFU device, variations in the tissue will provide the statistical variations in the formation of a thermal lesion (e.g., volume and displacement from the designed focus).

The HIFU source was modeled as a spherically focused, cylindrical traducer with a diameter of 20 mm. The f-number, the ratio of focal length to diameter, was set to 1, 1.5, and 2, which correspond to a geometric focus of 20, 30, and 40 mm, respectively. The frequency was set to 3, 4, and 5 MHz in the simulations. The applied acoustic power is proportional to the amplitude of the pressure at the transducer. Simulations were performed with $p_0 = 125$, 250, and 500 kPa. These pressure amplitudes and an f-number of one yield peak time-averaged intensities of approximately 200, 825, and 4100 W/cm^2, which span the range of values reported in the literature [2]. The last parameter investigated the duty cycle of an exposure condition for a fixed total acoustic power.

All simulations were conducted in a horizontally stratified biological medium. The propagation path includes a short (h = 6 mm) water stand-off, a layer of skin (3 mm), a layer of fat (7 mm) and muscle. The computation domain was truncated at a total depth of 50 mm from the HIFU source. Table 1 summarizes the material parameters assumed for each medium [16]. Of the parameters listed, the attenuation coefficient for skin indicates that skin will readily absorb acoustic energy and hence it may be susceptible to burning (depending on the HIFU exposure).

Figure 1 depicts the results of several numerical simulations. The time-averaged intensity is shown in Figs. 1(a)–(c) and the corresponding heat rated, given by Eq. (6), is shown in Figs. 1(d)–(f). The vertical lines indicate the interfaces that separate adjacent tissues. Each panel depicts the results of nine different simulations, (i.e., the combinations of three frequencies and three f-numbers). Clearly, the peak values in $\mathbf{I}$ and Q are achieved with an f-number of one. This implies that a thermal lesion can be created by a HIFU device with an smaller f-number with a shorter exposure time than by a device with a larger f-number at an equivalent exposure time. As expected, the full-width at half-maximum is much smaller for the HIFU devices with smaller f-numbers. In Figs. 1(a)–(c), peaks in $\mathbf{I}$ and Q for the 5 MHz signal exceed the peaks for 4 MHz, which

TABLE 1. Material parameters for the media in the path of propagation from the transducer to the focus.

Medium	c_0	ρ_0	B/A	α_0*	b	h
	m/s	kg/m^3		Np/m		mm
water	1500	1000	5.17	0.02	2.0	6
skin	1590	1100	7.87	28.0	1.0	3
fat	1430	928	10.0	7.0	1.1	7
muscle	1570	1040	7.5	6.4	1.0	34

* Reference frequency of $f_0 = 1$ MHz.

exceed the peaks at 3 MHz. This is a consequent of the relatively short distance and the frequency-dependent attenuation coefficient. For deeper penetration the predicted **I** and Q are comparable for the three frequencies.

Figure 2 shows the temperature along the acoustical axis of a transducer with a $f_0 = 3$ MHz signal, an f-number of one, and $p_0 = 500$ kPa. In the left panel, the HIFU was applied for 1 second and the temperature evolution, via Eq. (4), was tracked for four seconds. The right panel shows a total exposure of 1 second, but the exposure was done with a 25% duty-cycle (i.e., 0.25 s "on" time versus a 0.75 s "off" time). Hence, the total applied acoustic power is the same in each panel. A comparison of the images clearly shows a significant increase in the temperature in the skin layer and an accumulation of heat at the interface separating the fat and muscle layers. The thermal dose, Eq. (5), predicts that a thermal lesion will occur in the skin and to a lesser degree at the fat–muscle interface (not shown) while no lesions occur at these locations under the exposure conditions of the right panel. The thermal dose also predicts an ellipsoidal thermal lesion at the focus with an approximate axial length of 6 mm and width of 2 mm for the right panel conditions. Under the exposure conditions of the left panel, the thermal lesion at the focus is no longer ellipsoidal; rather the lesion is starting to advance towards the HIFU source with its proximal end flattening to give a bullet-shaped cross-sectional area.

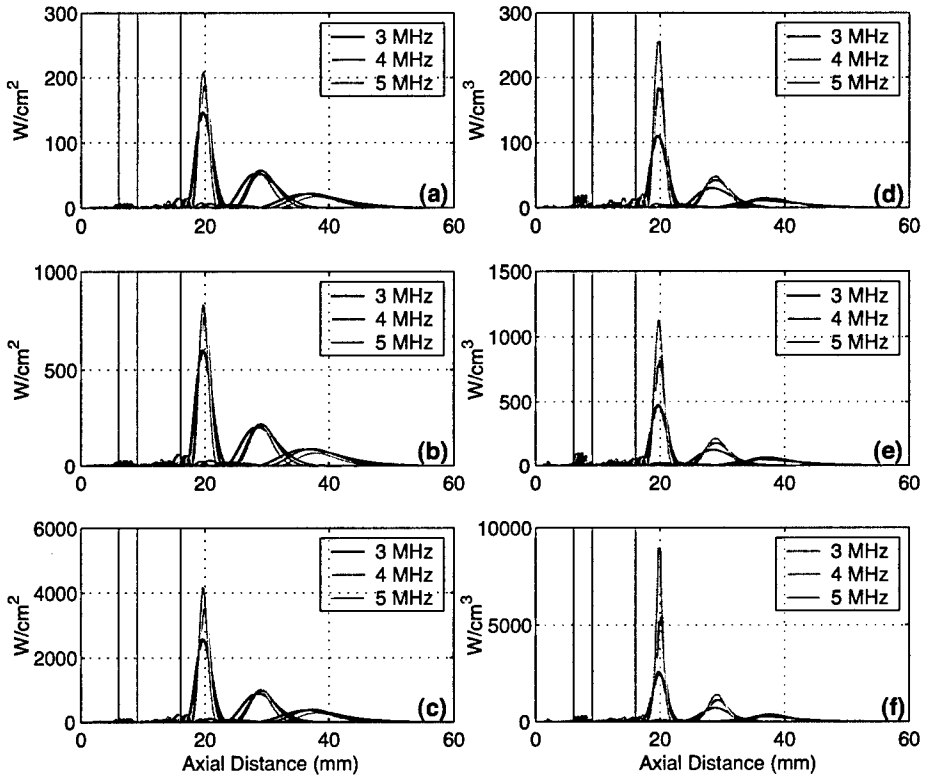

FIGURE 1. The time-averaged intensity (left) and heat rate (right column). The pressure amplitude at the source were $p_0 = 125$ kPa for (a) and (d), $p_0 = 250$ kPa for (b) and (e), and $p_0 = 500$ for (c) and (f).

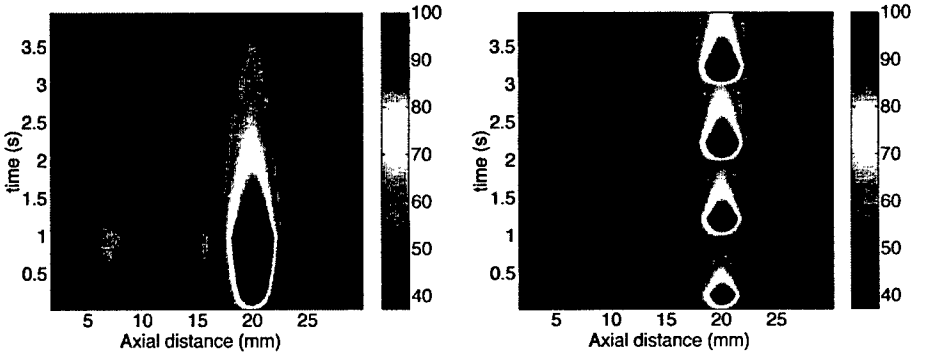

FIGURE 2. Axial temperature under two exposure conditions. Left panel: The acoustic field is on for 1 second. Right panel: The acoustic field is on for a total time of 1 second but with a 25% duty cycle.

CONCLUSION

For the ultrasound exposure conditions studied here, two scenarios were found to produce a thermal lesions while minimizing the heating of collateral tissues. For applications close to sensitive areas (e.g., the skin), we found that a HIFU device should possess a small aperture, high power, and a higher frequency ($f > 5$ MHz). Additionally, the exposure should consist of short "on" times and longer "off" times to produce more thermal lesion per unit volume. For applications that require penetration to deeper tissues, this study showed a large aperture, medium power, and a lower frequency ($f < 5$ MHz) were satisfactory in the creation of a thermal lesion. He exposure also required relatively longer "on"/"off" times, which produced less lesion per unit volume. In either application, it was determined that a low f-number was essential to produce a thermal lesion while minimizing deposition of heat at unwanted locations. Finally, we conjecture that the ideal HIFU source is an array, which permits control of the f-number by manipulating the amplitude and phase of the signal applied to each element.

ACKNOWLEDGMENTS

Partial support was provided by the U.S. Army Medical Research Acquisition Activity through The University of Mississippi under terms of Agreement No. DAMD17–02–2–0014. The opinions expressed herein are those of the author(s) and do not necessarily reflect the views of U.S. Army Medical Research Acquisition Activity or The University of Mississippi.

REFERENCES

1. Fry, W. J., *Amer. J. Phys. Med.*, **37**, 152–156 (1958).
2. Hill, C. R., and ter Haar, G. R., *Brit. J. Rad.*, **68**, 1296–1303 (1995).
3. Carstensen, E. L., and Bacon, D. R., "Biomedical Applications," in *Nonlinear Acoustics*, edited by M. F. Hamilton and D. T. Blackstock, Academic, San Diego, 1997, chap. 15, pp. 421–447.
4. Curra, F. P., Mourad, P. D., Khokhlova, V. A., Cleveland, R. O., and Crum, L. A., *IEEE Trans. Ultra. Ferro. Freq. Contr.*, **47**, 1077–1089 (2000).
5. Filonenko, E. A., and Khokhlova, V. A., *Acoust. Phys.*, **47**, 468–475 (2001).
6. Curra, F. P., *Medical Ultrasound Algorithm for Noninvasive High Intensity Ultrasound Applications*, Ph.D. thesis, University of Washington (2001).
7. Szabo, T. L., *J. Acoust. Soc. Am.*, **96**, 491–500 (1994).
8. Carcione, J. M., Kosloff, D., and Kosloff, R., *Geophysics*, **53**, 769–777 (1988).
9. Pennes, H. H., *J. Appl. Physiol.*, **2**, 93–122 (1948).
10. Separeto, S. A., and Dewey, W. C., *J. Rad. Onc. Biol. Phys.*, **10**, 787–800 (1984).
11. Fornberg, B., *A practical guide to pseudospectral methods*, Cambridge, New York, 1996.
12. Berenger, J. P., *J. Comp. Phys.*, **114**, 185–200 (1994).
13. Liu, Q.-H., and Tao, J., *J. Acoust. Soc. Am.*, **102**, 2072–2082 (1997).
14. Chew, W. C., *Microwave Opt. Tech. Lett.*, **15**, 363–369 (1997).
15. Ghist, M., Fornberg, B., and Driscoll, T. A., *SIAM J. Num. Anal.*, **38**, 718–741 (2000).
16. Duck, F. A., *Physical Properties of Tissue, A Comprehensive Reference Book*, Academic, London, 1990.
17. Nachman, A. I., Smith, J. F., and Waag, R. C., *J. Acoust. Soc. Am.*, **88**, 1584–1595 (1990).

Nonlinear Methods For Visualization Of HIFU-Induced Lesions

Yao Hui, Pornchai Phukpattarnont and Emad S. Ebbini

Department of Electrical and Computer Engineering, University of Minnesota Twin Cities, Minneapolis, MN 55455

Abstract. Nonlinear ultrasonic imaging methods (like pulse inversion [1] and quadratic imaging based second-order Volterra filter [2]) are used in visualization of lesion formation in freshly excised tissue. Both of these methods are more sensitive to nonlinear echoes (e.g., due to micro-bubbles) than standard B-mode imaging. While all three methods typically show increased echogenicity at the lesion location, the nonlinear methods exhibit more localized echo enhancement than B-mode imaging. Therefore, nonlinear methods are better suited to lesion mapping for purposes of image guidance. Quadratic images have the added advantage of a significant increase in image dynamic range and noise reduction (a major limitation of pulse inversion imaging). The results shown in this report continue to support the hypothesis that micro-bubbles play an important role of lesion formation. Furthermore, the presence of microbubbles provides significant opportunity for mapping the treated tissue and potentially characterizing the nature of damage.

INTRODUCTION

We have used a dual-mode array described in [3] to form HIFU-induced thermal lesions in freshly excised degassed tissue under a variety of *normal exposure* and *over exposure conditions*. Single-transmit focus images were collected for over 100 lesions before and after lesion formation. These images have consistently shown 5 - 7 dB enhancement in the echogenicity from the lesion location in the standard echographic images. These results were much more consistent than the reported "flashes" on the B-scan images when diagnostic ultrasound systems are used to monitor HIFU lesion formation. Motivated by the excellent investigation by P. P. Lele reported in [4], we hypothesized that this change in echogenicity is due to stable microbubbles that can occur even at low insonation levels. Lele found that subharmonic emission due to microbubbles showed a monotonic increase with intensity from 150 mW/cm^2 to 1500 W/cm^2 without a distinct threshold for emission (measurements done *in vitro* and *in vivo* at 2.7 and 1.8 MHz). The consistency of the increase in echogenicity at the lesion may be explained by the fact that the microbubbles may already be resonant at the imaging frequency (same as the therapeutic HIFU beam when the dual-mode array is is used), perhaps a result of rectified diffusion.

The standard echographic images at the fundamental, however, offer limited contrast enhancement due to the speckle phenomenon. Therefore, they could not provide a reliable method for mapping the boundaries of HIFU-induced lesions. This lead us to try to exploit the nonlinear nature of the microbubbles to enhance the visualization and mapping of thermal lesions. The idea was that, if microbubbles are indeed present at the lesion location, they will generate nonlinear echoes that may be better suited for

mapping. We have initially investigated second harmonic (SH) imaging as a means of enhancing the lesion contrast for improving the visualization of these images. SH images of thermal lesions have shown increase in the contrast on the order of 22 - 25 dB, but with decreased dynamic range of the resulting images [3]. A post-beamforming nonlinear compounding algorithm was shown to improve the contrast in lesion echogenicity to 30 - 35 dB without loss in dynamic range [5]. This was achieved by compounding the fundamental and the SH images using spatial compounding functions based on the receive beamforming characteristics of the dual-mode array at the fundamental and the SH frequencies. In this paper, we use a commercial imaging scanner with modifications to allow pulse inversion imaging in addition to standard B-mode imaging for the visualization of freshly excised tissue before, during, and after the formation of HIFU lesions.

NONLINEAR IMAGING METHODS

Pulse Inversion Imaging

This method was recently introduced by Burns and coworkers [6] for enhancing contrast echoes in contrast-assisted pulse-echo imaging. The basic implementation of this method entails the use of two pulses per image line. These pulses are carefully designed such that, $p_2(t) = -p_1(t - T_L)$, where T_L is some appropriate delay (on the order of the pulse-echo time from the maximum depth of interest). Summing the echoes resulting from the two pulses eliminates the odd-harmonic components from the echo signal (including the fundamental) while doubling the even-harmonic (mostly second) components. This method currently represents the leading approach for contrast-agent imaging, especially with low concentration and/or very low transmit signals to minimize the generation of tissue nonlinearity.

Quadratic Imaging Based On SVF

We have recently developed a new nonlinear imaging system based on the SVF [2]. This has a number of advantages when compared to PI imaging (e.g. requires only a single pulse per line and increased dynamic range).

Second-Order Volterra Model

Results from [2] have shown the validity of a second-order Volterra filer as a model for pulse-echo ultrasound imaging data from tissue mimicking media. In this section, the decomposition of received echo, i.e., output sequences only, into linear and quadratic components by using least-squares approach of second-order Volterra model will be considered and the detail of algorithm implementation to pulse-echo ultrasound imaging will be stated.

Signal Separation Model

The algorithm described in this section is adapted from [7]. The response of a quadratically nonlinear system, $y(n+1)$, can be predicted by a second-order Volterra model of past m values as follows:

$$\begin{aligned} y(n+1) &= y_L(n+1)+y_Q(n+1) \\ &= \sum_{i=0}^{m-1} y(n-i)h_L(i)+\sum_{j=0}^{m-1}\sum_{k=j}^{m-1} y(n-j)y(n-k)h_Q(j,k)+\varepsilon(n), \end{aligned} \quad (1)$$

where $h_L(i)$ is linear filter coefficients, $h_Q(j,k)$ represents quadratic filter coefficients and $\varepsilon(n)$ is a modelling error and/or a measurement noise which is assumed to be an independent, identically distributed(i.i.d) random variable with zero mean. That is, if the model coefficients are known, the echo signal can be decomposed into linear and quadratic components. The latter can be expected to better represent the quadratic response of the system than, say, the second harmonic component. The model coefficients can be obtained by setting the linear and quadratic prediction problem in Equation 1 to form a set of linear equations. Recognizing that the output is linear in terms of the (unknown) model coefficients, one obtains a matrix equation of the form:

$$\mathbf{f} = \mathbf{G}\mathbf{h}+\varepsilon, \quad (2)$$

where the vector $\mathbf{f}$, the matrix $\mathbf{G}$ and the error vector ε are

$$\begin{aligned} \mathbf{f} &= [y(n+1),y(n+2),\ldots,y(n+L)]^T \\ \mathbf{G} &= [\mathbf{y}(n),\mathbf{y}(n+1),\ldots,\mathbf{y}(n+L-1)]^T \\ \varepsilon &= [\varepsilon(n),\varepsilon(n+1),\ldots,\varepsilon(n+L-1)]^T. \end{aligned}$$

where the data vector, $\mathbf{y}$, is given by:

$$\begin{aligned} \mathbf{y}(n) = [&y(n),y(n-1),y(n-2),\ldots,y(n-m+1), \\ &y^2(n),y(n)y(n-1),\ldots,y^2(n-m+1)]^T \end{aligned}$$

and the filter coefficient vector, $\mathbf{h}$, is given by:

$$\begin{aligned} \mathbf{h} = [&h_L(0),h_L(1),h_L(2),\ldots,h_L(m-1), \\ &h_Q(0,0),h_Q(0,1),\ldots,h_Q(m-1,m-1)]^T. \end{aligned}$$

The details of the solution for the coefficients of the SVF model can be found in [8]. Briefly, a minimum-norm least-squares solution of (2) is obtained using *truncated singular value decomposition, TSVD*. To assess the performance of the signal separation model in enhancing the lesion visualization, we compute the contrast-to-tissue ratio:

$$CTR = 10\log_{10}\left(\frac{\|\mathbf{y}_{QC}\|_2^2}{\|\mathbf{y}_{QT}\|_2^2}\right) \quad (3)$$

where $\|\mathbf{y}_{QC}\|_2$ and $\|\mathbf{y}_{QT}\|_2$ are the l_2 norms of the quadratic components from the lesion and normal tissue regions, respectively. These regions are easily identified under various imaging conditions. For instance, for the application described in this paper, the contrast region is the expected location of the thermal lesion (often visible on the standard echographic image).

Implementation

The coefficients of the linear and quadratic components of the SVF model are obtained from the beamformed RF data. The implementation steps are as follows:

1. Using the standard echographic image, select a beamformed RF data segment from the expected lesion location.
2. Form the linear systems of equations according to (2).
3. Define contrast region (within the lesion) and normal tissue region for the computation of the mean-square error *MSE* and *CTR*.
4. Solve systems of linear equations by using TSVD regularization method.
5. Apply second-order Volterra filter to the beamformed RF data throughout the pulse-echo ultrasound image.
6. The quadratic component from the SVF can be displayed as a separate image or appropriately compounded with the linear component.

EXPERIMENTAL SETUP

Figure 1 shows a simple arrangement for the formation of HIFU lesions in freshly excised and degassed porcine livers samples. The therapy transducer is a 1.5 MHz single-element spherical-shell transducer with a radius of curvature equal to its diameter and equal to 63.5 mm (Etalon, Lizton, Indiana). The transducer is fixed to the back of a small tank as shown and driven by a power amplifier (ENI, Rochester, NY) and a programmable function generator. This assembly can be used in generating a variety of amplitude-modulated HIFU bursts from tens of milliseconds to several seconds long and intensities up to 3000 W/cm^2 (conservative estimate).

Real-time imaging is performed using a modified Technos MP system from ESAOTE, Genoa, Italy. The system is modified to allow imaging in pulse inversion mode in addition to normal B-mode imaging. In addition, a hardware module for capturing high-quality beamformed RF data allows us to capture and upload up to 60 seconds of full frame data with a specified frame rate. A CA 421 convex probe was used in acquiring image data for this paper. Image data was acquired in pulse inversion (PI) mode with a 2-cycle transmit pulse centered at 1.57 MHz. The imaging transducer was aligned so that the image plane is $x-z$ plane (to allow imaging the lesion along the axis of the therapy transducer.

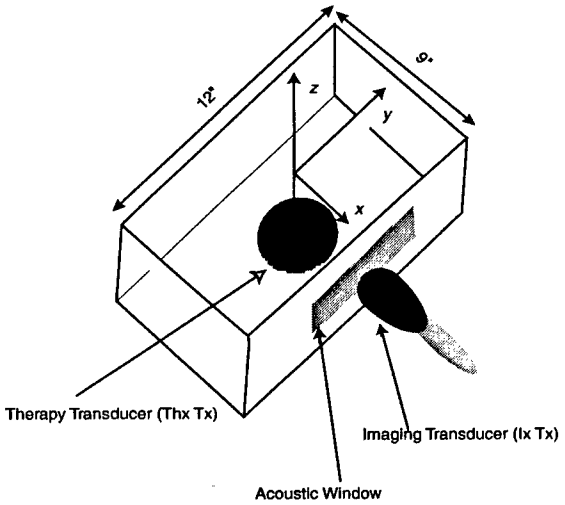

FIGURE 1. Experiment setup used for formation of HIFU lesions using a single-element transducer attached to the of the tank with an imaging probe monitoring a cross section of the lesion through an acoustic window.

RESULTS AND DISCUSSION

The experimental setup shown in Figure 1 was used in obtaining images of *ex vivo* tissue samples before, during and after thermal lesion formation with the spherical therapy transducer. This setup was designed to allow comparisons with our a dual-mode 64-element ultrasound phased array operating at 1 MHz described in [3]. Results shown in [3] confirmed that echoes from the lesion location exhibited increased levels of second harmonic generation even at normal exposure conditions. In this paper, we show imaging results from a single-shot slightly overexposure condition of a 5 second pulse at 1800 W/cm^2. This exposure typically produces a cigar-shaped lesion with average length of 10 mm and slight widening of the lateral extent of the lesion at the base (nearer to the therapeutic transducer). This is part of a study for characterization of different imaging modes at a full range of exposure conditions.

Figure 2 shows the RF data along a line through the lesion before lesion formation (upper left). The figure also shows spectrograms of the RF data (showing the frequency content of the RF echoes, lower left). Echoes from the tissue sample begin at depth 135 mm. The results show that the echoes before lesion formation cover the bandwidth of the CA4121 probe (fundamental at 1.57 MHz and some 2nd harmonic). This is confirmed by the corresponding PI data shown on the right hand side, which shows the second harmonic data just above the noise level.

On the other hand, the spectrogram of the RF data shown in Figure 3 from the same direction after lesion formation show strong fundamental and 2nd harmonic components at the lesion location (145 mm). This is also very clear in the PI data which shows a strong 2nd harmonic at the same location. In addition, the PI data consistently showed a significant component at 2.2 MHz (believed to be an ultra harmonic component).

Analysis of the 2nd harmonic and ultraharmonic components have revealed different (but consistent) transient behavior after lesion formation. These observations will be discussed in more detail in a future report.

Figure 4 shows 50 dB B-mode and PI images before (LHS pair) and immediately after lesion formation. Both imaging modes show enhanced echogenicity at the lesion location at an axial distance of 145 mm from the imaging transducer. The PI image shows a smaller size hyperechoic region with lateral extent of about 9 mm compared to 12 mm in the B-mode image. The actual lesion size determined by visual examination was 8 mm. This result is typical, i.e. the PI data gives a more accurate map of the lesion than B-mode data.

Using a beamformed echo data segment from the tissue region shown in Figure 2, the coefficients of linear and quadratic components of the SVF were estimated as described in Section . The quadratic components of the beamformed RF data were filtered out at all pixel locations. The images before and immediately after lesion formation are shown in Figure 5 at 90 dB dynamic range. One can see the speckle components conspicuous in the standard echo images is greatly reduced. This level of enhancement is typical and has been observed consistently in over 100 experiments similar to the one described in [3]. The reader can appreciate that the lesion boundaries are well defined in both the axial and lateral directions. With the significant increase in dynamic range, one can see that both detection and mapping of thermal lesions is significantly facilitated by the use of the quadratic filter based on the SVF model.

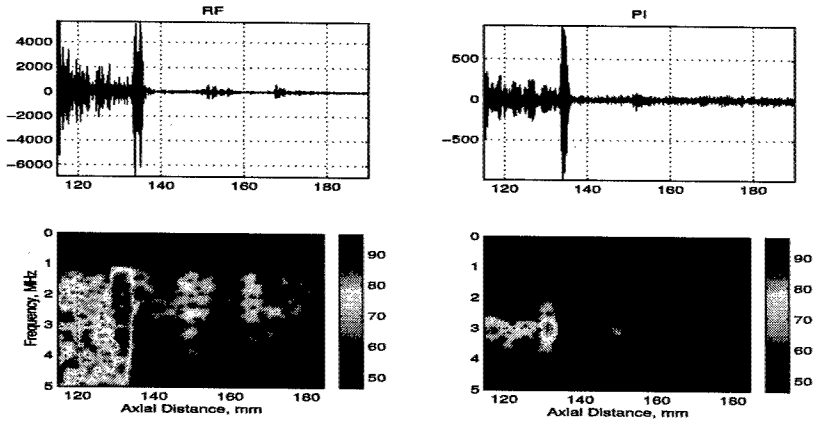

FIGURE 2. RF data and spectrograms from normal B-mode (left) and pulse inversion (right) *before lesion formation.*

CONCLUSIONS

Experimental results from *ex vivo* tissue samples provide compelling evidence that thermal lesions exhibit nonlinear behavior as a propagation medium. Nonlinear imaging methods were used to separate the linear and nonlinear components in the beamformed RF echo data. PI images confirmed the presence of strong 2nd harmonic component in

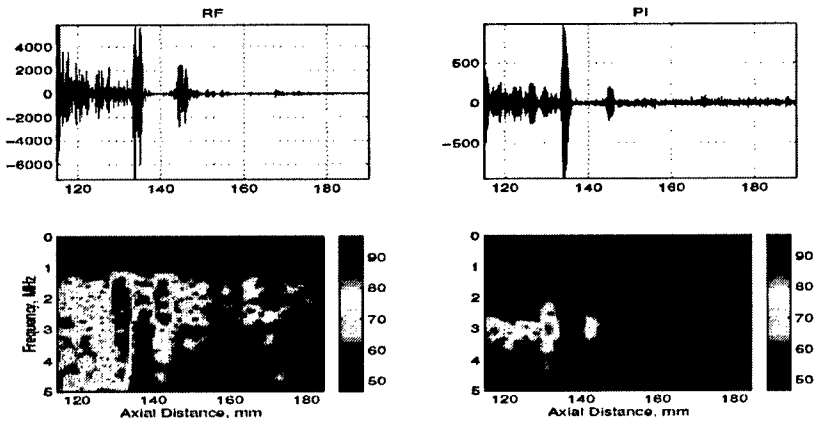

FIGURE 3. RF data and spectrograms from normal B-mode (left) and pulse inversion (right) immediately after lesion formation.

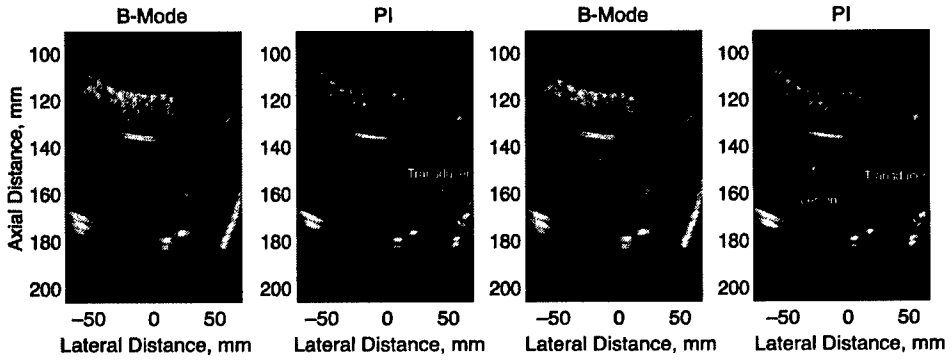

FIGURE 4. B-mode and pulse inversion images before (left pair) and immediately after (right pair) formation of lesion (50 dB dynamic range).

echoes from lesion location. The quadratic component images (obtained through SVF) show significant enhancement in lesion visualization due to:

1. They directly exploit the nonlinear nature of freshly formed thermal lesion (possibly due to formation of microbubbles).
2. Quadratic component combines both low frequency (close to dc) and harmonic frequency in forming nonlinear echoes. This simultaneously reduces speckle and beamforming artifacts without loss in spatial resolution.
3. The quadratic kernel of the SVF rejects the additive white Gaussian noise components which significantly improves the SNR of the imaging system and enhances the visualization of low echogenicity regions in the image.

We are currently conducting an experimental study to compare detection and mapping results using the three imaging methods for a full range of dose levels from

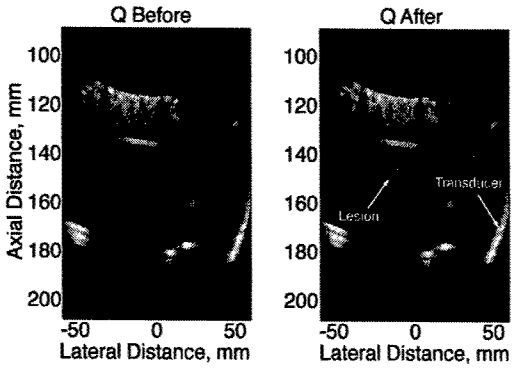

FIGURE 5. Quadratic images before (left) and immediately after (right) formation of lesion (90 dB dynamic range).

underexposure to *overexposure*. Preliminary data indicate that nonlinear imaging methods produce superior results compared to standard B-mode imaging.

ACKNOWLEDGMENTS

Funded by Grant DAMD 17-01-1-330 from the US Army Medical Research and Materiel Command and Esaote, S.p.A., Genoa, Italy.

REFERENCES

1. Burns, P.N., Wilson, S.R., and Simpson, D.H., *Invest Radiol*, **35**, 58–71 (2000).
2. Yao, H., Phukpattaranont, P., and Ebbini, E.S., "Post-beamforming second-order Volterra filter for nonlinear pulse-echo imaging," in *ICASSP*, **2**, pp. 1133–1136 (2002).
3. Ebbini, E., Bischof, J., and Coad, J., "Lesion formation and visualization using dual-mode ultrasound phased array," *2001 Ultrasonics Symposium*, **2**, pp. 1351–1354 (2001).
4. *Effects of ultrasound on solid mammalian tissue and tumors* in vivo, edited by M.H. Repacholi, M. Grandolfo, and A. Rindi, London: Plenum, 1987.
5. Steidl, C., Yao, H., Phukpattaranont, P., and Ebbini, E., "Dual-mode ultrasound phased arrays for noninvasive surgery post-beamforming image compounding algorithms for enhanced visualization of thermal lesions," *2002 Int. Symposium on Biomedical Imaging*, pp. 429–432 (2002).
6. Simpson, D.H., Chin, C.T., and Burns, P.N., *IEEE Trans. Ultrason., Ferroelect., Freg. Contr.*, **46**, 372–382 (1999).
7. Kim, K., Kim, S.B., Powers, E.J., Miksad, R.W., and Fischer, F.J., *IEEE J. Oceanic Eng.*, **19**, 183–192 (1994).
8. Phukpattaranont, P., and Ebbini, E., "Post-beamforming Volterra Filter for Contrast Agent Imaging, *2002 Ultrasonics Symposium* **2** (2002).

Dynamics Of Bubble Cloud In Focused Ultrasound

Yoichiro Matsumoto, Shin Yoshizawa, Teiichiro Ikeda

Dep. of Mech. Eng., The Univ. of Tokyo
Hongo, Bunkyo-ku, Tokyo 113-8656 JAPAN

Abstract. The behavior of a microbubble cloud in an ultrasound field shows multiple scale structures in time and space. The bubble size is the micro-scale, the distance between the bubbles is the meso-scale and the characteristic length in bubbly liquid, such as wavelength, is the macro-scale. It is essential to analyze the phenomena combining these scales reasonably. In this investigation the behavior of the bubble cloud in a focused ultrasound is simulated numerically taking the micro and meso-scale phenomena into account. An inward propagating shock wave is formed during the collapse of the bubble cloud, and the shock wave is focused at the cloud center. These phenomena generate violent bubble collapses. The bubble collapses emit high-pressure peaks, which are several hundred times larger than that of a single bubble collapse. These results are utilized for the lithotripsy of kidney stones *in vitro*. Two kinds of ultrasounds are focused on the stone. Cavitation bubble cloud is formed by the high frequency ultrasound at the front part of the stone and then, collapsed violently by the low frequency ultrasound field. The artificial and natural kidney stones are broken into tiny fragments efficiently.

INTRODUCTION

Ultrasound is widely applied in the clinical field today, such as ultrasonography [1], Extracorporeal Shock Wave Lithotripsy (ESWL), High Intensity Focused Ultrasound (HIFU) [2], sonodynamic therapy [3] and so on. Some of them have close relation to the dynamic behavior of microbubbles. In ultrasound imaging, microbubbles are used as contrast agents. In ESWL, the focusing of the shock wave causes cavitation and the impact pressure with bubble collapse damages not only the stone but also the surrounding body tissues. It has been reported that cavitation makes serious traumas to the human body tissues and its occurrence disturbs the propagation of ultrasound by scattering and absorbing the ultrasound energy [4]. On the contrary, the cavitation can be used as an energy transducer if it is well controlled. To utilize its energy efficiently, it is needed to understand its behavior under the ultrasound field.

In this paper, the dynamics of bubble clouds is discussed. Using the set of governing equations for the spherical bubble cloud, where the internal phenomena of each bubble and the compressibility of the liquid are taken into account, the bubble cloud motions in an ultrasound field are analyzed in detail. The numerical simulation and the experimental observation of the cavitation cloud using an ultra high-speed camera are exhibited. From these results, methods are developed to control and utilize the cavitation phenomena for lithotripsy. The experimental results show that the artificial and natural kidney stones are broken into tiny fragments efficiently.

BUBBLE CLOUD DYNAMICS

In considering medical applications of ultrasound, it is important to discuss the acoustic cavitation that is induced by the focused ultrasound field. In this section, the dynamic behavior of a microbubble cloud resulting from the volumetric change of the bubbles is simulated numerically. A spherical bubble cloud model [5] is employed to simulate the cloud cavitation behavior. Inwardly propagating shock wave, which results in a precursor wave, is formed during the collapse of the bubble cloud and it is focused in the cloud center. This produces violent bubble collapses in the central area and emits high pressure peaks from the bubbles.

Bubble Cloud Model

Figure 1 shows the schematic diagram of the bubble cloud model [5]. The simulation domain of the spherical bubble cloud is divided into three regions: (1) the outside of bubble cloud, which is the single-phase liquid region, (2) the inside of the bubble cloud, which is bubbly liquid, and (3) the inside of each bubble. Three sets of governing equations consisting of the equation of motion of the bubble cloud wall, the equations for bubbly liquid and the equations for bubble motion are formulated. To calculate the bubble cloud motion, Keller equation [6] is employed. To estimate the pressure within the bubble cloud, the pressure wave phenomena are examined by solving the set of equations formulated under the following assumptions: (1) Bubble cloud maintains a spherical shape. (2) Bubbly liquid inside the cloud is treated as a continuum fluid, whose mass and momentum are assumed to be equal to those of the liquid phase, since the mass per unit volume of the gas phase is much smaller than that of liquid phase, (3) Bubbles move with the surrounding liquid. Bubbles are small so that the slip between the bubble and the liquid can be neglected. (4) Coalescence and fragmentation of bubbles in the cloud are ignored. (5) Viscosity of the bubbly mixture is ignored in the bubble cloud because it has little influence on the wave phenomena. (6) The mass and momentum of gas phase are neglected in estimating those of the bubbly liquid, because they are much smaller than those of liquid phase due to low void fraction. (7) A bubble is assumed to be located at the center of the cloud to avoid the singularity therein. Each bubble motion is calculated using the numerical model [5], which is proposed by Matsumoto and modified by Shimada for the bubble cloud model. It takes into account the internal thermal phenomena of each bubble as well. To analyze the collapsing phenomena of the bubble cloud precisely, the internal thermal phenomena of each bubble and the liquid compressibility should be taken into account. The wall motion of the each bubble is described by the Fujikawa & Akamatsu equation [7]. The state of the liquid is estimated by the Tait equation.

Pressure Focusing In The Center Of Bubble Cloud

Figure 2 shows the time history of the pressure distribution in the bubble cloud for the case where the bubble radius is 20μm, the cloud radius is 5mm and the void fraction in the cloud is 0.1% as initial conditions. When the surrounding pressure increases, pressure waves propagate inward from the cloud boundary to the cloud

center. Kedrinskii [8] observed the precursor ahead of the shock wave propagating in the bubbly liquid in the case of the large pressure ratio. Present result also shows the precursor ahead of the shock wave. At the center of the cloud, the large oscillations are produced by the interaction between the shock wave and the precursor. The high peak pressure is observed at the cloud center because of shock wave focusing. Pressure waves propagating with higher velocities than that of the shock wave are observed ahead and behind the shock wave. This is because the high frequency pressure wave emitted from a collapsing and rebounding bubble behind the shock wave propagates with the sound velocity of the liquid [9].

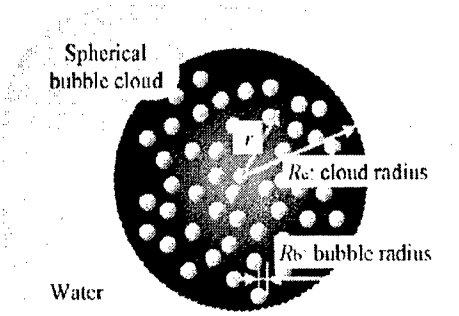

FIGURE 1. Concept of bubble cloud model.

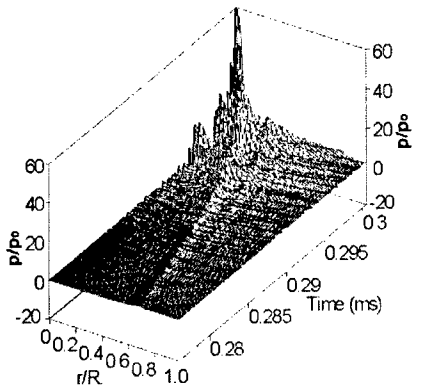

FIGURE 2. Time history of the pressure distribution in the cloud: Initial void fraction is 0.1%, initial bubble radius is 20μm and initial cloud radius is 5mm. The surrounding pressure decreases from 50kPa to 10kPa and then increases to 50kPa.

Bubble Cloud Behavior In The Ultrasound Field

The acoustic cavitation induced by an ultrasound field is considered to be much dependent on the ultrasound frequency. In medical applications, the typical frequency of ultrasound is around 0.5~5 MHz. When the ultrasound frequency is 4 MHz, the wavelength is about 0.4mm in water or in the human body. The focal region is considered to be around 2~4 times of the wavelength. In this simulation we assume that the region of acoustic cavitation is 0.75mm in radius, and the radius of each bubble in the bubble cloud is 1.0μm initially, with natural frequency about 4 MHz. The simulation condition is shown in Table 1.

Figure 3 shows the time histories of the ambient pressure at the center of the cloud and the radius of the center bubble when the bubble cloud is exposed to the ultrasound field. Figure 3 (a) and (b) show the results when the ultrasound frequency is 110 kHz. Figure 3 (c) and (d) show those of 2 MHz. When the bubble cloud oscillates resonantly (Figure 3 (a) and (b)), the center bubble collapses violently and the ambient pressure becomes larger than 20 MPa. However, in the case where the ultrasound frequency is higher (Figure 3 (c) and (d)) than the resonant one of the bubble cloud, no shock wave appears in the cloud. In this case, the pressure fluctuation amplitude is

less than the amplitude of the ultrasound field. This means that almost all of the acoustic energy of ultrasound is scattered, when the ultrasound frequency is higher than the resonant frequency of the bubble cloud.

Figure 4 shows the frequency response of the bubble cloud from 1 kHz to 10 MHz, in the case where the initial cloud radius is 0.75mm and the initial bubble radius is 1.0μm. The maximum pressure inside the bubble at the center of the cloud is shown. The resonant frequency of the bubble cloud is about 110 kHz, which is less than the natural frequency of the cloud, which is 163 kHz. The variation of the bubble cloud radius is very small in comparison with that of a single bubble. The increase of the amplitude of the ambient acoustic pressure has little influence on the volumetric oscillation of the bubble cloud because the initial void fraction is very small [10]. On the contrary, the pressure inside the bubble at the cloud center reaches approximately 500 MPa in the case where the surrounding acoustic frequency is the resonant one and the amplitude is 100kPa. This is very different from the case of a single bubble.

Figure 4 also shows that the frequency response of the bubble cloud is very much dependent on the amplitude of the surrounding ultrasound pressure. When the amplitude is 10kPa, the maximum pressure inside the bubble at the center is very small. In the case of 50kPa, although the maximum pressure reaches up to 2 MPa, the range of the resonant frequency where the pressure exceeds a few atmospheric pressures is very narrow (which is less than 100 kHz). However, in the case of 100kPa, the range of resonant frequency becomes broad. The frequency range where the maximum pressure exceeds 10 MPa becomes from 50 to 300 kHz. These results show that it is possible to control the collapsing phenomenon of cavitation bubbles in the ultrasound field. They suggest that cloud cavitation, which is formed by high frequency ultrasound, can be efficiently collapsed by low frequency ultrasound (about 0.1 times of higher frequency). The size of the bubble cloud and those of the bubbles in it are determined by the frequency of the exciting ultrasound. If the frequencies are selected carefully, it is technically possible to concentrate the high energy in restricted areas in the media such as water or human body.

Figure 5 shows the comparison of bubble behavior in the cloud center when the positive precedence wave and the negative precedence wave are applied in the lower frequency of the ultrasound. When the positive wave proceeds, the bubble cloud does not collapse at the first positive part. Then, after it stores the energy, it collapses with higher amplitude of the ambient pressure than the case when the negative wave proceeds.

TABLE 1. Calculation Conditions.

Parameter	Value
Initial Cloud Radius, R_{c0}	0.75 [mm]
Initial Bubble Radius, R_{b0}	1.0 [μm]
Initial Void Fraction, α_0	0.1 [%]
Ambient Ultrasound Pressure, p_∞	101.3 [kPa]
Temperature, T_0	293 [K]
Amplitude of Ambient Pressure, Δp	10, 50, 100 [kPa]
Range of Frequency	1 [kHz]~10 [MHz]
Natural Frequency of a Single Bubble	3.85[MHz]
Natural Frequency of Bubble Cloud	163[kHz]

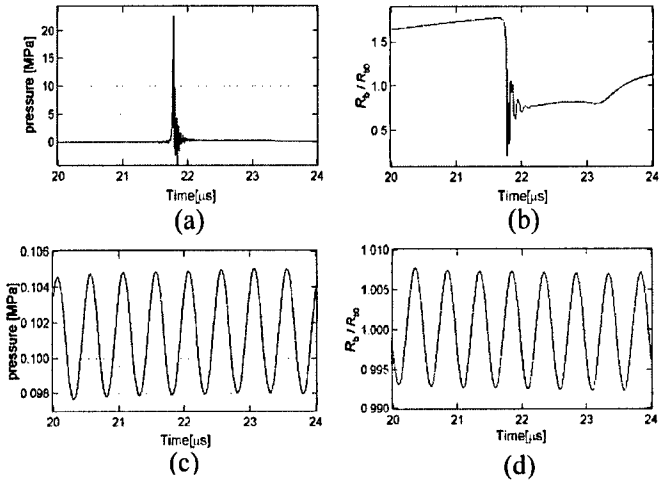

FIGURE 3. Time history of the center bubble oscillation (R_c=0): (a) Frequency 110 kHz. ambient pressure, (b) Frequency 110 kHz, center bubble radius, (c) Frequency 2 MHz, ambient pressure, (d) Frequency 2 MHz, center bubble radius.

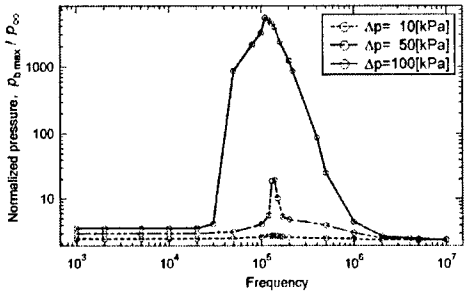

FIGURE 4. Response curve of bubble cloud: Maximum internal pressure of the center bubble.

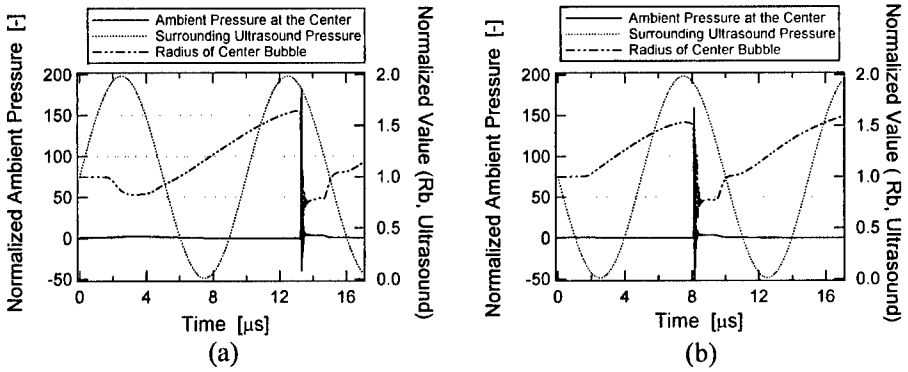

FIGURE 5. Time history of the ambient pressure at the center, the surrounding ultrasound and radius of the center bubble: Frequency is 100 kHz (a) Positive precedence wave, (b) Negative precedence wave.

OBSERVATION OF CLOUD CAVITATION

In this section, the observed results of cloud cavitation in the focused ultrasound field are discussed. Figure 6 shows the experimental set-up. The concave PZT ceramics diaphragms that have the natural frequencies of 1.0 MHz and 500 kHz are used as the ultrasound transducer. They transmit higher amplitude of ultrasound frequencies (2n+1) times of the fundamental frequencies than the other frequencies.

The artificial stone, which is used as the crushing test of ESWL machine, is fixed at the focal point. The cavitation phenomena at the focal point of the ultrasound field are recorded by the ultra high-speed camera (IMACON200, DRS Hadland). This camera has the ability to take 16 frames with 5ns in exposure time and 5ns in the minimum frame interval.

Figures 7 and 8 are the photographs of the cavitation around the stone. Figure 7 is the photograph of the focal region when the continuous ultrasound wave is focused. The cloud cavitation makes the bubble sheet over the artificial stone. The ultrasound energy is scattered at the surface of the cloud cavitation and the cavitation makes no damage to the stone. Figure 8 (a) shows the photographs of the time history of the cavitation bubbles when the 100 sinusoidal waves, whose frequency is 534 kHz, are focused. The cavitation region is about 3mm in width and large cavitation bubbles are observed. Figure 8 (b) shows the time history of the cloud cavitation when the focal acoustic frequency is 3.24 MHz. The region of the cloud cavitation is less than 1mm in diameter.

Figure 9 shows the controlled cavitation cloud around the stone. First, the high frequency ultrasound (3.815 MHz) is focused and small sized cloud cavitation is formed on the stone, then lower frequency ultrasound (545 kHz) is immediately focused. The cloud cavitation shrinks volumetrically at the sixth, tenth and thirteenth frames. It expands at the eighth and twelfth frames. Its volumetric oscillation has the frequency of about 500 kHz, which is the same order of the low frequency ultrasound. Thus, the violent collapse of the cloud cavitation is formed near the stone surface.

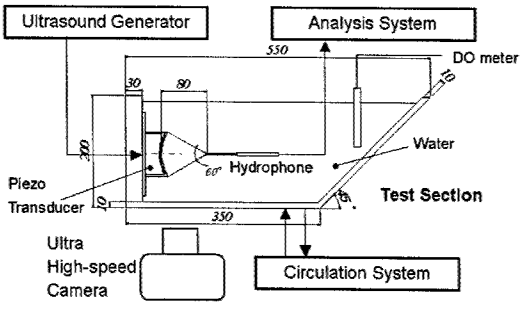

FIGURE 6. Summary of the experimental set-up.

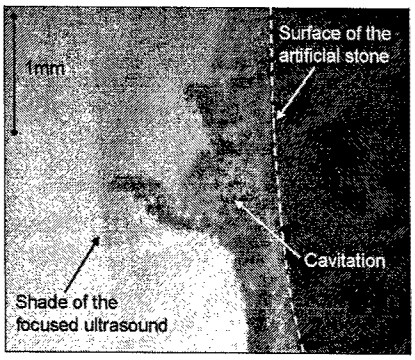

FIGURE 7. Photograph of cloud cavitation: The ultrasound is continuous and sinusoidal, frequency is 1.08 MHz and exposure time is 5 ns.

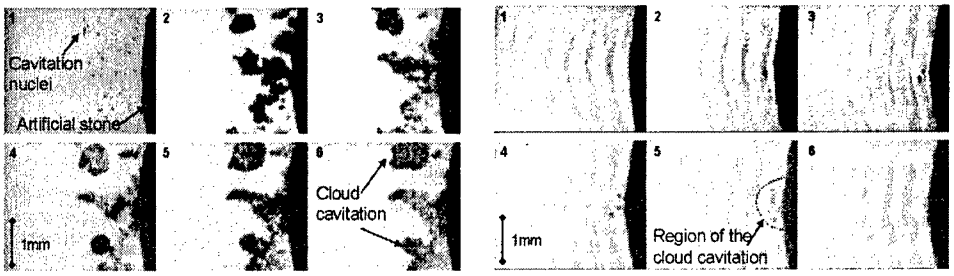

FIGURE 8. Photographs of cloud cavitation: Frame rate 100 kHz, (a) Ultrasound frequency is 534 kHz, (b) 3.24 MHz.

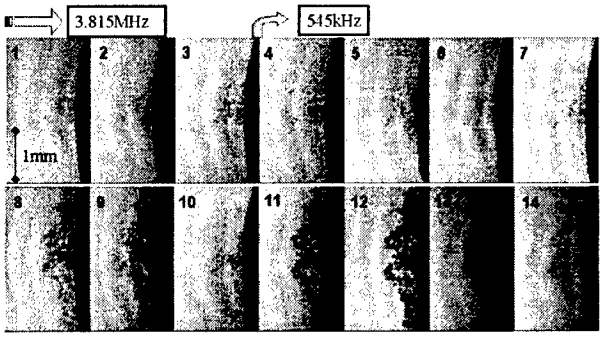

FIGURE 9. Photographs of cloud cavitation: Frame rate 2 MHz. Ultrasound frequency changes from 3.815 MHz to 545 kHz between the third frame and the fourth frame.

EXPERIMENT OF STONE CRUSHING

Based on the numerical simulation and the observation of the bubble cloud in the ultrasound field, the method of controlling cavitation collapse with high pressure in the restricted area is developed. Figure 10 shows the schematic diagram of the control method of the cloud cavitation. First, the cavitation nuclei, which consist of small bubbles, are formed by the high frequency ultrasound focused on the stone and cloud cavitation is concentrated near the surface of the stone. The reflection of the ultrasound at the solid surface amplifies the intensity almost twice. Next, the low frequency and high power ultrasound is exposed. The cloud cavitation oscillates when immediately exposed to low frequency ultrasound and the bubbles near the surface collapse violently.

Using this method, we conduct the crushing experiment of the stones. Figure 11 shows the broken model stones, which are used globally for the test of the ESWL, after the irradiation of focused ultrasound for 10 minutes. The model stone is made of activated aluminum. Figure 11 (a) shows the stone, which is crushed by the focused ultrasound combining the high frequency wave and the low frequency one. Figure 11 (b) shows the stone, crushed by the waveform when a delay of 50μs interval occurs

between the high and low frequency waves. This waveform results that the cavitation bubbles formed by the high frequency wave disappear during the interval so that violent collapse of cloud cavitation bubbles by the low frequency wave does not occur. Although the total ultrasound energies are the same in the case (a) and case (b), a deep hole about 1mm in diameter is observed at the center of the stone in Figure 11 (a). The cavitation erosion makes this hole. On the other hand, the stone in Figure 11 (b) does not have such a hole. The region of the center hole has the same scale of the focus region of the high frequency ultrasound (3.815 MHz). These results evidently indicate that the violent collapse of cloud cavitation can be induced in the restricted area by this method.

Finally, we conduct crushing experiment using the natural kidney stones. Figure 12 (a) shows the calcium oxalate stone fragments after the crushing test using the method shown in Figure 10. Figure 12 (b) shows the picture of a cystine stone after the crushing test. By using this method, the calcium oxalate stone is broken into very tiny fragments compared with the fragments by the present ESWL machine. Also the cystine stone, which is the hardest stone to break, is chipped away in tiny fragments.

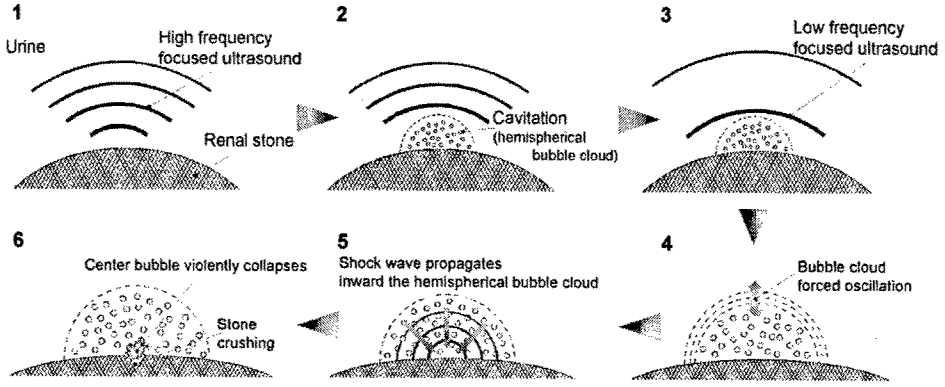

FIGURE 10. Mechanism of the control of cavitation phenomena.

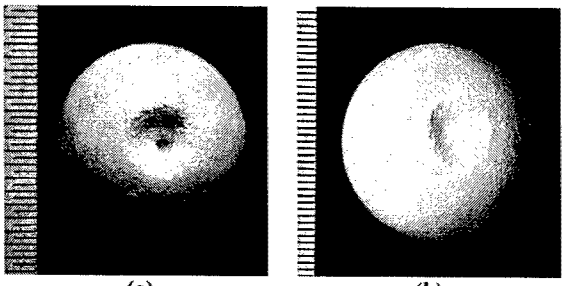

FIGURE 11. Result of the artificial stone crushing tests: (a) with the control of cavitation, (b) without the control of cavitation.

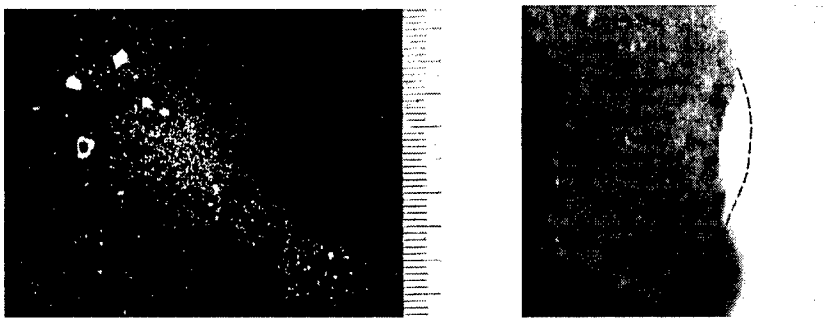

(a) (b)

FIGURE 12. Result of the natural kidney stone crushing tests: (a) Calcium oxalate stone fragments after the experiment, (b) Cystine stone after the experiment.

CONCLUDING REMARKS

A Set of governing equations for the motion of a spherical bubble cloud is formulated taking into account the internal phenomena of each bubble and the compressibility of the liquid. The pressure wave phenomena in a bubble cloud are simulated numerically in the ultrasound field. Inwardly propagating shock wave is formed during the collapse of the bubble cloud and it is focused in the cloud center. This creates the violent bubble collapse, with pressures more than several hundred times larger than that of a single bubble collapse. The numerical results reveal that the pressure waves emitted from bubbles in the cloud center area are amplified very much when the surrounding pressure oscillates in the resonant frequency of the cloud. The maximum pressure emitted from the bubble at the cloud center becomes much higher than that of a single bubble and high frequency pressure oscillation is observed in the central region. However, the maximum pressure of the cloud remains much lower than that of a single bubble when the applied ultrasound frequency coincides with the natural frequency of a single bubble. The response curve of the emitted pressure from the bubble in the center of the cloud is broadened with the ultrasound amplitude.

The cavitation behavior in the focused ultrasound field is observed by an ultra high-speed camera. The results reveal that the cloud cavitation can be generated in the restricted area by the high frequency ultrasound, and the cloud cavitation oscillates volumetrically by the successive low frequency ultrasound. In a continuous ultrasound field, the cloud cavitation covers the object at the focal area, and it does not transmit the energy into the cavitating cloud.

From the numerical simulation and the observation of cavitation, a method to induce the violent cavitation bubble collapse in the restricted area is proposed. That is, (1) High frequency focused ultrasound generates cloud cavitation in the narrow area. (2) Low frequency focused ultrasound; with wavelength exceeding the diameter of the bubble cloud, leads to resonantly oscillating cloud cavitation. (3) The bubble cloud efficiently collapses. By using this method, the artificial kidney stone is broken into tiny fragments efficiently. The natural kidney stones are also broken provided

that the ultrasound power is much less than the present ESWL machine. The break-up fragments are tiny enough to pass through the urethra without any pain.

ACKNOWLEDGEMENT

All the natural kidney stones were supplied from Professor Tadaichi Kitamura and Professor Nobutaka Ohta, at the Department of Urology, Faculty of Medicine, the University of Tokyo. We appreciate the offer and their discussions. We owed very much to Dr. Shinichiro Umemura at the Central Research Laboratory, Hitachi, Ltd. for the production of the PZT transducer. We would like to express our sincere appreciation for his help.

REFERENCES

1. Simpson, et al., "Pulse Inversion Doppler: a New Method for Detecting Nonlinear Echoes from Microbubble Contrast Agents," *IEEE Trans UFFC*, **46**, pp. 372-382 (1999).
2. Crum, L.A., "Acoustic Hemostasis," *Proceedings of the 15th Int. Symp. on Nonlinear Acoustics*, pp. 13-22 (1999).
3. Umemura, S, Kawabata, K., and Sasaki, K., "*In vitro* and *in vivo* Enhancement of Sonodynamically Active Cavitation by Second-harmonic Superimposition," *J. Acoust. Soc. Am.*, **101**, 1, pp. 569-577 (1997).
4. Delius, M., "History of Shock Wave Lithotripsy," *Proceedings of the 15th Int. Symp. on Nonlinear Acoustics*, pp. 23-30 (1999).
5. Shimada, M., Kobayashi, T., Matsumoto, Y., "Dynamics of Cloud Cavitation and Cavitation Erosion," ASME FEDSM, 99-6775, (1999).
6. Keller, J.B and Kolodner, I.I., "Damping of underwater explosion bubble oscillation," *J. Appl. Phys.*, **27** (1), pp. 1152-1161 (1956).
7. Fujikawa, S., Akamatsu, T., "Effect of the non-equilibrium condensation of vapour on the pressure wave produced by the collapse of a bubble in a liquid," *J. Fluid Mech.*, **97** (3), pp. 481-512 (1980).
8. Kedrinskii, V.K., "The propagation of perturbation in liquid with gas bubbles," *Journal of Applied Mechanics and Technical Physics*, **N4** (1968).
9. Commander, K.W. and Prosperetti, A., "Linear Pressure Waves in Bubbly Liquids: Comparison between theory and experiments," *J. Acoust. Soc. Am.* **85**, pp. 732-746 (1989).
10. Matsumoto, Y., Yoshizawa, S, "Behavior of Bubble Cluster in Ultrasound Field," Proceedings of the Fifth World Congress on Computational Mechanics (WCCM V), Vienna, Austria (2002).
11. Matsumoto, Y., Shimada, M., "Dynamics of Cavitation Bubble Cloud," ASME FEDSM, 97-3267 (1997).

Evaluation Of kHz-Frequency Surgical Devices

Fadi A. El-Khatib, Ph.D. and Inder Raj S. Makin, M.B.B.S., Ph.D.

Ethicon Endo-Surgery, 4545 Creek Road, Cincinnati, OH 45242

Abstract. Use of kHz-frequency devices for surgical procedures is a well-known medical application of ultrasound energy. In these systems a piezo-ceramic stack in the device handle generates an ultrasound signal that is guided through a stepped titanium horn. The distal half-wavelength of the titanium rod is used to clamp tissue by using a passive, non-vibrating jaw. It is hypothesized that the vibrational energy at the end-effector of this device is primarily converted to heat, leading to tissue coagulation and cutting. A basic model will be presented to better understand the distribution of heat resulting from mechanical energy being input in the system in this clamp-like configuration. Experimental results validating some of the theoretical predictions for temperature profiles will be presented.

INTRODUCTION

Ultrasound devices operating at kHz frequencies are currently being successfully used in various surgical procedures to cut and coagulate tissue using a single instrument. This tissue effect is hypothesized to result from frictional heat generated between the vibrating blade and the tissue.

Further optimization of these surgical devices is anticipated to achieve better cutting speed and tissue coagulation. One of the significant factors that controls instrument performance is the heat generated at the tip of the blade, and the temperature reached at the blade-tissue interface. The methods used to develop such devices and assess temperatures are solely based on experiments and empirical design. Such an approach is costly and time consuming.

Hence, computer simulation to model the functionality of kHz-frequency surgical devices can provide an appropriate means to evaluate and predict the heat generated and temperature distribution. Simulation can predict temperatures of parts like the interface between tissue and the blade that are hard to reach experimentally. This approach provides flexibility in changing design parameters easily and test out novel physical constructs.

The objective of this research is to develop a thermal analytical method to predict the temperature of the blade-tissue-blade construct and to use the method to better design and optimize kHz-frequency surgical devices.

This paper is divided into four sections. The thermal model is described in the first section. The governing thermal equations involved in the model are described in the second section. Validation of the model with experimental results is presented in the third section. Discussion and conclusions are presented in the last section.

THERMAL MODEL

The cutting edges of the clamp-like device consist of two blades: the Titanium blade and the Teflon/Stainless Steel blade (Figure. 1). The latter is a stationery blade and helps in clamping the tissue.

The heat is generated at the titanium tissue interface. The direction of the heat flux is downwards (+x-direction) from the titanium to the tissue (Figure. 2). The problem is divided into three one-dimensional problems. The thermal equations are attained for each direction then combined to form the general solution [2, 3].

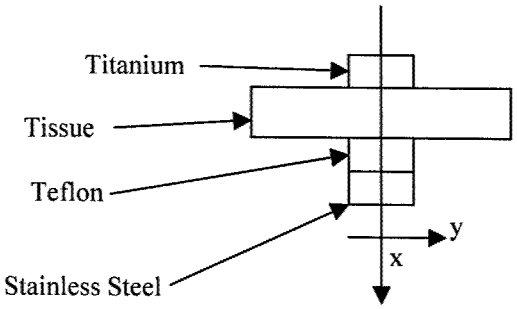

FIGURE 1. The blade – tissue – blade construct.

Assumptions

1. All the heat coefficients are constant (i.e. ρ (density), Cp (specific heat), & k (conductivity)).
2. The initial temperature and the ambient temperature are constants.
3. There are no internal resistances at the interfaces between the layers (i.e. the temperatures are identical)
4. There is no heat generation within the materials (i.e. no internal reactions between atoms that cause heat generation).

THERMAL EQUATIONS

The governing differential equations, in the x-direction, are

$$\frac{\partial T_1}{\partial x^2} = \frac{1}{\alpha_1}\frac{\partial T_1}{\partial t} \quad 0 \le x \le a \quad , t > 0 \tag{1}$$

$$\frac{\partial T_2}{\partial x^2} = \frac{1}{\alpha_2}\frac{\partial T_2}{\partial t} \quad a \le x \le b \quad , t > 0 \tag{2}$$

$$\frac{\partial T_3}{\partial x^2} = \frac{1}{\alpha_3}\frac{\partial T_3}{\partial t} \quad b \le x \le d \quad , t > 0 \tag{3}$$

$$\frac{\partial T_4}{\partial x^2} = \frac{1}{\alpha_4}\frac{\partial T_4}{\partial t} \quad d \le x \le L_x \quad , t > 0 \tag{4}$$

where a, b, c, L_x are the thickness shown in figure 2, and t is the time to cut the tissue, and α is the thermal diffusivity ($\alpha = k/\rho C_p$).

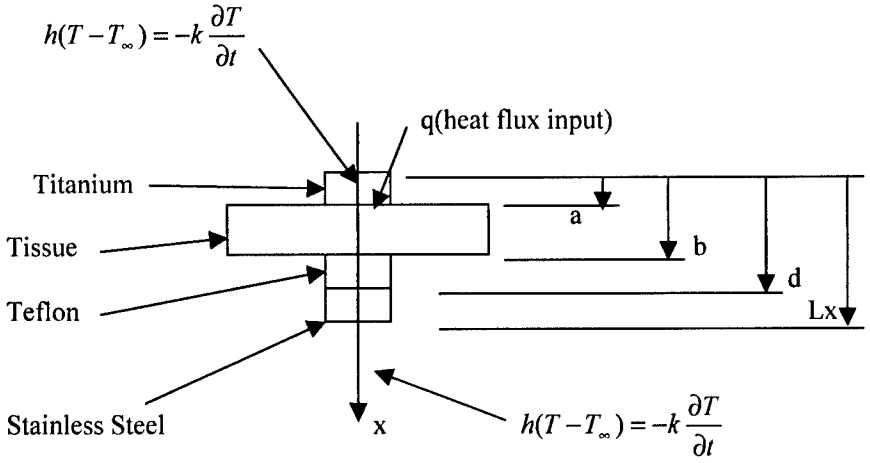

FIGURE 2. The boundary conditions of the blade – tissue – blade construct.

The solution is divided into a steady state solution and a transient solution. Both are solved separately and the solutions are added up at the end.

Thus, the general form will be,

$$\theta_j(x,t) = \psi_j(x,t) + \phi_j(x) \tag{5}$$

The differential equations for the transient part are,

$$\frac{\partial^2 \psi_j}{\partial x^2} = \frac{1}{\alpha}\frac{\partial \psi_j}{\partial t} \tag{6}$$

and for the steady part,

$$\frac{\partial^2 \phi_j}{\partial x^2} = 0 \tag{7}$$

Therefore, the solution, in the x-direction, will have the form

$$\theta_j(x,t) = \varphi_j(x) + \sum_{n=1}^{\infty} A_n X_{jn}(x,t) e^{-\alpha_j \lambda^2_{jn} t} \tag{8}$$

where

$$\begin{aligned} \varphi_j(x) &= C_j x + D_j \\ X_{jn} &= A_{jn} \sin \lambda_{jn} x + B_{jn} \cos \lambda_{jn} x \end{aligned} \tag{9}$$

and A_n, is the weighting coefficient.

The governing differential equation, in the y-direction, is

$$\frac{\partial T}{\partial y^2} = \frac{1}{\alpha}\frac{\partial T}{\partial t} \quad 0 \le y \le L_y \quad , t > 0 \tag{10}$$

where, L_y is half the width of the blades.

Therefore the solution, in the y-direction, can be expressed in non-dimensional form as,

$$\theta = \sum_{n=1}^{\infty} B_n \cos \lambda_n y \tag{11}$$

where B_n are the coefficients for the n-eigenvalues.

The analysis in the z – direction, is similar, to the analysis in the y – direction.

Therefore the temperature distribution as a function of x, y, z and t (time) can be expressed as,

$$\theta_{total} = \theta_{x,t} * \theta_{y,t} * \theta_{zy,t}$$

$$\theta_{total} = \left(\frac{T_{(x,t)} - T_{(ambient)}}{T_{(initial)} - T_{(ambient)}} \right) * \left(\frac{T_{(y,t)} - T_{(ambient)}}{T_{(initial)} - T_{(ambient)}} \right) * \left(\frac{T_{(z,t)} - T_{(ambient)}}{T_{(initial)} - T_{(ambient)}} \right) \tag{12}$$

Consequently, the absolute temperatures are expressed as,

$$\theta_{total} = \frac{T_{(x,y,z,t)} - T_{(ambient)}}{T_{(initial)} - _{(ambient)}} \tag{13}$$

Water Vaporization

Empirical formulas are used to express the heat transfer coefficient (h) during water vaporization [1]. It has been suggested that the total heat transfer coefficient be calculated as,

$$h = h_{conv} + \frac{3}{4} h_{rad} : h_{rad} < h_{conv} \tag{14}$$

Equation (14) shows that during vaporization the heat transfer coefficient consists of a convection term and a radiation term.

Heat Loss

Significant heat losses exist due to the extended length of the Titanium blade in the z–direction and the tissue in the y-direction. The amount of heat losses are estimated as described in [1].

Heat Flux Input

The value of heat flux or power delivered to the tissue is required as input in the thermal model. The heat flux delivered to the tissue is assumed to be the difference between the power input from the generator when the device is loaded and unloaded.

Thus,

Heat flux = electrical power input when loaded with tissue – electrical power input when unloaded

The electrical power is expressed as P(electrical) = I(rms) * V(rms) cos (phase angle), where I is electric current and V is the voltage.

RESULTS

Several tests have been conducted to measure the temperature of these devices using IR camera and thermocouples. Two different sizes of titanium blades were tested: 0.07 in and 0.085 in diameters. The 0.07 in blade had higher temperature than the 0.085 in blade. The average peak temperature for the 0.07 in blade was 284° C where the average peak temperature for the 0.085 in blade was 214° C. The thermal model predicted a peak temperature of 245° C for the 0.07 in blade (Figures 5, 6) and 200° C for the 0.085 in blade (Figures 3, 4).

Additionally, a 3D finite element model has been developed and predicted peak temperatures of 257° C and 192° C for the 0.07 in blade and 0.085 in blade, respectively.

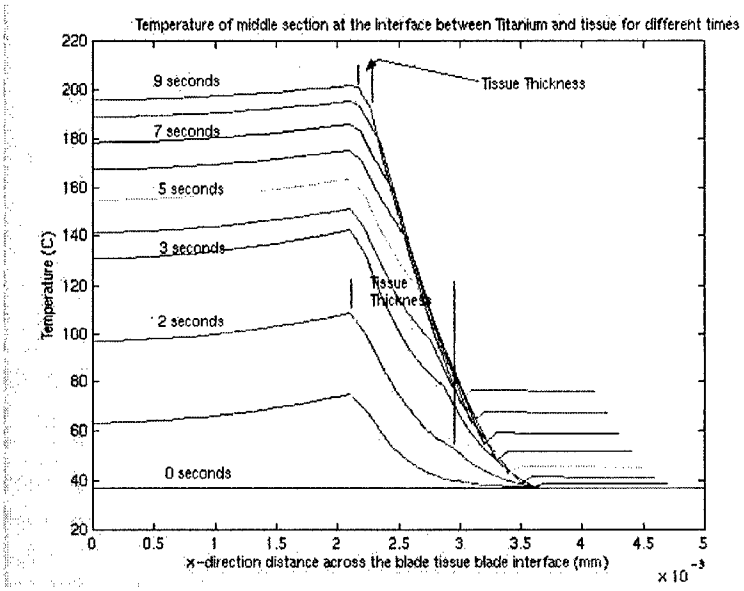

FIGURE 3. Temperature distribution of the 0.085 in blade across the blade – tissue – blade construct.

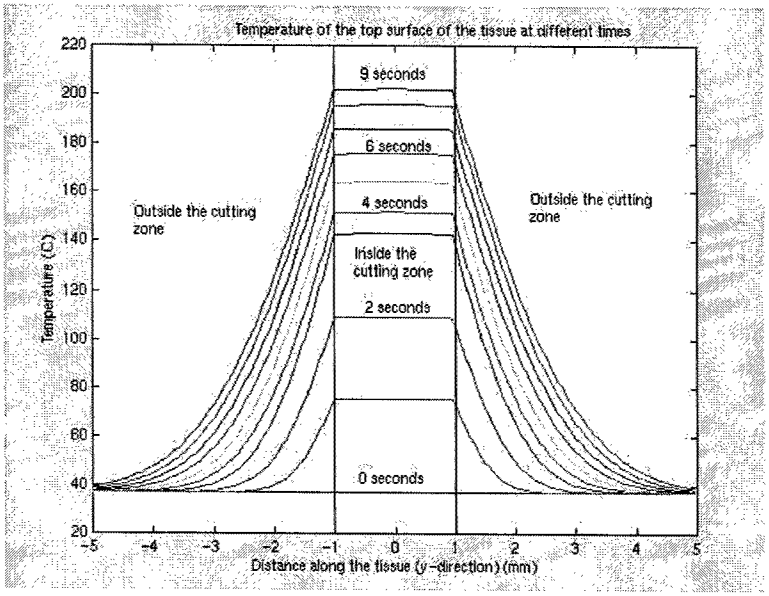

FIGURE 4. Temperature distribution of the 0.085 in blade along the tissue.

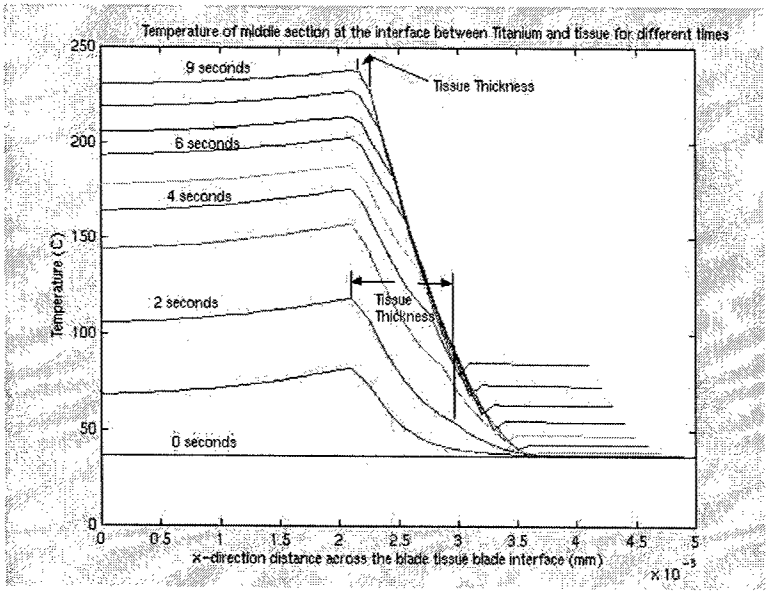

FIGURE 5. Temperature distribution of the 0.07 in blade across the blade – tissue – blade construct.

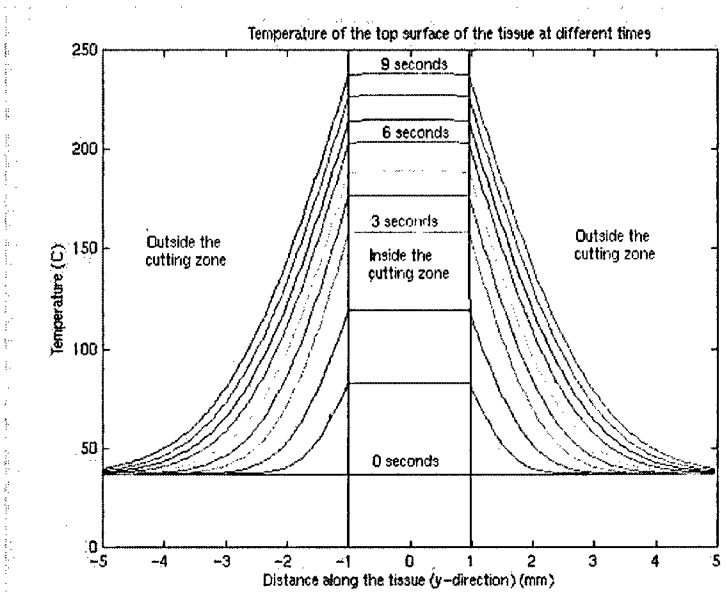

FIGURE 6. Temperature distribution of the 0.07 in blade along the tissue.

CONCLUSION

The thermal model provides understanding of the thermal behavior of kHz-frequency ultrasound devices. It can be used as a quick assessment of the temperature distribution and heat generated in the blades and the tissue.

The results show good agreement between the thermal model, finite element results and experimental outcome. The results show that the temperature of the smaller blade is higher. However, the difference in temperature results is attributed to the difference in geometry of the Titanium blade between the model and the experiment. The thermal model considered a rectangular cross section to match the geometry of the tissue, Teflon and Stainless Steel blades. In reality, the Titanium blade has a circular cross section while the Teflon and Stainless steel blades have rectangular cross section. Furthermore, placing the thermocouples between the blade and the tissue caused extra heat generated due to friction between the blade and the thermocouple, which lead to higher temperature results.

REFERENCES

1. Incropera, F., and Dewitt, D., "Introduction to Heat Transfer," 3rd edition, 1996.
2. Ozisik, M., "Heat Conduction," 2nd edition, John Wiley and Sons, Inc., 1993.
3. Ozisik, M., "Boundary Value Problems of Heat Conduction," 1st edition, 1968.

4. DOSIMETRY

HIFUS Treatments: Dosimetric Considerations

Gail ter Haar[a], James Kennedy[b], Feng Wu[c]

[a]*Joint Dept. of Physics, Royal Marsden Hospital, Institute of Cancer Research, Downs Road, Sutton, Surrey, SM2 5PT, England; gail@icr.ac.uk*
[b]*Dept. of Urology, Churchill Hospital, Oxford, OX3 7LJ, England.*
[c]*Clinical Center for Tumor Therapy, 2nd Affiliated Hospital of Chongqing University of Medical Sciences, 76 Linjiang Road, Chongqing 400010, P.R. China*

Abstract. As the use of high intensity focused ultrasound (HIFUS) increases, it becomes increasingly important to develop common consensus as to how exposures and clinical treatments are described. A regime for tissue ablation may be quantified in a number of different ways. Details of the ultrasound therapy source and of the acoustic field it produces either in water or in tissue are required to describe the "exposure" of the targeted tissue volume. In addition, a description of the mode of energy delivery, whether as single "shots" or in "scanned tracks" is needed. Dose is a concept used to relate the "exposure" to effects produced in tissue. In HIFUS dose has most usually been expressed in terms of thermal dose. Clinically, the parameters of most interest are the dimensions and positioning accuracy of the ablation achieved, and practically the volume ablated per unit time may be important. Ultimately a target tissue response such as complete ablation (CA) or incomplete ablation (IA) may prove more useful.

INTRODUCTION

In radiotherapy treatments, a clear distinction is made between "exposure" and "dose", with exposure describing the ionising radiation incident on the tissue, and "dose" being a concept that takes into account the effects tissue has on the incident field, and is therefore a useful predictor of tissue response. Historically, for ultrasound, exposure and dose have been used interchangeably, particularly in diagnostic applications. Ultrasonic fields are generally characterised under "free field" conditions in water. Some attempt is made to allow for the effects introduced by tissue by using *in situ* intensity values, which take into account the energy lost from the beam by transit through tissues overlying the volume of interest.

HIFUS presents different challenges to dosimetry than diagnostic ultrasound. It is important to form a consensus on this topic for a number of reasons. As the field develops, it becomes more important that the acoustic fields and energy delivery modes are properly described in order that findings can be compared, and where appropriate, reproduced. In addition, once patient trials become more commonplace, good communication between clinical colleagues becomes essential, and it may be most appropriate to compare ablation rates and tissue response. Here, a simple statement of the treatment parameters needed to ablate a given volume would be most useful.

DOSIMETRIC CONSIDERATIONS

Exposure

Requirements for description of the ultrasonic exposure to tissue stem from a need to understand the mechanisms for tissue destruction. Where purely thermal ablation is sought, the acoustic parameters of interest for determining the temperature rise are the acoustic power, peak intensity, acoustic frequency, the timing of the energy delivery and the beam dimensions. Where cavitation occurs, the peak negative pressure amplitude is also of interest.

Transducer Characteristics

In general, transducers used for HIFUS are either plane transducers combined with lenses or reflectors, or are focused bowls driven as single elements or as phased arrays. Whatever the configuration, the source and the acoustic field it produces can be characterised in a number of ways. The transducer diameter, effective radius of curvature, focal length and fundamental frequency should be given. Other parameters that are sometimes quoted are the F-number, active area and aperture angle.

Beam Characteristics

Complete acoustic field characterisation comprises two parts. The total power emitted at the transducer face can be measured using a radiation pressure balance technique. The beam profile is most readily measured by mapping the pressure distribution using a hydrophone. This is mainly performed at low pressure amplitudes to minimise the non-linear propagation effects that arise in water at high pressures and to avoid damage to the hydrophone from acoustic cavitation.

Hydrophone measurements allow an estimate of the free field spatial peak intensity at the levels used for ablation. They also allow determination of the full width of the pressure (and hence intensity) profile at half its peak intensity in both axial and radial directions (beam half widths).

Using the spatial peak intensity value, I_{SP}, it is possible to estimate the peak intensity within a target tissue volume (peak intensity *in situ*), $I_{in\ situ}$, if the attenuation coefficients, α, of the overlying tissue (of thickness x) are known.

$$I_{in\ situ} = I_0\, e^{-\alpha x}$$

where I_0 is the focal peak intensity measured in water.

When a sharply focused ultrasonic beam travels through tissue in conditions for which finite amplitude effects are important, there is transfer of energy from the fundamental frequency to harmonics, which leads to changes in beam shape and the effective absorption coefficient. In an attempt to define a dosimetric parameter that minimises this problem, Hill *et al* [1] have proposed I_{SAL} – the acoustic intensity spatially averaged over the area enclosed by the half maximum pressure contour as determined under linear conditions. In order to derive I_{SAL}, it is necessary to measure acoustic power at the levels used for ultrasound surgery, and to map the pressure

profile under low amplitude conditions using a hydrophone with high spatial resolution, (which does not need to be calibrated). I_{SAL} can be shown to be 0.557 I_{SP}.

It has been shown that before thermal diffusion dominates, or boiling or cavitation occur, the lesion diameter is close to the full width half maximum pressure. I_{SAL} appears to be an appropriate parameter for predicting the temperature achieved at the lesion boundary.

Energy Delivery Mode

In order to obtain volume ablation, energy is delivered in one of two ways. In one regime, successive contiguous exposures are made with the transducer being held stationary during each "shot". A "shot" may last 1-5s and a time interval typically of 1 minute is left between successive exposures to allow overlying tissues to cool [2]. In the other commonly used regime, the transducer is scanned in some fashion (usually linearly) through the tissue while the sound is on. This method speeds up the rate of ablation of volumes at depth, but increases the ultrasound exposure to skin.

A description of the delivery mode necessitates detailing the exposure time per "shot" and the time delay and spatial separation between them for the "shot" by "shot" regime, or the scanning speed, track length and number of passes over each track for the moving transducer technique.

Dose

As discussed above, HIFUS tissue destruction is obtained predominantly by a thermal mechanism, but acoustic cavitation can also contribute, and these mechanisms are interdependent. There is no dosimetric parameter for acoustic cavitation although the integral of the subharmonic signal during exposure has been shown to be a good predictor of cell survival *in vitro* [3]. This approach would probably not be appropriate *in vivo* where cytotoxic temperatures are also occurring.

The field of hyperthermia has used the concept of thermal dose with some success. As is well known, the toxic effect of high temperatures on cells depends both on the temperature achieved, and the time for which it is maintained. The relationship between the times (t_1 and t_2) needed at two different temperatures (T_1 and T_2) to obtain the same biological effect has been described by Overgaard & Suit [4] as

$$t_2 = t_1 R^{(T_1 - T_2)} \tag{1}$$

where R is a constant found to be 0.25 for temperatures below 43° C and 0.5 for those above.

Sapareto and Dewey [5] have suggested a technique whereby as the temperature varies, numerical integration is used to calculate the equivalent time that would give the same biological effect at a constant chosen reference temperature. In hyperthermia a standard reference temperature of 43° C is used. The thermal dose is then defined as the equivalent time at 43° C, t_{43}, where

$$t_{43} = \sum R^{(43-T)} \Delta t \tag{2}$$

where T is the average temperature during the time interval Δt.

Various authors have suggested that t_{43} = 240 minutes is a suitable threshold for tissue necrosis in HIFUS [6,7]. Damianou *et al* [7] have shown that in fact this value varies for different tissue types. It has been shown that for a 1-2s lesion, the temperature at the boundary is approximately 56° C [1,8]. Using the above formulation (eqn 1.) t_{43} = 240 minutes is equivalent to a time at 56° C of 1.7s. It would seem more rational to use 56° C as the reference temperature for HIFUS where exposure times are typically seconds rather than minutes.

TABLE 1. Thermal dose for different tissue types [7].

Tissue	t_{43}(min)	t_{56}(s)
Muscle	120-240	0.8-1.7
Brain	30-100	0.2-0.7
Liver	45-60	0.3-0.4
Skin	120	0.8
Kidney	250	1.8

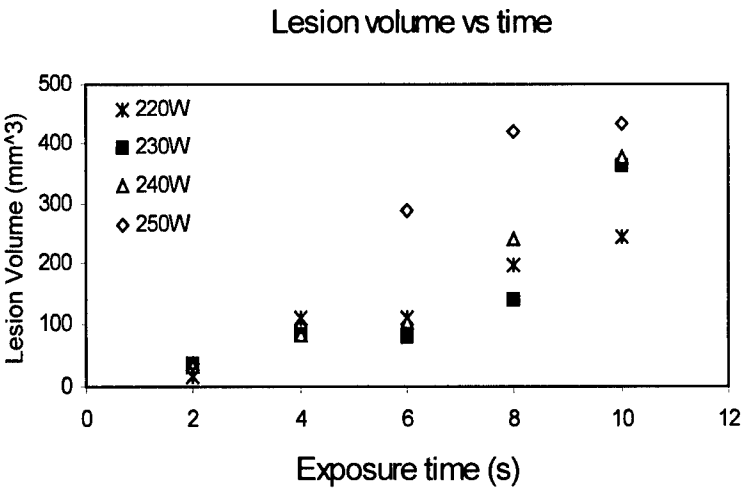

FIGURE 1. Graph showing relationship between lesion volume and exposure time for different acoustic powers.

Tissue Effects

Assessment of ablation success in the laboratory is made in terms of the volume of tissue necrosed and its position relative to that targeted. A clinically useful lesion for the "shot" by "shot" approach is one that follows the shape predicted by the free field focal volume and which falls in the expected position across the focal plane. For the scanned track, the volume should have the axial dimensions of a single exposure, and

extend the full scanned length. For a single lesion, the volume increases with exposure time if all other parameters remain constant (Fig. 1). The thickness of the scanned slice may vary from the radial extent of a single lesion to several times this value, depending on the number of times the track path is scanned (see Figure 2). A parameter that is predictive of the volume ablated under given exposure conditions would be useful for treatment planning. A number of different parameters may be explored here. The energy needed to create a given volume is useful for determining the exposure parameters (Fig.3), whereas the volume ablated per unit time (Fig 4.) may be of more interest to the clinician.

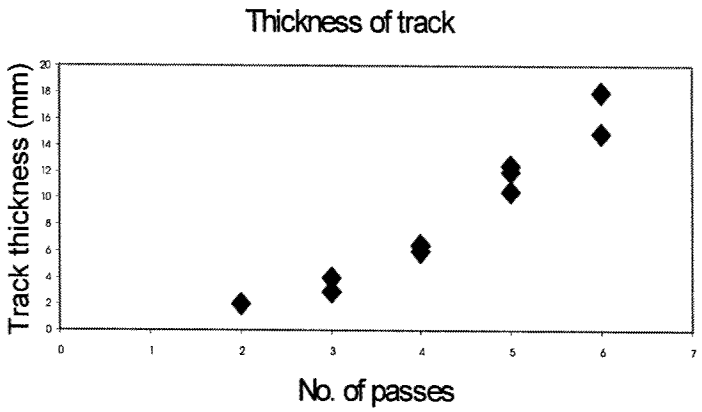

FIGURE 2. Graph showing relationship between thickness of tissue volume ablated and number of passes over the same track for a fixed acoustic power and scan speed (230 W; 4 mm/s; 35 mm track).

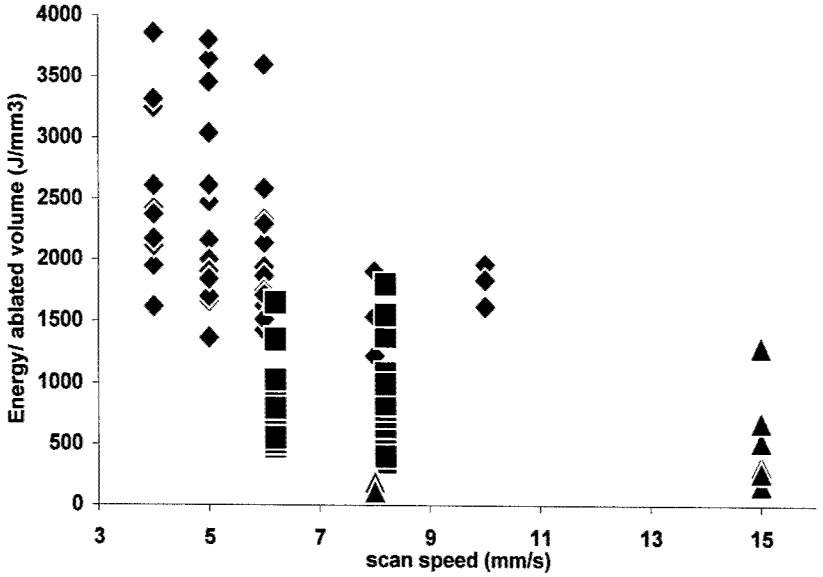

FIGURE 3. Graph showing relationship between energy required to ablate unit volume and scan speed. ◆ 1 pass over track, ■ 2 passes over track, ▲ 4 passes over track (graph courtesy of Alison Crum).

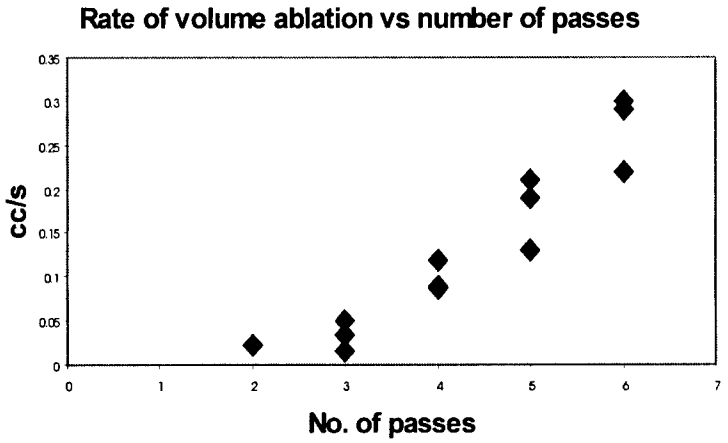

FIGURE 4. Graph showing rate of volume ablation as a function of the number of passes over the same track (230 W; 4 mm/s; 35 mm track length).

Clinical Effects

Conventionally in chemo- or radiotherapy, response to treatment is graded in terms of complete response (CR), partial response (PR) or no response (NR). These terms seem inappropriate for HIFUS. Here tissue response and targeting success may be better described using terms such as complete ablation (CA), incomplete ablation (IA), no ablation (NA) where complete ablation infers 100% of the targeted tissue (tumour plus normal tissue margin where appropriate) being destroyed at the time of treatment. Tumour tissue does not respond to thermal ablation in the same way as it does to other treatment modalities. Initially, the tumour volume, as assessed by "anatomical" imaging methods such as MRI, CT or ultrasound, may increase in response to the thermal insult. Resorption of the ablated volume is slow, and verification of HIFUS ablation during the first 4 weeks following treatment is best done using functional imaging techniques such as contrast enhanced MRI or CT, Doppler ultrasound, DSA, PET or SPECT.

DISCUSSION

The aim of dosimetry is two-fold. Firstly, it should give a meaningful description of the acoustic exposure to tissue, and from that allow prediction of the ablative effects that may be achieved. In describing the acoustic field it is relatively easy to define a minimum set of parameters that should be declared. These are: transducer diameter, focal length and frequency, axial and radial beam half widths, acoustic power and I_{SAL}. From these, comparisons of different sources can be made. I_{SAL} has been chosen in preference to I_{SP} as it is easier to measure with confidence in non-linear fields, it

bears a close relationship to the lesion extent, and allows direct calculation of I_{SP} from the relationship $I_{SAL} = 0.557 I_{SP}$.

Prediction of the volume that will be ablated from a given set of exposure parameters is more problematical. Tissue factors such as temperature, homogeneity and vascular status play an important part in the success of lesion creation. It is therefore still important that HIFUS treatments be monitored as they are carried out, using either diagnostic ultrasound techniques or magnetic resonance imaging.

This discussion has centred on dosimetry of HIFUS for the purpose of describing ablation. Another important factor in clinical treatments will be dose limiting effects. The primary site for damage is the skin. Skin dosimetry is therefore an essential component of treatment planning about which very little is as yet known, although it is generally recognised that treatment through overlying scars can lead to burns.

CONCLUSIONS

Informative dosimetry is an important aspect of understanding HIFUS and in performing successful treatments. It is therefore important that some common ground is reached between the different groups and disciplines involved. A minimum set of "exposure" parameters has been suggested for the reporting of HIFUS treatments and studies.

ACKNOWLEDGMENTS

The authors would like to thank Qi Zhong for his invaluable help in obtaining some of the experimental data obtained in this work, and Drs Mark Allen, Ian Rivens, Zhibao Wang, Peter Kaczkowski, and Bob Clarke for helpful and thought provoking discussions.

REFERENCES

1. Hill, C.R., Rivens, I., Vaughan, M.G., and ter Haar, G.R., *Ultrasound in Med. & Biol,* **20**, 259-269 (1994).
2. Malcolm, A.L., and ter Haar, G.R., *Ultrasound in Med. & Biol.*, **22,** 659-669 (1996).
3. Morton, K.I., ter Haar, G.R., Stratford, I.J., and Hill, C.R., *Ultrasound in Med. & Biol,* **9**, 629-633 (1983).
4. Overgaard, J., and Suit, H.D., *Cancer Res.,* **39**, 3248-3253 (1979).
5. Sapareto, S., and Dewey, W., *Int.J.Rad. Oncol.Biol. Phys,* **10**, 787-800 (1984).
6. Damianou, C., and Hynynen, K., *J.Acoust.Soc.Am.,* **95**, 1641-1649 (1994).
7. Damianou, C.A., Hynynen, K., and Fan, X., *IEEE Trans UFFC,* **42**, 182-187 (1995).
8. Robinson, T.C., and Lele, P.P., *J.Acoust.Soc.Am,* **51**, 1333-1351 (1972).

The Benefit Of Electronic Scanning In Extra-Corporeal Hifu

F. Lacoste**, J. Schlosser*, G. Vallancien*

*Department of Urology and Research (CERA) Institut Montsouris, 75013 Paris. France
** Edap, 69120 Vaulx-en-Velin. France

Abstract. Objectives: To study the immediate tissue effects of High Intensity Focused Ultrasound (HIFU) with electronic scanning and to determine acoustic treatment parameters on two perfused organ models.
Method: 17 livers and 23 kidneys, taken from 17 pigs, were perfused and treated by HIFU. The macroscopic and histological appearance of the lesions induced by focal scanning ranging from 3 x 3 mm to 10 x 10 mm, focal acoustic intensities ranging from 1,700 to 17,000 W/cm2 and pulse energy increasing by 20% steps were studied.
Results: Focal intensities lower than 3,600 W/cm2 allowed homogeneous " coagulation " of the tissues. Over 3,600 W/cm2, the tissues were heterogeneously lacerated when using electronic scanning. For equivalent scanning, the destruction of renal parenchyma required more energy than the destruction of hepatic parenchyma. The energy required for destruction of a tissue volume was inversely proportional to the scanned volume and the focal intensity.
Conclusion: Electronic scanning provides an energy gain in HIFU. Focal intensity can change the homogeneity and the precision of the focal destruction. The choice of focal intensity will depend on the treatment objectives.
Key-Words: HIFU, Extracorporal Circulation, Electronic scanning.

INTRODUCTION

The objective of High Intensity Focused Ultrasound (HIFU) is to induce rapid, irreversible and selective destruction of deep benign or malignant tumors [1]. In most systems, only a small volume is destroyed with each ultrasound pulse due to the highly focused nature of the ultrasound beam. Electronic scanning allows this volume to be increased as desired. Various studies [2,3] have demonstrated the potential value of this new technique to increase the rate of treatment of large tumors. The aim of this study was to verify this hypothesis in vitro on two different perfused organ models.

MATERIAL AND METHOD

The HIFU Device (Edap, France)

The treatment head is composed of 160 flat piezoelectric ceramics arranged within a 320 mm radius spherical dish and operating at 1 MHz. The focal point has an ovoid shape, 2 mm in diameter and 10 mm long (Figure 1). The ceramics can be excited with

various power levels, allowing adjustment of the peak acoustic power between 150 and 6200 W.

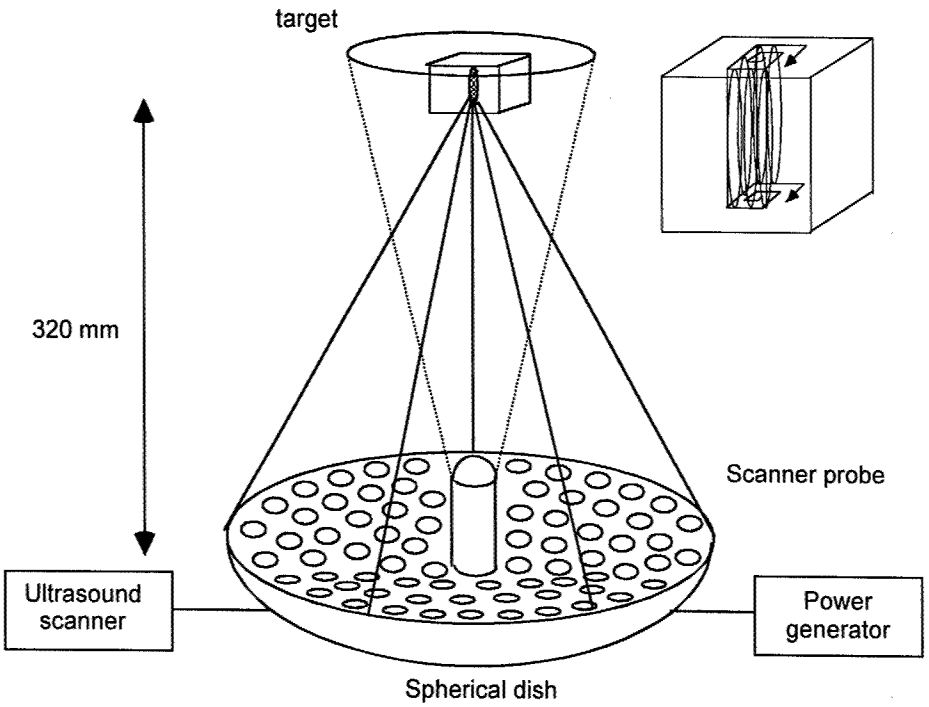

FIGURE 1. Schematics of the treatment head and of the motion of the focus.

Each ceramic in this new treatment head can be activated asynchronously and independently. By adjusting the relative phases very rapid electronic movement of the focal point within the target volume can be obtained, without any mechanical movement of the treatment head.

The volume scanned during each ultrasound pulse is a cube with dimensions ranging from 3 x 3 x 10 mm to 15 x 15 x 10 mm. Larger volumes can be treated by mechanical displacement of the treatment head.

Ultrasonic detection of the target volume is ensured by a real time ultrasonic probe (3.5 MHz, 120° scanning angle, with a fixed focal length of 80 mm) located in the center of the treatment head.

Perfusion Circuit

The perfusion circuit (Figure 2) consisted of a reservoir with filter Minimax 1316 (Medtronic France SA, Rueil Malmaison, France), two Stöckert monoblock peristaltic pumps ensuring precise control of blood flow rates, an oxygenator with a heat exchanger Minimax Plus 3381 (Medtronic France SA, Rueil Malmaison, France) mounted on the arterial line, a non sterile experimentation circuit especially designed for this study and comprising a DIDECO D624 pediatric bubble trap mounted on the venous line (Sofracob SA, Reventin-Vaugris, France). The heat exchanger was

supplied with water heated on a Gambro HYP 10-200 hot block. The temperature of perfused blood, maintained at 37° C, was controlled by a YSI tele-thermometer (Simpson Electric Co., USA) connected to the heat exchanger. Oxygenation of arterial blood, verified before and at the end of the experimentation, maintained as close as possible to physiological values (PaO2 between 80 and 100 mm Hg, PaCO2 between 35 and 45 mm Hg, SaO2 between 80% and 100%, pH around 7.40), was ensured by a SECHRIST air-oxygen mixer connected to the laboratory's wall supply.

Method

17 livers and 23 kidneys of 17 female Large White x Land Race pigs were removed under anesthesia, according to a surgical procedure. The kidneys were removed first, cannulated, perfused and stored in Euro-Collins solution at 4° C until treatment. The common bile duct and hepatic vessels were immediately cannulated and connected, within fifteen minutes, to the perfusion circuit composed of heparinised blood taken from the animal before sacrifice.

During the experimentation, the organs were maintained in an ultrasound-transparent tank connected to the treatment head (Figure 3). The flow rates of the hepatic artery (between 245 and 320 ml/min) and of the portal vein (between 430 and 560 ml/min) were determined as a function of the animal's weight. The renal artery blood flow rate was systematically set at 150 ml/min.

The focal acoustic intensity I was varied by modifying the electrical power supply to the ceramics. For each scanning dimension, dx, and each value of focal intensity, I, the pulse duration and consequently the focal energy EcF was gradually increased by 20% steps until homogeneous volumes of destruction, of adequate dimensions, were obtained. Altogether, 144 hepatic lesions and 90 renal lesions were created.

After treatment, the organs were fixed in 10% formaldehyde solution. The volumes destroyed were measured. Their shape, macroscopic and histological appearance, examined by light microscopy, were described. The standard stain used was Haematein-Eosin-Saffron. The lesions were then classified according to their size and homogeneity.

RESULTS

Focal Energy According To Focal Acoustic Intensity I

EcFm, expressed in kJ/cm2, is the mean focal energy per unit of surface area scanned, necessary to obtain adequate dimensions of tissue destruction (Table 1 and Figure 4). For equivalent scanning, EcFm is inversely proportional to focal acoustic intensity I. For equivalent intensity and scanning, destruction of renal parenchyma requires more energy than destruction of hepatic parenchyma.

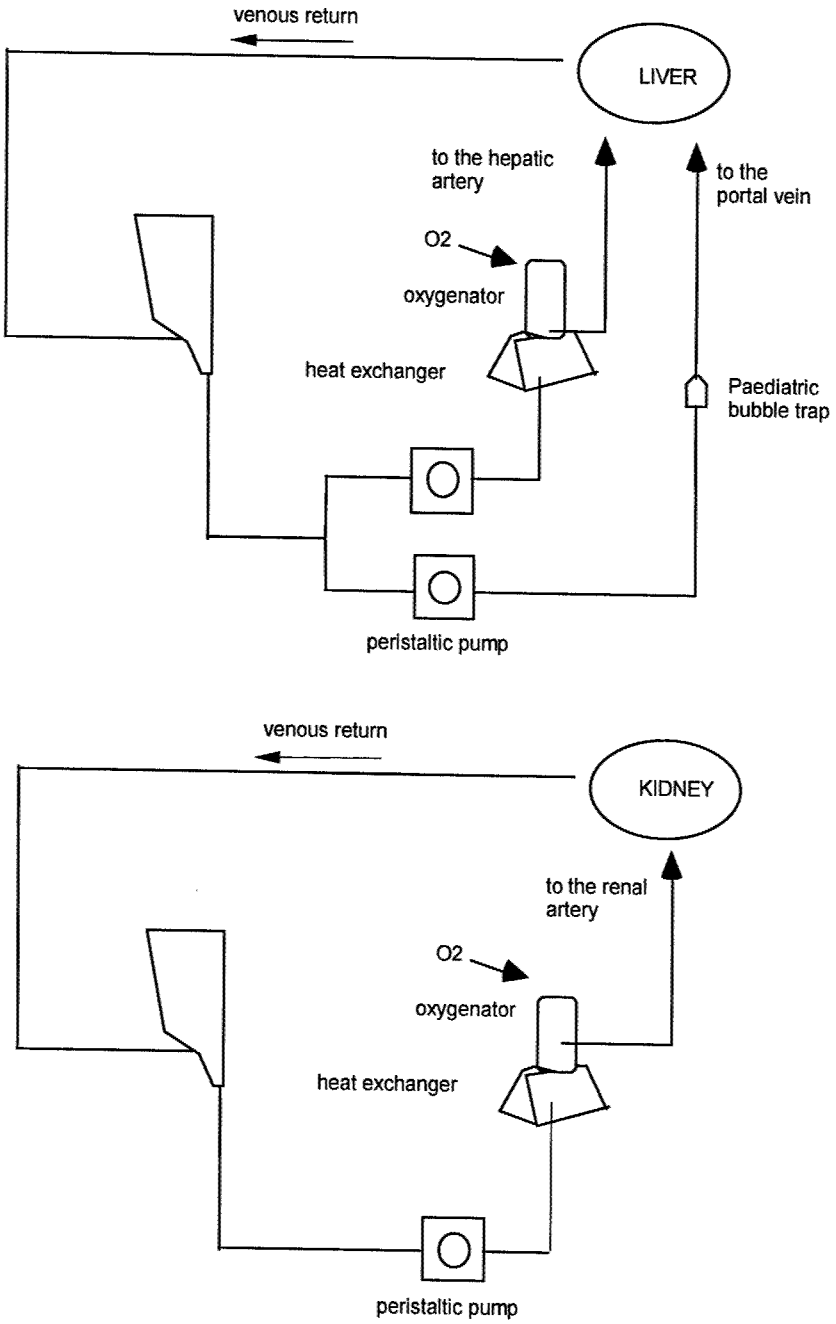

FIGURE 2. Experimental perfusion circuits for isolated perfused liver and kidney.

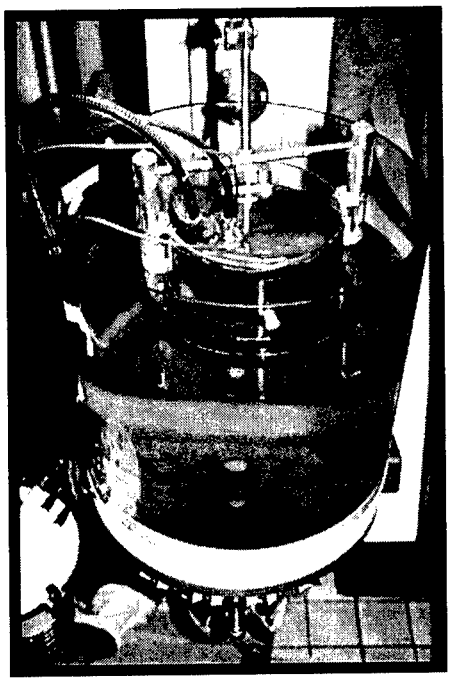

FIGURE 3. The perfused organ is immersed in a tank, itself located over the treatment head.

TABLE 1. Hepatic and renal treatment parameters for various values of focal intensity (I) and focal scanning dimensions (dx).

FOCAL INTENSITY (W/cm2)	**MEAN FOCAL ENERGY EcFm (kJ/cm2)**					
	Kidney dx: 2mm	kidney dx: 5mm	Liver Dx: 2mm	liver dx: 3mm	liver dx: 5mm	liver dx: 10mm
1700			16,6	15,8	15,2	12,1
2180	22,6					
3870				7,7	4,9	4,5
5020		7,3				
6580			7,6	6,8	3,3	3,3
8520	9,45	6,1				
12960		3,6				
13650			3,33	3,3	1,9	1,4
17040	4,59	3,2				

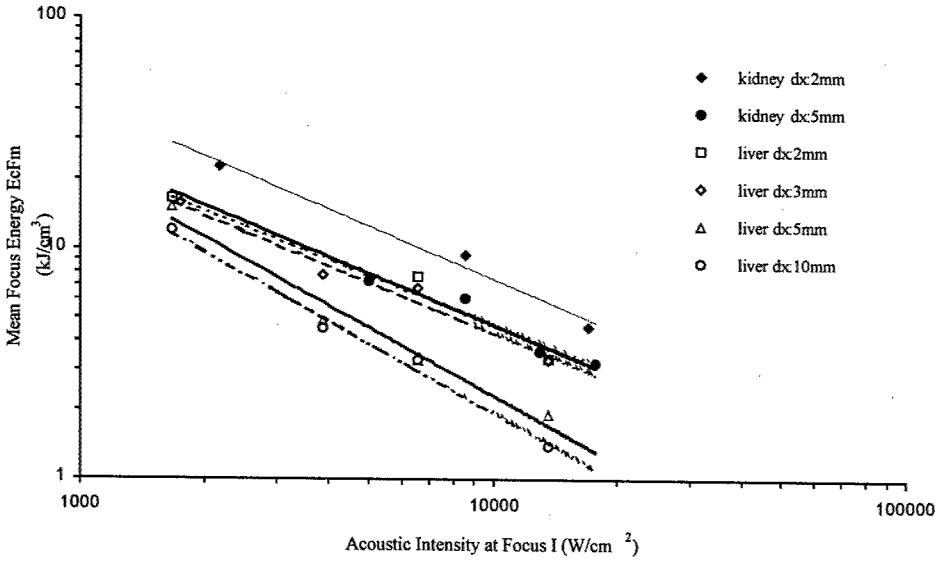

FIGURE 4. Hepatic and renal treatment parameters for various values of focal intensity (I).

Focal Energy vs. Size Of Scanning

On the hepatic and renal model, for equivalent intensity, the energy necessary to produce lesions EcFm diminishes when the size of scanning increases. This energy gain due to scanning increases with focal intensity.

Influence Of Focal Acoustic Intensity On Tissue Destruction

At low focal intensity (I ≈ 1,700 W/cm2 for the liver / I ≈ 2,200 W/cm2 for the kidney), no alteration of tissue echogenicity after treatment was observed. The tissues did not present any macroscopic or microscopic structural modifications. The whitish lesions had a homogeneous, oval shape, regardless of the scanning dimensions used. Tissues appeared to be " coagulated " (Figure 5).

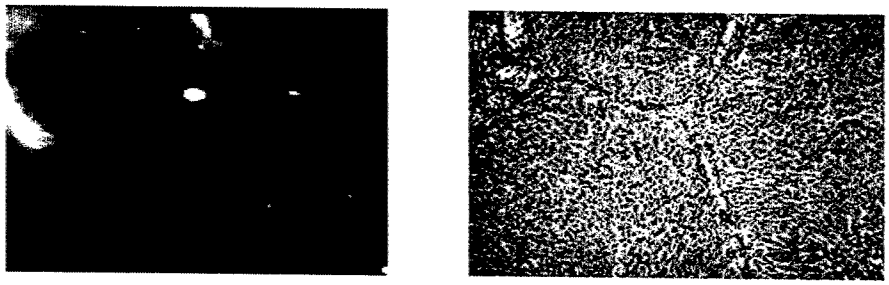

FIGURE 5: Juxtaposition of " thermal " lesions in perfused isolated liver (macroscopic and microscopic images).

At higher intensity (I > 3,600 W/cm2 for the liver and kidney), all of the focal lesions commenced at a satisfactory depth, but had a conical shape when focal scanning was used. They all resulted in hyperechogenicity of the tissue after treatment. The tissues were always histologically lacerated and more severely destroyed in the proximal part of the focal spot (Figure 6).

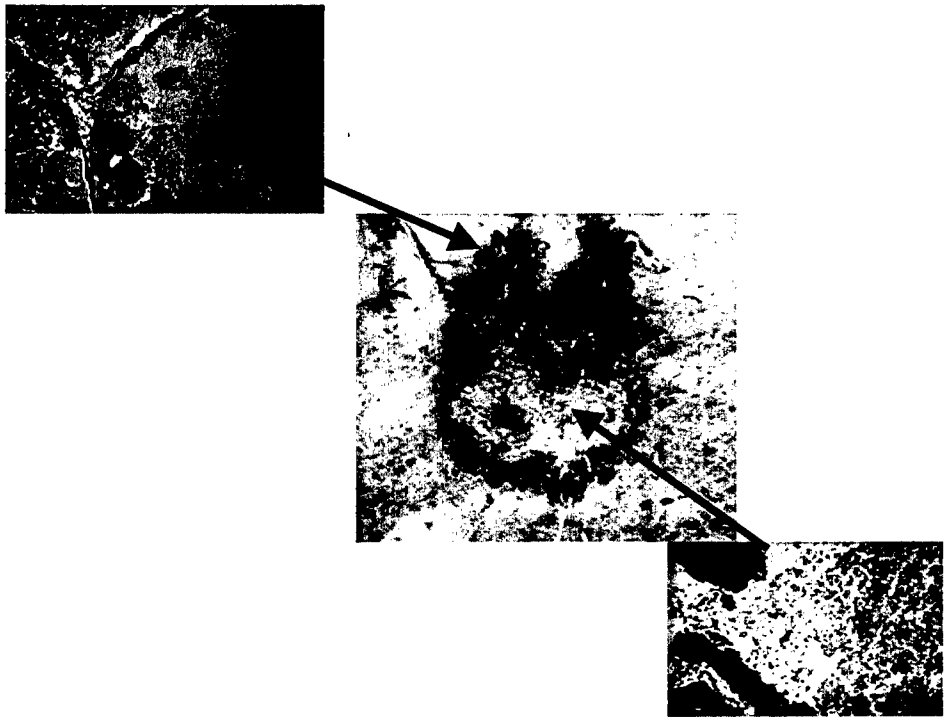

FIGURE 6. Juxtaposition of high intensity lesions in perfused isolated liver (macroscopic and microscopic images).

DISCUSSION

Depending on the intensity and frequency of the acoustic beams, the mechanism of tissue destruction is thermal or by cavitation. At low intensity, thermal effect is obtained, but treatment time is longer than at high intensity where tissue destruction occurs mainly by cavitation.

This model allowed the selection of precise acoustic parameters. The absence of intervening tissues ensured that all the emitted acoustic energy precisely reached the target. Since the tissue was perfused in this model, the heat sink effect of blood perfusion was taken into account. This is particularly important in the case of low intensity – longer time sonifications.

The results of the experimentation finally confirmed the energetic advantage of electronic scanning for tissue destruction at the focal point. The energy required for

destruction of a hepatic or renal volume is inversely proportional to the scanned volume and the focal acoustic intensity. Energy gain was relatively low at moderate intensities (about 1700 W), but reached 2 with 6500 W power and scanning size about 4 times the focal spot.

However, the focal acoustic intensity determines the mechanism, shape and homogeneity of tissue destruction. Low intensity lesions, without mechanical damage, are homogeneous and oval shape. With high intensities, lesions start at the same plane and seem to grow towards the transducer. The appearance of gas cavities trapped in the tissues, due to tissue boiling or cavitation, may be responsive of this phenomena [4], because the cavities increase the ultrasound absorption.

It is important to take this concept into account, as, in anticancer therapy, tissues must be destroyed as homogeneously as possible. On the other side, cavitation could also increase the risk of metastases [5], contrary to thermal tissue destruction [6]. For the treatment of malignant tumors, low focal intensity therefore appears to be necessary.

In other indications, the homogeneity of tissue destruction is not a sine qua non condition. In benign tumors or hyperplasia, the objective of treatment is to decrease a volume [7]. In superficial bladder tumors, treatment is designed to "resect" the tumour extracorporeally [8,9]. The choice of a high focal intensity should then allow immediate mechanical destruction of the tissues and should be energetically more advantageous.

CONCLUSIONS

These experiments showed that electronic scanning provides an energy gain directly proportional to the scanning dimensions and focal intensity. Focal intensity can modify the quality and precision of ultrasound destruction. Thus, electronic scanning in Extracorporal High Intensity Focused Ultrasound offers more flexibility in selecting treatment options, with focal intensity chosen to meet specific treatment objectives.

ACKNOWLEDGMENTS

The authors want to thank Drs A. Arefief and Chapelon (INSERM U556 - Lyon), Dr F. Laborde, and all members of the CERA - Fondation de l'Avenir research laboratory for their technical assistance in this research.

REFERENCES

1. Vallancien, G., Chartier-Kastler, E., Bataille, N., Chopin, D., Harouni, M., Bougaran, J., "Focused Extracorporal Pyrotherapy," *Eur Uro*, **23**, 48-52 (1993).
2. Fan, X., Hynynen, K., "Control of the necrosed tissue volume during noninvasive ultrasound surgery using a 16-element phased array," *Med Phys*, **22**, 297-306 *(1995)*.

3. Fan, X., Hynynen, K., "Ultrasound surgery using multiple sonications - Treatment time considerations," *Ultrasound Med Biol*, **22**, 471-482 *(1996)*.
4. Watkin, N.A., Rivens, I.H., ter Haar, G.R., "The intensity dependence of the site of maximal energy deposition in focused ultrasound surgery," *Ultrasound Med Biol*, **22**, 483-491 (1996).
5. Oosterhof, G.O., Cornel, E.B., Smits, G.A., Debruyne, F.M., Schalken, J.A., "The influence of high-energy shock waves on the development of metastases," *Ultrasound Med Biol*, **22**, 339-44 (1996).
6. Oosterhof, G.O., Cornel, E.B., Smits, G.A., Debruyne, F.M., Schalken, J.A., "Influence of high-intensity focused ultrasound on the development of metastases," *Eur Urol*, **32**, 91-95 (1997).
7. Maderbacher, S., Kratzik, C., Susani, M., Marberger, M., "Tissue ablation in benign prostatic hyperplasia with high intensity focused ultrasound," *J Urol*, **152**, 1956-1961 (1994).
8. Vallancien, G., Harouni, M., Guillonneau, B., Veillon, B., Bougaran, J., "Ablation of superficial bladder tumors with focused extracorporeal pyrotherapy," *Urology*, **47**, 204-207 (1996).
9. Watkin, N.A., Morris, S.B., Rivens, I.H., Woodhouse, C.R.J., ter Haar, G.R., "A feasibility study for the non-invasive treatment of superficial bladder tumors with focused ultrasound," *Br J Urol*, **78**, 715-721 (1996).

Control Of The Size And Shape Of Myocardial Lesions Produced By HIFU

Robert Muratore*, Frederic L. Lizzi*, Sarayu N. Ramachandran*, David Engel†, Shunichi Homma†, and Charles C. Marboe†

*Riverside Research Institute 156 William St Fl 9, New York NY 10038-2609 USA

†Columbia University College of Physicians and Surgeons, 161 Fort Washington Ave, New York NY 10032-3713 USA

Abstract. Management of cardiac arrhythmias and potential revascularization of the myocardium in patients with ischemic heart disease might be possible with therapeutic ultrasound. For example, lesion formation in the ventricular wall can disrupt arrhythmias. Damage to the endocardium or other areas of the ventricle may promote revascularization of the cardiac tissue. In order to guide these therapies, a taxonomy of ultrasound lesions was compiled. High-intensity focused ultrasound (HIFU) was used to create lesions in canine left and right ventricular cardiac tissue *ex vivo*. Sectioning, trichromic staining and photomicrography revealed denatured proteins in areas exposed to lower intensity ultrasound and mechanical damage surrounded by a "halo" of denatured protein in areas exposed to higher intensity ultrasound. Control of conventional beam parameters including focal region diameter and depth allowed the formation of intramyocardial lesions without involvement of the myocardial surfaces. This is potentially important because it avoids the formation of blood clots associated with damage to the inner surface of the heart. In addition, unique beam parameters including radial asymmetry via the use of annular array and linear strip-electrode spherical-cap therapy transducers produced "custom" lesion shapes corresponding to beam focal-region shapes, as revealed by photomicrographs.

INTRODUCTION

Sustained ventricular tachycardia is a grave instance of cardiac arrhythmia. Blockages in coronary arteries produce a ventricular "dead zone" surrounded by ischemic tissue. The electrical impulses that regulate contraction travel more slowly in ischemic than in healthy regions. The transit time through an ischemia can be greater than the refractory period of the muscle fibers, but much less than the period required to efficiently pump blood. The result is an extremely rapid heart rate and a severe drop in blood pressure [1].

Therapies to reduce recurrence include those aimed at blocking the electrical current through the ischemic region by forming a lesion, and those aimed at decreasing the electrical impulse transit time by promoting healing through re-established blood flow (revascularization).

Lesion-forming therapies often utilize radio-frequency (RF) ablation. We have investigated the use of high-intensity focused ultrasound (HIFU) as an alternative means of lesion formation, or ablation [2]. HIFU is potentially safer (minimizing

endocardial damage and associated clot formation), less invasive (avoiding catheterization) and more accurate (being guided ultrasonically).

At the cellular level, revascularization therapies include lasers, which require catheterization. HIFU can potentially operate from outside the heart, and might offer the ability to tune revascularization attempts to the proper depth in tissue, including the endocardial surface [3, 4].

Thus, an understanding of HIFU in cardiac tissue will provide a basis for its potential use as a lesion-forming tool and a cardiac revascularization tool, among other uses [5].

We have made a variety of HIFU lesions in canine cardiac tissue *ex vivo*, and in a simple model tissue (chicken breast). We have performed extensive computer simulations of the lesion formation process. All approaches are qualitatively consistent. We have begun to look at nonlinear effects that we hope will produce quantitative consistency.

METHODS

Canine Cardiac Lesions

Hearts were harvested from mongrel dogs recently sacrificed for other purposes. Strips of ventricular and atrial tissue were degassed in normal phosphate-buffered saline and insonified with various transducers to form lesions.

Cardiac lesions were made with Sonocare model CST-100 ultrasound therapy systems [6] which feature 80 mm diameter, 90 mm focal length spherical-cap PZT-4 transducers, excited at 4.67 and 4.75 MHz, with acoustic power ranging from 22 to 60 W, for durations from 1 to 10 seconds; and with a strip-electrode transducer of the same size (see Simulations, below) excited at 4.65 MHz, with acoustic power ranging from 10 to 30 W, for durations from 0.1 to 5 seconds. Ambient temperature for all lesions was room temperature, about 22° C. Power was measured with the radiation force technique. Additional characterization of the transducers was made with 0.2 mm diameter PVDF hydrophones.

Lesioned regions were excised, placed in normal buffered 10% formalin, sectioned, stained with Masson's trichrome stain, mounted and photographed.

Model (Chicken) Lesions

Supermarket chicken breasts were brought to room temperature, degassed in normal phosphate-buffered saline, and insonified with various transducers to form lesions.

Chicken lesions were made with Sonocare model CST-100 ultrasound therapy systems (see Canine Cardiac Lesions, above), excited at 4.67 MHz, with acoustic power ranging from 22 to 60 W, for durations from 1 to 5 seconds.

Lesioned regions were exposed by scalpel and photographed.

Computer Simulations

Three transducer designs were considered. Each transducer is of identical physical design: spherical-cap PZT-4 with a diameter of 80 mm and a focal length of 90 mm. The front of each is electrically identical, with a single common electrode formed by the plated concave surface. The rear differs in the number and size of electrodes: one transducer has a single, full-surface rear element, one has multiple wide linear strips, of which the outer two, 20 mm wide, were excited [7], and one has multiple narrow linear strips, of which the outer two, 10 mm wide, were excited. Each transducer was modeled linearly. Frequency was set to 4.5 MHz, focal point intensity was set to 5 kW/cm^2, and exposure duration was set to 1 second.

Beam Pressure

Standard diffraction integrals [8] were evaluated numerically to determine the three-dimensional beam pressure profile.

Absorbed energy

The computation for absorbed energy used representative attenuation and absorption coefficients (attenuation = 0.5 $dBMHz^{-1}cm^{-1}$, absorption = 75% attenuation) [9]. The tissue sample was set to 1 cm thick, with the beam focused in the middle.

Temperature

The bio-heat transfer equation [9,10] was evaluated to determine the three-dimensional temperature distribution as a function of time.

Lesions

The thermal dose integral was used to compute the equivalent time of exposure at 43° C. Lesions were determined at points where the dose was greater than or equal to 240 minutes [11].

RESULTS

Canine Cardiac Lesions

Lesions of distinct types were obtained. Protein-denaturing lesions, PDLs, (gently produced thermal lesions in which mechanical effects are minimized) can be distinguished from "bubbly" lesions (Fig. 1). A magnified image of a bubbly lesion shows a large vacuole within a myocyte. Transmural lesions can be distinguished from and intramural lesions in ventricular tissue (Fig. 2). Also, lesions could be formed by placing the transducer on the endocardial side and aiming at the epicardial side, and by

placing the transducer at the epicardial side and aiming at the endocardial side. Finally, the length of 19 measured lesions tended to increase with acoustic power, as shown in the dose-response curve in Fig. 3.

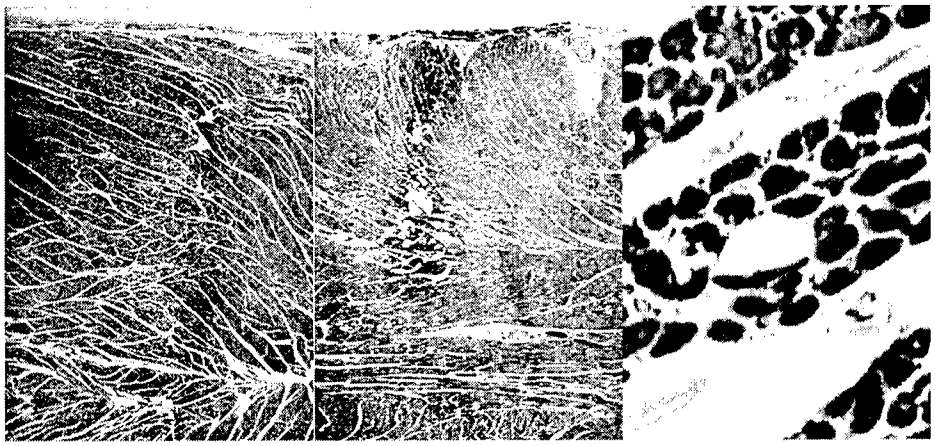

FIGURE 1. Photomicrographs show protein-denaturing lesion (PDL) (left), bubbly lesion (center), and myocyte vacuole (right) in canine ventricular myocardium. Slices were stained with Masson's trichrome stain, and scanned images were globally color-enhanced in Photoshop. Left and center images are approximately 0.8 cm high, with transducer located endocardially. Notice the halo of protein-denatured tissue around the bubbly lesion. Lesions were produced near 4.7 MHz, at approximately 30 W. The myocyte vacuole, near the center of the right image, appears to be a thermally produced bubble within the cell membrane.

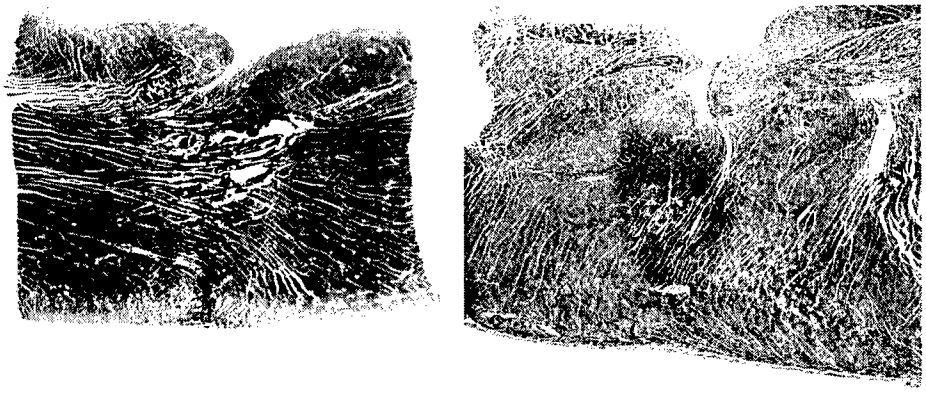

FIGURE 2. Photomicrographs show a transmural lesion (left) and an intramural lesion (right) in canine ventricle. Slices were stained with Masson's trichrome stain, and scanned images were globally color-enhanced in Photoshop. Images are approximately 1 centimeter high. Transducer was located on endocardial (top) side. Transmural lesion was made with a full-aperture transducer at 4.67 MHz, with acoustic power equal to 29 W for 3 seconds. Intramural lesion was made with a full-aperture transducer at 4.67 MHz, with acoustic power equal to 46 W for 1 second.

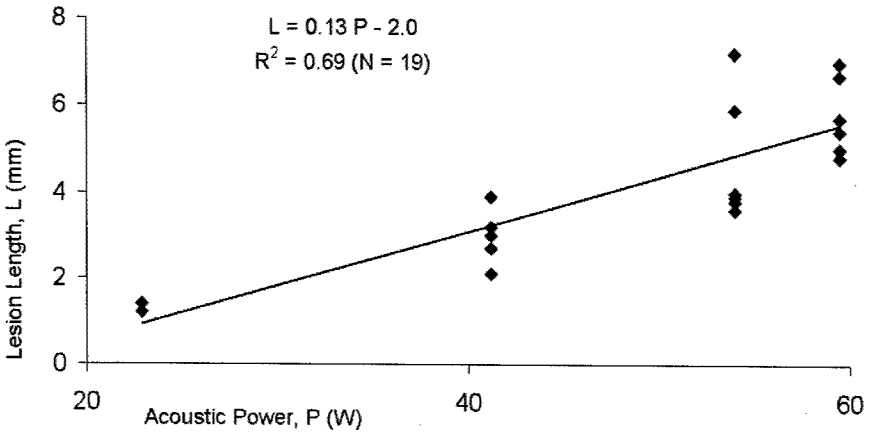

FIGURE 3. Dose-Response curve for 19 canine cardiac ventricular lesions made with full-aperture 80 mm diameter, 90 mm focal length spherical-cap transducers operated near 4.7 MHz. Lesion length was measured axially. Line was regression-fit.

Model (Chicken) Lesions

Chicken lesions were obtained that were similar to the cardiac lesions. The chicken lesions (Fig. 4) followed the simulation predictions (Fig. 5), with the strip-electrode transducer producing wider and less transversely symmetrical lesions than the full-aperture transducer.

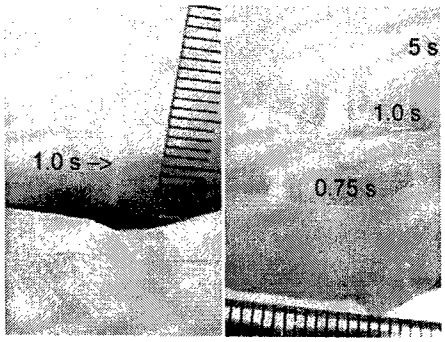

FIGURE 4. HIFU lesions in chicken breast were made with full aperture transducer at 4.67 MHz, 29 W, 1 second (left) and 20 mm strip-electrode transducer at 4.75 MHz, 25 W, various exposure times (right). Right sample was insonified from the opposite surface. Rulings are in millimeters. Strip-electrode lesions are wider than full-aperture lesions, consistent with simulations (see Fig. 5).

Computer Simulations

The beam pressure profiles, temperature fields produced in representative tissue by the incident beam, and resulting lesions vary dramatically and systematically as the aperture of the spherical-cap transducer is reduced to narrow parallel strips (Fig. 5). The strip-electrode transducers produce transverse asymmetry.

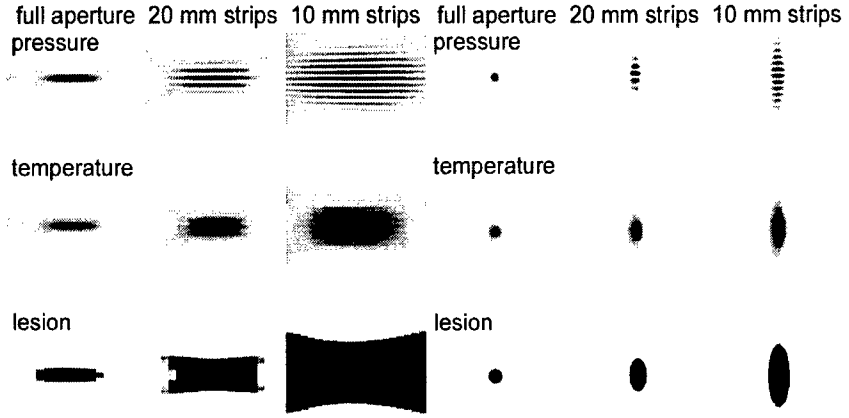

FIGURE 5. Normalized pressure profile, normalized temperature field, and lesion extent as calculated in 1 cm of tissue with attenuation = 0.5 $dBMHz^{-1}cm^{-1}$, absorption = 75% attenuation. Full aperture is 80 mm diameter, 90 mm focal length PZT-4 spherical-cap transducer focused 5 mm into tissue, at 4.5 MHz, 5 kW/cm^2 focal point intensity for 1 second. 20 mm strips and 10 mm strips are outer strips of strip-electrode transducers, otherwise identical to full aperture transducer. Left set of images shows broader transverse-axial plane. Beam enters sample from left. Right set of images shows focal plane. Transverse asymmetry is clearly evident in these simulations.

DISCUSSION

Our suite of computer simulations was able to suggest appropriate doses for the formation of lesions and to predict the variation in lesion width with transducer design in the chicken and cardiac tissues. Furthermore, it demonstrates that a new transducer similar to our existing 20 millimeter-strip-electrode transducer, but with narrower 10 millimeter strips, will produce an even wider, less symmetric beam, useful for quickly "painting" lesions in tissue.

We were able to form protein-denaturing lesions (PDLs) and bubbly lesions endocardially, epicardially, transmurally, and intramurally.

Producing a wide variety of *ex vivo* ventricular lesions with an exposure of less than 1 second is no guarantee that *in vivo* ventricular HIFU will be easy. Nonetheless, Williams et al. [12] have been successful in producing atrial HIFU lesions in live, open-chest dogs.

With a fine-grained striated structure and thickness of between 1 and 2 cm, chicken breasts serve as a convenient model of the myocardium.

Finally, we note that we have seen several higher harmonics in a hydrophone characterization of our long water path transducers, suggesting that nonlinear effects might play a role in accurate determination of delivered dose [13,14].

ACKNOWLEDGMENTS

The authors thank Gayle Denman, who produced the chicken lesions, and Cheri X. Deng, who developed some of the computer simulation algorithms.

This research was supported in part by Bioengineering Research Partnerships grant 5R01 CA84588, awarded by the National Cancer Institute and the National Heart, Lung, and Blood Institute.

REFERENCES

1. Netter, F. H., *Heart (The CIBA Collection of Medical Illustrations, Vol. 5)*, Summit NJ: CIBA, 1978.
2. Kluiwastra, J.-U., Zhang, Y., VanBaren, P., et al., "Ultrasound Phased Arrays for Noninvasive Myocardial Ablation: Initial Studies" in *1995 IEEE Ultrasonics Symposium Proceedings*, New York: Institute of Electrical and Electronic Engineers, 1995, pp. 1605-1608.
3. Smith, N. B., and Hynynen, K., *Ultrasound Med. & Biol.* **24**, 1045-1054 (1998).
4. Sanghvi, N. T., Fry, F. J., Zaitsev, A., and Olgin, J., "Cardiac Ablation Using High Intensity Focused Ultrasound: A Feasibility Study" in *1997 IEEE Ultrasonics Symposium Proceedings*, edited by S. C. Schneider et al., New York: Institute of Electrical and Electronic Engineers, 1997.
5. Lee, L. A., Simon, C., Bove, A. L., et al. *Echocardiography.* **17**, 563-566 (2000).
6. Silverman, R. H., Vogelsang, B., Rondeau, M. J., and Coleman, D. J., *Am. J Ophthal.* **111**, 327-337 (1991).
7. Lizzi, F. L., Astor, M., Deng, C. et al., "Strip-Electrode Ultrasonic Arrays for the Production of Asymmetric Therapeutic Thermal Lesions" in *1997 IEEE Ultrasonics Symposium Proceedings* **2**, edited by S. C. Schneider et al., New York: Institute of Electrical and Electronic Engineers, 1997, pp. 1331-1336.
8. O'Neil, H. T., *J Acoust. Soc. Am.* **21**, 516-526 (1949).
9. Lizzi, F. L., Driller, J., Lunzer, B., et al., *Ultrasound Med. & Biol.* **18**, 59-73 (1992).
10. Curra, F. P., Vogelsangourad, P. D., Khokhlova, V. A., et al., *IEEE Trans Ultrason., Ferroelec., & Freq. Contr.* **47**, 1077-1089 (2000).
11. Damianou, C. A., Sanghvi, N. T., Fry, F. J., and Maass-Moreno, R., *J Acoust. Soc. Am.* **102**, 628-634 (1997).
12. Williams, M. R., Kourpanidis, S., Casher, J., et al., *Circulation* **104**, II409 (2001).
13. Muir, T. G. and Carstensen, E. L., *Ultrasound Med. & Biol.* **6**, 345-357 (1980).
14. Duck, F. A. and Perkins, M. A., *IEEE Trans Ultrason., Ferroelec., & Freq. Contr.* **35**, 232-241 (1988).

Experimental Apparatus And Method For *In Vitro* HIFU Dose Response Studies

Marilee Andrew[1], Peter Kaczkowski[1], Andrew Brayman[1], Bryan Cunitz[1], Ajay Anand[1], Cyril Lafon[2], and Lawrence Crum[1]

[1]*Center for Industrial & Medical Ultrasound, Applied Physics Laboratory, University of Washington. Box 355640, 1013 NE 40th St. Seattle WA 98105-6698*
[2]*INSERM Unité 556, 151, Cours Albert Thomas 69003 Lyon, France*

Abstract. In order to develop treatment protocols for High Intensity Focused Ultrasound (HIFU) therapy it is necessary both to make quantitative comparisons between numerical simulations and experimental results, and also to develop appropriate means to parameterize the therapeutic dose. We have developed an experimental apparatus and analytical procedure that enables us to create reproducible HIFU lesions *in vitro*, measure their properties, and investigate the associated bioeffects. Our method consists of 1) measurement of bulk sound speed and attenuation, 2) computer-controlled delivery of HIFU, 3) precise tissue sectioning and image capture, and 4) computer-aided optical analysis to quantify and reconstruct lesion geometries in 3-D. The test chamber accommodates a sample of dimensions 45x45x65 mm^3; tissue samples are degassed in phosphate buffered saline (PBS) and warmed to 37°C in a test tank filled with degassed PBS. Specially-designed positioning stands provide the means to establish accurate registration using either a needle hydrophone or HIFU transducer transmit/receive signals. Dose parameters and position are pre-programmed using software developed with LabView. After HIFU exposure the tissue sample and chamber are frozen for approximately 1.5 hours to facilitate slicing. A threaded push-rod allows precise slicing of 1.27 mm thick sections, which are captured with a digital camera and downloaded to a PC. Image reconstruction software was developed using Matlab. Dose response data from initial experiments with freshly excised bovine liver demonstrate the utility and repeatability of the technique.

INTRODUCTION

The dose response of High Intensity Focused Ultrasound (HIFU) is becoming an important consideration as treatment applications in cancer and hemostasis progress toward clinical evaluation and use. Of growing interest is the ability to compare experimental data with theoretical predictions in order to develop treatment protocols and therapy planning systems. This paper describes an apparatus and method for creating reproducible HIFU lesions *in vitro*, quantifying lesion characteristics, and evaluating various dose response parameters.

MATERIALS AND METHODS

Tissue Preparation

Initial dose response studies were performed using freshly excised bovine liver obtained from a local slaughterhouse on the day of the experiments. Samples were cut to fit the test chamber (45 mm by 45 mm by 55 mm) and degassed in chilled phosphate buffered saline (PBS) for a minimum of 30 minutes. Samples were then warmed for approximately 45 minutes in order to reach a temperature of 37 °C prior to treatment with HIFU.

Test Tank And Positioning

The experimental setup is shown in Figure 1. A plexiglass test tank was filled with degassed PBS and heated to 37 °C. The tank was continuously degassed using a custom-built, vacuum-membrane degassing system. Each HIFU transducer (all were manufactured by Sonic Concepts, Inc. of Woodinville, WA USA) was mounted to a 3-axis positioning system and interfaced to a PC using LabView software. An HP 33120 function generator and ENI A150 amplifier were used to provide signal conditioning; a Lecroy oscilloscope was used to monitor signals and establish registration. Tissue samples were placed in a specially-designed aluminum tissue chamber; three windows in the chamber allow for HIFU treatment, bulk property measurement and ultrasound imaging. A special registration base for the chamber allowed for precise registration of HIFU treatment.

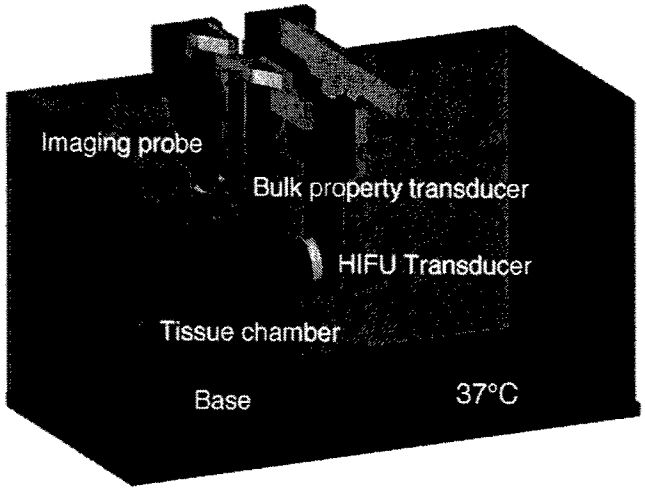

FIGURE 1. Test tank and instrument setup for HIFU dose response experiments.

Transducer Registration

The transducer face was first registered to the plane perpendicular to the axis by snugging the element face against the delrin base as shown in Figure 2(a) and securing the delrin transducer holder to the positioner rod. Figure 2(b) shows the test chamber equipped with a special registration footing. Four needles mounted in the footing allow for precise across- and along-axis positioning of the HIFU focus within the tissue sample. For these experiments, a transmit/receive switch was connected to the HIFU transducer, and the acoustic signal was observed on the oscilloscope. The 3-axis positioner was adjusted by hand until the acoustic reflection off the first needle was maximized in the vertical, horizontal and axial directions. This position was then stored in the positioner control software as the reference position, or origin. As an alternative to the transmit/receive method, the transducer may also be registered using a needle hydrophone which attaches to the delrin chamber base.

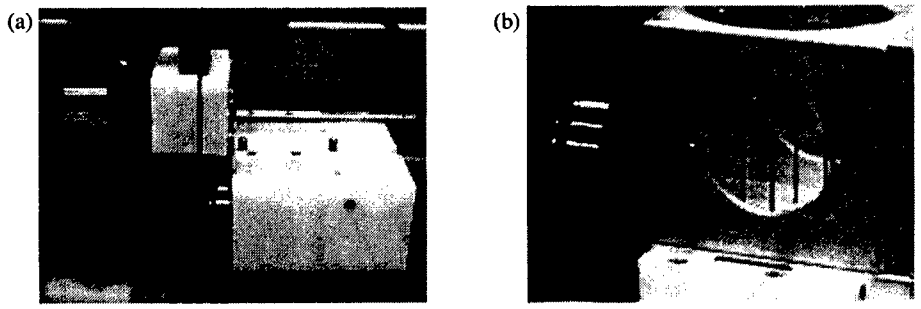

FIGURE 2. (a) Aligning transducer face with tissue chamber base. (b) Tissue chamber with needle registration footing.

BULK PROPERTY MEASUREMENT

Figure 3 shows the "acoustic calipers" used to acquire tissue sound speed and acoustic attenuation data. A pair of transducers was mounted on a set of digital calipers to enable precise measurement of the transmission path length. The broadband acoustic signal was transmitted first through a water path (reference signal) and then through the tissue; the received reference and tissue signals were acquired, averaged and compared in order to recover sound speed and attenuation as detailed in [1].

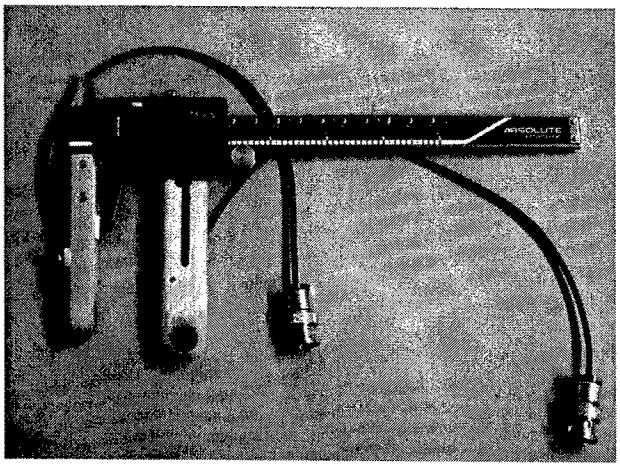

FIGURE 3. "Acoustic Calipers" used to determine tissue bulk properties.

Treatment Protocols

HIFU positioning and dose parameters were computer-controlled using LabView software. Two protocols, one for creating point lesions and one for creating scanned lesions, were developed for dose response studies. Figure 4(a) shows the laydown pattern programmed in Labview. A total of 9 lesions were formed on 8 mm centers in a single tissue sample; three lesions each were created for CW exposure times of 1, 2 and 4 s while holding the input electrical power constant. Exposure time was programmed from shortest to longest to reduce thermal buildup during treatment. A slice from near the focus of a tissue sample treated with 5 MHz HIFU at 20 W input electrical power is shown in Figure 4(b) and demonstrates the reproducibility of lesions within a single sample.

The scanned lesion laydown pattern is shown in Figure 4(c). A total of 8 tracks of 15 mm length were programmed. Scan direction was from center to edge, with 10 mm horizontal and 8 mm vertical separation between tracks. Results from a slice near the focus treated with 3.5 MHz HIFU with 30 W input electrical power and scan rates from 2 mm/s to 5.33 mm/s are shown in Figure 4(d). Note that due to the short standoff distance, shadowing of the transducer field by the tissue chamber reduced the amount of energy delivered in the top pair of scans (choice of geometry is transducer dependent and should be made carefully). The pair of tracks above the bottom row were made at the same scan rate of 2.67 mm/s; these demonstrate the reproducibility of scanned lesions within a single tissue sample. However, the tracks also illustrate that, while general lesion dimensions can be reproduced, lesion thickness along the track varies.

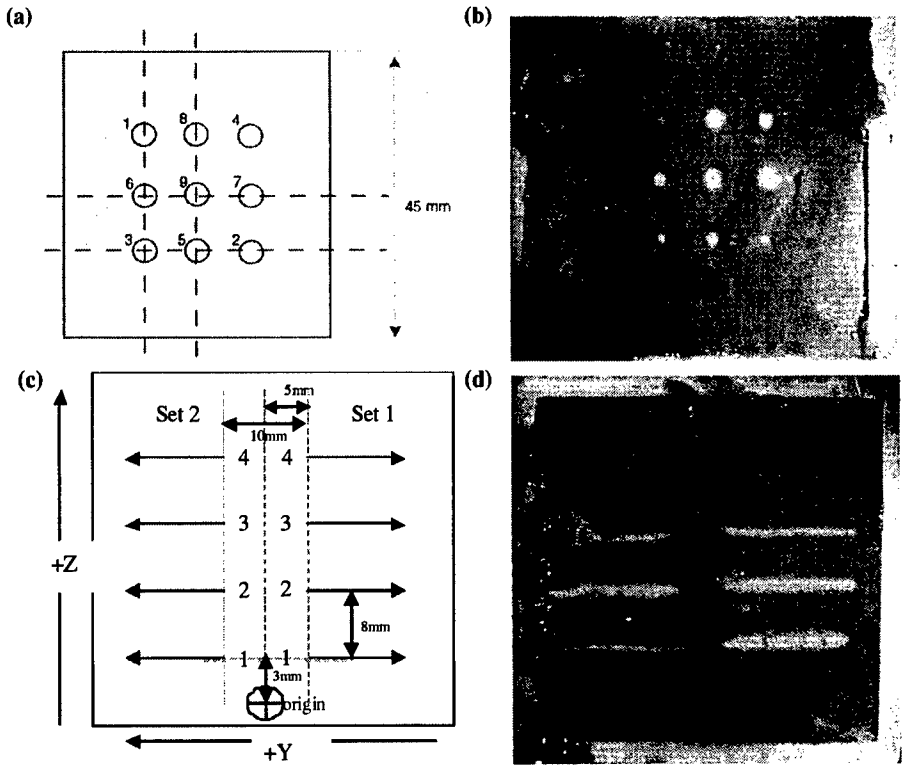

FIGURE 4. Treatment protocols: (a) laydown pattern for point lesions. (b) slice through tissue sample near focus showing results in bovine liver for a 5 MHz transducer at 20W electrical power. (c) laydown pattern for scanned lesions. (d) results near focus in bovine liver tissue for 3.5 MHz, 30 W input electrical power. Note that the top pair of tracks did not receive full treatment due to transducer field shadowing.

Tissue Sectioning And Lesion Image Capture

In order to ensure optimal sectioning, tissue samples were frozen to -10 °C for a minimum of 1 hour prior to slicing. This ensured sufficient stiffness was achieved to facilitate slicing while minimizing the amount of tissue expansion. The sectioning setup using a specially-modified deli-slicer is shown in Figure 5(a). A threaded pushrod was mounted into the back of the chamber, as shown in Figure 5(b), until it snugged against a square delrin push-pad behind the tissue block. The chamber was then placed in a custom slider box, which was set into grooved runners on the slicer assembly. The tissue sample was advanced until the tissue face was even with the plane of the slicer blade; the tissue surface was then photographed with a digital camera. The pushrod was rotated 360°, advancing the tissue 1.27 mm as shown in Figure 5(c). The excess tissue was cut away, and the newly exposed face was photographed. The process was repeated until no lesions were observed for at least three consecutive slices. Image files were then downloaded to computer further processing.

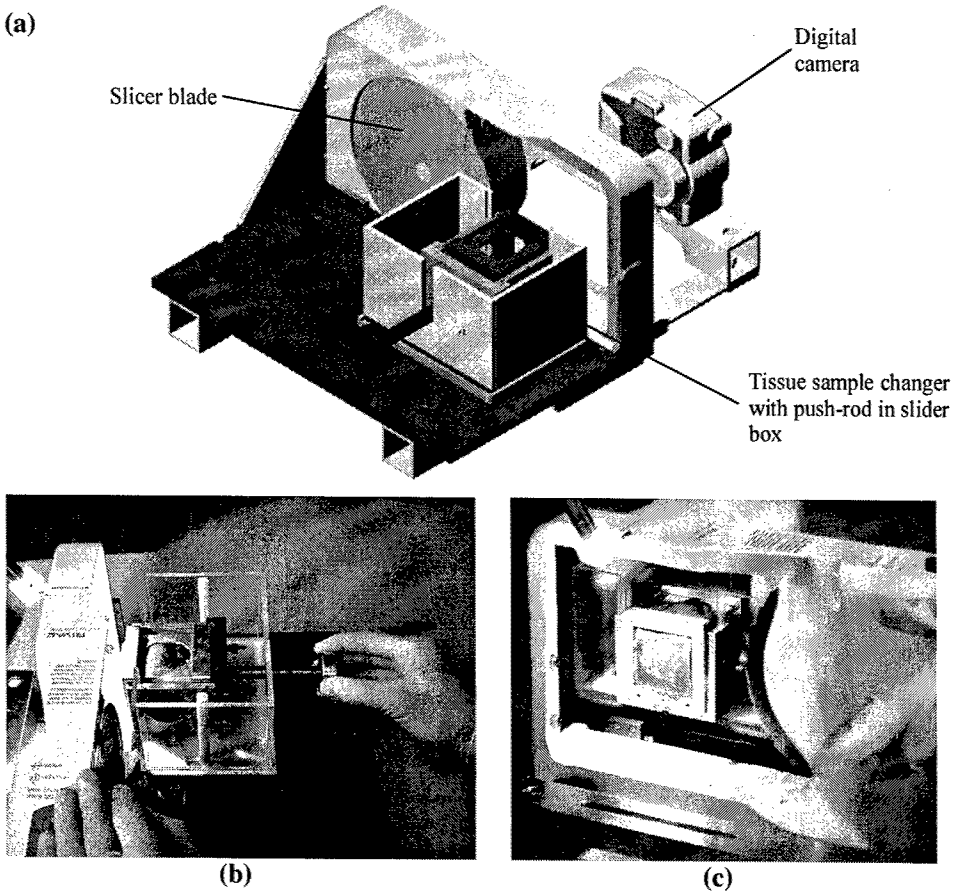

FIGURE 5. Set-up for tissue sectioning and image capture. (a) drawing showing tissue chamber with push-rod in slicer mounted in specially-designed slider box. The exposed face is captured on a digital camera. (b) overhead photo of setup. (c) photo showing exposed tissue face.

RESULTS

Tissue Bulk Properties

Sound speed and acoustic attenuation measurements in freshly excised bovine liver tissues are presented in Figures 6(a) and (b), respectively. Data were collected from 33 different tissue samples taken from 10 different bovine livers. Sound speed varied from 1577 to 1606 m/s, with an overall mean of 1589.1 and STD of 8.2, while attenuation varied from 0.4 to 1.48 dB/cm/MHz with an overall mean of 0.76 dB/cm/MHz and STD of 0.25. Such variability can be expected in liver given its inhomogeneity; the results agree well with those reported in the literature [2].

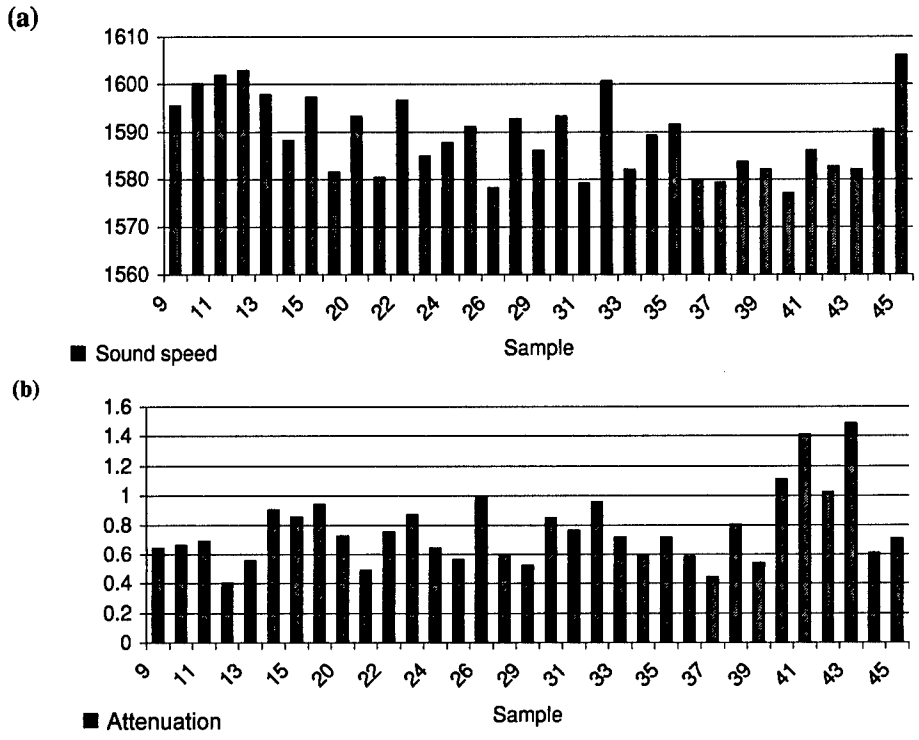

FIGURE 6. (a) sound speed and (b) acoustic attenuation of freshly excised bovine liver measured using acoustic calipers.

Image Processing And Lesion Reconstruction

Point Lesion Data

Point lesion image processing and 3-D reconstruction routines were implemented using Matlab software with the Image Processing Toolkit. RGB slice images were first converted to grayscale; an example is shown in Figure 7(a). The mean background was computed and subtracted to reduce noise. Morphological processing was then used to produce binary slice images; an example is shown in Figure 7(b). Individual lesions were selected from the binary slice data and 3-D reconstructions were produced. Figure 8 shows 3-D reconstructions for 1s, 2s and 4 s exposures with a 5 MHz transducer at 30 W input electrical power. The transducer focal length was 35 mm; the focus was set to a tissue depth of 15 mm. Note that as exposure time increased lesion shape transitioned from elliptical to tadpole and the energy was deposited increasingly prefocally. These observations are consistent with results previously reported [3].

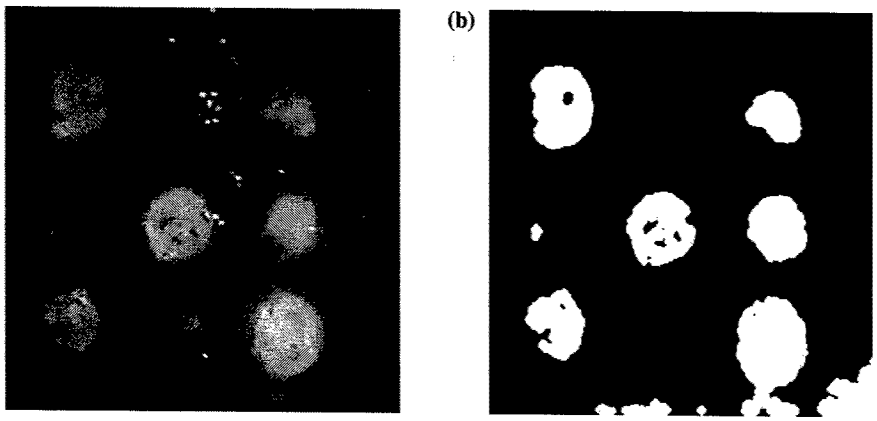

FIGURE 7. Example of point lesion slice image processing for a 2 MHz transducer using the laydown pattern shown in Figure 4 (a) above: (a) gray scale image of slice through treated liver tissue. (b) morphologically processed binary image of the same tissue slice. Individual lesions are selected for 3-D reconstruction; image processing parameters can be adjusted to optimize image morphology.

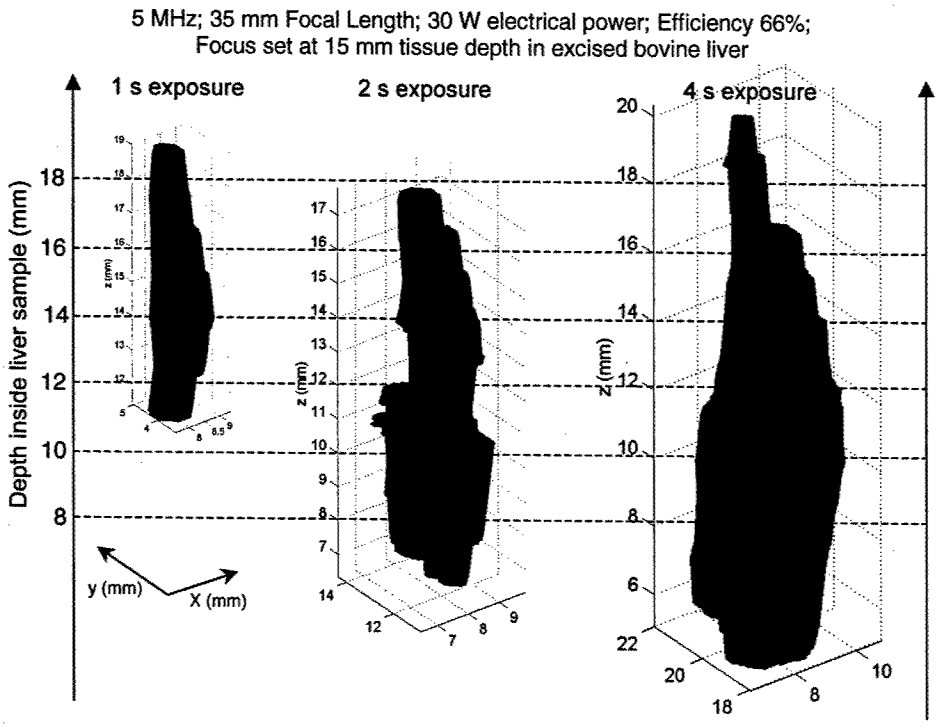

FIGURE 8. Point lesion 3-D reconstruction for 1, 2 and 4 s exposures.

In addition to 3-D reconstruction, lesion characteristics including maximum diameter, length and distance from transducer to lesion start can be collected and averaged to study the dose response. Figure 9 presents averaged lesion dimensions for the 5 MHz, 30 W input electrical power case. Of the parameters measured, only lesion diameter is observed to vary linearly with exposure duration.

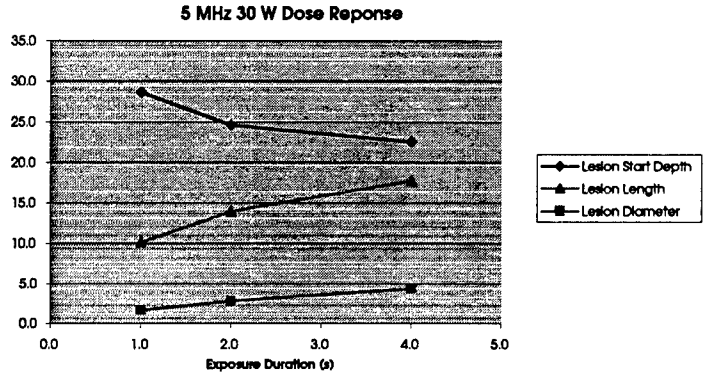

FIGURE 9. Lesion characteristics plotted as a function of exposure duration for a 5 MHz transducer and 30 W input electrical power.

Scanned Lesion Data

Image processing techniques applied to the scanned lesion data were similar to those applied to the point lesion data. Figure 10(a) presents a gray-scale image of a typical slice through tissue treated with scanned HIFU; Figure 10(b) presents the morphologically processed binary image of the slice. In the scanned case, 3-D reconstructions are less useful; of greater interest are the statistics related to the variability of the lesion along the scan path. In particular, the binary image data can be processed to obtain instantaneous lesion thickness across the scan; averaging the data yields lesion thickness (equivalent to point lesion diameter) mean and standard deviation. Figure 11 presents lesion statistics obtained for a 3.5 MHz case; along-scan instantaneous and mean lesion thickness are show in Figure 11(a), while mean lesion thickness versus axial depth is shown in Figure 11(b). Note that the scanned lesion is centered post-focally; additional samples must be processed, however, before this can be considered a trend.

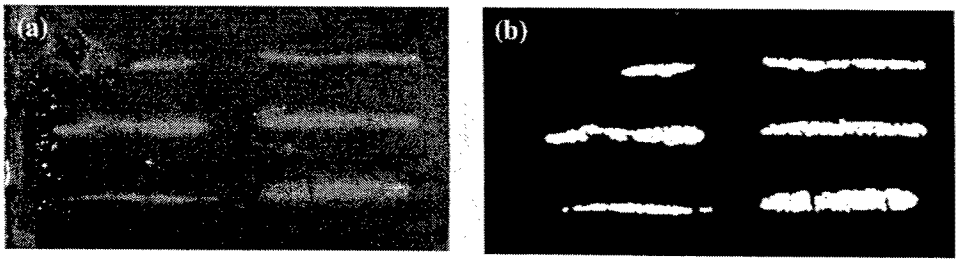

FIGURE 10. Example of scanned lesion slice image processing for a sample treated with a 3.5 MHz HIFU transducer using the laydown pattern shown in Figure 4(c). (a) gray scale image. (b) morphologically processed binary image.

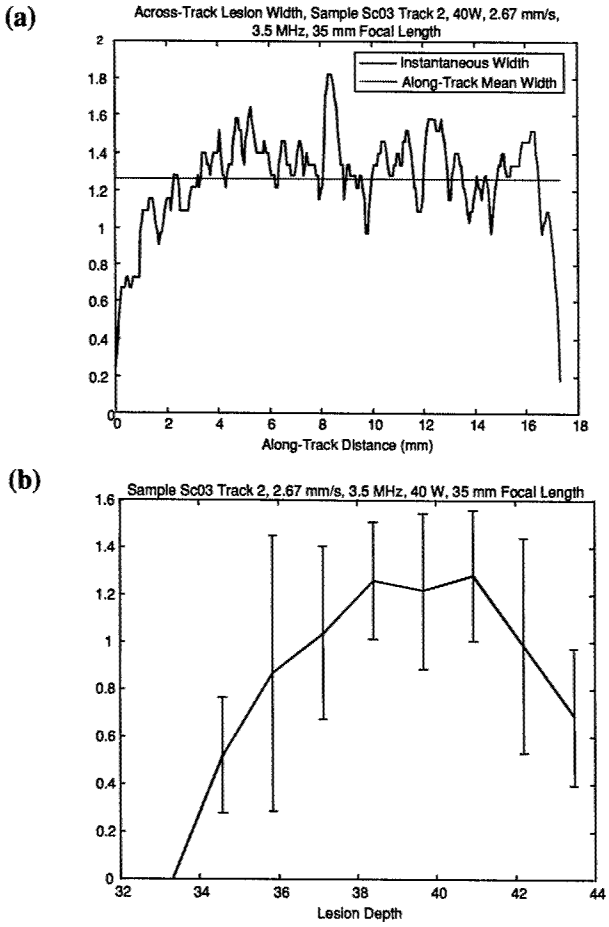

FIGURE 11. Scanned lesion characteristics. (a) Across-track lesion instantaneous and mean thickness obtained from a slice near the transducer focus. (b) Lesion mean radial thickness versus axial depth.

CONCLUSIONS

The apparatus and method presented above demonstrate that reproducible point and scanned lesions can be created *in vitro* and their characteristics assessed. The resulting data can be used to study HIFU dose response in a variety of tissues. Dose response analysis for a series of experiments in bovine liver are discussed in detail in the accompanying proceedings paper by Kaczkowski et al. beginning on page 339.

ACKNOWLEDGMENTS

This publication was made possible through support provided by the U.S. Army Medical Research Acquisition Activity under terms of Agreement No. DAMD17-00-2-0063. The opinions expressed herein are those of the author(s) and do not necessarily reflect the views of U.S. Army Medical Research Acquisition Activity, 820 Chandler Street, Fort Detrick, MD 21702-5014.

This publication was also made possible through support from the Office of Naval Research, Code 341, via BOA N00014-01-G-0460 (order 0003).

REFERENCES

1. Keshavarzi, A., Vaezy, S., Kaczkowski, P. J., Keilman, G., Martin, R., Chi, E. Y., Garcia, R., and Fujimoto, V., *J. Ultrasound Med.*, **20** (5), 473-480 (2001).
2. Duck, F. A., *Physical Properties of Tissue*, New York. Academic Press, 1990, pp. 79-116.
3. Watkin, N. A., ter Haar, G. R., and Rivens, I., *Ultrasound in Med. & Biol.*, **22** (4), 483-491 (1996).

In Vitro Examination Of Non-linear Heat Deposition In HIFU Lesion Formation

Peter Kaczkowski[1], Marilee Andrew[1], Andrew Brayman[1], Steve Kargl[1], Bryan Cunitz[1], Cyril Lafon[2], Vera Khokhlova[3], and Lawrence Crum[1]

[1]*Center for Industrial & Medical Ultrasound, Applied Physics Laboratory, University of Washington. Box 355640, 1013 NE 40th St. Seattle WA 98105-6698*
[2]*INSERM Unité 556, 151, Cours Albert Thomas 69003 Lyon, France*
[3]*Department of Acoustics, Faculty of Physics, Moscow State University, Moscow 119992 Russia*

Abstract. Numerical simulations of HIFU lesion formation in tissue indicate that under some conditions, acoustic non-linearity should result in substantially higher heating rates in a narrow axial region within the fundamental focal zone. Surprisingly, these models indicate that in the absence of cavitation, non-linear "enhancement" does not appear to increase the overall size of a lesion over that predicted by linear models. However, the highly localized heating can lead very rapidly to boiling cavitation and substantial changes in local attenuation [1]. In order to examine this regime in tissue, carefully controlled experiments are conducted in which model input parameters and lesion shapes are measured. Static HIFU-induced lesions, in which the transducer is spatially fixed with respect to the target tissue, were created using frequencies of 2, 3.5, 5, 7.5 and 10 MHz, and using a range of exposures for which the linear dose, defined by the product *Dose* = *Intensity* x *Exposure_Time* was held constant. Resulting lesions were measured by photographing successive 1.27 mm thick transverse slices of the tissue sample, and reconstructed on a computer for quantitative comparison. Differences in shape and size appear to be generally explained by boiling cavitation, inferred from our observations of results in gel phantoms and tissues, and through numerical modeling (*ad hoc* creation of gas voids in a nonlinear acoustic model, [2]). In primarily thermal lesions created near the boiling threshold, a small pinhole void is often visible on the acoustic axis, indicating the likelihood that boiling was initiated there. Scanned lesion formation, in which the HIFU source is continuously moved transverse to the acoustic axis, is examined using a transparent tissue-mimicking phantom to elucidate the initiation of boiling. Scanning or "painting" lesions using this highly non-linear regime should prove to be an efficient method of depositing highly targeted heat in a large volume of tissue.

INTRODUCTION

High intensity focused ultrasound (HIFU) is gaining importance as a new therapeutic tool for applications in tissue ablation [3,4] and hemostasis [5,6]. Treatment protocols take selective advantage of HIFU's thermal (e.g. heating-induced protein denaturization) and mechanical (e.g. cavitation-induced emulsification) bioeffects. However, precise control over these effects (e.g. lesion size & location), within the treatment area is difficult to achieve because the observed bioeffects appear to be sensitive to local conditions near the focal region [7-9] as well as to the acoustic and thermal properties along the intervening acoustic path [10,11].

Developing accurate numerical models for individual patients thus requires detailed information such as tissue geometry, thermal and acoustic parameters, and perfusion rates. Such modeling is becoming increasingly important as HIFU moves toward more non-invasive implementations, and will be integral in the development of HIFU therapy planning systems. Two important investigations arise from this need for treatment planning: 1) determining useful ways to correlate HIFU exposure with the resulting bioeffect(s) – that is, categorize the HIFU dose response, and 2) benchmarking numerical bio-acoustic models against precisely controlled experiments to assess, and in turn improve, model accuracy.

We are engaged in such long-term investigations and are particularly interested in exploring the role of acoustic non-linearity in HIFU lesion formation. The apparatus and method for acquiring *in vitro* experimental data using freshly excised bovine liver was described in the previous paper (Andrew et al.). In this paper we summarize the dose response methodology and data that we have collected as of June 2002. Our preliminary results indicate that non-linear heat deposition may produce enhanced local heating as has been previously observed in gel phantoms [1], and at lower temperatures than might be expected [2]. Our results also illustrate the variability of the bioeffect due to tissue inhomogeneity near the focal zone and along the acoustic path. We present a glossary of terms and acoustic regime properties that we find useful to standardize. We also offer photographic examples of the dose response data we have collected.

DEFINITIONS

Dose is defined by Merriam Webster's Dictionary as the "quantity of radiation delivered or absorbed" at any given site. This quantity, representing the real energy absorbed at every point, depends on system settings and on a great number of tissue parameters that are essentially unknowable. Clearly, the dose is a statistical quantity, but it is a unique deterministic quantity for any given case. To determine what value it has, however, requires careful *in situ* measurement: this is the meaning of **dosimetry**, namely, "measurement of the dose". We distinguish between *predicted* dose (theoretical, planned, modeled, simulated, intended) and *measured* dose (that is, actual, experimental, *in situ*). Because of its inherently statistical nature, the dose is often simply described by its mean value, but regrettably the reference to this "average" is often omitted along with any quantification of the variance and higher order moments, and of the underlying probability distribution.

Exposure, by contrast, is the energetic "input" to the body, and does not usually take into account the local conditions that lead to absorption at a particular site. Practical units for the exposure vary widely as there is no accepted HIFU standard (see the paper by ter Haar on page 305). The exposure can be simply related to settings on the instrument (for example, electrical Watts out of the amplifier), or to the expected value of the intensity field at the focus for a particular propagation path (e.g., the acoustic field in the treatment zone, as measured in water, or inferred from such measurements and a simple model for the tissue). Even then, there are many different

ways in which power in the treatment zone is reported, often making direct comparisons across publications very difficult.

In summary, we use the term ***dose*** to refer to actual energy absorbed, and use the term ***exposure*** to describe the applied acoustic field. Both quantities vary spatially, and thus we find it convenient to measure HIFU system power electrically and relate those global exposure readings to power in the focal zone through an acoustic model, thus effectively 'derating' the power incident on the tissue surface by the attenuation of the tissue path. We have not yet confirmed these values with *in situ* hydrophone measurements, but have made bulk attenuation measurements for each tissue sample using a pair of transducers dedicated to this purpose, and use this value in modeling.

The **dose response** of tissues to HIFU exposure relates the bioeffect to the dose, usually in terms (units) related to the efficacy of therapy for a particular clinical objective. In this work, we quantify the thermal denaturation of tissue by measuring and delineating the discoloration of the sample using digital photography. Other studies have interpreted the discoloration in terms of histological changes (typically as coagulative necrosis) but we do not address the nature of the damage and assume that any error in estimating the spatial extent of acute necrosis using color alone is small.

We also find it helpful to describe different acoustic regimes that lead to formation of HIFU-induced lesions. Here, we enumerate the characteristics we feel identify and qualitatively distinguish acoustic regimes by the underlying physical mechanisms at play, and the characteristics of the lesions they create.

A. Linear Regime

- Acoustic field is accurately modeled using the linear wave equation.
- Negligible harmonic generation.
- Negligible cavitation.
- Heat source given by $Q \propto 2\alpha I$.
- Lesion is smooth and symmetrical, and looks like the intensity beam pattern; well modeled by the basic bioheat equation.
- Lesions are 'cigar-' or 'grain-of-rice' shaped.
- AKA: "purely thermal", "linear", "PDL" (protein-denatured lesion).

B. Non-Linear Acoustic Regime

- Non-linear acoustic model required (e.g., KZK, FD or FE codes).
- Harmonic generation occurs with propagation.
- Steepened & possibly "shocked" and asymmetric pressure waveforms.
- Increased heat deposition (compared to the linear estimate) → "non-linear attenuation" is a term describing the combined effect of increased attenuation of higher harmonics.
- No cavitation is assumed: bubbles are absent.
- Heat source is harmonic content dependent: $Q \propto 2\,\alpha(f)\,I(f)$.
- Heating is axially symmetrical, but no longer looks quite like Intensity beam pattern (sharper on axis).
- Lesion is smooth and symmetrical, and indistinguishable from a 'linear regime' lesion.
- *Non-Linear Heating near axis can be huge!*

C. Acoustic Cavitation regime – below the vapor phase transition

- "More" non-linearity than in B above.
- Bubbles grow only at nucleation sites: i.e., if no nuclei, then no bubbles form.
- Bubbles grow by rectified diffusion, up to several microns at which point they are likely to get destroyed and may reform as a multitude of small bubbles.
- Bubbles change local acoustic medium bulk properties significantly, by lowering the sound speed (higher compressibility) and increasing the attenuation.
- Complicated and significant harmonic generation / bubble cloud scattering.
- Greatly increased heat deposition.
- Need for a good theoretical model for an "effective medium" representation of a HIFU-induced cloud of bubbles in tissue: c, ρ, α, and non-linearity parameters.
- Heating pattern (and the resulting lesion) generally progresses back toward transducer.
- Lesion no longer symmetrical; can take on "tadpole" or "carrot" or "conical" shape, where the larger end is toward the transducer [12].
- *Still difficult to model, consistently observable: "stochastically reproducible."*

D. Boiling Cavitation Regime

- Vapor (water) bubbles form suddenly, often under superheated conditions; "*popcorn*" audible sound often detectable, stops as soon as HIFU is turned off
- With continued HIFU vapor bubbles grow rapidly - to as much as 100s of microns in size - and change local acoustic medium properties dramatically.
- Complicated harmonic generation / bubble scattering.
- Greatly increased heat deposition.
- Recent theoretical models for "effective" heat source from a "cloud" of rapidly evolving bubbles need examination.
- Heating pattern is much more random than in acoustic cavitation regime & generally progresses back toward transducer, but can also produce off-axis lesions.
- Lesions have distinct voids in them visible to the naked eye and under magnification, either long "needle holes" on axis, or cavities distributed throughout the lesion.
- *Very difficult to model due to large variance in results, but experimentally consistent: "stochastically reproducible."*

MODELING: LINEAR VERSUS NONLINEAR REGIMES

Several authors have noted the possibility of enhanced absorption of nonlinearly propagating acoustic waves [13-15]. The following considerations arise in contemplating the importance of non-linearity, that must ultimately be explored numerically and experimentally:

1. The nonlinear heating rate can be much higher than that of the pure linear estimate (fundamental frequency alone).
2. Harmonics are continuously generated along the propagation path, and they represent a small part of the total energy in the beam (typically a few percent).
3. Geometry of harmonics is such that higher frequencies focus more tightly (aperture "contains" more wavelengths for higher frequencies).
4. Non-linear heating (due to harmonics alone) is localized to an interior subset of the focal region (as defined for the fundamental frequency).
5. Harmonics are attenuated more rapidly over the path than the fundamental, because the attenuation increases nearly proportionally to frequency.
6. Modeling is required to sort out the quantitative importance of competing effects for different HIFU system parameters.

Using the KZK model [16], the results in Figure 1 are obtained, indicating the difference in heating rate due to conversion of energy into harmonics of the emitted wave. However, the overall effect on lesion formation could be expected to be *small*, since little *total* energy is converted to harmonics at HIFU intensities in tissue. Indeed, the models suggest that for typical HIFU parameters, the calculated position of the 60 degree contour of temperature is very similar for linear and non-linear models. Consequently, the location of the (visible) lesion boundary is not sensitive to the degree of non-linearity in the acoustic propagation. (Recall that lesion boundary might approach that of ~ 60° contour because thermal dose at 57° C is about 2 s, and even a very short time of exposure at 60° is almost always enough to produce a lesion.) This numerical result, for non-cavitating regimes, is illustrated in Figure 2.

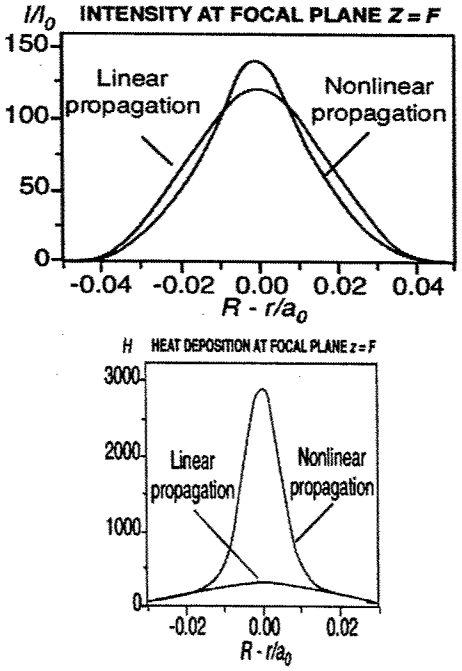

Figure 1. Transverse intensity profiles (upper) and heat deposition rates (lower) for linear and non-linear acoustic models, with I_p = 1500 W/cm^2.

The upper plot indicates that the ***near-axis intensity*** value is somewhat higher for propagation modeled including non-linear contributions than for the linear (fundamental alone) calculation. This modest increase is due primarily to harmonic content: higher frequencies will focus more tightly than the fundamental, thereby further concentrating the beam energy.

More dramatic is the difference in ***heating rates*** between the linear and non-linear calculations (lower plot). The nearly linear increase of the attenuation as a function of frequency leads to a much greater proportion of beam energy being converted to heat for the higher harmonics.

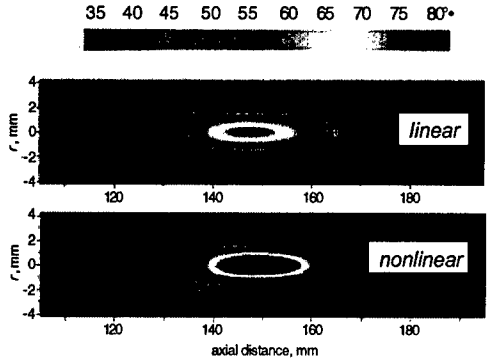

Figure 2. Spatial distributions of temperature in liver after 0.8 seconds, with I_s = 1500 W/cm^2 exposure.

The T = 60° C contour (approximately in the middle of the green band) indicates the approximate extent of necrosed tissue, and in both models the boundary is similar. This result implies that non-linear heat deposition would not be easily observable simply using overall lesion size.

Under such conditions, the effects of acoustic non-linearity would be difficult to observe by lesion size estimation, and would hardly matter in the design of treatment protocols. This result also implies that the use of simple linear models would be adequate. However, propagation effects alone do not explain the sudden and rapid movement of the lesion boundary toward the HIFU source observed by many authors.

If the production of bubbles is considered, non-linear heat deposition can make a significant impact precisely because it is so spatially concentrated. Under our typical HIFU exposure conditions, axial temperatures do rise very quickly and readily reach 70° C or more before the time that the linearly predicted lesion boundary has reached the dimensions of the 6 dB focal zone contour (the latter represents a reasonable dosimetric end point for a static lesion). Such relatively high temperatures on axis, combined with the very low (negative half-cycle) pressure in the focal zone due to the intense field there, may produce cavitation, either due to simple phase change of water (boiling cavitation) or to the extraction of dissolved gases from blood and tissue (acoustic cavitation). Cavitation should initiate preferentially on the acoustic axis where the combination of heating and low negative pressure is maximal (unless a large number of gaseous nuclei exist nearby).

In gel phantoms, the appearance of bubbles during HIFU is sudden and it radically changes the local acoustic characteristics of tissue in such a way as to convert acoustic energy to heat more efficiently [1]. This positive feedback mechanism does lead to an extremely rapid increase in heating along the path between the bubbles and the transducer, and is the dominant hypothesis for lesions growing preferentially toward the transducer once this regime is initiated [12]. Because the appearance of bubbles so fundamentally changes the medium's acoustic properties, the relatively small region over which non-linearities play a role nevertheless makes a big difference in the efficiency of HIFU energy conversion. We see evidence of this process in our experiments as described in the following section.

EXPERIMENTAL RESULTS

Studies In Gel Phantoms

We have exposed our BSA-loaded acrylamide gel phantoms to a range of static HIFU field intensities and filmed the process using a video camera. Two time lapse sequences appear in the figure below. The top row illustrates a typical 'linear regime' sequence (with elapsed time increasing from left to right), in which the lesion appears, grows monotonically with HIFU exposure and then dissipates as the gel cools due to significant reversibility of the opacification process. The bottom row is an example of a boiling cavitation sequence in which the lesion grows in a regular manner until the first bubble forms, after which the bubbles appear and disappear chaotically. After HIFU is turned off, bubble formation halts and the lesion relaxes to a final equilibrium state that typically proves to be more opaque than in the 'linear' cases. This as an indication that the appearance of bubbles has indeed greatly increased the amount of heat deposited, even though the exposure was almost identical. Note the small increase in drive signal: linear: 154 mV; boiling: 158 mV. We consistently observed very sharp demarcation between no cavitation and cavitation regimes. (The signal voltage applied to the input of the power amplifier is linearly related to high power electrical drive voltage and HIFU amplitude.).

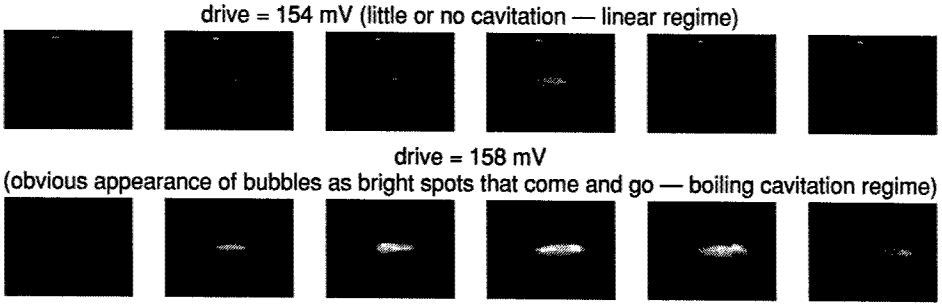

Figure 3. Transverse view of the focal zone in gel. A video camera was used to observe the temporal evolution of HIFU lesions in a protein-loaded acrylamide gel. These frames are extracted from the video: approximate elapsed time is two seconds, with time increasing from left to right.
Top panels:, Bottom panels:.

Preferential boiling near the beam axis is observed consistently, and the collapse and resurgence of bubbles is hypothesized to be due to the effectiveness of shielding of the field once a bubble has appeared, allowing the vapor to cool enough to condense again. We observe end-points in tissue that appear to be consistent with our observations in gel.

In Vitro Point Lesions In Bovine Liver

We have observed the formation of cavitation-induced voids and tissue emulsification in the centers of static lesions (in which the transducer does not move

with respect to the tissue) in preliminary dose response studies. We observe end-points in tissue that appear to be consistent with our observations in gel (see Figure 4).

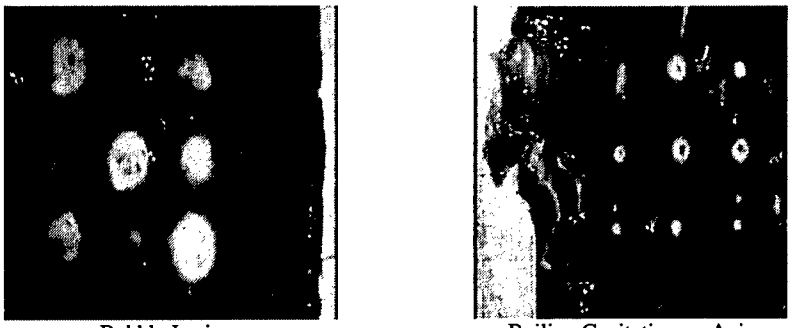

Bubbly Lesions Boiling Cavitation on Axis

Figure 4. Evidence of bubbles in tissue, for static HIFU-induced lesions.
Left: Cavitation and boiling regimes (mixed). Transverse sections of point lesions at three different exposure levels, in bovine liver, in which lesions have grown toward the transducer (out of the page) and 'bloomed' in the transverse dimension.
Right: Onset of boiling cavitation on-axis: Transverse sections of lesions that exhibit axial cavities, hypothetically formed by vapor bubbles on or near the acoustic axis.

In Vitro Scanned Lesions In Bovine Liver

Scanning protocols allow additional control over the delivery of HIFU energy, and they provide a new opportunity to investigate nonlinear enhancement. We hypothesize that the initial appearance of large vapor bubbles may be rapid, but further heat deposition is prevented by shielding. Moving the location of the focal zone would permit continued rapid heating in a controlled manner. Experiments conducted wherein the HIFU transducer is translated at a uniform velocity along a linear track led to the lesion tracks imaged in Figure 5.

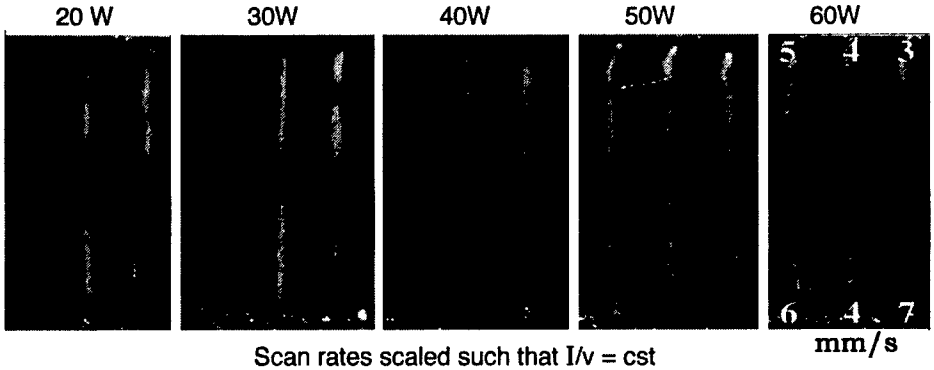

Figure 5. Linear lesion tracks in bovine liver. Five different exposure power values (20, 30, 40, 50 and 60 W), and 5 different transducer velocities (3, 4, 5, 6, and 7 mm/s in a direction transverse to the beam axis) were used to examine the response of tissue to scanning protocols. Each frame consists of 6 tracks, with velocities the same in each frame, but with the speeds indicated on the rightmost frame. All images are taken from the depth slice at focal maximum. The top and bottom center tracks in each frame were made at the same scan rate (4 mm/s) to verify the repeatability of the technique.

Clearly visible is the random nature of the bioeffects given uniform exposure conditions. Track deflections and lesion "fades" are likely due to distortions in the HIFU beam due to the acoustic path. Distinct gaps are recognized as vessels (water filled) and other biological structures, and in the case of the 60W input power exposures there is clear evidence of cavitation. We will examine the data to obtain statistical descriptions of the bioeffect as a step toward building stochastic models for dose response. Figure 6 illustrates the result of quantification of the lesion width along the track using image processing, and the compilation of that data for several depths within the focal zone.

Realistic scanning protocols will require complex, application-dependent trajectories. Tumor treatment, for example, will depend on tumor geometry and acoustic window, while blunt trauma hemostasis protocols might require scanning of multiply-located lines, planes and/or points. In addition, all such complex trajectories will be subject to tradeoffs in the therapy delivery control parameters that depend on system capabilities and treatment planning algorithms. To investigate a simple extension of the linear scan, perhaps useful for treating spheroidal tumors or cauterizing a volume, we developed a circular scanning protocol. We explored similar tradeoffs between exposure power and translational velocity along track, as well as the inter-track spacing. Given the experience gathered in preliminary scans, we studied the role of accumulated heat on lesion width. Of particular interest is the accumulation of heat that occurs in an interior region as circular tracks are placed in a sequence of decreasing radius (we did not use spiral scans because of the difficulty of programming the motion stage).

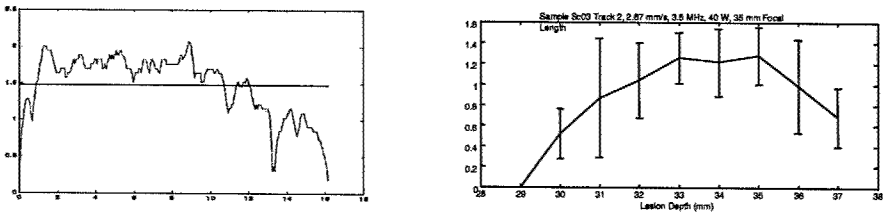

Figure 6. Lesion width along track (left), and lesion width as a function of axial distance from the transducer (right). Image processing using color value thresholding leads to the plots above. The values are obtained from the *observed* track; different results are obtained along the *planned* track.

The images of transverse slices in Figure 7 illustrate the results of just such experiments. It is easy to see how scanned tracks provide a wealth of information on lesion size and character from a single tissue sample, and how treatment protocols can benefit from the rapidity with which HIFU-induced thermal ablative therapy can be conducted using moving transducers.

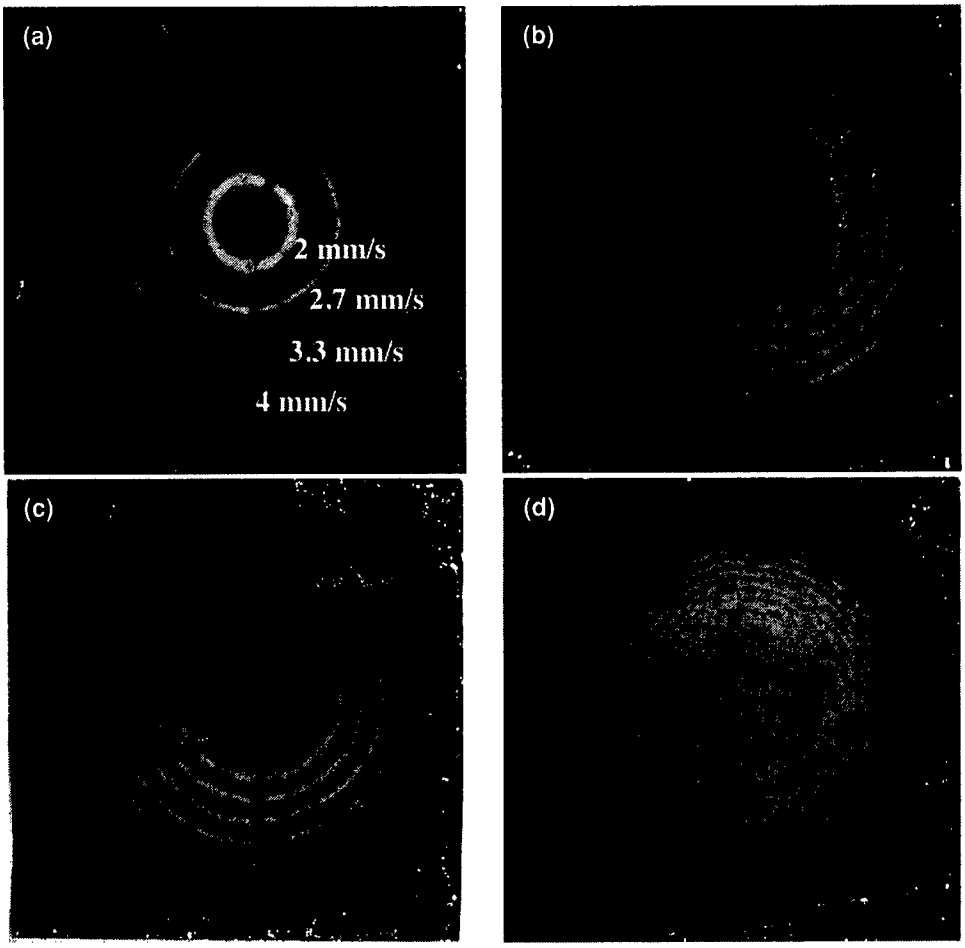

Figure 7. Examples of circular scans in excised bovine liver tissue: (a) shows different scan rates for a single input power of 50 W. (b) shows constant scan rate (2 mm/s) and power (50 W), stepped from outside toward the center at constant decrements of radial distance of 2 mm. Note that heat is beginning to build in the center and causes tissue denaturation without focal exposure. (c) constant scan rate (2.7 mm/s), and results in less thermal buildup and resulting denaturation in the center. (d) 50W, 2.7 mm/s, 1 mm radial decrement; a total of 8 tracks were made, moving about half-way toward the center, and the entire central area has been denatured.

DISCUSSION AND CONCLUSIONS

Our results indicate that non-linear heat deposition likely spurs the development of water vapor bubbles by boiling. Non-linear heating is due to absorption of higher harmonics of the field generated *only* by acoustic propagation (here through tissue) and has greatest effect on axis in the focal zone. Boiling provokes an extremely sudden (highly non-linear) increase in local heating as elucidated by Holt and Roy in

gel [1]. It appears that such boiling cavitation happens below 100° C, because the large negative pressures in the focal region lower the boiling point significantly. The extremely small spatial extent of the effect makes it very difficult to measure directly.

Our investigation of the bio-response associated with HIFU exposures that heat to temperatures near the boiling cavitation threshold indicates that local dose in tissue can fluctuate significantly for a constant exposure setting. This fluctuation has two important components that stem from the natural heterogeneity of tissue: variable absorption in the focal zone, and variable acoustic power at the focus due to scattering along the acoustic path. A good therapy planning system must consider the random nature of the local dose resulting from a constant applied exposure, and a stochastic model for bioeffect should be an integral part of HIFU therapy planning and real-time control.

Nonlinear (propagation) effects may be avoided or enhanced by adjusting the HIFU source parameters (under the constraints of device aperture and acoustic window). Bubble creation can be tailored with some control; lower intensities would permit 'stable cavitation', while boiling is initiated with high focal intensities. Non-linear heating is itself enhanced by a combination of high focal gain and high initial power.

Scanning the HIFU transducer has many advantages: treatment is faster, because it allows optimal use of the non-linear regime which is hampered in static configurations by vapor bubble shielding. Motion leads to more consistent bioeffect, since vapor bubbles lead to relatively uncontrolled lesion formation. Nevertheless, sources of randomness and uncertainty still exist. We believe that there is a need for stochastic models to better characterize dose response in a heterogeneous, random medium in which many parameters will not be known.

ACKNOWLEDGMENTS

This publication was made possible through support provided by the U.S. Army Medical Research Acquisition Activity under terms of Agreement No. DAMD17-00-2-0063. The opinions expressed herein are those of the author(s) and do not necessarily reflect the views of U.S. Army Medical Research Acquisition Activity, 820 Chandler Street, Fort Detrick, MD 21702-5014.

This publication was also made possible through support from the Office of Naval Research, Code 341, via BOA N00014-01-G-0460 (order 0003).

REFERENCES

1. Holt, R.G. and R.A. Roy, "Measurements of bubble-enhanced heating from focused, MHz-frequency ultrasound in a tissue-mimicking material," *Ultrasound Med Biol*, **27** (10), p. 1399-412 (2001).
2. Curra, F.P., et al., "Numerical simulations of heating patterns and tissue temperature response due to high-intensity focused ultrasound," *IEEE Transactions on Ultrasonics, Ferroelectrics and Frequency Control*, **47** (4), p. 1077-1089 (2000).
3. Goldberg, S.N. and M. Ahmed, "Minimally invasive image-guided therapies for hepatocellular carcinoma. *J Clin Gastroenterol*, **35** (5 Suppl 2), p. S115-29 (2002).

4. ter Haar, G., D. Sinnett, and I. Rivens, "High intensity focused ultrasound--a surgical technique for the treatment of discrete liver tumours," *Physics In Medicine and Biology*, **34** (11), p. 1743-50 (1989).
5. Vaezy, S., et al., "Liver hemostasis using high-intensity focused ultrasound," *Ultrasound Med Biol*, **23** (9), p. 1413-20 (1997).
6. Vaezy, S., et al., "Hemostasis of punctured blood vessels using high-intensity focused ultrasound," *Ultrasound Med Biol*, **24** (6), p. 903-10 (1998).
7. Hill, C.R., et al., "Lesion development in focused ultrasound surgery: a general model," *Ultrasound Med Biol*, **20** (3), p. 259-69 (1994).
8. Watkin, N.A., G.R. ter Haar, and I. Rivens, "The intensity dependence of the site of maximal energy deposition in focused ultrasound surgery," *Ultrasound Med Biol*, **22** (4), p. 483-91 (1996).
9. Chen, L., G. ter Haar, and C.R. Hill, "Influence of ablated tissue on the formation of high-intensity focused ultrasound lesions," *Ultrasound Med Biol*, **23** (6), p. 921-31 (1997).
10. Sumino, Y. and R.C. Waag, "Measurements of ultrasonic pulse arrival time differences produced by abdominal wall specimens," *J Acoust Soc Am*, **90** (6), p. 2924-30 (1991).
11. Hinkelman, L.M., T.L. Szabo, and R.C. Waag, "Measurements of ultrasonic pulse distortion produced by human chest wall," *J Acoust Soc Am*, **101** (4), p. 2365-73 (1997).
12. Bailey, M.R., et al., "Use of overpressure to assess the role of bubbles in focused ultrasound lesion shape *in vitro*," *Ultrasound Med Biol*, **27** (5), p. 695-708 (2001).
13. Carstensen, E.L., et al., "Nonlinear propagation and the output indices," *J Ultrasound Med*, **18** (1), p. 69-80 (1999).
14. Bacon, D.R. and E.L. Carstensen, "Increased heating by diagnostic ultrasound due to nonlinear propagation," *J Acoust Soc Am*, **88** (1), p. 26-34 (1990).
15. Dalecki, D., et al., "Absorption of finite amplitude focused ultrasound," [published erratum appears in *J Acoust Soc Am*, **90** (5), p. 2855 (1991)]. Journal Of the Acoustical Society Of America. **89** (5), p. 2435-47 (1991).
16. Khokhlova, V.A., et al., "Numerical modeling of finite-amplitude sound beams: Shock formation in the near field of a cw plane piston source," *J Acoust Soc Am*, **110** (1): p. 95-108 (2001).

5. ENGINEERING

Development And Application Of Therapeutic Ultrasound Technology For Tumor Therapy

Fucheng Sun[1], Liang Zhai[1], Jiwei Jiang[2], Xiaoping Qian[1], Yikang Wang[1], Xiangling Xiao[1], Renkang Yu[1], Fan Yang[3]

[1]*Department of Biomedical Engineering Shanghai Jiao Tong University, 1954 Hua Shan Road, Shanghai 200030, P.R.China*
[2]*Shanghai A&S Science Technique Development Co., Ltd. 201203, P.R.China*
[3]*720 Rutland Avenue, Traylor 6th floor Baltimore, MD 21205, U.S.A.*

Abstract. This paper will introduce the work we have done on therapeutic ultrasound technology for tumor therapy since the 1970s. Our first ultrasound applicator for hyperthermia was developed in 1984, which was a single-element machine. From 1984 to 1997, we successively developed several multiple-element ultrasound machines whose probes were 2×2 or 3×3 planar transducer arrays. They had been successfully applied in the clinic for tumor hyperthermia. We have also been devoted to research on high-intensity focused ultrasound (HIFU) applications for tumor therapy since the middle of 1980s. After a large amount of in vitro and in vivo experiments, we've found that HIFU has many merits when used for tumor ablation and can be an effective method for tumor treatment. In 2001, we successfully built a double-focusing HIFU system for tumor therapy, whose probe consists of six self-focusing transducers where all the foci of the transducers aim at the same point. Each element is independently controllable. The ultrasound frequency is 1 MHz, and the ultrasound intensity is above 3000 W/cm^2 at a focal area, which is 3 mm×3 mm×8 mm. The system has been used in three hospitals in China for clinical experiments. More than 157 patients with tumors or cancerous diseases have been treated and good curative effect has been achieved.

INTRODUCTION

Due to its excellent focusing and penetration abilities, ultrasound has been used for hyperthermia for a long time. Generally, heating techniques can be categorized as conventional hyperthermia or high temperature hyperthermia according to the temperature in target regions. Conventional ultrasound hyperthermia is usually used as an adjuvant to radiotherapy or chemotherapy, and elevates target regions to temperatures in the 41-45° C range. The biological rationale is twofold: hyperthermia is directly cytotoxic, especially in deprived microenvironments with low blood supply, hypoxia, and low pH, such as are commonly encountered in portions of a malignant tumor; and hyperthermia is a "sensitizer" that can increase damage induced by radiotherapy and chemotherapy and prevent subsequent repair. In high temperature hyperthermia, temperatures of the target regions will be elevated above 50° C by high intensity focused ultrasound. It can be used alone to selectively destroy or permanently alter tissue regions.

We began research on ultrasound technology for tumor treatment in the late 1970s. From conventional hyperthermia to high temperature hyperthermia, we have designed and constructed several systems for tumor therapy. In this paper, we will introduce the work we have done.

CONVENTIONAL HYPERTHERMIA

Our first ultrasound applicator was built in 1984 and consisted of a single-element therapeutic ultrasound applicator, shown in Fig. 1. It was also the first such applicator

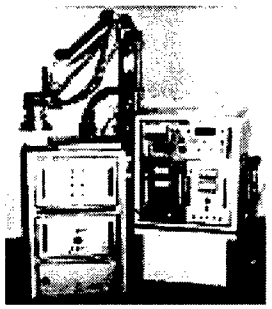

FIGURE 1. Single-elemental ultrasound applicator built in 1984.

in China at that time. This applicator can heat a 5 cm×5 cm×5 cm area to the temperature range of 42-44° C. To achieve the optimal therapeutic effect, we designed several different applicators to match the ultrasound field with the target tissue area. In 1992, we built a multi-element ultrasound applicator shown in Fig. 2. The main probe is a 3×3 planar transducer array. Electrical scanning was used to achieve the uniformity of the temperature distribution. An improved multi-element ultrasound applicator was built in 1997, as is shown in Fig. 3.

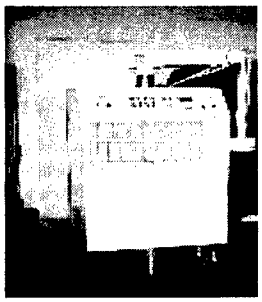

FIGURE. 2. Multi-element ultrasound applicator built in 1992.

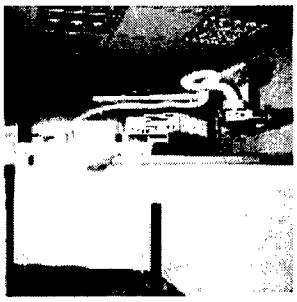

FIGURE 3. Improved multi-element ultrasound applicator built in 1997.

HIGH TEMPERATURE HYPERTHERMIA

High intensity focused ultrasound can be used to selectively destroy tissue deep within human body non-invasively. Because the energy can be concentrated precisely,

the boundaries of the coagulated volume are sharply demarcated, and damage to the overlying or surrounding tissue is avoided. Typically, ultrasound intensities at the focus range from 1-10 kilowatts/cm^2. Such high intensities will result in instantaneous tissue coagulation. In 2001, we built the HIFUNIT-9000 Ablation Knife, as is shown in Fig. 4. Up until now, we have completed more than 60 clinical experiments and found very good results.

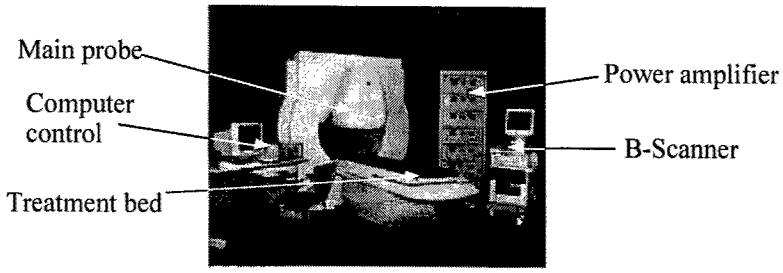

FIGURE 4. HIFUNIT-9000 Ultrasound Ablation Knife.

The main applicator of the HIFUNIT-9000 Ablation Knife consists of a B-scanner probe and an array of six self-focusing transducers. Each transducer is of concave aperture, with a diameter of 60 mm, which can produce a focus at 157 mm. Each transducer is controlled independently, and operates at 1 MHz. The electrical input for each transducer can be adjusted continuously within the range of 0–100 W. The maximum acoustic output of a single transducer is 68 W. The transducers are equally distributed on a concave surface and geometrically aim to the same focus of size $3\times3\times8$ cm^3. When all transducers are switched on and all inputs are set at full, the acoustic power will exceed 3000 W/cm^2. The B-scanner probe is placed in the center of the applicator, and can diagnose and localize the tumor within the human body as well as monitor the treatment process. A sketch of the main probe is shown in Fig. 5.

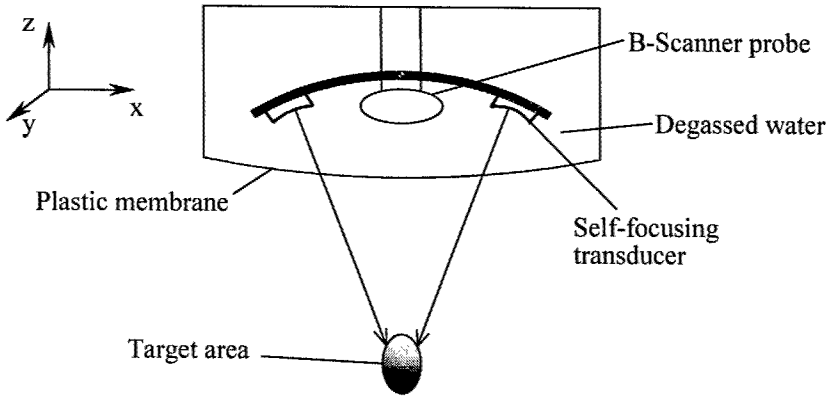

FIGURE 5. Sketch of the main probe of the HIFUNIT 9000. It consists of six self-focusing transducers and a B-scanner probe.

The applicator of the HIFUNIT9000 has two advantages. First, it is especially designed to enable the patients to lie in the supine, rather than the prone, position, which makes them feel relatively comfortable. This is especially important to those patients who have been very weak. Second, the probe has great flexibility in movement. It can move 0–100 mm in the x,- y-, and z-directions, and can also rotate in the range of 0-30° around the x-axis and 0–20° around the y-axis. Combined with the movement of the treatment bed (0-240 mm in the x-axis, 0–1200 mm in the y-axis, and 0–300 mm in the z-axis), the main probe can reach any part of the human body with ease, which means the machine can be used to eliminate tumors wherever the B-scanner can detect them.

Operation of the HIFUNIT 9000 is very convenient. First, doctors use the B-Scanner to localize the tumor. Once the doctors set up the tumor area and determine the exposure dosage, the treatment process is automatically executed by computer-control. The dosage is determined by four factors: the number of transducers used, the power of each transducer, the exposure time, and the interval time of each exposure. Usually the exposure time is 0.1 with a 0.2 s interval. Mechanical scanning is adopted to cover the entire tumor area. During the therapy, doctors can change the dosage according to patients' responses. For example, if a patient feels too much pain, the power can be reduced and exposure times increased.

The treatment is safe for patients. Most patients don't need to be anaesthetized and others only need local anaesthetic. They can talk with doctors about what they are feeling at any time during the therapy. And the B-Scanner can also monitor the treatment process in real time, because images are changing due to changes in US attenuation or in the stiffness of the tissue during therapy.

To evaluate the efficiency, we classified pain into four levels. Level zero: no pain at all; level one: slight bearable pain, but need no analgesic; level two: twinge, has some influence on sleep and requires analgesic; level three: have great pain that influences sleep seriously and requires anesthetics. If the pain degree of a patient has dropped more than two levels, we define it as evidently effective; if the pain degree of a patient has reduced one level, we define it as effective; and otherwise there is no effect.

In all the patients who accepted the treatment and have reported to us, 87 patients had pain, among which 24 at level one, 39 at level two, and 24 at level three. After the treatment, 43 were classified as evidently effective, 41 as effective, and 3 had no effect. Data for relief after treatment are shown in Table 1.

TABLE 1.

Symptom	Cases	Relief cases		
		Evidently effective	Effective	No effect
Pain	87	43	41	3
Bellyache	21	12	7	2
Anus distension	27	0	24	3
Frequent urine	16	16	0	0
Blood urine	17	17	0	0
Blood feces	1	1	0	0

After treatment, tumor tissue histology analysis was done in 19 patients. The histological results indicated that all tissues in the tumor area were coagulatively necrosed. Shown in Fig. 5 are the histological pictures of a mammary tumor after treatment. Pictures shown in Fig. 6 are the histological pictures of a recurrent transferred rectum tumor after treatment.

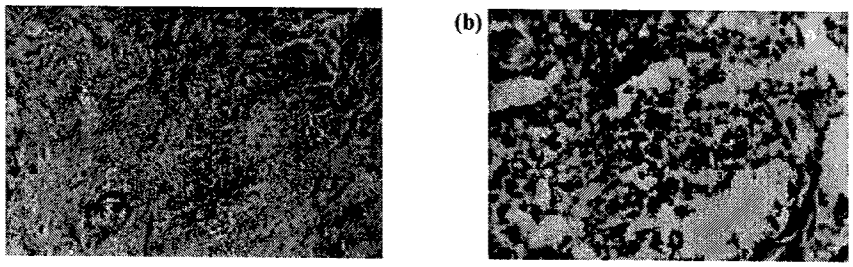

FIGURE 5. Histological analysis of a mammary tumor after treatment. (a) Necrosis of the tissue accompanied by cell inflammatory response. Tumor tissue structure is greatly destroyed. (b) Remains of the necrosed capillary wall is seen in the middle, with surrounding structure inflammatory.

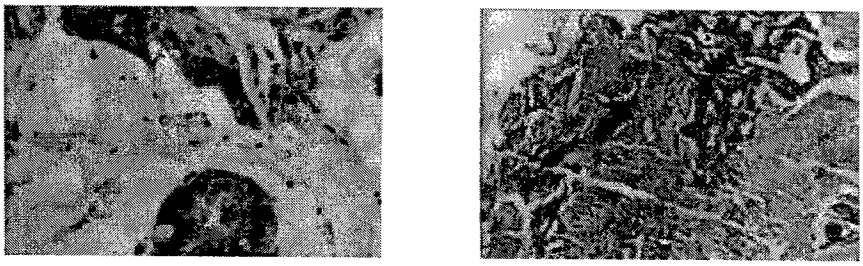

FIGURE 6. Jejunum mucosa glands are destroyed; no clear cell boundary can be seen, accompanied by formation of capillary thrombus.

From the information about patients who have accepted treatment, we believe the HIFUNIT-9000 can effectively eliminate tumors in the abdomen, pelvis and limbs, and superficial tumors. Generally, it can be used to treat tumors wherever the B-scanner can detect them.

ACKNOWLEDGMENTS

We sincerely acknowledge the following personnel and institutes:

- Faculty, staff and students of the Shanghai Jiao Tong University
- All staff of Shanghai A&S Science Technique Development Co,. Ltd, China
- Shanghai Hua Shan Hospital, China
- The Eighty First Tumor Center, Nanjing, China
- The Second Affiliate Hospital of ZhengZhou University, China
- Hunnan Tumor Hospital, China

And we especially thank Professor Lawrence Crum and Professor Shahram Vaezy for their valued opinions for our work.

REFERENCES

1. Rivens, I.H., Clarke, R.L., and ter Haar, G.R., *IEEE Transaction on Ultrasonics, Ferroelectrics and Frequency Control*, **43**, (6), (1996).
2. Diederich, C.J., and Hynynen, K., *Ultrasound in Med. & Biol.*, **25** (6), 371-887 (1999).
3. Nyborg, W.L., *Ultrasound in Med. & Biol.*, **27** (3), 301-333 (2001).
4. Shiyan, L., and Ruiying, L., *Modern Tumor Hyperthermia: Theories, Methods and Clinic*, China, Xueyuan Publisher, 1997, pp. 12-34.

Water Cooled Intraoperative HIFU Applicators With Frequency Tracking

Roy W. Martin[1,3,4], Shahram Vaezy[1,4], Carol Cornejo[2], Jerry Jurkovich[2]

University of Washington, Center for Industrial and Medical Ultrasound[1], and Departments of Surgery[2], Anesthesiology[3] and Bioengineering[4], Seattle, Washington, USA

Abstract. HIFU applicators with solid cone coupling offer a new method of producing hemostasis in trauma. Water-cooled applicators of two tip styles, which operate at 5.7 MHz, were fabricated and tested *in vitro* and *in vivo*. These applicators were found to be highly resonant (Q of 327). The resonant frequency was discovered to shift -0.6 KHz /° C increase in the cone temperature depending on the applicator. A frequency tracking circuit was developed to maintain the excitation on peak resonance as the applicators warmed with use. Standing wave ratios were thus sustained below 1.6 for applied electrical power levels up to 150 Watts. A maximum of -15 KHz shift occurred in use. Acute *in vivo* studies were conducted with anesthetized juvenile swine. Trauma models included: blunt trauma by a high velocity impact to the chest and surgical punctures, incisions and transections of blood vessels, liver lobes and spleen. The general findings were that there is no smoke generated or charring of the tissue, no interference in the ECG, volume and surface cauterization can be performed, cauterization can be performed in the face of profuse bleeding and hemostasis is achieved in all organs and vessels. In blunt trauma injuries large liver fractures were treated and rendered hemostatic with an average of 15 minutes of HIFU treatment and a 54 minute surgery. Almost all the treated sites were found hemostatic after reopening the surgical site after an average of 3.6 hours of abdominal closure. Large veins (greater than 3 mm in diameter) posed problems and required the aid of sutures to stem bleeding. On the average the amount of fluid found in the abdomen per weight of the animal was much less than reported in the literature with a similar injury and observation protocol but different treatment modality. We have found some build up of clotted blood on the more pointed applicator, which must be periodically removed. The frequency tracking technique worked well—no fading of acoustic power level was found during procedures, a problem previously encountered.

INTRODUCTION

We have demonstrated the potential of HIFU in the surgical environment for producing hemostasis in a number of studies [1-7]. Most of this early work was performed using a single transducer element with a concave spherically focusing piezoelectric element [2-5]. Attached to the transducer was a conical shell that was filled with water and truncated proximal to the focal point of the transducer (Figure 1A). The shell was sealed with an acoustic transparent membrane to maintain the fluid in the shell and also provide an acoustic window for the ultrasound to pass

through. This truncated tip was then placed against the hemorrhaging tissue or blood and the ultrasound passed through it to the focal site. Intensities of 2000 W/cm^2 were generally produced at the focus. The major mechanism for producing hemostasis was found to be tissue heating and coagulative necrosis. Streaming, radiation pressure and cavitation also plays a role. In solid organs such the liver, spleen and more recently the lung [8] the creation of a blood and tissue emulsion has been found to be very important. This emulsion if left undisturbed quickly hardens and provides a seal over injured parenchyma.

The use of water filled cones for coupling the ultrasound from the transducer to the tissue is technically simple but it poses problems from a practical method in the operating room. We found it was necessary to change membranes several times during a study because holes developed in them. This required refilling the cone with water and removing all bubbles each time the membrane was changed. The distraction and time to accomplish this in human surgery is unacceptable let alone the problem of maintaining sterility while accomplishing this task. We therefore investigated other coupling methods that would be more practical in the operating room. Solid material was considered and a prototype aluminum coupler was developed [9]. A spherical concave piezoelectric element was bonded to a matching convex surface at the base of

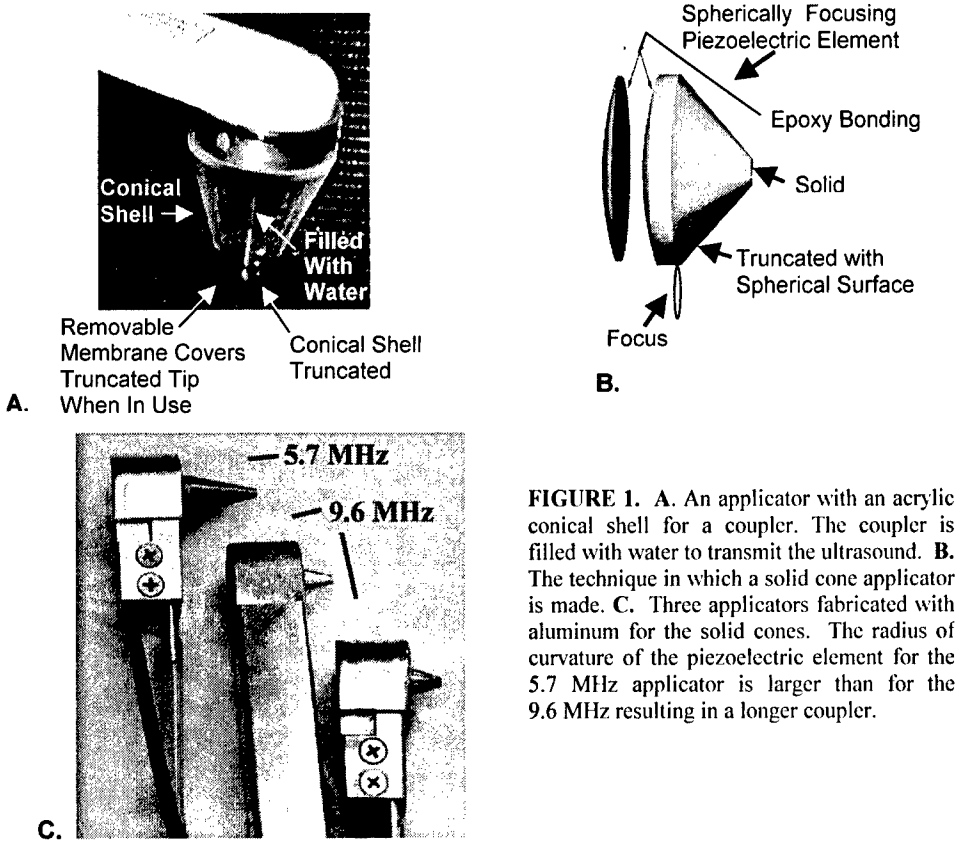

FIGURE 1. **A.** An applicator with an acrylic conical shell for a coupler. The coupler is filled with water to transmit the ultrasound. **B.** The technique in which a solid cone applicator is made. **C.** Three applicators fabricated with aluminum for the solid cones. The radius of curvature of the piezoelectric element for the 5.7 MHz applicator is larger than for the 9.6 MHz resulting in a longer coupler.

the conical shaped applicator (Figure 1B). The outer dimensions of the cone were made larger than the natural focusing beam pattern to avoid the longitudinal waves from encountering the boundary and being converted to shear waves. Avoiding shear waves is important. The slower speed that they propagate with respect to longitudinal waves in solids can interfere with the phase coherence of waves arriving at the tip of the applicator. Lack of coherence diminishes the efficiency of an applicator. A number of applicators were fabricated (Figure 1C.) and tested *in vitro* and *in vivo*. Based on these results a second generation of applicators was developed as well as a custom electronic drive and cooling system. This has then been employed in a number of animal studies and is presented here.

APPLICATORS AND DRIVE SYSTEM

Two problems were found with the early aluminum applicators. First, we found the tip tended to erode with use due the softness of aluminum and the presence of cavitation adjacent to the tip, and second we had a high failure rate of the devices. Changing the tip material to titanium solved the first problem. Titanium has high tensile strength, good heat conduction, and although it is heavier than aluminum, it is lighter than many other metals. We have found no erosion with this material.

The second problem has been more complicated with several contributing factors. First, we discovered the piezoelectric to cone bonding material initially used could not tolerate a very high temperature. Consequently, a heat cured epoxy was identified that could withstand temperatures up to 200° C. A curing fixture was developed and used that applied and maintained high pressure on the piezoelectric element forcing it against the base of the cone during heat curing. This technique provided bonds that didn't fail at elevated temperature. Nevertheless, since the efficiency of the electrical to acoustic conversion was between 50%-60%, depending on the device, a lot of heat was generated in the applicator and would eventually affect the piezoelectric material and the units would deteriorate. Water cooling was then introduced into the design and that made major improvements in the life of the units and allowed us to run them at much higher power. We then discovered that the resonant frequency would shift down in frequency as the units were used. We realized that since the applicators are very resonant ($Q \sim 327$), a small shift in frequency produced a considerable mismatch between the transmitter and the transducer, and that further decreased the efficiency of the system. Thus more power had to be applied for the same acoustic output power which added further to heating the applicator. We found even with the water cooling the applicators would warm with heavy use, enough to produce about a 20 KHz frequency shift. An example of frequency change occurring in one applicator is given in Figure 2.

The cause of the shift was determined to be due to the speed of propagation in the titanium decreasing as the temperature increased. This affects the resonance because the high Q results from energy reflecting back forth along the body of the cone between the tip and the piezoelectric element. Therefore the speed of sound in the body of the cone plays an important role in establishing the resonant frequency.

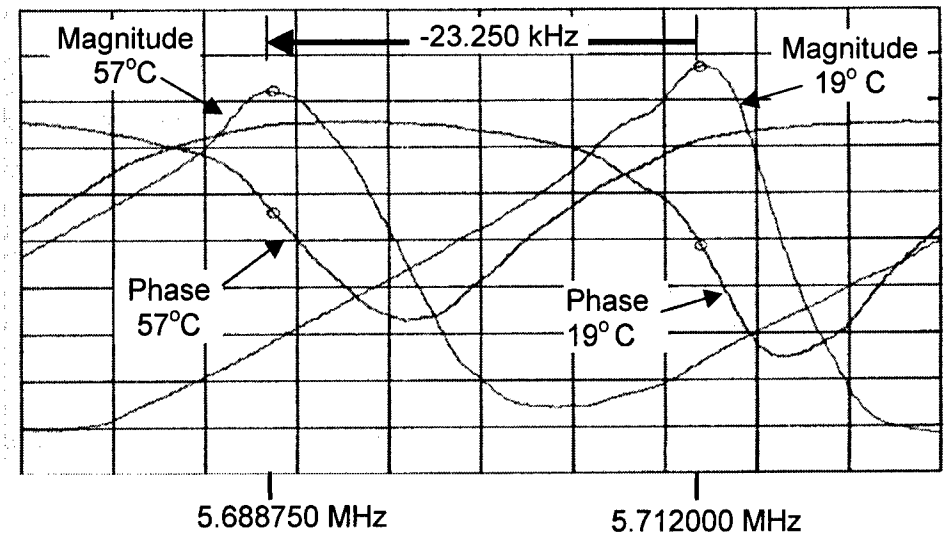

FIGURE 2. Impedance (magnitude and phase) plot of an applicator at two temperatures. Note the peak magnitude shifts a -23.250 KHz for a 38° C increase in temperature (0.611 KHz/° C).

There are multi-resonating frequencies that result in the applicator with spacing between them related to the length of the cone and the speed of propagation. The most efficient resonant mode is when the resonance of the applicator falls on the center of the natural resonance of the piezoelectric element. Efficient operation then required a transmitter that operates at this frequency and could track the frequency change that occurs with temperature change in the cone maintaining the excitation continually at optimal resonance point.

We consequently developed such an excitation system. This was accomplished by incorporating a directional coupler between the transmitter and the transducer. The reflected voltage from the coupler was then mixed against the excitation frequency. A signal was thus obtained that increased in amplitude as the reflected voltage increased (due to the excitation frequency being increasingly off resonance). Further, the polarity of the signal was related to whether the excitation frequency was above or below resonance. This signal was used to control a digital frequency generator stepping it down or up in 100 Hz steps as needed in order to minimize the signal and track the frequency. The resulting system maintained the standing wave ratios below 1.6 for applied power up to 150 Watts. By preserving the excitation on resonance the applicator was more efficient, and a maximum of -15 KHz shift was recorded during *in vivo* use. This change resulted from about a +17° C temperature rise in the water cooled applicator.

A dual channel excitation and cooling system was built (Figure 3A.) in order to allow two applicators to be used simultaneously or to allow the surgeon to change quickly between two types of applicators, using the one most desirable for a particular bleeding situation (Figure 3A). The cooling part of the system allows pumping cooling fluid through each applicator at a flow rate of 630 ml/min each. The system can deliver 220 Watts to each channel (50 ohm load at 5.5 MHz) under continuous use. Since the system is still a prototype it was mounted on a cart to allow it to be

easily moved to different investigative sites. Two titanium applicator styles have been used in a variety of animal investigations (Figure 3B &C).

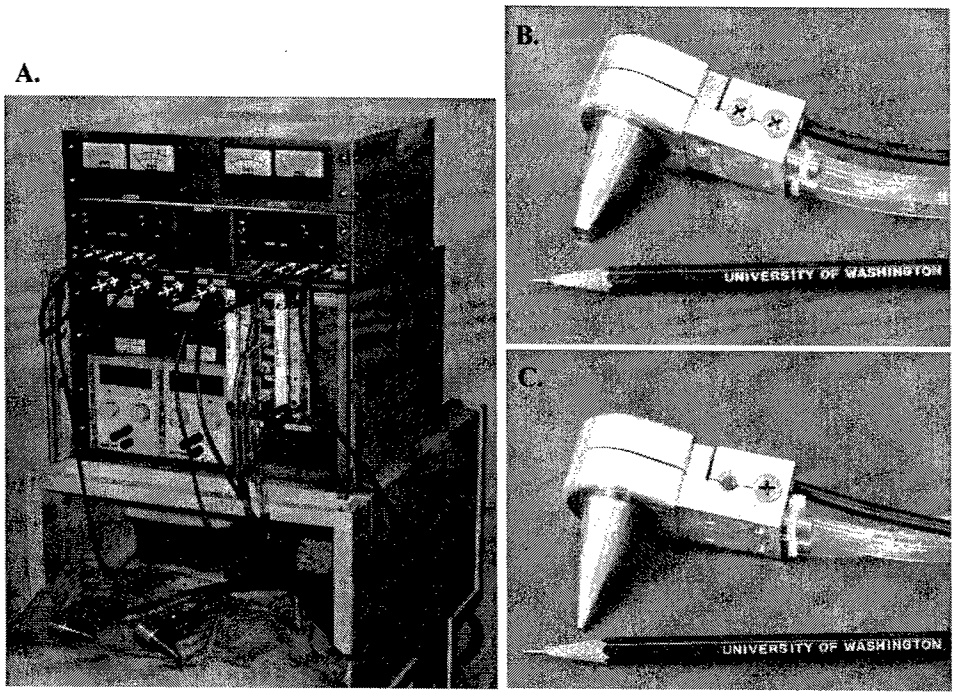

Figure 3. A. The electronic and cooling system for two channels. **B.** Water-cooled titanium HIFU applicator (5.7 MHz). The piezoelectric element is 2.54 cm in diameter with a spherical curvature with a radius of curvature of 6.35 cm at f/# 2.5. The cone is truncated so the applicator focuses at a distance of 1.3 cm from the tip. **C.** An applicator similar to B, but the tip is truncated closer to the natural focus of the spherical piezoelectric element. The focus centers at 5 mm from the tip.

IN VIVO ANIMAL HEMORRAGE STUDIES

Numerous studies have been conducted with our solid cone applicators but a recent one involved investigating HIFU therapy for blunt trauma. In this investigation 11 juvenile swine (31.7 ± 4.1 kg) were studied along the guidelines approved by National Institutes of Health for laboratory animals and a protocol approved by the University of Washington's Animal Care and Use Committee. The animals were anesthetized and then received a blunt impact to the abdomen over the area of the liver utilizing a nail driving gun impacting on a 5 cm diameter and 1.3 cm thick aluminum disk placed on the skin. This blow resulted in a variety of injuries to the liver varying from trauma level II to III. It was observed that these injuries were similar to those that people receive with accidents that produce blunt abdominal trauma. The animals were maintained anesthetized during laparotomy, the injured liver was exposed, and HIFU was administered to all the bleeding sites using a 5.7 MHz water-cooled titanium coupled applicator. Electrical power levels were applied up to 150 W continuous to

the applicator. On the average 15 minutes of HIFU exposure time was used for each animal but that depended considerably on the extent of the injury. When all the bleeding sites that were found had been treated to the level to achieve hemostasis, all fluid was suctioned from the abdomen, and the animal was closed. The average surgery time was 54 $\pm$ 23 minutes. The animals then were kept anesthetized, fluid was given intravenously to try to maintain blood pressures, and the animals were given heparin throughout to try to model a state of coagulopathy as is often encountered in blunt trauma patients. At 3.6 $\pm$ 0.4 hours the animals were reopened and the injury and treated sites were inspected for bleeding. Any new fluid that had accumulated during that period was aspirated and measured. On the average 8.6 $\pm$ 6.2 ml/kg was found. This was less than that reported by Cohn, et al. [10] in a study of 14 pigs insulted similarly. Seven of their animals were treated with normal surgical approach, which included packing the bleeding site before closing. The other 7 were treated in a similar manner except, instead of packing, fibrin glue was used. They reopened the animals at about 1.5 hours and recovered on the average 51 ml/kg for those packed and 17.6 ml/kg for those who received fibrin glue. Although their protocol was similar to ours it was not identical in several areas. We therefore cannot make an absolute comparison but it appears that our HIFU approach did perform well when contrasted with their study. Perhaps the most positive finding was that in almost all cases the treated sites were still hemostatic at the time of reopening. Nevertheless, we found we had missed some bleeding sites in some of our initial laparotomies and one of our animals died at 2.6 hours. All the other animals had viable vital signs at the time of reopening. The biggest problem found with the HIFU method (as with other techniques) was when large veins (greater than 3 mm diameter) were ruptured. They required suturing in addition to HIFU but that was not always completely satisfactory. It was discovered in the animal that died that a large vein of about 1 cm in diameter had ruptured but was hidden by the gall bladder.

SUMMARY

Overall the water-cooled applicators when operated with frequency tracking performed very well. The frequency tracking maintained standing wave ratios below 1.6 with power of up to 150 Watts applied. There was no smoking generated or charring from the HIFU technique, hemostasis could be achieved with blood in the fracture, surface and volume cauterization was produced, and there was no interference with the ECG. However, large veins required the assistance of sutures or other means. The applicator shown in Figure 2B worked the best for large fractures. The other applicator tended to have dried or clotted blood build up on it which required removing by an abrasive action. The applicators tolerated gas sterilization with no problems developing. One applicator was used over 1. 7 hours in the study. The unit and applicators were also used successfully in another study in treating pig lungs that is reported in this proceeding [8].

ACKNOWLEDGMENTS

This research was supported by grants from the National Institute of Health grant number NIH 8 R01 EB00292-03 and Department of Defense DAMD 17-002-0063.

REFERENCES

1. Vaezy, S., Martin, R., Schmiedl, U., Caps, M., Taylor, S., Beach, K., Carter, S., Kaczkowski, P., Keilman, G., Helton, S., Chandler, W., Mourad, P., Rice, M., Roy, R., Crum, L., "Liver hemostasis using high intensity focused ultrasound," *Ultrasound in Med and Biol*, **23** (9), 1413-1420 (1997).
2. Vaezy, S., Martin, R.W., Keilman, G., Kaczkowski, P., Chi, E., Yaziji, H.,Caps, M., Poliachik, S., Carter, S., Sharar, S., Cornejo, C., Crum, L.A., "Control of splenic bleeding using high intensity ultrasound," *J Trauma*, **47** (3), 521-525 (1999).
3. Martin, R.W., Vaezy, S., Helton, S., Caps, M., Kaczkowsk,i P., Keilman, G., Carter, S., Chandler, W., Mourad, P., Beach, K., Crum, L., "Acoustic liver cauterization: A potential tool for bloodless surgery," *Proceedings of 16th ICA/135th ASA Meeting*, **2**, 721- 722 (1998).
4. Vaezy, S., Martin, R.W., Yaziju, H., Kaczkowski, P., Keilman, G., Carter, S., Caps, M., Crum, L.A., "Hemostasis of punctured blood vessels using high intensity focused ultrasound," *Ultrasound in Med and Biol*, **24** (6), 903-910 (1998).
5. Martin, R.W., Vaezy,S., Kaczkowski, P., Keilman, G., Carter, S., Caps, M., Beach, K., Plett, M., Crum, L., "Hemostasis of punctured vessels using Doppler-guided high-intensity ultrasound," *Ultrasound Med and Biol*, **25** (6), 985-990 (1999).
6. Vaezy, S., Martin, R.W., Kaczkowski, P., Keilman, G., Goldman, B., Yaziji, H., Carter, S., Caps, M., Crum, L.A., "Use of high intensity focused ultrasound to control bleeding," *J Vasc. Surg.*, **29** (3), 533-542 (1999).
7. Noble, M.L., Vaezy, S., Keshavarzi, A., Paun, M., Prokop, A.F., Chi, E.Y., Cornejo, C., Sharar, S.R., Jurkovich, G.J., Martin, R.W., Crum, L.A., "Spleen hemostasis using high-intensity ultrasound: Survival and healing," *J of Trauma*, **53** (6) (In Press Dec 2002).
8. Vaezy, S., Cornejo, C., Martin, R., Crum, L., "Hemostasis and Sealing Air Leaks in Lung using High Intensity Focused Ultrasound," *2nd International Symposium on Therapeutic Ultrasound AIP Conference Proceedings* (In press 2002).
9. Brentnall, M.D., Martin, R.W., Vaezy, S., Kaczkowski, P., Forster, F., Crum, L., "A new high intensity focused ultrasound applicator for surgical applications," *IEEE Trans Ultrasonics, Ferroelectrics, & Frequency Control*, **48** (1), 53-63 (2001).
10. Cohn, S.M., Cross, J.H., Ivy, M.E., Feinstein, A.J., Samotowka, M.A., "Fibrin glue terminates massive bleeding after complex hepatic injury," *J of Trauma*, **45** (4), 666-672, (1998).

Cylindrical Array For Intraductal Thermal Ablation

D. Melo de Lima[1], C. Lafon[1], F. Prat[2], Y. Theillère[1], A. Birer[1] and D. Cathignol[1]

[1]*INSERM Unit 556, 151 Cours Albert Thomas 69424 Lyon, France*
[2]*Centre Hospitalier Bicètre, 78 Avenue G^{al} Leclerc 94275, France*

Abstract. Intraductal thermal surgery has been shown to be a useful therapeutic option when external ultrasound applicators cannot be used as their beam may not reach the target site. In this study the feasibility of developing a cylindrical array (10-mm O.D.) for the treatment of oesophageal tumours was evaluated. If plane transducers are used the ultrasound beam has to be rotated in order to generate a sufficiently large volume of necrosis. Furthermore, rotating intraductal applicators and controlling their shooting direction present technical difficulties. To solve this problem, the feasibility of an array has been evaluated using a 10-mm cylindrical prototype, which is composed of 16 transducers working at 4.55 MHz and arranged on a quarter of the cylinder. In order to treat depth sector-based or circular area, plane waves were generated by exciting eight successive elements of the array with appropriate excitation delay times. The shot direction was changed by exciting a different set of eight elements, thereby electronically rotating the ultrasound beam through the tissues. *Ex vivo* experiments were carried out on pig liver and permit to generated three reproducible well-defined lesions up to 15-mm, separated from each other by a 22.4° angle. In all sets of experiments, the sonication time and the intensity were 20 seconds and 17 W/cm² respectively. This work was support by a grant from the French ministry of industry (N° CNC02F).

INTRODUCTION

A large proportion of digestive tumours develop initially inside the circumference of the lumen. This is the case for many oesophageal tumours. Results obtained by surgery or the use of systemic methods (radiotherapy or chemotherapy) does not allow us to envisage curative prospects. Local destruction by physical means is one of the research themes which, it is hoped, will lead to therapeutic progress. For this reason, endoscopic techniques to clear the oesophagus ducts are routine. Of these methods, laser photocoagulation [1,2] is often used, but it is relatively expensive and demanding because tissue destruction is superficial and several sessions are generally needed to achieve symptomatic improvement. In the past, high intensity ultrasound has proved to be highly efficient, both experimentally and clinically, in inducing homogeneous and reproducible tumour destruction by thermal coagulation necrosis [3,4,5]. In the case of oesophageal cancers, one of the problems is to be able to treat a tumoral volume which is sometimes sector-based and extends to variables depths. To solve this problem, Melo de Lima [6] reconsidered the idea of plane rotating transducers [7], already applied to biliary ducts [8]. This solution provides deep coagulation necrosis (up to

10 mm) on a short time scale (around 10 seconds). This system requires mechanical rotation of the shaft of the applicator to treat large volumes so that successive shots cannot follow on rapidly, as already noted by many authors [9,10,11]. If the active part consists of several transducers, the form and intensity of the pressure field created can be controlled electronically by modulating the amplitude and phase applied to each element. The location of the heat point can then be moved without the need for mechanical movement. Several layouts have been suggested. Applicators with linear-mounted elements are rare, because they do not completely dispense with the need for mechanical movement [12]. Elements disposed on the concave surface of a focused applicator combine electronic and geometric focusing [13,14,15]. Since it is possible to create several focal points simultaneously, the time take for a complete treatment is also greatly reduced [16,17].

To solve the problems of treating oesophageal tumours, we suggest the use of a cylindrical phased array ultrasound applicator, 10 mm in diameter, consisting of 64 transducer elements, operating at 4.55 MHz, disposed around the entire periphery of the cylinder. In this configuration, the ultrasound field is naturally divergent. To produce plane propagation, eight consecutive elements are excited with the appropriate delay times. Mechanical movement of the applicator is replaced by electronic rotation of the ultrasound beam using eight other elements to change the shot direction. This method guarantees more accurate shooting angles, and sonication sequences which are not dependent on mechanical constraints.

The aim of this work is to study the feasibility of a 64-element applicator using a prototype consisting of 16 transducers disposed over a quarter of the cylinder. Coagulation necroses were produced on pig's liver. Initially, elementary lesions were formed by generating, with the array, a plane wave to ensure that appropriate delay times collimate the ultrasound beam so that it is comparable with a lesion generated by a plane source. By rotating the beam electronically, we studied the correspondence between the position of the lesion and the three groups of transducers with an angular distance of 22.4° between them, which were used to induce these lesions. Then, choosing a finer angular step (6°), contiguous lesions were induced to ensure that all the region of interest was treated. Finally, the acoustic intensity was modulated during a series of 9 ultrasonic shots to generate a lesion, the depth of which varied according to the angular position.

MATERIALS

The prototype applicator consisted of a biocompatible silicone tube 12 mm in diameter with a 1.5 mm thick wall ending with two 15 mm diameter brass sleeves which mechanically hold the active part, a 10.6 mm diameter cylinder. This sector-based phased array is composed of 16 plane transducer elements 70 μm apart. Each is 390 μm thick and works at a frequency of 4.55 MHz. Their dimensions are 0.45×15 mm^2 and they are disposed over 90°. RF connections were made via a miniature coaxial cable 150 cm long, 50Ω, with a 0.52 mm OD. The outer ground conductor was connected to the external face of the transducers. The aft wave is

dissipated in a hollow rigid cylindrical backing which gives the active part its mechanical rigidity. The transducer elements are cooled by a continuous flow of degassed water which circulates along the front of the transducers, then goes inside the backing. The cooling circuit water, maintained at 25°C, is driven by a Masterflex peristaltic pump (Cole Parmer Instrument Co., Chicago, USA) at a speed of 0.21 L/min. maintaining the temperature of the transducer elements at about 45° C during sonication. The cooling circuit water also provides ultrasonic coupling between the transducer and the target tissues, so that, if necessary, the depth of treatment can be increased by moving the maximum temperature zone further away from the front of the transducer. The active part of the applicator is covered by a 65-μm thick latex balloon attached with 4/0 polydioxanone (PDS) suture thread (Ethnor, Neuilly, France) and covered by watertight seal. This envelope produced 9% of the ultrasonic pressure loss. A tube (1 mm OD) over the whole length of the applicator, holds a guide wire which, during future use *in vivo*, will first be inserted into the oesophagus to guide the probe to the treatment zone. Electricity was provided by 16 AHF 855 power amplifiers (Adece, Artannes, France) which put into sinusoidal form the TTL signals generated by a 50 channels pattern generator (PG1050 Acute, Hsin Chuang City, Taiwan). Sixteen channels of the generator were used in this study. The delay can be adjusted for each channel with a resolution of 10 nanoseconds. 0-10V digital-analog output cards are used to adjust the gain on each amplifier. Input cards capture analog voltages (delivered by the amplifiers) directly proportional to the direct and reflected power. A Pentium 4 PC controls the input-output cards and the generator. An I/O card management program developed under Dynamic C is used to capture and store the values of gain and power provided during each ultrasonic shot. A significant increase in reflected power indicates a problem (vaporization of cooling water, incorrect acoustic coupling between the transducer and the target tissues, formation of bubbles or accidental heating of the transducer) which can damage the active part of the applicator. This is why, if reflected power is 10% more than incident power the program returns a null value to all amplification gains.

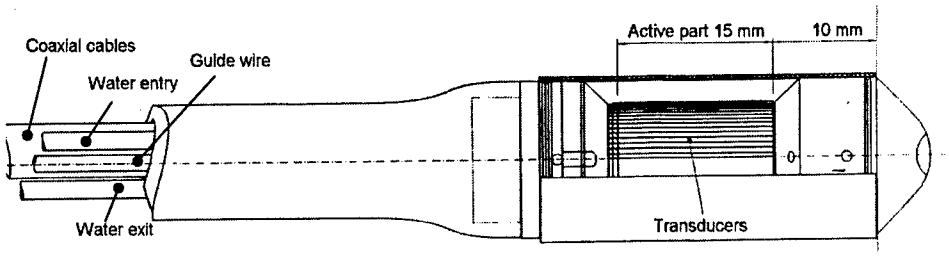

FIGURE 1. Schematic drawing of our cylindrical ultrasound phased array.

METHODS

Trials were performed *ex vivo* on a total of 18 samples of butcher's pig's liver. Before the experiment, each sample of liver was degassed in a vacuum (0.7 bars for 30 min) to remove microbubbles initially present in the tissue. During the tests, each

sample was immersed in a tank of degassed water maintained at 37° C. A thermocouple was inserted in each sample to ensure that the temperature was close to 37° C before starting the shots. The ultrasound applicator, inserted in the middle of a rectangular parallelepiped of liver (100x100x30 mm^3), was attached to a PVC support to prevent any movement (Figure 2). This experimental protocol using pig's liver was the same for all three studies described below.

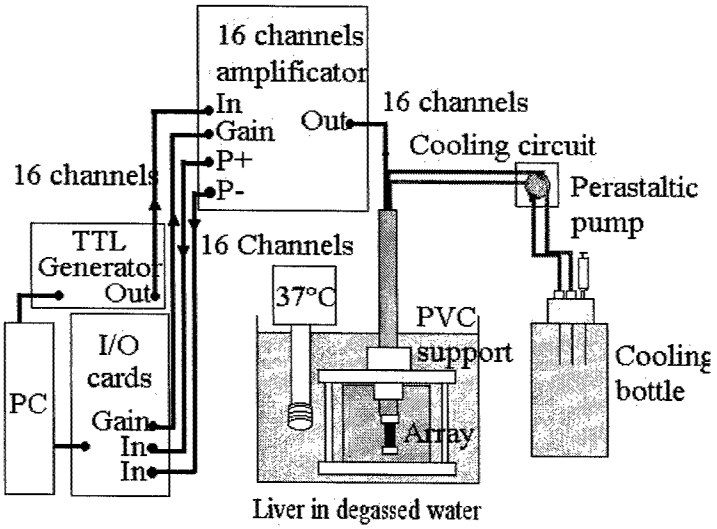

Figure 2. Experimental system and electrical equipment for the *ex vivo* experiments

The lesion generated by 8 elements excited to collimated the beam were compared with lesions induced by a plane transducer [8]. The delays applied to elements 1 to 7 were 10, 110, 180, 210, 200, 170, and 100 nanoseconds respectively, element 8 being used as reference. The eight elements delivered an acoustic intensity of 17 W/cm^2 during 20 seconds. To show that it is possible to rotate the ultrasonic beam electronically, a series of three separate lesions, 22.4° apart, were produced. Each elementary lesion was obtained by exciting three groups of eight transducers successively. During each shot, the active elements delivered an acoustic intensity of 17 W/cm^2 for 20 seconds. To obtain the separate lesions, the pause duration was set to one minute. Elements 1 to 8, 5 to 12 and 9 to 16 were used during shots one, two and three respectively. During examination of the necroses obtained, the angular distance between each lesion was measured by tracing three lines joining the centre of the applicator and the middle of the lesions to ensure that electronic rotation wad accurately transmitted. During the second *ex vivo* study, contiguous lesions were produced by 9 successive ultrasound shots. As before, plane waves were recreated from 8 elements for each shot. Acoustic intensity and sonication time were also the same, 17 W/cm^2 and 20 seconds respectively. For each new ultrasound shot, we used 8 elements displaced by one transducer with respect to the previous shot, corresponding to the finest possible angular distance (5.6°). The time between two consecutive shots was 10 seconds. Using the same procedure, lesions were induced by modulating the acoustic intensity of the shots. As before, 9 ultrasonic shots, offset by an angle of 5.6°,

were realised successively every 10 seconds. Sonication time was 20 seconds for each shot. The first three lesions were produced using an acoustic intensity of 12 W/cm², the next three at an intensity of 17 W/cm² and the last three at an intensity of 12 W/cm². Using the same protocol, we also produced lesions through 4 successive shots, every 10 second, at an intensity of 12 W/cm² during 20 seconds, then 5 shots every 10 seconds were performed at 17 W/cm² during 20 seconds. In this study we restricted ourselves to a power of 17 W/cm² to avoid damaging the transducers
Liver samples were frozen just after treatment to make the lesion easier to cut and examine. When the tissue temperature was close to –6°C, the tissues were sliced along a plane perpendicular to the acoustic axis, at mid-height from the transducer. The coagulation necroses were inspected macroscopically at the end of the experiment. The distinction between the surrounding non treated tissues can clearly be seen in a medium like pig liver; the lesion has an off-white colour, sometimes dark at the most heated points, similar to that of cooked liver.

RESULTS

All the coagulation necroses obtained were distinct and reproducible. The cross-sections made perpendicular to the applicator axis were used to measure the depth and width of the lesions. Figure 3a shows 7 lesions induced by a 5.1 MHz plane applicator at an ultrasound intensity of 19 W/cm² during 20 seconds. The necrosis reached a depth of 20 mm from the applicator surface. Figure 3b shows an elementary lesion induced by 8 elements of the array generating a plane wave. Ultrasound intensity was set to 17 W/cm² during 20 seconds. The lesion reached a depth of 15 mm from the applicator surface. Figure 3c shows the three basic lesions produced by electronic rotation of the ultrasonic beam. Each lesion is 14±1 mm deep and 5±1 mm wide. The angle between lesions one and two is 26°. The angular difference between lesions two and three is 24°. Considering the positioning and size of the transducers, the theoretical difference between two consecutive lesions produced using hit experimental protocol was 22.4°. Angular differences were thus respected at ±5° which corresponds approximately to measurement uncertainty. The average acoustic intensities emitted by each element of the array during this experiment were 17.0, 16.5 and 17.1 W/cm² for shots one, two and three respectively. Figure 3d shows a continuous coagulation necrosis, 19 mm deep and occupying a sector of 90°. The average acoustic intensity emitted by the elements during all the shots generating this lesion was 16.6 W/cm². A dark area corresponding to the part of the tissue which was strongly heated is visible in the center of the necrosis. Figure 3e shows the lesion obtained by modulating the power emitted according to the angular position. Average acoustic intensities were 11.8 W/cm², 17.2 and 12.3 W/cm² for shots 1-3, 4-6 and 7-9 respectively. As before, the zones in the centre of the lesion are brown. Figure 3f shows a lesion also obtained by modulating the power emitted according to the angular position. Average acoustic intensities were 12.0 W/cm² and 17.3 W/cm² for shots 1-4 and 5-9 respectively. A brown area is visible in the centre of the lesion. The lesions shown in Figures 6 and 7 are 5±2 mm and 15±1 mm deep for tissues exposed to intensities of 12 and 17 W/cm² respectively.

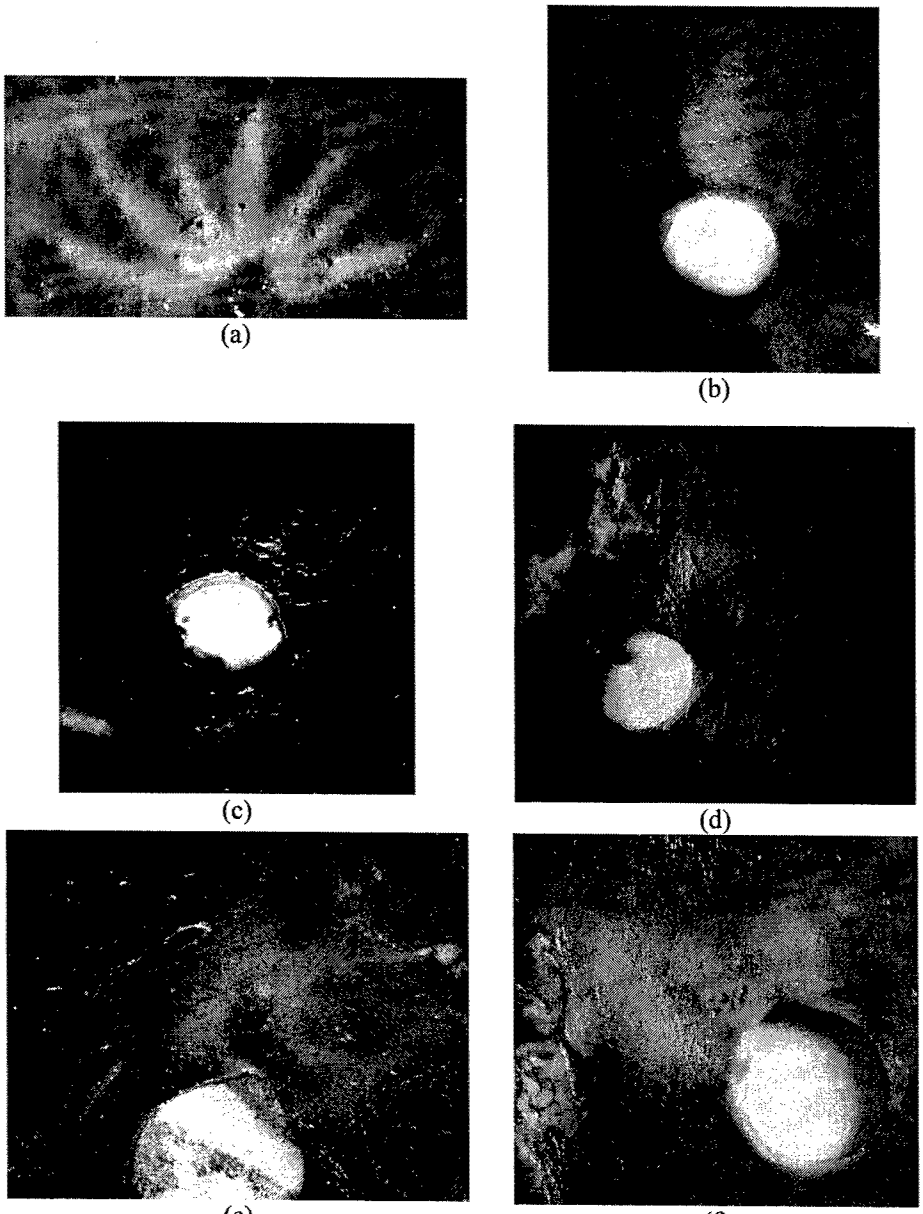

FIGURE 3. (a) 7 lesions induced by a 5.1 MHz plane applicator at an ultrasound intensity of 19 W/cm^2 during 20 seconds. (b) Elementary lesion induced by 8 elements of the array generating a plane wave. Ultrasound intensity: 17 W/cm^2 during 20 seconds. (c) Three elementary lesions obtained by 22.4° rotation of the beam. Intensity fixed at 17 W/cm^2 for 20 seconds; one minute pause between each shot. (d) 9 ultrasound shots every 10 seconds. Angular step 5.6°. Intensity and exposure time were set at 17 W/cm^2 and 20 seconds respectively. (e) 9 ultrasound shots every 10 seconds. Angular step 5.6°. Shots 1-3 and 7-9: 12 W/cm^2 for 20 seconds. Shots 4-6: 17 W/cm^2 for 20 seconds. (f) 9 ultrasound shots every 10 seconds. Angular step 5.6°. Shots 1-4: 12 W/cm^2 for 20 seconds. Shots 5-9: 17 W/cm^2 for 20 seconds.

DISCUSSION

All the lesions obtained *ex vivo* are clear and reproducible. When eight consecutive elements of the array are excited with a phase law permitting the recreation of a plane wave, the coagulation necroses obtained are in the form of a flame. For shooting times of 20 seconds at acoustic intensities of 17 W/cm², the depth of treatment observed is, on average, 16±2 mm. This lesion geometry is that routinely observed when using a plane transducer as is the depth of the necrosis as shown in Figure 3a[7]. The height of the lesions is essentially the same as that of the transducer, as has always been the case when using plane transducers[6]. Electronically rotating the beam in the tissues has produced a series of deep lesions. When the waiting time between each ultrasound shot is long (1 minute), the lesions are all separate. It is then easy to measure the angular distance between two consecutive lesions. The angular value expected (22.4°) according to the geometry and size of the active part is relatively close to the experimental results (24±2°) which confirms the possibility of generating precise electronically rotating plane waves (Figure 3c). So that there is no untreated area during sonication of a tumoral mass, we have also shown that a fine angular step (6°) can be used to obtain continuous necroses. These are logically deeper than basic lesions (19 mm instead of 17 mm) because with a short pause (10 seconds) each lesion benefits from the heat generated by the previous ultrasound shot. When two successive shots are displaced by one transducer, the central elements are also most often used, so that the tissues opposite these transducers receive a greater thermal dose, generating the brown areas observed in Figures 3b, c and d. The sectoral aspect and variable extension in depth of oesophageal tumours pose major problems in treatment by physical means. These difficulties can be solved using this approach which combines electronic rotation and modulation of acoustic intensity of shots according to the angular position. The minimum angular step in our applicator also means that healthy tissue immediately adjacent to the cancerous area can be preserved when a sector-based tumour is being treated.

CONCLUSION

This work enabled us to study and develop a prototype circular array of 16 elements. We have shown that an appropriate phase law can be used to recreate a plane wave with a directivity comparable to that generated by a plane transducer. In addition, the elementary lesions obtained are the same as those generated by a plane applicator, both in terms of depth of treatment and necrosis geometry. It was also shown that the electronic apparatus controlling the transducers provides electronic rotation of the ultrasonic beam which complies with the array geometry and ensures a precise control of the deposit power. The principle of a plane rotating beam permit to adjust the treatment depth according to the angular position.

ACKNOWLEDGMENTS

This work was partially supported by a grant from the French ministry of industry. N°CNC02F

REFERENCES

1. De Palm,a G.D., Galloro, G., Siciliano, S., Donisi, M. and Cantanzano, C., "Endoscopic palliation of locally recurrent esophageal and gastric carcinoma after surgery," *Gastroenterology International*, pp. 69-72 (1999).
2. Sharma, P., Jaffe, P.E., Battacharyya, A., and Sampliner, R.E., "Laser and multipolar electrocoagulation ablation of early Barrett's adenocarcinoma: Long-term follow-up," *Gastrointestinal Endoscopy*, pp. 442-446 (1999).
3. Fry, F.J., and Johnson, L.K., "Tumour irradiation with intense ultrasound," *Ultrasound Med. Biol.*, pp. 337-341 (1978).
4. Chapelon, J.Y., Ribault, M., Vernier, F., Souchon, R., and Gelet A., "Treatment of localised prostate cancer with transrectal high intensity focused ultrasound," *European Journal of Ultrasound:* Official Journal of the European Federation of Societies for Ultrasound in Medicine and Biology, pp. 31-38 (1999).
5. Gelet, A., Chapelon, J.Y., Bouvier, R., Rouvière, O., Lasne, Y., Lyonnet, D., Dubernard, J.M., "Transrectal high-intensity focused ultrasound: minimally invasive therapy of localized prostate cancer," *Journal of Endourology* / Endourological Society, pp. 519-528 (2000).
6. Melo de Lima, D., Prat, F., Theillère, Y., Arefiev,A., and Cathignol, D. *Ultrasound applicator for destruction of oesophagus tumours: First Animals Trials.* Proceeding of the congress of the revue IEEE UFFC, Atlanta, Georgia, USA, 2001, pp. 1365-1368.
7. Lafon, C., Chapelon, J.Y., Prat, F., Gorry, F., Margonari, J., Thellière, Y., and Cathignol, D, "Design and preliminary results of an ultrasound applicator for interstitial thermal coagulation." *Ultrasound in Med. and Biol.*, pp. 113-122 (1998).
8. Prat, F., Lafo, C., Margonari,J., et al., "A high-intensity US probe designed for intraductal tumor destruction: experimental results," *Gastrointestinal Endoscopy.*, pp. 388-392 (1999).
9. Damianou, C. and Hynynen K., "Focal spacing and near-field heating durinf pulsed high temperature ultrasound hyperthermia treatment," *Ultrasound in Med. Biol.*, pp. 777-787 (1993).
10. Fan, X. and Hynynen, K., "Ultrasound surgery using multiple sonications-treatment time considerations," *Ultrasound in Med. Biol.*, pp. 471-482 (1996).
11. Daum, D.R. and Hynynen, K., "Thermal dose optimization via temporal switching in ultrasound surgery," *IEEE Trans. Ultrason., Ferroelect., Freq. Contr.*, pp. 208-215 (1998).
12. Chopra, R., Bronskill, M.J., and Foster, F.S., "Feasibility of linear arrays for interstitial ultrasound thermal therapy," *Med. Phys.*, pp. 1281-1286 (2000).
13. Hutchinson, E.B., Buchanan, M.T., and Hynynen, K., "Intracavitary ultrasound phased array for non invasive prostate surgery," *IEEE Trans. Ultrason., Ferroelect., Freq. Contr.*, pp. 1032-1042 (1996).
14. Cain, C.A., and Umemura, S.I., "Concentric-ring and sector-vortex phased-array applicators for ultrasound hyperthermia," *IEEE Trans. Microwave Theory Tech.*, pp. 1803-1813 (199).
15. Curiel, L., Chavrier, F., Souchon, R., Birer, A., Chapelon, J.Y., "1.5-D high intensity focused ultrasound array for non-invasive prostate cancer surgery," *IEEE Transactions on Ultrasonics, Ferroelectrics, and Frequency Control*, pp. 231-242 (2002).
16. Fan, X., and Hynynen, K., "A study of various parameters of spherically curved phased arrays for noninvasive ultrasound surgery," *Phys. Med. Biol.*, pp. 591-608 (1996).
17. Wan H., VanBaren P;, Ebbini E.S. and Cain C.A., *Ultrasound surgery: Comparison of strategies using phased array systems.* IEEE Trans. Ultrason., Ferroelect., Freq. Contr., 1996, pp. 1085-1097.

200 Elements Fully Programmable Random Sparse Array For Brain Therapy: Simulations And First *Ex Vivo* Experiments

M. Pernot, J-F. Aubry, C. Dorme, M. Tanter and M. Fink

Laboratoire Ondes et Acoustique,ESPCI, France, Paris 75005.

Abstract. A fully programmable random sparse array has been specially designed and built for noninvasive transskull brain therapy. Due to the strong increase of sound absorption of the skull with frequency, the frequency of the transducers has been set to 1 MHz. In order to correct the phase and amplitude distortion induced by the skull, the active element size has to be smaller than the correlation length of the skull (approximately 1 cm at 1 MHz). Moreover, the element size has to be small enough to permit beam steering in a sufficiently large volume. The array is made of 200 high power transducers (Imasonic, Besançon, France) with a 0.5 cm^2 active area, enabling us to obtain 300 bars at focus. In order to optimize the focus, several transducers distributions on a spherical surface have been simulated (hexagonal, annular, and semi-random distribution). Secondary lobes were significantly reduced by using a semi-random array. Furthermore, simulations and experiments showed the capability of the random array to electronically move the focal spot in the vicinity of the geometrical focus (up to +/- 15 mm at 140 mm depth). The semi-random array has been assembled. A good agreement between simulated and experimental focusing patterns is shown. 260 bars have been measured at focus and *ex vivo* experiments are under investigation.

INTRODUCTION

The feasibility of the practical clinical realization of noninvasive surgery using High Intensity Focused Ultrasound in order to burn tumors has been demonstrated [1] and is today widely studied [2,3,4,5,6]. However ultrasonic brain tumor hyperthermia remains limited due to the strong aberrations and absorption induced by the skull. In order to build an array that can correct for these aberrations, a number of design considerations have been discussed [2] and a first prototype was recently developed by Clement *et al* [3]. During the last two years, a prototype devoted to brain HIFU has also been designed and built in our lab. As suggested by clement and Hynynen, we used a F/D number lower than one in order to reach the maximum antenna gain. This new system is working at a higher frequency (1 MHz) than the one built by Hynynen's team. An higher frequency improves resolution and increases the cavitation threshold but also increases the overheating of the skull surface and the aberrations induced by the skull on the beam pattern. First *ex-vivo* experiments are under investigation.

ARRAY DESIGN AND SPECIFICATIONS

A 1 MHz driving frequency was chosen for the array. This operating frequency has been chosen by considering several factors: The F/D aperture of the array, the focal spot size, the absorption coefficient, the cavitation threshold and finally the electrical matching of the transducers (linked to ration between the size of the transducer and the wavelength). On the one side, at low frequencies, the absorption coefficient is smaller and necrosis is harder to reach. Moreover, cavitation occurs sooner as the cavitation threshold decreases with frequency. On the other side, it is obvious that a higher frequency can achieve a more localized focus, but above 1.3 MHz the absorption and scattering loss of the skull increase very rapidly, and a high fraction of the wave energy is absorbed by the skull [8]. Moreover, at high frequency, the constraints imposed by steering abilities and electrical matching are incompatible with a reasonable number of transducers, as ones has to maximize the array aperture to avoid skin and skull heating.

Several transducers spatial repartitions have been investigated in order to minimize the secondary lobes and optimize the beam steering capabilities of the system. Thus, in order to optimize the number of transducers and their size, several considerations have been taken into account. The array must be able to focus at its geometric center, correcting the aberrations induced by the skull, which means that the active element size has to be smaller than the correlation length of the skull (~ 10 mm at 1 MHz). Moreover the array must be large enough to distribute energy evenly across the skull bone in order to avoid undesired skull heating. A 140 mm geometrical focus and 180 mm array diameter were chosen in decrease at best the F/D ratio [clement]. Finally, the number of transducers must also be sufficient to deliver therapeutic power level at focus. The acoustic power required in ablation operating regime is typically 1500 $W.cm^{-2}$ at 1 MHz, which corresponds to a overpressure of 70 bars at focus when passing through the skull. Considering the absorption of soft tissues (0.7 $dB.cm^{-2}$), and the absorption induced by the skull (an average loss of 11 dB), the pressure obtained at focus in water without the skull must be approximately 400 bars. All transducers of the array have been characterized individually. Each transducer was linked to its 50 Ohms electrical matching and reached a 60 % efficiency. The electrical power delivered by each of the 200 electrical channels is 18 Watts. Consequently, each transducer can generate 2 bars at focus (140 mm) in water during 5 seconds. Therefore the array will be composed of approximately 200 elements.

SIMULATIONS

The performance of several transducers distributions, as hexagonal, concentric shifted rings and quasi-random, was investigated (Fig. 1). For each array the 3D acoustic field was calculated by using the impulse diffraction code SIMULPA developed by D. Cassereau. The different sparse phased arrays have the characteristics previously described. According to Gavrilov et al. [9], the sparseness (52%) was within the limited range 40 to 70 %, allowing beneficial effects of randomization. In order to assess the performance of the different arrays we calculated the acoustic field

when focusing at geometrical focus, and finding the maximum intensity in grating lobes.

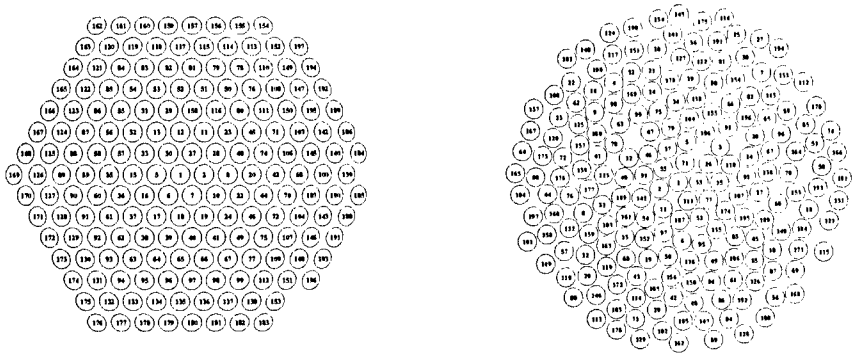

FIGURE 1. Hexagonal and quasi-random transducers distributions.

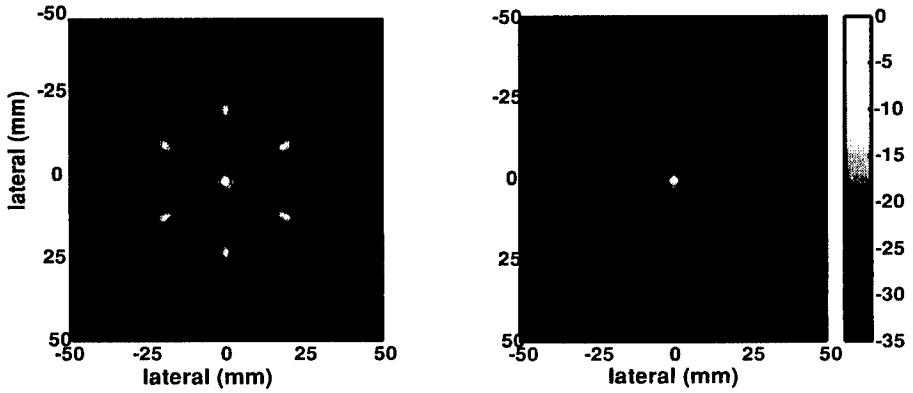

FIGURE 2. Acoustic field in the focal plane for the hexagonal (left) and quasi-random (right) arrays.

Figure 2 shows the intensity distributions in the focal plane for the hexagonal and quasi-random arrays. Grating lobe levels associated with an aperiodic distribution (concentric shifted rings and quasi-random arrays) are 10 to 12 dB less than those associated with periodic element spacing (hexagonal array). The concentric rings and quasi-random arrays have quite similar performance in the focal plane, the maximum grating lobe level is lower than –20 dB. However the quasi-random array has better performance in the near field: on the acoustical axis the pressure amplitude of the quasi-random array was found 10 dB lower than the one of the concentric rings array, see Fig 3 (and Fig. 7b for the experimental validation).

We have also investigated the increase of the grating lobes level when electronically shifting the focus in the lateral direction. Figure 4 shows the intensity distributions in the focal plane for the concentric rings array when the focus is shifted from 0 to 20 mm off the acoustical axis.

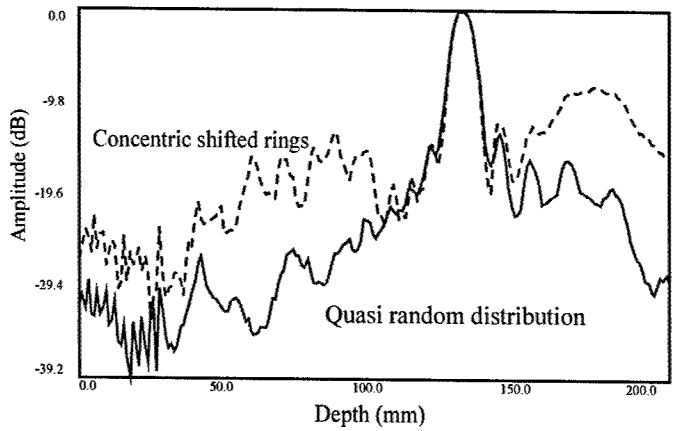

FIGURE 3. Simulated Intensity versus depth for the concentric ring and quasi random arrays.

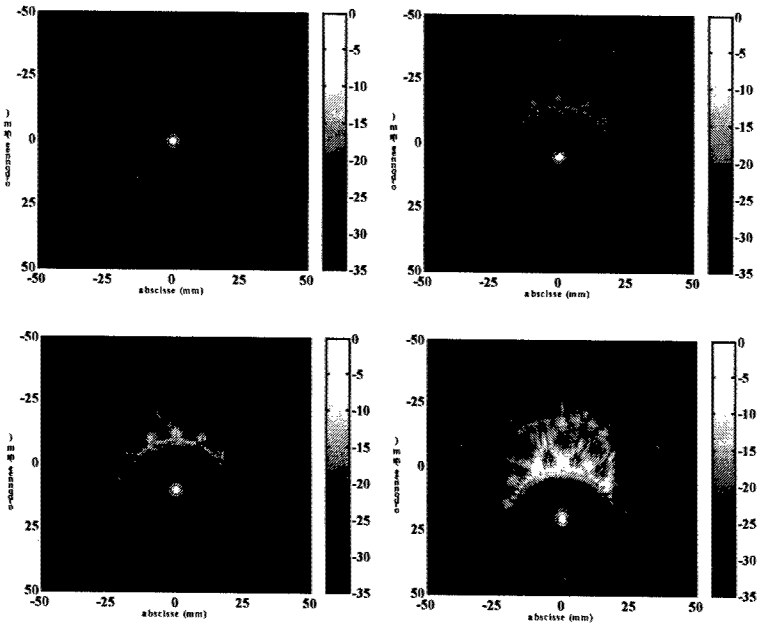

FIGURE 4. Intensity distribution for the concentric ring array, with the focus steered a) 0 mm, b) 5 mm, c) 10 mm, d) 20 mm in the y lateral direction.

The intensity distribution was deemed acceptable if the maximum intensity in the grating lobes were at least 10 dB lower than that in the main lobe, which is the commonly accepted level for safe delivery of treatment [10]. The steering range was very poor with the hexagonal distribution (± 3mm), but quite good with the aperiodic distributions (± 15 mm), see Fig 5. The grating lobes remain below -6dB up to a

20 mm steering distance. Consequently, the quasi-random distribution was finally chosen as it gives the lowest level of grating lobes in the focal plane as well as in the near field and it presents good steering capabilities.

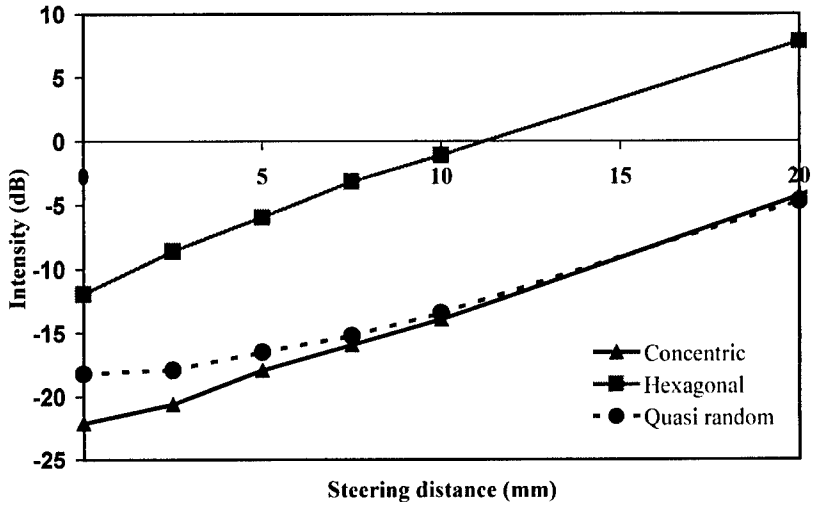

FIGURE 5. Intensity of the maximum grating lobe as a function of the steering distance from the geometrical focus. Three distributions are studied: Concentric shifted rings, hexagonal distribution and quasi random distribution.

EXPERIMENTS

The quasi-random sparse array previously designed was constructed. The 197 high power piezocomposite transducers (8 mm diameter, 0.5 cm^2 active area, Imasonic) were mounted in a sealed spherically curved holder made of a mixture of Ureol 6414B and Ureol 5075 A (Vantico Ltd). This material was selected for its thermal, mechanical and acoustical properties. Each transducer element was individually matched to the 50 Ω output impedance of the generator. The matching boxes were placed in a PVC box totally water proof, Fig. 6. The coaxial lines from the matching boxes were connected to a 197-channel driving system. Each channel could provide 18 electrical Watts. A computer was used to control the operation of the 197-channel driving system. The pressure was measured in water with a Golden Lipstick calibrated hydrophone (SEA, Soquel, CA), at low power. At focus, we measured an average value of 1.8 bars contribution for each transducer.

We also scanned the acoustic field by moving the hydrophone in the x, y and z directions. The experimental fields are very close to the one obtained with the simulation; see Fig. 7.a and 7.b. The –6dB dimension of the focus is 1.5×1.5×10.5 mm^3, and the grating lobes are lower than –20 dB.

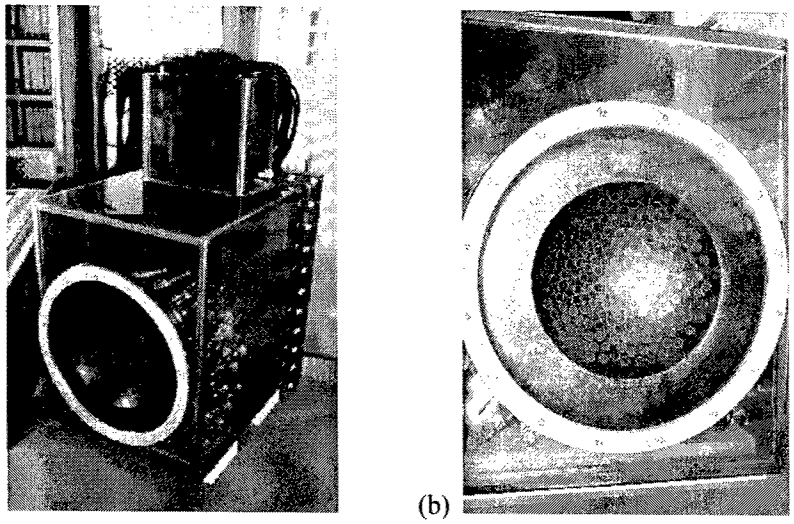

FIGURE 6. (a) 200 elements sparse array prototype and the electronic system. The waterproof rectangle contains the 200 electrical matching boxes. (b) Quasi random distribution of transducers embedded in spherical shaped Ureol.

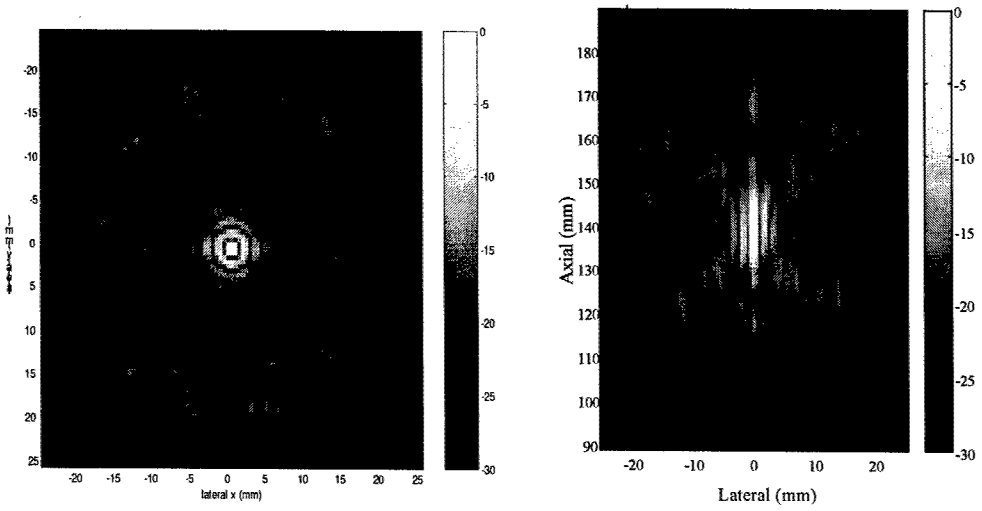

FIGURE 7. (a) Experimental scan of the intensity distribution for the quasi-random array in the focal plane (XY plane). This beam pattern was found to be in good agreement with the numerical simulation in Fig. 2b. The amplitude is in a dB scale between 0 and -30 dB. (b) Experimental scan of the intensity distribution in the XZ plane. The amplitude is in a dB scale between 0 and -30 dB.

In a next step, a skull and a piece of cow liver were inserted in water between the hydrophone and the array. The water tank temperature was 25° C. A time reversal process combined with amplitude compensation was performed in liver at the

geometric center of the array in order to correct for phase and amplitude aberrations induced by the bone on the ultrasonic beam [4]. The resulting intensity field was scanned in the focal plane. It is shown in figure 9 and compared with the field obtained without any aberration corrections. The uncorrected beam is strongly degraded by the skull. The focal spot is not at the desired location and is widely spread in comparison with the corrected one. Moreover, an important point is that the pressure amplitude at focus of the corrected beam (70 Bars) is 2.25 times higher than the pressure amplitude of the uncorrected one. Consequently, it results in a 5 times higher heat deposit.

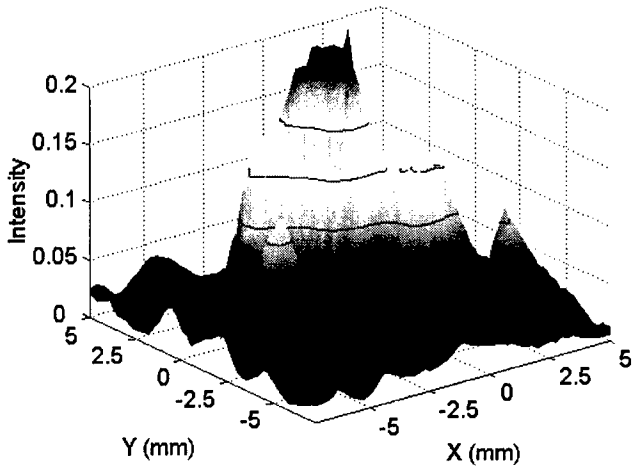

(a)

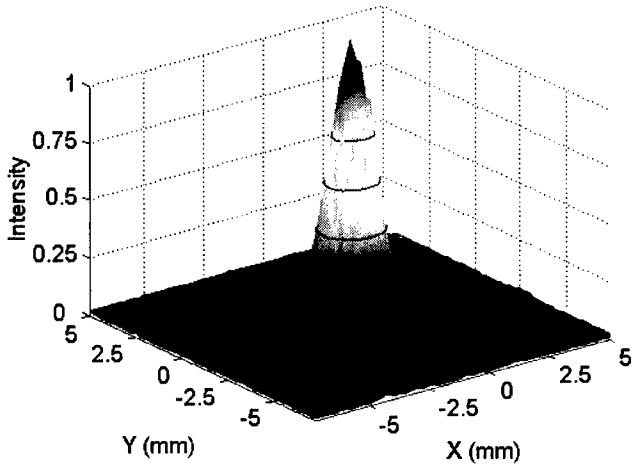

(b)

Figure 9. Experimental distribution of the normalized intensity in the focal plane (a) without aberrations corrections and (b) with corrections. Black lines correspond to -3 dB, -6 dB and -9 dB.

In order to check experimentally the heating pattern and the steering capabilities obtained through the skull a plexiglas slice (10 mm width) was placed behind the skull so that its first interface is located in the focal plane of the system. A 2 seconds

insonification was achieved and induced a burning at the plexiglas interface. The emission signals were then tilted electronically in order to focus at 7.5 mm in the four cardinal directions. As one can notice in figure 10, the targets are clearly defined, the "plexiglas necrosis" size is about 1.5 mm diameter. The impact is more important at the geometrical center of the system as the focal pressure amplitude decreases when tilting the beam.

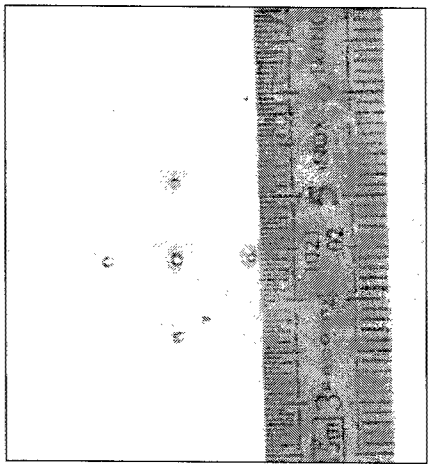

FIGURE 10. Impacts induced in a slice of plexiglas located in the focal plane (Z = 140 mm) through the skull. The impact size is about 2 mm. Aberration corrections were achieved at center by using an hydrophone and next impacts were achieved by tilting electronically the beam.

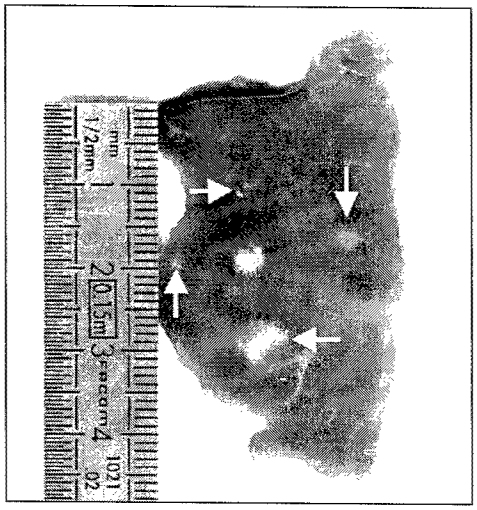

FIGURE 11. Lesions induced in liver through the skull. The target is located at depth Z = 140 mm from the array. Lesion size is about 2 mm diameter for the center spot, 4mm for the one below, 2mm for the right one. The spatial pitch between each lesion is 7.5 mm. Aberration corrections were achieved at center by using an implanted hydrophone and next impacts were achieved by tilting electronically the beam. Distance between horizontal necrosis is 7.5 mm. Distance between between vertical necrosis is about 9 mm as the liver slice was involuntarily stretched during the cut slice by slice.

The same kind of experiments were conducted in liver samples. An implanted hydrophone allows first to correct the skull aberrations for one location. The beam is then electronically tilted 7.5 mm away from the initial focus in the four cardinal directions. Two high intensity focused beams of duration 7s (with a waiting time of 10 s between each shot) were first emitted at the initial hydrophone location in the liver sample, see Fig. 11. The necrosis size is about 3 mm diameter. Then, the same procedure was used when tilting electronically the beam 7.5 mm up and 7.5 mm to the left, Fig. 11. As one can notice, the necrosis is smaller according to the intensity decrease regarding to the tilting angle. In order to increase the thermal dose for the next tilting angles, four shots were used for the right target and six shots were used for the last focus (down). The necrosis size increases with the thermal dose. The thermal dose allowed to predict the size of the necrosis which is in good agreement with the measurements.

Finally, the overheating induced at the skull surface was checked in several locations on the outer table for a 10s insonification at maximum power with a 50 % duty cycle. An average 2.5° C temperature increase (from the initial 25° C temperature of the water tank) was found without any watercooling system. Figure 12 shows the temperature elevation for a given thermocouple location.

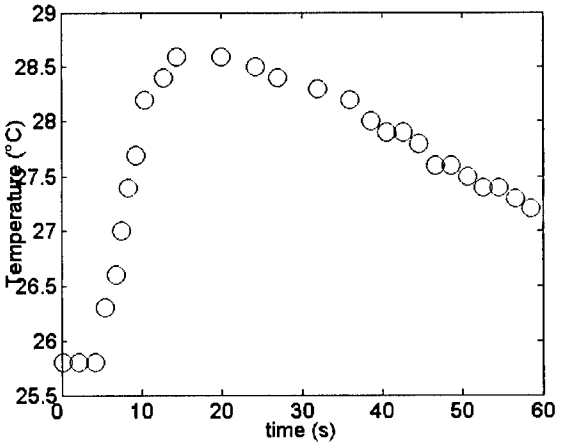

FIGURE 12. Temperature elevation on the skull surface for a 10s insonification at maximum power of the system with a 50% duty cycle. Average overheating was found to be about 2.5° C without any watercooling system.

SUMMARY AND CONCLUSIONS

A 200 elements sparse array was designed and built for brain H.I.F.U. It capabilities in terms of aperture, working frequency, electrical matching and electronic steering were optimized. Each transducer is linked to its own Emission/Reception electronic channel. After correction of skull aberrations using the time-reversal process achieved with an implantable hydrophone, overpressures of about 70 Bars are reached through the particular skull we used in experiment. A large number of *ex-vivo* experiments of H.I.F.U. through the skull bone were finally performed on liver pieces.

The steering capabilities of the system were also demonstrated on several liver samples. Further works will be investigated *in vivo* on 20 sheep.

REFERENCES

1. R.H. Britt, D.W. Pounds, B.B. Lyons, "Feasibility of treating malignant brain tumors with focused ultrasound," *Prog.exp.Tumor Res.*, **28**, 232-245, (1984).
2. G. Clement and K. Hynynen, "Criteria for the Design and Characterization of Large-Area Arrays for Transkull Ultrasound Surgery and Therapy," *IEEE Ultras Symp* (2000).
3. G.T. Clement, J.P. White, and K. Hynynen, "Investigation of a large area phased array for focused ultrasound surgery through the skull," *Phys. Med. Biol.*, **45**, 1071-1083 (2000).
4. J-L. Thomas, M. Fink, "Ultrasonic beam focusing through tissue inhomogeneities with a time reversal mirror: application to transskull therapy," *IEEE Trans. Ultrason., Ferroelect., Freq. Contr.*, **43**, (6), 1122-1129 (1996).
5. M. Tanter, J-L. Thomas, and M. Fink "Focusing and steering through absorbing and aberating layers: Application to ultrasonic propagation through the skull," *J. Acoust. Soc. Am*, **103** (5), 2403-2410 (1998).
6. J. Sun, K. Hynynen, "Focusing of therapeutic ultrasound through a human skull: A numerical study," *J. Acoust. Soc. Am.*, **104** (3), 1705-1715 (1998).
7. J. Sun and K. Hynynen, "The potential of transskull ultrasound therapy and surgery using the maximum available surface area," *J. Acoust. Soc. Am.*, **105**, 2519-2527 (1999).
8. F. Fry and J. Barger, "Acoustical properties of the human skull," *J. Acoust. Soc. Am.*, **63** (5), 1576-1590 (1978).
9. L. Gavrilov and J. Hand, "A theoretical Assesment of the Relative Performance of Spherical Phased Arrays for Ultrasound Surgery," *IEEE Trans. Ultrason., Ferroelect., Freq. Contr*, **47**, (1), 125-137 (2000).
10. S. Goss, L. Frizzell, J. Kouzmanoff, J. Barich and J. Yang, "Sparse Random Ultrasound Phased Array for Focal Surgery," *IEEE Trans. Ultrason., Ferroelect., Freq. Contr*, **43** (6), 1111-1121 (1996).

Theoretical Results For New Cylindrical Ultrasound Phased Array For Prostate Treatment

Leon A. Frizzell, Joseph S. Tan and Gary M. Warren

Bioacoustics Research Laboratory, Department of Electrical and Computer Engineering, University of Illinois, 405 N. Mathews Ave., Urbana, IL 61801

Abstract. Several groups have examined the design of ultrasound phased arrays for transrectal treatment of the prostate. An effective design must utilize the entire aperture of the array and maintain relatively low grating lobe intensities, ideally while minimizing the number of elements and associated phasing circuitry. In this continuation of our studies to design an array that meets these requirements we examined theoretically a new approach to the design of a cylindrical array. Previous designs have subdivided the cylindrical aperture into several columns of elements oriented along the array length, each with the same center-to-center spacing between adjacent elements. Columns of elements are paired, with the same phasing applied to each of the two corresponding elements within a pair, due to symmetry that applies when focus formation and scanning are limited to a plane bisecting the array in the lengthwise direction. Here we report the results obtained for a novel array where the center-to-center spacing is different for different column pairs. This results in a different location for the grating lobes associated with each column pair, which then no longer reinforce each other. When performance was examined by determining the ratio of the peak focal intensity relative to the maximum intensity of unwanted lobes, G, this array design performed much better than previous designs that we have examined. It was possible to achieve values for G that stayed above 7 when steering the focus 15 mm in either depth or lengthwise directions from its unsteered location.

INTRODUCTION

Two diseases of the prostate, benign prostatic hyperplasia (BPH) and prostate cancer (PC), increasingly afflict our aging male population. Benign prostatic hyperplasia is a nonmalignant enlargement of the prostate that may result in difficulty and discomfort during urination. Fifty percent of all men over the age of 55 suffer from prostate enlargement, and histological evidence of BPH is found in almost all men if they live long enough [1]. Due to its prevalence, treatment costs for BPH represent a substantial portion of the total health expenditures in many countries [2].

Occurrence of prostatic cancer is second to skin cancer in men. It is also the second leading cause of cancer death in American men. In the year 2002, it is estimated that there will be 189,000 new cases and 30,200 deaths due to prostate cancer. Current treatment options include surgery, drugs, and radiotherapy. These treatments can be fairly expensive and are associated with a high incidence of impotence and urinary incontinence, as well as the risks associated with surgical procedures [3]. Since none

of these treatment options are ideal, alternative therapies are currently being sought [2,3].

In recent years, there has been a rise in interest in the use of high intensity focused ultrasound (HIFU) for thermal therapy of the prostate [4,5]. It can produce well-defined regions of thermal necrosis within tissue when applied in a minimally invasive manner, without damaging surrounding and overlying tissue. Local prostate cancer can be controlled with low morbidity, and symptomatic relief of BPH can be provided. It has been shown that HIFU does not enhance metastatic spread of cancer, avoids damage to the rectal wall, and treatment can be repeated for recurrent cancers, unlike radiotherapy.

In the treatment of prostatic disease, ultrasound is applied transrectally. This approach minimizes intervening tissue, which allows the use of higher frequencies with a larger absorption coefficient and more efficient heating of the treatment region. Transrectal treatment limits the size of the acoustic aperture that can be used, but the aperture has been shown to be adequate [4,5]. The thermal sink provided by the cooled coupling fluid surrounding the transducer provides protection for the rectal wall.

Current devices used for HIFU treatment of the prostate use a spherically curved transducer with a fixed focal length. With these systems the focal region is scanned to treat a large volume of tissue by mechanical movement of the transducer. While this mechanical scanning has worked quite successfully [4,5], it is necessary to replace the transducer with one of a different focal length in order to vary the treatment depth.

Several groups have investigated the use of phased arrays to decrease the reliance on mechanical scanning of the transducer, reduce the overall treatment time, and eliminate the need to change transducers. Whereas for some HIFU applications sparsely filled arrays of random distributed elements can be used to decrease grating lobe intensities [6,7], that approach is not possible for transrectal probes as virtually the entire aperture must be used. Thus, other approaches have been examined. For example, it has been shown that the peak intensity of unwanted grating lobes in the field could be decreased by random placement of elements with two different widths within the array [8]. This randomization of element sizes interrupts the regular center-to-center spacing between elements, which significantly decreases constructive interference outside of the intended focal region. However, this approach makes array fabrication more difficult and results in output impedance mismatches between elements, which need to be taken into account.

Previously we examined the effect of array geometry on performance. Studies were conducted on spherical segment, cylindrical, and curved cylindrical arrays to determine their ability to steer in depth and along the length of the prostate [9]. In this study we continue our investigation of the design of phased array transducers that will provide steering in both depth and along the length of the prostate. The goal is to design an array that will provide an acceptable acoustic field, with grating lobes that are acceptably low intensity, while minimizing the number of elements in the array. Herein we report a new approach to decreasing the grating lobes while maintaining a reasonable number of elements.

ARRAY CONFIGURATION

The phased array configuration examined in this study was a cylindrical array which was chosen on the basis of simplicity of design (and therefore ease of manufacture) and superior performance when steered in the y direction (see Fig. 1). The focus of the array was scanned in two dimensions, along the prostate (or y direction) and in depth (or the z direction). It is well known that for such an array grating lobes occur primarily at intervals along the y direction and that their positions are directly dependent upon the center-to-center spacing of the transducer elements. The angular position of the first (strongest) grating lobe in the far field of a one-dimensional linear array is given by the inverse sine of the ratio λ/d, where λ is the wavelength and d is the center-to-center spacing of the elements. The actual angular location of the first grating lobe associated with a cylindrical array is slightly different from that for the linear array, but shows a similar dependence upon d and good agreement for $d/\lambda > 3$.

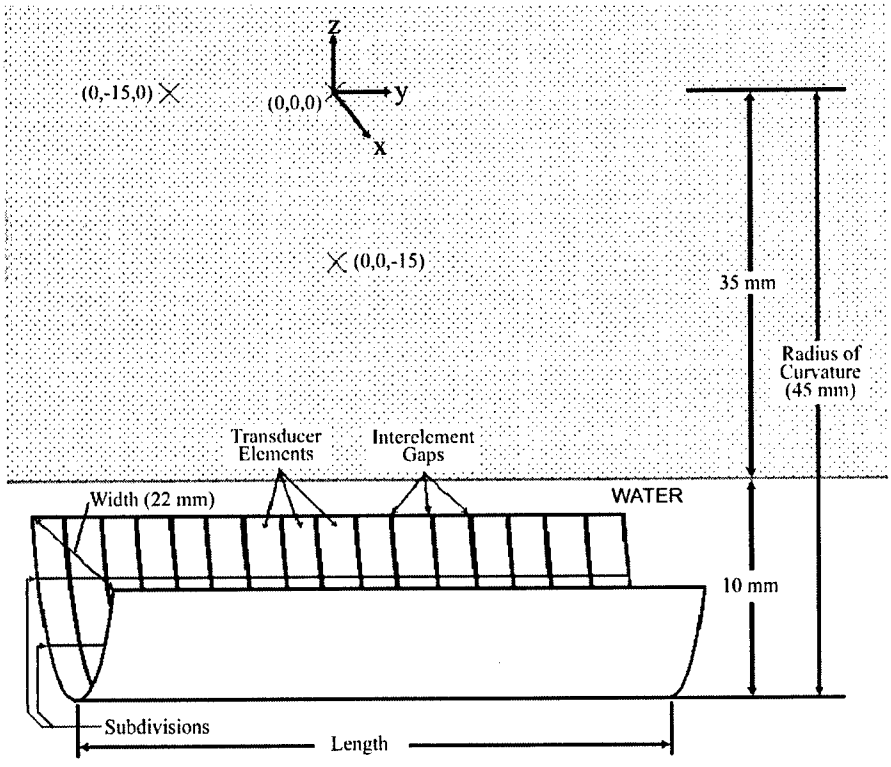

FIGURE 1. Diagram of cylindrical transrectal HIFU applicator, water standoff, tissue, and relevant coordinates.

In order to obtain reasonable grating lobe levels when steering a cylindrical array in the z direction it is necessary to divide the array into several columns of elements [9,10]. These columns are symmetric about a line bisecting the array along its length.

Thus, the array columns can be defined as pairs such that corresponding elements within the pair will each have the same phase for steering and may be connected in parallel to minimize the number of electrical lines in the cable and associated amplifiers. The configuration examined in this study employed a different center-to-center spacing of the elements (a different element width) for each column pair, as shown in Fig. 2. Each element width for this multiwidth cylindrical array applied to a pair of columns symmetrically positioned relative to the y axis, e.g. columns 2A and 2B in Fig. 2. Therefore, each of the paired columns generated grating lobes at different locations in the field. Thus, the array could be designed so that grating lobes produced by different column pairs did not overlap spatially, while the steered foci of each pair of columns still interfered constructively. Note that the column width was adjusted to maintain a constant surface area for all elements and therefore each element exhibits approximately the same impedance.

METHODS

Pressure fields were calculated using the point radiator method [11], which divides the active surface area of the elements into subelements each small enough (one tenth of a wavelength) to produce an acoustic field approximating that of a point source. The total pressure at a given point in the field was calculated as the sum of the complex pressures contributed by each subelement, taking into account the relative phase of the signal applied to the transducer element to which the subelement belongs. Thus the total acoustic pressure at the point (x, y, z) is given by

$$p(x,y,z) \cong j\frac{\rho c k U_0 \Delta A}{2\pi} \sum_{\text{array surface}} \frac{e^{-[\alpha_W R_W + \alpha_T R_T + jk(R_W + R_T)]}}{R_{Tot}} \qquad (1)$$

where the summation is over the entire active surface of the array, ρ is the density and c is the speed of sound of the medium (taken as 1,000 kg/m^3 and 1,500 m/s, respectively, for both water and tissue), k is the acoustic propagation constant (from $k=2\pi/\lambda$, where λ is the wavelength), U_0 is the velocity amplitude of the surface of the source (calculated from $U_0=(2I_0/\rho c)^{1/2}$, where I_0 = 10,000 W/m^2), ΔA is the area of the subelement, α_W is the attenuation coefficient in water (taken as zero), R_W is the distance that the beam traveled through water, α_T is the attenuation coefficient in tissue (taken as 32.24m^{-1}), R_T is the distance that the beam traveled through tissue, and $R_{Tot} = R_W + R_T$ is the total distance that the beam traveled along the straight line from the source subelement to the field point. All simulations were carried out at a frequency of 4 MHz and the spacing between elements was maintained as half a wavelength.

For a given array configuration, the pressure field was calculated for the focus steered to the anticipated extremes of the treatment region, -15 mm in the y (lengthwise) or z (depth) directions, as well as at the geometric center of the array, 45 mm from the array surface which was defined as the origin of the coordinate system, see Fig. 1. Array performance was assessed by first calculating the acoustic

intensity at each field point, using the equation $I = p^2/2\rho c$, and then finding G, the ratio of intensity at the focus, I_{focus}, to the intensity of the largest unwanted lobe, $I_{max,unwanted}$.

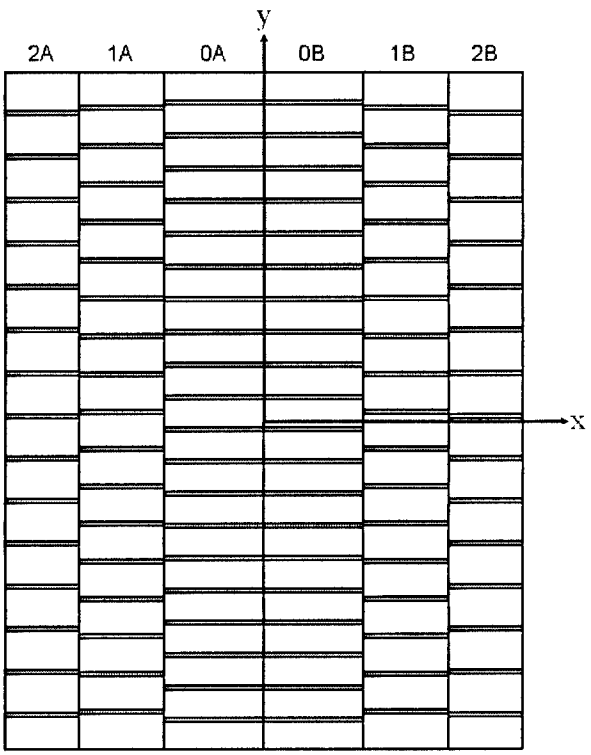

Figure 2. Front face of multiwidth cylindrical transrectal HIFU applicator.

RESULTS

The calculated intensity profile in the y-z plane is shown for two cylindrical transducers with six columns of elements (three column pairs) steered to (0,0,-15) mm, in Fig. 3. The left panel of Figure 3 shows results for an array with a common element width for all columns. This differs significantly from the field shown in the right panel calculated for a multiwidth array (different element width for each of the three column pairs) with the same number of total element pairs. Note that, in contrast to the left panel, the three non-overlapping sets of grating lobes in the right panel have intensities that are very small relative to the focal intensity, and thus are barely visible on the linear scale used.

The performance of several different multiwidth arrays was evaluated by determining the value of G when they were focused at the three positions shown in Fig. 1. The lengths of the arrays examined were 40, 50, and 60 mm, and the number of column pairs was two, three or four. The results consistently showed better performance by a factor of two to three at all three focal positions. When the total

number of element pairs was only 200 it was possible to obtain G values of at least seven.

The shortest arrays seemed to perform best when comparing G versus the total number of element pairs. However, using a sliding subaperture (i.e., a segment of the total array) of a longer array could provide some significant advantages for steering in the y direction. Arrays with two column pairs generally performed best, on a per element basis, at the two focal positions (0,0,0) and (0,-15,0) mm, whereas the four-column-pair arrays performed best with the focus at (0,0,-15) mm. The three-column-pair array appeared to provide the best overall performance when all steering locations were considered.

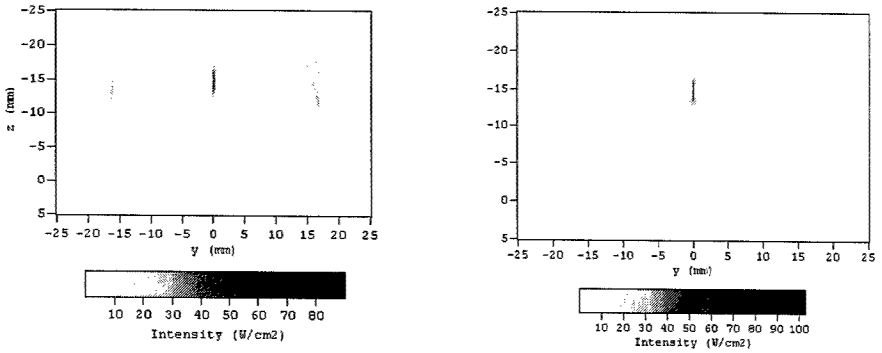

FIGURE 3. Plots of the intensity profile in the z-y plane for a cylindrical array with the same element width for all column pairs (left) and for different element widths (right) for each of the three column pairs.

CONCLUSION

It is apparent that, in all cases, the various multiwidth arrays outperform significantly their single element-width counterparts for a given number of element pairs. The multiwidth array appears to be a promising candidate for HIFU of the prostate.

REFERENCES

1. Grayhack, J.T., Kozlowski, J.M., and Lee, C., *J. Urol.*, **160**, 2375-2380 (1998).
2. De la Rosette, J.M.C.H., D'ancona, F.C.H., and Debruyne, F.M.J., *J. Urol.*, **157**, 430-438 (1997).
3. Parkins, T., *J. Natl. Cancer Inst.*, **86**, 897-898 (1994).
4. Sanghvi, N.T., Foster, R.S., Bihrle, R., Casey, R., Uchida, T., Phillips, M.H., Syrus, J., Zaitsev, A.V., Marich, K.W., and Fry, F.J., *Eur. J. Ultrasound*, **9**, 19-29 (1999).
5. Gelet, A., Chapelon, J.Y., Bouvier, R., Pangaud, C., and Lasne, Y., *J. Urology*, **161**, 156-162 (1999).
6. Frizzell, L.A., Goss, S.A., Kouzmanoff, J.T., and Yang, J.M., *Proc. 1996 IEEE Ultrasonics Sym.*, San Antonio, Texas, Nov. 4-6, 1996, pp. 1319-1323.

7. Goss, S.A., Frizzell, L.A., Kouzmanoff, J.T., Barich, J.M., and Yang, J. M., *IEEE Trans. Ultrason., Ferroelect., Freq. Contr.*, **43**, 1111-1121 (1996).
8. Hutchinson, E.B., Buchanan, M.T., and Hynynen, K., *Med. Phys.*, **23**, 767-776 (1996).
9. Tan, J. S., Frizzell, L. A., Sanghvi, N.T., Seip, R., Wu, J., and Kouzmanoff, J. T., *J. Acoust. Soc. Am.*, **109**, 3055-3064 (2001).
10. Curiel, L., Chavrier, F., Souchon, R., Birer, A. and Chapelon, J. Y., *IEEE Trans. Ultrason., Ferroelect., Freq. Contr.*, **49**, 231-242 (2002).
11. Ocheltree, K.B. and Frizzell, L.A., *IEEE Trans. Ultrason., Ferroelect., Freq. Contr.*, **36**, 242-248 (1989).

Focused Ultrasound Therapy Of The Uterus: A Device For Potential Treatment Of Leiomyoma

Arthur H. Chan[1], Grace Huynh[1], Marla Paun[1], Victor Y. Fujimoto[2], Donald E. Moore[3], and Shahram Vaezy[1]

[1]*Center for Industrial and Medical Ultrasound, Applied Physics Laboratory and Dept. of Bioengineering, University of Washington, Seattle, WA, 98105*
[2]*Department of OB/GYN, University of California, San Francisco, CA, 94117*
[3]*Department of OB/GYN, University of Washington, Seattle, WA, 98105*

Abstract. The objective of this study was to design, manufacture and test a prototype device intended for image-guided high intensity focused ultrasound (HIFU) treatment of uterine fibroids. Tests using tissue mimicking phantom and a sheep model were performed. Ergonomics and imaging capabilities were evaluated in human volunteers. The device consisted of a transvaginal HIFU applicator (3.6 MHz) integrated with an abdominal ultrasound image probe. The applicator used a 25.4 mm diameter transducer affixed to an aluminum lens (fixed focal length 40 mm). The half-pressure maximum focal dimensions were 11 mm by 1.2 mm. A water-filled condom covering the applicator ensured sterility, and provided acoustic coupling, cooling, and controlling of treatment location. Coagulative necrosis lesions (ISATA 1400 - 1700 W/cm2, duration 5 s) formed in tissue mimicking phantom had lengths of 13.3 ± 0.9 mm and widths of 2.5 ± 0.8 mm. Lesions formed in vivo in sheep uterus (ISATA 1000 - 2000 W/cm2, duration 3 - 10 s) appeared as hyperechoic spots on the ultrasound image. Histological analysis showed HIFU disrupted smooth muscle tissue and damaged glandular structure. Testing in six human volunteers (age 23 - 49 years, body mass index 20.4 - 29.9) demonstrated that the device had potential to treat fibroids located in the cervix and mid-uterus (average distance of 22.3 mm and 34.6 mm respectively), and in the fundus within 40 mm. No discomfort was experienced by volunteers. These results show ultrasound image-guided transvaginal HIFU has potential to provide a non-invasive treatment for uterine fibroids.

INTRODUCTION

We report on the *in vitro* and *in vivo* testing of an ultrasound image-guided High Intensity Focused Ultrasound (HIFU) device designed for treating uterine fibroids. HIFU has become a precise, minimally-invasive treatment modality for benign and malignant tumours. Uterine fibroids, or leiomyoma, are benign tumours of the uterus that affect 25% of all women of reproductive age [1-3]. Symptoms may include abnormal bleeding, pelvic pain, and reproductive complications. Fibroids are the most common indication for hysterectomy (removal of the uterus), a procedure not suitable for women who wish to retain reproductive potential. By using HIFU to ablate uterine fibroids, the uterus can be retained. A previous study in our lab has also shown that HIFU was effective in treating uterine leiomyoma in nude mice [4]. Within 3 months

of treatment, tumour reductions of 90% were observed and tumour recurrence (a common result of alternative fibroid treatment methods such as myomectomy and drug therapy [5,6]) after complete treatment was not noticed. A device that combines a transvaginal HIFU applicator and an abdominal image probe has been developed. We hypothesize that this device can potentially be used for precise image-guided treatment of the uterus and describe experiments that lead to the confirmation of this hypothesis.

MATERIALS AND METHODS

Device Overview

The prototype device, depicted in Figure 1 and described in detail elsewhere [7], combined a custom built transvaginal HIFU treatment applicator with a commercially available abdominal ultrasound image probe (the Sonosite C60 4-2 MHz probe was used for the experiments reported in this article). The image probe was aligned such that the focus of the HIFU applicator was in the image plane allowing for visualization of the applicator and focal region. The HIFU applicator, designed to fit inside the vagina, operated at a center frequency of 3.6 MHz, an electrical impedance matched efficiency of 58%, and had an aperture size of 25.4 mm (diameter) and a fixed focal length of 40 mm (F-number = 1.57). The -6 dB focal dimensions measured using a PVDF needle hydrophone (active diameter of 0.5 mm) were 11 mm (axial) by 1.2 mm (lateral). The HIFU applicator was powered using a RF amplifier and the source signal was generated using a waveform generator, which was used to control the frequency, duty cycle and amplitude. Real-time visualization of the HIFU treatment was enabled using a pulse-synchronization method [8], controlled with a notebook computer. The HIFU applicator was operated at a 50% duty cycle. A latex condom was attached to the HIFU applicator and water channels machined into the transducer housing allowed the condom to be filled with degassed water during treatment. This water-filled condom serves three functions: acoustic coupling from the transducer to the site of treatment, a variable stand-off when the amount of water is adjusted, and transducer and treatment area cooling using a custom built water circulation system.

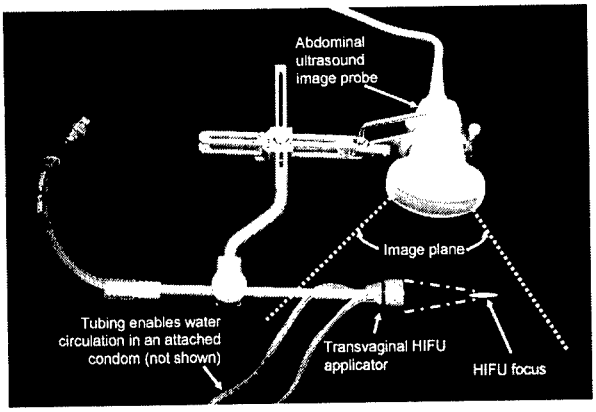

FIGURE 1. The prototype device is shown with the transvaginal HIFU applicator and abdominal ultrasound image probe aligned such that the HIFU focus is within the image plane.

In Vitro Testing

The device was used to perform image-guided HIFU treatment of a tissue mimicking phantom [9]. The optically transparent phantom consisted of polyacrylamide and bovine serum albumin, a thermally indicative protein that causes the phantom to turn opaque upon onset of HIFU treatment. The speed of sound and attenuation of the phantom were 1544 m/s and 0.012 NP/cm/MHz respectively. The device and phantom were suspended in distilled degassed water. Ten treatments of each of the following scenarios were performed: (a) the transducer was directly on the phantom surface, (b) the transducer was 1.2 cm away from the phantom surface separated by a water filled condom, and (c) the transducer was 1.2 cm away from the phantom surface without condom separation. Lesions were produced using 46 W of acoustic power for 5 seconds at 50% duty cycle. This corresponded to focal intensities of 1407 W/cm^2 with the transducer on the surface of the gel and 1587 W/cm^2 with the transducer and gel separated by 1.2 cm of water. Lesion dimensions were measured using digital photographs taken of the phantom immediately after the 5 second treatment.

An experiment was also performed to determine the transducer temperature during a simulated treatment scenario in 37°C water. The thermal data from an internally mounted thermocouple was recorded for a 10-cycle treatment where, in each cycle, HIFU ($I_{SATA} \sim 1900$ W/cm^2) was on for 3 seconds and off for 7 seconds.

In Vivo And Ergonomics Testing

The device was used *in vivo* in a sheep model to examine imaging and lesion forming capabilities, and to study the effects of HIFU treatment on uterus *in situ*. A female sheep, approximately 1 year of age and 85 kg, was used. The animal was sedated intramuscularly with xylazene (0.3 mg/kg) and atropine (1 mL/9 kg), transferred onto an operating table, connected to a ventilator, and placed under anesthesia (isofluorane). The abdominal region of the sheep was shaved to allow ultrasound imaging. The device was placed in the ewe.

HIFU was applied to various areas of the uterus and vaginal canal at focal intensities (I_{SATA}) between 500 and 1400 W/cm^2 at 7 seconds exposure duration per treatment. At the completion of treatment, anesthetic was increased to 5% for 5 minutes and the animal was euthanized using an overdose of Pentasol. A surgical incision was made in the lower abdomen, and the vaginal canal and uterus were removed. Photographs were taken of the treated regions using a digital camera, a qualitative gross macroscopic analysis to determine the appearance of HIFU treated area was performed, and selected sections of treated uterus were placed in a 10% neutral buffered formalin solution for fixation. These sections were sent to the histopathology laboratory for staining with hematoxylin and eosin and mounting on microscope slides. The completed slides were analyzed using bright field light microscopy.

Ergonomics testing was performed in 6 healthy human volunteers ranging in age from 23 - 49 and in body mass index from 20.4 - 29.9. The study involved a transabdominal ultrasound scan with the HIFU applicator inserted in the vagina

(i.e. the device was positioned in the volunteer as if treatment were to be administered). A sterile condom was secured to the HIFU transducer, lubricated, and filled with water prior to insertion into the vagina. Once the HIFU transducer was inside the vagina, the image probe was positioned to visualize pelvic structures and the HIFU transducer. The length and width of the uterus were measured, and the potential treatable region based on a fixed HIFU focal length of 4 cm was determined for various transducer positions. These positions corresponded to how the transducer would be placed for targeting the cervix, the mid-uterus region, and the fundus. A survey was administered at the end of each study to determine comfort of the device during use.

RESULTS AND DISCUSSION

In Vitro Testing

A HIFU lesion produced in the gel phantom and visualized with ultrasound is shown in Figure 2. This image depicts the treatment scenario where the transducer and gel were separated by a distance of 1.2 cm using a water filled condom. The HIFU transducer and the water-filled condom were clearly seen in the ultrasound image.

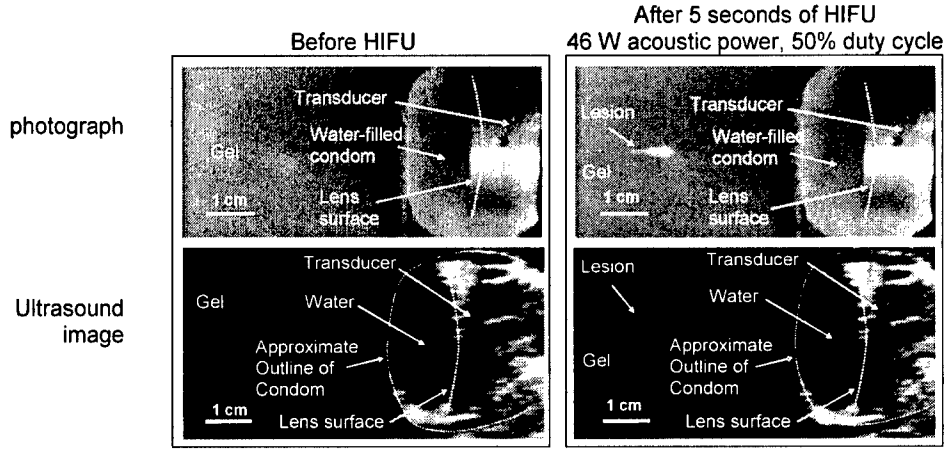

FIGURE 2. Left: a photograph of the optically transparent tissue mimicking phantom and ultrasound image prior to treatment. Right: after treatment, an opaque lesion is shown in the photograph of the phantom and a hyperechoic spot is visible in the ultrasound image.

A lesion is characterized by the white opaque spot in the transparent gel, and the bright hyperechoic spot in the ultrasound image. All lesions were visualized with ultrasound. The measured lesion dimensions for the three treatment scenarios are shown in Table 1. A two-sample two-tailed t-test indicated no statistically significant difference between lesions created with the water filled condom and without ($P<0.05$).

TABLE 1. Lesion dimensions in tissue mimicking phantom.

Treatment Scenario (n=10 for each)	Focal Intensity	Lesion Length	Lesion Width	Ultrasound Visualization
Transducer directly on gel	1407 W/cm^2	11.2 ± 0.8 mm	2.2 ± 0.6 mm	10 / 10
2 cm separation, no condom	1587 W/cm^2	13.5 ± 1.1 mm	2.6 ± 0.7 mm	10 / 10
2 cm separation, with condom	1587 W/cm^2 [a]	13.3 ± 0.9 mm	2.5 ± 0.8 mm	10 / 10

[a] attenuation of the 0.07 mm thin condom (Trojan Brand Non-Lubricated, CWI Carter Products Div., New York, NY) was assumed to be zero.

The measured transducer temperature during the simulated 10 cycle treatment is shown in Figure 3. With 150 mL/min water circulation in the latex membrane, transducer operating temperatures for 10 repeated cycles of 3 seconds HIFU on followed by 7 seconds rest stabilized to 0.6° C within 3 cycles whereas the temperature increase approached 4.5° C without water circulation.

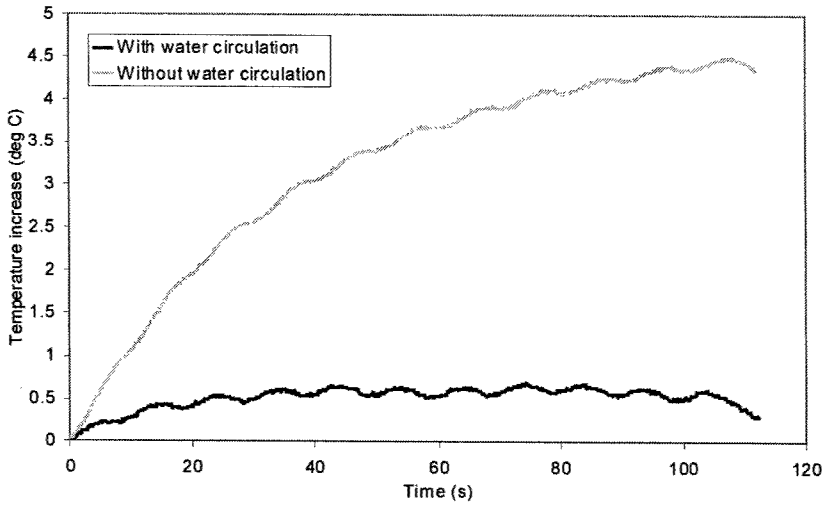

FIGURE 3. Transducer temperature increase for a 10 cycle (3 seconds on, 7 seconds off) treatment was monitored using an internally mounted thermocouple. A 4° C difference in temperature increase was noted when water was circulated within the latex condom. Temperatures also stabilized sooner.

In Vivo And Ergonomics Testing

Macroscopic analysis of the treated areas revealed regions of necrosis surrounded by hemorrhage. The treated areas, exemplified in Figure 4, showed necrotic tissue as blanched tissue, and hemorrhage as dark red borders surrounding the necrosis. It can be seen in the cross section of the treated area that the coagulative necrosis extended through the depth of the tissue layer. Treatment effects appeared to be localized and well demarcated.

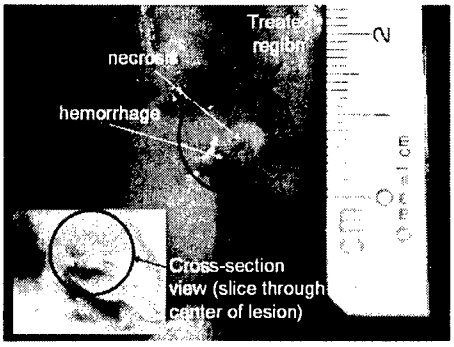

FIGURE 4. A HIFU lesion created in sheep uterus shows characteristics of coagulative necrosis, with a blanched necrosis area surrounded by a dark ring of hemorrhage.

Figure 5a shows a light microscopy image of normal sheep uterus at 10X magnification. This image was taken at the border between the myometrium and the endometrium. The myometrium, or uterine wall, is comprised of densely packed smooth muscle organized in interlacing bundles that are oriented randomly. The endometrium consists of straight, tubular uterine glands. This structural composition is similar to human uterus. Figure 5b and 5c depict areas of HIFU treatment. A well demarcated region of HIFU induced gland shrinkage, glandular wall disruption and resulting fluid leakage, and separation of the glands from surrounding tissue can be seen in Figure 5b. Smooth muscle disruption and separation can be observed in Figure 5c.

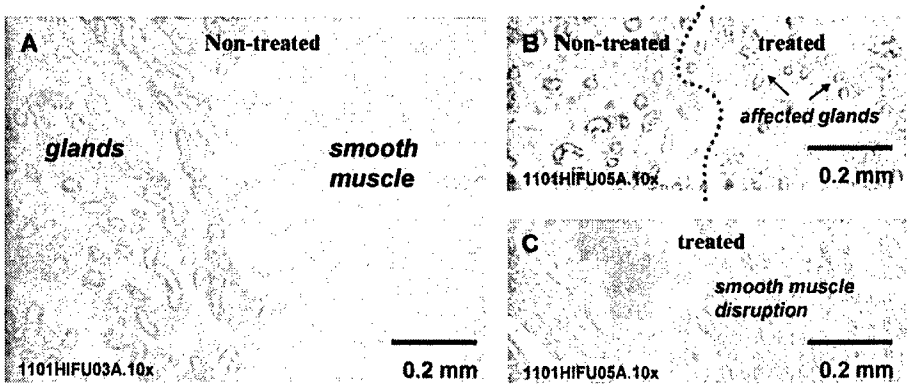

FIGURE 5. Light microscopy analysis of uterus tissue under 10x magnification and H&E staining. A: regular uterus tissue showing smooth muscle bundles and uterine glands. B: shows the differences in glandular structure between a well-demarcated HIFU treated area with non-treated area. C: smooth muscle disruption in myometrium can be seen after treatment.

Placement of the sterilized device in human volunteers demonstrated successful visualization of the HIFU transducer and the uterus. Figure 6 illustrates the device placement and an ultrasound image showing the water filled condom, the applicator and the uterus and bladder. Uteri length ranged between 5.90 and 8.49 cm and width ranged between 3.21 and 4.63 cm, with the exception of a volunteer with a fibroid

located at the fundus whose total uterus length and width including fibroid were 11.7 cm and 8.03 cm, respectively. Figure 7 shows how the transducer can be positioned to target various areas of the uterus. It was determined that if treatment was to be administered, a 4 cm focal length would be sufficient for treating fibroids located in the cervix and mid-uterus of all volunteers (average distance of 2.23 cm and 3.46 cm respectively). According to the survey completed by the volunteers after the study, entrance into the vagina was comfortable if lubrication was used and sufficient water was inside the condom to act as a cushion between the vaginal wall and the HIFU transducer. No discomfort was experienced while the probe was in the vagina and when the probe was removed from the vagina.

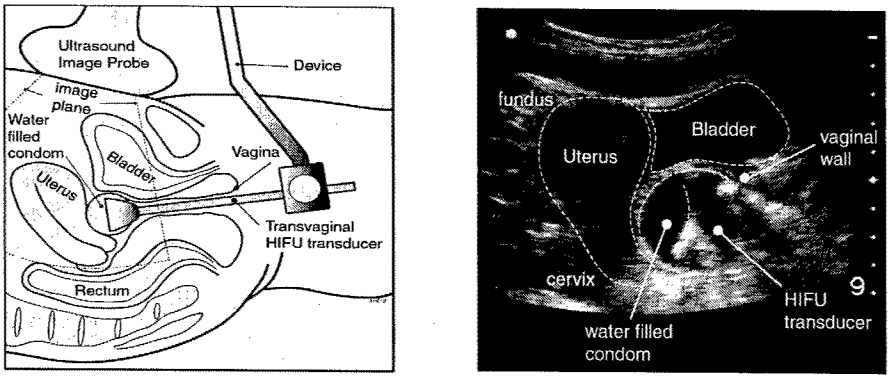

FIGURE 6. Left: Illustration of the device placed in a human. Right: An ultrasound image of the device placed in a human volunteer. The uterus, bladder, and HIFU transducer was visualized.

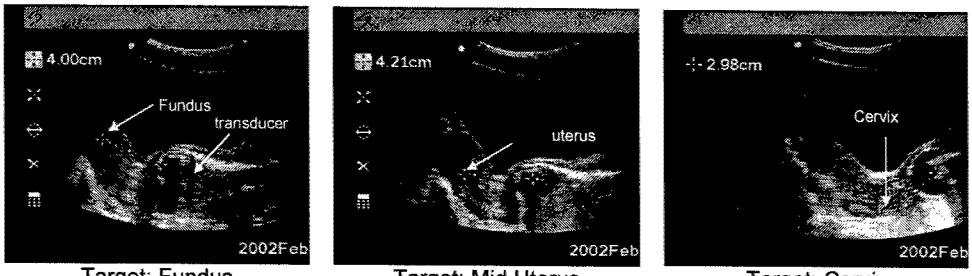

Target: Fundus Target: Mid Uterus Target: Cervix

FIGURE 7. Mobility within the vagina and varying the amount of water in the condom (effectively adjusting the stand-off distance) allowed various parts of the uterus to be treated.

Discussion

The capability of this device to produce repeatable and consistent HIFU lesions has been demonstrated in tissue mimicking phantom and also in a dosimetry experiment using turkey breast tissue (not shown here).[7] Although all lesions were visualized with ultrasound during treatment of the phantom, there appears to be an intensity threshold (approximately 1800 - 2000 W/cm^2) below which the hyperechoic spot does not show up in the ultrasound image. This threshold is hypothesized to be associated

with frequency dependent cavitation and vaporization, resulting in bubble formation at the treatment site. Therefore, there is a possibility that treated tissue may not have been visualized. Nevertheless, relying on the hyperechoic spot for targeting and treatment confirmation is not optimal since treatment will have already taken place once the spot appears on the ultrasound image. A HIFU control system and targeting system, that uses position sensors for tracking the focus and treatment area, is being developed. This system will automate the exposure duration, temperature measurement, targeting and treatment operation, and will be tested *in vivo*.

The *in vivo* studies have shown that this device has the potential to be used for human uterus treatment. We are intending to treat submucosal uterine fibroids, the most symptomatic type of fibroid, as we believe they are candidates for HIFU treatment (generally small and easily accessible using the transvaginal treatment approach). Fibroids may exist that are too large or in hard to access locations (i.e. very close to bowel) rendering HIFU treatment impractical (resulting in the procedure lasting too long or risking damage to surrounding tissue). HIFU may also be used as an adjunct treatment to drug therapy, myomectomy or uterine artery embolisation to ensure complete resection of the fibroid. This device can be used with any commercially available ultrasound machine and is intended for use as an OB/Gyn procedure. Since it was shown that fibroids located in the fundus may exceed the 4 cm focal length for midline uteri, the focal length may need to be increased or a transabdominal approach (combined with transvaginal imaging) may be used for such cases. Prior to clinical testing, this device will undergo efficacy and safety studies in a sheep model. In the future, this device has the potential for other gynecological applications.

CONCLUSION

A prototype ultrasound image-guided HIFU device was tested *in vitro* and *in vivo*. The imaging was performed using an abdominal probe, and the treatment administered using a vaginal HIFU applicator. *In vitro* testing in tissue mimicking phantom, and *in vivo* testing in a sheep model showed consistent lesion formation and uterus treatment potential. Ergonomics testing in humans showed visualization of potential treatment area and HIFU transducer, and demonstrated no discomfort during use. A targeting system is being developed and efficacy and safety studies will be performed using a sheep model. We believe that ultrasound image-guided transvaginal HIFU has potential to provide a non-invasive treatment for uterine fibroids.

ACKNOWLEDGMENTS

This project was funded by the Whitaker Foundation, the National Institutes of Health, NSERC of Canada, and the Royalty Research Fund at the University of Washington. The authors wish to thank Dr. Emil Chi, Dr. Lawrence Crum, Dr. Peter Kaczkowski, Dr. Roy Martin, Francis Olson, Andrew Proctor, and Rusty Starr for their assistance.

REFERENCES

1. N.F. Chavez and E.A. Stewart, "Medical treatment of uterine fibroids," *Clin Obstet Gynecol,* **44** (2), 372-84 (2001).
2. R.A. Nowak, "Fibroids: pathophysiology and current medical treatment, " *Baillieres Best Pract Res Clin Obstet Gynaecol*, **13** (2), 223-38 (1999).
3. E.A. Stewart, "Uterine fibroids, " *Lancet,* **357** (9252), 293-8 (2001).
4. S. Vaezy, V.Y. Fujimoto, C. Walker et al., "Treatment of uterine fibroid tumors in a nude mouse model using high- intensity focused ultrasound, " *Am J Obstet Gynecol,* **183** (1), 6-11 (2000).
5. M. Filicori, D.A. Hall, J.S. Loughlin et al., "A conservative approach to the management of uterine leiomyoma: pituitary desensitization by a luteinizing hormone-releasing hormone analogue, " *Am J Obstet Gynecol*, **147** (6), 726-7 (1983).
6. L. Fedele, F. Parazzini, L. Luchini et al., "Recurrence of fibroids after myomectomy: a transvaginal ultrasonographic study," *Hum Reprod,* **10** (7), 1795-6 (1995).
7. A.H. Chan, V.Y. Fujimoto, D.E. Moore et al., "An image-guided high intensity focused ultrasound device for uterine fibroids treatment, " Accepted for publication in *Med Phys*., (2002).
8. S. Vaezy, X. Shi, R.W. Martin et al., "Real-time visualization of high-intensity focused ultrasound treatment using ultrasound imaging, " *Ultrasound Med Biol*, **27** (1), 33-42 (2001).
9. C Lafon, P. Kaczkowski, S. Vaezy et al., "Development and characterization of an innovative synthetic tissue-mimicking material for high intensity focused ultrasound (HIFU) exposures, " presented at the International Congress on Acoustics, Rome, Italy, 2001 (unpublished).

Mechanisms Of Lesion Formation In High Intensity Focused Ultrasound Therapy

*Wen-Shiang Chen, †Cyril Lafon, *Thomas J. Matula, *Shahram Vaezy, *Andrew A. Brayman and *Lawrence A. Crum

*Center for Industrial and Medical Ultrasound, Applied Physics Laboratory, University of Washington, Seattle WA 98105, USA
†INSERM Unité 556 151, Cours Albert Thomas, 69003 Lyon, France

Abstract. Lesions generated by 1.1- or 3.5-MHz high-intensity focused ultrasound (HIFU) were studied in tissue phantoms with/without pre-mixed ultrasound contrast agent (UCA). At 1.1 MHz and without UCA, small bubble generation preceded cigar-shaped thermal lesion formation, but lesion origins were independent of these bubbles. After further exposure, boiling occurred, and resulted in a loss of lesion symmetry and tadpole-shaped growth toward the transducer. At 3.5 MHz and without UCA, bubble generation did not precede lesion formation, but onset of boiling was followed by loss of lesion symmetry. Absent UCA, passive cavitation detection results did not indicate inertial cavitation (IC) occurrence at either HIFU frequency. UCA inclusion in the phantoms delayed lesion formation at both frequencies, and produced larger lesions than in gels lacking UCA. Broadband noise emissions indicative of IC were detected in phantoms with UCA exposed to 1.1 MHz HIFU. The broadband emission extinguished in seconds, while lesion growth continued for tens of seconds. Broadband emission was not detected in phantoms without UCA exposed at 3.5 MHz. The presence of UCA resulted in pronounced lesion distortion at 1.1 MHz, with almost all of the lesion volume in the pre-focal region. With UCA and 3.5 MHz HIFU, lesion morphology remained approximately cigar-shaped. These results indicate that while gas bodies can alter thermal deposition patterns and thus affect HIFU lesion morphology, the primary determinant of asymmetric lesion growth in phantoms without UCA is the occurrence of boiling. Inclusion of UCA can induce lesions to form in the pre-focal region of the HIFU field, and enlarge the size of lesion at equivalent exposure duration. Better control of lesion formation and placement might be achieved by selection of exposure parameters that do not result in tissue boiling.

INTRODUCTION

The minimally invasive nature of the high-intensity focused ultrasound (HIFU) has been a focus of different therapeutic applications in recent years, especially tumor ablation [1-7]. However, in some cases the lesions were not formed as expected, either in shape, or in location relative to the geometric focus [8,9]. Theoretically, for a pure thermal process, the lesion should be cigar-shaped (fusiform) and should form around the transducer focus. This shape corresponds to the focal area (full-width, half intensity) and thus the area of highest thermal deposition. The unexpected experimental observations cannot be explained sufficiently either by nonlinear wave propagation, or by the changes in acoustic properties of a denaturing tissue. The

presence of bubbles was proposed to be the main mechanism [9-11]. However, it is not clear whether these bubbles are generated by inertial cavitation (IC) or boiling.

TABLE 1. The composition of a 40 ml tissue phantom.

BSA (Bovine Serum Albumin)	2.8 g (7 % w/w)
Distilled water	28.644 ml
40% v/v Acrylamide	7 ml
1M TRIS (Trishydroxymethyl Ammoniomethane), pH=8	4 ml
10% w/v APS (Ammonium Persulfate)	0.336 ml
TEMED ((N,N,N,N -Tetramethyl-Ethylenediamine))	0.02 ml
Sonazoid contrast agent (if added)	5 µl/350 ml (about 20 bubbles/mm^3)

Recently, a transparent tissue-mimicking phantom was developed in our laboratory that provides two unique benefits: (1) real-time visualization of the HIFU-induced lesions; and (2) adjustable attenuation by varying the protein concentration [12]. This special phantom gives us a chance to understand the detailed mechanism of the lesion formation process in HIFU therapy. Therefore, our goals in this study are: (1) to observe in real time the HIFU lesion-formation process at different intensity levels; (2) to study the mechanism of the 'tadpole-shaped' (pyriform) lesion transformation; (3) to evaluate the role of IC and tissue boiling in the lesion formation process; and (4) to investigate the changes of lesion size and mechanism of lesion formation after the addition of ultrasound contrast agent (UCA).

METHODS

Tissue Phantom

The phantom used in this study was based on a polyacrylamide gel mixed with Bovine Serum Albumin (BSA), a protein used as a temperature-sensitive indicator. Detailed components are as listed in Table 1. Since the phantom is transparent at 7% BSA, HIFU-induced denaturation could be easily observed and highly contrasted. The attenuation of this material can be adjusted with changing the BSA concentration. In the current study, 7% BSA was used, yielding an acoustic attenuation of 0.017 Np/cm/MHz. The sound speed and the density, which are independent of the protein concentration, are 1544 m/s and 1044 kg/m^3, respectively [12].

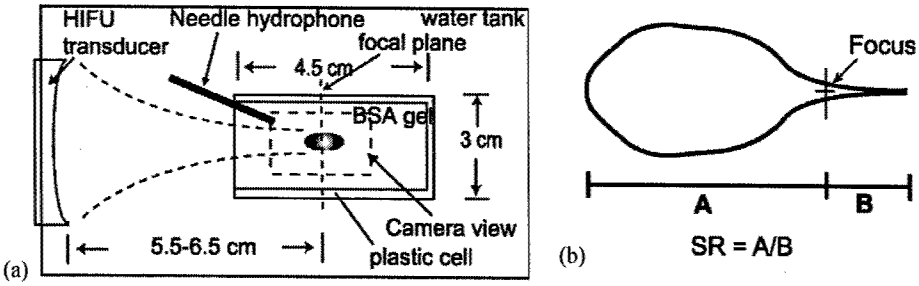

FIGURE 1. Experimental setup and definition of SR. (a) Experiment setup of the exposure tank; (b) definition of symmetry ratio (SR), where A and B are lesion lengths proximal and distal to the focus.

The mixture of all the necessary components was poured into a 30-ml plastic cell, sealed with a parafilm membrane, and agitated gently for 30 min. Afterwards, the cell (with the parafilm membrane removed) was mounted on a positioning system (Velmex, Bloomfield NY) and immersed in a water-filled tank (Fig. 1a).

Experimental Setup

Ultrasound energy was delivered through the front opening of the cell by either a 1.1 MHz (f = 1.0, focal diameter = 1.43 mm) or a 3.5 MHz (f = 1.6, focal diameter = 1.00 mm) high-intensity focused ultrasound (HIFU) transducer (Sonic Concepts, Woodinville, WA) operating in continuous wave (CW) mode. The total exposure time was 90 s. Compared with other HIFU studies [8;10;13;14], longer exposure durations, but lower intensities were used, because we planned to observe the response of the gel phantom at different stages of exposure. The focus of the HIFU transducer was set at the center of the sample cell. A PVDF needle hydrophone, used as a passive cavitation detector (PCD), was inserted into the phantom through the front opening at ~ 30° to the axis of the HIFU transducer (Fig. 1a). Gel phantoms with and without Sonazoid UCA were exposed to pre-selected pressure levels ranging from 3 to 5.2 MPa (SATA Intensity: ~1400 to 2000 W/cm^2). The concentration of the UCA was about 20 bubbles/mm^3. The lesion formation process was recorded in real time by a CCD camera and a VCR. The recorded images were digitized and processed by programs written in Matlab (MathWorks, Natick, MA). To quantify the shape transformation of lesions, the symmetry ratio (SR) measurement was used, which was defined as the length of the lesion in front of the focus, divided by the length behind (Fig. 1b).

Experimental Series

Two series of experiments were performed. In Series 1, no Sonazoid was pre-mixed with the phantom. Each phantom was exposed to a pre-selected pressure level for 90 s at either 1.1 or 3.5 MHz. After the completion of the ultrasound treatment, the used phantom was replaced by a new one, and exposed to a higher pressure level. A total of 4 to 5 pressure levels ranging between 3 and 5.2 MPa were tested for each frequency. The lesion development was recorded by a CCD camera for off-line analysis as described earlier.

In Series 2, a fixed concentration of Sonazoid microbubbles (20 bubbles/mm^3) was mixed with the gel phantom before polymerization was completed. Gentle hand rotation was performed for 30 min to ensure a uniform distribution of bubbles inside the gel. The adequate concentration of Sonazoid microbubbles was determined by several pilot studies. Briefly, high concentrations of Sonazoid caused the lesions to form totally on surface of the gel phantom, while very low concentrations of Sonazoid produced the same lesion as in phantoms without UCA. Cavitation detection using PCD was performed in both series of experiments.

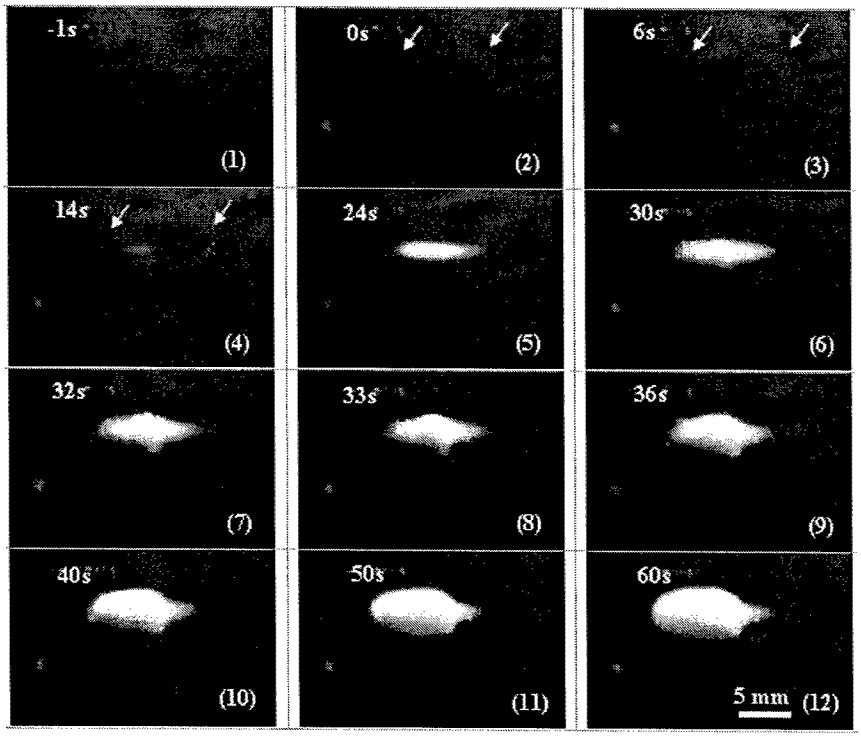

FIGURE 2. Formation of a tadpole-shaped lesion by 1.1 MHz HIFU at P- pressure = 5.2 MPa. No UCA was added. Details are described in the text. The white arrows in frames 2 to 4 are the white reflective dots described in the text.

RESULTS

Series 1: Phantoms Without Sonazoid

The series of photos in Figs. 2 and 3 show the real-time formation of HIFU lesions at HIFU frequencies of 1.1 and 3.5 MHz, respectively. The HIFU transducer (not shown) was located on the left side of these photos. The occurrence of HIFU exposure is indicated by an LED in the lower left corner. The elapsed time is displayed on the upper left corner. Time zero is the beginning of the HIFU exposure.

In this first set of experiments, no UCA was added to the phantoms. In Fig. 2, no bubble or lesion was seen before the HIFU exposure (frame 1). Small white reflective dots were observed immediately after switching on the HIFU transducer operating at 1.1 MHz in CW mode (frames 2 and 3). These dots were primarily found in the path of the acoustic wave, but not necessarily at the focus (white arrows in frames 2, 3 and 4). The cigar-shaped thermal lesion was not formed until the 14^{th} s of exposure. The lesion was formed at the focus and extended its length bidirectionally, *i.e.*, toward and away from the HIFU transducer (frames 4 and 5). Some white dots were later merged with the growing lesion, but the lesion did not originate from the white dots. The first

trace of the boiling-like phenomenon was found at the 30th s of exposure (frame 6). Rapid increases in lesion size and tadpole-shape transformation were observed after the onset of the boiling-like phenomenon (frames 9 to 12), after which the lesion was developed primarily in front of the focus. PCD failed to detect any broadband noise during the entire exposure, including the stage of the boiling-like activity.

The upper margin of all photos in Fig. 3 shows a well developed cigar-shaped thermal lesion produced at a lower pressure level (3.2 MPa) at 3.5 MHz. The new lesion at a higher pressure level (3.8 MPa) was formed in a lower location of the phantom. Unlike the situation at 1.1 MHz, no white reflective dots were seen in the phantom at 3.5 MHz (frame 2, 0 s). However, the thermal lesion formed much faster than did the one at 1.1 MHz (frame 3, 1 s). The white arrow at the first second of the HIFU exposure shows the first trace of the cigar-shaped thermal lesion. Similar to the 1.1 MHz condition, the lesions changed from cigar to tadpole-shape soon after vigorous boiling-like activity (frame 5). A sequence of events, most likely related to boiling, but less vigorous than the boiling-like activity at 1.1MHz, forced the lesion to move toward the transducer rapidly (frames 5 to 9). The tadpole-shaped lesion was then formed.

Figure 4a shows the effect of pressure on the lesion-formation process at 1.1 MHz. Results of measurements at three pressure levels (4.5, 4.8, and 5.2 MPa) are shown. Boiling-like phenomena were seen both at 4.8 and 5.2, but not at 4.5 MPa. The lesion size (in pixels) increased gradually with increasing exposure duration. The slope of the lesion area *vs.* time curve was not altered when the vigorous boiling-like activity occurred at ~ 38th s (5.3 MPa) and ~ 82nd s (4.8 MPa). Higher pressure levels generated larger lesions. However, for the same pressure levels, the symmetry ratio

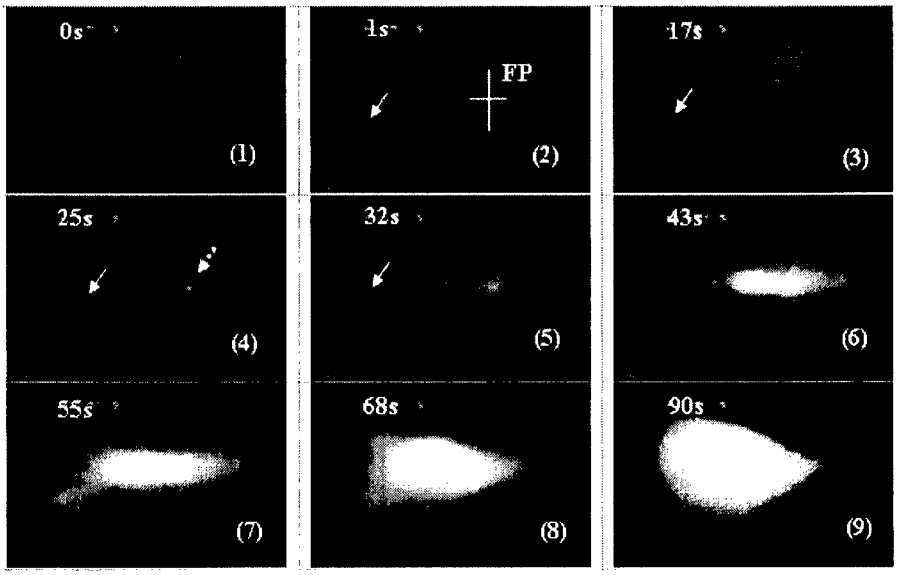

FIGURE 3. Lesion formed in phantom containing Sonazoid and exposed to 1.1 MHz HIFU at P- = 4.8 MPa. Details are described in the text. White arrows: areas of numerous small white dots; dashed arrows: starting point of lesion formation; FP: focal point.

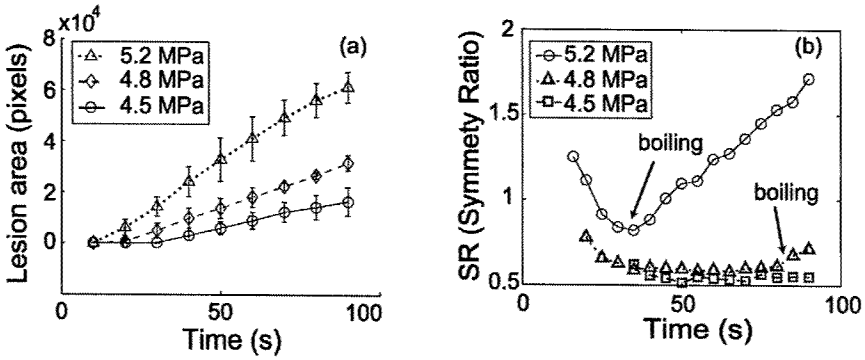

FIGURE 5. Lesion growth and transformation. (a) The changes of lesion size at 3 pressures are shown as a function of exposure time at 1.1 MHz; (b) The changes of SR for 3 selected pressure levels are shown as a function of exposure time.

(SR) of the formed lesion increased after the occurrence of the boiling-like activity (Fig. 4b). At 5.2 and 4.8 MPa, boiling-like activity and SR increase occurred after the 38th and 82nd s of exposure, respectively.

Series 2: Phantoms With Sonazoid

The lesion-formation process in phantoms containing UCA was substantially different from that in phantoms without UCA. Immediately upon switching on the HIFU transducer, numerous small white dots were observed between the focal plane

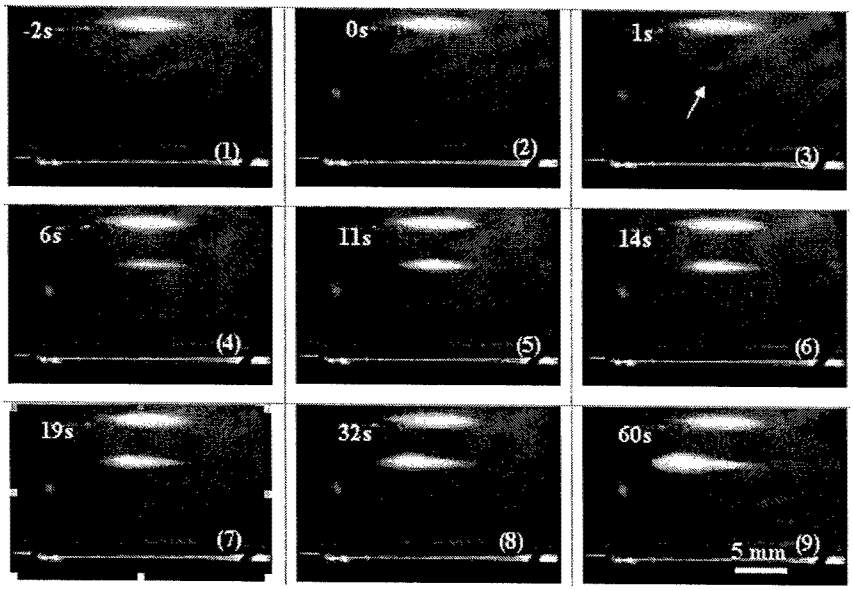

FIGURE 4. Formation of a tadpole-shaped lesion by 3.5 MHz HIFUat P- pressure = 3.8 MPa. No UCA was added. Details are described in the text. White arrow in frame 3: first trace of the thermal lesion. The symmetric lesion near the upper margin of each subplot is a cigar-shaped thermal lesion formed at P- pressure = 3.2 MPa.

and the front surface of the phantom (Fig. 5, solid arrows, frames 2, 3, and 4). Unlike the phantoms without UCA, the lesion origin seemed to be related to the enhanced heating of those small white dots, and started at a position near the focus (frames 4 and 5, dashed arrows). Although the final lesions formed in gel with UCA at 90 s looked tadpole-shaped, they didn't experience the boiling-like activity and shape transformation process. They are probably reflecting the beam profile of the transducer itself. The boiling-like activity was not seen at either frequency, but the final lesion sizes increased substantially (Fig. 6); phantoms with UCA created larger lesions at equivalent pressure and exposure duration.

At 3.5 MHz, the lesion started as a long lesion near the focus, and extended simultaneously and rapidly both toward and away from the transducer (Fig. 7). Unlike the experience of the phantom with UCA at 1.1 MHz, no visible 'white dots' occurred throughout the whole exposure period. The first trace of the thermal lesion was not seen until the 12^{th} second. For a phantom without UCA, the lesion was formed at the first second of exposure at equivalent pressures. The lesion formed in the phantom with UCA at 3.5 MHz was generally a long slender lesion without the occurrence of visible boiling-like activity. The final volume of the lesion (frame 9, Fig. 7) was also larger than the lesion formed in a phantom at an equivalent pressure level but without the addition of UCA (Fig. 6c, d).

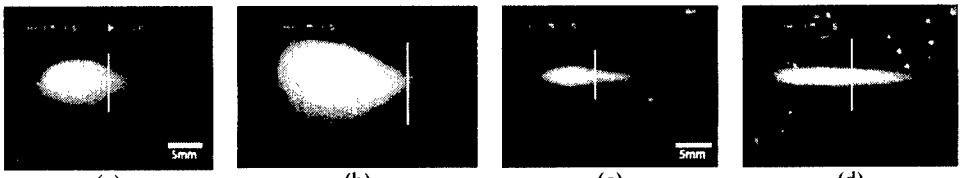

FIGURE 6. Phantoms with UCA created larger lesions. Lesions formed for phantoms without UCA (a, c) and with UCA (b, d), at 1.1 (a, b) and 3.5 MHz (c, d). The peak negative pressures for all four experiments were 4.8 MPa, while the exposure durations were 90 s. The white vertical lines indicate the focal plane. Scale bar: 5 mm. All photos are in the same scale.

For phantoms without UCA, broadband noise was not detected during the entire exposure period for either frequency, including the vigorous boiling-like stage. Broadband noise was also not observed in the first few seconds of the PCD recording in phantoms without UCA (Fig. 8a), although the creation of a few small 'white dots' was observed at 1.1 MHz. It is uncertain if the lack of an IC signature was due to sensitivity issues (too few bubbles created by IC) or the mechanism reason, *i.e.*, 'white dots' were not bubbles or were bubbles but created by mechanisms other than IC.

For the phantoms with UCA, besides the fundamental frequency (1.1 MHz), harmonics, subharmonics, and typical broadband noise from approximately 2 to 6 MHz were recorded (Fig. 8b). The broadband noise occurred in the first few seconds and died out fast (Fig. 8c), while the lesion kept enlarging over the entire exposure period. Intermittent bursts of activity were observed occasionally (solid arrow). In phantoms with or without UCA at 3.5 MHz, there was no broadband noise during the entire exposure period.

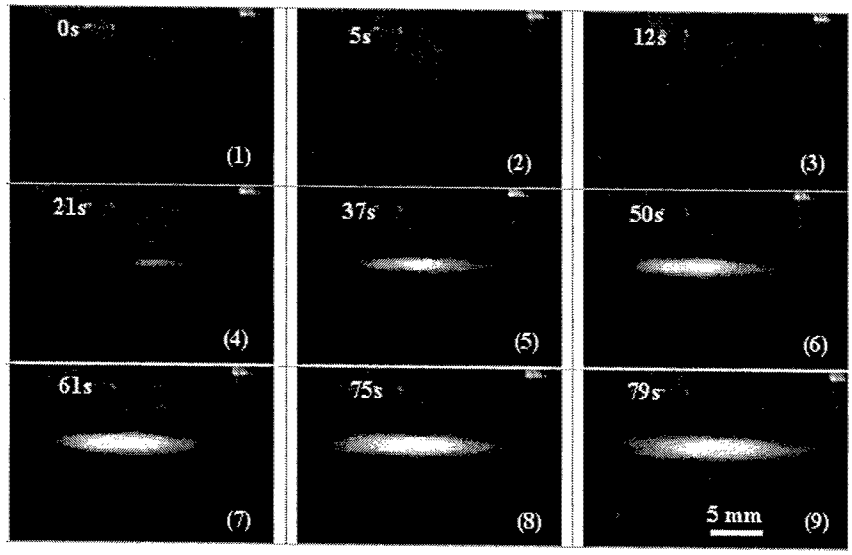

FIGURE 7. A lesion formed in a phantom containing Sonazoid and exposed to 3.5 MHz HIFU at P- = 4.2 MPa. Details are described in the text.

Examples of the final lesion formed at both frequencies for phantoms with or without UCA are shown in Fig. 6. Lesions formed in phantoms with UCA were larger than in those without UCA.

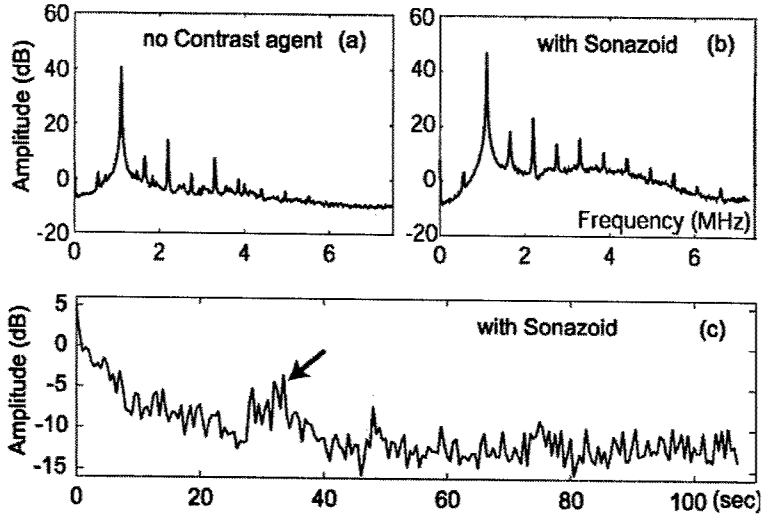

FIGURE 8. Broadband noise recorded in phantoms with or without UCA. The frequency spectra of the recorded signals at 1.1 MHz are shown: (a) first 2 s in phantom without UCA; (b) first 2 s in phantom with UCA; and (c) peak amplitude of the broadband noise (between 2nd and 3rd harmonics) over the entire exposure period. Solid arrow: intermittent burst of the broadband noise after the continuous stage.

DISCUSSION

Two possible sources of bubbles could be used to explain the tadpole-shaped lesion formation during HIFU therapy. First, bubbles may already exist *in situ* or be generated by IC from existing nuclei [14]. Chavrier's simulation estimated that at 2.25 MHz and an intensity level of 4300 W/cm^2, tadpole-shaped lesions will be generated when the concentration of micrometer-sized bubbles is greater than 500 bubbles/mm^3 [10]. In our phantoms with UCA at a concentration of 20 bubbles/mm^3, the existing UCA was apparently already enough to impede the sound transmission and force the lesion to form with a maximal heating area several centimeters in front of the focus at 1.1 MHz. In phantoms without UCA, one would expect that a high concentration of bubbles should be nucleated and concentrated at the focal area only. However, no broadband noise was detected at the onset of lesion formation or trans-formation. Note also that degassing agar gel fails to change the pressure threshold of enhanced heating [14]. The second possibility assumes that the bubbles are created from tissue boiling at the focus. In our observations, pressure-dependent IC did occur at the beginning of some exposures and created bubbles. Those bubbles undergoing IC could deposit enough heat [14] to denature the surrounding albumin and turn it white ('white dots'). However, the subsequent lesion formation did not originate from these 'white dots'. Cigar-shaped lesions started near the geometric focus. Also, boiling-like activity and lesion transformation occurred much later than the generation of white dots, and was therefore considered to be a separate process (Fig. 2 and 3).

We believe that the boiling activity occurred before the lesion transformation. Several reasons lead us to this conclusion. First, the creation of a millimeter-sized bubble was observed during the stage of boiling-like activity, which was not typical for the tiny IC-generated bubbles (on the order of a few microns or submicrons). Second, PCD recordings during the stage of vigorous boiling-like activity revealed no evidence of IC activity (broadband noise) in Fig. 2 (frame 6) and 11th s in Fig. 3 (frame 5). Third, the delayed onset of the boiling-like activity further suggested that thermal deposition, rather than nucleation (bubble generation from existing nuclei by IC), was responsible for the vigorous bubble creation. Nucleation is a pressure-dependent process that should occur whenever the threshold pressure is met and adequately sized nuclei are present; that is, in the beginning of the HIFU exposures in our experiments. Furthermore, a delay of 30 s and the 'explosive' creation of bubbles resist explanation by either IC or rectified diffusion [15-17].

Similar white dots were observed in greater number during the initial few seconds of exposure in phantoms with UCA at 1.1MHz (Fig. 5), when broadband noise was detected. At 3.5 MHz, elongated fusiform lesions were formed in phantoms with UCA, and started later compared with phantoms without UCA at equivalent pressure. The delay was caused by diminished acoustic energy arriving at the focus. This was due to the scattering effect of the existing UCA microbubbles. Insufficient bubbles, if any, were generated by IC to effectively block the sound transmission and induce tadpole-shape transformation at this frequency (3.5 MHz). At both tested frequencies, the final size of the lesions for phantoms with UCA at equivalent acoustic pressure and exposure duration was larger than in those without UCA (Fig. 6). The enhanced

heating of the existing UCA bubbles or their derivatives (fragments, free IC-generated bubbles, *etc.*) might be the major mechanism of the lesion enlargement.

Attempts have been made to use UCA to enhance the lesion-formation process. Tran *et al.* introduced UCA to the target tissue, and showed the reduction of the threshold intensity for lesion formation and the requisite duration of HIFU therapy [18]. In our study with 1.1 MHz HIFU and UCA, the maximally-heated area of the final lesion located centimeters away from the focus, which might produce unacceptable damage to intervening structures.

Lesion formation during HIFU therapy is a complicated process that involves both thermal and cavitation effects. The initial lesion is formed thermally. Boiling of the tissue causes lesion shape transformation and asymmetric advancement. In phantoms premixed with UCA, the enhanced heating from the bubble fragments or the IC-generated bubbles is the dominant mechanism for lesion formation, especially at low frequency.

REFERENCES

1. Daum, D.R., Smith, N.B., King, R., and Hynynen, K., *Ultrasound Med. Biol.*, **25**, 1087-1098 (1999).
2. Chapelon, J.Y., Ribault, M., Vernier, F., Souchon, R., and Gelet, A., *Eur. J. Ultrasound*, **9**, 31-38 (1999).
3. Sanghvi, N.T., Foster, R.S., Bihrle, R., Casey, R., Uchida, T., Phillips, M.H., Syrus, J., Zaitsev, A.V., Marich, K.W., and Fry, F.J., *Eur. J. Ultrasound*, **9**, 19-29 (1999).
4. Wu, F., Chen, W.Z., Bai, J., Zou, J.Z., Wang, Z.L., Zhu, H., and Wang, Z.B., *Ultrasound Med. Biol.*, **27**, 1099-1106 (2001).
5. ter Haar, G.R., *Echocardiography*, **18**, 317-322 (2001).
6. He, S.X., Xiong, L.L., Yao, S.S., Yu, J.S., Lan, J.M.X., He, C.J., Shan, S.S., Zeng, J.Q., Zang, Y., and Du, R.U., *Chinese Med. J.*, **114** (2001).
7. Vaezy, S., Shi, X., Martin, R.W., Chi, E., Nelson, P.I., Bailey, M.R., and Crum, L.A., *Ultrasound Med. Biol.*, **27**, 33-42 (2001).
8. Watkin, N.A., ter Haar, G.R., and Rivens, I., *Ultrasound Med. Biol.*, **22**, 483-491 (1996).
9. Bailey, M.R., Couret, L.N., Sapozhnikov, O.A., Khokhlova, V.A., ter Haar, G., Vaezy, S., Shi, X., Martin, R., and Crum, L.A., *Ultrasound Med. Biol.*, **27**, 695-708 (2001).
10. Chavrier, F., Chapelon, J.Y., Gelet, A., and Cathignol, D., *J. Acoust. Soc. Am.*, **108**, 432-440 (2000).
11. Meaney, P.M., Cahill, M.D., and ter Haar, G.R., *Ultrasound Med. Biol.*, **26**, 441-450 (2000).
12. Lafon, C., Vaezy, S., Noble, M., Kaczkowski, P.J., Martin, R., and Crum, L.A., *2001 Proc. IEEE Ultrason. Symp.*, **2**, 1295-1298 (2002).
13. Clarke, R.L. and ter Haar, G.R., *Ultrasound Med. Biol.*, **23**, 299-306 (1997).
14. Holt, R.G. and Roy, R.A., *Ultrasound Med. Biol.*, **27**, 1399-1412 (2001).
15. Church, C.C., *J. Acoust. Soc. Am.*, **83**, 2210-2217 (1988).
16. Crum, L.A. and Hansen, G.M., *Phys. Med. Biol.*, **27**, 413-417 (1982).
17. Lewin, P.A. and Bjorno, L., *J. Acoust. Soc. Am.*, **69**, 846-852 (1981).
18. Tran, B.C., Seo, J., Fowlkes, J.B., and Cain, C.A., *2001 Proc. IEEE Ultrason. Symp.*, **2**, 1389-1392 (2002).

Ultrasonic Attenuation Of Necrotic Soft Tissues

Christakis Damianou

Frederick Institute of Technology (FIT)
18, Mariou Agathangelou, 3080, Limassol, Cyprus

Abstract. Absorption of soft tissues is the main ultrasonic parameter that affects the size and shape of necrosis during the application of High Intensity Focused Ultrasound. Absorption is the major contributor to attenuation, and therefore attenuation can be a good indicator of the thermal effects of Ultrasound.

The main goal was to measure the attenuation at body temperature and at the state where tissue is necrosed. The attenuation of muscle, kidney, brain, liver, fat, and prostate was measured. All tissues were extracted from adult pigs. The thermal dose of 1000 mins referenced at 43° C was used to necrose the tissues, which is above the threshold of necrosis of all six tissues under investigation. Attenuation was measured using 2 low-intensity transducers operating at 4 MHz. Attenuation of a specific tissue was measured at body temperature and after it was heated by circulating warm water above the threshold of necrosis, it was measured again.

In all six tissues the attenuation for a necrotic tissue was much higher that the attenuation before necrosis. The attenuation of necrotic tissue in fat was 1.8 times bigger than the attenuation before necrosis, whereas the corresponding figure for muscle was 2.5. The other tissues exhibit an intermediate behavior. The main conclusion of this study is that necrotic tissue attenuation is about two times bigger than the value at body temperature.

INTRODUCTION

The main goal of this study was to measure the attenuation of a soft tissue at body temperature and then at the state where tissue is necrosed. The attenuation of muscle, kidney, brain, liver, fat, and prostate was measured. Extensive search revealed that a lot of research is underway for the above tissues in the area of HIFU (High Intensity Focused Ultrasound). Representative studies are given as a reference for the reader: liver [1-2], prostate [3-5], kidney [6-7], brain [8-10], muscle [11], and fat [12]. The research on muscle and fat is justified because these two tissues usually surround other vital organs (for example liver, kidney) which are of ultrasonic importance.

The current study is a continuation of a previous study [13] that also explored the effect of thermal dose on attenuation. In that study attenuation was measured in dog liver, kidney and muscle, over a broad range of thermal dose. This paper is simplistic in the sense that attenuation is measured at body temperature (thermal dose is zero) and then it is measured at a dose of 1000 mins referenced at 43° C. The choice of heating a tissue at 1000 mins ensures that all six tissues of interest are necrosed [14]. Moreover, this study includes attenuation measurements for prostate, fat, and brain.

The value of attenuation (which gives a very good indication of absorption) was measured using the transmission and reception method [15]. The attenuation was measured using a system that includes 2 low-intensity transducers, a signal generator, a

data acquisition card and a PC. Attenuation includes absorption, scattering and reflection but when minimizing scattering and reflection, attenuation will reflect mostly losses due to absorption.

Previously [16] studied the changes in attenuation (from 30° C to 90° C) in cat brain and shows that the attenuation stays essentially constant up to 50° C, and then increases rapidly. The studies by [13] and [17] also showed that attenuation increases at high temperatures.

MATERIALS AND METHODS

The system consists of a signal generator (HP 33120A Hewlett Packard, now Agilent technologies), a 12 bit/50 MHz A/D acquisition card (CS1250, GAGE, Lachine, Canada) and two identical flat/circular transducers made from piezoelectric ceramic PZT4 (Etalon, Lebanon, Indiana) of 10 mm diameter. The transducers operate at 4 MHz. Figure 1 shows an illustrated block diagram of the system using the actual photos of the instruments. One transducer is connected to the signal generator and functions as the transmitter. The transmitter is attached in a small container, which is filled with degassed water. The tissue under measurement is placed inside the small container. In the other side of the container and opposite to the transmitter the other transducer (receiver) is placed. The output of the receiver is connected to the A/D acquisition card. Circulating thermally regulated water though a heating coil controlled the temperature of the tissue. A 50-μm diameter T-type copper-costantan

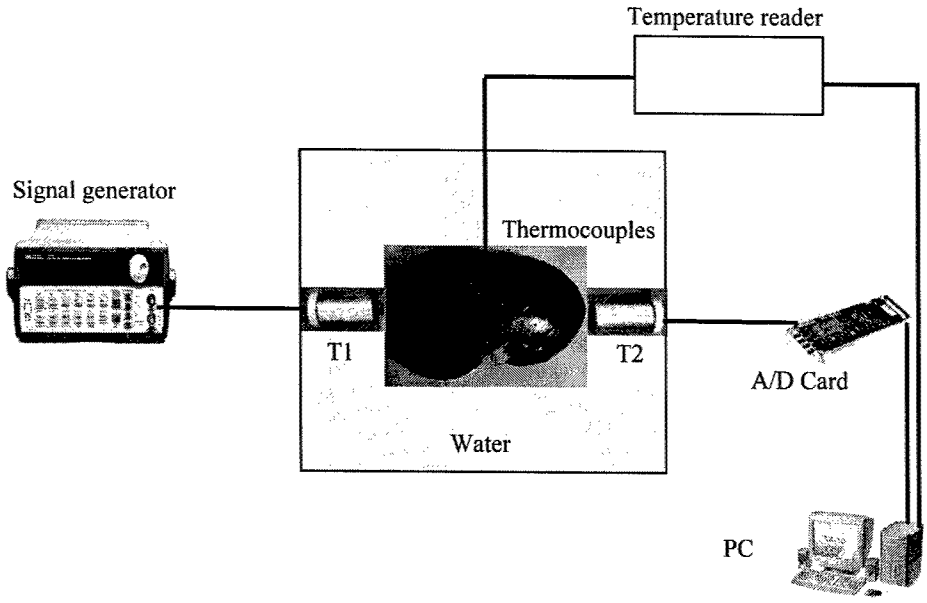

FIGURE 1. Block diagram of the attenuation measurement system.

thermocouple (Physitemp) was inserted in the tissue in order to measure the tissue temperature. Based on the elapsed time and measured temperature the thermal dose referenced at 43° C is estimated. The temperature was measured using an HP 7500 series B system and an HP 1326B multimeter.

Initially the signal through the water was measured (V_W) with the A/D card and the software that supports the card. Then the signal V_T is measured with the presence of a tissue sample. The following equation gives the value of attenuation α in dB/cm:

$$\alpha = 20 \log (V_W/V_T)/d \quad (1)$$

where d is the sample thickness measured in cms.

Initially the attenuation of a tissue at body temperature was measured. Then heating the bath at 60° C increased the temperature of the tissue. The heating at this temperature was maintained until the thermal dose of a tissue referenced at 43° C was 1000 mins. At this dose the tissue became necrotic, and the attenuation was measured again.

RESULTS

Table 1 shows the attenuation of porcine kidney cortex, muscle, fat, prostate, brain and liver at a zero dose (body temperature) and at 1000 mins referenced at 43° C (state of necrosis). The measurements were made at a frequency of 4 MHz.

TABLE 1. Attenuation of various soft tissues at body temperature (0 mins at 43° C) and at the state of necrosis (1000 mins referenced at 43° C) at a frequency of 4 MHz.

Tissue Type	Attenuation at 0 mins at 43° C (dB/cm)	Attenuation at 1000 mins at 43° C (dB/cm)
Kidney	3.1	6.5
Muscle	3.8	6.8
Fat	8.1	14.6
Prostate	4.2	8.3
Brain	3.1	6.3
Liver	3.2	8

DISCUSSION

The success of this study depends on the accuracy of measuring attenuation. Therefore the results of other studies were tabulated in order to compare. The comparison was made for liver, since for this tissue a lot of results were available. Table 2 shows attenuation of liver at 4 MHz of other studies. The main conclusion is that attenuation in liver varies between 1.8 to 5 dB/cm. From Table 2 it appears that the typical value is around 3-3.5 dB/cm. Thus the value of 3.2 dB/cm that we found in this study is vary close to the typical value found by other authors, which proves that the methods used in this paper are very accurate.

TABLE 2. Attenuation of liver at 4 MHz measured by other authors.

Tissue Type	Attenuation dB/cm at 4 MHz	Reference
Bovine liver	4.2	[17]
Human liver	2.5	[17]
Porcine liver	3.6	[18]
Bovine liver	3.5	[19]
Human liver	3	[20]
Human liver	1.8-3.5	[21]
Human liver	3.5	[22]
Hog liver	5	[23]
Human liver	4	[23]

This study confirms that the variation of attenuation within ultrasonic-important tissues (kidney, liver, prostate, and brain) is small. The lowest attenuation at 4 MHz at body temperature was measured in kidney and brain (3.1 dB/cm) whereas the maximum was measured in fat (8.1 dB/cm).

In all six tissues the attenuation for a necrotic tissue was much higher that the attenuation at body temperature. The attenuation of necrotic muscle was 1.8 times bigger than the attenuation before necrosis, whereas the corresponding figure for liver was 2.5. The other tissues exhibit an intermediate behavior. The main conclusion of this study is that soft tissue attenuation after necrosis is about double the value at body temperature.

The increase of attenuation with temperature has been observed also by [24]. The difference in that experiment is that the tissue was heavily degassed, whereas in this study the experiment was initiated immediately after the animal was killed, thus in terms of bubble content, this study was more realistic. The increase of attenuation that we observed can be attributed to the change in the tissue structure (protein denaturation) due to the heating. Since in this experiment only one measurement is taken (after necrosis) it is difficult to assess whether there is more than one process that characterizes the changes during heating

The importance of this study is that during real time ultrasound guidance of HIFU the signal might decrease during heating. Whether this drop is sufficient to provide good contrast between necrotic and normal tissue, it cannot be established yet. The study by [24] shows that the changes in backscattering due to heating are comparable to changes from point to point in the tissue. Since backscattering does not show a similar increasing trend as the attenuation [24], then the increase of attenuation may be attributed mostly to absorption (already observed by [13]). This result can be very important during HIFU. One example that demonstrates the importance of increasing attenuation is the case of a target that must be covered with necrosis by moving the transducer along the axial direction twice. A good strategy is to start heating the part of the target that is deeper in the tissue. Then the transducer can treat the rest of the target. If the opposite was followed, then during the heating of the deeper part, an acoustical barrier of high attenuation would have been created in the front part. Thus

the information of increased attenuation could be very useful during HIFU treatment planning.

ACKNOWLEDGEMENT

The study was supported by the Research Promotion Foundation of Cyprus (contract 25/99).

REFERENCES

1. ter Haar, G., Sinnett, D., Rivens, I., *Phys. Med. Biol.*, **34** (11), 1743-50 (1989).
2. Prat, F., Centarti, M., Sibille, A., Fadil, F., Henry, L., Chapelon, JY., Cathignol, D. *Hepatology*, **21** (3), 832-6 (1995).
3. Sanghvi, N., Fry, F., Foster, R., Chua, R., Chua, G., Griffith, S., Birhle, R., Yang, R., Zink, J., Hennige, L., *Med. Biol. Eng. Comp.*, **29**, 748 (1991).
4. Bihrle, R., Foster, R., Sanghvi, N., Donohue, J., Hood, P., *Journal of Urology*, **151** (5), 1271-5 (1994).
5. Chapelon, JY., Ribault, M., Vernier, F., Souchon, R., et al., *Eur. J Ultrasound*, **9** (1), 31-8 (1999).
6. Chapelon, JY., Margonari, J., Theillere, Y., Gorry, F., Vernier, F., Blanc, E., Gelet, A., *Eur. Urol.*, **22** (2), 147-52 (1992).
7. Hynynen, K., Damianou, C., Colucci, V., Unger, E., Cline, H., Jolesz, F., *Journal of Magnetic Resonance Imaging*, **5** (3), 259-66 (1995).
8. Fry, W., Mosberg, W., Barnard, J., Fry, F., *J Neurosurg.*, **11**, 471-9 (1954).
9. Lele, P., *J. Physiol.*, **160**, 494-512 (1962).
10. Vykhodtseva, N., Hynynen, K., Damianou, C., *Ultrasound Med. & Biol.*, **20** (9), 987-1000 (1994).
11. Hynynen, K. *Ultrasound Med. & Biol.*, **13** (2), 85-91 (1987).
12. Hynynen, K., McDannold, N., Mulkern, R., Jolesz,F., *Magn. Reson. Med.*, **43** (6), 901-4 (2000).
13. Damianou, C., Sanghvi, N., Fry, F., Maass, R., *J. Acoust. Soc. Am.*, **102** (2), 628-634 (1997).
14. Damianou, C., Hynynen, K., Fan, X., *IEEE Trans. on Ultrasonics, Ferroelectrics, and Frequency Control*, **42** (2), 182-187 (1995).
15. Kossoff, G., Kelly-Fry, E., Jellins, J., *J. Acoust. Soc. Am.*, **53** (6), 1730-1736 (1973).
16. Robinson, T., Lele, P., *J. Acoust. Soc. Am.*, **51** (4), 1333-51 (1972).
17. Bamber, J., and Hill, C., *Ultrasound in Med. & Biol.*, **5**, 149-157 (1979).
18. Bamber, J., and Nassiri, D., *Ultrasound in Med. & Biol.*, **11** (2), 293-298 (1985).
19. Bamber, J., Fry, M., Hill, C., Dunn, F., *Ultrasound in Med. & Biol.*, **3**, 15-20 (1977).
20. Bamber, J., Hill, C., *Ultrasound in Med. & Biol.*, **7**, 121-133 (1981).
21. Stuart Foster, F., Hunt, J., *Ultrasound Med. Biol.*, **5**, 257-268 (1979).
22. Chivers, R., Hill, C., *Ultrasound Med Biol.*, **2**, 25-29 (1975).
23. Gammell, P., Le Croissette, D., Heyser, R., *Ultrasound in Med & Biol.*, **5**, 269-277 (1979).
24. Gertner, M., Wilson, B., Sherar, M., *Ultrasound in Med. &Biol.*, **23** (9), 1395-1403 (1997).

Development Of An Intra-Operative HIFU System And Its New Techniques — Focus Control Technique Using An "Unbalanced Checker" Phased Array, And Intermittently Monitoring Technique During Sonication —

[1]Katsuhiko Fujimoto, [1]Yoshiharu Ishibashi, [2]Kentaro Tasaki, [2]Hiroshi Yamamoto, [3]Hideaki Miyauchi, [3]Taihei Ito, [3]Satoru Kondo, [3]Michihiro Maruyama, [3]Osamu Kainuma, and [2,4]Takehide Asano

[1]*Medical Systems R&D Center, Toshiba Co. Medical Systems Company, 1385 Shimo-Ishigami, Otawara-shi, Tochigi 324-8550, JAPAN*
[2]*Department of Digestive Surgery,* Chiba Cancer Center, 666-2 Nitona, Chuo-ku, Chiba 260-8717, JAPAN
[3]Department of Surgery, *Chiba University, 1-8-1 Inohana, Chuo-ku, Chiba 260-8670, JAPAN*
[4]*Medical Team Leader*

Abstract. In recent years, High Intensity Focused Ultrasound (HIFU) therapy has received heightened attentions in the field of minimally invasive cancer therapy. We have developed a new intra-operative HIFU system, which has the following new functions – the focus expansion technique using an "Unbalanced Checker" phase-shifted driving method, and the intermittently monitoring technique during treatment.

In this paper, we introduce this new system and investigate effects of these techniques in computer simulations and *in vitro* experiments

INTRODUCTION

In recent years, minimally invasive treatments (MIT) have become important in various medical fields. Thermal ablation such as radiofrequency tissue ablation (RFA) or microwave coagulation therapy (MCT) has become one of the standard tools of minimally invasive therapy for liver tumor. However these methods still need to puncture the tumor with a needle-type electrode and carry risks of tumor cell implantation and dissemination. As a new method to overcome these problems, High Intensity Focused Ultrasound (HIFU) therapy attracts a great deal of attention. Focused ultrasound energy was chosen as the therapeutic energy since it can coagulate deep-lying region within the body extracorporeally better than most other forms of energy. This technique seems to have been originally used for the destruction of small

volumes in the field of neurosurgery.[1,2,3] However, it was found that local energy absorption increased significantly due to the onset of transient cavitation,[4] and this was expected to have adverse effects on its heating capability, such as displacement of the heated part[5,6] and near-field heating during focus scanning.[7] We have already developed a Cavitation Suppression Technique (CAST) and confirmed that it is able to suppress any adverse effects due to cavitation.[8]

Although a conventional spherical ultrasound source was used, the focus was formed very sharply creating several problems. Because of its small denaturation size, the total treatment time tended to be extended. However, the biggest problem was the strong focal intensity which could mechanically the tissue around the focal point.[9]

Several focus expansion methods have already been reported which expand the focus and reduce the intensity.[10,11,12] We have developed a new technique called the "Unbalanced Checker" method to obtain a uniform ultrasound energy distribution around the focal area, and represents a remarkable improvement over current methods.

This paper reports the basic examination results obtained with an intra-operative HIFU system incorporating the "Unbalanced Checker" technique and intermittently monitoring, *in vitro* and *in vivo* experimental data are presented to demonstrate its effectiveness for HIFU therapy.

Intra-Operative HIFU System

Our developed intra-operative HIFU system is shown in Figure 1.

The system is composed of a main component (system controller and drivers), a diagnostic ultrasound imaging system (Toshiba PowerVision model SSA-380A), and an ultrasound generator (applicator).

The applicator consists of 12 pieces of piezo-ceramic transducers (diameter 57.2 mm, curvature 65.8 mm, frequency 1.5-1.6 MHz), a B-mode ultrasound probe (5 MHz) and a water coupler. Each transducer has its own drivers (total electrical output is 1.0 kW).

Figure 2 shows in its left half the principle of intermittently monitoring built into this system. The right half shows the clinical experience. The intensity of therapeutic ultrasound is much higher than that of imaging ultrasound which adds severe acoustic noise to the ultrasound images and prevents the doctor from monitoring during sonication.

FIGURE 1. Intra-operative HIFU system (for clinical trials) and ultrasound generator (applicator: lower right).

To overcome this problem, we prepare short intervals (0.05 seconds) intermittently during continuous HIFU sonication, acquire one frame of the ultrasound image within the interval and display it.

Clinical trials have confirmed the effectiveness of this new method as well as its safety improvement qualities during HIFU treatments.

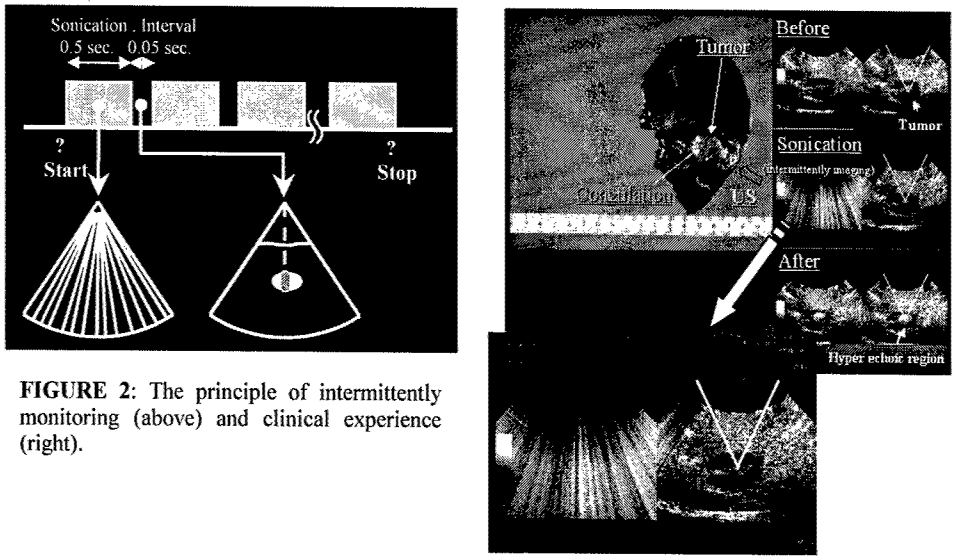

FIGURE 2: The principle of intermittently monitoring (above) and clinical experience (right).

Materials And Methods

The principle of the "Unbalanced Checker" method is shown in Figure 3.

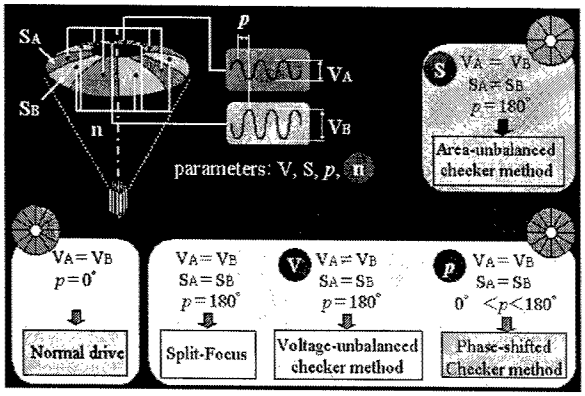

FIGURE 3. "Unbalanced Checker" method description.

The "Unbalanced Checker" method disperses the ultrasonic energy around the geometrical focal point by driving two groups of transducers with different waves. Focus expansion was investigated with computer simulations by changing the

following parameters: driving phase (p), driving voltage ratio (V), number of divided transducers (n) and transducer area ratio (S).

The ultrasound distributions were then measured experimentally at several driving conditions confirmed with these simulations. The experimental setup is shown in Figure 4. The ultrasound generator (applicator) is driven by an intra-operative HIFU system and the ultrasound images are obtained using a Toshiba SSA-380A diagnostic ultrasound imaging system. Positioning and scanning IMOTEC needle-type hydrophone are performed with an XYZ automatic stage, and ultrasound distributions are measured. Data acquisitions are controlled with Labview^{TM} on a personal computer. Several "Unbalanced Checker" conditions were applied to bovine liver *in vitro*. After sonication, the liver sections were compared with each other.

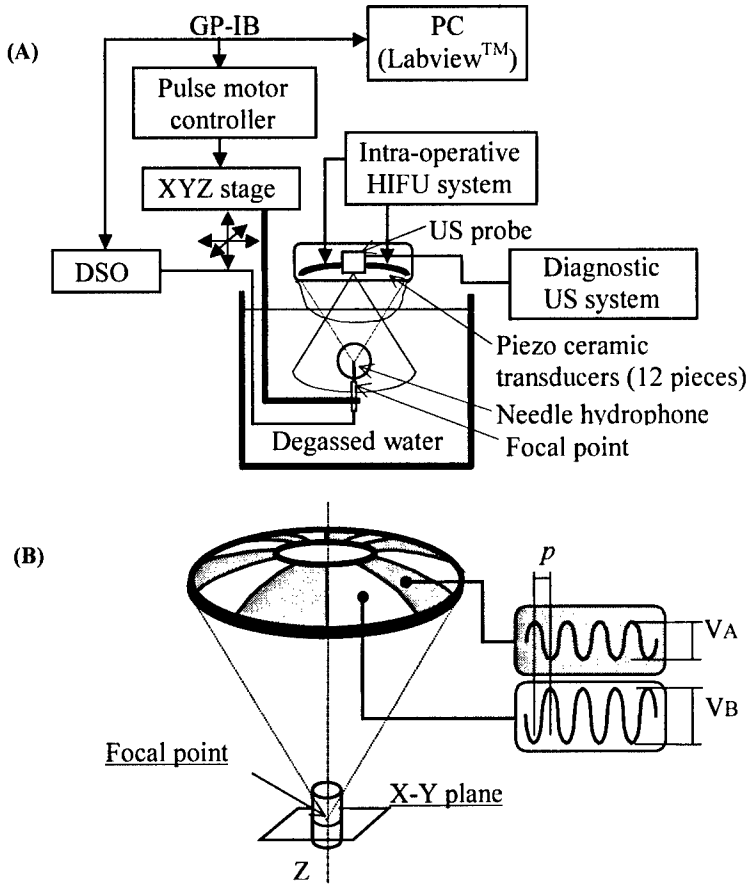

FIGURE 4. Schematic diagram of the experimental setup.

RESULTS AND DISCUSSION

Driving Parameters For Focus Expansion

Figure 5 shows how the ultrasound distributions change when the driving phase (*p*) is varied. In these simulations, the most uniform sound field was obtained when *p* was between 126 and 144 degrees.

Figure 6 shows how the lateral distribution changes when the driving voltage ratio (**V**) is set to p=180 degrees. As can be seen, the most suitable driving voltage ratio was approximately 1 to –2. The driving power ratio for these values of **V**, however, was approximately 1 to 4, which could heavily load the transducers. The Voltage-unbalanced Checker method was thus deemed unsuitable for use.

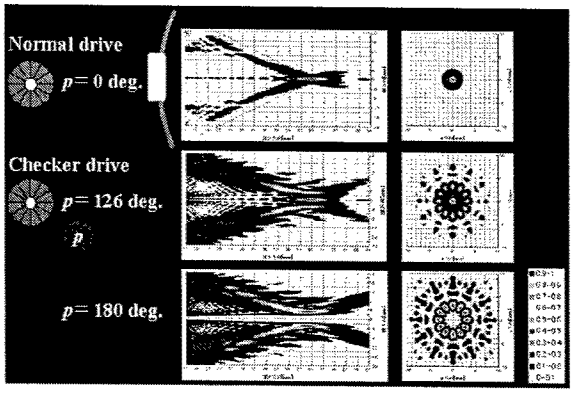

FIGURE 5. Phase-shifted Checker method: ultrasound distribution changes with varying driving phase (*p*).

- Computer simulation -

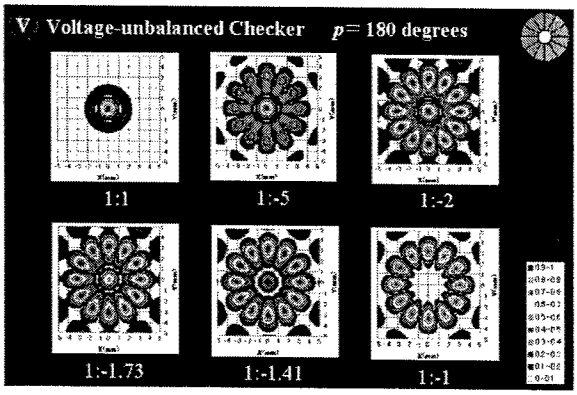

FIGURE 6: Voltage-unbalanced Checker method: lateral distributions at different driving voltage ratios (**V**).

- Computer simulation

Figure 7 shows how the ultrasound distributions change when the number of divided transducers (**n**) is varied at *p*=126 degrees. The focal size becomes smaller as **n** is reduced. On the other hand, the ultrasound intensity around the front path of the focal point becomes quite high with increasing **n**. This may cause unexpected heating around the ultrasonic path.

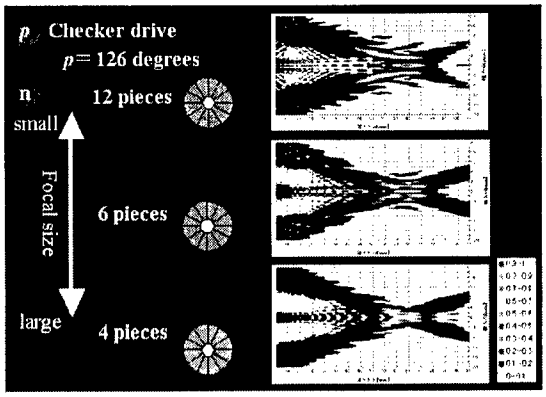

FIGURE 7. Ultrasound distributions for different numbers of divided transducers (**n**).

- Computer simulation

Sound Distribution In Water

Figure 8 shows the ultrasound distributions measured with an IMOTEC needle-type hydrophone in degassed water. When the peak ultrasound intensity is given the same value, the ultrasound intensity at Z = -30 mm of large focus was about 5 times higher than that at the middle focus. This shows that not only the focal ablation size but also the heating in front of the focus can be controlled.

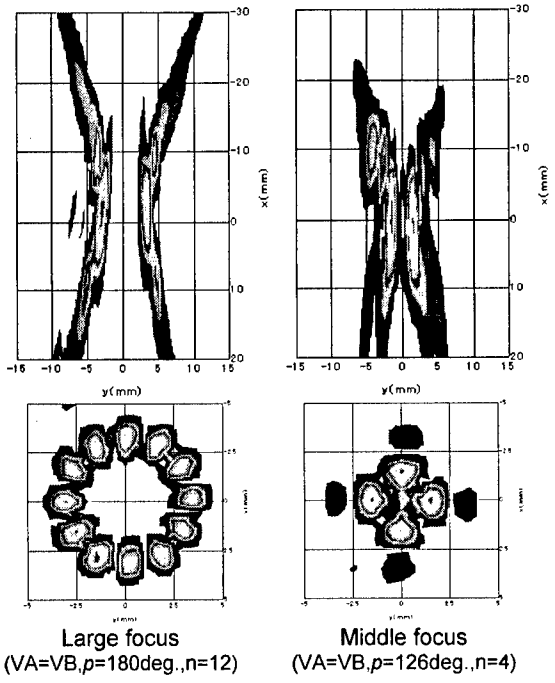

FIGURE 8. Ultrasound distributions measured with a hydrophone in degassed water.

- Experimental data

Vitro Experiments

Figure 9 shows *in vitro* bovine liver sections after sonication. With normal focus (left), the coagulated region was small, heavily denatured and partially destroyed. On the other hand, with a large focus (right), the coagulated region became large and exhibited mild denaturation. However, the coagulation expanded towards the transducers, which could have adverse effects on the HIFU treatment. The middle image shows moderate coagulation with neither tissue destruction nor expansion of tissue coagulation.

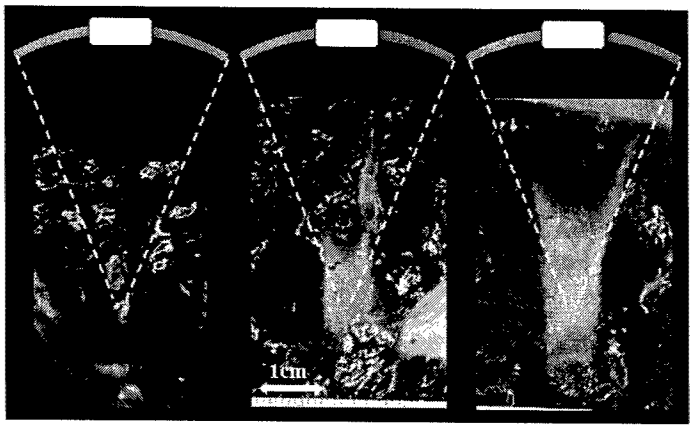

Normal (V_A=V_B,p=0°, [n=1]) Middle focus (VA=VB,p=126°, n=4) Large focus (VA=VB,p=180°, n=12)

FIGURE 9. *In vitro* bovine liver sections after sonication.

CONCLUSION

It was confirmed that our developed new "Unbalanced Checker" technique enables us to easily control the focal size. And, since focal size is closely related to the extent of tissue coagulation and destruction, this focus size control technique becomes important for HIFU therapy.

REFERENCES

1. Fry, W.J.; "Intense ultrasound in investigation of the central nervous system," *Advances in Biol. Med. Phys.*, Vol.6, Academic Press Inc. 1958.
2. Fry, F.J., et al; "Threshold ultrasonic dosages for structural changes in the mammalian brain," *J. Acoust. Soc. Am.*,.**48**, (6), 1413-1417 (1970).
3. Britt, R.H., et al.; "Feasibility of treating malignant brain tumors with focused ultrasound," *Prog. Exp. Tumor Res.* **28**, 232-245 (1984).
4. Hynynen, K.; "The threshold for thermally significant cavitation in dog's thigh muscle *in vivo*," *Ultrasound in Med. Biol.*, **17**, (2), 157-169 (1991).

5. ter Haar, G.R., et al.; "High intensity focused ultrasound - a surgical technique for the treatment of discrete liver tumors," *Phys. Med. Biol.*, **34**, No.11, 1743-1750 (1989).
6. Fujimoto, K., et al.; *WFUMB'94 Book of Abstracts 1-16-2(S95)*, 17-22 July, 1994 (Sapporo, JAPAN).
7. Damianou, C., et al.; "Focal spacing and near-field heating during pulsed high temperature ultrasound therapy," *Ultrasound Med. Biol.*, **19**, No.9, 777-787 (1993).
8. Fujimoto, K., et al.; "A new cavitation suppression technique for local ablation using high intensity focused ultrasound," *IEEE Ultrasonics Symposium Proceedings*, 1629-1632 (1995).
9. Sugamoto, Y., Asano T., et al.; "Thermal coagulation therapy forn liver tumors using a newly developed high intensity focused ultrasound apparatus (HIFU)," *Soc. of Minimally Invasive Therapy 9th Annual International Meeting*, Kyoto, Japan (1997).
10. Fan, X., Hynynen, K.; "Control of the necrosed tissue volume during noninvasive ultrasound surgery using a 16-element phased array,". *Med. Phys.* **22**, No.3, 297-306 (1995).
11. Hoffelner, J., et al.; "Self-focussing HIFU source for large therapy volumes," *IEEE Ultrasonics Symposium,* PB-6 (1998).
12. Umemura, S.-I., et al.; "Advantages of split-focus approach in coagulation therapy," *IEEE Ultrasonics Symposium,* PA-7, 1998.

Orthogonal Focusing HIFU System With Lens And Linear Array

Ishida Kazunari*, Kubota Jun*, Sato Yutaka*,
Azuma Takashi**, Sasaki Kazuaki**, Kawabata Ken-ichi**,
Umemura Shin-ichiro**

** Research & Development Center, Hitachi Medical Corporation, Chiba, 277-0804, JAPAN*
*** Hitachi Central Research Lab., Tokyo, 185-8601, JAPAN*

Abstract. Aiming to develop a non-invasive ultrasonic treatment technology enabling coagulation treatment with a highly enhanced throughput [1,2], we are developing a Variable Focal length High Intensity Focused Ultrasound (VFHIFU) system for coagulation therapy. In order to treat tumors at a wide range of depth in tissue by ultrasonic coagulation therapy, it is necessary to increase range of variable transmitting focal length. In this study, we considered array transducer design method for transmitting high intensity ultrasound. And as an evaluation result of prototype based on the method, the prospect of dynamic focusing ultrasound therapy was obtained.

INTRODUCTION

A focal spot size is around 2 mm in diameter and 100 mm in length for the particular application to treat prostate cancer from rectum. It needs exchanging of transducer while the treatment process proceeds when the transducer has fixed focal length (Fig. 1). It is possible to treat prostate without pulling out and reinstalling the transducers (Fig. 2).

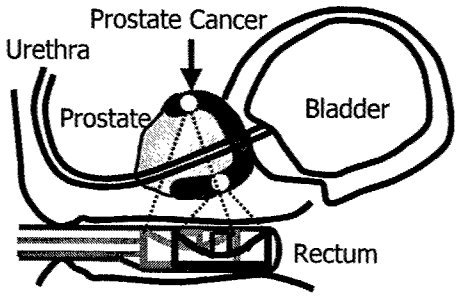

FIGURE 1. Trans rectal HIFU for prostate.

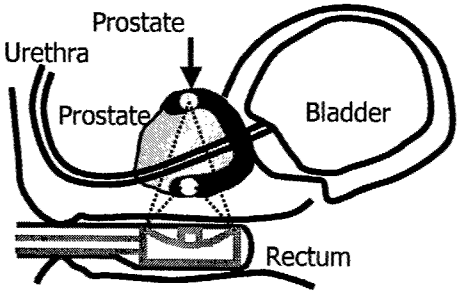

FIGURE 2. VFHIFU for trans rectal prostate treatment.

A prototype variable focal length array transducer system for a high-throughput HIFU is constructed and tested in order to treat benign and malignant

tumors at a wide range of depth in tissue. Lesion of coagulation necrosis is formed and observed at the focused region in a sample of liver tissue removed by using the system made on trial.

METHODS

The variable focal length technology with linear array and acoustic lens was employed to expand the treatment zone. The applicator consists of two pieces of power array transducers with an elevational mechanical lens for the treatment, and a small diagnostic array probe located between them for targeting and monitoring. The each power array transducer with small f-number is formed as phased array to make the focal length variable.

They can converge an ultrasound beam at several distances from the contact surface by using the transmitting circuits of several channels that drive each corresponding elements of the transducer independently to cauterize a sample of tissue removed. The transmitting control unit consisting of the circuits is shown with ultrasound scanner for imaging in Fig. 3, while Fig. 4 shows a head part of the system containing all the transducers' assembled as is shown in Figs. 5 and 6 respectively. Schlieren apparatus monitors the focused ultrasound beam profiles, while acoustic power is measured by a radiation force balance method.

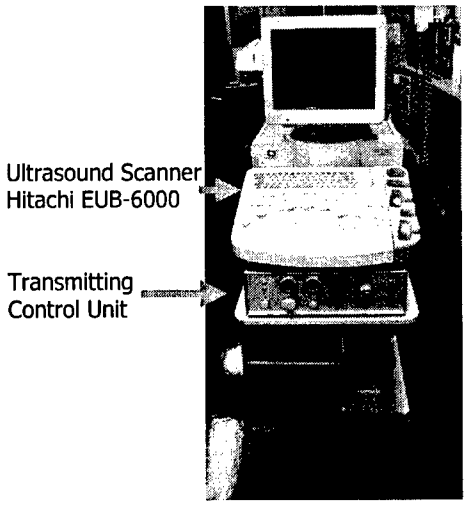

FIGURE 3. Front view of the trial made apparatuses.

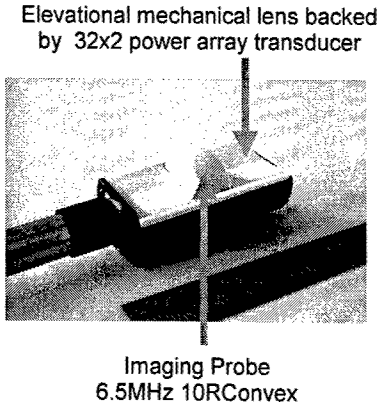

FIGURE 4. External view of transducer head.

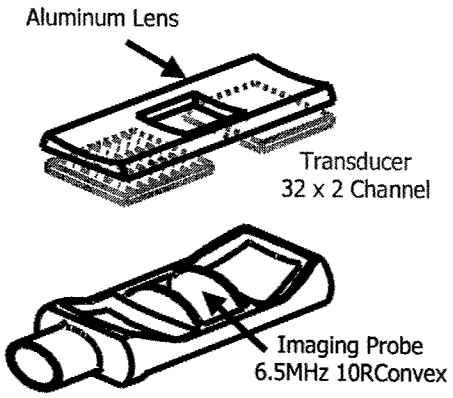

FIGURE 5. Structure of the head.

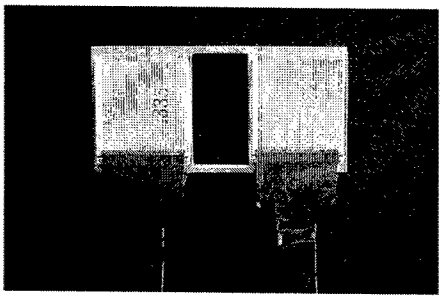

FIGURE 6. Rear view of the array transducers below aluminum lens.

RESULTS

Fig. 7 shows total acoustic power radiated from HIFU transducers vs. peak-to-peak voltage applied to the array elements. The frequencies for power array transducers and single element (fixed focusing) transducers are 2.66 MHz and 4.3 MHz respectively. More than forty watts of acoustic power was measured in water irradiated by both array transducers assembled in the head, as shown in Fig. 7, when applying 100 Vp-p to the each array transducer elements. Since canine prostate was cauterized to generate coagulation lesion by continuous wave ultrasound beam of 17W at 4.3 MHz at the former experiment [3] that is equivalent to 43 W at 2.7 MHz, the power is expected to be sufficient for coagulation.

The focal points are targeted at different depth from 30 to 65 mm in water as shown in Fig. 8. Although the beam is weakly focused by the acoustic lens for short axis, it cannot be focused properly without electrical phase control. Therefore electronic phase control for the HIFU beam focusing proved to be effective.

Fig. 9 shows the result of animal experiment, the swine liver cut surface, cut after the irradiation of the VFHIFU along the section.

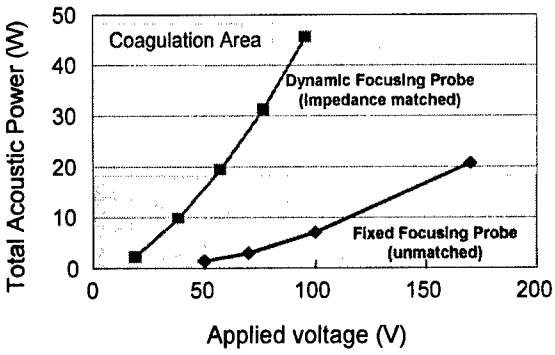

FIGURE 7. Total acoustic power radiated from HIFU transducers vs. peak-to-peak voltage applied to the array elements.

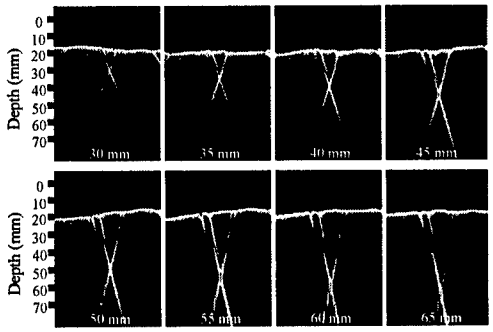

FIGURE 8. Beam pattern of dynamic focusing probe obtained by schlieren technique

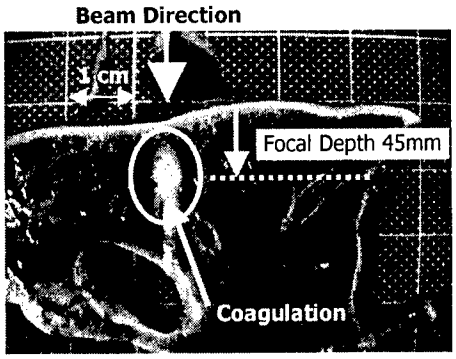

FIGURE 9. Necrotic lesion in swine liver caused by VFHIFU irradiation

It was confirmed that lesion of coagulation necrosis is formed at the regions around focal point which were monitored by schlieren method as shown in Fig. 9.

CONCLUSIONS

Total acoustic power of more than 40W was achieved in water using our power array transducer with elevational mechanical lens.

The transducer can generate coagulation lesion upon necrosis (swine liver) around focal point, deep at 45 mm, total acoustic power of more than 40 W, and Intensity 1.9 kW/cm^2.

This study demonstrated that our new prototype HIFU system can coagulate tissue at focal points without exchanging applicators.

ACKNOWLEDGMENTS

This research was partly supported by NEDO. (New Energy and Industrial Technology Development Organization of Japan).

REFERENCES

1. Umemura, S., Sasaki, K., Kawabata, K., Azuma, T. and Sanghvi, N. T., "Coagulation of swine liver and canine prostate with a prototype split-focus transducer," IEEE Ultrasonic Symposium (1999).
2. Umemura, S., Sasaki, K., Kawabata, K. and Azuma T., "Non-circular multi-sector split-focus transducer for coagulation therapy," IEEE Ultrasonic Symposium (2000).
3. Ishida, K., Sato, Y., Umemura, S., Kawabata, K., Sasaki, K., Azuma, T., "Development of therapy head for ultrasonic therapy system," *JSUM Workshop for Basic Technology proceedings*, **100**, (1), pp.21-26 (20/5/2000)
4. Ishida, K., Sato, Y., Azuma, T., Sasaki, K., Kawabata, K., Umemura, S., "Development of Dynamic Focus HIFU System," AUIM Annual Convention (2001).
5. Ishida, K., Kubota J., Sato, Y., Azuma, T., Sasaki, K., Kawabata, K., Umemura, S., "Variable focal length HIFU system with power array transducer," AUIM Annual Convention (2002).

New Piezocomposite Transducers For Therapeutic Ultrasound

Gérard Fleury, Rémi Berriet, Olivier Le Baron, Bertrand Huguenin

Imasonic, 15 Rue Alain Savary, 25000 Besançon, France

Abstract. The development of therapeutic applications of ultrasound depends notably on the availability of high-performance transducers. New piezocomposite technologies offer performances that have proved to be particularly well adapted for such applications thanks to high power density generation with high efficiency. Moreover this technology enables a wide variety of shapes and the design of array transducers for electronic focusing, scanning and steering of the beam. This article details these advantages as well as other interests such as a large bandwidth or the MRI compatibility allowing the imaging / therapy association.

Furthermore, the feasibility of highly focused transducers and complex array structures will be illustrated through various examples.

INTRODUCTION

Ultrasound therapy has been the subject of research for many years [1,2,3], but it is only recently that this technique has found effective and widespread medical applications. The potential of this technique is extremely promising, but there remains progress to be made, notably in the area of the generation of ultrasonic waves.

The large range of potential applications creates a wide range of different objectives. The main parameters are the required action on the biological tissue, the volume and location of the treatment zone inside the body, the acoustic access to the target area, the limitations on treatment time, the limitations on the acoustic exposure of surrounding tissues, the associated imaging techniques.

Compared with other medical ultrasonic techniques like those used in medical diagnostic this will lead to specific requirements:

- Generate high power acoustic waves that are precisely localized and precisely controlled in amplitude,
- Provide 3D scanning of the beam with a high degree of flexibility,
- Have a physical compatibility with imaging equipment and associated sensors,
- Guarantee an improved degree of reliability and safety taking into account the use of a larger amount of electrical and acoustical energy

Based on the above application requirements the transducer designer will have to take into account transducer specifications that includes:

- The production of high acoustic power at the surface of the transducer,
- 2D large active radiating apertures with f-number ~1.

Maintaining the treatment time in a reasonable range is often an important objective. Flexibility of operation and easiness of control are also important criteria.

On those aspects electronic beam synthesis focusing and steering with transducer arrays opens many routes for solutions.

When MRI imaging technique is to be used the material compatibility with MRI environment of transducer and other parts of the system is required.

When ultrasonic imaging technique is chosen it makes necessary to combine diagnostic requirements and therapeutic ones. Various configurations can be used:

- different transducers in separated housings mechanically positioned one to the other in order to obtain a precisely controlled location of respective beams in the same setting mark. The position of one transducer relative to the other may be adjustable or not.
- different transducers with a fixed position in the same mechanical assembly or in the same housing in order to obtain a very stable and constant positioning of one transducer relatively to the other.
- using the same transducer or the same group of transducer elements having the capability to function in both modes. This will obviously require transducers with a high power capability, at least at the chosen frequency for the therapeutic use, and a wide band capability, at least in the frequency range of imaging for diagnostic use.

State of the art technologies developed for high power ultrasound as well as technologies developed for low power ultrasound like medical diagnostic, non destructive testing, flow and distance measurement, etc., have many limitations with respect to the above mentioned requirements.

In order to solve these limitations and develop new transducers for therapeutic ultrasound new high-power technologies using piezocomposite technology have been searched and evaluated [3]. Continuous research and development in this piezocomposite route offers now a broad range of technological solutions.

State Of The Art In Piezoceramic And Piezocomposite Technology

It is well known that one can use piezoceramic bowls or plates made from low losses PZT materials to produce high power transducers. The piezoelectric layer is then excited on its first or third harmonic. These transducers are generally air-backed and array structures can be obtained by making deep grooves in the ceramic layer. This approach allows the manufacturing of high-intensity transducers with high efficiency but involves the following limitations:

- Lateral vibrations in ceramic layer may create parasitic waves producing spurious hotspots,
- Cross talk between array elements may limit beam control performances,
- Producing large size plates or bowls may be difficult,
- Due to the low resilience of piezoceramic materials and due to the presence of grooves in arrays the transducer structure may be fragile under mechanical shocks or pressure,
- Most of these designs give narrow band transducers.

On the other hand 1-3 and other piezocomposite technologies have received a large interest in low power applications like medical diagnostic [4] and non destructive testing. 1-3 piezocomposite technique is based on the use of materials including a

large number of piezoceramic rods embedded into a matrix of polymer material (Fig 1).

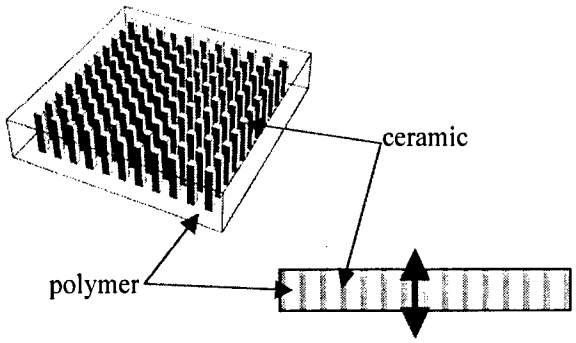

FIGURE 1. 1-3 Piezocomposite after W. A. Smith.

The main benefit of a properly designed 1-3 piezocomposite material is an enhanced vibration in thickness mode and a reduction of the influence of lateral modes. The good properties in the thickness mode can be described by the coupling coefficient that is higher than the coupling coefficient of a plate made of the same ceramic material.

The most current design of so called 1-3 piezocomposite transducers based on the use of 1-3 piezocomposite materials implies the following choices:

- Use of low glass transition temperature (Tg) polymer filler: epoxy or polyurethane
- Thermal shaping of the piezocomposite structure in order to create a shell. This shell structure may be used to produce the mechanical focusing characteristics of the transducer.
- Create an array structure by using a pattern of engraved electrodes and making profit of the low lateral cross talk
- Use of solid backing material with relatively low acoustical impedance in order to have a good mechanical resistance and a high efficiency.

The use of 1-3 piezocomposite technology facilitates the reduction of lateral waves in large transducer shells as demonstrated by Cathignol et al. [5] and provided that the piezocomposite is properly designed, one can obtain beam patterns with an excellent correlation with predicted beams from theoretical models.

Based on the above reasons the use of piezocomposite technology is attractive for therapeutic applications.

One important point must be remembered at this stage. High power ultrasound cannot be produced without electrical and mechanical losses inside the materials of the transducer and such losses make a part of the electrical and mechanical energy to be converted into thermal energy inside the transducer itself. As for instance it is well known that losses play an important role in the power capability of transducers based on ceramic technology and in that case one must take care to use special low loss piezoceramic materials in order to obtain high power characteristics. In addition one

must take care of the losses in the used electrical interconnections, cables and matching networks.

Also it is well known that 1-3 piezocomposite materials have relatively high losses compared to ceramic materials used in power applications. The existence of losses implies that high power generation cannot be envisaged without a special and careful design of the thermal properties of materials and structures. As for instance maximum inside temperature of the currently used piezocomposite materials in low power applications is limited by low thermal glass transition temperature (Tg) usually around 60°C (140 °F). A transducer built with piezocomposite technologies designed for low power applications will rapidly be damaged under high power excitations. Therefore the use of 1-3 piezocomposite technology for therapeutic applications requires specific structural design and adapted materials.

New High-Power Piezocomposite Technologies

Due to above mentioned variety of requirements in therapeutic applications and due to the limitations of state of the art technologies we have been willing to overcome encountered limitations and we have designed several piezocomposite materials and structures for therapeutic applications.

This work was based upon the development and the combination of three key technological aspects:

- The use of new 1-3 piezocomposite materials using high Curie temperature ceramic rods embedded into high glass transition temperature (Tg above 120°C) polymer matrices.
- The use of special shaping processes allowing the making of highly curved shells. These processes are not revealed in this article due to their proprietary aspect.
- The use of newly designed structures combining piezocomposite layer with matching layers and backing. These new structures have been made necessary in order to keep low mechanical stress and thus keep the structure integrity under the inherent variations of the inside temperature that are produced by losses under high power generation.

In our team we have developed two technologies named HI1 and HI2.

HI1 technology has been designed and the first prototypes have been manufactured on the very beginning of 1991. Following a demand from the French "Institut National de la Santé et de la Recherche Médicale – Inserm" and in the framework of a feasibility study made in collaboration with Inserm our objective was to demonstrate the feasibility of transducers for the thermal ablation of tissues. Considering the limitations of existing technologies we decided in our team to experiment the use of technological results including materials structures and processes from previous research and development works dedicated to high temperature transducers for NDT applications. Other results were also available at that time in our lab for the shaping of relatively large transducers with F-number close to 1. First prototypes were characterised by Inserm and high power performances were shown demonstrating the capability to produce high power ultrasound at levels adapted for the thermal ablation

of tissues. Previously demonstrated shaping processes were then used to produce the first piezocomposite HIFU transducers.

Considering the date of initial works it may appear that these works are no more really new. However one must consider that therapeutic ultrasound development is a long term process and that the qualification of materials, processes and methods is quite long due to the overall complexity of the objectives including the definition of the treatment itself, the design and realisation of devices, the process of laboratory and clinical experiments.

More recently HI2 technology has been developed with the objective to have more power capability in some applications. A solid backing that is not described in this paper gives better thermal cooling while keeping a good bandwidth. In addition this HI2 technology allows the design of transducers which are extremely resistant to mechanical and thermal shocks.

Both developed technologies have been shown suitable to produce high power ultrasound for therapeutic applications. Other characteristics are as follows:

TABLE 1. Characteristics of Imasonic HI-1 and HI-2 technologies.

Characteristics of Imasonic HI1 and HI2 technologies	
Common features	– Flexibility in shapes, sizes and array patterns – Mechanically robust
Imasonic HI-1	
Transducer efficiency	60% to 70%
Working frequency range	200 kHz to 10 MHz
Maximum acoustical power	5 to 10 W / cm²
Backing	Air
Imasonic HI-2	
Transducer efficiency	40% to 60%
Working frequency range	200 kHz to 5 MHz
Maximum acoustical power	up to 30 W / cm²
Backing	Solid

HI1 AND HI2 PERFORMANCES THROUGH SOME EXAMPLES

Access to array technique: the structure of the piezocomposite material allows a significant reduction of spurious modes of vibrations and privileges the thickness mode. This property makes possible the design of array transducers as the elements can be made acoustically independent. It is also beneficial for avoiding the generation of parasitic radiation. Both HI1 and HI2 technologies can be used to make arrays and this is illustrated in various following examples.

Acoustical power and efficiency: thanks to a high coupling coefficient, superior to that of the ceramic material, and a lower acoustic impedance (8 to 12 Mrayl) that facilitates the transfer of energy to water, and due to their specific thermal and mechanical design, transducers based on HI1 and HI2 piezocomposite technologies can generate acoustical power that can be as high as 30 Watts/cm^2 with a high efficiency. In order to meet therapeutic applications, Ultrasonic transducers have to

withstand the applied electrical power in a continuous manner for several seconds, or even several minutes. Under such conditions, the internal heating due to electrical or mechanical losses constitutes a first source of limitations. The efficiency of the HI1 and HI2 piezocomposite transducers, typically around 50 - 60%, remains stable at high level of power over a long time.

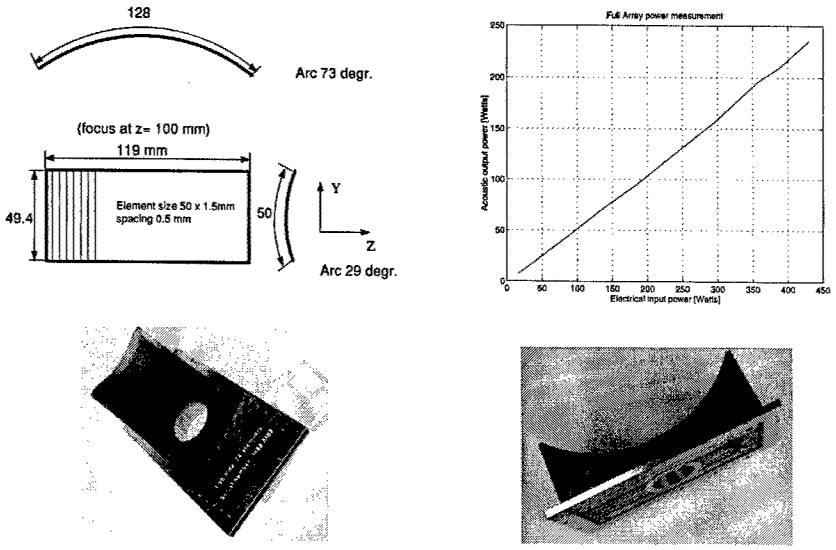

FIGURE 2. HI1 linear concave array — 64 elements with measurements of total acoustic output power as a function of electrical input power.

The following example illustrates the stability of efficiency in the case of HI2 transducers:

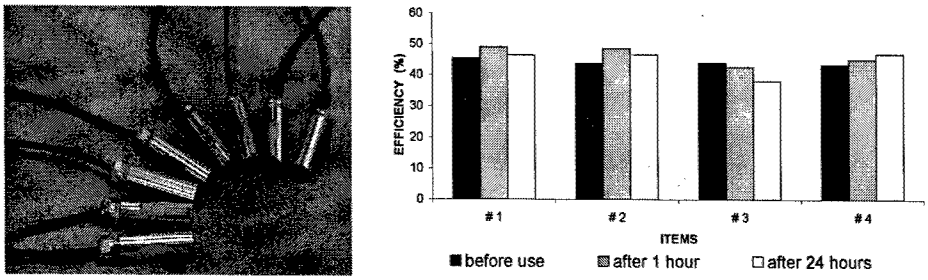

FIGURE 3. Single element transducers – Evolution of the efficiency after 1 hour and 24 hours. (Emitted acoustical power: 10 W/cm² - Duty cycle : 10 sec. ON – 60 sec. OFF)

Bandwidth, Beam Quality and **Imaging / Therapy association**: The structure of the piezocomposite material privileges the thickness mode of vibration of the active element. Typically, the thickness mode coupling coefficient k_T is on the order of 0.60. Beyond the interest for energy conversion, it facilitates also the widening of the bandwidth. This feature has an interest in many cases. First it facilitates the tuning with the electrical circuit. This means that the transducer can operate in a relatively

wide frequency range around the nominal value with an efficiency that remains high. In some applications this allows to sweep the frequency in order to obtain specific effect like the reduction of grating lobes [6]. Moreover this allows to adjust the frequency according to some parameters of the treatment like the depth of tissue, the nature of tissue, etc.

More recently came an increasing interest in making transducers allowing a combined use in therapeutic mode and imaging mode. For instance, the wide band characteristic of HI1 combined with innovative signal processing was used by Ebbini et al. [10] in order to produce images from a linear array transducer initially developed for therapeutic purpose. This opens new paths for the combination of Therapeutic ultrasound with Imaging ultrasound. The following figure shows the transmit temporal and frequential characteristics of a HI1 linear array transducer.

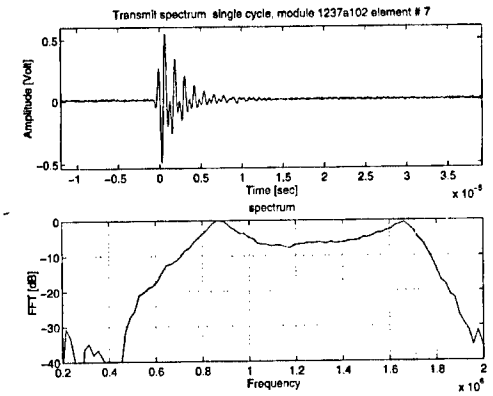

FIGURE 4. Temporal response and frequential analysis of a high-power HI1 transducer.

In the same goal of making therapeutic transducers compatible with imaging techniques HI-1 and HI2 based transducers have been developed using MRI compatible materials in order to use them under MRI imaging and hence to associate ultrasonic treatment with MRI monitoring.

The picture in Fig 5 shows HI1 2D arrays for Focused Ultrasound Surgery under MRI imaging and Fig 6 shows an MRI image with the transducer in the bottom part of the image.

Another important requirement in most therapeutic applications is the high level of control of beam quality. This is particularly important in HIFU techniques were a precise volume of tissue is being ablated.

This is also important in methods including the synthesis of beams with special spatial distribution in order to treat a larger volume of tissue and to reduce the time of the treatment. Fig 7 shows an example of beam distribution from a 2D array made in HI 1 technology.

FIGURE 5. 104 elements high power MRI compatible transducers.

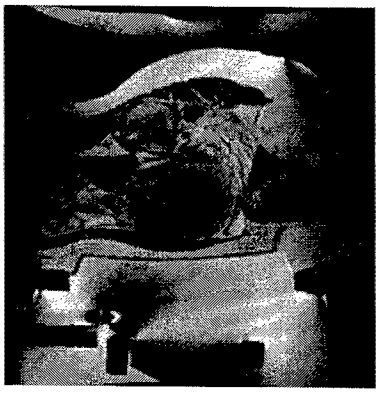

FIGURE 6. MRI imaging with therapeutic transducer.

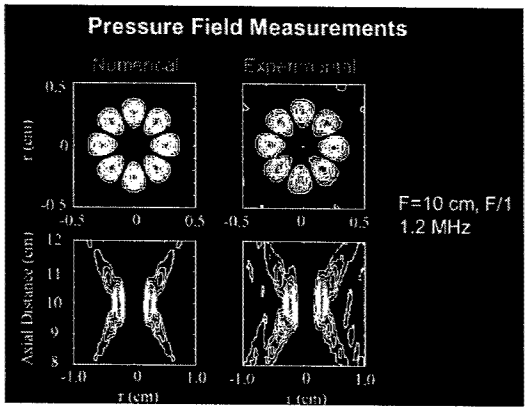

FIGURE 7. Pressure field measurements of a 104 elements 2D array. Note that the results obtained are very close to the simulations (after J.L. Raymond, R. King, and K. Hynynen)

CONCLUSIONS

The evolution of ultrasonic therapy and the variety of applications and combinations with imaging techniques make increasingly necessary to take into account the specific nature of each application. Imasonic HI-1 and HI-2 technologies have been developed to bring adapted technological solutions in a wide range of cases including array techniques. Theses technologies make feasible efficient transducers with a high degree of confidence in beam predictability. Solutions are also designed to be electrically and mechanically safe and compatible with other constraints like MRI imaging. Moreover, routes are being opened to obtain echographic images with the same transducers.

ACKNOWLEDGEMENTS

We would like to thank all researchers and members of companies developing therapeutic systems who gave us the opportunity to design and manufacture transducers for therapeutic applications.

REFERENCES

1. G. ter Haar, R.L. Clark, M. G. Vaughan, and C.R. Hill , "Trackless surgery using focussed ultrasound: technique and case report," *Min Inv.Ther.*, **1**, 13-19 (1991).
2. J.Y. Chapelon, P. Faure, M. Plantier, D. Cathignol, R. Souchon, F. Gorry and A. Gelet, "The Feasibility of Tissue Ablation Using High Intensity Electronically Focused Ultrasound," IEEE Ultrasonics Symposium 1993, 1211-1214.
3. J.Y. Chapelon, D. Cathignol, C. Cain, E. Ebbini, J.U. Kluiwstra, O. Sapozhikov, G. Fleury, R. Berriet, L. Chupin and J.L. Guey, "New Piezoelectric Transducers for Therapeutic Ultrasound'" *Ultrasound in Med. & Biol.*, 153-159 (2000).
4. W.A. Smith, "The role of piezocomposites in ultrasonic transducers," IEEE Ultrasonics Symposium 1989, 755- 766.
5. D. Cathignol, O.A. Sapozhnikov, J. Zhanz, J.Y. Chapelon, "Comparison of acoustic fields radiated from piezoceramic and piezocomposite highly focused transducers", IEEE Ultrasonic Symp. Proc. 1995b, 983-896.
6. F. Dupenloup, J.Y. Chapelon, D. Cathignol and O. Sapozhnikov, "Reduction of the Grating Lobes of Annular Arrays Used in Focused Ultrasound Surgery," *IEEE*, **43** (6), 991-998 (1996).
7. J.Y. Chapelon, F. Prat, A. Arefiev, D. Cathignol, R. Souchon and Y. Theillère, "Development of Small High Intensity Focused Transducers for Ultrasound Endotherapy," IEEE Ultrasonics Symposium, 1996, 1265-1268.
8. J.-U. Kluiwstra, R.J. McGough and C.A. Cain, "Therapeutic Ultrasound Phased Arrays : Practical Consideration and Design Strategies," IEEE Ultrasonics Symp., 1997, 1277-1280.
9. P. VanBaren, C. Simon, R. Seip, T. Solf, C.A. Cain and E. Ebbini, "Image-Guided Phased Array Systems for Ultrasound Thermotherapy," IEEE Ultrasonics Symp., 1999, 1269-1272.
10. E.S. Ebbini, C. Simon, H. Lee, W. Choi, "Self-Guided Phased Arrays for Noninvasive Surgery," IEEE Ultrasonics Symposium, 1999, 1427-1430.
11. L. Curiel, F. Chavrier, R. Souchon, A. Birer and J.Y. Chapelon, "1.5D Multi-Elements Phased Array Applied to High Intensity Focused Ultrasound," IEEE Ultrasonics Symposium, 1999, 1451-1454.
12. D.R. Daum and K. Hynynen, "A 256-Element Phased Array System for the Treatment of Large Volumes of Deep Seated Tissue," *IEEE Trans. on UFFC*, **46** (5), 1254-1268 (1999).
13. L. Curiel, F. Chavrier, R. Souchon, A. Birer and J.Y. Chapelon, "1.5-D high Intensity Focused Ultrasound Array for Non-Invasive Prostate Cancer Surgery," *IEEE Trans. on UFFC*, **49** (2), 231-242, (2002).

Power Supply Requirements For HIFU

Bruce J.P. Mortimer*, Renier Morkel*, Ian DeVries* and Gary A. Zets†

*Centre for Instrumentation Research, Cape Technikon, South Africa
†Engineering Acoustics Inc. (EAI-DigiPower), 933 Lewis Drive Suite C, Winter Park, FL 32789

Abstract. HIFU has gained importance as a therapy modality. Various acoustic transducer systems have thus far been presented but very little work has been done on optimally driving these transducers. Piezoelectric loads present a non-linear frequency and power dependant load that is incompatible with most conventional RF amplifiers. This paper presents work done on developing a switching type RF power source suitable for driving piezoelectric transducers at high frequencies. This design approach presents several cost and reliability advantages and also a dramatic increase in efficiency compared to conventional linear amplifier designs opening up the potential for portable applications.

INTRODUCTION

High-intensity focused ultrasound (HIFU) is becoming an accepted method of non-invasive hemostasis and tumor treatment. Hemostasis systems typically consist of a single-element concave piezoelectric transducer load and are required to deliver powers ranging from 30 W to 250 W [1]. Several different configurations have been reported for tumor ablation including; multiple transducers in an array [2], single or multiple concave transducers [3], and a single flat piezoelectric transducer in combination with an acoustic lens [4]. All systems are designed to operate at relatively high frequencies between 0.8 and 6 MHz.

Thus far, conventional RF linear amplifiers and external matching networks have been used to drive the transducers at a resonant mode. Further, no HIFU applications currently drive the transducers with anything other than continuous or pulsed sinusoidal driving voltages. Therefore, the extensive bandwidth and linearity offered by linear amplifiers is not required in HIFU and a size, weight and cost penalty is associated with this approach. Further, these amplifiers have a reputation for low reliability (ruggedness) due to their low tolerance for VSWR. This paper examines the piezoelectric load under high power drive and introduces results from a specially designed high frequency switch mode energy source, optimized to drive HIFU loads at power.

DYNAMIC BEHAVIOR OF THE PIEZOELECTRIC LOAD

It is important to be able to accurately predict the behavior of the load under the operating conditions before attempting to design the driver amplifier for maximum power transfer and efficiency. The piezoelectric transducer operating near or at its

resonant frequency can be characterized by the simple equivalent circuit [5] of Fig. 1, where:

Co	*is the capacitance of the clamped disc,*
Ro	*is the parallel resistance representing dielectric losses of the transducer,*
Rm	*is the internal resistance representing mechanical losses and*
R_L	*is the external (useful) load resistance representing radiated energy while*
Lm and *Cm*	*represent the mechanical compliance and mass of the transducer.*

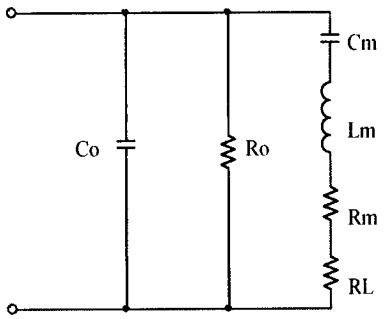

FIGURE 1. Equivalent circuit of a piezoelectric transducer.

R_L + *Rm* is the load pure resistance when the disc is driven at mechanical resonance. It is to this resistance that the maximum power transfer must take place and its value is an important factor that is considered when designing or matching to the driver amplifier. The behavior of the load is usually measured using network analyzer however care must be taken when interpreting these small-signal results as these may be somewhat different when driven at the rated power. Practical loads are usually complex and highly non-linear which results in several unique challenges for the amplifier; loads are usually highly reactive, have multiple-resonant modes and are capable of acting as source under certain loadings. Losses and power transfer invariably result in a change in temperature and a shift in the resonant characteristics. These can be easily tracked using a control strategy [6] or including the frequency varying elements as part of the resonant circuit in power oscillators [7]. Multiple resonant modes usually render the power-oscillator approach unreliable and most ultrasonic systems make use of an external oscillator and frequency control system [6].

The static capacitance of the transducer can be eliminated or reduced using either a series or parallel compensation inductor. This practice is both common and necessary when using linear amplifiers, however compensation requirements are different for switching supplies and is usually accomplished via a filter network.

HALF-BRIDGE SWITCH MODE POWER SUPPLY

Linear RF amplifiers are bulky; the amplifier will dissipate large amounts of power during normal operation (with efficiencies usually less than 65%). This, together with the demands and variability of a resonant load often results in problems with

reliability. In contrast, switch-mode systems have excellent efficiencies, typically more than 90%.

In the Class-D switch mode configuration shown in Fig. 2, switching is employed to create an AC current flow through the load from a DC source (voltage fed topology). This configuration is often called an inverter, but it can also be called a switching amplifier since both cycles of the voltage waveform, measured on the midpoint, is an amplified version of the combined inputs to this configuration. Two N-channel MOSFETs are tied by their drain and source terminals on the midpoint. They are alternately switched on by each half cycle of the generated square-wave signal for half a period at the switching frequency. Fig. 2(b) shows an alternative way of representing the inverter action. The diodes across the switches in Fig. 2(b) represent the reverse-recovery diodes typically found inside MOSFETs.

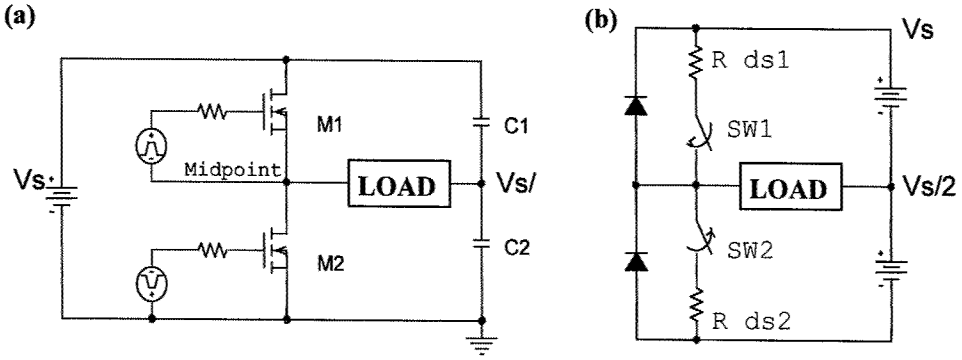

FIGURE 2. (a) Schematic of a class-D half-bridge inverter; (b) simplified version.

Class D power supplies have been used extensively for low frequency ultrasonic applications [6]. In HIFU, the minimum operation frequency for the power supply is of the order of 1 MHz and this introduces several complications into designing a switch-mode topology. The MOSFETs and lumped circuit elements cannot be considered as ideal elements at these high frequencies. Further, the following practical problems must be managed; the reverse recovery time of the internal diode is finite which can create losses and switching noise especially when driving resonant loads, the MOSFET output capacitance must be discharged one each cycle introducing losses and Millers effect increases the input capacitance making gate switching lossy. Most of the parameters including the effects of stray inductance can be managed by careful layout, component and inverter operating point selection. In our approach we have made use of an energy-recovery driving circuit in the gate driving circuit; thus reducing the conventional high frequency switching losses associated with MOSFETs (discussed below).

Attempting to drive the piezoelectric transducer into resonance with a square wave is not desirable since the additional harmonic content in square waves will introduce multiple transducer modes. Since the transducer has more than one resonant frequency, it is necessary to introduce some form of filtering to ensure its operation in the chosen mode of vibration. Despite the fact that the transducer is driven at resonance, it still appears as a largely capacitive load to the driver amplifier because of

Co. For this reason we make use of a novel resonant coupled matching network as a low impedance source and impedance matching network to the transducer. This configuration has several practical advantages compared to conventional impedance transformers.

Energy Recovery Gate Driver Circuit

At high frequencies, the MOSFET driver must be able to drive large capacitive type loads with high charge and discharge currents, fast rise and fall times and low power consumption. We have made use of an energy recovery circuit that typically uses less than half the power of conventional drivers over its entire frequency range. It can also provide high peak sink and source currents of up to 8.5 A for large capacitive loads over 3 MHz and it is able to drive the gate capacitance of a MOSFET to more than +15 V to -10 V while being powered by a single rail 5 V supply.

An inductor has to be used in conjunction with the capacitance load (gate of the MOSFET). The value of the inductor depends on the size of the capacitance driven as well as the voltage swing needed across the capacitance. The principle of operation of the topology is that of a resonant circuit whereby the energy stored in the capacitor is recycled via the inductor and stored back in the capacitor but with the opposite polarity voltage [8]. Depending on the size of the inductor L, this circuit is capable of driving a capacitive load with a higher voltage than its own supply voltage.

Resonant Load Matching

Q-Matching [9] is a transducer image impedance transformation circuit that can be viewed as being a special case of series-parallel resonant load coupling (known in switched mode power inverter systems). Q-Matching replaces compensation inductor elements and the need for a matching transformer. Further, the system can be adjusted and optimized in-situ by varying capacitor values; which is much less time consuming than changing magnetic element component values. Q matching is inherently a filter which means than it can couple directly to switch mode amplifiers (without the need for an additional low pass filter or matching transformer) and it presents a very low source impedance (especially at high frequencies).

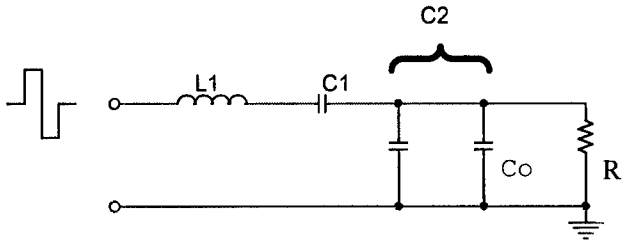

FIGURE 3. Q-matching filter network (showing a simplified equivalent of the transducer at resonance).

The Q-matching topology is shown in Fig. 3. C2 is the total value of the parallel capacitance, including the measured capacitance of the transducer. This configuration produces the frequency spectrum of Fig. 4 showing the fundamental frequency and some limited harmonic content (depending on the Q of the filter).

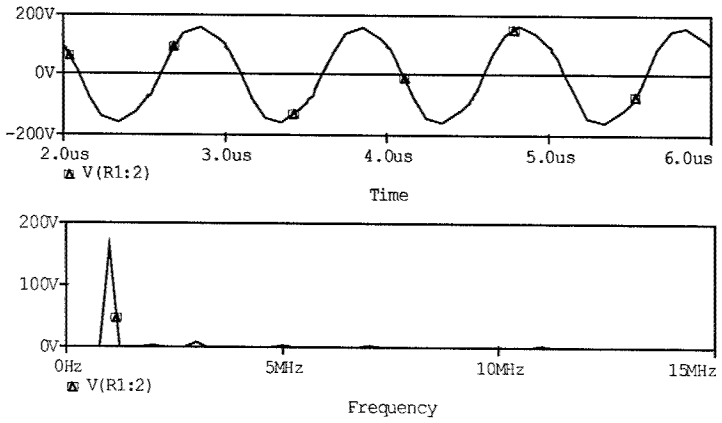

FIGURE 4. Sinusoid voltage across load and frequency spectrum for Q = 1.3 and a 1 MHz piezo load.

Choosing the *C1*, *C2* and *L1* component values carefully, the input current into the filter slightly lags the input voltage in phase, meaning that the impedance reflected to the midpoint of the inverter is slightly inductive (which is desirable for avoiding switching noise on the inverter) and it is possible to obtain a good sinusoidal excitation of the load.

EXPERIMENTAL RESULTS

Two prototype Class D HIFU power supply units were constructed using either IRFP460 or APT6025BLL MOSFETs. Loads were either a dummy resistive load, a purpose built 1.1 MHz nebulizer, or a 3.5 MHz HIFU concave transducer obtained from the University of Washington. Measured and calculated efficiencies corresponded at 94% for the topology. The energy recovery circuit dramatically reduced switching losses (leading to the high efficiencies).

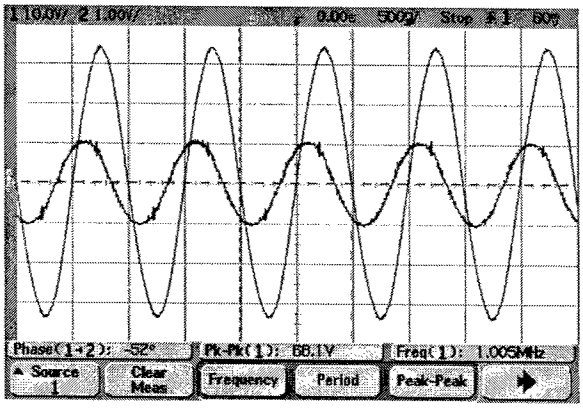

FIGURE 5. Output voltage (lagging) and current measured for a 1.1 MHz piezoelectric transducer.

Very little external inductance was required when driving the APT MOSFETs due to this device's internal construction and lead inductance. Power control was achieved by varying the inverter DC supply (duty cycle was optimum at 35%). Typical drive waveforms are shown in Fig. 5.

CONCLUSIONS

Switch-mode inverters hold potential for high efficiency power supplied for ultrasonic systems although high frequencies introduce several problems which have thus far limited research into this area. We have combined an energy recovery circuit and a resonant matching topology to overcome the high frequency switching losses and difficulties in driving piezoelectric loads. A Class D prototype has successfully driven two HIFU transducers and the unit is capable of delivering 200 W. This approach represents a practical solution for high-efficiency HIFU systems and offers cost, size and performance advantages over existing RF linear amplifiers.

REFERENCES

1. Kaczkowski, P., Keilman, G., Martin, R., Vaezy, S., Carter, S., Crum, L., "Engineering development of image guided therapy using high intensity focused ultrasound," Proceedings First International Workshop on the Application of High Intensity Focused Ultrasound (HIFU) in Medicine, Chonquing, China, 2001, 52-54.
2. Zhu, H., "Measurement of Ultrasonic Focusing Transducer and its Application in HIFU," Proceedings First International Workshop on the Application of High Intensity Focused Ultrasound (HIFU) in Medicine, Chonquing, China, 2001, 5-7.
3. Qian, X., "Research in HIFU tumor therapeutic instrument with multiple-element array," Proceedings First International Workshop on the Application of High Intensity Focused Ultrasound (HIFU) in Medicine, Chonquing, China, 2001, 58.
4. Wang, Z., Wu, F., Bai, J., Li, F., Du, Y., Xu, G., Wen, S., "The Concept of Biological Field and the Theraputic HIFU Dose," Proceedings First International Workshop on the Application of High Intensity Focused Ultrasound (HIFU) in Medicine, Chonquing, China, 2001, 61-64.
5. Mason, W.P., "Electromechanical Transducers and Wave Filters," Van Nostrand, Princeton, New Jersey, 1942.
6. Mortimer, B.J.P., Tapson, J., Davies, J., Du Bruin, T., "High Power Resonance Tracking Ultrasonic Amplifier using admittance Locking," *Ultrasonics International,* **39,** 257-261 (2001).
7. Abramov, O.V., "Sources of Ultrasonic Energy," in *High-Intensity Ultrasonics*, Gordon and Breach Science Publishers, 1998, 371-377.
8. de Vries, I.D.,"A Resonant Power MOSFET / IGBT Gate Driver," Applied Power Electronics Conference Proceedings, Dallas, Texas, March 2002.
9. Mortimer, B.J.P., Ensign, T., "High Power Sonar Amplifiers," SBIR Topic N01_034: Report, US Office of Naval Research, October 2001.

Investigation Of The Opacification Of High-Intensity Ultrasound-Induced Thermal Lesions In A Tissue-Mimicking Phantom

Misty L. Noble, Shahram Vaezy, and Lawrence A. Crum

Center for Industrial and Medical Ultrasound, Applied Physics Laboratory, Dept. of Bioengineering, University of Washington, Seattle, WA 98105, USA

Abstract. We have developed a transparent tissue-mimicking phantom ideal for studying High Intensity Focused Ultrasound (HIFU) applications. Opaque lesions are produced after applying HIFU in this phantom, and are believed to be caused by protein denaturation and protein aggregation. We have observed that lesions in the phantom would after a certain period of time. Spectral analysis was used to investigate both the opacification and its subsequent reversal.

INTRODUCTION

Dosimetry studies involving different kinds of heat therapy often require the use of a phantom in order to demonstrate and investigate lesion formation and its behavior. Traditionally, excised tissues have been used to study these biological effects. Tissues are generally opaque, which do not allow real-time observation of lesion development, and they contain inhomogeneities that lead to inconsistencies in lesion formation. A transparent homogeneous phantom with properties similar to tissues is ideal in performing dosimetry studies.

A tissue-mimicking phantom for high-intensity focused ultrasound (HIFU) and image-guided therapy applications has been developed and characterized [1]. The phantom is based on a polyacrylamide (PA) gel matrix, embedded with a protein Bovine Serum Albumin (BSA), which acts as a thermal indicator. The properties of the PA-BSA phantom can be adjusted to be similar to that of soft tissue. Table 1 lists some properties of the phantom compared to soft tissue, and water.

TABLE 1. Properties of PA-BSA Phantom, Soft Tissue, and Water.

Property	PA-BSA Phantom	Soft Tissue	Water
Density, ρ (kg/m^3)	1.044	1.065	1.000
Sound Speed, c (m/s)	1544	1549	1480
Attenuation Coefficient, α (dB/cm-MHz)	0.08-0.17	0.40	0.0022
Thermal Conductivity, K (W/m-°C)	0.70	0.50	0.60
Specific Heat, C_p (J/kg-°C)	5075	3600	4185

The PA-BSA phantom is transparent at room temperature, but turns opaque as temperature increases making it ideal for studying HIFU lesion formation [2]. At lower intensities, a uniform change in opacity of the PA-BSA phantom from transparent to a cloudy appearance can be observed. At higher HIFU intensities, significant bubble activity with accompanying popping sounds was noted. These observations may indicate that both thermal and mechanical effects of HIFU are involved in the formation of a focal lesion in the phantom. However, we have observed that these HIFU-induced lesions fade after a certain period of time as seen in Figure 1. One day after applying HIFU, the lesions were not as distinct. Mechanical lesions were observed to fade faster compared to their thermal counterparts.

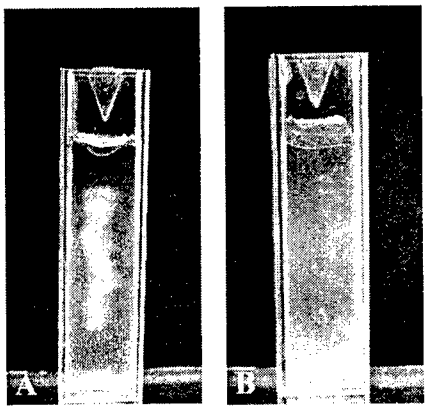

FIGURE 1. HIFU-induced thermal lesions in PA-BSA phantoms usually fade after a certain period of time. **A,** Lesions can be seen distinctly inside the transparent phantom immediately after application of HIFU. **B,** One day after HIFU application, lesions are not as distinct.

This study aims to investigate the opacification of HIFU-induced thermal lesions in the PA-BSA phantom and its subsequent reversal. Our goal is to have a better understanding of the features of the PA-BSA phantom, which could lead us to develop a more effective phantom for HIFU and image-guided therapy applications.

MATERIALS AND METHODS

Preparation Of PA-BSA Phantom

The properties of PA-BSA phantom can be modified by changing the concentration of the polymer in the gel matrix, and the amount of BSA in the solution. Details of the preparation are provided elsewhere [1]. Briefly, BSA was dissolved in distilled water, 1 M TRIS solution, and 40% (w/v) acrylamide solution. For this particular study, we have used 5% (w/v) BSA protein, and diluted the acrylamide solution to 7% (w/v). The solution was degassed for about half an hour prior to addition of catalyzing agents: 10% ammonium persulfate (APS), and N,N,N',N'-tetramethylethylenediamine

(TEMED). The mixture was transferred in clear plastic boxes for the calibration study, and in disposable cuvettes for the spectral analysis.

Determination Of HIFU Parameters

The HIFU transducer used was a single element, concave piezoelectric disk, with a frequency of 3.5-MHz, a diameter of 35-mm, and a focal length of 55-mm. The transducer was operating at approximately 56% efficiency.

A calibration curve was first obtained to determine the HIFU parameters involved in producing purely thermal lesions. HIFU was applied to the PA-BSA phantom at different intensities, and the time when the lesion starts to form, and the time when microbubbles first appear were recorded to determine the calibration curve.

Application Of HIFU

Figure 2 shows the set-up used for the study. A plastic cuvette, with two faces cut out, was used to hold the PA-BSA phantom while HIFU was being applied. The transducer was held by an X-Y-Z positioner, which was manually moved to relocate the focus. The entire set-up was placed inside a water tank. From the calibration curve, the suitable HIFU intensity and duration was chosen. HIFU was applied in 10-s bursts, with 2-s "off" time. An average of about 30 lesions (total HIFU "on" time of 300-s) were created for each sample for the absorbance studies mentioned below. Each lesion was spaced such that they overlap, or they are about 1-mm apart.

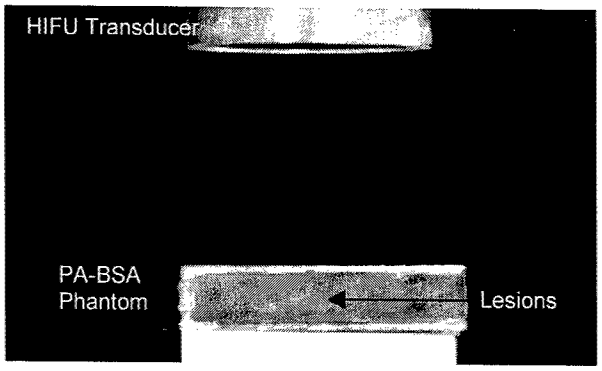

FIGURE 2. In a water tank, the transducer was positioned such that the HIFU focus is inside the PA-BSA phantom.

Absorbance Studies

To investigate the change in opacification of these HIFU-induced thermal lesions in the PA-BSA phantom, absorbance measurements were collected using a UV-visible spectrophotometer (UV-1601, Shimadzu, Columbia, MD). The background absorbance was obtained using distilled water. Prior to the application of HIFU, a baseline absorbance spectra for each of the samples used was recorded.

Measurements were collected immediately after the application of HIFU (0-Hr Post), and at different time points (0.5, 1, 1.5, 2, 2.5, 3, 3.5, 4, 5, 6, 24, and 48-Hr Post). The absorbance maximum of each spectrum was noted. The baseline absorbance was subtracted from each of the spectra to determine the change in absorbance maximum.

RESULTS

To determine the suitable HIFU parameters in producing purely thermal lesions, we looked at peak-to-peak input electrical voltages between 150 mV and 195 mV, with corresponding focal intensities of 2750 W/cm^2 and 4420 W/cm^2, respectively. The lesion start time and bubbling start time were plotted against the focal intensities as seen in Figure 3.

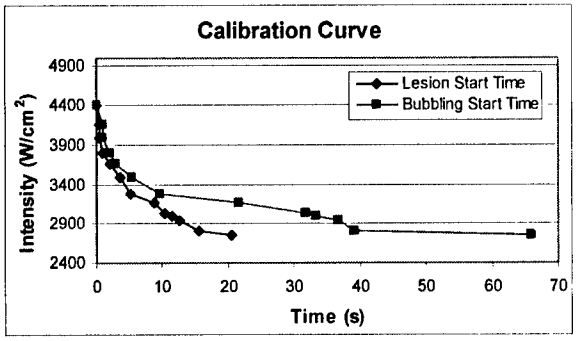

FIGURE 3. Plot of *in situ* intensities as a function of lesion start time, and bubbling start time.

Figure 4 shows the absorbance spectra of water, 5% BSA solution, PA-BSA phantom immediately before and immediately after application of HIFU. The BSA spectra revealed a maximum absorbance at 298 nm. A change in absorbance maxima before and after HIFU application in the PA-BSA phantom was observed.

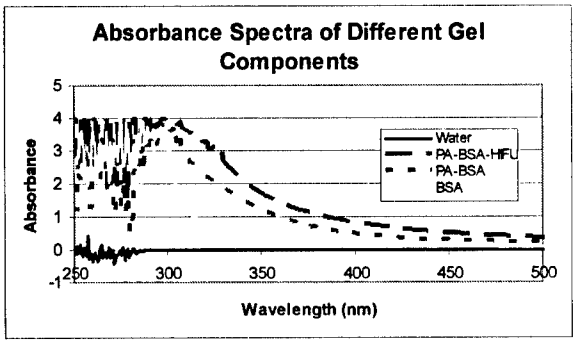

FIGURE 4. Absorbance spectra of water, 5% BSA solution, PA-BSA phantom, and PA-BSA phantom after HIFU application.

The application of HIFU to the transparent PA-BSA phantom produced opaque lesions that gradually reduced their opacity with time as seen in Figure 5. This observation was further supported by looking at absorbance spectra. A significant change in the absorbance spectra was observed immediately after application of HIFU. However, as time passed the peak absorbance gradually returned to the absorbance maximum seen before HIFU was applied to the PA-BSA phantom as seen in Figure 6.

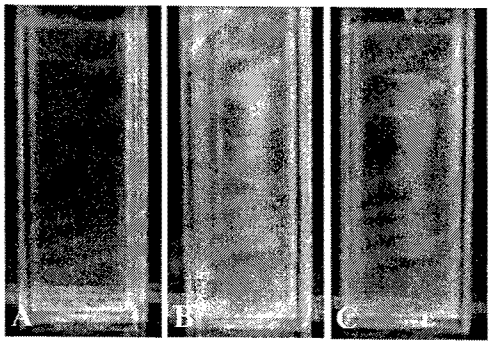

FIGURE 5. HIFU-induced thermal lesions in PA-BSA phantom. **A,** The phantom is transparent before applying HIFU. **B,** Opaque thermal lesions in the PA-BSA phantom were seen immediately after applying HIFU. **C,** One hour after applying HIFU, opacity of the thermal lesions was reduced in the PA-BSA phantom.

The change in absorbance maxima was determined by subtracting the wavelength where the peak was seen before HIFU was applied from the wavelength where the peak was seen after HIFU. The average change in absorbance maxima was plotted as a function of time as seen in Figure 7. Error bars indicate +/- one standard deviation.

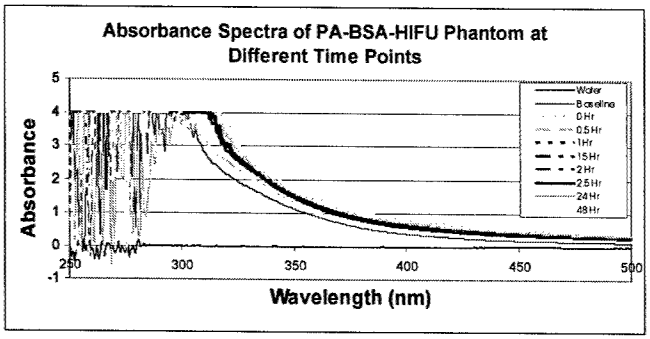

FIGURE 6. A representative plot of absorbance spectra of PA-BSA phantom after application of HIFU at different time points.

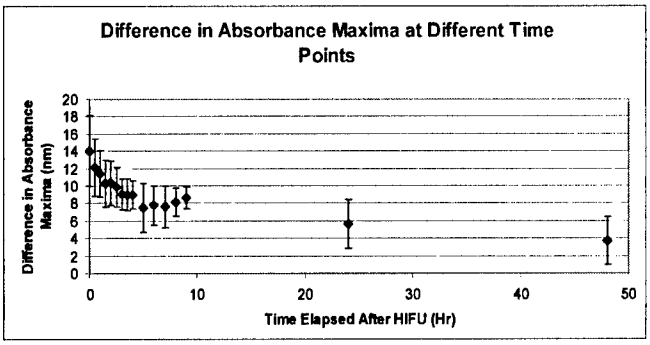

FIGURE 7. The average difference in absorbance maxima from the baseline was plotted as a function of time.

DISCUSSION

The development of this PA-BSA phantom has been essential in studying HIFU effects. The phantom possesses several important characteristics, which makes it an ideal phantom material for HIFU. First, it has acoustic properties similar to soft tissue. Secondly, it is optically transparent allowing real-time visualization of lesion formation. And lastly, it demonstrates a dramatic change in color, or opacity, when subjected to HIFU. The homogenous structure of the phantom allows for studying the thermal effects of HIFU in real-time without the complexities of nonlinear acoustics.

The opacification of the PA-BSA phantom due to HIFU application is thought to be attributed to protein denaturation, and protein aggregation. The amount of energy delivered at the focus when HIFU is applied increases the temperature to above 70 °C within seconds causing the BSA to denature, and as a result producing an opaque lesion. However, reversible unfolding of the BSA prevents permanent protein denaturation [3] allowing the thermal lesions to fade with time. The gel structure of the PA-BSA phantom enables suspended particles, like the BSA, to move within the matrix. The protein aggregates resulting from HIFU application will gradually diffuse into the surrounding area, consequently reducing the opacity of the lesion [4].

This study showed by spectral analysis the reversal of the opacification of HIFU-induced thermal lesions. There are several factors limiting the accuracy of this study. The spectrophotometer would only allow absorbance measurements of up to 4.000. The gel concentration had to be kept constant, so dilution was not an option. Also, the amount of scattering in the samples could have contributed to the absorbance saturation. The region of interest (λ = 280-350 nm) picked up interference, and as a result, was not well-defined. Perhaps, the use of ultraviolet (UV) cuvettes will allow noise reduction

Further analysis of this PA-BSA phantom will enable us to improve and develop a more accurate HIFU phantom allowing us to study lesion formation behavior, and other HIFU biological effects. The PA-BSA phantom is not only a laboratory tool to demonstrate HIFU lesion formation, but it can also be a potential aid in HIFU treatment planning.

ACKNOWLEDGMENTS

We gratefully acknowledge support from DARPA (#N00014-96-1-0630), NIH (#HL64208-02), and NSF (#BES-0002932).

REFERENCES

1. Lafon, C., Kaczkowski, P.J., Noble, M.L., Sapozhnikov, O.A., Yuen, J.C., Crum, L.A., and Vaezy, S., *Ultrasound Med Biol,* Submitted (2002).
2. Yuen, J.C., Noble, M.L., Lafon, C., Wyzgala, M., Bailey, M.R., Kaczkowski, P.J., Crum, L.A., and Vaezy, S., *Ultrasound Med Biol,* Submitted (2002).
3. Pico, G.A. *Int J Biol Macromol,* **20**, 63-73 (1997).
4. Benedek, G.B. *CIBA Found Symp,* **106**, 237-47 (1984).

Polyacrylamide Gel As An Acoustic Coupling Medium For Focused Ultrasound Therapy

Adrian Prokop, Shahram Vaezy, Misty Noble, Roy Martin

Center for Industrial and Medical Ultrasound, Applied Physics Laboratory
Department of Bioengineering
University of Washington, Seattle WA

Abstract. A hydrogel acoustic coupling medium was investigated as a practical alternative to water for clinical applications of focused ultrasound therapy. The gel's high water content provides favorable acoustic properties, while its cross-linked, polymer structure allows the material to be formed into a durable object with a specific shape. Material characterization and functional testing of polyacrylamide gel couplers was performed. Acoustic, bulk, and thermal properties were measured. Conical couplers were designed to fit a 3.5-MHz, spherically concave HIFU transducer. Functional tests included schlieren imaging, power efficiency measurements, field maps of focal region, failure tests, and in-vivo hemostasis experiments. Polyacrylamide was shown to have acoustic properties that varied linearly with acrylamide concentration. Attenuation, sound speed, and impedance ranged from 0.08 to 0.14-dB/cm at 1-MHz, 1546 to 1595-m/s, and 1.58 to 1.68-Mrayl, respectively. Thermal conductivity and heat capacity were found to be 0.84-W/m/°C and 6500-J/kg/°C, respectively. An in-vivo hemostasis experiment in a sheep model demonstrated that the polyacrylamide-coupled transducer was capable of inducing hemostasis in actively bleeding splenic and hepatic incisions. The feasibility of extracorporeal HIFU therapy without producing skin burns has been demonstrated by using impedance-matched gel couplers. Moderate material costs and straightforward manufacturing and storage methods allow for the possibility of inexpensive, custom-designed, disposable HIFU coupling devices.

INTRODUCTION

An important component in any type of ultrasound therapy system is the mechanism for coupling the acoustic energy into the patient. The acoustic coupling device provides an efficient path for ultrasound propagation from the transducer to the tissue. The ideal coupler is a homogeneous medium that has low attenuation and acoustic impedance similar to that of the tissue being treated. The goal of this research was to characterize and develop a disposable, hydrogel, acoustic coupling device suitable for clinical therapy applications of high intensity focused ultrasound (HIFU).

Previous studies have shown hydrogels to be efficient coupling media for both diagnostic and therapeutic ultrasound [1,2,3]. Hydrogels are hydrophilic, cross-linked, polymer networks that are swollen in water. Unlike the ultrasound transmission gels typically used for diagnostic scans, hydrogels have mechanical properties similar to rubber, and can be formed into rigid, three-dimensional shapes. Since hydrogels consist mostly of water, they inherently have low attenuation and acoustic impedance similar to tissue. The additional advantages that they have relatively low material

costs, and can be easily mounted to an ultrasound transducer makes them attractive candidates as disposable acoustic couplers for HIFU devices.

Polyacrylamide (PA), a hydrogel, was investigated as a potential acoustic coupler for HIFU devices. The structure and properties of PA have been extensively researched for the past 30 years [4,5]. It can have very high water content, ranging from 70% to greater than 90% water by weight, and it can be prepared relatively easily and quickly at room temperature. The gel's physical properties, such as density and stiffness, can be varied in a straightforward manner simply by changing the overall concentration of acrylamide monomer. This study involved the material characterization and functional testing of PA gel as an acoustic coupler. While much of the results can be applied to HIFU therapy in general, this work focused on the specific application of an intra-operative hemostasis device, which targets bleeding regions close to the surface of the tissue.

MATERIALS AND METHODS

Material Characterization

Acrylamide concentrations used in this study ranged from 10% to 20% weight in volume (w/v). The percent concentration was determined by the ratio of the mass of total acrylamide to the volume of pre-polymerized solution. An aqueous solution of 40% w/v acrylamide with a 19:1 monomer to cross-linker ratio (LIQUI-GEL; *ICN Biomedicals, Aurora, Ohio*) was used to prepare the gels. The hydrogels were formed in solution by free radical, chain-reaction polymerization. The initiated solution was transferred to a cylindrical mold, which was held upright so that the top face of the gel formed parallel to the bottom face. Each gel was allowed to polymerize for approximately 30 minutes. The resulting cylindrical gels were 2.5-cm in diameter and approximately 3-cm in height (Fig. 1). The gels were either tested within one hour after polymerization, or stored in vacuum-sealed, plastic bags to avoid dehydration if left in air, or swelling if placed in water.

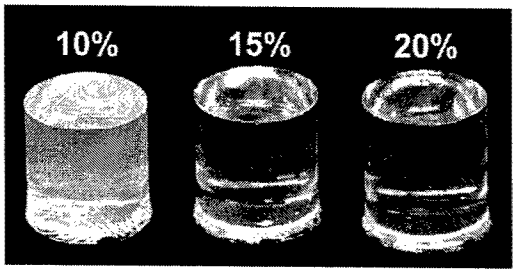

FIGURE 1. 10% to 20% w/v PA gel test plugs. Stiffness and transparency increase with acrylamide concentration.

Bulk Properties

Water content was determined by comparing the mass of the hydrated gel immediately after polymerization to the mass of the dehydrated gel. Six gel samples were tested for each concentration. Density was calculated using the measured mass (electronic scale) and volume (water-displacement technique). Seven gel samples were tested for each concentration.

Acoustic Properties

Sound speed, c (m/s), acoustic impedance, Z (Mrayl), and attenuation coefficient, α (dB/cm), were measured for gels of five different concentrations: 10%, 12.5%, 15%, 17.5%, and 20%. For each concentration, seven gel samples were tested at 25°C. In addition, acoustic properties were measured for one 15% acrylamide gel sample at different temperatures ranging from 23° C to 45° C. A pulse transmission technique was used to measure the attenuation coefficient and sound speed in PA. Calculations were based on the well-known substitution method, where two acoustic paths were compared [6]. The sample path contained the gel sample with approximately two centimeters of water on either side, and the reference path contained only water [7]. The attenuation coefficient was measured at frequencies of 1 to 5-MHz.

Thermal Properties

The thermal conductivity, k (W/m/° C), and specific heat capacity, C_p (J/kg/° C), of PA were measured by monitoring the thermal dissipation of a heat impulse. A heating wire was pulled taut through the center of a custom-made measurement cell. The initiated polyacrylamide solution was poured into the measurement cell and allowed to polymerize. Needle thermocouples were placed within the gel at precise distances from the heating wire. An equation based on Fourier's law of heat conduction in cylindrical coordinates was derived and used to describe the radial temperature distribution at some time after heating. Thermal properties were measured for three different acrylamide concentrations: 10%, 15%, and 20%.

Functional Testing

Conical gel couplers, designed to fit to a specific transducer, were produced using a custom-built mold (Fig. 2). A 3.5-MHz, spherically concave, single element, HIFU transducer with a 5.5-cm focal length and a 3.5-cm aperture diameter were used for these tests. The gel cones had spherically convex bases that matched the curvature of the transducer. Conical plastic housings held the gel couplers to the transducer (Fig. 2). Full-length, flat tip cones were 4.9-cm long, which placed the center of the HIFU focus 0.6-cm from the tip. The tip shape and height were varied to place the focus at different locations from the tip. For the majority of the tests, convex tips 0.3-cm in height were used, which placed the center of the HIFU focus 0.3-cm from the tip.

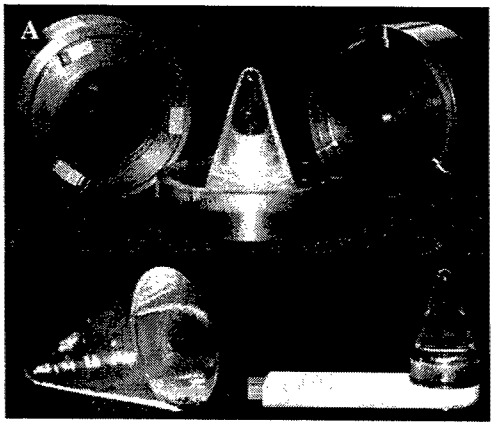

FIGURE 2. A: Top: Three-part gel mold with polymerized PA gel in bottom portion of mold. Bottom Left: View of conical gel coupler laying on its side. Bottom Right: Gel coupler resting on face of HIFU transducer. B: Assembly diagram of PA coupler and transducer.

Schlieren Imaging

Four 15% gel cones of different shapes were tested: 2-cm truncated cone; 3-cm truncated cone; full-length cone with flat tip; and full-length gel cone with convex rounded tip.

Power Efficiency

Overall power efficiency, $E_{Overall}$, of the transducer-coupler device was defined as the ratio of output acoustic power delivered to a water bath, to input electrical power supplied to the transducer. $E_{Overall}$ was defined as:

$$E_{Overall} = E_{Transducer} \times E_{Coupler} \ , \qquad (1)$$

where $E_{Transducer}$ is the transducer efficiency, and $E_{Coupler}$ is the coupler efficiency. $E_{Transducer}$ was determined by measuring output acoustic power without any coupler attached. The efficiency of the coupler was then calculated from equation 1. For comparison, a water-filled coupling cone, with the same dimensions as the full-length gel couplers, was also tested. A reflecting force balance (UPM-DT-IOE; *Ohmic Instruments Co., Easton, MD*) was used to measure the output acoustic power for various input electrical power levels. Efficiency was measured for full-length, convex-tip, gel couplers with different concentrations. These data were compared to theoretical efficiency based on the attenuation of the gel, $E_{Coupler\_Theory}$, calculated using the following equation:

$$E_{Coupler\_Theory} = \exp(-2\alpha d) \, , \qquad (2)$$

where α (nepers/cm) was the measured attenuation coefficient of the gel at 3.5-MHz, and d (5.2-cm) was the length of the gel.

In-Vivo Testing

A total of four intra-operative hemostasis treatments were performed, two on the spleen and two on the liver of an anesthetized sheep. In each case, an incision about 3-cm long and 0.5-cm deep was made. A new, full-length, convex tip, gel cone was used for each treatment. Immediately after injury, the tip of the gel cone was scanned along the bleeding incision site, using 5 to 10-sec intervals of HIFU application. A focal intensity of approximately 2,000-W/cm^2 was used. The treatment time to hemostasis was recorded. Any change in or damage to the gel coupler during treatment was noted.

RESULTS

Material Characterization

Bulk Properties

Water content of PA decreased from 87% to 76% as a linear function of increasing acrylamide concentration. The density was found to be slightly greater than the density of water, increasing from 1.02 to 1.05-g/ml as a linear function of increasing concentration.

Acoustic Properties

The acoustic properties increased as linear functions of increasing acrylamide concentration. Sound speed ranged from 1546 to 1595-m/s (Fig. 3.A). Impedance ranged from 1.58 to 1.68-Mrayl (Fig. 3.B). Attenuation ranged from 0.08 to 0.14-dB/cm at 1-MHz (Fig. 4.A). The attenuation coefficient was also shown to have a quadratic dependence on frequency (Fig. 4.B). Sound speed and impedance were shown to increase with temperature, while attenuation was shown to decrease with temperature.

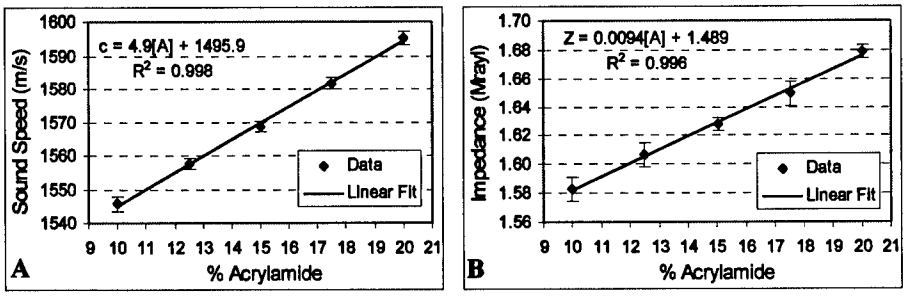

FIGURE 3. A: Sound speed in PA gel (AVG ± SD) vs. concentration, with linear fit to data (N = 7). B: Acoustic impedance of PA gel (AVG ± SD) vs. concentration, with linear fit to data (N = 7).

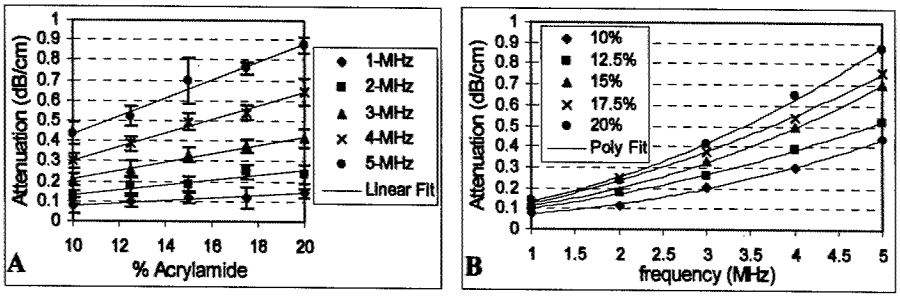

FIGURE 4. A: Attenuation coefficient of PA gel (AVG ± SD) vs. concentration at frequencies of 1 to 5-MHz (N = 7). B: Attenuation coefficient (AVG) vs. frequency for different concentrations.

Thermal Properties

Thermal conductivity and heat capacity did not vary with concentration. The overall average thermal conductivity and heat capacity of PA gel, 0.84-W/m/° C and 6470-J/kg/° C respectively, were slightly higher than the corresponding values for water.

Functional Testing

Schlieren Imaging

The schlieren images showed that the HIFU field was essentially unchanged by the presence of the various gel couplers. Fig. 5 shows the ultrasound fields produced by the different couplers.

Power Efficiency

Table 1 lists the measured and theoretical efficiency for the different couplers. The transducer efficiency was measured at 56%. Attaching the 5.2-cm gel cone to the transducer dropped the overall efficiency to between 22% and 29%, for 20% and 10% acrylamide concentration, respectively. Normalizing the overall efficiency to the transducer efficiency showed the gel cones to have coupler efficiencies from 40% to 51%. For comparison, the coupler efficiency of the water-filled cone was measured to be 65%. The measured coupler efficiency of the gel cone was 14% to 23% less than its calculated theoretical efficiency.

TABLE 1. Power efficiency at 3.5-MHz of various full-length couplers.

Coupler Type	Measured Overall Efficiency (%)	Measured Coupler Efficiency (%)	Theoretical Coupler Efficiency (%)
No Coupler	55.8	100	100
Water-filled Cone	36.4	65.3	100
10% PA 5.2-cm	28.6	51.3	74.2
15% PA 5.2-cm	26.3	47.3	61.7
20% PA 5.2-cm	22.4	40.1	53.8

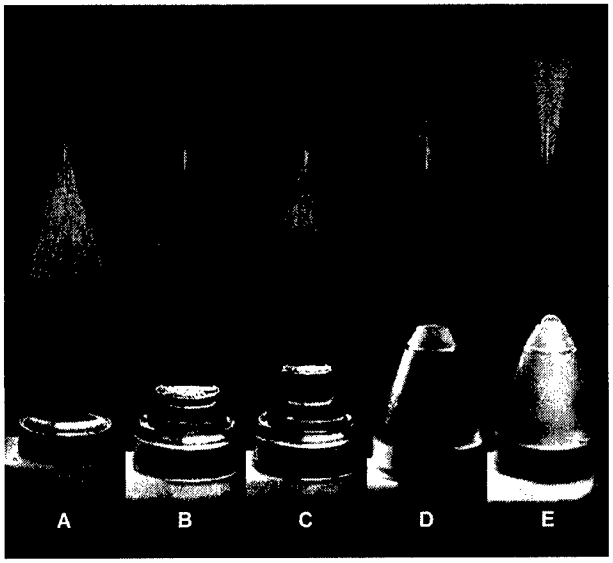

FIGURE 5. Schlieren images of ultrasound field produced by 3.5-MHz spherically concave transducer (A) without coupler, (B) with 2-cm truncated gel cone, (C) with 3-cm truncated gel cone, (D) with full-length, flat tip gel cone, and (E) with full-length, convex tip gel cone. Approximately 35-W input electrical power, and 1000 to 2000-W/cm^2 focal intensity.

In-Vivo Testing

For the two spleen injuries, complete hemostasis was achieved after 41-sec and 39-sec of treatment. For the liver injuries, complete hemostasis was achieved in only one of the cases, which occurred after 68-sec. For the other case, major hemostasis occurred after 61-sec. When the gel tips were analyzed after the experiment, varying degrees of blood adhesion, erosion, and pitting were observed (Fig. 6.A, minimal damage; Fig. 6.B, significant damage). In addition, blood was observed to have penetrated into the interior of the gel tip.

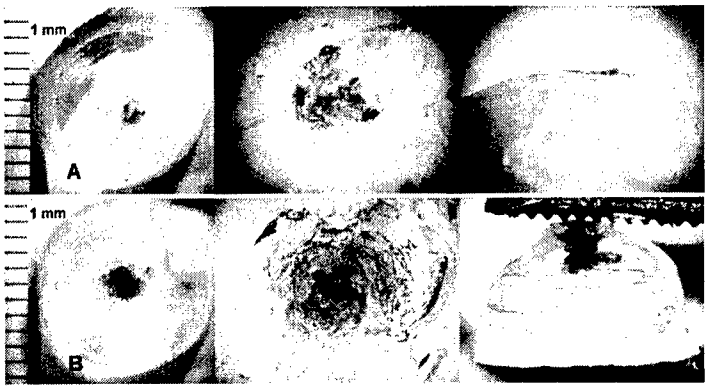

FIGURE 6. Gel cone tips after in-vivo hemostasis experiment. A: Left & Middle: Top view of gel tip; minimal damage to gel. Right: Side view of gel tip. B: Left & Middle: Top view of gel tip; significant amount of erosion and pitting. Right: Side view of gel tip; blood has penetrated into interior of gel.

DISCUSSION

As a result of the gel's high water content, the acoustic properties of PA were found to be similar to those for water. Attenuation, sound speed, and impedance were found to increase as linear functions of increasing acrylamide concentration. The linear dependence allows for straightforward modification of the gel's acoustic properties simply by varying the monomer concentration. This property lends itself naturally to the application of impedance matching of the coupler to a particular type of tissue. This technique has been experimentally demonstrated in in-vivo transabdominal treatments to minimize the occurrence of skin burns caused by reflections and standing waves at the coupler-tissue interface [8].

The thermal conductivity and heat capacity of PA were found to be similar to, although slightly higher than, the corresponding values for water, and did not depend on acrylamide concentration. These properties are important when considering heating effects in the device. During HIFU treatment, heat is generated at the transducer crystal and within the gel coupler. Elevated transducer temperatures can reduce its efficiency and eventually lead to irreversible damage to the crystal. Although thermal conductivity of the gel is about two times greater than most plastics, PA is a relatively poor conductor of heat. In addition, it does not support convection like water does. Preliminary measurements (not reported in this paper) showed that heat dissipation from the front of the transducer was slower for a PA coupler than for a water-filled coupler. Cooling of the transducer during HIFU operation may be a critical issue. Heating of the gel coupler was observed during the hemostasis experiment. Since the acoustic properties of the material were shown to be temperature dependent, changes in coupling efficiency could occur as a result of heating. A next step in this research would be to model and experimentally measure the temperature distributions within the gel coupler during HIFU treatment.

Due to its low attenuation, the PA coupler was found to have good power transfer efficiency, which decreased as a function of increasing concentration. The measured efficiency was found to be lower than the theoretical efficiency that was calculated based on its attenuation coefficient alone. This result, along with the fact that the water-filled cone with negligible attenuation had efficiency less than 100%, suggests that power was lost in the couplers due to mechanisms other than attenuation. The reduction in efficiency may be related to the geometry or boundary of the cone. Nevertheless, attenuation in the gel is largely responsible for output power loss. Efficiency could potentially be improved by using shorter coupling cones. A transducer having short focal distance, thus requiring a short coupler, might be more suited for superficial HIFU procedures.

The in-vivo hemostasis experiment demonstrated that a HIFU transducer fitted with a PA coupler was capable of inducing hemostasis in actively bleeding splenic and hepatic incisions. In three out of four cases complete hemostasis was achieved. In addition, a paste was generated during treatment in these cases. The production of this homogenized tissue has been observed in previous HIFU hemostasis studies, and is capable of plugging the incision, which helps stop bleeding [9]. For the case in which complete hemostasis was not achieved, slow bleeding persisted despite additional ultrasound treatments. The same scenario has been observed in previous hemostasis

studies, where excessive treatment of injured tissue can increase stiffness and change the tissue properties in such a way that they no longer support HIFU-induced hemostasis. Surgical technique plays an important role in HIFU hemostasis procedures.

The hemostasis experiment also revealed several limitations of the full-length PA coupler. The tips of the cones sustained various degrees of damage. In two of the cases, damage was minor, consisting of erosion on the surface of the coupler tip. These markings may have resulted from abrasion due to the tip moving across the tissue, and not necessarily from HIFU-related effects. In the cases where damage to the coupler was more significant, in the form of pitting in the tip, HIFU was likely a major cause. One possibility is that the high acoustic intensity at the focus induced cavitation in the blood. Collapsing bubbles at the surface of the coupler tip might have created jets of fluid that impacted the polymer gel. Another possibility is that a large enough portion of the focal region overlapped the coupler tip to cause damage. The extreme temperatures and pressures associated with the high focal intensity may have melted or ablated regions of the polymer matrix. It should be noted, however, that despite the damage sustained by the gel tips, no noticeable degradation in performance was observed. The wetness of the treatment region may have helped provide additional coupling. The fact that blood had penetrated into the tips of the damaged couplers indicates that blood filled the cavity region during treatment.

With the potential medical applications for HIFU continuing to emerge, the need for more efficient, yet more practical, devices will increase. Although many components in ultrasound systems work well in research or industrial environments, they are not necessarily suited for a medical environment. As a result of certain, practical limitations in our own ultrasound therapy devices, we investigated the use of an alternative acoustic coupling medium. This study has shown that PA gel is a promising coupling material for HIFU therapy applications. The gel's high water content provides favorable acoustic properties, while its cross-linked, polymer structure allows the material to be formed into a durable object having a specific shape. Moderate material costs and straightforward manufacturing methods allow for the possibility of inexpensive, custom-designed, disposable HIFU coupling devices.

REFERENCES

1. Hayakawa, K., Takeda, S., Kawabe, K., Shimura, T., *Ultrason Symp*, 969-972 (1989).
2. Klucinec, B., Scheidler, M., Denegar, C., Domholdt, E., Burgess, S., *Physical Therapy*, **80**, 469-476 (2000).
3. Young, S.R., Dyson, M., *Ultrasonics*, **28**, 175-180 (1990).
4. Furukawa, H., *J Molec Stuct*, 11-19 (2000).
5. Tanaka, T., *Polymer*, **20**, 1404-1412 (1979).
6. Madsen, E.L., *J Ultrasound Med*, **18**, 615-631 (1999).
7. Keshavarz,i A., Vaezy, S., Kaczkowski, P., et al., *J Ultrasound Med*, **20**, 473-480 (2001).
8. Vaezy, S., Martin, R., Kaczkowski, P., et al., "Hemostasis and Tumor Treatment Using High Intensity Focused Ultrasound: Experimental Investigations and Device Development," First International Workshop on the Application of High Intensity Focused Ultrasound (HIFU) in Medicine Proceedings, 2001, 46.
9. Vaezy, S., Martin, R., Keilman, G., et al., *J Trauma*, **47**, 521-525 (1999).

Ocular Drug Delivery Using Ultrasound

Vesna Zderic[1,2], John I. Clark[3], Roy W. Martin[1,2], and Shahram Vaezy[1,2]

[1]*Center for Industrial and Medical Ultrasound, Applied Physics Laboratory, University of Washington, Seattle, WA 98105, USA*
[2]*Department of Bioengineering, University of Washington*
[3]*Department of Biological Structure, University of Washington*

Abstract. Our objective has been to explore whether ultrasound can provide the enhancement in transcorneal drug delivery without causing damage to the eye tissues. We reported previously that 20 kHz ultrasound at I_{SATA} of 2 W/cm^2 applied for 60 min produced up to 4 times increase in the corneal permeability of rabbit cornea *in vitro*. In this study, we investigated the morphological changes induced in the cornea after the application of 20 kHz ultrasound. The damage was observed in all layers of the corneal epithelium using light and transmission electron microscopy. No gross damage appeared to be present in the stroma. It appeared that ultrasound application at 20 kHz may not be an optimal choice in transcorneal drug delivery. The application of 880 kHz ultrasound at 0.4 W/cm^2 for 5 min caused 4 times increase in the corneal permeability for fluorescein sodium in rabbit cornea *in vitro*. Future research will focus on the exploration of the ultrasound enhancement of transcorneal drug delivery at medium frequencies (400-900 kHz).

INTRODUCTION

Delivery of drugs into the eye for treatment of different ocular diseases is a significant challenge. Systemic drug delivery is inefficient due to the different eye-blood barriers [1]. The cornea is the dominant route for penetration of topically applied drugs. However, the cornea also acts as a biological barrier and usually only 1% of the drug can penetrate into the eye [2,3]. If the corneal permeability is increased, more of the drug can pass through, and, subsequently, a smaller amount of the drug may be used to achieve therapeutic concentrations inside the eye while reducing the chance of unwanted systemic effects.

The barrier properties of the cornea have been shown to be modified by the application of ultrasound [4,5,6]. Ultrasound at frequencies of 470-880 kHz and intensities of 0.2-0.3 W/cm^2 applied for 5 min in a continuous mode produced up to 10 times increase in the corneal permeability in a rabbit model, *in vivo* [6,7].

The enhancement of drug delivery through the cornea by 880 kHz ultrasound (phonophoresis) has been used successfully for the last 40 years in the treatment of eye diseases in Russia and the USSR [4,5,8,9]. The diseases of the anterior as well as the posterior regions of the eye have been treated. For example, phonophoresis was used in the treatment of keratitis and corneal burns [9,10], and the combination of phonophoresis and iontophoresis has been used in the treatement of chorneoretinal dystrophy [5].

The goal of our research project has been to explore whether ultrasound can provide the enhancement of penetration of topically applied drugs into the eye without causing damage to the eye tissues. We reported previously that 20 kHz ultrasound applied at I_{SAPA} of 14 W/cm^2 (I_{SATA} of 2 W/cm^2) for 60 min produced up to 4 times increase in the corneal permeability to glaucoma drugs of different lipophilicity (atenolol, carteolol, timolol, and betaxolol) in a rabbit model, *in vitro* [11]. In this study, we investigated the effects of 20 kHz ultrasound in the cornea using light and electron microscopy.

When experiments with 20 kHz ultrasound were being performed, we found USSR and Russian publications on using ultrasound at 470-880 kHz for the enhancement of drug delivery through the cornea. It was also found that an ultrasound instrument for transcorneal drug delivery is commercially available in the Russian Federation (UZT-1.04, Electrical and Medical Apparatus, Moscow). The instrument was obtained and used to perform preliminary experiments with 880 kHz ultrasound.

MATERIALS AND METHODS

Application Of 20 kHz Ultrasound

Eyes of the New Zealand albino rabbits were obtained within 30 min of euthanasia. The eyes were kept in saline at 4°C until the experiment (within 10 h of sacrifice). The cornea was placed in a vertical diffusion cell (PermeGear, Hellertown, PA). The receiver compartment was filled with a phosphate-buffered saline and the donor compartment was filled with a drug solution. The ultrasound transducer was positioned at 0.5 cm distance from the cornea. Ultrasound at 20 kHz was applied with I_{SAPA} of 14 W/cm^2 (I_{SATA} of 2 W/cm^2) and exposure duration of 60 minutes.

The corneas were prepared using the protocol for sample preparation for transmission electron microscopy (TEM) observations. The corneas were fixed in Karnovsky half-strength solution, postfixed in osmium tetroxide, stained with uranyl acetate, passed through alcohol series, and embedded in Spurr Epoxy. Semithin sections (1 μm) of the cornea were stained with Richard's stain (methylene blue/azure II) and observed with light microscopy. Thin sections (~ 100 nm) were post-stained with uranyl acetate and lead citrate and observed with the Phillips CM 100 TEM.

Application Of 880 kHz Ultrasound

The instrument for transcorneal drug delivery (UZT-1.04) was characterized with the radiation force balance and hydrophone measurements (Figure 1). The instrument works at 880 kHz and has control panel settings of 0.05, 0.2, 0.4, 0.7 and 1 W/cm^2. The actual ultrasound intensity was measured to be approximately 40% of the corresponding intensity written on the control panel. UZT-1.04 has a non-focused transducer with the diameter (d) of 1.13 cm. The near-field far-field transition distance (d_{FF}) was calculated to be 1.9 cm.

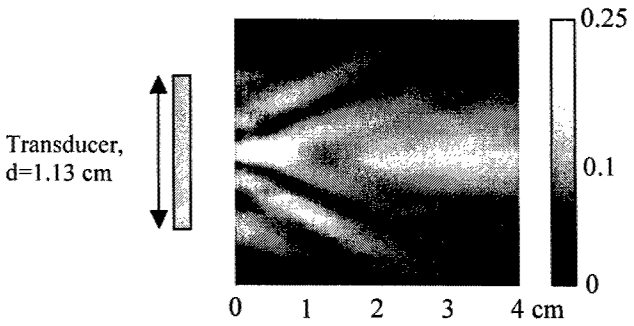

FIGURE 1. Beam plot of UZT-1.04 at intensity of 0.4 W/cm^2 (linear scale). The intensity maximum observed in the near field of the transducer was likely an artifact.

Fluorescein Sodium

We explored the efficiency of UZT-1.04 in increasing the corneal permeability for fluorescein sodium. Fluorescein sodium, a hydrophilic dye with a molecular weight of 376 Daltons, can be used as a model for small hydrophilic drugs for which the permeability of the cornea is low [2]. Fluorescein sodium (Sigma, St. Louis, MO) was used to make 0.25% solution in Dulbecco phosphate buffered saline (DPBS, D6650, Sigma) (pH 7.3). The solution was kept in a dark place at room temperature until the experiment.

Storage Medium For Cornea

It was reported previously that superficial layers of the epithelium were damaged when rabbit corneas were exposed to saline for 4 h *in vitro* [12]. In our experiments with 20 kHz ultrasound, eyes were kept in saline for up to 10 h and saline storage may have caused the epithelial damage and the change in barrier properties of the cornea. We investigated the influence of storage medium on the corneal permeability in a rabbit model *in vitro*. It appeared that the corneal permeability to fluorescein sodium was 8 times lower when DPBS was used as a storage medium instead of saline. Therefore, DPBS was used as a storage medium in our subsequent experiments with 880 kHz ultrasound.

Experimental Procedure

The rabbit eyes were enucleated within 15 minutes of euthanasia, placed in DPBS, and kept in the refrigerator at 4° C until the experiment (within 4 h of sacrifice). The eyes were examined and those with the corneal damage were discarded. The cornea was dissected on a dental wax sheet and placed between the donor and receiver compartment of a diffusion cell such that the epithelial layer was facing the donor compartment (Figure 2). A vertical diffusion cell (PermeGear), made of borosilicate glass, with an orifice diameter of 1.13 cm was used. The receiver compartment was filled with DPBS and the donor compartment was filled with the fluorescein sodium

solution in DPBS. The cornea was exposed to the dye solution for 60 min in both control and treatment experiments. The receiver compartment was stirred at 700 rpm using a magnetic stir bar.

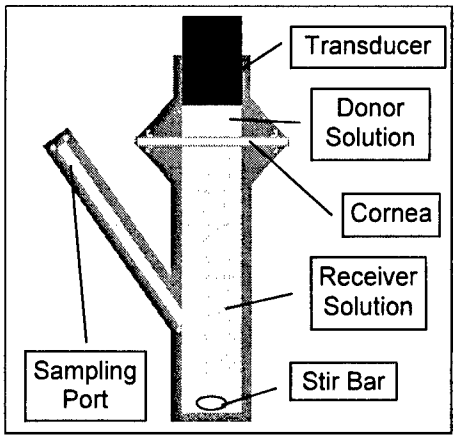

FIGURE 2. *In vitro* measurements in diffusion cell. The diameter of the transducer tip is 1.13 cm.

Ultrasound was applied at 0.4 W/cm^2 for 5 min. The distance between the transducer and cornea was 0.3 cm or 1.3 cm. Ultrasound application started immediately after the dye solution was placed in the donor compartment. After the ultrasound application, the diffusion cell was placed in the water bath with an immersion circulator (Model 1112, VWR, West Chester, PA). The cornea was kept at a temperature of approximately 34° C, corresponding to the physiological temperature of the cornea [13]. In the control experiments, the donor compartment was filled with the dye solution, the diffusion cell was placed in the water bath, and the cornea was kept at the temperature of 34° C.

After 60 min of the dye exposure, the receiver compartment solution was sampled and the solution absorbance was measured with an UV-visible spectrophotometer (UV-1601, Shimadzu, Columbia, MD). Fluorescein sodium has an absorbance maximum at 490 nm. The calibration curve of the fluorescein sodium concentration vs. absorbance was obtained, and was used to calculate the dye concentration in the receiver compartment. The increase in the permeability of the cornea was approximated as the ratio of the receiver compartment concentration in the treatment and control cases [11].

RESULTS AND DISCUSION

Application Of 20 kHz Ultrasound

Ultrasound application for 60 min at I_{SAPA} of 14 W/cm^2 (I_{SATA} of 2 W/cm^2) produced significant disorganization of the corneal epithelium in rabbit model, *in vitro* (Figures 3, 4, and 5). The surface layers of the epithelium were mostly absent and the inner layers lost its compact structure. The membranes of epithelial cells were

ruptured, cells were swollen due to hydration, and cell nuclei were also swollen. The necrotic cells could be easily distinguished from the viable cells by their increased electron transparency, i.e. lighter color (Figure 4a). No gross damage appeared to be present in the stroma (Figure 3a). Endothelium was absent in both control and treated samples likely due to sample processing artifacts, and therefore no conclusion on the ultrasound effect on the endothelium could be obtained. The control cornea is shown in Figures 3b and 5b. Corneal disorganization was likely caused by ultrasound-induced cavitation [14]. The disorganization and damage of the cornea may explain the observed enhancement in the drug delivery.

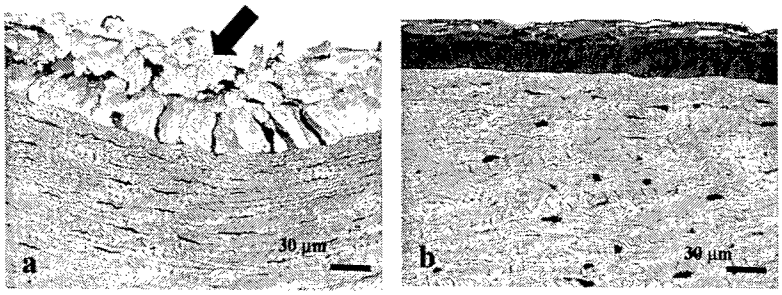

FIGURE 3. Light microscopy observations. a) Disorganization of the epithelium after 60 minutes of ultrasound exposure (20 kHz, I_{SAPA} of 14 W/cm^2) (arrow). b) Control cornea.

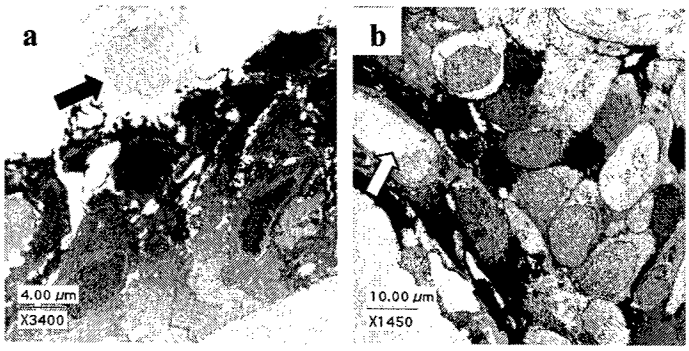

FIGURE 4. TEM observations. Epithelial damage after 60 minutes of ultrasound exposure (20 kHz, I_{SAPA} of 14 W/cm^2). a) The epithelial cells are disorganized. Necrotic cell with increased electron transparency (arrow). b) Rupture in the outer layer of epithelium (arrow).

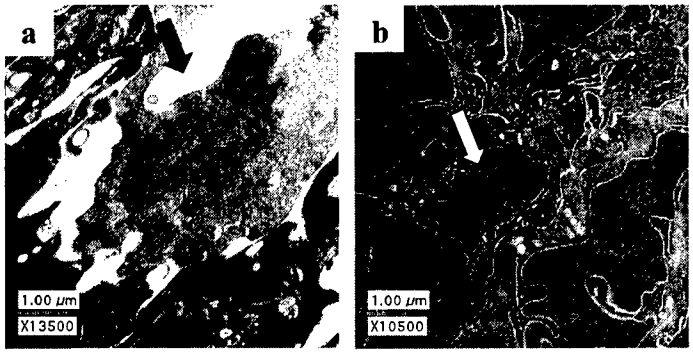

FIGURE 5. TEM observations. a) Damaged epithelial cell observed at higher magnification (20 kHz, I_{SAPA} of 14 W/cm^2, exposure of 60 min). Voids surrounding the nucleus of the ruptured cell (arrow). b) Epithelium of the control cornea. Cell nucleus (arrow).

Application Of 880 kHz Ultrasound

The treatment corneal permeability was measured to be $3.22\pm0.83\text{x}10^{-6}$ cm/s, and the control permeability was measured to be $0.78\pm0.34\text{x}10^{-6}$ cm/s after the application of 880 kHz ultrasound at 0.4 W/cm^2 for 5 min (Figure 6). Therefore, the application of 880 kHz ultrasound caused 4.1 times increase in the corneal permeability to fluorescein sodium in rabbit eyes, *in vitro* ($p<0.001$). This value corresponded well with the 4.6 times increase in the corneal permeability to fluorescein sodium in rabbit cornea *in vivo* obtained after the application of 880 kHz ultrasound at 0.2 W/cm^2 for 5 min, as reported by Nuritdinov [7]. The cavitation-induced pitting of the epithelium was reported responsible for the corneal permeability enhancement. The epithelial pitting was shown to be healed in 6 hours [7].

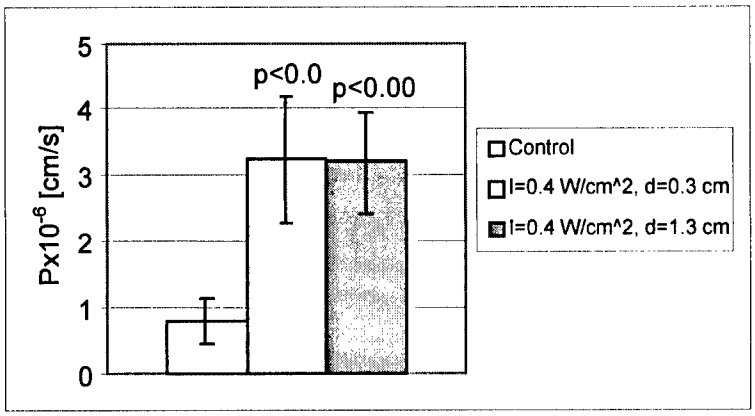

FIGURE 6. Corneal permeability in control and treatment case. d = distance between the transducer and cornea. n=5-6 in all cases. The data are given as mean ± S.D.

CONCLUSION

The application of 20 kHz ultrasound at I_{SATA} of 2 W/cm^2 for 60 min produced significant disorganization of the corneal epithelium and up to 4 times increase in the corneal permeability [11]. Therefore, it appears that, due to the significant damage to the corneal epithelium, 20 kHz ultrasound may not provide optimal results in transcorneal drug delivery. The application of 880 kHz ultrasound at 0.4 W/cm^2 for 5 min resulted in 4 times increase in the corneal permeability for a hydrophilic compound, fluorescein sodium. The corneal damage after the application of 880 kHz ultrasound at similar ultrasound dose as used in our experiments was reported to be minor, consisting of pits in the epithelium that healed in 6 hours [7]. Therefore, we have decided to focus our future research on the exploration of ultrasound enhancement of transcorneal drug delivery at medium frequencies (400-900 kHz).

ACKNOWLEDGEMENTS

This work was supported by the Center for Industrial and Medical Ultrasound and the Seattle Foundation.

REFERENCES

1. Sasaki, H., Yamamura, K., and Mukai, T., *Crit Rev Ther Drug Carrier Syst,* **16**, 85-146 (1999).
2. Ke, T.L., Clark, A.F., and Gracy, R.W., *J Ocul Pharmacol Ther,* **15**, 513-523 (1999).
3. Lee, V.H., *J Ocul Pharmacol*, **6**, 157-64 (1990).
4. Cherkasov, I.S., Marmur, R.K., and Radkovskaia, A.I., *Oftalmol Zh,* **29**, 114-118 (1974).
5. Gvarishvili, E.P., and Dushin, N.V., *Vestn Oftalmol,* **115**, 19-21 (1999).
6. Tsok, R.M., Gereliuk, I.P., Tsok, O.B., and Kaminskii, I.M., *Oftalmol Zh*, 46-49 (1990).
7. Nuritdinov, V.A., *Vestn Oftalmol*, 56-58 (1981).
8. Filippenko, V.I., and Tretiak, V.V., *Voen Med Zh*, 30-31 (1989).
9. Marmur, R.K., Moiseeva, N.N., and Korkhov, S.S., *Oftalmol Zh,* **34**, 68-73 (1979).
10. Iakimenko, S.A., Chalanova, R.I., and Artemov, A.V., *Oftalmol Zh*, 492-497 (1989).
11. Zderic, V., Vaezy, S., Martin, R.W., and Clark, J.I., *Ultrasound Med Biol,* **28**, 823-829 (2002).
12. Doughty, M.J., *Ophthalmic Physiol Opt,* **15**, 585-599 (1995).
13. Efron, N., Young, G., and Brennan, N.A., *Curr Eye Res,* **8**, 901-906 (1989).
14. Frenkel, V., Kimmel, E., and Iger, Y., *Ultrasound Med Biol,* **25**, 1295-1303 (1999).

6. LITHOTRIPSY

Lithotripter Shockwaves With Cavitation Nucleation Agents Reduce Tumor Growth And Induce Gene Transfer *In Vivo*

Douglas L. Miller and Jianming Song

Department of Radiology, University of Michigan, Ann Arbor MI 48109

Abstract. Cavitation nucleation agents (CNA) can greatly enhance nonthermal bioeffects of ultrasound *in vivo*. RENCA tumor cells were implanted on the hind legs of syngeneic BALB/c mice and grown to about 500 µl tumor volumes. Mice were anesthetized, the tumor region was shaved and depilated, and a DNA plasmid coding for marker proteins was injected into the tumor. As a CNA, either saline, Optison® ultrasound contrast agent, a vaporizing perfluoropentane droplet suspension or air bubble was also injected intratumorally at 10 percent of tumor volume. Two sets of tests were completed: (i) a plasmid coding for β-galactosidase was used with tumor growth and local gene expression assessed after four days and (ii) a plasmid coding for luciferase was used with overall luciferase production assayed after two days. Shockwaves were generated from a spark-gap lithotripter at 7.4 MPa peak negative pressure amplitude. For sham exposure, the growing tumors increased to 3.6 times the original volume after four days. All of the nucleation agents performed approximately the same, with 500 SW treatment reducing four-day tumor growth to 1.2 to 1.9 times the original volume. β-galactosidase expression was enhanced with CNA but was generally localized to the needle injection path. All the agents with 500 SW, except saline, produced statistically significant increases of 11.8 to 14.6 fold in luciferase expression, relative to shams. These results demonstrate the efficacy of CNA *in vivo* for simultaneous SW tumor ablation and local gene transfer.

INTRODUCTION

Bioeffects of acoustic cavitation provide a potential means for nonthermal therapeutic applications of ultrasound. Cavitation produces micro-scale bioeffects on cell membranes, which include sonoporation and cell death. In tissue, cavitation activity can produce larger scale bioeffects such as hemorrhage and fragmentation of tissue. Many of these bioeffects may be impossible to produce by any other non-invasive method. The application of cavitation bioeffects for therapy requires some strategy for overcoming the natural lack of cavitation nuclei, which tends to minimize cavitation activity in mammalian tissue. At very high pressure amplitudes, cavitation can occur during shockwave lithotripsy, aiding in stone breakup and sometimes causing hemorrhage [1]. The cavitation threshold has been found to be in the range 1.5-3.5 MPa in human tissue for relatively low frequency lithotripsy shockwaves [2]. However, cavitation bioeffects tend to be infrequent random events *in vivo*, even above this threshold. Since cavitation bioeffects depend on the presence of cavitation nuclei in the tissue, the development of a safe and efficacious cavitation nucleation

agent (CNA) for tissue would facilitate the development of nonthermal therapy applications.

One application of nonthermal ultrasound therapy might be to cancer treatment, provided that cavitation can be induced in tumors. Prat, et al. utilized bubbles mixed into gelatin and infused into the abdominal cavity of rats to enhance cavitational tissue destruction and cancer chemotherapy with lithotripter shockwaves [4]. Cavitation can also enhance gene transfer into treated cells by sonoporation, which provides another tool for cancer therapy in addition to cell killing for tumor ablation. Cavitation-induced cell killing has been combined with sonoporation for gene transfer in mouse melanoma tumors by injecting free air into the tumor together with a DNA plasmid solution [5]. Simple injection of saline with DNA coding for a marker gene produced some transfection, but addition of lithotripter shockwave exposure produced a 15 fold enhancement of gene expression. Injection of air into the tumor gave an additional 7 fold enhancement, which shows the benefit of the augmentation of cavitation nucleation even for lithotripter shockwaves [5]. Injection of saline or air into tissue provides cavitation nucleation; however, these are not optimum methods. Improved CNA are needed to provide more efficient cavitation nucleation *in vivo* with reduced risk of air embolization.

Several CNAs have recently been tested in whole blood, which normally has very few cavitation nuclei owing to the natural filtering processes in the body [3]. Fresh canine whole blood with added agent was exposed in 1.3 ml disposable pipette bulbs to lithotripter shockwaves. Saline and a retained air bubble were compared to Optison® ultrasound contrast agent and a stabilized perfluoropentane droplet suspension (SDS). The contrast agent consists of stabilized perfluoropropane bubbles that can act as cavitation nuclei, and the droplets in the SDS vaporize upon exposure to provide gaseous nuclei. Cavitation activity was assessed by measuring hemoglobin released by lysis of red blood cells (hemolysis). The droplet suspension performed nearly as well as retained air bubble when added at a concentration sufficient to provide a roughly equal volume of gas after vaporization. Optison® also yielded nucleation, but a concentration of 10-20% was needed for large enhancement of hemolysis comparable to 5% SDS. The ultrasound contrast agent and the stabilized perfluoropentane droplet suspension appeared to be suitable for use as CNA in nonthermal ultrasound therapy applications.

The purpose of this present study was to compare the CNAs, which were compared previously *in vitro* [3], in a mouse tumor model. The RENCA mouse tumor model was tested with direct intratumoral injection of saline, air bubbles, contrast agent, or droplet suspensions. The efficacy of lithotripter shockwave treatment with these enhanced nucleation methods was evaluated both for tumor growth rate reductions and for transfer and expression of marker genes. This combination of tests provided data for optimization of tumor cell killing and gene transfer for ultrasound enhanced cancer gene therapy.

METHODS

All *in vivo* procedures throughout the study were in accord with the guidance and approval of the University of Michigan Committee on the Use and Care of Animals. The renal carcinoma (RENCA) mouse tumor model was used for this research. RENCA cells were cultured by standard methods and implanted in the right thigh of female Balb/c mice (Charles River Laboratories) 14-15 days before treatment.

The four cavitation nucleation agents used in this research have been described previously [3]. Some minimal nucleation is provided by the sterile saline used as the DNA injection vehicle. Injected air reliably nucleates cavitation activity. Optison® ultrasound contrast agent (Mallinckrodt Inc., St. Louis MO) contains 500-800 $\cdot 10^6$ perfluoropropane gas bodies per ml, with a mean diameter of 2 to 4.5 μm. Stabilized droplet suspension (SDS) was prepared, as described previously [3]. Briefly, vials containing saline with 0.085% albumin and 10% by volume of perfluoropentane (PFP) liquid were agitated using a vial shaker to produce a suspension of droplets [6]. The stock suspension was diluted to contain 0.65% perfluoropentane so that the gas produced by vaporization would equal the initial volume of liquid (assuming ideal gas conditions and complete vaporization). This stabilized droplet suspension (SDS) contained about 60 million droplets per ml. An average 3 μm diameter droplet vaporizes to yield a roughly 16 μm diameter bubble (calculated by neglecting the surface tension and diffusion of gases into and out of the bubble, which can be important under some conditions [6,7]. This agent was also used after dilution by a factor of 10 in saline (DSDS).

The laboratory lithotripter system was similar to a Dornier HM-3 lithotripter and was fitted with standard spark gaps (Dornier Medical Systems, Kennesaw, Ga), as described previously [5]. Prior to filling, the exposure bath water was degassed for 1 hr by vacuum, and then continuously filtered and maintained at 37° C. The shock wave (SW) amplitude was measured at the focus using a bilaminar shielded hydrophone with a 0.5 mm sensitive spot (Marconi Type Y-34-3598, National Physical Laboratory, Middlesex, UK) coupled to a 500 MHz bandwidth digital oscilloscope. The spatial peak pressure amplitude averaged 42.6 MPa ($\pm$1.4 MPa standard deviation) positive and 7.4 MPa ($\pm$1.9 MPa s.d.) negative. For treatment, 500 SWs were delivered at a 2 Hz rate.

DNA plasmids coding for the two readily detectable markers luciferase and β-galactosidase were used in this research in 2 mg/ml solutions obtained from the University of Michigan Vector Core Laboratory. For treatment, the tumor area of anesthetized mice was shaved and depilated, and the volume of each tumor was estimated. A volume of plasmid solution equal to 10% of the tumor volume was mixed with an equal volume of a CNA and injected into the tumor approximately 5 min prior to SW treatment. The mouse was then mounted on a plastic board in the water bath with the tumor centered at the lithotripter focus. For mice injected with the β-galactosidase plasmid, tumor volumes were measured on the second and fourth day after treatment. On the fourth day, the excised tumor was stained with an X-gal staining kit (Gene Therapy Systems, San Diego CA) for the presence of expressed ß-galactosidase protein and observed with a dissecting microscope. For mice injected with the luciferase plasmid, the mouse was euthanized and the tumor was excised after

two days. These samples were lysed and the luciferase activity was measured with a luminometer. Total protein content was also measured in each sample to provide the luciferase concentration per gram of total protein.

RESULTS

Results are shown in Fig. 1 in bar graphs with the error bar extending one standard error beyond the mean. Sham groups tested for each CNA produced statistically indistinguishable results, and the sham results were pooled for comparison to the SW exposure results. Except as noted below, each luciferase-plasmid test was performed five times, and each growth rate test was performed four times. The tumor volumes are normalized to the volume on the treatment day, so that a value of 1.0 indicates complete cessation of tumor growth. The sham-exposed tumors grew to 3.6 times the initial volume after four days. Shockwave exposure significantly reduced this growth rate to 1.9 for saline, to 1.6 for an air bubble, to 1.5 for diluted SDS (three values), to 1.2 for SDS and to 1.5 for Optison® injection. The staining for expression of β-galactosidase indicated that the cell transfection occurred primarily around the injection track. For the luciferase expression tests, plasmid injection produced some transfection and expression of luciferase even for the shams. SW exposures with saline produced approximately a three-fold, statistically significant increase in luciferase expression compared to shams. All the other nucleation agents performed about the same, with 11.8- to 14.6- fold enhancements of luciferase expression relative to sham exposure.

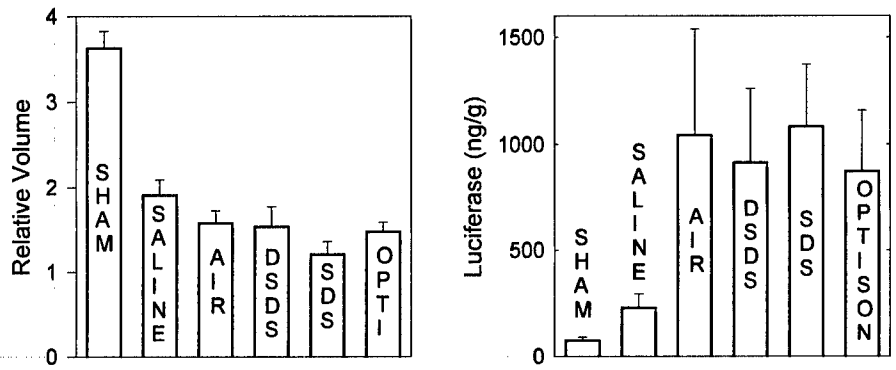

FIGURE 1. Sham and 500 SW exposure results for intratumoral injection of cavitation nucleation agents (SDS=stabilized droplet suspension, DSDS=diluted SDS, Opti=Optison). Results are presented as mean values with standard error bars. Tumor volume after four days is plotted on the left and overall expression of the luciferase marker gene is plotted on the right.

DISCUSSION AND CONCLUSIONS

In this study, saline, air bubbles, an ultrasound contrast agent and perfluoropentane droplets, which vaporize upon exposure to yield gas bubbles, were injected into mouse

RENCA tumors to nucleate cavitation activity during shockwave exposure. The cavitation activity enhanced cell transfection with marker plasmids injected with the agents, and induced tumor growth rate reductions. Cell transfection appeared to be localized around the injection track, and involved a small fraction of the total number of tumor cells, which agrees with earlier findings [8]. All the agents provided nucleation, with the gaseous agents performing better than saline. These results demonstrate the efficacy of the alternative CNAs *in vivo* for simultaneous SW tumor ablation with local gene transfer.

ACKNOWLEDGMENTS

We thank Dr. Michael Peacock, University of Michigan Vector Core Laboratory for preparing the DNA plasmid solutions and Dr. Oliver Kripfgans, Department of Radiology, for help with the droplet suspension. This research was supported by PHS grant CA83904 awarded by the National Institutes of Health, DHHS.

REFERENCES

1. Delius, M., "Medical applications and bioeffects of extracorporeal shock waves," *Shock Waves,* **4**, 55-72 (1994).
2. Coleman, A.J., Kodama, T., Choi, M.J., Adams, T., and Saunders, J.E., "The cavitation threshold of human tissue exposed to 0.2 MHz pulsed ultrasound: preliminary measurements based on a study of clinical lithotripsy," *Ultrasound Med Biol.,* **21**, 405-417 (1995).
3. Miller, D.L., Kripfgans, O.D., Fowlkes, J.B., and Carson, P.L., "Cavitation nucleation agents for nonthermal ultrasound therapy," *J. Acoust. Soc. Am.,* **107,** 3480-3486 (2000).
4. Prat, F., Chapelon, J.Y., El Fadil, F.A., Theillere, T., Ponchon, T., and Cathignol, D., "*In vivo* effects of cavitation alone or in combination with chemotherapy in a peritoneal carcinomatosis in the rat," *Br. J. Cancer,* **68,** 13-17 (1993).
5. Bao, S., Thrall, B.D., Gies, R.A., and Miller, D.L., "*In vivo* transfection of melanoma cells by lithotripter shock waves," *Cancer Res.,* **58,** 219-221 (1998).
6. Kripfgans, O.D., Fowlkes, J.B., Miller, D.L., Eldevik, O.P., and Carson, P.L., "Acoustic droplet vaporization for therapeutic and diagnostic applications," *Ultrasound Med. & Biol.,* **26,** 1177-1189 (2000).
7. Kabalnov, A., Klein, D., Pelura, T., Schutt, E., and Weers, J., "Dissolution of multicomponent microbubbles in the bloodstream: 1. Theory," *Ultrasound Med Biol.,* **24,** 739-749 (1998).
8. Miller, D.L, Bao, S., Gies, R.A., and Thrall, B.D., "Ultrasonic enhancement of gene transfection in murine melanoma tumors," *Ultrasound Med. & Biol.,* **25,** 1425-1430 (1999).

Dual Frequency High Intensity Focused Ultrasound To Control Bubbles

Michael R. Bailey, David J. Halaas, Justin A. Reed, Tanya Khokhlova, Erin Graf, Peter J. Kaczkowski, Roy Martin, Andrey A. Chulichkov,[†] and Vera A. Khokhlova[†]

Center for Industrial and Medical Ultrasound, Applied Physics Laboratory
College of Ocean and Fishery Science, University of Washington, Seattle, WA 98105 USA
[†]Department of Acoustics, Physics Faculty, M. V. Lomonosov Moscow State University, Moscow, 119899, Russia

Abstract. Bubble activity plays an important role in tumor necrosis, hemostasis, and drug delivery induced by high intensity focused ultrasound (HIFU). On the negative side, cavitation can cause unpredictable lesion distortion or form a barrier to deep sound penetration. On the positive side, bubbles are hyperechoic and useful in ultrasound-guided targeting and are an apparent mechanism of stimulated local drug delivery and immune response. Superposition of different frequencies was used here to study the effect of acoustic waveform on bubbles and cavitation. A 250-kHz continuous wave and 3.5-MHz pulses (50% duty cycle at 250 kHz) were superimposed. The Gilmore-Akulichev model for bubble dynamics was used to numerically calculate the bubble dynamics. Sonochemical yield was measured in a KI solution, and bubbles were imaged optically by CCD camera and acoustically with B-mode ultrasound. Bubble activity with the waves superimposed was greater than either wave alone. However, synchronizing the high frequency pulses with the positive phase of the low frequency wave produced more bubble activity than when the pulses coincided with the negative phase.

INTRODUCTION

Bubbles play a double-edged role in ultrasound therapy. On the beneficial side of HIFU therapy, bubbles appear to cause hyperecho on B-mode ultrasound that can be used for targeting. [1-5] Bubbles also appear to accelerate treatment by viscous heating and re-radiation due to their oscillations. [6,7] On the detrimental side, bubbles cause distortion in lesion shape, [8,9] can shield ultrasonic propagation, [10] and can cause mechanical tissue disruption that may lead to metastases of tumors. [11] Bubbles play a host of other roles when we consider other types of ultrasound therapy such as hemostasis [12] and drug delivery. [13,14] Since bubbles play this varied role, controlling cavitation (the formation, growth and collapse of bubbles) in HIFU is important. The goal of this paper is to report initial progress in controlling cavitation for HIFU.

Two techniques were used: overpressure and waveform manipulation. Overpressure, increased static pressure, is a common research tool to suppress cavitation. Hill [15] used overpressure to suppress ultrasound-induced cavitation in biological systems *in vitro*, and Lele [16] used overpressure and HIFU *in vivo*. By

suppressing bubbles with overpressure, Bailey et al. [17] demonstrated bubbles cause lesion distortion. Overpressure is useful for elucidating the role of bubbles; however, it is of limited use in clinical practice.

Waveform manipulation is a means of controlling cavitation that may be used clinically. In shock wave lithotripsy, Cathignol et al. [18] and Evan et al. [19] have manipulated the acoustic waveform to suppress cavitation and found reduced tissue injury and kidney stone comminution, which showed cavitation was important in both bioeffects. In HIFU, studies to date have primarily focused on how the waveform affects bubbles and not yet on the bioeffects. Chapelon et al. [20] used pseudorandom signals and found cavitation was reduced. Umemura and Kawabata, [21] Dezhkunov et al., [22] and Madanshetty [23] have mixed two frequencies of continuous waves to see increased sonochemistry, sonoluminescence, and surface erosion by bubbles. Deng et al. [24] used two frequencies to enhance echo-contrast in ultrasound imaging. And Grandia and Bar-Cohen [25] have described a method to mix frequencies in HIFU. Ciaravino et al. [26] have examined cavitation enhancement by pulses compared to continuous–wave (cw) HIFU.

In this paper, overpressure is used to assess the role of bubbles in lesion size and image. Two changes to the waveform – frequency sweeping and mixing high frequency pulses with low frequency cw – are investigated numerically and experimentally.

METHODS

Numerical Method

The radial oscillations of a single spherical bubble in response to the applied acoustic waves were simulated. The bubble radius is described by the Gilmore equation, [27]

$$\left(1-\frac{\dot{R}}{C}\right)R\ddot{R}+\frac{3}{2}\left(1-\frac{\dot{R}}{3C}\right)\dot{R}^2=\left(1+\frac{\dot{R}}{C}\right)H+\left(1-\frac{\dot{R}}{C}\right)\frac{R\,dH}{C\,dt}\,, \qquad (1)$$

where a dot signifies a time derivative, C is the sound speed in the liquid at the bubble wall, H is the difference between the specific enthalpy in water at the bubble wall relative to the specific enthalpy in the water far from the bubble. The numerical solution has been described previously. [28,29]

Pressure Chamber

Experiments with elevated static pressure were conducted in the pressure chamber shown in Fig. 1. The HIFU transducer (3.5 MHz, 38-mm diameter, 64-mm radius of curvature) is mounted in the chamber. A gel phantom [30] made of polyacrylamide and 5% bovine serum albumin was placed in degassed water in the chamber. Pressure was increased with a hand pump. Ultrasound images (Phillips ATL HDI –1000, L11-5 probe) and CCD camera images were made through the 25-mm thick acrylic windows

in the chamber. HIFU heat deposition caused the albumin to denature and turn white in the transparent gel, which revealed the HIFU lesion.

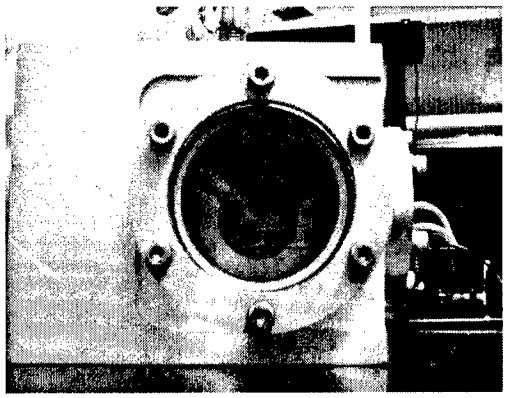

FIGURE 1. Pressure chamber.

Sonochemistry

Sonochemistry – measurement of products of free radical reactions produced by inertial cavitation – was used to quantify cavitation activity. [31] Low-density polyethylene pipette bulbs (Sigma Chemical Company, St. Louis, MO), 30 mm in length, 10 mm in diameter and 0.5 mm in wall thickness were used as exposure vessels. Pipette bulbs were filled with an iodide solution, consisting of 0.1 M KI and 0.51 mM ammonium molybdate [$(NH_4)_2MoO_4$] adjusted to pH 5. Because of the time-sensitivity of the iodine reaction, a small volume of iodide solution was freshly prepared prior to each experiment, and a control sample was measured for every such volume.

The high temperatures generated inside cavitating bubbles mediate a series of chemical reactions. Specifically, hydrogen peroxide is formed from the pyrolysis of water and reacts with the iodide to form iodine. The iodine and iodide react to form triiodide, which was spectrophotometrically analyzed ($\varepsilon_{352} = 2.2 \times 10^4$ L/mole/cm) with a double beam spectrophotometer (Shimadzu UV-1601). Control values were subtracted from corresponding experimental values and the concentration of hydroxl radicals was estimated as 1/2 the concentration of triiodide.

Sonochemistry experiments and photography were done in a water tank shown in Fig. 2. A low frequency transducer (250 kHz, 100-mm diameter, 78-mm radius of curvature) and a high frequency transducer (3.5 MHz, 35-mm diameter, 55-mm radius of curvature) were mounted confocally in the tank. The sample pipette was placed at this focus. Two series of chemistry experiments were completed. One, the four conditions shown in Fig. 3 were examined to compare the effect of mixing low frequency and high frequency bursts. Pressure amplitudes were 3.2 MPa (low frequency) and 8 MPa (high frequency). Exposures were 1 ms on, 1 ms off for five minutes. The focal spot size was sufficiently small that phase changes in the pipette were small. Two, a frequency chirp 240-290 kHz (swept over 1 ms) was compared to single frequency 250 kHz exposure. Exposure was 100 ms on, 100 ms off for ten

minutes. Because the frequency response of the transducer was not flat, comparison was by maintaining the same time averaged spatial peak intensity between the single frequency and the frequency chirp. Intensity was determined by measuring the peak pressure for the range of frequencies and then calculating and averaging the intensity over the frequency range.

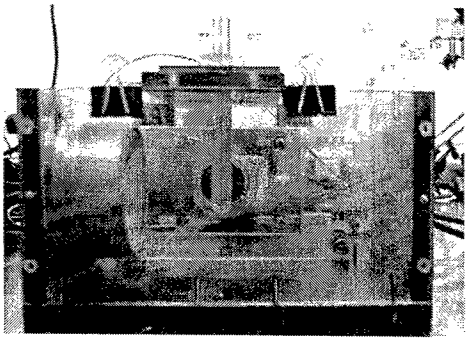

FIGURE 2. Two confocal transducers.

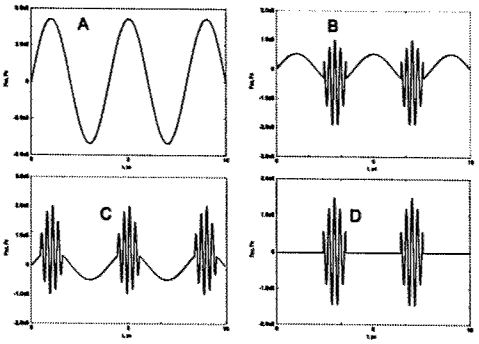

FIGURE 3. Frequency mixing waveforms.

EXPERIMENTAL RESULTS

Overpressure, which suppresses bubbles, yielded smaller lesion size and no hyperecho on B-mode imaging. Figure 4 shows CCD camera images of the lesion formed in gel after 5 s at 1500 W/cm^2 and the simultaneous B-mode image of the lesion. The images at the top were obtained at 1 bar and on the bottom at 100 bar. The lesion is larger at 1 bar and a hyperechoic region is seen on the B-mode. At 100 bar, the lesion created is smaller and B-mode images does not reveal a hyperechoic region. These results are consistent with the idea that cavitation can increase heating and that bubbles are responsible for the hyperecho seen in HIFU treatment.

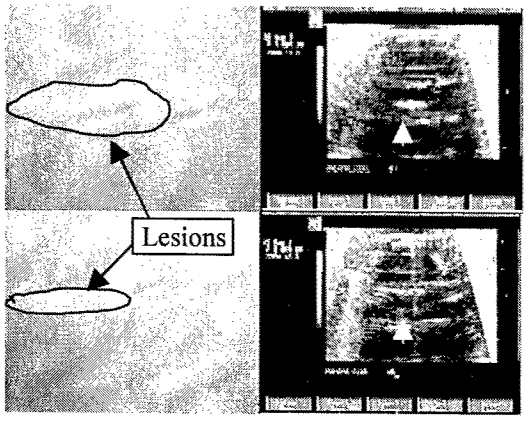

FIGURE 4. Lesions (left) and ultrasound images (right) at 1 bar (top) and 100 bar (bottom). Lesion is smaller and no hyperecho (arrow) is seen at 100 bar.

Although useful in elucidating the cavitation mechanism, the overpressure experiments are of limited direct applicability *in vivo*, but cavitation can be controlled by the acoustic waveform. Figure 5 shows sonochemistry results for duplicate experiments comparing the four waveforms in Fig. 3. Absorbance is on the y-axis and the spectrum along the x-axis. The peak around 350 nm corresponds to the amount of triiodide produced. The high frequency bursts (D in Fig. 3) produced negligible chemistry. The low frequency produced more. But adding the two frequencies together produced significantly greater cavitation and sonochemistry. Synchronizing the high frequency with the positive phase of the low frequency wave produced more cavitation and chemistry than synchronizing with the negative phase, but the difference was small. The nonlinear increase in cavitation when two frequencies are added is consistent with others findings. [21-23]

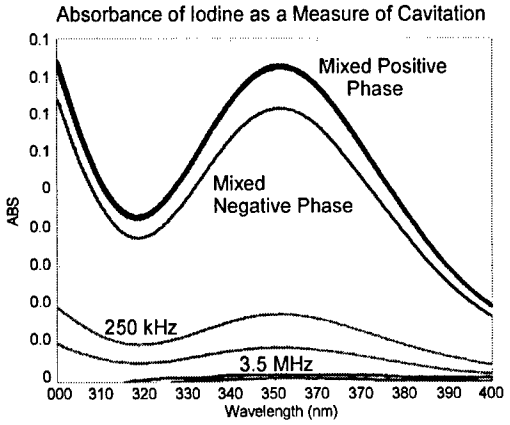

FIGURE 5. Absorbance vs. frequency measures for the four cases in Fig. 3. Mixing the frequencies give more chemistry (350 nm) than either frequency alone.

Figure 6 shows sonochemistry for a monoharmonic 250 kHz wave and a chirped wave. The single frequency produced measurable chemistry whereas the chirp suppressed cavitation and chemistry.

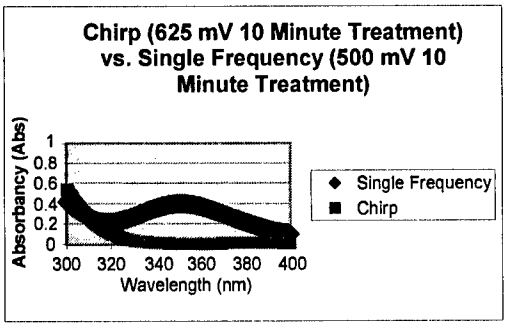

FIGURE 6. Absorbance vs. frequency. The chirp yields less cavitation and chemistry than the single frequency.

NUMERICAL RESULTS

Numerical calculations reveal that an increase in the minimum bubble size correlates well with an increase in sonochemistry. Number of bubble collapses does

not correlate well. Fig. 7 shows radius versus time curves calculated for 4 waveforms. Clockwise from the top left, the driving acoustic waves are a 3.5 MHz wave, a 250 kHz wave, 3.5 MHz bursts riding on the negative phase of the 250 KHz wave, and 3.5 MHz bursts riding on the positive phase of the 250 KHz wave. The mixed cases yield the smallest minimum bubble radii and the most sonochemistry. Synchronizing the high frequency with the positive phase of the low frequency wave produced the smallest radii numerically consistent with the most chemistry experimentally. The 3.5 MHz wave produced the most bubble collapses but the least sonochemistry. Similar calculations showed the chirp waveform produced lower amplitude radial oscillations than the monofrequency wave, which was in agreement with the sonochemistry results in Fig. 6.

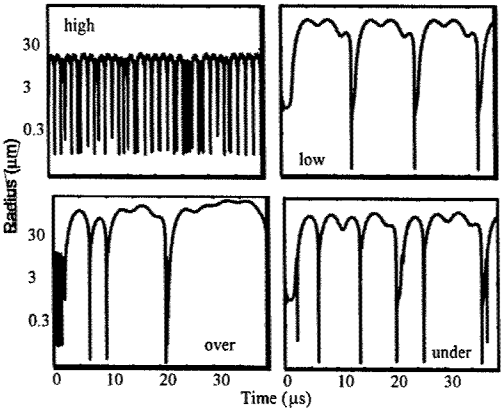

FIGURE 7. R(t) curves for the four cases in Fig. 3.

DISCUSSION

Overpressure experiments have shown that bubbles play an important role in HIFU therapy and imaging. Watkin et al. [9] were careful to work below a threshold pressure in an effort to avoid lesion distortion caused by bubbles. Vaezy et al. [5] have shown hyperecho on B-mode imaging useful in targeting the treatment appears before gross damage to tissue, which indicates at least in some exposure conditions bubbles precede the therapeutic effect. Bubbles may be unavoidable. Hence we investigated how the HIFU waveform might be manipulated to control bubbles and cavitation.

Mixing of two frequencies can increase cavitation activity. Our goal was to apply the high frequency bursts synchronized with the positive phase of the low frequency wave. The hope was that the low frequency wave could act as an overpressure and suppress cavitation activity. However, we found for these parameters the low cavitation threshold of the low frequency wave dominated, and in fact with either phasing, cavitation was increased.

Frequency sweeping or chirping was used to reduce cavitation as measured by sonochemistry. Our hypothesis is that a single bubble cannot oscillate in resonance with chirped frequencies unless the chirp happens to exactly track the growth or dissolution of a bubble. Therefore oscillations are less violent and bubbles do not all conform to a single resonant size by rectified diffusion. We plan to use chirp

frequencies in the MHz range but because little chemistry occurred in this frequency band, the results reported here were at a lower frequency.

The results reported here are preliminary but demonstrate that the HIFU wave can be manipulated to reduce cavitation. Once the cavitation effect in understood it can be correlated with bioeffect such as heating efficiency or hyperechogenicity. The parameters have not been optimized. In part because it was not known what the important parameters were in our model. However maximum and minimum bubble size seem to be the important parameters for sonochemistry. The goal will be to establish the ideal frequencies for mixing and chirping. In summary, HIFU waveform manipulation is a way to control cavitation.

ACKNOWLEDGMENTS

This research was supported by grants from the National Space Biomedical Research Institute (NSBRI SMS00203) through NASA, National Science Foundation (NSF 0002932), Civilian Research Development Foundation (CRDF RP2-2384-MO-02), and National Institutes of Health (NIH R44 CA83244).

REFERENCES

1. Fry, F.J., "Ultrasonic visualization of ultrasonically produced lesions in brain," *Confin. neurol.* **32**, 38-52 (1970).
2. Lizzi, F.L., Coleman, D.J., Driller, J., Silverman, R.H., Lucas, B., and Rosado, A., presented at the 1986 Ultrasonics Symposium, Institute of Electrical and Electronic Engineers, New York, 1986.
3. Gelet, A., Chapelon, J.Y., Margonari, J., Theillere, Y., Gorry, F., Cathignol, D., and Blanc, E. , "Prostatic tissue destruction by high-intensity focused ultrasound: experimentation on canine prostate," *J Endourol,* **7**, 249-253 (1993).
4. Sanghvi, V.I., Fry, F.J., Bihrle, R., Foster, R.S., Phillips, M.H., Syrus, J., Zaitsev, A., and Hennige, C., "Microbubbles during tissue treatment using high intensity focused ultrasound," IEEE 95 UFFC Symposium, 1249-1253 (1995).
5. Vaezy, S., Shi, X., Martin, R.W., Chi, E., Nelson, P.I., Bailey, M.R., and Crum, L.A., "Real-Time Visualization of Focused Ultrasound Therapy," *Ultrasound Med Biol*, **27**, 33-42 (2000).
6. Fry, F.J., Sanghvi, V.I., Foster, R.S., Bihrle, R., and Hennige, C., "Ultrasound and microbubbles: their generation, detection, and potential utilization in tissue and organ therapy - experimental," *Ultrasound Med Biol*, **21**, 1227-1237 (1995).
7. Holt, R.G., and Roy, R.A., "Measurements of bubble-enhanced heating from focused, MHz-frequency ultrasound in a tissue-mimicking material.," *Ultrasound Med Biol*, **27**, 1399-1412 (2001).
8. Crum, L.A., and Law, W., The relative roles of thermal and nonthermal effects in the use of high intensity focused ultrasound for the treatment of benign prostatic hyperplasia, Presented at the Proceedings of the 15th International Congress on Acoustics, Trondheim, Norway, 1995.
9. Watkin, N.A., ter Haar, G.R. and I. Rivens, G.R., "The intensity dependence of the site of maximal energy deposition in focused ultrasound surgery," *Ultrasound Med Biol*, **22**, 483-491 (1996).

10. Meaney, P., Cahill, M.D., and ter Haar, G.R., "The intensity dependence of lesion position shift during focused ultrasound surgery," *Ultrasound Med. Biol*, **26** (2000).
11. Fry, F.J., Johnson, L.K., "Tumor irradiation with intense ultrasound." *Ultrasound Med Biol*, **4**, 337-341 (1978).
12. Vaezy, S., Martin, R., Keilman, G., Kaczkowski, P., Chi, E., Yazaji, E., Caps, M., Poliachik, S., Carter, S., Sharar, S., Cornejo, C., and Crum, L., "Control of splenic bleeding by using high intensity ultrasound," *J Trauma*, **47**, 521-525 (1999).
13. Tachibana, K. Sugata, K., Meng, J., Okumura, M., and Tachibana, S., "Liver tissue damage by ultrasound in combination with the photosensitizing drug, photofrin II," *Cancer Letters*, **78**, 177-181 (1994).
14. Everbach, E.C., and Francis, C.W., "Cavitational mechanisms in ultrasound-accelerated thrombolysis at 1 MHz.," *Ultrasound Med Biol*, **26**, 1153-1160 (2000).
15. Hill, C.R., "Ultrasonic exposure thresholds for changes in cells and tissues," *J. Acoust. Soc. Am.*, **52**, 667-672 (1971).
16. Lele, P.P., "Effects of ultrasound on "solid" mammalian tissues and tumors in vivo," in *Ultrasound: Medical applications, biological effects and hazard potential* (Plenum, New York, 1986), pp. 275-306.
17. Bailey, M.R., Couret, L.N., Sapozhnikov, O.A., Khokhlova, V.A., ter Haar, G., Vaezy, S., Shi, X., Martin, R., and Crum, L.A. "Use of overpressure to assess the role of bubbles in focused ultrasound lesion shape in vitro," *Ultrasound Med. Biol*, **27**, 696-708 (2000).
18. Cathignol, D., Tavakkoli, J., Birer, A., et al., "Comparison between the effects of cavitation induced by two different pressure-time shock waveform pulses," *IEEE Trans. Ultrason Ferroelectr Freq Control*, **45**, 788-799 (1998).
19. Evan, A.P., Willis, L.R., McAteer, J.A., Bailey, M.R., Connors, B.A., Shao, Y., Lingeman, J.E., Williams Jr., J.C., Fineberg, N.S., and Crum, L.A., "Kidney damage and renal function changes are minimized by waveform control that suppresses cavitation in SWL," *J. Urol.*, **168** (2002) in press.
20. Chapelon, J.Y., Dupenloup, F., Cohen, H., and Lenz, P., "Reduction of cavitation using pseudorandom signals," *IEEE Trans. Ultrason Ferroelectr Freq Control*, **43**, 623-625 (1996).
21. Umemura, S., and Kawabata, K., "Enhancement of sonochemical reaction by second-harmonic super-imposition," *Proc. IEEE Ultrason. Symp.*, 917-920 (1993).
22. Dezhkunov, N.V., Francescutto, A., Ciuti, P., Kulak, A.I., and Koltovich, V.A., "Multibubble sonoluminescence in interacting fields of different frequencies," AIP-Conference-Proceedings. **524**, 447-50 (2000).
23. Madanshetty, S.I., "Method and apparatus for utilizing acoustic coaxing induced microcavittion for submicron particulate eviction." US Patent number 5,681,396.
24. Deng, C.X. Lizzi, F.L., Kalisz, A., Rosado, A., Silverman, R.H., and Coleman, D.J., "Study of ultrasonic contrast agents using a dual-frequency band technique." *Ultrasound Med Biol.*, **26** (5), 819-31 (2000).
25. Grandia, C., and Bar-Cohen, "Medical noninvasive operations using focused modulated high power ultrasound," US Patent number 5,827,204.
26. Ciaravino, V., Flynn, H.G., and Miller, M.W., "Pulses enhancement of acoustic cavitation: a postulated model." *Ultrasound Med Biol.*, **7** (2), 159-66 (1981).
27. Gilmore, F.R., "The growth or collapse of a spherical bubble in a viscous compressible liquid" (Report No. Rep. 26-4,California Institute of Technology, Pasadena, California, 1952) pp. 1-40.
28. Church, C.C., "A theoretical study of cavitation generated by an extracorporeal shock wave lithotripter," *J. Acoust. Soc. Am*, **86**, 215-227 (1989).

29. Sapozhnikov, O.A., Khokhlova, V.A., Bailey, M.R., Williams, Jr., J.C., McAteer, J.A., Cleveland, R.O., and Crum, L.A., "Effect of overpressure and pulse repetition frequency on shock wave lithotripsy," *J. Acoust. Soc. Am.*, **112** (3) in press (2002).
30. Lafon, C., Vaezy, S., Noble, M., Kaczkowski, P.J., Martin, R., and Crum, L.A., "A new synthetic tissue-mimicking phantom for high intensity focused ultrasound," in *Proc. 17th International Congress on Acoustics* (Rome, Italy, 2001).
31. Leighton, T.G., *The Acoustic Bubble*, London: Academic Press I, 1994, p. 613.

The Role Of Stress Waves And Cavitation In Stone Comminution In Shock Wave Lithotripsy

Songlin Zhu[*], Franklin H. Cocks[*], Glenn M. Preminger[#], and Pei Zhong[*,#]

[*]*Department of Mechanical Engineering and Materials Science*
[#]*Comprehensive Kidney Stone Center/Urologic Surgery*
Duke University, Durham, North Carolina 27708, USA

ABSTRACT. Using an experimental system that mimics stone fragmentation in the renal pelvis, we have investigated the role of stress waves and cavitation in stone comminution in shock wave lithotripsy (SWL). Spherical plaster-of-Paris stone phantoms (D = 10 mm) were exposed up to 500 shocks at the beam focus of a Dornier HM-3 lithotripter operated at 20 kV and a pulse repetition rate of 1 Hz. The stone phantoms were immersed either in degassed water or in castor oil to delineate the contribution of stress waves and cavitation to stone comminution. It was found that after 500 shocks while in degassed water there is a progressive disintegration of the stone phantoms into small pieces (66%<2mm), the fragments produced in castor oil are fairly sizable (11%<2mm). On the other hand, if a stone is exposed only to cavitation bubbles induced in SWL, the resultant fragmentation is much less effective compared to that produced by the combination of stress waves and cavitation. It is concluded that, although stress wave-induced fracture is important for the initial disintegration of kidney stones, cavitation is necessary to produce fine passable fragments, which are most critical for the success of clinical SWL. Stress waves and cavitation work synergistically, rather than independently, to produce effective and successful disintegration of renal calculi in SWL.

INTRODUCTION

Disintegration of renal calculi in a lithotripter field is the consequence of dynamic fracture of stone materials due to the mechanical stresses produced either directly by the incident lithotripter shock wave (LSW) or indirectly by the collapse of cavitation bubbles [1]. In shock wave lithotripsy (SWL), two basic mechanisms of stone fragmentation have been well documented, namely, spalling at the posterior surface and at internal crystalline-matrix interfaces of a stone due to reflected tensile waves [2-4], and cavitation erosion at the anterior surface of a stone due to violent collapse of bubbles [5-8]. The damage produced inside the stone material have been attributed to stress waves generated by the impingement of LSWs, which are enhanced by internal wave focusing, superposition, and squeezing effects [9-11]. In contrast, cavitation damage is produced primarily on the surface of the stone and the resultant fragments are usually small due to the highly localized stresses generated by a collapsing bubble [7,8]. The damage patterns produced by these two mechanisms, however, are distinctly different [12] and their relative contribution to the overall success of stone comminution in SWL has not been investigated.

In this work, a series of experiments were carried out using a phantom system that mimics *in vivo* stone comminution in the renal pelvis. Emphasis is placed on delineating the contribution of various working mechanisms to the overall success of stone comminution, and on understanding of the progressive development of stone comminution in SWL in relation to the contributing mechanisms

MATERIALS AND METHODS

Lithotripter. In this study, an HM-3 lithotripter operated at 20 kV was used. Figure 1 shows the typical pressure waveform measured at the lithotripter focus (F2).

Stone samples. Spherical stone phantoms (D = 10 mm) were made of plaster-of-Paris (powder/water ratio = 2 : 1 by weight). The acoustical properties of the plaster-of-Pairs stone phantom are comparable to that of magnesium ammonium phosphate hydrogen (MAPH) stones [13,14]. In addition, six pairs of kidney stones of different compositions, surgically removed from patients, were used for comparison of stone comminution in different fluid media. Each pair of the stones were selected based on their similarity in composition, size, color, and weight (Table 1), with their primary chemical composition determined to be calcium oxalate monohydrate (COM), the most commonly observed crystalline material in kidney stones [15].

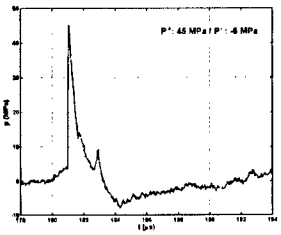

FIGURE. 1. A typical pressure waveform produced at the focus of an HM-3 lithotripter operated at 20 kV, measured using a fiber optical probe hydrophone. P^+/P^- = 45/-8 MPa, t^+/t^- =2/9 μs, –6 dB beam size: 75(L) x 8(T) mm.

Table 1. Dimension and chemical compositions of the kidney stones.

		Dimension (L×W×H, mm)	Initial Weight (g)	Component						
				COM	MAPH	$CaPO_4$	UA	COD	CA	PTN
Stone Group 1	A	9.23×8.48×7.28	0.4860	50	20	30				
	B	10.77×9.03×7.03	0.6768							
Stone Group 2	A	13.18×10.18×5.96	0.7167	88			12			
	B	17.81×9.89×7.42	0.9871							
Stone Group 3	A	9.64×6.93×7.46	0.3817	88			12			
	B	9.54×8.17×5.12	0.3163							
Stone Group 4	A	14.17×11.03×7.40	0.7620	90		10				
	B	14.4×11.87×7.79	0.8983							
Stone Group 5	A	13.25×10.28×10.55	1.1968	60	15	25				
	B	16.76×9.51×10.32	1.1281							
Stone Group 6	A	11.03×7.05×6.84	0.3912	42				38	17	3
	B	10.99×7.22×5.14	0.2830							

COM, calcium oxalate monohydrate; MAPH, magnesium ammonium phosphate hydrogen; $CaPO_4$, calcium phosphate; UA, uric acid; COD, calcium oxalate dihydrate; CA, carbonate apatite; and PTN, platinum triamine ion.

Experimental protocol. A phantom system that mimics stone comminution in the renal pelvis was used (Fig. 2). The stone sample was placed in a plastic holder with disposable finger cot (VWR Scientific Products, Suwanee, GA) at the end. The holder was filled with either degassed water (a cavitation supportive medium) or freshly poured caster oil (a cavitation inhibitive medium) to delineate the contribution of stress waves and cavitation to stone comminution. Using this set up, the finger cot and the test fluid inside the sample holder can be replaced easily following each test. The stone holder was immersed in an acrylic testing chamber (254×254×152~216 mm, L×W×H) filled with caster oil and with a slab of 25-mm thick tissue-mimicking phantom placed at the bottom to simulate tissue attenuation on the incident LSWs [16].

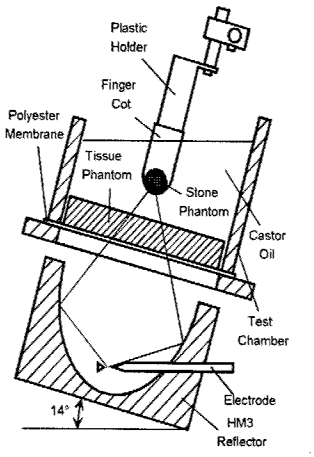

FIGURE. 2. Schematic diagram of the experimental set up.

The stone phantoms were randomly divided into two sets for shock wave treatment either in degassed water or in castor oil. Samples in each set were further subdivided into six groups and exposed from 25 to 500 shocks. For kidney stones, the comparison was made at 200 shocks only. Before the experiment, the weight of each sample in dry state was measured. Prior to shock wave treatment, each stone sample was immersed in the prospective test fluid (degassed water or caster oil) for at least 20 minutes until no visible bubbles could be seen at the stone surface. Alignment of the stone phantom to F2 was aided by a pointer and verified by the fluoroscopic imaging system of the HM-3 lithotripter. Following the shock wave treatment, all the fragments in the finger cot was carefully removed and spread out on a dry paper. For samples treated in castor oil, facial tissue was used to gently absorb excessive oil left on the specimen surface. After air dry for 48 hours, the fragments were collected and their size distribution was determined by sequential sieving [17].

To identify the contribution of cavitation alone to stone comminution in SWL, another set of experiments was performed using the plaster-of-Paris stone phantoms in an experimental HM-3 lithotripter [10]. High-speed shadowgraph was used to visualize the bubble dynamics near the stone. To eliminate the contribution of stress waves, the stone phantom was placed in the focal plan but with its center shifted transversely by a 13-mm distance from the shock wave axis to position the stone just outside the lithotripter beam focus (see Fig. 5b). Cavitation bubbles, however, were still produced at F2 in water and collapsed near the lateral surface of the stone. In the experiments, the stone sample was placed inside a thin-wire net affixed to an inverted U-shape holder, and exposed to LSWs in degassed water without tissue-mimicking materials. For comparison, another group of stone phantoms were treated at F2.

RESULTS

Dose-dependency of stone comminution in degassed water. In degassed water, stone phantoms break up progressively as the number of shocks increases (Fig. 3a). The size distribution of the fragments at different number of shocks is shown in Fig. 3a. Initially, after 25 to 50 shocks the stone was broken into several large pieces (> 4 mm), which accounts for more than 90% of the fragments by weight. As the shock number increased, more medium- (2-4 mm) and small-size (< 2 mm) fragments were produced, indicating a progressive comminution of the initial large fragments. After 200 shocks, the large fragments was reduced to 28% of the total weight, while the medium fragments reached a maximum of 36%, and the small fragments contributed to the remaining 36%. As the shock wave exposure continued, the percentage of small fragments increased further while the percentage of large and medium fragments decreased.

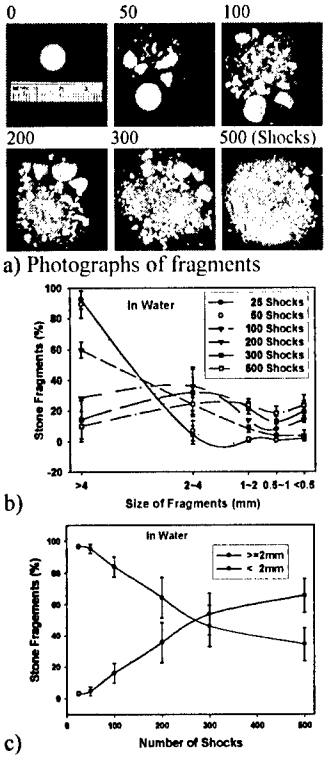

FIGURE. 3. Photographs and dose-dependent size distribution of the fragments of plaster-of-Paris stone phantoms in water after shock wave treatment in an HM-3 lithotripter at 20 kV.

Figure 3c shows the dose dependency in stone comminution using the 2-mm criterion for passable fragments, based on the clinical observation that stone fragments less than 2 mm can be discharged spontaneously following SWL [2]. Initially (< 50 shocks) stone comminution increases slowly with the shock number. Between 50 and 300 shocks, there is a rapid, linear increase in fragmentation, and after 300 shocks, the comminution rate slows down. At this point, it was noticed that significant amount of small fragments were settled down at the bottom of the finger cot, which may attenuate the ensuing LSWs and thus decreasing stone comminution [4].

The contribution of stress waves. To determine the contribution of stress waves, stone phantoms were immersed in castor oil to suppress cavitation [18]. Under this circumstance, stone phantoms were fragmented primarily by the stress waves produced by the incident LSWs [1,9,10]. The result, shown in Fig. 4a, demonstrates that although stone phantoms were disintegrated into multiple pieces in castor oil, the fragments remained fairly sizable even after 500 shocks. Quantitatively, large and medium fragments were produced after 25 shocks accounting for 75% and 20% of the stone weight, respectively (Fig. 4a). With continued shock wave exposure, the large fragments were reduced to medium-size pieces, which, however, were not further comminuted into small fragments. For example, after 500 shocks only 1.5% of the stone mass was

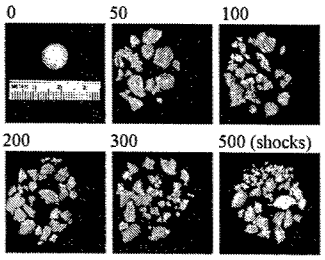

a) Photographs of fragments

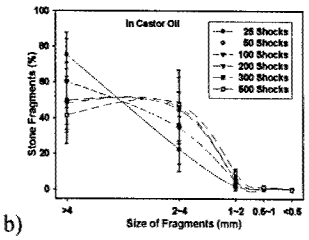

b)

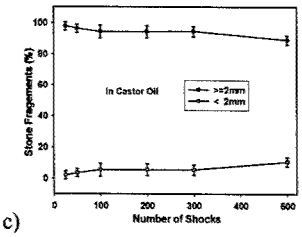

c)

FIGURE. 4. Photographs and dose-dependent size distribution of the fragments of plaster-of-Paris stone phantoms in castor oil after shock wave treatment in an HM-3 lithotripter at 20 kV.

reduced to less than 1 mm and no fragments less than 0.5 mm were produced (Fig. 4b). This is in great contrast to the progressive comminution of stones into fine fragments in degassed water (Fig. 3). Clearly, under the influence of stress waves alone there is an apparent limitation on the smallest fragments that can be produced.

The contribution of cavitation. To isolate the contribution of cavitation alone to stone comminution in SWL, a plaster-of-Paris stone phantom was placed off-axis transversely from F2 by 13 mm. As shown in Fig. 5b, the incident LSW propagated through F2 in water sweeping by the lateral surface of the stone (the number above each image frame indicates the time delay in microseconds after the lithotripter spark discharge). With this arrangement, stress waves produced inside the stone could be minimized. Yet, cavitation bubbles were still generated by the incident LSW around F2. The bubbles first expand to a maximum size in about 200 μs and then collapsed violently near the lateral surface of the stone, emitting secondary shock waves (see circular rings at 600 μs in Fig. 5b). Some bubbles were also seen to aggregate on the lateral surface of the stone, and their subsequent collapse could be asymmetric with resultant formation of microjets impinging towards the stone [5, 6]. Overall, the bubble dynamics in the off-axis arrangement is similar to that generated when the stone is placed at F2 (Fig. 5a), except that in the later case the bubbles collapse primarily near the proximal surface of the stone facing the incident LSW (frames at 500 μs and 680 μs in Fig. 5a).

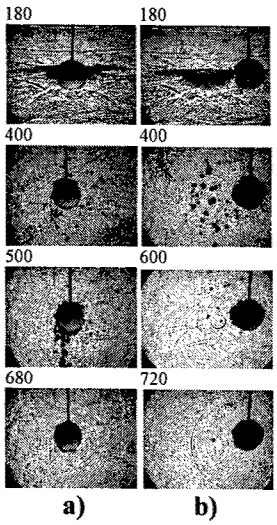

FIGURE. 5. Representative high-speed image sequences of the bubble dynamics produced by a laboratory HM-3 lithotripter in water at 24 kV. The stone phantom (10 mm in diameter) was placed **a)** at F_2, **b)** at a 13 mm distance transverse from F_2.

When the stone phantom was placed off-axis, only 3% of the stone mass was fragmented to less than 2 mm after 30 shocks at 24 kV in the experimental HM-3 lithotripter. In comparison, when placed directly at F2, 27% of the stone mass was disintegrated into passable fragments. It should be noted that these results could not be compared directly with the ones (see Fig. 3)

obtained using the renal pelvis mimicking phantom system because of the significant differences in the experimental setup. Macroscopically, damage to the stones placed off-axis was primarily surface erosion produced by the collapse of cavitation bubbles without any bulk disintegration of the stone. Whereas stones placed at F2 were fragmented into pieces of different sizes. These results suggest that with cavitation alone, although damage to the stone (primarily surface erosion) can be produced, the comminution efficiency is significantly reduced compared to that produced by the combination of stress waves and cavitation.

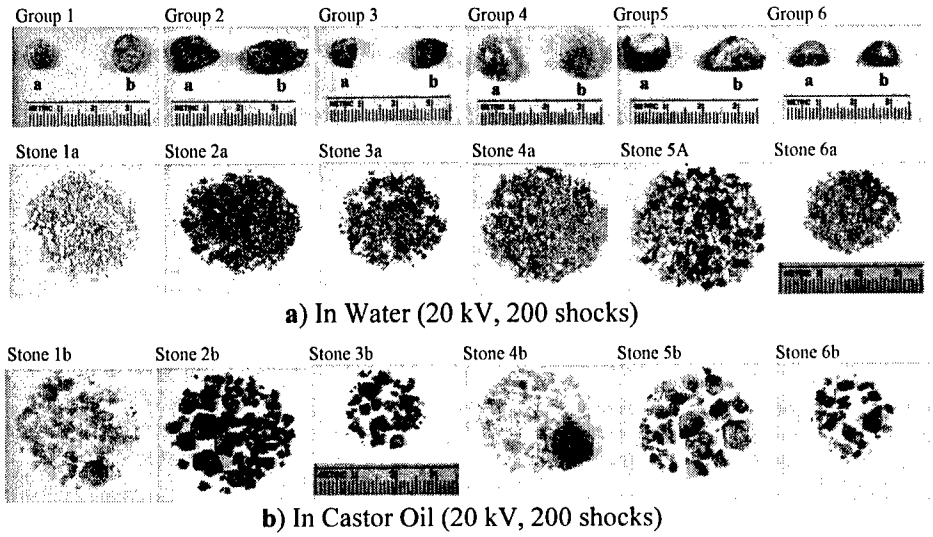

FIGURE 6. Photographs of original pairs of kidney stones and their corresponding fragments after being treated by 200 shocks produced by a HM-3 lithotripter at 20 kV, **a)** in water and **b)** in castor oil.

Paired kidney stones of similar composition, size, shape, and weight were exposed to 200 shocks at 20 kV in the HM-3 lithotripter either in degassed water or in castor oil. The results, shown graphically in Fig. 6 and quantitatively in Fig. 7, revealed that in water most stones were comminuted into passable pieces whereas in castor oil most fragments remained large in size. For example, in water no fragments were larger than 4 mm and the residual weight for 2-4 mm, 1-2 mm, and ≤ 1mm fragments were 11%, 37%, and 52%, respectively. In contrast, in caster oil the fragments > 4 mm and 2-4 mm were 51% and 28%, respectively (Fig. 7). Using the 2-mm criterion, the percentage of passable fragments were 89% and 22% for the kidney stones treated in water and in caster oil, respectively. All together, these experimental findings confirm that with stress waves alone, kidney stones will be disintegrated primarily into large, impassable pieces.

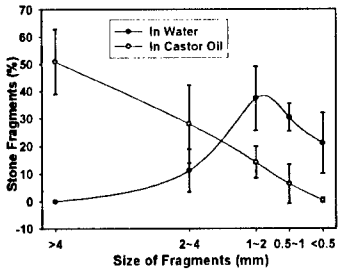

FIGURE 7. Size distribution of kidney stone fragments after 200 shocks in an HM-3 lithotripter at 20 kV.

DISCUSSION

The fragmentation of kidney stones in SWL is the consequence of dynamic fracture of stone materials in response to the mechanical stresses produced either by LSW or cavitation [1]. Kidney stones, like most crystalline materials, have pre-existing flaws or microcracks randomly distributed at the crystalline-matrix interface or at the grain boundary of the crystalline materials. Under the mechanical stresses imposed by the LSWs, these pre-existing microcracks may extend if the accumulated stress-intensity factor at the crack tip exceeds a threshold value, also known as the fracture toughness of the material [1]. The fracture toughness for kidney stones of various compositions has been measured in the range of 0.056 MPa*m$^{1/2}$ for MAPH stones to 0.120 ~ 0.136 MPa*m$^{1/2}$ for brushite and COM stones, corresponding to their varying fragilities in SWL [13]. These values are an order of magnitude lower than the fracture toughness of ceramic materials [19]. It has been suggested that the nucleation, growth, and coalescence of the microcracks in the stone material under repeated bombardments of the LSWs eventually leads to the fragmentation of kidney stones in SWL [1].

The observation that stone phantoms and kidney stones immersed in castor oil cannot be fragmented into passable pieces (see Figs. 4a and 6b) indicates that there is a size limitation on the fragments produced by stress waves alone in SWL. Among various proposed mechanisms, this finding is most consistent with the spalling mechanism. A simple analysis of wave reflection and superposition at the stone boundary may provide some critical insights to this problem. Let's consider the reflection of a transmitted longitudinal wave at the posterior surface of a kidney stone, a critical process involved in the production of spalling damage [9, 10]. Because of the decrease in acoustic impedance from stone material to surrounding tissue or fluid, the leading compressive component of the wave will be inverted in phase, generating a reflected tensile wave. This reflected tensile wave, propagating back into the stone material, will first superimpose with the remaining portion of the compressive component of the incident wave, resulted in a mutual reduction of their respective amplitudes [10]. Subsequently, as the reflected tensile wave propagates further into the stone and superimposes with the trailing tensile component of the incident wave, a strong tensile stress will be produced at some distance from the posterior surface of the stone. This is the reason why in cylindrical stone phantoms (LSW propagating along the axis of the cylinder), spalling damage always occurs at a distance from the posterior surface of the stone [10]. On a first order approximation, the reflected tensile wave has to travel at least half of the positive pulse duration (t^+) of the incident longitudinal wave in order to build up a sufficient tensile stress. Taking a typical value of t^+ = 2.0 μs for a HM-3 LSW (see Fig. 1) and the longitudinal wave speed (c_L) in kidney stones [13], this minimal distance ($\sim c_L * t^+ /2$) is estimated to be in the range from 2.7 mm for MAPH to 4.5 mm for COM stones, which are greater than the 2-mm critical size for spontaneous discharge following clinical SWL. When the size of the residual fragments becomes less than this minimal distance, there will be destructive superposition of the stress waves reverberating inside the fragment. Consequently, the net stress imposed on the stone material will be significantly reduced. If the corresponding stress-intensity factor at the tip of pre-existing microcracks in the fragment falls below the fracture toughness of the stone material, subsequent shock

wave exposure will not cause the microcracks to extend and, therefore, no further disintegration of the fragment will occur. Based on this analysis, if only stress waves contribute to stone comminution in SWL most renal calculi will not be comminuted to fragments small enough (< 2 mm) for spontaneous discharge, as demonstrated by the stone comminution results in castor oil.

On the other hand, when cavitation is the only contributory force for stone comminution the resultant fragmentation efficiency is very low, compared to that produced by the combination of stress waves and cavitation. Cavitation-induced damage is primarily surface erosion and it does not penetrate much into the bulk of the stone material. Despite this, cavitation damage may weaken the surface structure of large residual fragments (Fig. 8), making them much more fragile to the impact of subsequent LSWs. With the progression of shock wave exposure, liquid may enter into the bulk of the stone material through crevices produced on the surface [7]. The expansion of bubbles inside the stone by ensuing shock waves may generate large tensile stress at the crevice root, leading to crack expansion [20,21]. The analogy to SWL-induced tissue injury is the tensile rupture of small blood vessels due to large intraluminal bubble expansion [22]. As the number of fragments increase, the total surface area of the fragments will increase rapidly, which would favor the progression of cavitation-facilitated damage. Although the contribution of each individual cavitation bubble to the overall stone comminution is small, the accumulative effect from numerous bubbles generated during the course of SWL treatment could be significant. It is conceivable that although stress wave-induced fracture, such as spalling and squeezing damage, is responsible for the initial fragmentation of the stone, cavitation is necessary to produce fine passable fragments, which are most critical for the success of clinical SWL treatment.

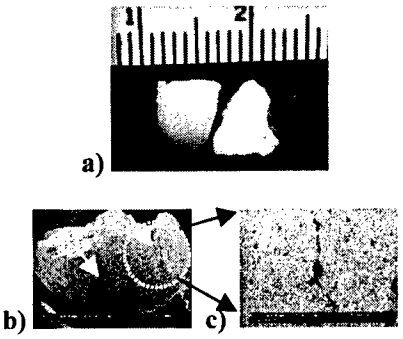

FIGURE 8. Photograph and SEM pictures of large fragments of plaster-of-Paris stone phantoms produced by 100 shocks in an HM-3 lithotripter at 20 kV, **a)** comparison of surface damage of the fragments produced in water (right) with numerous pittings observed on the surface and in castor oil (left) without pitting. **b)** another fragment in water showing deep pitting (indicated by arrows) with radial crack formation, and **c)** an enlarged view of the circled area in **b)**.

As observed in this and other studies [4,23], the scattering of LSWs by small fragments surrounding large residual stone pieces is a significant efficiency-limiting factor for the success of SWL treatment. Therefore, strategies to alleviate the scattering of LSWs by small fragments surrounding large residual stones should be explored in future investigations in order to improve the treatment efficiency of SWL.

In conclusion, stress waves and cavitation have both been found to be important for the success of stone comminution in SWL. While stress waves are important for the initial fragmentation of kidney stones into distributed pieces, their effectiveness is hindered when the size of residual fragments becomes less than half of the compressive wavelength in the stone material, due to destructive superposition of the

stress waves inside the residual fragments. Cavitation, on the other hand, while working at a much slow rate of stone comminution, can significantly weaken the structure of the stone surface, making it much more fragile to the impact of ensuing LSWs and associated bombardments of cavitation bubbles. Therefore, stress waves and cavitation work synergistically, rather than independently, to produce effective and successful disintegration of renal calculi in SWL. Optimal utilization of the stress waves and cavitation in SWL may help to improve treatment efficiency while reducing adverse tissue injury.

ACKNOWLEDGEMENTS

This work was supported in part by NIH through Grants No. RO1-DK52985 and RO1-DK58266, and by a Research Grant from the Whitaker Foundation.

REFERENCES

1. Lokhandwalla, M., and Sturtevant, B., "Fracture mechanics model of stone comminution in ESWL and implications for tissue damage," *Phys. Med. Biol.*, **45**, 1923-1940 (2000).
2. Chaussy, C., Schmiedt, E., Jocham, D., Walther, V., Brendel, W., Forssmann, B., Hepp, W., *Extracorporeal shock wave lithotripsy: New aspects in the treatment of kidney stone disease*, edited by C. Chaussy, (S Karger, 1982).
3. Khan, S.R., Hackett, R.L., and Finlayson, B., "Morphology of urinary stone particles resulting from ESWL treatment," J. *Urol.*. **136**, 1367-1372 (1986).
4. Whelan, J.P. and Finlayson, B., "An experimental model for the systematic investigation of stone fracture by extracorporeal shock wave lithotripsy," *J. Urol.*, 140, 395-400 (1988).
5. Coleman, A.J., Saunders, J.E., Crum, L.A., and Dyson, M., "Acoustic cavitation generated by an extracorporeal shockwave lithotripter," *Ultrasound Med. Biol.*, **13**, 69-76 (1987).
6. Crum, L.A., "Cavitation microjets as a contributory mechanism for renal calculi disintegration in ESWL," *J. Urol.*, **140**, 1587-1590 (1988).
7. Sass, W., Braunlich, W,M., Dreye,r H.P., Matura, E., Folberth, W., Priemeyer, H.G.and Seifert, J., "The mechanisms of stone disintegration by shock eaves," *Ultrasound in Med. & Biol.*, **7** (3), 239-243 (1991).
8. Zhong, P., Chuong, C.J., and Preminger, G.M., "Propagation of shock waves in elastic solids caused by the impact of cavitation microjets: Part II. application to extracorporeal shock wave lithotripsy," *J. Acoust. Soc. Am.*, **94**, 29-36 (1993).
9. Gracewski, S.M., Dahake, G., Ding, Z., Burns, S.J. and Everbach, E.C., "Internal stress wave measurements in solids subjected to lithotripter pulses," *J. Acoust. Soc. Am*, **94**, 652-661, (1993).
10. Xi, X.F. and Zhong, P., "Dynamic photoelastic study of the transient stress field in solids during shock wave lithotripsy," *J. Acoust. Soc. Am.*, **109**, 1226-1239 (2001).
11. Eisenmenger, W., "The mechanisms of stone fragmentation in ESWL," *Ultrasound Med. Biol.*, **27**, 683-693 (2001).
12. Chuong, C.J., Zhong, P., Arnott, H.J. and Preminger, G.M., "Stone damage modes during piezoelectric shock wave lithotripsy", in *Shock Wave Lithotripsy II: Urinary and Billiary*, edited by J.E. Lingeman and D. M. Newman (Plenum, New York, 1989), Chap. 20, pp. 103-106.
13. Zhong, P., Chuong, C.J. and Preminger, G.M., "Characterization of fracture toughness of renal calculi using a microindentation technique," *Journal of Materials Science Letters*, **12**, 1460-1462 (1993).

14. Chuong, C.J., Zhong, P. and Preminger, G.M., "A comparison of stone damage caused by different modes of shock wave generation," *J. of Urology*, **148**, 200-205 (1992).
15. Sutor, D.J., "The nature of urinary stones", *Urolithiasis: Physical Aspects*, B. Finlayson, L.L. Hench, and L.H. Smith (eds.), National Academy of Sciences, Washington, DC, 1972, pp. 43-63.
16. Zhong, P. and Zhou, Y.F:, "Suppression of large intraluminal bubble expansion in shock wave lithotripsy without compromising stone comminution: Methodology and *in vitro* experiments," *J Acoust Soc Am.*, **110**, 3283-3292 (2001).
17. Akers, S.R. Cocks, F.H., and Weinerth, J.L., "Extracorporeal shock wave lithotripsy: the use of chemical treatments for improved stone comminution," *J Urol.* **138**, 1295-1300 (1987).
18. Howard, D. and Sturtevant, B., "In vitro study of the mechanical effects of shock-wave lithotripsy," *Ultrasound Med. Biol.* **23**, 1107-1122 (1997).
19. Hertzberg, R.W., *Deformation and fracture mechanics of engineering materials*, 3rd edition, John Wiley & Sons, New York, NY, 1989.
20. Field, J.E., "The physics of liquid impact, shock wave interactions with cavities, and the implications to shock wave lithotripsy," *Phys. Med. Biol.*, **36**, 1475-1484 (1991).
21. Delius, M., "Minimal static excess pressure minimises the effect of extracorporeal shock waves on cells and reduces it on gallstones," *Ultrasound Med. Biol.* **23**, 611-617 (1997).
22. Zhong, P., Zhou, Y.F. and Zhu, S.L., "Dynamic of bubble oscillation in constrained media and mechanisms of vessel rupture in SWL," *Ultrasound in Med. Biol.*, **27**, 119-134 (2001).
23. Mueller, S.C., Wilbert, D., Thueroff, J.W., Alken, P., "Extracorporeal shock wave lithotripsy of ureteral stones: clinical experience and experimental findings," *J. Urol.* **135**, 831-834 (1986).

Mechanisms Of Cell And Tissue Damage In Shock Wave Lithotripsy

James A. McAteer*, James C. Williams, Jr.*, Andrew P. Evan*, Lynn R. Willis*, Michael R. Bailey†, Lawrence A. Crum† and Robin O. Cleveland‡

*Departments of Anatomy & Cell Biology, and Pharmacology & Toxicology
Indiana University School of Medicine, Indianapolis, IN 46202 USA
†Center for Industrial and Medical Ultrasound, Applied Physics Laboratory
University of Washington, Seattle, WA 98105 USA
‡Department of Aerospace and Mechanical Engineering,
Boston University, Boston, MA 02215 USA

Abstract. Shock wave lithotripsy (SWL) is a highly effective treatment for urinary stones. Lithotripters generate an acoustic pulse in the range ~35-115 MPa P^+, ~-10 MPa P^-, focused to a zone only a few mm wide (estimated I_{SPTP}~80,000 W/cm^2). Lithotripter SW's are effective at breaking stones, but collateral kidney injury can be severe. A clinical dose of SW's (2,000 SW, 24 kV) delivered to the juvenile pig kidney using the Dornier-HM3 lithotripter created a hemorrhagic lesion measuring 6.1±1.7 volume percent. The same dose, but using a time-reversed SW that suppresses cavitation, produced minimal bleeding—injury too small to quantitate. Lysis of red blood cells in vitro was lower with the time-reversed waveform than with conventional SW's, and high overpressure (>120 atm) reduced red cell lysis with conventional SW's. These observations support the idea that cell/tissue injury is related to cavitation. However, red cell lysis at high overpressure was significantly greater than untreated controls, and breakage of ~100 nm diameter phospholipid membrane vesicles was unaffected by overpressure. Overall, these results suggest that cavitation plays an important role in renal injury in SWL, but the *in vitro* cell and vesicle lysis experiments demonstrate that lithotripter SW's also cause damage by mechanisms other than cavitation—possibly strong pressure gradients that cause shear. Further, the vesicle data show that SW damage may not be linked to cavitation when target dimensions are small. Thus, multiple mechanisms appear to be at play in SW damage to biological targets in SWL.

INTRODUCTION

Shock wave lithotripsy (SWL) for the treatment of urinary stones can be viewed as one of the first successful applications of therapeutic ultrasound. SWL was introduced to clinical practice in the early 1980's and even with the refinement of endourologic methods for stone removal such as ureteroscopy and percutaneous nephrostolithotomy, SWL remains the treatment of choice for upper urinary tract calculi [1]. The principal advantage of SWL is that it is a non-invasive treatment to comminute stones. That is, SWL is a non-surgical approach for stone removal and treatment can commonly be performed on an outpatient basis. For treatment, patients

are usually sedated or anesthetized. The urologist controls the number of SW's, the power of the pulses and the rate of SW administration. In a typical treatment session 1,000 to 4,000 SW's are delivered to fragment a stone, and treatment is usually completed in about an hour.

Although SWL is considered to be highly successful, lithotripsy is plagued by the occurrence of adverse effects. Clinical experience and studies with experimental animals have shown that a dose of SW's sufficient to comminute a stone invariably causes trauma to the kidney [2-4]. The renal injury associated with SWL can be severe and can lead to long-term complications such as new-onset hypertension [5]. Still, the benefits of SWL are considerable. As such there is great interest in research to understand the mechanisms of SW action in stone breakage and renal injury with the goal of devising strategies to make lithotripsy safer and more effective.

In SWL a high-intensity acoustic pulse is generated by one of three mechanisms: electrohydraulic spark discharge, electromagnetic deflection of a plate or piezoelectric transduction. The majority of clinical devices are either electrohydraulic or electromagnetic. The acoustic pulse is focused to a cigar-shaped region that, depending on the lithotripter design, is 3-12 mm wide and 50-80 mm long. Electrohydraulic lithotripters typically have a larger focal zone than electromagnetic or piezoelectric lithotripters.

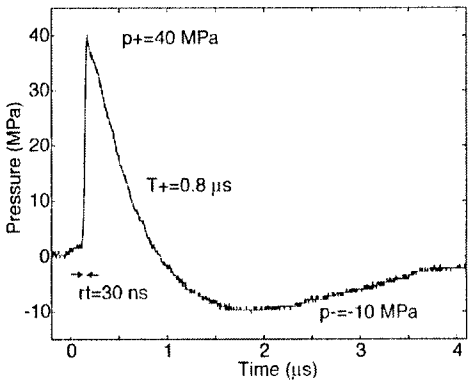

FIGURE 1: Typical shock wave at the focus of an electrohydraulic lithotripter.

A representative focal waveform is shown in Fig. 1. The pulse consists of a compressive phase with a peak amplitude of 35—115 MPa and duration ~1 μs, followed by a tensile tail with peak amplitude ~-10 MPa and duration ~3 μs. The pulse leads with a shock wave of ~ 10 ns rise time (measured in water). However, this measurement is affected by the limited bandwidth (<100 MHz) of available hydrophones, and the Taylor shock thickness for a shock of these amplitudes is of the order 0.1 ns. The waveform measured in vivo is very similar to that shown in Fig. 1 except that the rise time is lengthened to ~70 ns [6]. For comparison with high intensity focused ultrasound, the peak intensity at the focus is I_{SPTP} = 80,000—880,000 W/cm^2. However, because in the clinical setting shock waves are delivered at ~1 s intervals the temporal average of the intensity is I_{SPTA}= 0.08—0.88 W/cm^2. Therefore, the biological actions of lithotripsy are dominated by non-thermal mechanisms [7]. Although considerable progress has been made in recent years to understand how

lithotripter SW's work, the exact mechanisms by which SW's fragment stones and cause damage to tissue are still under investigation.

The adverse effects of SWL have been linked to the cavitation induced by the tensile phase of the lithotripter shock wave. It is well recognized that lithotripter SW's generate cavitation in the body [8], and studies using diagnostic ultrasound and passive detection methods have localized cavitation to the renal parenchyma [9]. The renal lesion in SWL is characterized by vascular trauma — damage primarily to capillaries, small veins and small arteries [2,3,10,11]. Precisely how cavitation causes this vascular damage has yet to be determined. The renal parenchyma is occupied by myriad epithelial tubules and small blood vessels. There is very little fluid space outside the lumens of vessels and renal tubules where cavitation might be expected to occur. Hemorrhage leads to pooling of blood in the kidney interstitium and beneath the kidney capsule. Such bleeding could provide sites for cavitation to develop. Cavitation detection has localized bubble noise and echogenicity to subcapsular hematomas, but has not been able to resolve bubble activity to vessels of the size that are damaged by SWL [9]. However, large pools of blood may not be necessary for cavitation to occur and recent in vitro studies [12] lend support to the idea that bubble expansion within the lumen could cause small blood vessels to rupture. Thus, SW-bubble interactions appear to play an important role in the renal trauma associated with SWL.

The purpose of this report is to summarize our observations from in vivo studies with pigs [13] and in vitro experiments with biological targets (isolated cells and membrane vesicles) [14,15] showing that cavitation is involved in SWL injury. In addition, we present evidence suggesting that mechanisms other than cavitation may contribute to cell and tissue injury in lithotripsy.

METHODS

Lithotripters And Shock Wave Reflectors

Animal experiments were performed using an unmodified (80 nf) Dornier HM3 clinical lithotripter. This lithotripter has a brass ellipsoidal reflector. Pressure release reflectors (PRel) were milled from polyurethane foam and machined to nest inside the brass reflector. Thus, the PRel reflector conformed to an ellipse of slightly smaller dimensions, but with the same foci (F1 and F2) as the brass reflector. The normal pressure amplitude reflection coefficient, R, for this polyurethane foam is nearly pressure release (R = -0.88). R for brass is 0.94. Thus, neither reflector was perfectly rigid (R = 1) or pressure-release (R = -1) acoustically.

The PRel reflector was developed as a means to suppress cavitation generated by an electrohydraulic lithotripter [16-18]. The polyurethane insert reverses the compressive and tensile components of the lithotripter pulse so that the tensile phase precedes the compressive phase (Fig. 2). Cavitation bubbles that may begin to grow under influence of the leading tensile wave are crushed by the trailing compressive wave. Thus, the cavitation cycle is interrupted before bubbles can undergo forceful inertial

collapse. The PRel reflector does not change the position of the spark gap, the position of F2 or the dimensions of the focal zone of the lithotripter [17,18].

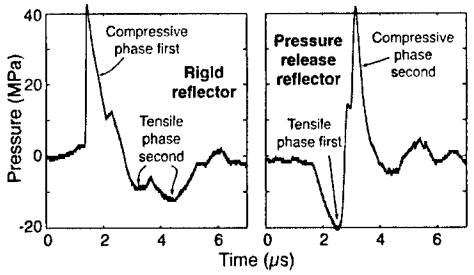

FIGURE. 2: Waveforms from rigid and pressure release (PRel) reflectors.

In vitro studies on isolated cells and membrane vesicles were performed using a research electrohydraulic lithotripter with acoustic output similar to that of the Dornier HM3 [19,20].

Experimental Animals And Assessment Of Kidney Injury In The Pig

Female farm pigs, 6-7 weeks of age with an average weight of 14.0±0.6 kg were used. Three groups of animals were studied: Group 1 (rigid reflector), Group 2 (PRel reflector), and Group 3, (sham SWL). Animals were anesthetized and prepared for SWL as previously described [10,11]. SW's (2000 SW's, 24 kV, 2 Hz) were administered to the lower pole calyx for the rigid and PRel reflector groups, while sham animals were placed in the lithotripter but not treated.

Following SW treatment both kidneys were then infused with fixative in situ and removed for morphological analysis. Four kidneys from each study group were embedded and serial sectioned for morphometric analysis to determine the size of the hemorrhagic lesion produced by SWL. [21]

In Vitro Lysis Of Red Blood Cells And Phospholipid Membrane Vesicles

Fresh red blood cells collected from one donor were heparinized, washed and diluted to a concentration of 3.1% in buffered saline (PBS), and loaded to 2 ml screw cap polypropylene cryovials [14]. Since bubbles in such vials enhance SW-lysis vials that contained bubbles were discarded [22]. For studies using the pressure release reflector, vials were positioned at F2 and 75 shock waves were administered (22 kV, 1Hz). For comparison, cohort vials were treated with SW's using the rigid reflector. Cell lysis was determined by assay of hemoglobin in the supernatant [23].

Carboxyfluorescein-loaded phospholipid membrane vesicles were prepared from egg phosphatidylcholine by the extrusion method [24]. Repeated passage of phosphatidylcholine in carboxyfluorescein buffer through a 0.1 μm polycarbonate filter produced unilamellar vesicles ~120 nm in diameter. Extravesicular carboxyfluorescein was removed by passing the vesicles through a Sephadex G-25 column. Vesicle lysis was determined by measuring carboxyfluorescein in the extravesicular fluid following SW exposure.

Overpressure Experiments With Cells And Vesicles

The overpressure chamber used in these experiments was a bronze-aluminum alloy cylinder capped with plates milled from a plastic (polyphenylene oxide) that allowed passage of the shock wave with minimal attenuation and no appreciable alteration in waveform [25]. Vials of cells or membrane vesicles were placed within the chamber, at F2 of the lithotripter, the chamber was filled with water and the end-caps secured. The chamber was pressurized with nitrogen to ~120 atm and SW's were administered. Non-pressurized vials were exposed to SW's in the chamber. Zero-SW controls were handled in the same way, but were not exposed to SW's.

RESULTS AND DISCUSSION

Pig kidneys treated with SW's from the standard rigid reflector showed damage that was evident even on gross inspection. These kidneys typically developed a subcapsular hematoma that covered their anterior and posterior surfaces. Subcapsular bleeding was most pronounced in the treated pole (lower pole) of the kidney but frequently extended to portions of the upper pole as well. Histologic analysis of the renal parenchyma showed a focal hemorrhagic lesion that involved both the cortex and medulla and commonly spanned the entire width of the kidney [10,11,13]. This zone of damage was focal, in that the parenchyma of the upper pole was never involved and there were broad areas of the treated, lower pole that appeared undamaged (Fig. 3). At the tissue level the lesion was characterized by breaks in veins, capillaries and other thin-walled vessels. Some small arteries were also damaged. The vascular endothelium of damaged vessels was disrupted, exposing patches of basement membrane. Renal tubules were broken and were filled with blood. The peritubular interstitium was filled with extravasated blood and this region of hemorrhage contained a large number of inflammatory cells such as polymorphonuclear leucocytes and platelets. The hemorrhagic lesion produced by treatment with the rigid reflector occupied 6.1±1.7% of kidney parenchymal volume (determined by quantitative histomorphometry) [13].

Very little damage occurred to kidneys treated with the PRel reflector (Fig. 3) [13]. These kidneys did not develop hematomas. On histologic analysis the renal cortex was virtually undamaged and evidence of injury was limited to slight intraparenchymal bleeding in renal papillae (Fig. 3, arrowhead on right panel) that fell within the F2 focal zone of the lithotripter. Although such regions of bleeding were visible in histologic sections these areas of hemorrhage were too slight to register by morphometric analysis (i.e. 0.0% of kidney parenchymal volume). Our previous studies have shown that the PRel reflector suppresses cavitation in vitro [18]. Thus, the observation that renal injury is dramatically reduced when the polyurethane PRel reflector is used strongly suggests that the damaged that occurs with the standard rigid reflector is caused by cavitation.

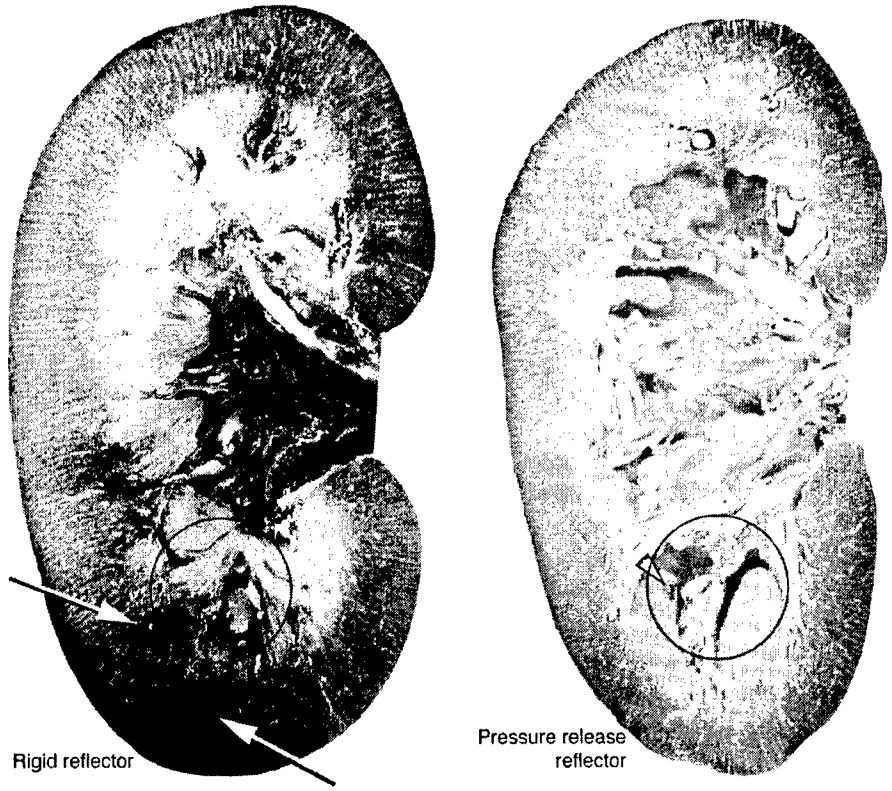

FIGURE 3: Damage to pig kidney tissue using rigid (left) or PRel (right) reflector. Circles mark location in kidney lower pole targeted during SW treatment.

Isolated red blood cells (RBC's) suspended in physiologic buffer are commonly used in lithotripsy research as a sensitive marker SW damage [23]. When vials of RBC's were treated with a dose of 75 SW's using the standard rigid reflector, lysis (~1.1%) was significantly higher ($p<0.0001$) than untreated controls (~0.25%) (Fig. 4). Cell lysis with the PRel reflector was significantly lower ($p<0.0001$) than

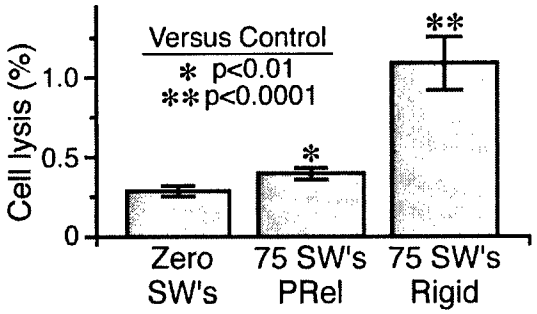

FIGURE 4: Red blood cell lysis with rigid and pressure release reflectors.

when the rigid reflector was used. This suggests that cavitation was responsible for most of the cell lysis that occurred with the rigid reflector. Hemolysis with the PRel reflector was reduced, but still significantly higher ($p<0.01$) than the baseline cell lysis observed in untreated controls.

Our previous studies [18] have shown that the lifetime (bubble duration) of cavitation bubbles with the PRel reflector is 50 times shorter, and the amplitude of the calculated acoustic emission of the collapsing bubbles is 13 times smaller than with the rigid reflector. Also, cavitation pits in target foils treated with PRel reflector SW's measure 8 times smaller than with the rigid reflector. That is, cavitation bubbles with the PRel reflector do not grow as large and they collapse with less force than the cavitation bubbles that are generated with the rigid reflector. Thus, it is clear that cavitation is substantially reduced by inverting the lithotripter pulse, but, bubble activity is not entirely eliminated. Therefore, it is possible that the RBC lysis with PRel greater than untreated controls was caused by cavitation. At the same time this does not rule out the possibility that this increased hemolysis was due to a mechanism other than cavitation.

It has been shown by numerical modeling [26] and by experiment [14,27] that lithotripter shock pulses have the potential to cause cell lysis by non-cavitational mechanisms such as shear. In order to separate damage to isolated cells caused by cavitation from cell lysis due to non-cavitational forces we used overpressure to suppress cavitation [14,25,28,29]. In theory, overpressure (OP) in excess of the amplitude of the tensile phase of the lithotripter pulse should prevent bubble growth and, thereby, prevent cavitation from occurring. In actuality, cavitation in the free field can be suppressed by relatively low (~3-5 atm) excess hydrostatic pressure [28,29]. To make certain that cavitation would be eliminated we exposed isolated RBC's to SW's in an overpressure chamber capable of achieving >120 atm excess static pressure. The chamber was constructed with acoustic windows that had minimal effect on the waveform characteristics or amplitude of the pressure pulse [25]. Vials of RBC's placed in the chamber were exposed to SW's at atmospheric pressure or at >120 atm overpressure. Lysis of cells treated with SW's at OP was significantly lower ($p<0.01$) than cell lysis when SW's were administered at atmospheric pressure (Fig. 5). This hemolysis at overpressure sufficient to preclude cavitation still was significantly higher than cell lysis in untreated (but pressurized) controls. This suggests that whereas most of the SW-cell lysis was due to cavitation, significant cell damage occurred by a mechanism other than cavitation. This non-cavitational damage was

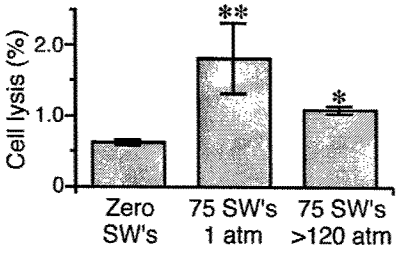

FIGURE 5: Red blood cell lysis at atmospheric and high overpressure (OP). *$p<0.04$ compared to control; ** $p<0.003$ compared to control and high OP.

dependent on the kilovoltage of the shock source, with lysis significantly higher ($p<0.05$) at 24 kV than at 16 kV and 20 kV (Fig. 6).

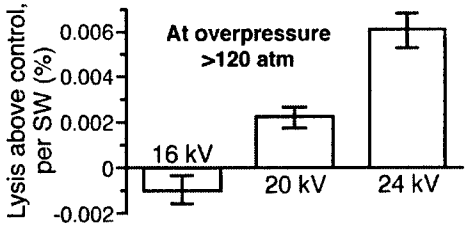

FIGURE 6: Red blood cell lysis at high OP is dependent on SW voltage.

Isolated RBC's in vitro are relatively large targets. With a diameter in fluid suspension of 7-9 μm RBC's approximate the size of circulating cells in the blood vasculature, and some tissue structures such as the walls of capillaries and small veins. Our in vitro studies with OP showed (above) that significant SW damage was due to forces other than cavitation. Numerical modeling of SW propagation through a tissue-like medium predicts that the stress upon a target object is related to the size of the object [20,26,27]. Thus, larger targets should be under greater stress than smaller targets, but the size limit for target damage is difficult to estimate. In order to determine if lithotripter SW's might be capable of causing damage to biological targets smaller than isolated cells, we conducted SW exposure experiments on phospholipid membrane vesicles similar in size (~100-150 nm) to intracellular organelles. Vesicles were more difficult to break than isolated cells. The lysis rate of vesicles was approximately 0.03% per 100 SW's compared to 2.3% per 100 SW's for isolated RBC's. To determine whether SW lysis of vesicles was dependent on cavitation, vials of vesicles were placed in the OP chamber and exposed to SW's at atmospheric pressure or at ~130 atm OP. Vesicle lysis at OP was not different from lysis at atmospheric pressure (Fig. 7). This indicates that SW damage to membrane vesicles was not due to cavitation. That is, biological targets the size of intracellular organelles can be damaged by lithotripter SW's, but cavitation does not contribute to this damage.

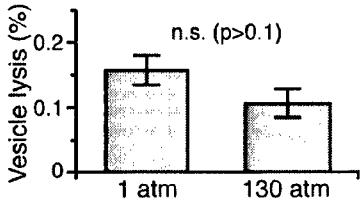

FIGURE 7: Phospholipid vesicle lysis at atmospheric and high OP.

Overall, the results of these studies using biological targets as diverse as whole animals, isolated cells and membrane vesicles suggest that lithotripter SW's cause damage to tissue by more than one mechanism. Cavitation appears to be the dominant mechanism, but other forces appear to be at play as well. These studies also point to

the value of approaching the problem of SW injury at different levels, that is, with models that have different levels of biological complexity. The data show that our understanding of how SW's injure the kidney is helped by use of simpler models which may in themselves seem far from tissue. For example, cells in suspension lack the structural organization of tissues, so this simple system is not a particularly compelling model of a complex organ such as the kidney. However, with isolated cells it is possible to rigidly control the environment during SW exposure and this proves to be an important advantage. For example, isolated cells can be exposed to SW's while at high overpressure, a manipulation that is not feasible with a living animal. Use of this strategy to control cavitation has shown convincingly that SW-induced cell lysis is not due to cavitation alone [14,27].

The idea that lithotripter SW's may cause tissue damage by mechanisms other than cavitation has been suggested by others. Lokhandwalla and Sturtevant [26] demonstrated by computation that SW's are capable of causing cell rupture by inducing unsteady flows in the surrounding media. Subsequent experimental studies [27] using overpressure to eliminate cavitation and a parabolic reflector to refocus the wave field within the sample vial showed that even in the absence of cavitation SW's could deform foils and that cell lysis was significantly enhanced by SW-focusing. This supports the idea that cell lysis can be caused by gradients in shock strength and validates shear as a damage mechanism.

How shear might contribute to renal injury is not known. The PRel reflector data with pigs [13] suggest that the magnitude of damage caused by cavitation far outweighs the injury caused by shear. However, the contribution of shear may not be entirely inconsequential. It is possible that damage caused by shear might potentiate damage caused by cavitation. That is, it seems feasible that vessel rupture due to shock gradients could initiate bleeding into the kidney interstitium and that this pooling of blood could then support cavitation.

In conclusion, taken together these studies using whole animals and isolated in vitro targets suggest that cavitation is the principal mechanism by which lithotripter SW's cause tissue damage. Shock wave shear has the potential to cause damage to the kidney, perhaps even initiating vascular injury, but SW-bubble interactions appear to be the major mechanism responsible for renal injury in SWL.

ACKNOWLEDGEMENTS

We thank Erin Hatt and Drew Rietjens for excellent technical support, and Philip Blomgren for the images of shock wave damage in kidneys. This research was supported by grants from the National Institutes of Health (NIH DK55674, DK43881).

REFERENCES

1. Kerbl, K., Rehman, J., Landman, J., Lee, D., Sundaram, C., Clayman, R.V., *Jour Endourol,* **16**, 281-288 (2002).
2. Evan, A.P., McAteer, J.A., Q-Effects of shock wave lithotripsy, in *Kidney Stones: Medical and Surgical Management*, edited by F.L. Coe, M.J. Favus, C.Y.C. Pak, G.M. Preminger, Lippincott-Raven, Philadelphia, 1996, pp. 549-570.

3. Evan, A.P., Willis, L.R., Lingeman, J.E., McAteer, J.A., *Nephron,* **78**, 1-8 (1998).
4. Lingeman, J.E., Newmark, J.R., Adverse bioeffects of shock-wave lithotripsy, *in Kidney Stones: Medical and Surgical Management,* edited by F.L. Coe, M.J. Favus, C.Y.C. Pak, G.M. Preminger, Lippincott-Raven, Philadelphia, 1996, pp. 605-614.
5. Janetschek, G., Frauscher, F., Knapp, R., Hofle, G., Peschel, R., Bartsch, G., *J Urol,* **158**, 346-351 (1997).
6. Cleveland RO, Lifshitz DA, Connors BA, Evan AP, Willis LR, Crum L.A., *Ultrasound Med Biol,* **24**, 293-306 (1998).
7. Filipczynski, L., Wojcik, J., *Ultrasound Med Biol,* **17**, 715-721 (1991).
8. Coleman, A.J., Choi, M.J., Saunders, J.E., *Ultrasound Med Biol,* **22**, 1079-1087 (1996).
9. Sapozhnikov, O.A., Bailey, M.R., Crum, L.A., Miller, N.A., Cleveland, R.O., Pishchalnikov, Y.A., Pishchalnikova, I.V., McAteer, J.A., Connors, B.A., Blomgren, P.M., Evan, A.P., *Proc IEEE Ultrasonics Symp,* 1437-1440 (2001).
10. Willis, L.R., Evan, A.P. Connors, B.A., Blomgren, P., Fineberg, N.S., Lingeman, J.E., *J Am Soc Nephrol,* **10**, 1753-1762 (1999).
11. Evan, A.P., Connors, B.A., Pennington, D.J., Blomgren, P.M., Lingeman, J.E., Fineberg, N.S., Willis, L.R., *J Endourol,* **13**, 619-628 (1999).
12. Zhong, P., Zhou, Y., Zhu, S. *Ultrasound Med Biol,* **27**, 119–134 (2001).
13. Evan, A.P., Willis, L.R., McAteer, J.A., Bailey, M.R., Connors, B.A., Shao, Y., Lingeman, J.E., Williams, J.C. Jr., Fineberg, N.S., Crum, L.A., *J Urol,* **168** (In Press: 2002).
14. Williams, J.C. Jr., Woodward, J.F., Stonehill, M.A., Evan, A.P., McAteer, J.A., *Ultrasound Med Biol,* **25**, 1445-1449 (1999).
15. Williams, J.C. Jr., Rietjens, D.L., Zarse, C.A., McAteer, J.A., *Proc 17th Int'l Cong Acoust,* **VII**, 182-183 (2002).
16. Bailey, M.R., *Control of acoustic cavitation with application to lithotripsy.* Ph.D. dissertation, The University of Texas at Austin, 1997. Also issued as Technical Report ARL-TR-97-1, Applied Research Laboratories, The University of Texas at Austin, Texas, March 1997.
17. Bailey, M.R., Blackstock, D.T., Cleveland, R.O., Crum, L.A. *J Acoust Soc Am.* **104**, 2517-2524 (1998).
18. Bailey, M.R., Blackstock , D.T., Cleveland, R.O., Crum, L.A. *J Acoust Soc Am,* **106**:1149-1160 (1999).
19. Cleveland, R.O., Bailey, M.R., Hartenbaum, B., Lokhandwalla, M., McAteer, J.A., Sturtevant, B., *Rev Scientific Instr,* **71**, 2514-2525 (2000).
20. Howard, D., Sturtevant, B. *Ultrasound Med Biol,* **23**, 1107-1122 (1997).
21. Blomgren, P.M., Connors, B.A., Lingeman, J.E., Willis, L.R., Evan, A.P., *Anat Rec,* **249**, 341-348 (1997).
22. Williams, J.C. Jr., Stonehill, M.A., Colmenares, K., Evan, A.P., Andreoli, S.P., Cleveland, R.O., Bailey, M.R., Crum, L.A., McAteer, J.A., *Ultrasound Med Biol,* **25**, 473-479 (1999).
23. Delius, M., Ueberle, F., Gambihler, S., *Ultrasound Med Biol,* **21**, 707-710 (1995).
24. MacDonald, R.C., MacDonald, R.I., Menco, B.P.M., Takeshita, K., Subbarao, N.K., Hu, L., *Biochim Biophys Acta Bio-Membr,* **1061**, 297-303 (1991).
25. Stonehill, M.A., Williams, J.C. Jr., Bailey, M.R., Lounsbery, D., Cleveland, R.O., Crum, L.A., Evan, A.P., McAteer, J.A., *Meth Cell Sci,* **19**, 303-310 (1998).
26. Lokhandwalla, M., Sturtevant, B., *Phys Med Biol,* **46**, 413-437 (2001).
27. Lokhandwalla, M., McAteer, J.A., Williams, J.C., Jr., Sturtevant, B., *Phys Med Biol,* **46**, 1-20 (2001).
28. Delius, M., *Ultrasound Med Biol,* **23**, 611-617 (1997).
29. Sapozhnikov, O.A., Khokhlova, V.A., Bailey, M.R., Williams, J.C. Jr., McAteer, J.A., Cleveland, R.O., Crum, L.A., *J Acoust Soc Am,* (In Press: 2002).

7. ULTRASOUND-ENHANCED DRUG DELIVERY

Enhanced Gene Transfer By Echo Contrast Agents

Katsuro Tachibana*, Tieli Li†, Motomu Kuroki†, Masahide Kuroki†

*Department of Anatomy Fukuoka University School of Medicine 7-45-1 Nanakuma, Jonan Fukuoka 814-0180 Japan
†Molecular Oncology Center Fukuoka University 7-45-1 Nanakuma, Jonan Fukuoka 814-0180 Japan

Abstract. The purpose was to determine if commercially available echo contrast agent microbubbles could be used to increase gene transfection efficiency by relatively low intensity ultrasound-mediated microbubble destruction. Cell viability in the presence of Optison™ was significantly different from Albunex at the same 5% microbubble concentration (73.1±2.7 vs 33.3±1.0, $p<0.01$, ANOVA). Cell killing rate by Optison™ remained approximately the same level at bubble concentration of 10 and 20%. On the other hand, cell viability tended to decrease at higher bubble concentrations (62.0±4.3, 54.8±1.4%) in the case with Albunex. Optison™ was diluted to a concentration of 2% whereas Albunex was adjusted to 10%. Levovist microbubble concentration was adjusted to 10 mg/ml. Cell viability under these conditions after ultrasound irradiation was approximately 60% for each of the agents tested, however the mean number of GFP transfected cells in the presence of Optision was approximately 8-folds greater than in groups that contained Albunex or Levovist. Low intensity therapeutic ultrasound in the presence of Optison™ echo contrast agent induced efficient gene transfer but not with Albunex or Levovist.

INTRODUCTION

Recent studies have shown that therapeutic ultrasound can induce or increase cell membrane permeabilization of various agents including genes. It is currently suggested that the mechanism of this phenomenon is closely related with acoustic cavitation. High ultrasound intensities are required to create cavitation within tissues such as the skeletal muscles and myocardium. Ultrasound alone could lead to temperature increase and mechanical damage to the tissue itself. This study addressed the hypothesis that echography contrast agent microbubbles that are commercially available could be used to increase gene transfection efficiency by relatively low intensity ultrasound-mediated microbubble destruction. Gene transfection rates were measured *in vitro* in the presence of various types of echo contrast agents.

MATERIALS AND METHODS

Plasmid Preparations

A commercial reporter plasmid pQBI25 (TAKARA Biomedicals, Japan) encoding green fluorescent protein (GFP) and Rhodamine-labeled plasmid pGeneGrip™ (GTS inc., San Diego, CA) with hCMV IE promoter/enhancer driving green fluorescent protein gene were used for insertion and subsequent transient expression within the cells. The plasmid DNA from Escherichia coli DH5 cultures was prepared with Qiagen Maxi kit according to the company protocol (Qiagen Inc., Chatsworth, CA). Finally, agarose gel electrophoresis was performed before and after restriction endonucleases digestion to verify the identity and purity of the plasmid DNA.

In Vitro Studies

The Chinese hamster ovary (CHO) cells were maintained in alpha minimal essential medium (Life Technologies, Inc., Gaithersburg, MD) supplemented with 10% heta-inactived fetal bovine serum (Bio-Whittaker, Walkersville, MD), 2 mM glutamine, 100 units/ml penicillin, and 100 μg/ml streptomycin. The cell cultures were maintained at 37° C in a humidified atmosphere of 5% CO_2 in air. Exponentially growing cells were used in all experiments. Cell viability was determined by trypan blue dye exclusion.

Echo Contrast Agents

Culture cells were harvested and washed once in Phosphate buffered saline (PBS) and re-suspended at 2×10^6 cells/ml of plain PBS/well of 48-well plate (Corning, New York, NY). Three different types of ultrasound contrast agent microbubbles were evaluated: Albunex is a albumin shelled ultrasound contrast agent composed of air-filled micrrobubbles with a median diameter of 3 to 4 μm, Optison™ is a second-generation perfluorocarbon-filled contrast agent with similar microbubble diameter and concentration (5 to 8 $x10^8$ bubbles per milliliter), Levovist is a galactose-based, air-filled microbubble contrast agent, 99% of which are smaller than 7 μm. Each pf the contrast agents was added to the cell medium and diluted to various concentrations. Plasmid encoding green fluorescent protein were then added immediately into cell supernatant to a final DNA concentration of 20 μg/ml at a volume of 1 ml.

Ultrasound Exposure

The ultrasound probe and well plate were firmly fixed to a stand to avoid dislocation during ultrasound irradiation. Immediately after addition of plasmid DNA and microbubbles into the well, the cells were exposed with 1.0 MHz ultrasound for 20 seconds at an intensity of 0.5 or 1.0 W/cm^2, duty cycle 20% (Sonitron 1000, Rich Mar Inc, Inola, OK). The ultrasound probe was inserted directly into the cell suspension. A miniature stirrer was placed within the well and revolved at a speed of 300 RPM by a magnetic rotator placed under the container (PC-220, Corning, Boston, MA). The cells

were placed at least a row apart from each other to prevent overlap or interaction by transmission of ultrasound along the plastic well container. Immediately after exposure, the cell viability was tested by counting cells stained with trypan blue. To verify that ultrasound exposure did not produce thermal effects, the temperature in the sample was measured before and immediately after ultrasound exposure by a needle type digital thermometer (PTC-201, Unique Medical Co, Tokyo, Japan). The rise in temperature within the samples was found to be less than 1° C. Thus any ultrasound bioeffects observed in this study were considered to be non-thermal.

Quantification of GFP Expression

After the cell viability analysis, the cell suspensions were harvested from the wells, separated by centrifugation and re-suspended in alfa-MEM. Viable cells (2×10^5) were plated into 6-cm dishes. After 48 hours culture, the GFP positive cells were detected on Digital Camera FUJIX HC-300 (FUJIFILM, Tokyo, Japan), ARGUS-20 image processor and chilled CCD Camera (Hamamatsu Photonics K.K., Hamamatsu, Japan) from a ECLIPSE E 600 fluorescence microscopy (Nikon Inc., Tokyo, Japan) with plain apochromat lenses using an FITC-HYO filter (EX 450-490, DM 505, BA 520). Cell images were printed out by FUJIX Pictrography 3000 (FUJIFILM, Tokyo, Japan).

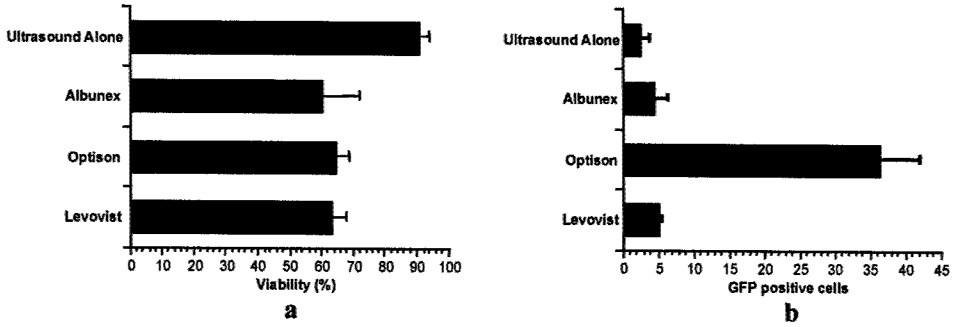

FIGURE 1. a) Bar graph shows cell viability (mean ± SD, n=5) after 1 MHz, 20% duty cycle, 20 second duration. Concentration of each echo contrast agents were Levovist: 10 mg/ml, Albunex: 10% and Optison™: 2%. b) Bar graph shows the percentage of GFP positive cells at identical conditions.

RESULTS

Preliminary measurement of cell viability after ultrasound irradiation alone at various intensities (0.5, 1.0 W/cm^2) and duration (10, 20, 40 sec) were performed. Ultrasound alone had minimal cell killing effects at the conditions examined. Whereas addition of echo contrast agents resulted in significant reduction of cell viability by ultrasound irradiation. Addition of 10 mg/ml Levovist resulted in cell viability reduction from 90.6±2.2% baseline to 60.7±5.3% ($p<0.01$). Similar cell viability percentages were observed with addition of Levovist concentrations of 20 and 40 mg/ml. Addition of Albunex and Optison™ also induced significant cell killing compared to ultrasound irradiation alone. Cell viability in the presence of Optison™ was

significantly different from Albunex at the same 5% microbubble concentration (73.1±2.7 vs 33.3±1.0, $p<0.01$, ANOVA). Cell killing rate by Optison™ remained approximately the same level at bubble concentration of 10 and 20%. On the other hand, cell viability tended to decrease at higher bubble concentrations (62.0±4.3, 54.8±1.4%) in the case with Albunex. Based upon these results, the concentration of each echo contrast agents were adjusted to induce similar cell killing rates at identical ultrasound irradiation conditions in the following gene transfection experiments. Optison™ was diluted to a concentration of 2% whereas Albunex was adjusted to 10%. Levovist microbubble concentration was adjusted to 10 mg/ml. Cell viability under these conditions after ultrasound irradiation was approximately 60% for each of the agents tested, however to our surprise, the mean number of GFP transfected cells in the presence of Optision was approximately 8-folds greater than in groups that contained Albunex or Levovist.

DISCUSSION

In the present study, commercially available echo contrast agents, Optison™, Albunex and Levovist were evaluated *in vitro* to see if there are differences in inducing gene transfer. Perfluorcarbon- filled, second generation Optision proved to be more effective compared to the other agents in increasing the rate of gene transfection.

It has been previous reported by others that certain microbubbles significantly increases drug uptake into cells and gene transfection [1-16]. Although the exact mechanism that causes this phenomenon is still unclear, the rapid collapse of microbubbles is thought to play a major role. It is also speculated that the presence of microbubbles can significantly reduce the acoustic pressure amplitude threshold for cavitation. Miller MW et al [12] have supported this hypothesis with the use of a 20-MHz passive cavitation detector system. Greenleaf et al. [5] demonstrated an increase in the transfection rate of DNA *in vitro*, in the presence of albumin microbubbles, Albunex. Unger et al. [4] described similar results with microbubble liposomes. Guzman et al [13] succeeded in quantification of molecular uptake of drugs in DU145 prostate cancer and aortic smooth muscle cells. High acoustic pressure resulted in greater uptake of drugs per cell in the presence of Optison™. Furthermore, comparison has recently been performed by several groups between different type of microbubbles such as Albunex and Optison™. It was reported by Miller MW et al [2] that Optison™ had greater sonolytic potential than Albunex in terms of destruction of human erythrocytes *in vitro*. Others have similarly shown more lysis of cervical cancer cells (HeLaS3) in the presence of Optison™ rather than Albunex [14].

Although the exact mechanism is still unknown, it is believed that microbubbles, upon rupture, create a local increase in membrane fluidity, thereby enhancing cellular uptake of the therapeutic compound. Furthermore, as Optison™ has a longer life span as a bubble, gene transfection may be attributed to repeated or slower bubble destruction during ultrasound irradiation resulting in greater number of cell membrane poration. Next generation echo contrast agents could be developed as a carrier of genes to targeted locations and pure plasmid DNA can be attached either to the outside or inside of the microbubble capsule wall [15]. Bubbles can be collapsed by extracorporeal

ultrasound or by intravascular ultrasound catheter [16], permitting the DNA to penetrate directly into the tissue and cells. Nevertheless, more experiments are anticipated to determine the optimal echo contrast agent and ultrasound conditions for drug/gene delivery.

REFERENCES

1. Tachibana, K, Tachibana, S. *Echocardiography,* **18**, 323-328 (2001).
2. Tachibana, K, Tachibana, S. *Circulation,* **92**, 1148-1150(1995).
3. Tachibana, K, Uchida, T, Ogawa, K, Yamashita, N, Tamura, K. *Lancet,* **353**, 1409 (1999).
4. Unger, EC, McCreery, TP, Sweitzer, RH. *Invest Radiol,* **32**, 723-727 (1997).
5. Greenleaf, WJ, Bolander, ME, Sarkar,G, Goldring, MB, Greanleaf, JF. *Ultrasound in Med & Biol,* **24**, 587-595 (1998).
6. Shohet, RV, Chen, S, Zhou, YT, Wang, Z, Meidell, RS, Unger, RH, Grayburn, PA. *Circulation,* **101**, 2554-2556 (2000).
7. Lawrie, A, Brisken, AF, Francis, SE, Cumberland, DC, Crossman, DC, Newman, CM. *Gene Therapy,* **7**, 2023-2027 (2000).
8. Newman, CM, Lawrie, A, Brisken, AF, Cumberland, DC. *Echocardiography,* **18**, 339-347 (2001).
9. Porter, TR, Xie, F. *Echocardiography,* **18**, 349-353 (2001).
10. Manome, Y, Nakamura, M, Ohno, T, Furuhata, H. *Human Gene Therapy,* **11**, 1521-1528 (2000).
11. Taniyama, Y, Tachibana, K, Hiraoka, K. *Circulation,* **105**, 1233-1239 (2002).
12. Miller, MW, Everbach, EC, Cox, C, Knapp, RR, Brayman, AA, Sherman, TA. *Ultrasound in Med & Biol,* **27**, 709-721 (2001).
13. Guzman, HR, Nguyen, DX, Khan, S, Prausnitz, MR. *J Acoust Soc Am,* **110**, 588-596 (2001).
14. Huber, PE, Jenne, J, Debus, J, Wannenmacher, MF, Pfisterer, P. *Ultrasound in Med & Biol,* **25**, 1451-1457 (1999).
15. Lindner, JR, Kaul, S. *Echocardiography,* **18**, 329-337 (2001).
16. Amabile, PG, Waugh, JM, Lewis, TN, Elkins, CJ, Janas, W, Dake, MD. *J Am Coll Cardiol,* **37**, 1975-1980 (2001).

Comparison Of Two Albumin-Based Echocardiographic Contrast Agents For Ultrasound-Induced Gene Transfer

S.V. Pislaru[a], C. Pislaru[b], R.R. Kinnick[b], R. Singh[a], R. Gulati[a], J.F. Greenleaf[b], and R.D. Simari[a]

[a]*Cardiovascular Research Department, Mayo Clinic and Foundation, Rochester MN, USA*
[b]*Basic Ultrasound Research Laboratory, Mayo Clinic and Foundation, Rochester MN, USA*

Abstract. Background. Various contrast agents have been shown to enhance ultrasound (US) induced gene transfer. The aim of our study was to directly compare Optison™ and perfluorocarbon exposed sonicated dextrose albumin (PESDA), agents with very similar structure. By doing so, any observed difference in gene transfer would be attributable to mechanisms beyond cavitation.
Methods and results. A plasmid encoding for the firefly luciferase was used as a reporter. DNA mixed with either Optison™ or PESDA (25% v/v) was added to vascular smooth muscle cells or endothelial cells. US exposure was performed in continuous wave mode at 1 MHz, 0.5 or 0.75 W/cm^2, for 5–30 sec. Measurements of luciferase activity 24 h after exposure showed a several hundred-fold enhancement of gene transfer with both Optison™ and PESDA in comparison with plasmid alone, plasmid + US, plasmid + contrast agents without US, and several fold increase over plasmid lipofection.
Conclusions. In this experimental setup, both Optison™ and PESDA enhanced gene transfer to levels superior to standard plasmid lipofection. However, PESDA was superior to Optison™, suggesting that mechanisms beyond cavitation may be involved in US enhancement of gene transfer.

INTRODUCTION

Several echocardiographic contrast agents have been shown to enhance ultrasound (US) induced gene transfer [1-4]. The suggested mechanism responsible for this effect is lowering the threshold for inertial cavitation. However, the relative efficacy of different contrast agents was never evaluated. Furthermore, the possible intervention of other mechanisms remains unknown.

The aim of our study was to directly compare Optison™ and Perfluorocarbon Exposed Sonicated Dextrose Albumin (PESDA), two contrast agents with very similar structure and size. By doing so, any observed difference in gene transfer would be attributable to mechanisms beyond cavitation.

METHODS

Reporter Genes And Cell Culture

We have used a plasmid encoding for the firefly luciferase as reporter of gene transfection. Porcine vascular smooth muscle cells (VSMC) and human endothelial cells (EC) were cultured in 199 and EmBM growth media, respectively. Cells grown in 6-well plates to >70% confluence were used for gene transfer experiments.

Contrast Agents And Ultrasound Exposure

PESDA was prepared from human albumin, 5% glucose solution and decafluorbutane. Optison™ was purchased and used within 24 hours after opening. The concentration of microbbubles in stock solutions of Optison™ and PESDA was measured with a hemocytometer. The size distribution of microbubbles was evaluated on microscopic images of fresh dilutions (1:100 in 5% glucose) of Optison™ and PESDA with the ImagePro Plus software. (See Figure 1.)

Four 35-mm diameter air-backed US transducers were fixed in a frame so that the bottoms of the corner wells on the 6-well culture plate were aligned parallel with the transducers. The frame was immersed in a water tank; the distance between the top of the transducers and the bottom of the well was three millimeters. US exposure was performed in continuous wave mode at 1 MHz, 0.5 or 0.75 W/cm^2 average power, for 5–30 seconds.

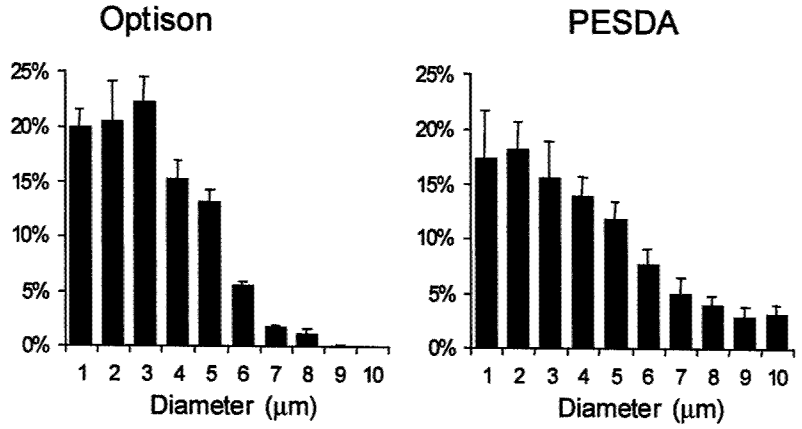

FIGURE 1. Size distribution of Optison™ (left panel) and PESDA (right panel). Over 90% of the microbubbles had diameters in the 0-8 μm range. Both agents have albumin shells containing a perfluorocarbon gas.

Gene Transfer Protocols And Efficacy Assays

A plasmid dose of 10 μg/well was used throughout the study. Luciferase plasmid was diluted in 750 μl serum-free media and mixed with 250 μl contrast. The mixture was added to the culture well, and exposure to US was performed. After 2 hours, complete media was added to stop the transfection; cells were incubated for another 24 hours prior to assessment of gene transfer efficacy. Growth media, plasmid alone, plasmid plus US, plasmid plus contrast media without US, and plasmid lipofection (20 μg lipofectamine mixed with 10 μg DNA/well) were used as controls. Twenty-four hours after transfection, the cells were lysed, luciferase activity was measured with a commercially available kit (Promega) and expressed in light units per microgram protein.

RESULTS

Luciferase activity measurements are summarized in Table 1 and Figure 2 (data from 6-8 experiments; mean ±SEM). Exposure to US in the presence of both Optison™ and PESDA enhanced gene transfer several hundred-fold in comparison with plasmid DNA alone, and was superior to plasmid lipofection. Addition of microbubbles in the absence of US, and US exposure in the absence of contrast agents were associated with luciferase activities similar to plasmid DNA alone.

In both vascular smooth muscle cells and endothelial cells, PESDA was associated with significantly higher transfection efficacy than Optison™ (Figure 2). This effect became evident for exposure times above 10 seconds. Longer exposure to US resulted in higher luciferase activities, tending to reach a plateau at 30 seconds.

The endothelial cells were more difficult to transfect *in vitro*, with luciferase activities 3-5 times lower than those observed in vascular smooth muscle cells.

Table 1. Luciferase activity (in light units/μg protein).

	VSMC	EC
Growth media	0.0 ± 0.0	0.0 ± 0.0
DNA alone	0.1 ± 0.0	0.1 ± 0.2
DNA + US	0.1 ± 0.0	0.3 ± 0.1
DNA + Optison™ / PESDA	0.0 ± 0.0	0.1 ± 0.0
DNA + lipofectamine	12.9 ± 4.1*	1.7 ± 0.3*
DNA + Optison™ + US	37.6 ± 20.1*†	5.6 ± 0.6*†
DNA + PESDA + US	72.6 ± 33.7*†	17.2 ± 9.9*†

All data given as mean ± SEM. VSMC: vascular smooth muscle cells. EC: endothelial cells. DNA: luciferase plasmid; US: 30 seconds exposure at 0.75 W/cm^2. * $p<0.05$ vs. DNA alone; † $p<0.05$ vs. DNA + lipofectamine

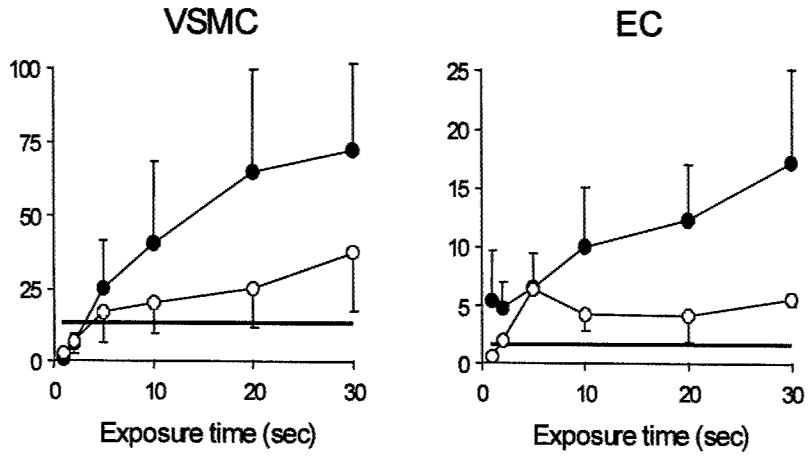

FIGURE 2. Luciferase activity 24 hours after transfection in vascular smooth muscle cells (left panel) and endothelial cells (right panel). Both Optison™ (open circles) and PESDA (solid circles) were superior to the level of plasmid lipofection (solid line). However, PESDA was associated with higher transfection efficacy in both cell cultures tested.

DISCUSSION AND CONCLUSIONS

Optison™ and PESDA are echocardiographic agents with very similar structure. Both agents are based on albumin shells containing a perfluorocarbon gas (octafluorpropane in Optison™, decafluorbutane in PESDA). Both have microbubble concentrations of 4-8X10^8 /ml, and an average diameter of 2-6 μm. Therefore, their ability to enhance inertial cavitation should be similar.

In this experimental setting, Optison™ and PESDA enhanced US gene transfer to different extent. We could not find an obvious explanation for this effect. However, our results suggest that mechanisms beyond cavitation might also play a role in US induced gene transfer. Differences in DNA binding to the albumin shells, the presence in PESDA of microbubbles with diameters above 8 μm, and different cellular uptake of PESDA and Optison™ microbubbles could have been responsible for these results. Further studies of the mechanisms responsible for plasmid DNA transport through the cellular and nuclear membranes upon exposure to US seem warranted.

REFERENCES

1. Greenleaf, W.J., Bolander, M.E., Sarkar, G., Goldring, M.B., Greenleaf, J.F., *Ultrasound in Medicine and Biology*, **24**, 587-595 (1998).
2. Porter, T.R. Iversen, P.L., Li, S., Xie, F., *Journal of Ultrasound in Medicine*, **15** (8), 577-584 (1996).
3. Lawrie, A., Briskin, A.F., Francis, S.E., Cumberland D.C., Crossman, D.C., Newman, C.M., *Gene Therapy*, **7**, 2023-2027 (2000).
4. Shohet, R.V., Chen, S., Zhou, Y.T., Wang, Z., Meidell, R.S., Unger, R.H., Grayburn, P.A., *Circulation*, **101** (22), 2554-2556 (2000).

Catheter-Directed Radial Ultrasound For Facilitating Thrombolysis Within Cerebral Arteries

Floyd Karp & Wolfgang Janas

EKOS Corporation, Bothell, WA 98021

Abstract. Background and Purpose: Ultrasound energy in the mega-hertz frequency range has been found to increase the rate of thrombolysis *in vitro*. Current medical interventions for the treatment of acute ischemic stroke can be effective; however, quicker recanalization times may result in improved neurological outcomes. Locally directed ultrasound can enhance the physiologic breakdown of clots and a catheter-directed local delivery system for thrombolytics allows a reduction in the total systemic dose. Together this is expected to reduce the time to recanalization and reduce the rate of follow-on intracerebral hemorrhage common when large doses of systemic thrombolytic agents are used over longer time periods.
Materials and Methods: 30 patients were enrolled prospectively, ages 18 to 77 years. The EKOS ultrasound microcatheter was placed into the proximal portion of thrombus. Thrombolytic was delivered and local ultrasound energy was concurrently applied for a set time or until recanalization was achieved. Time to recanalization, intracranial hemorrhage and mortality were assessed as well as neurological and functional disability at 90 days post-treatment.
Results and Conclusions: There have been no known instances of adverse events associated with the use of the EKOS MicroLysUS catheter or its low-energy ultrasound. There has been no increase in the mortality rate or the rate of intracranial hemorrhage when compared to other local drug delivery studies using thrombolytics. Additionally, there is preliminary evidence of accelerated thrombolysis and improved clinical outcomes for patients treated with thrombolytics delivered by the EKOS MicroLysUS ultrasound catheter.

INTRODUCTION

The purpose of developing an ultrasound-microcatheter system suitable for treating cerebral vascular thrombus can be summarized with the three following key assumptions: First, the localized application of directed high-frequency, low- intensity ultrasound generated by the EKOS system accelerates fibrinolysis. Secondly, an increased rate of recanalization should translate into a better neurological outcome in patients with acute ischemic stroke. And lastly, a decrease in total dose of thrombolytic should result in decreased hemorrhagic complications.

The EKOS ultrasound infusion system used in these clinical studies consists of three principle components. An electronics control unit provides the ultrasound frequency wave generation. A laptop computer controls the system and provides data collection. A microcatheter incorporates an ultrasonic transducer on the distal tip, and has a central lumen for guidewire placement and drug infusion.

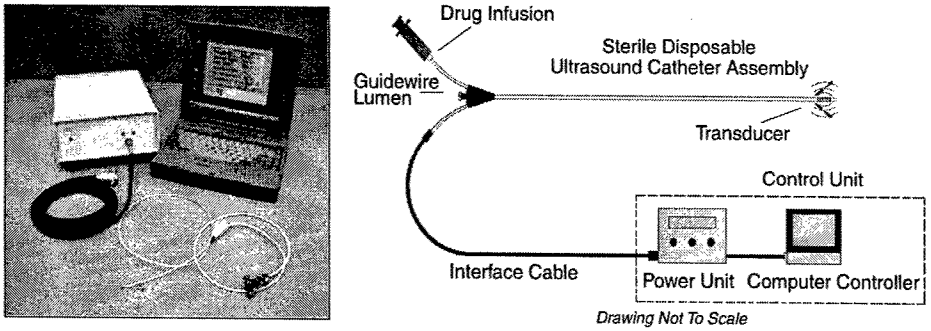

FIGURE 1. The EKOS Ultrasound Infusion System. (photograph and schematic diagram).

Mechanisms Of Ultrasound Enhanced Thrombolysis

There are many interacting mechanisms which contribute to enhanced thrombolysis by the EKOS ultrasound infusion system. *In vitro* investigations[1] have demonstrated that there is a reversible change to the fibrin structure. The mechanical actions of micron scale vibrations enhance the transport of drug molecules into the fibrin bundles. This leads to increased fluid permeation. The catheter supplies a constant infusion of fresh drug locally to the clot. The micron scale vibrations increase the surface interactions of drug molecules and clot components. All of these mechanisms interact and contribute to enzymatic clot dissolution, rather than mechanical disruption. A further perceived advantage of this approach is the introduction of thrombolytic enzyme to the downstream circulation which tends to further dissolve any distal emboli which are dislodged from the local occlusion site.

Selection Criteria For Initial Clinical Subjects

Subjects ranged in age from 18 - 77 years. It was important that they had no prior confounding neurologic event. Because some cerebral arteries are difficult to access, an angiogram was required to confirm that the occlusion was situated in a treatable artery. The subjects' symptoms needed to be extant for greater than three-hours, but less that six hours for anterior occlusions, or less than twenty-four hours for posterior occlusions. Each subject was assessed using the National Institute of Health Stroke Scale (NIHSS). No hemorrhage was observable on a CT scan. An Informed Consent from each subject was required.

Clinical Procedures

An angiogram confirmed the position of the occlusion and assessed flow to the region. The tip of the EKOS MicroLysUS catheter was placed into the proximal portion of thrombus. Each clinic selected a thrombolytic drug of choice.

All subjects received low-dose intravenous heparin as a bolus' followed by an infusion of several hours. The thrombolytic agents were infused over one to two hours, with ultrasound activated for the initial 45-60 minutes. Angiography was

performed every 15 minutes to assess progress and the catheter was advanced as indicated to keep the tip in the proximal portion of the remaining thrombus. Treatment was stopped at the end of two hours or when complete recanalization was achieved.

Outcome Measurements And Results For The Initial Clinical Subjects

The primary purpose of these investigations was to prove the safety of the EKOS ultrasound infusion catheter system. The secondary purpose was to learn about the efficacy of the device immediately post-treatment and during the following thirty and ninety days.

Thirty subjects were enrolled prospectively. Fourteen subjects were diagnosed as anterior circulation occlusions. Thirteen subjects were diagnosed as posterior circulation occlusions. Three subjects were treated off-protocol and are included only in the safety analysis. For all subjects the NIHSS and modified Rankin Scale (mRS) were assessed. All surviving subjects were evaluated at multiple intervals including: pre-treatment, immediately post-treatment, twenty-four hours, one week, one month and three months post-treatment.

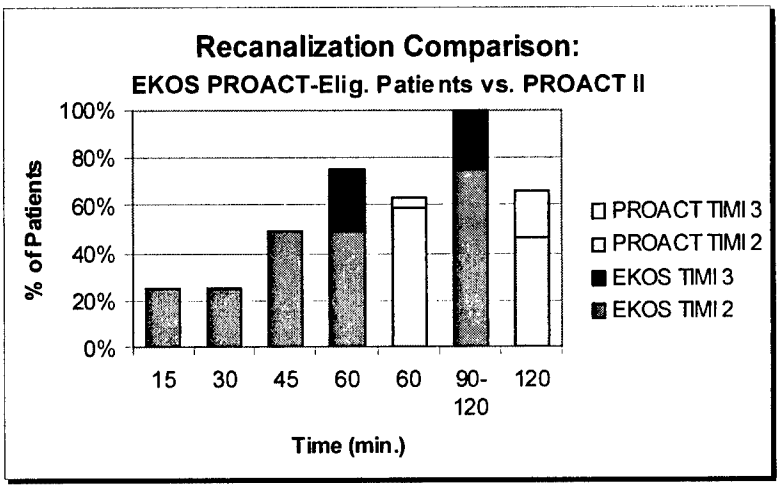

FIGURE 2. Comparison of EKOS microcatheter outcomes over time compared to the larger PROACT II Study.[2]

As safety of the device was of primary concern, the outcome was encouraging. No adverse events were reported relating to the use of the EKOS microcatheter itself (e.g., no perforations, dissections). Deaths and intracranial hemorrhage occurred consistent with the severity of acute ischemic stroke in the patient population. The data has been analyzed based on the site of the occlusion.

CONCLUSIONS

Most importantly, the EKOS ultrasound infusion catheter appears to be safe. The speed of recanalization appears faster and is associated with improvement in neurologic outcome. A larger scale study of this technology is justified.

ACKNOWLEDGMENTS

Sponsored in part by NIH-NHBLI Grant-No. 64434-01 and EKOS Corporation, Bothell, WA 98021. Douglas Hansmann, PhD was the Principal Investigator.

REFERENCES

1. Blinc, A., Francis, C.W., Trudnowski, J.L., Carstensen, E.L., "Characterization of Ultrasound-Potentiated Fribrinolysis In Vitro," *Blood*, **81**, (10), pp. 2636–2643 (May 1993).
2. Furlan, A., et al., "Intra-arterial Prourokinase for Acute Ischemic Stroke. The PROACT II Study: A Randomized Controlled Trial," *JAMA*, **282**, (21), (1999).

Evaluation Of Transcranial Ultrasonic Thrombolysis: *In Vivo* Study In A Thromboembolic Model Of Rats

Takayuki Saguchi[1,2], Hiroshi Furuhata[2], Toshihiro Ishibashi[1], Hisashi Onoue[1], and Toshiaki Abe[1]

Medical Engineering Laboratory[1], Department of Neurosurgery[2]
Jikei University School of Medicine
3-35-8 Nishishinbashi, Minatoku, Tokyo 105-8461 Japan

Abstract. Background: We are developing intracranial thrombolytic therapy by maens of transcranial ultrasonication (TUS). The efficacy of thrombolysis with transcranial ultrasonication in a rat autologous thromboembolic model was investigated. Methods: Thirty Male Wistar rats weighing 300-400 g were used for the autologous cerebral thrombosis model. Animals were classified into three groups; 1) no therapy: NT group (n=8), 2) an intravenous administration of 1.2 mg tissue plasminogen activator (tPA; monteplase) at three hours after embolization: TPA group (n=11), and 3) 2) with TUS: TUS group (n=11). TUS conditions were 488.2 kHz, 0.8 W/cm^2 with a 60-minute intermittent application. Twenty hours after the treatment, neurological examination was re-evaluated and the brain was carefully removed. A thrombus dissolution rate and a cerebral infarction ratio (CIR) were evaluated. Results: Thrombolysis ratio in the TUS group was significantly high than that of the TPA group and the NT group. Each CIR in the TPA and TUS group was significantly decreased than that of the NT group. However, the significant difference was not confirmed between TPA and TUS groups. CIR was lower in the TUS group than that of the TPA group among the neurologically improved cases. Remarkably, among the neurologically non-improved cases, CIR was higher in the TUS group than the TPA group. Conclusion: Thrombolysis by means of TUS was very effective in terms of thrombolytic effect. However, a potential risk of re-perfusion damage to ischemic brain should be always considerd in the treatment of thrombolysis by means of TUS as well as by means of a thrombolytic drug (tPA) alone.

INTRODUCTION

Thrombolytic effects by means of transcranial ultrasonication (TUS) *in vitro* have been reported by many investigators [1,2]. We have reported the efficacy of thrombolysis by means of TUS *in vivo*. However, an *in vivo* evaluation of ultrasonic thrombolysis using a cerebral thrombosis model has not been reported. We are developing intracranial thrombolytic therapy by means of TUS. In this study, the efficacy of transcranial ultrasonic thrombolysis was evaluated using a rat autologous thromboembolic model.

METHODS

Thirty Wistar male rats were used in this study. On the previous experiment day, blood was drawn into 50 cm PE50 polyethylene tube from a right femoral artery. Just before each experiment, 25 mm length autologous thrombus was prepared from the tube. Under general anesthesia the thrombus was inserted from the right external carotid artery in a retrograde fashion, then the origin of the right middle cerebral artery (MCA) was embolized via the right internal carotid artery (ICA) [3].

Neurological evaluation with the five-point scale was performed at the time of three hours after thrombus was inserted [3,4]. The case which presented an apparent left hemiparesis with the neurological score 3 or 4 was entered into this study.

The animal models were classified into the following three groups; 1) no therapy: NT group (n=8), 2) an intravenous administration of 1.2 mg tissue plasminogen activator (tPA; monteplase) at three hours after embolization: TPA group (n=11), and 3) 2) with TUS: TUS group (n=11).

TUS condition was the frequency of 488.2 kHz and the intensity of 0.8 W/cm2. Figure 1 shows the picture of installation procedure of the TUS apparatus. In the other experiment, it was confirmed that the ultrasonic power was decreased to the level of 0.3 W/cm^2 when the ultrasound of this condition get through the rat cranium.

FIGURE 1. The picture of installation procedure of the TUS apparatus on the rat skull.

Intermittent TUS was applied in cycles of 2 minutes, with a pause of 30 seconds, over a period of 10 minutes. TUS was not applied for 5 minutes. These 10-minute cycles, which followed 5-minute breaks, were repeated four times. The total intermittent application time of TUS was 32 minutes. Intermittent TUS was applied in order to avoid tissue heating.

Neurological evaluation was re-performed 24 hours after thrombus insertion. The case which score was improved into score 2 or score 1 was judged to be a

neurologically improved case. Then, the brain was carefully removed and the thrombus dissolution at the origin of right MCA was checked with the naked eye. Thrombolysis ratio was calculated by that the number of cases with thrombus dissolution which was divided by the number of total cases of each group. Furthermore, cerebral infarction ratio was calculated by that the volume of cerebral infarction which was divided by the volume of contralateral side of a cerebral hemisphere.

All data were analyzed with the Mann-Whitney's U test. All values are presented as means ± S.D. Significant difference was $p<0.05$.

RESULTS

Thrombolysis Ratio

In the NT group, three cases among eight ones, in the TPA group, six cases among eleven ones, in the TUS group, ten cases among eleven ones presented the complete thrombolysis at the origin of the right MCA. The thrombolysis ratio between the NT group and the TUS group was significant. (Figure 2)

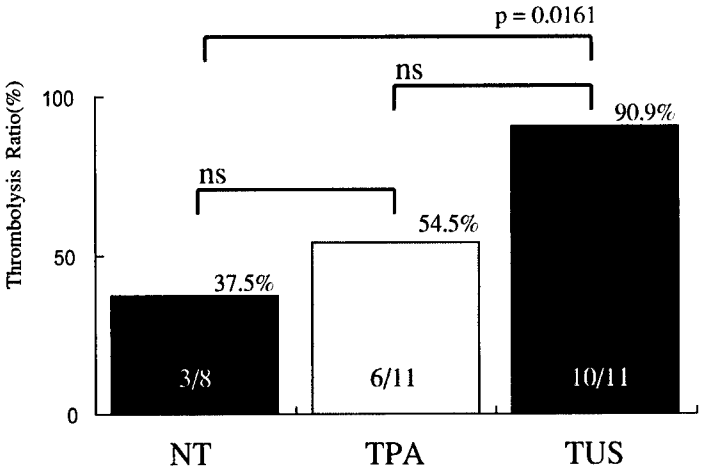

Figure 2. Thrombolysis ratio.

Cerebral Infarction Ratio

Regarding the cerebral infarction ratio (CIR), the TPA group and the US group were significantly low as compared with the NT group. However CIR between the TPA group and the TUS group was not significant and CIR in the TUS group became a little bit higher than that of the TPA group. (Figure 3-1)

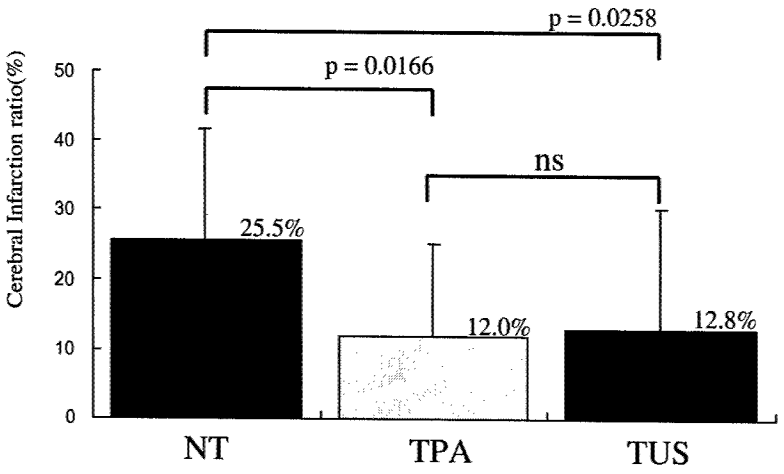

FIGURE 3-1. Cerebral infarction ratio.

CIR was evaluated from the aspect of neurological findings. In the TPA group, four cases were neurologically improved and seven cases were neurologically non-improved. It was not significant between the average CIRs of neurologically improved and non-improved cases. In the TUS group, seven cases were neurologically improved and four cases were neurologically non-improved. It was significant between the average CIRs of neurologically improved and non-improved cases in the TUS group. CIR was low in the TUS group than that of the TPA group among the neurologically improved cases. However, among the neurologically non-improved cases, CIR was high in the TUS group than that of the TPA group. (Figure 3-2)

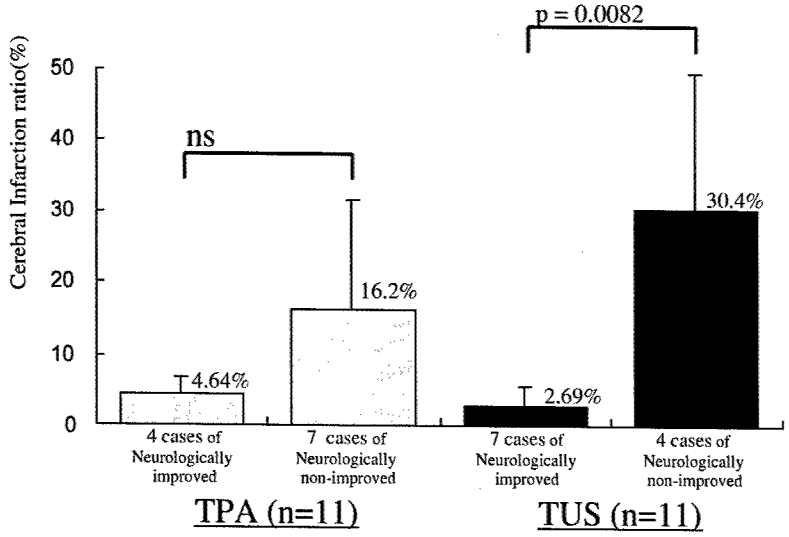

FIGURE 3-2. Cerebral infarction ratio.

DISCUSSION

The reason for a high cerebral infarction ratio in the TUS group among neurologically non-improved cases is considered to be as follows. It is possible that thrombolysis by means of TUS might lead to re-perfusion damage of the ischemic brain because of the higher thrombolytic effect in the TUS group. In the clinical situation, some risk factors that can cause hemorrhagic transformations when performing thrombolysis are well known [3,4]. For example, an occlusion in a major vessel such as the internal carotid artery or a large cerebral ischemia might lead to a higher risk of hemorrhagic transformation.

Clinical Application In The Future

The TUS conditions (488.2 kHz and 0.8 W/cm^2) used in this study were set in due consideration of the safety for human application. The level of ultrasound (US) intensity was almost as same as the upper limit of intensity that required by FDA (0.72 W/cm^2 $_{spta}$) for the commercially available diagnostic US instruments. Furthermore, to minimize the intracranial temperature rise that occurs under the ischemic condition, the thermal index was set to be less than 2. On the other hand, mechanical index (MI) was set to be 0.25, which is one-fourth of the upper limit level of avoiding cavitation, namely the mechanical index "1.0". Therefore, the TUS conditions used in this study were within the range of practical use, suggesting that the possibility of clinical application of transcranial ultrasonic thrombolysis in the near future may be high.

In this study, the occlusion site of the vessels (i.e. ICA or MCA or anterior cerebral artery) and the severity (i.e. extent) of cerebral ischemia were not evaluated. However, these above-mentioned findings should be carefully considered when performing thrombolysis with TUS. In order to avoid brain damages, appropriate patient selection for the thrombolytic therapy with TUS seems to be very important as well as the conventional thrombolytic therapy with tPA [5,6].

CONCLUSIONS

Thrombolysis by means of TUS was effective in terms of a thrombolytic effect. However, a potential risk of re-perfusion damage to the ischemic brain should be always considered in the treatment of thrombolysis by means of TUS as well as a treatment with a thrombolytic drug (tPA) alone.

There was a tendency for the cerebral infarction ratio in the TUS group to be lower in the neurologically improved cases and higher in the neurologically non-improved cases compared to that of the TPA group. These results were supported by the histological findings.

ACKNOWLEDGMENTS

This work was supported in part by grant H11-001 from the Research on Advanced Technology of Ministry of Health and Welfare.

REFERENCES

1. Behrens, S., Daffertshofer, M., Spiegel, D., Hennerici, M., "Low-frequency, low-intensity ultrasound accelerates thrombolysis through the skull," *Ultrasound Med Biol.* **25**, 269-273 (1999).
2. Akiyama, M., Ishibashi, T., Yamada, T., Furyhata, H., "Low-frequency ultrasound penetrates the cranium and enhances thrombolysis *in vitro*," *Neurosurgery,* **43**, 828-832; comment 832-833 (1998) .
3. Zhang, R.L., Chopp, M., Zhang, Z.G., Jiang, Q., Ewing, J.R., "A rat model focal embolic cerebral ischemia," *Brain Research,* **766**, 83-92 (1997).
4. Longa, E.L., Weinstein, P.R., Carlson, S., Cummins, R., "Reversible middle cerebral artery occlusion," *Stroke,* **20**, 84-91 (1989).
5. del Zoppo, G.J., Poeck, K., Pessin, M.S., Wolpert, S.M., Furlan, A.J., Ferbert, A., Alberts, M.J., Zivin, J.A., Wechsler, L., Busse, O., Greenlee, Jr., R., Brass, L., Mohr, J.P., Feldmann, E., Hacke, W., Kase, C.S., Biller, J., Gress, D., Otis, S.M., "Recombinant tissue plasminogen activator in acute thrombotic and embolic stroke," *Ann Neurol,* **32**, 78-86 (1992).
6. Okada, Y., Yamaguchi, T., Minematsu, K., Miyashita, T., Sawada, T., Sadoshima, S., Fujishima, M., Omae, T., "Hemorrhagic transformation in cerebral embolism," *Stroke,* **20**, 598-603 (1989).

Towards Intra-Operative Treatment Of High-Grade Gliomas With HIFU

Pierre Mourad PhD[1,2], Brett Anderson[1], Mike Bobola PhD[2], Elizabeth Dahl[1], Richard Ellenbogen MD[2], Lindi Farrell MS[2], Ali Mesiwala MD[2], Rick Morrison PhD[2], Andy Nemecek MD[2], Lisa Nguyen[1], Ryan Ollos[1], Tyrone Porter PhD[1], Paul Santiago MD[2], Daniel Silbergeld MD[2], Louis Stamps[2], Sara Vaezy[1]

1Center for Industrial and Medical Ultrasound, Applied Physics Laboratory
University of Washington, Seattle, WA, 98195
2Department of Neurological Surgery, University of Washington, Seattle, WA, 98195
For more information contact Pierre D. Mourad: pierre@apl.washington.edu

Abstract. High-grade gliomas, uniformly fatal primary brain tumors, form bulk (i.e. macroscopic) tumor that can be imaged and treated via surgery, radiotherapy, and in principle, HIFU. However, individual cells from these tumors invade microscopically beyond the bulk tumor in a fashion that cannot be imaged, and requires other means of treatment (chemotherapy, whole-brain radiation, etc). The purpose of this abstract is to propose that a viable strategy for treating these tumors may someday be through resection of the bulk tumor, then HIFU applied to the resection margin to enhance drug delivery, or to selectively attack residual bulk tumor or the remaining invaded tumor cells. This could be followed by systemic chemotherapy and radiation therapy. We first review the biology of one type of a high-grade glioma – glioblastoma multiforme – then review what HIFU investigators have shown HIFU to do to brain using acoustic parameters suitable for intra-operative application. Then, we will bring these facts together to propose a new strategy for high-grade glioma treatment that involves both surgical intervention and HIFU treatment.

REVIEW OF HIGH-GRADE GLIOMAS

Glioblastoma Multiforme (GBM) is the most common primary supratentorial cerebral neoplasm in adults [1]. This tumor is diffusely infiltrative and rapidly and uniformly fatal [2, 3], with a median survival of 12 months [4]. Current therapeutic modalities, including cytoreductive surgery [5], and adjunctive therapy such as radiation applied in a number of ways [6], implanted biodegradable polymer wafers (Gliadel®) that gradually elute a chemotherapeutic agent [7], and systemic chemotherapy [3, 8], are generally undertaken to reduce the number of viable tumor cells in or just adjacent to the bulk tumor, as delineated by MRI. This is an important treatment strategy because the bulk tumor often leads to acute symptoms, which must be addressed to improve the short-term survival of these patients. In particular, surgically removing the bulk tumor directly addresses tumor mass affects and

attendant reduction of brain function, as well as providing tissue for accurate histological diagnosis that guides the adjunctive therapy.

The major impediment, however, to accurate diagnostic imaging and successful therapeutic intervention is the diffuse, invasive nature of these tumors. Individual GBM cells invade beyond abnormalities detected with MRI [9], usually invading more than 2 cm beyond the bulk tumor as defined by MRI [10]. Also, Silbergeld and colleagues demonstrated that MRI normal human brain, beyond the MRI borders of bulk tumor, is histologically normal, but contains GBM cells that can be grown in culture [11]. Mourad et al [12] showed with a rat model of GBM that by three days after implantation of GBM cells in the brain, those cells had invaded throughout the brain, and achieved a stable tumor cell density until near the time of death. These invading tumor cells are problematic for a number of reasons [13]: they cannot be surgically removed; they are protected from systemically applied chemotherapeutic agents by an intact blood-brain-barrier (BBB) that curtails the flux of many chemicals from the blood into the brain; and they rarely cycle, which makes these cells difficult to treat effectively with radiation therapy and with whatever chemotherapeutic agents that make it past the BBB. Moreover, these invading cells are responsible for GBM recurrence at the resection margin [1] (even after hemispherectomy [14]). Finally, these cells, by unknown mechanisms, can lead to progressive neurologic dysfunction without evidence of mass effects or recurrence of bulk tumor [15].

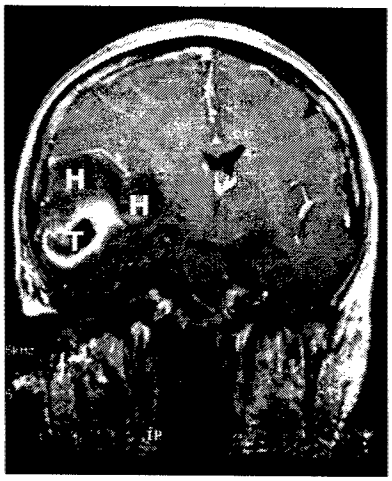

FIGURE 1. Enhanced T-1 weighted MRI image of a high-grade glioma (T) surrounded by regions of hemorrhage (H). Note the displacement of normal brain by bulk tumor, which can eventually cause loss of function and, if unchecked, lead to death. This image also shows the enhancing rim of this tumor – the bright oval shape in this figure. A significant increase in length of survival is associated with removing the tumor, including this enhancing rim, if this can be achieved without an unacceptable reduction in the quality of survival. However, successful treatment of the bulk tumor does not cure the patient, due to microscopically invading tumor cells well beyond the imaged tumor.

REVIEW OF HIFU APPLIED TO THE BRAIN

HIFU has been shown to irreversibly affect brain tissue in several ways, in vitro and in vivo. As reviewed by Mourad [16], early work on therapeutic ultrasound focused primarily on the brain. Dominant in the field at the middle of the twentieth century were the Fry brothers, whose work culminated in successful, short-term treatment of patients with movement disorders. Their ablative therapy required a craniotomy and a 'water hat' placed above the skull defect, into which transducers were lowered to apply the appropriate acoustic protocol. Following the development of L-dopa and other anti-Parkinsonian medicines, however, HIFU for treatment of the brain fell into disuse almost without exception until recently, when Hynynen and colleagues began efforts to treat brain disorders with HIFU with a special focus on transcranial application of ultrasound (discussed elsewhere in this volume).

Intra-operative use of HIFU for treating the brain, while requiring surgery, gives the user a wider range of acoustic protocols from which to choose. This is because intra-operative HIFU avoids the problem of unacceptably high heat deposition in the skull by HIFU. With this in mind, we note that Patrick et al [17] showed tissue destruction and BBB opening in association with severe damage to brain tissue. Vykhodtseva et al [18] showed tissue destruction and BBB opening in association with lesions that produced cavitation in the brain. (Hynynen et al [19] saw similar effects, using acoustic protocols that can be applied transcranially.) Vykhodtseva et al [20] showed that in the periphery of thermal lesions such as the one shown in figure 2, a few percent of cells underwent apoptosis, that is, received sufficient stress from HIFU to undergo delayed cell death.

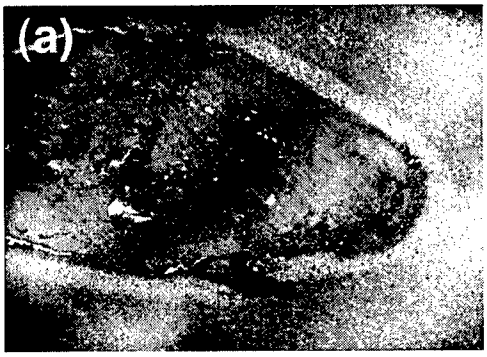

FIGURE 2. A thermal lesion placed in pig brain showing a central region without intact cells with a penumbra of edema surrounded by normal tissue. The halo of edema measures approximately 100 microns in thickness.

Mesiwala et al [21] showed that HIFU applied intra-operatively in the rat can open the BBB without inflicting collateral brain damage as determined histologically in acute studies, with comparable results in extended survival studies (Vaezy et al [22]). Work is currently underway to develop an inter-operative HIFU delivery system that consistently opens the BBB without damage (Ollos et al [23]). Mesiwala et al [21] also showed that HIFU-induced BBB opening persisted for at least three days following

HIFU application. Finally, they [21] showed electron microscopy images of the BBB consistent with the hypothesis that HIFU opens the BBB by disrupting the tight junctions between the specialized endothelial cells that constitute the major functional component of the BBB.

Nemecek et al [24] showed in vitro that a cavitating HIFU field could immediately destroy rat GBM or human medulloblastoma cells, and could also temporarily reduce the net proliferation of surviving cells. Preliminary analysis suggests that HIFU-induced apoptosis plays a role in this reduced proliferation rate.

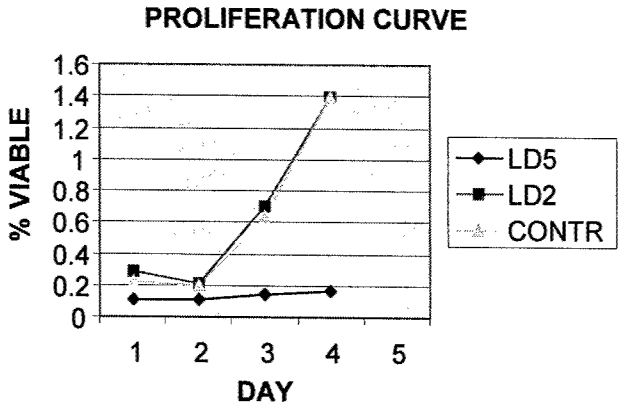

FIGURE 3. Human medulloblastoma cells, from another infiltrative brain tumor, suspended in growth medium, were subjected to either HIFU that immediately killed 25% (LD25) or 50% (LD50) cells, as demonstrated by Trypan exclusion test, or to sham HIFU applications (control). Cells were then plated at equal number density, and viable cells were counted after re-suspension one, two, three or four days after the initial experiment. In this sample study, all three cohorts showed no change in proliferation rate for the first two days. On days three and four, however, the LD25 and control groups showed marked proliferation of comparable amounts, while the number density of the LD50 did not change. Preliminary morphological analysis suggests HIFU-induced apoptosis may explain this difference.

Nemecek et al [24] also showed in vitro that a cavitating field permitted delivery of vital dyes and viable DNA into rat GBM cells, consistent with earlier work reviewed in Mourad [16]. Consistent with earlier work, significant cell death accompanied successful dye and DNA delivery.

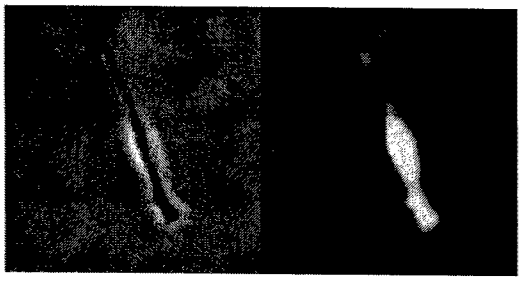

FIGURE 4. Rat GBM cells were suspended in growth medium and subjected to a cavitating field of HIFU while in the presence of naked DNA that coded for green fluorescent protein (GFP). Following insonation, the cells were plated and allowed to grow for a day before fixation and imaging under bright field (left image) and fluorescent (right image) microscopy. The figure shows a viable, migrating GBM cell that expressed GFP within its cytoplasm.

STRATEGY FOR INTRA-OPERATIVE USE OF HIFU TO TREAT HIGH-GRADE GLIOMAS TUMORS

Successful treatment of high-grade gliomas and other infiltrative brain tumors requires a strategy that targets not only the bulk tumor but also the microscopically invading individual tumor cells. The bulk tumor typically requires immediate treatment – usually surgery – to relieve acute symptoms. As noted before, surgery also allows diagnosis of the brain tumor type, which guides the adjunctive therapeutic strategy. This strategy leaves behind the invaded tumor cells that are inadequately attacked by current adjunctive therapies, and which ultimately form a bulk tumor at the resection margin. Of relevance later, recent unpublished results show that Gliadel® increased the length of survival of patients by six weeks relative to a placebo wafer. This successful drug delivery strategy suggests that for these tumors, getting chemotherapeutic agents beyond the BBB for an appreciable time can be of benefit.

HIFU can easily destroy cells including tumor cells. While destroying cells, HIFU can also deliver proxy drugs or DNA into a significant percentage of surviving cells. While creating damage, it can also open the BBB and allow proxy drug flux from the blood stream into brain tissue. There are also indications that HIFU can open the BBB without associated tissue damage.

Can HIFU play a role in the management of high-grade gliomas? We hypothesize that while HIFU can, in principle, be used to directly destroy the bulk tumor, the need for quickly reducing the mass of the tumor to manage its acute effects with minimal inflammation as well as the need for adequate tissue samples for accurate diagnosis will require surgical intervention, at least for a biopsy in conjunction with HIFU application to the bulk tumor. Given this hypothesis, there may also be a role for HIFU in the management of the residual tumor cells. Specifically, if the tumor margin does not contain eloquent brain, HIFU applied at and near the resection margin that causes acceptable levels of damage may be used to directly deliver drugs or DNA into surviving tumor cells. Such protocols are also likely to open the blood-brain barrier, which should allow increased delivery into tissue near the resection margin of systemically applied chemotherapeutic agents. If the resection margin does contain eloquent brain, however, then HIFU strategies are significantly limited, given that most HIFU-based drug delivery strategies cause significant collateral damage. Given the state of the art, only HIFU that consistently opens the blood-brain barrier without collateral damage may be applied to the resection margin when eloquent brain is present at that margin.

Much work still needs to be done before any of the strategies presented here can be shown to make a meaningful impact on patient care. However, given the dismal prognosis of patients with high grade brain tumors, any new treatment strategy would be welcomed.

ACKNOWLEDGMENTS

This work was supported in part by a training grant (K-25 NS02234-01) from the National Institutes of Health, National Institute of Neurological Disorders and Stroke

(PDM) as well as the McDonnell Center for Cellular and Molecular Biology Award #26275D, and training grants (KO8 NS01730 and NS69640) from the National Institutes of Health (DLS).

REFERENCES

1. Nazzaro, J.M., Neuwelt, E.A:, "The Role of Surgery in the Management of Supratentorial Intermediate and High-Grade Astrocytomas in Adults," *J Neurosurg*, **73**, 331-344 (1990).
2. Frankel, S.A., German, W.J., "Glioblastoma Multiforme: Review of 219 Cases with Regard to Natural History, Pathology, Diagnostic Methods, and Treatment," *J Neurosurg*, **15**, 489-503 (1958).
3. Salford, L.G., Brun, A., Nirfalk, S., "Ten-Year Survival Among Patients with Supratentorial Astrocytomas Grade III and IV," *J Neurosurg*, **69**, 506-509 (1988).
4. Salcman, M., Scholtz, H., Kaplan, R.S., *et al.*, "Long Term Survival in Patients with Malignant Astrocytoma," *Neurosurgery*, **34**, 213-220 (1994).
5. Silbergeld, D.L., "Controversies in Neurosurgery - Primary Brain Tumors: Resective Surgery Versus Biopsy and Adjuvant Therapy: The Case for Biopsy and Adjuvant Therapy," *Clinical Neurosurg*, **45**, 218-220 (1999).
6. Gannett, D.E., Wisbeck, W.M., Silbergeld, D.L., *et al.*, "The Role of Postoperative Irradiation in the Treatment of Oligodendroglioma," *Int J Rad Oncol Biol Phys*, **30**, 567-573 (1994).
7. Sampath, P., Brem, H., "Implantable Slow-Release Chemotherapeutic Polymers for the Treatment of Malignant Brain Tumors," *Cancer Control*, **5**, 130-137 (1998).
8. Thomas, D.G.T., Darling, J.L., Paul, E.A., *et al.*, "Assay of Anti-Cancer Drugs in Tissue Culture: Relationship of Relapse Free Interval and in vitro Chemosensitivity in Patients with Malignant Cerebral Glioma," *Br J Cancer*, **51**, 525-532 (1985).
9. Kelly, P.J., Daumas-Duport, C., Kispert, D.B., *et al.*, "Image-based Stereotactic Biopsies in Untreated Intracranial Neoplasms," *J Neurosurg*, **66**, 865-874 (1987).
10. Burger, P.C., Dubois, P.J., Schold, S.C., *et al.*, "Computerized Tomographic and Pathologic Studies of the Untreated, Quiescent and Recurrent Glioblastoma Multiforme," *J Neurosurg*, **58**, 159-169 (1983).
11. Silbergeld, D.L., Chicoine, M.R., "Isolation and characterization of human malignant glioma cells from histologically normal brain," *J Neurosurg*, **86**, 525-31 (1997).
12. Mourad, P.D., Farrell, L., Stamps, L.D., Santiago, P., Fillmore, H.L., Broaddus, W.C., Silbergeld, D.L., "Quantitative assessment of Glioblastoma invasion *in vivo,"* Submitted to *Cancer Letters.*
13. Chicoine, M.R., Silbergeld, D.L., "Assessment of brain tumor cell motility *in vitro* and *in vivo*," *J Neurosurg*, **82**, 615-622 (1995).
14. Bell, E., Karnosh, L.J., "Cerebral hemispherectomy," *J Neurosurg*, **6**, 285-293 (1949).
15. Silbergeld, D.L., Rostomily, R.C., Alvord, E.C., "The Causes of Death in Patients with Glioblastoma is Multifactorial: Clinical Factors and Autopsy Findings in 117 Cases of Supratentorial Glioblastoma in Adults." *J Neuro-Oncol*, **10**, 179-185 (1991).
16. Mourad, P.D., "Biological effects of ultrasound" in *Encyclopedia of Electronics and Electrical Engineering, V2*, edited by J.L. Webster, Philadelphia: John Wiley & Sons, 1999, pp. 368-386.
17. Patrick, J.T., et al., "Clinical Practice in Cancer Treatment," in *Advances in Experimental Medicine and Biology: Consensus on Hyperthermia for the 1990s, Vol. 267*, edited by H.I. Bicher, J.R. McLaren, G.M. Pigliucci, New York, New York: Plenum Press, 1990. pp. 369-381,

18. Vykhodtseva, N.I., Hynynen, K., Damianou, C., "Histologic effects of high intensity pulsed ultrasound exposure with subharmonic emission in rabbit brain in vivo," *Ultrasound Med Biol*, **21**, 969-979 (1995).
19. Hynynen, K., McDannold, N., Vykhodtseva, N., Jolesz, F.A., "Noninvasive MR imaging-guided focal opening of the blood-brain barrier in rabbits," *Radiology*, **220**, 640-646 (2001).
20. Vykhodtseva, N., McDannold, N., Martin, H., Bronson, R.T., Hynynen, K., "Apoptosis in ultrasound-produced threshold lesions in the rabbit brain," *Ultrasound Med Biol.*, **27** (1), 111-7 (2001).
21 Mesiwala, A.H., Farrell, L., Wenzel, H.J., Crum, L.A., Silbergeld, D.L., Winn, H.R., and Mourad, P.D., "High Intensity Focused Ultrasound Selectively Disrupts the Blood-Brain Barrier in vivo," *Ultrasound in Medicine and Biology*, **28** (1), 389-400 (2002).
22. Vaezy, S., Mesiwala, A.H., Farrell, L., Anderson, B., Dahl, E., Nguyen, L., Silbergeld, D.L., Mourad, P.D., "Survival studies of the ability of High intensity focused ultrasound to open the blood-brain barrier *in vivo*, In Preparation.
23. Ollos, R., Anderson, B., Cooksey, G., Mourad, P.D., "An intra-operative applicator of high-intensity focused ultrasound for the purpose of opening the blood-brain barrier," In Preparation.
24. Nemecek, A., Dahl, E., Bobola, M., Ellenbogen, E., Morrison, R., Porter, T., Santiago, P., Silbergeld, D.L., Mourad, P.D.", High intensity focused ultrasound alters both the survival and proliferation rates of brain tumors in vitro," In Preparation.

8. SONODYNAMIC THERAPY

Enhancement Of Ultrasonic Absorption By Microbubble Agent For HIFU Treatment

Shin-ichiro Umemura, Ken-ichi Kawabata,
Narendra Sanghvi*, Kazuaki Sasaki

Central Research Laboratory, Hitachi Ltd., Kokubunji, Tokyo 185-8601, Japan
**Focus Surgery, Inc. Indianapolis, Indiana 46226, U. S. A.*

Abstract. Ultrasonic power absorbed and scattered by a microbubble was calculated through numerically solving the Rayleigh-Plesset equation to analyze its nonlinear breathing motion. At an ultrasonic intensity of 1 W/cm^2 and a frequency of 2 MHz, a resonant microbubble, approximately 1.2 μm in radius, absorbed and scattered ultrasonic power in the order of 10 μW and 1 μW, respectively. Ultrasound was more absorbed than scattered by microbubbles smaller than approximately 3 μm in radius. It was predicted that tissue ultrasonic absorption will be increased by more than twice if microbubbles are delivered to the tissue at a concentration in the order of 10^8 microbubbles/kg. An exteriorized murine kidney was exposed to HIFU at 3.2 MHz in degassed saline and the tissue temperature change was measured. With administration of Optison™ at a dose of 0.2 ml/kg, the temperature elevation induced by HIFU exposure was multiplied by three to four times. This effect may have a potential use to enhance the selectivity as well as the throughput of HIFU treatments.

INTRODUCTION

Ultrasound has two kinds of bioeffects which can be utilized for therapeutic application: thermal and nonthermal effects. The bioeffects induced by ultrasonic cavitation are studied normally in the latter category. For example, use of cavitation to sonochemically activate a certain drug has been being studied to obtain a localized therapeutic effect.[1-3] Ultrasonic cavitation consists of two stages: 1) nucleation and growth of microbubbles under acoustic pressure, and 2) their rapid collapse. While most of cavitational bioeffects are induced at the second stage, the cavitation threshold normally means the ultrasonic intensity required for the first rather than the second stage because the first stage requires much higher intensity. However, the first stage is not needed in the existence of a stabilized microbubble agent. Consequently, the ultrasonic intensity for inducing cavitational bioeffects can be reduced by orders of magnitude with administration of such an agent.

Recently, it was reported that the thermal bioeffect of ultrasound was also enhanced with a microbubble agent. With administration of Albunex, a several times larger volume of tissue was coagulated in a canine prostate than its absence with the same highly focused beam at the same ultrasonic intensity and exposure time.[4] If the ultrasonic absorption of tissues can be significantly increased in a well-controlled manner with administration of such a microbubble agent, it will be especially useful

for the ultrasonic treatment of deep-seated tissues, to where ultrasonic power high enough for the treatment with ultrasound alone is relatively difficult to deliver.

In this study, the ultrasonic power absorbed and scattered by a microbubble is calculated through numerically solving the Rayleigh-Plesset equation to analyze its nonlinear breathing motion.[5] It is followed by *in vivo* HIFU exposure experiments of a murine kidney with and without adiminstration of Optison™.

THEORETICAL PREDICTION

Method Of Analysis

The nonlinear oscillation of a microbubble subjected to an acoustic pressure was analyzed by numerically solving the Rayleigh-Plesset equation,

$$\rho \{R(d^2R/dt^2) + (3/2)(dR/dt)^2\} = P_B(t) - P_0 - 2\sigma/R - 4\mu(dR/dt)/R - P_A(t) \quad (1)$$

where

$$P_B(t) = (P_0 + 2\sigma/R_0)(R_0/R)^{3\kappa}, \quad (2)$$

P_0: the hydrostatic pressure, $P_A(t)$: the acoustic component of pressure of the surrounding liquid, $P_B(t)$: the gas pressure in the microbubble, R(t): its radius, R_0: the radius in equilibrium, ρ: the density of the liquid, σ: its surface tension, μ: its viscosity, and κ: the polytropic exponent of the internal gas. To simplify the numerical analysis, the following further approximations were also applied:

1) the microbubble is small enough to assume the isothermal change of the internal gas, i. e. $\kappa = 1$, and
2) the microbubble is stabilized so that the surface tension of the microbubble can be neglected, i. e. $\sigma = 0$.

The acoustic pressure radiated by the microbubble was calculated as

$$p = \rho (d^2V/dt^2)/ 4\pi r = \rho R [R(d^2R/dt^2) + 2(dR/dt)^2] / r \quad (3)$$

assuming that R is much smaller than the wavelength. Here, the oscillatory factor of radial change was ignored, r: distance from the microbubble, and $V = 4\pi R^3/3$: the volume of the microbubble. The acoustic power was then calculated as

$$W_A = 4\pi r^2 p^2/\rho c = \rho(d^2V/dt^2)^2/4\pi c = 4\pi r R^2 [R(d^2R/dt^2) + 2(dR/dt)^2]^2 /c \quad (4)$$

assuming that r is much larger than the wavelength where c: the sound speed. This gives the acoustic power scattered by the microbubble.

The fourth term on the right hand side of (1) gives the acoustic power dissipated due to the viscosity as

$$W_H = 4\pi R^2 (dR/dt) \cdot 4\mu(dR/dt)/R = 16\pi\mu R (dR/dt)^2 = 4\mu (dV/dt)^2/ 3V \quad (5)$$

This gives the acoustic power absorbed by the microbubble. The total attenuation of the acoustic power is then given as

$$W_A + W_H = \rho(d^2V/dt^2)^2/ 4\pi c + 4\mu(dV/dt)^2/3V. \quad (6)$$

RESULTS AND DISCUSSION

Absorbed and scattered acoustic power in continuous-wave response at 2 MHz is plotted against the microbubble radius in Figure 1. The total attenuated acoustic power is also plotted. They are plotted for peak acoustic drive pressure of 0.01 and 0.06 MPa. Both absorbed and scattered power have maximum peaks at the resonant radius. As the drive pressure increased from 0.01 to 0.06 MPa, the resonant radius shifted a little to the smaller side, and the secondary peak emerged near a half the radius of resonance. These are due to the nonlinear acoustic behavior of the microbubble.

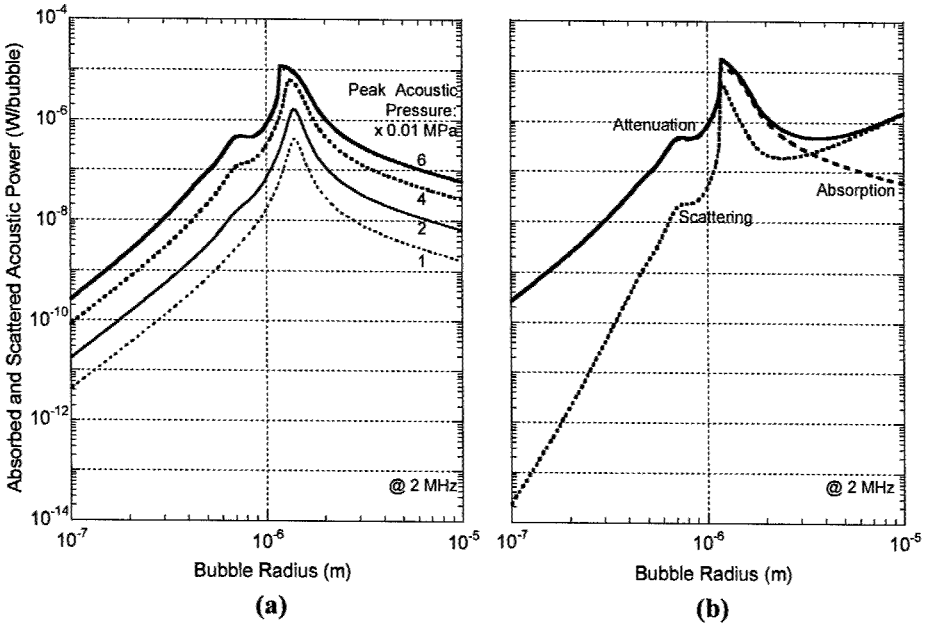

FIGURE 1. Acoustic power absorbed and scattered by microbubble in numerically obtained continuous-wave response: (a) acoustic power absorbed by a microbubble at a peak acoustic pressure of 0.01 to 0.06 MPa at an ultrasonic frequency of 2 MHz, and (b) acoustic power absorbed, scattered, and attenuated by a microbubble at a peak acoustic pressure of 0.06 MPa. Surface tension and shell parameters were ignored, and isothermal change was assumed for the internal gas.

At acoustic pressure of 0.06 MPa, corresponding to acoustic intensity about 0.12 W/cm^2, a resonant microbubble absorbed acoustic power of 13 μW. At the same acoustic pressure and frequency, typical tissue absorbs acoustic power at a rate about 40 μW/mm^3, assuming that tissue attenuation is 0.7 dB/MHz/cm and that the attenuation is mostly due to absorption. These lead an estimation that approximately three resonant microbubbles per cubic millimeter of tissue are needed to multiply the tissue absorption by twice. This corresponds to a concentration in blood of 60 bubbles/mm^3 and to a total number of 2×10^3 bubbles in a whole human body, which is typically a tenth of a vial.

Ultrasonic power is much more absorbed than scattered by a microbubble approximately in the resonant size or smaller although it is much more scattered than

absorbed by a microbubble more than a few times larger than the resonant size. Therefore, in order to maintain the ultrasonic penetration enough for efficient heating, the microbubble size should be controlled to have no bubbles larger than the resonant size by more than a few times. This will be an important consideration even in case that a microbubble agent is delivered selectively to the tissue volume to be treated, typically through a catheter rather than systemic injection, unless the volume is as small as a HIFU focal spot.

IN VIVO EXPERIMENT

Method

HIFU Transducer

A prototype split-focus transducer with two elements, constructed for transrectal treatment of a prostate, was used in exposure experiments in water. The dual element PZT transducer (Fuji Ceramics) had a resonant frequency of 3.2 MHz, a spherical curvature radius of 35 mm, and an aperture of 40 mm × 20 mm. The aperture of each element is 40 mm × 10 mm. It was contained in an aluminum housing in combination with a small imaging probe (EUP-F331, Hitachi Medical) at 6.5 MHz having a convex array curvature radius of 10 mm. The position and angle of the imaging probe, relative to the HIFU transducer, was calibrated and adjusted prior to the experiment.

Preparation of Animal

After surgical anesthesia with sodium pentobarbital was given to a female SD rat (approximately 250 g), a kidney was mobilized and exteriorized through an incision. A 0.25-mm diameter sheathed chromel-almel thermocouple (Sukegawa Electric, Japan) was inserted into the cortex tissue for temperature measurement during and after HIFU exposure. A cannula 0.8 mm in diameter was also inserted into a jugular vein for systemic administration of Optison™. The rat was held vertically in degassed saline at 33°C and its position was adjusted to locate the thermocouple right in the middle of the HIFU focal zone by using B-mode images taken with the probe.

The experimental animals were treated according to the guidelines proposed by the Science Council of Japan.

Results and Discussion

The kidney tissue temperature was continuously measured every 0.2 s during a series of four time HIFU exposures for 10 s at the same peak ultrasonic intensity of 290 W/cm^2. The temperature change is shown in Figure 2. Right before the second HIFU exposure, 0.05 ml Optison™ (0.2 ml/kg) was injected through the indwelling needle. The ultrasonic intensity at the split focus mode was chosen so that HIFU alone would not induce significant irreversible changes to the tissue.

The tissue temperature rise immediately after the Optison™ administration was approximately four times higher than that before the administration and approximately three times higher than that 15 min after the administration. Therefore, this dose of Optison™ is considered to be able to enhance the ultrasonic absorption at least by three times. Assuming that 15 min was enough for the microbubles to be washed away from the tissue, it may be further considered that the temperature elevation immediately after the administration may have been increased by 30% due to some irreversible change in the tissue such as destruction of capillaries.

Since Optison™ contains 5-8 $\times$ 10^8 microbubles in each milliliter, the dose of 0.2 ml/kg corresponds to 1.0-1.6 $\times$ 10^8 bubbles/kg or 100-160 microbubbles per cubic millimeter of tissue. This dose is approximately 30-50 times higher than the dose theoretically predicted to be needed for enhancing the tissue absorption by twice. Therefore, these results suggest that approximately a tenth of the microbubbles in the tissue acted as resonant bubbles to convert acoustic power into heat. This may be reasonable when the size distribution of Optison™ and the destruction of microbubbles during HIFU exposure are considered.

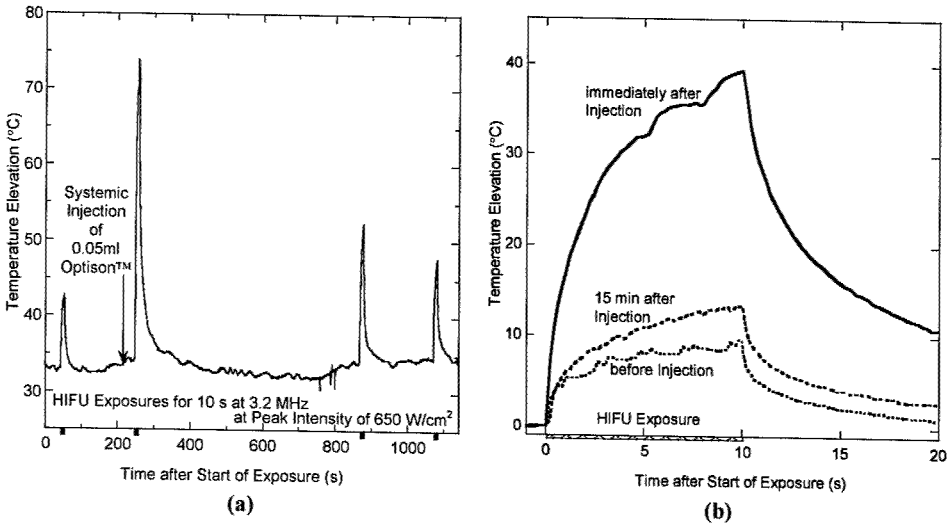

FIGURE 2. Temperature change in murine kidney tissue during and after HIFU exposure: (a) the temperature change in a series of four time exposures, and the temperature elevation after the start of each exposure. Each HIFU exposure at 3.2 MHz was continued for 10 s at the same peak intensity of 650 W/cm^2.

CONCLUSION

The ultrasonic power absorbed by a microbubble in the resonant size was calculated to be approximately 13 μW at a peak acoustic pressure of 0.06 MPa at 2 MHz. This leads a predicted enhancement of ultrasonic absorption in tissue by twice with 3 resonant micobubbles in a cubic millimeter of the tissue. The temperature elevation in an exteriorized murine kidney induced by HIFU exposure at 3.2 MHz was enhanced by

three to four times with administration of Optison™ at a dose of 0.2 ml/kg, which corresponds to 100-160 micobubbles in a cubic millimeter of tissue. The observed level of enhancement in tissue temperature elevation can be explained by assuming that approximately a tenth of the microbubbles in the tissue acted as resonant bubbles to convert acoustic power into heat. This effect may have a potential use to improve the selectivity as well as the throughput of HIFU treatments.

ACKNOWLEDGMENTS

Authors thank to Dr. Takao Iwasaki and Professor Yoichiro Matsumoto for the discussions of using microbubbles in ultrasonic treatments. They also thank to Dr. Kunio Hashiba and Mr. Shu-ichi Iino for discussions and cooperation in the analysis of microbubble oscillation, and Mr. Takashi Azuma for cooperation in the experiment. This work was partly supported by the National Research and Development Program for Medical and Welfare Apparatus under entrustment by the New Energy and Industrial Technology Development Organization of Japan.

REFERENCES

1. Yumita, N., Nishigaki, R., Umemura, K., and Umemura, S., "Synergetic effect of ultrasound and hematoporphyrin on sarcoma 180," *Jpn. J. Cancer Res.*, **81**, pp. 304-308, (1990).
2. Umemura, S., Yumita N., Nishigaki R., and Umemura, K., "Mechanism of cell damage by ultrasound in combination with hematoporphyrin," *Jpn. J. Cancer Res.*, **81**, pp. 962-966, (1990).
3. Umemura, S., Kawabata, K., and Sasaki, K., "Enhancement of sonodynamic tissue damage production by second-harmonic superimposition: Theoretical analysis of its mechanism," *IEEE Trans. Ultrason., Feroelec., Freq. Contr.*, **UFFC-43**, pp. 1054-1062, (1996).
4. Sanghvi, N. T., Fry, F. J., Foster, R. S., Bihre, R., Zaitsev, A., and Hennige, C., "High intensity focused ultrasound treatment of prostate tissue in the presence of US contrast agent," *J. Ultrason. Med.*, **14**, S17, (1995).
5. Umemura, S., Kawabata, K., and Hashiba, K., "Enhancement of ultrasonic absorption by microbubbles for therapeutic," *Proc. 2001 IEEE Ultrason Symp.*, **2**, pp. 1311-1314, (2001).

Correlation Of Bubble Lifetime With Bioeffects Of Acoustic Cavitation *In Vitro*

Pavel P. Kamaev, Hector R. Guzman, and Mark R. Prausnitz

School of Chemical Engineering, Georgia Institute of Technology, Atlanta, GA 30332-0100, USA

Abstract. Acoustic cavitation has been shown to deliver molecules into viable cells, which is of interest for drug and gene delivery applications. This work was intended to measure the lifetime of albumin-stabilized cavitation bubbles (Optison™) and correlate it with desirable (intracellular uptake of molecules) and undesirable (loss of cell viability) bioeffects. Optison™ was exposed to 500 kHz ultrasound either with or without the presence of DU145 prostate cancer cells bathed in calcein, a cell-impermeant tracer molecule. Bubble lifetime was determined using a Coulter counter, while uptake of calcein and cell viability was quantified by flow cytometry. It was shown that the lifetime of Optison™ cavitation nuclei decreased and bioeffects increased (i.e., molecular uptake and loss of cell viability) with increasing acoustic energy exposure. The bioeffects were shown to correlate well with disappearance of bubbles, suggesting that Optison™ bubble destruction either directly affected cells or indirectly affected cells, involving unstabilized cavitation nuclei created upon the destruction of Optison™. Additional experiments showed that Optison™ solutions presonicated to destroy all detectable bubbles also caused significant bioeffects, which suggests that the indirect mechanism is more likely.

INTRODUCTION

Ultrasound-mediated drug delivery is a novel strategy for targeted transport of drugs and genes into cells and tissue [1-3]. In contrast to systemic procedures, delivery enhanced by ultrasound can be focused onto target tissues, thereby requiring lower whole body doses of a drug and allowing delivery of molecules to precise locations in the body, which can reduce side effects and treatment costs [4]. By transiently permeabilizing cell membranes using ultrasound and thereby causing uptake of molecules into the cells (sonoporation), this approach has applications in gene and protein delivery both *in vivo* and *in vitro* [5,6].

Despite successful demonstrations of intracellular delivery of molecules into viable cells, robust control and reproducible bioeffects have been difficult to achieve. This is in part because most studies have concentrated on controlling acoustic conditions, rather than directly controlling cavitation, which is the main mechanism through which ultrasound causes bioeffects. Therefore, the aims of this study were to measure the lifetime of cavitation bubbles and correlate them with bioeffects on cell suspensions *in vitro*.

MATERALS AND METHODS

For experiments involving cells, DU145 human prostate cancer cells (American Type Culture Collection, Rockville, MD) suspended in RPMI-1640 media (10^6 cells/ml) were exposed to focused 500 kHz ultrasound in the presence of 10 μM calcein and 1.7 % v/v albumin-stabilized gas bubbles (Optison™, Amersham Health, Princeton, NJ) at the conditions described by Guzman et al. [7,8]. Cell viability and calcein uptake were determined by means of flow cytometry, as described previously [7,8].

For experiments without cells, Optison™ bubbles were added to RPMI-1640 media to achieve a final concentration of 1.7 % v/v and exposed to the acoustic conditions in the same range as in the experiments with cells. Samples were diluted 200-fold with Isoton II (Beckman Coulter) [9] and immediately examined by electrical zone sensing with a Coulter Multisizer II (Beckman Coulter, Fullerton, CA) to determine the size distribution and concentration of bubbles. The Coulter instrument was fitted with a 100 μm orifice, the aperture current was fixed at 1600 μA, the gain factor was set at 2 and the siphon volume was fixed at 500 μl. Each experiment was performed in triplicate.

These bubble-only experiments were carried out without the presence of cells to eliminate difficulty in distinguishing cells and cell debris from bubbles in the Coulter instrument. To verify that removal of cells did not alter bubble dynamics, bubble size distribution and concentration were compared using data from (i) data from Optison™ bubbles without cells, (ii) data from cells without Optison™ subtracted from data from cells with Optison™ and (iii) data from cells initially with Optison™ and then exposed to vacuum (30 min at 0.6 atm) to remove bubbles subtracted from data from cells with Optison™. Bubble concentrations and size distributions were approximately the same for each of these comparisons both before and after sonication, suggesting that cells do not have a protective (or destructive) effect on bubbles during sonication.

RESULTS AND DISCUSSION

The effect of ultrasound exposure over the range of 0.6 – 3.0 MPa and 120 – 2000 ms on DU145 prostate cancer cell viability and intracellular calcein uptake was previously investigated by Guzman et al. [7,8]. These data show that the number of calcein molecules delivered per viable cell increased and cell viability decreased in good correlation with the acoustic energy exposure (Fig.1).

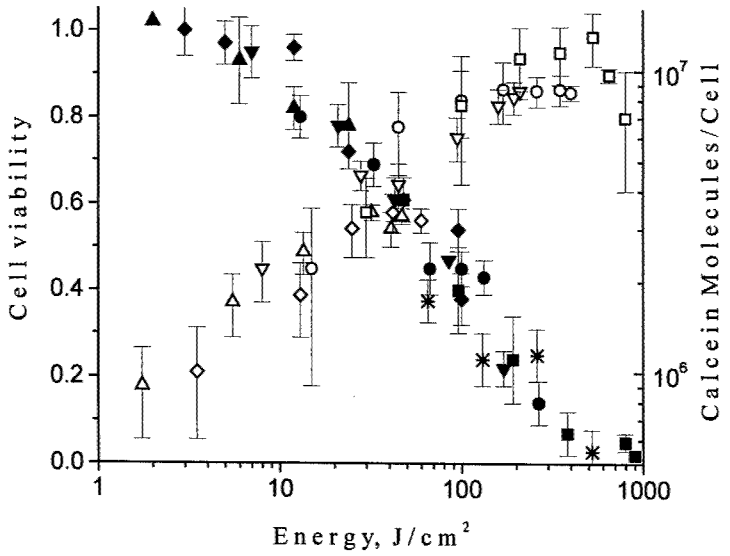

FIGURE 1. Cell viability (black symbols) and calcein uptake (white symbols) as functions of acoustic energy exposure. (acoustic pressures : •, ○ – 2 MPa, ▲, Δ – 0.6 MPa, ♦, ◊ – 1.2 MPa, ▼, ∇ – 1.6 MPa, ■, □ –2.4 MPa, ✱ – 2.8 MPa). Data are from Guzman et al. [7].

Our goal is to relate these observed bioeffects directly to cavitation bubble activity. We therefore used a Coulter counter to measure the number of bubbles present after Optison™ suspensions were exposed to ultrasound over a range of different energy exposures. The Coulter counter is capable of measuring the presence of bubbles greater than 1 μm, meaning that bubbles larger than 1 μm were counted and bubbles made smaller than 1 μm were classified as "destroyed". It is known that acoustic energy exposure mediates cavitation, which is the main mechanism of the observed effects of ultrasound on cells [10]. In our study Optison™ plays a key role in nucleation of cavitation activity in cell suspensions.

Figure 2 shows that the lifetime of bubbles nucleated from Optison™ suspension depends on the ultrasound energy exposure. Although the ultrasound conditions used in this study covered a range of different pressures and exposure times, the results collapse into a single curve when plotted versus energy exposure, indicating that this is a unifying acoustic parameter. As energy exposure increased, bubble concentration decreased, where almost all were destroyed by energies of 30 - 50 J/cm^2. It is interesting to note that this range of energies is close to the optimal exposure conditions observed by Guzman et al. [7] for DU145 cells.

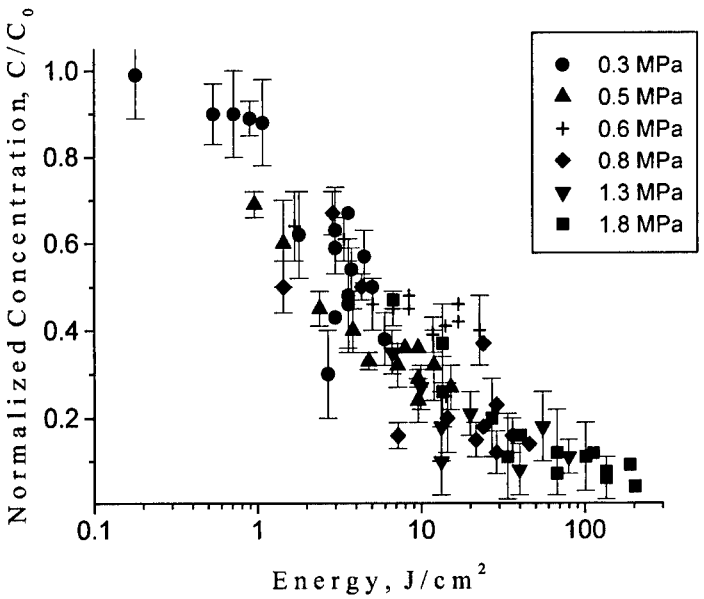

FIGURE 2. Destruction of Optison™ bubbles as a function of acoustic energy exposure following sonication in RPMI-1640 media at different pressures and exposure times. Initial concentration of Optison™ was $C_0 = 4 \times 10^6$ bubbles/ml. Based on the Coulter counter's detection limit of 1 μm, bubbles smaller than 1 μm could not be detected and were considered destroyed.

To determine the relationship between bubble activity (Fig. 2) and bioeffects (Fig. 1), we made a comparison between the fraction of destroyed bubbles and both molecular uptake and cell viability over a broad range of energy exposures. The results presented in Fig. 3 show that calcein uptake increases and cell viability decreases with the destruction of Optison™ bubbles.

It is interesting to note that when 60 – 70% of the bubbles are destroyed, there are significant levels of molecular uptake at high viability. Once more than 80% of bubbles are destroyed, viability steeply decreases. This suggests that destruction of a critical number of nucleation sites is sufficient to desirable bioeffects and further destruction causes large losses in cell viability. This suggests that careful regulation of bubble activity could help to maintain both molecular uptake and cell viability high during ultrasound exposure.

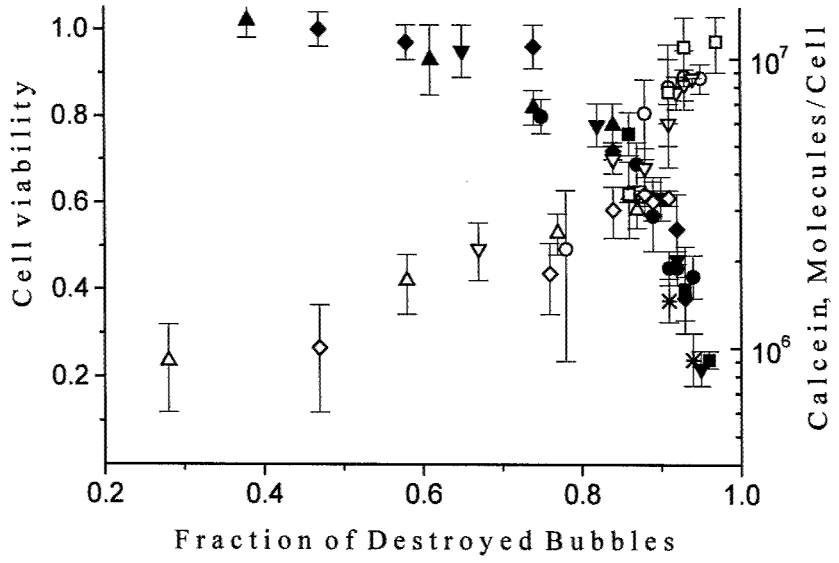

FIGURE 3. Dependences of cell viability (black symbols) and calcein uptake (white symbols) on the fraction of Optison™ bubbles destroyed during sonication. (acoustic pressures : •, ○ – 2 MPa, ▲, Δ – 0.6 MPa, ♦, ◊ – 1.2 MPa, ▼, ∇ – 1.6 MPa, ■, □ –2.4 MPa, ✱ – 2.8 MPa).

The significant bioeffects observed at large acoustic energies, after most Optison™ bubbles had been destroyed, could arise as a consequence of "derivative" microbubbles created when the stabilizing shells surrounding Optison™ are broken and the encapsulated gas escapes. Recent studies with human erythrocytes and 1 MHz ultrasound revealed that gas bodies capable of nucleating violent cavitation activity persist even after the rapid destruction of albumin-covered contrast agent Albunex [11]. Theoretical considerations predict that free bubbles liberated from contrast-agent gas bodies are expected to be much more active than the stabilized shell-encapsulated gas bubbles [12, 13].

To further confirm the hypothesis that "derivative" bubbles cause bioeffects, we presonicated a suspension of Optison™ bubbles at 130 J/cm^2 to remove almost all bubbles. Then, cells were added and sonicated again at 130 J/cm^2. Despite the removal of almost all detectable bubbles, cell viability decreased to 60 ± 10 % and calcein uptake reached (1.2 ± 0.5) x 10^6 molecules/cell. In contrast, sonication of cells under the same ultrasound conditions using media that never contained Optison™ bubbles led to no significant uptake or loss of viability [7].

CONCLUSION

In this study we found that acoustic energy exposure correlates with not only cell viability and calcein uptake, but the lifetime of Optison™ cavitation nuclei too. Almost all Optison™ bubbles (with diameters of at least 1 μm) were destroyed by energies of 30 – 50 J/cm^2, which is approximately the same energy previously reported to be optimal for producing desirable bioeffects. Carefully regulating the kinetics of destruction of cavitation nuclei during ultrasound exposure could be a useful approach to keep both cell viability and molecular uptake high. Significant cell death observed at high acoustic energies is probably a consequence of cavitation dynamics of free gas microbubbles liberated after rupture of Optison™ bubbles.

REFERENCES

1. Terahara, T., Mitragotri, S., Kost, J., Langer, R., *Int. J. Pharm,* **235**, 35 - 42 (2002).
2. Boucaud, A., Garrigue, M.A., Machet, L., Vaillant, L., Patat, F., *J. Control. Release,* **81**, 113 - 119 (2002).
3. Whelan, J., *Drug Discov Today,* **7**, 585-586. (2002).
4. Miller, M.W., *Ultrasound Med. Biol.* **26**, Suppl. 1, S59 – S62 (2000).
5. Miller, D.L., Bao, S., Gies, R.A., Thrall, B.D. *Ultrasound Med. Biol.*, **25**, 1425 - 1430 (1999).
6. Ward, M., Wu, J., Chiu, J-F., *Ultrasound Med. Biol.*, **26**, 1169 – 1175 (2000).
7. Guzman, H.R., Nguyen, D.X., Khan, S., Prausnitz, M.R., *J. Acoust. Soc. Am.*, **110**, 588 – 596 (2001).
8. Guzman, H.R., Nguyen, D.X., Khan, S., Prausnitz, M.R., *J. Acoust. Soc. Am.*, **110**, 597 – 606 (2001).
9. Sontum, P.C., Christiansen, C. J., *Pharm. Biomed. Analysis,* **12**, 1233 – 1241 (1994).
10. Bao, S., Thrall, B.D., Miller, D.L., *Ultrasound Med. Biol.*, **23**, 953 – 959 (1997).
11. Brayman, A.A., Miller, M.W., *Ultrasound Med. Biol.*, **23**, 793 – 796 (1997).
12. Miller, D.L., *J. Acoust. Soc. Am.*, **104**, 2498 – 2505 (1998).
13. Wu, J., *Ultrasound Med. Biol.*, **28**, 125 – 129 (2002).

Sonodynamic Cancer Treatment With Cavitation-Promoting Agent

Ken-ichi Kawabata, Nami Sugita, Kazuaki Sasaki,
and Shin-ichiro Umemura

Medical Systems Research Department, Central Research Laboratory, Hitachi, Ltd., Japan

Abstract. The combinational anti-tumor effects of ultrasound exposure with second-harmonic superimposition and tumor accumulative rose bengal (RB) derivatives were investigated. The combination was found to exhibit anti-tumor effect at acoustic intensity at which almost no effect was obtained when ultrasound was used solely. The anti-tumor effects were improved by rotating phase difference between the fundamental and the second-harmonic at an optimum period of 300 ms.

INTRODUCTION

Cavitation is a typical non-thermal bio-effect induced by ultrasound. Although its therapeutic application is much less studied than thermal effects, cavitational effects may be useful for therapeutic application if they can be induced in controlled ways. As an approach, we are studying for "sonodynamic therapy" [1] which utilizes chemical effects induced by acoustic cavitation and enhanced by certain sensitizers. Sonodynamic therapy has the potential for low-invasive and highly selective tumor treatment if it is combined with suitable ultrasound exposure methods and sensitizers. We have been developing second-harmonic superimposition [2,3] and xanthene dyes [4] as such a method and sensitizers.

The second-harmonic superimposition method superimposes the second-harmonic wave onto the fundamental at target. The method has been revealed to be an effective way to induce cavitational effects both *in vitro* and *in vivo*.

The sensitizers for sonodynamic treatment must possess three properties:

(1) lower acoustic intensity threshold of cavitation,

(2) accumulate into tumor tissues, and

(3) enhance cavitational anti-tumor effects.

Until now, certain porphyrin dyes have been found to show properties (2) and (3) [1], and certain xanthene dyes have been found to show (1) and (3) [4]. Still, chemicals with all three properties have not yet been found. Accordingly, we synthesized new chemicals aimed at attaining all three properties. Our approach is to add property (2) to xanthene dyes, which already possess properties (1) and (3).

Results on the effects of newly synthesized xanthene derivatives with the second-harmonic superimposition method on mouse tumor will be described in this paper.

MATERIALS AND METHODS

Chemicals

Figure 1 shows the structures of synthesized rose bengal (RB) derivatives. RB was reacted with brominated alkane or brominated carboxylic acid in DMF at 70° C for 4-8 hours. The resulting derivatives were purified by open column chromatography. The reagents for derivatives were purchased from Wako Chemical Industries (Osaka, Japan).

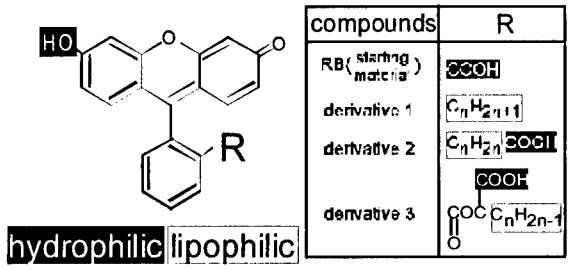

FIGURE 1. Newly synthesized RB derivatives for sonodynamic treatment.

Setup For Sonodynamic Treatment Of Tumor Bearing Mice

Derivatives were administered into tumor-bearing CDF1 mice under the same conditions as described in the previous section. Mice were exposed to ultrasound at 0.5 and 1.0 MHz 6 hours after administration with a focused type ultrasound transducer (spherical curvature radius of 35 mm, F number = 1) in a water tank filled with degassed water.

Setup For Measuring Subharmonic Emission *In Vitro*

Subharmonic emission from sample was used to detect the occurrence of cavitation in this series of experiments [2]. Subharmonic emission in aqueous solution was measured by using a focused type PVDF hydrophone. A 2.5 ml aliquot of 25% (V/V) alcohol aqueous solution was filled in 0.02-thick polyethylene bag (30 x 25 mm) and placed in a degassed water tank in front of a plane ultrasound transducer (1.0 and 2.0 MHz, 24-mm in diameter). The PVDF hydrophone was also placed in the water tank and acoustic signals from the bag were recorded while ultrasound was exposed for 60 seconds. Time averaged subharmonic emission intensity was calculated and used as a measure of cavitation intensity.

RESULTS AND DISCUSSION

Among RB derivatives synthesized this time (Figure 1), derivative 3 was found to accumulate in tumor tissues most significantly. Figure 2 shows the outlook of murine tumors 7 days after focused ultrasound exposure with second harmonic superimposition at 0.5 and 1.0 MHz (4 + 16 W/cm^2). When ultrasound was exposed in the presence of RB derivative 3, damage could be seen in tumor tissue along the ultrasound path, while almost no damage was seen when ultrasound was exposed solely. Results of measuring the tissue temperature rise and second-harmonic generation suggest that this anti-tumor effect be obtained by cavitation-promoting effect of RB derivative 3.

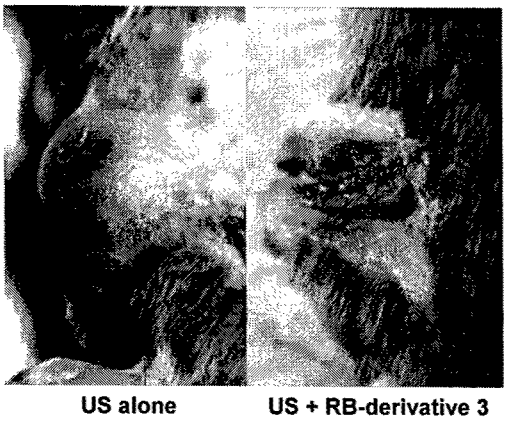

FIGURE 2. Effect of RB-derivative on murine tumor.

Figure 3 shows the tumor growth curve after ultrasound exposure. While ultrasound alone has almost no effects, tumor growth was significantly suppressed by the combinational treatment with RB derivative 3 and ultrasound. Still, reduction of tumor size could not be achieved.

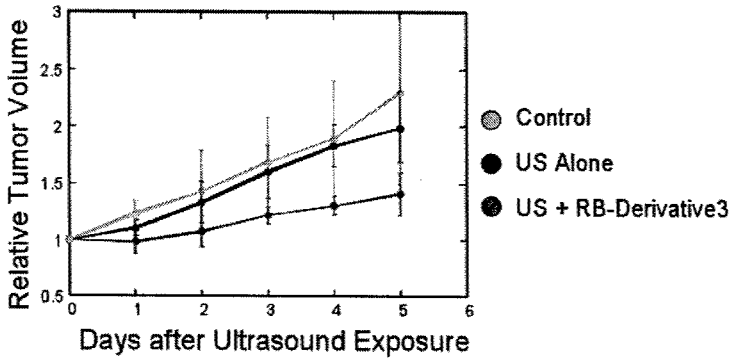

FIGURE 3. Effect of RB-derivative on murine tumor (growth curve).

To improve the combinational anti-tumor effect of ultrasound with second-harmonic superimposition and RB derivative 3, the effect of rotating of relative phase difference between the fundamental and the second harmonic was investigated. Figure 4 shows the effect of relative phase difference on generation of cavitation with second-harmonic superimposition in aqueous solution. Cavitation was generated most significantly when waveform C was used and almost no cavitation was generated when waveform A was used.

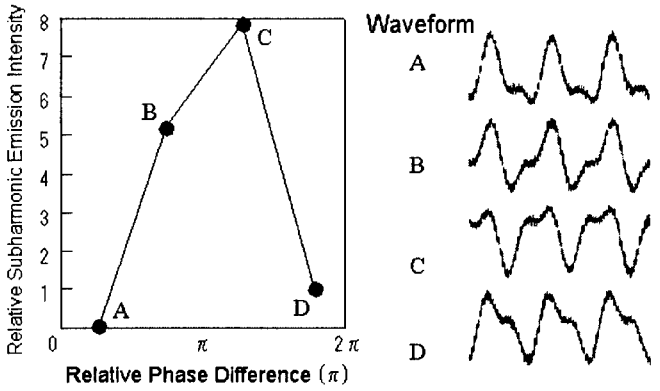

FIGURE 4. Effect of relative phase difference on generation of cavitation with second-harmonic superimposition *in vitro*.

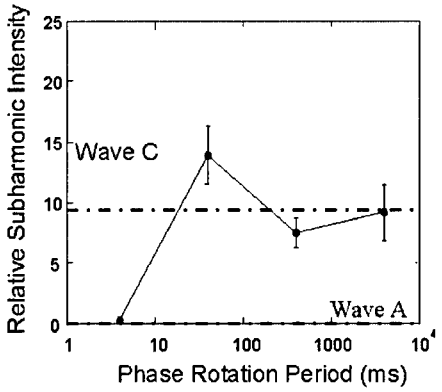

FIGURE 5. Effect of phase rotation on generation of cavitation with second-harmonic superimposition *in vitro*.

Figure 5 shows the effect of phase rotation period on generation of cavitation in aqueous solution. When the period was short (3 ms), cavitation was not generated. However, when the period was longer than 300 ms, cavitation was generated about as much as when waveform C, the optimal waveform, was used. Moreover, when the period was 30 ms, the intensity of cavitation was significantly higher than that obtained with waveform C. Further investigations are needed to clarify the mechanism why rotating phase difference can promote cavitation as much as the optimum

waveform. It is possible that the phase rotation works as a kind of agitation such as pulsed ultrasound [5] and switched spiral focal field [6].

Figure 6 shows the effect of phase rotation on the suppression of murine tumor growth with second-harmonic and RB derivative 3. All the rotation period used this time was effective for suppressing the tumor growth. Reduction of tumor size was obtained only when the period was 300 ms. The optimum period was ten times longer than that in aqueous solution. This may be related to the chemical properties such as viscosity or ion concentration between water and tissues. Further investigations are needed; still, it is very interesting that the phase rotation was effective both *in vitro* and *in vivo*.

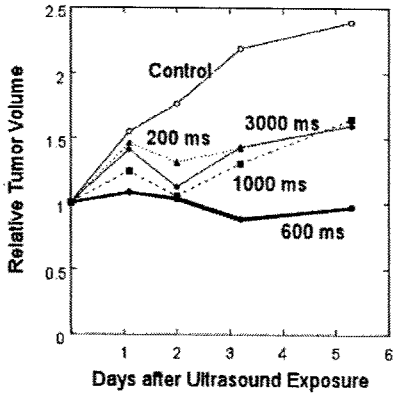

FIGURE 6. Effect of phase rotation on tumor growth suppression with second-harmonic superimposition and RB derivative 3 *in vivo*.

ACKNOWLEDGMENTS

Part of this work was partly supported by the National Research and Development Program for Medical and Welfare Apparatus under entrustment of the New Energy and Industrial Technology Development Organization (NEDO), Japan.

REFERENCES

1. Umemura, S., et al., *Jpn J. Cancer Res*, **84**, 582-588 (1993).
2. Kawabata, K. and Umemura, S., *J. Phys. Chem.*, **65**, 2503-2504 (1994).
3. Umemura, S., et al., *J. Amer. Soc. Acoust.*, **101**, 569-577 (1997).
4. Kawabata, K. and Umemura, S., *J. Ultrasonics*, **35**, 469-474 (1997).
5. Henglein, A., *Ultrasonics Sonochem.*, **2**, S115-S121 (1995).
6. Kawabata, K. and Umemura, S., *J. Ultrasonics*, **31**, 457-462 (1997).

The Use Of Shockwaves And Pressure Pulses For The Transfer Of Molecules Into Cells

Friedrich Ueberle[1,3], Michael Delius[2], Lei Guo[1], Wolfgang Hepp[1]

[1]*Dornier MedTech, Wessling, Germany*
[2]*Institut für Chirurgische Forschung, Universität München, Germany*
[3]*University of Applied Sciences, Hamburg, Germany*

Abstract. A mixture of mouse lymphocytes (L1210) and fluorescent marker molecules are subjected to shockwaves *in vitro*. Due to the transient cavitation generated by the shockwaves, the cells take up the marker molecules. Cavitation is characterized by the bubble collapse times. An electrohydraulic generator XL-1 and a piezoelectric generator PR-II were used: PR-II was more effective. Depending on the pulse energy and number of pulses, up to 70% of the surviving cells took up the molecules. Shock-wave-mediated molecule transfer provides a useful tool for the transfer of molecules into cells, which can be used as a research tool in the medical and biotechnological fields. Due to the large penetration potential of shockwaves into the body, the method may be further developed for *in vivo* transfer of drugs and cell transfection use.

INTRODUCTION

Since the first time shockwaves were used for the disintegration of kidney stones, researchers were also interested in their effect on tissue and cells. In the beginning the main interest was in potential side effects of lithotripsy, but soon further medical applications of shockwaves beyond lithotripsy were considered. Reports on the experimental treatment of tumours were published. The effect of the shockwaves was mainly attributed to a significant reduction of tumour blood perfusion, lasting for several hours. But as the application of shockwaves alone did not yield satisfactory results, the next research step was the combination with cytotoxic agents, which gave more promising results. The experiments showed, that the majority of cells was not killed by the effects of the shockwaves, but more than 90% of the cells were penetrated by the toxic molecules. After the insonication the cell membranes closed again, the cells survived and were able to make use of the molecules, which could be shown by a change in the expression of proteins [7].

MECHANISM OF SOUND PORATION

Several reports on the permeabilization of cell membranes by acoustic wave effects can be found in literature. It is common agreement that the dominating effect is cavitation, but also shear forces contribute to the ripping of the cell membrane.

Hypothetically transient cavitation is the cause of the biological effect of sound poration. After the passage of a pressure pulse or shock wave, large bubbles are grown from pre-existing seeds of a few micrometers size. The bubbles then collapse after another 100 ... > 1000 µs. The time until the bubble collapses is influenced both by the ambient conditions of the bubble and the impinging pres-sure pulse. At the moment of collapse the bubble transmits part of the stored elastic energy as a secondary shockwave. Inside the bubble temperatures exceeding 5000°K can occur. Amplitude and duration of the negative part of the exciting pressure pulse mainly determine the occurrence of transient cavitation.

Cavitation generated by pressure pulses in the microsecond range causes sonoluminescence, secondary shock waves and free radicals, but it does not lead to a complete disintegration of the cells. The rapid change in bubble radius causes adiabatic compression of the bubble as a prerequisite for high internal temperatures [2].

Cell disintegration (Lysis) mainly occurs due to shear forces in the vicinity of oscillating bubble walls when stable cavitation is present. Erythrocytes are disintegrated by bubble motion amplitudes of more than 18 µm [1]. Bubbles having sufficient size to exert effective shear forces are mainly generated by continuous ultrasound means, e.g. by sonotrodes, which are in use for the disintegration of cells.

Shockwave – Bubble – Interaction

In lithotripsy, the interaction of shock waves with bubbles that were generated by a preceding shockwave is identified as one (amongst other mechanical effects) cause of stone disintegration and side effects [2]. Cavitation bubbles leave a residual cloud of small bubbles, which in water have a typical diameter of 40 µm and which can be found more than 1 second after the generating shockwave. When these residual bubbles are hit by another shock wave, they collapse in a few microseconds. For bubbles of 0,15-2 mm diameter collapse times of 1-9 µs are reported [3]. During the collapse a water jet, which can reach jet speeds of 400-800 m/s at a bubble size of 0,5-0,6 mm, is directed towards the next surface, which might be a cell membrane.

Cavitation Threshold

The cavitation threshold was evaluated *in vitro* by different scientists in dependence on the sound frequency and on the pulse duration. Starting at 0,7 MPa, an increase of the cavitation threshold to 1,3 MPa was found [4] when the pulse duration was reduced from 100 µs to 1 µs. A significant number of bubble seeds reduces the cavitation threshold.

In vivo the cavitation threshold of 7 MPa at 20 ms pulse duration was estimated by morphological changes. Another author reports a threshold of 12 MPa when using sound bursts of 30 µs duration.

Many cavitation threshold experiments are made with sound bursts, which are composed of several positive and negative pressure changes. In contrast, typical shockwaves only have one leading (positive) pressure pulse of 0,2 to 2 µs duration and

one trailing rarefaction (negative) phase with 3 – 6 times longer duration, but with only 1/3 to 1/10 of the positive pressure amplitude. According to several authors the cavitation threshold for shock waves also is in the range of 1 – 12 MPa.

Sub-cellular level reactions on shockwaves are vacuoles in the cytoplasma, changes of the membrane surface and defects of the cell membrane. Depending on the pulse intensity integral of the shockwaves different cell organelles are affected [5]. It was reported that large pores occur for a short time, which can support the passage of molecules up to 2 millions relative weight into the cells [6]. After the end of the sonication the cells do not take up new molecules any more, thus the pores only last for a few seconds or even shorter time.

MATERIALS AND METHODS

Mouse lymphocytic (L1210) cells in a nutrient solution were used. As the marker-molecule Fluoreszin-Dextran (FD) was added. 3,5 ml cells with a concentration of 106 cells per milliliter were mixed with 1,75 ml FD and filled in 5 ml PVC test tubes, carefully avoiding to trap gas bubbles. Besides the sonicated samples, unsonicated control samples were prepared the same way. After sonication the cells were washed and centrifuged. Trypan blue staining gives the number of disintegrated cells. 10.000 surviving cells were the analysed by FACS to evaluate the fluorescence distribution in comparison to the unsonicated control cells (Figure 1).

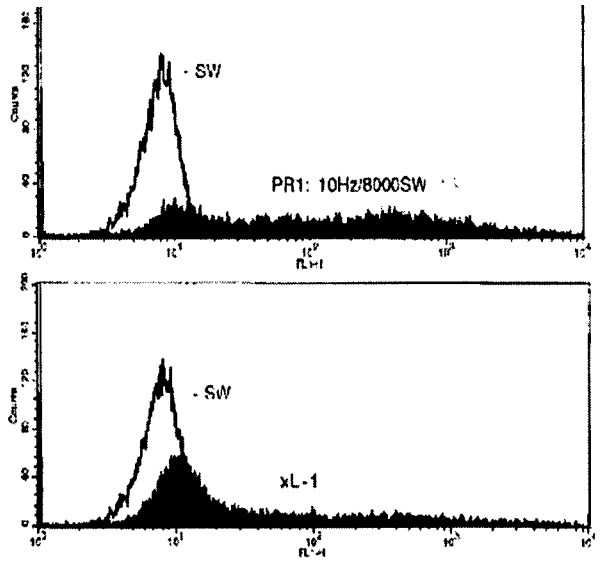

FIGURE 1. FD-uptake is measured by comparing the fluorescence distribution of sonicated and unsonicated (-SW) samples. Only those channels having a higher fluorescence than a threshold are counted. The threshold is determined by the right flank of the fluorescence distribution of –SW. In our experiments, fluorescence channels > 40 are used as a rule.

At least three cell samples per experimental parameter set were used. The experiments were repeated several times during the last months with different breeds of cells.

Two different pressure pulse sources were used for sonication:

+ Electrode-shocksource XL-1 (Dornier MedTech)
+ Piezoelectric transducer PR-II (Dornier MedTech)

By the use of confocal laser pointers the test tubes were positioned in the focal area such that the focus was ca. 5 mm inside the tubes. The pulse intensity, the number of pulses and the repeat rate of the pulses was varied.

The collapse time of the cavitation bubbles was determined by a pressure probe with a steel membrane of 5 mm diameter (PCB, USA) placed in the focus of the pressure pulse source (Figure 2).

RESULTS

After the passage of the pressure pulse a bubble grows at the probe surface, which collapses after the time tc (Figure 2). At the XL-I the probe was placed perpendicular to the direction of the sound path, therefore the collapse time tc (Figure 3) is about twice the time as compared to the collapse time in the test tube in absence of strongly reflecting surfaces.

To evaluate the relative amount of cells that have taken up FD molecules, the fluorescence of the unsonicated samples was taken as a reference. The natural FD-uptake of the unsonicated control cells was 3,2% +- 0,9.

Additionally, with every experiment with the piezoelectric device the fluorescence of samples treated with 250 shocks of XL-1 at 25 kV was measured. Repeating XL-1 experiments gave a mean FD-uptake of 36% +- 8. The number of disintegrated cells was 48% +- 8 (Figure 4).

The FD uptake increases linear with the number of pressure pulses (Figure 5). At the same time the number of lost cells also increases (Figure 6). In our present series, the best FD uptake of 70% was achieved with the piezoelectric source at the maximum energy setting using 8000 pulses (Figure 5).

The overall efficacy of the procedure is defined as the number of surviving cells that have taken up FD per total number of cells before sonication (1 Mio / ml). The repeated experiments with XL-1 yielded an efficacy of 18% +- 4 for the L1210 cells (Figure 4). The best overall transfer efficacy (28%, Figure 7) was achieved with the piezoelectric source PR-II at the maximum energy setting using 4000 shocks.

FIGURE 2. Cavitation bubble building up at the 5 mm diameter membrane of a PCB-pressure probe in the focal plane of a shock source (on the left outside the image region). After the shockwave hit the probe (approx. 2nd image frame) a bubble occurs, which is significantly larger than the other bubbles in the sound field. After 500 µs (approx. 12th frame) the large bubble collapses for the first time. (Image interframe delay 50 µs; Images courtesy of Luderer/Bohris, Dornier MedTech [8])

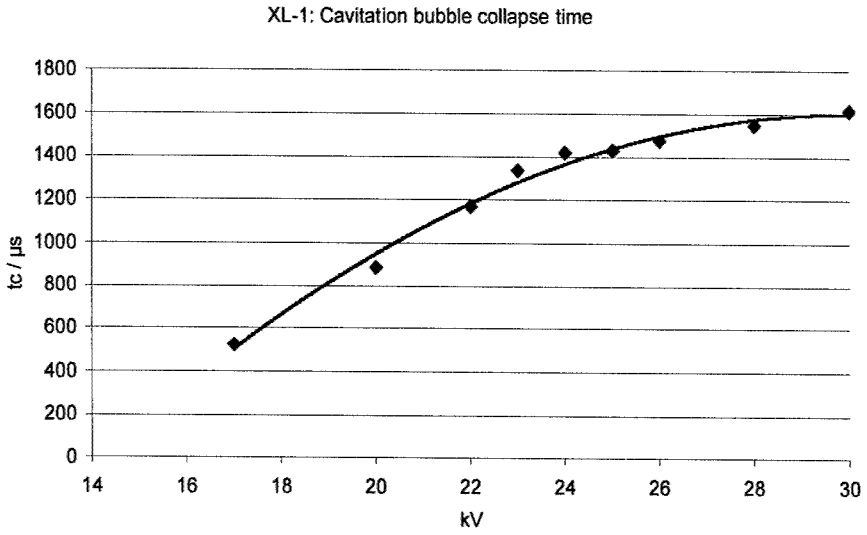

FIGURE 3. Collapse time (tc) of the focal cavitation bubbles in the presence of a PCB steel-membrane hydrophone in the focus of the XL-1.

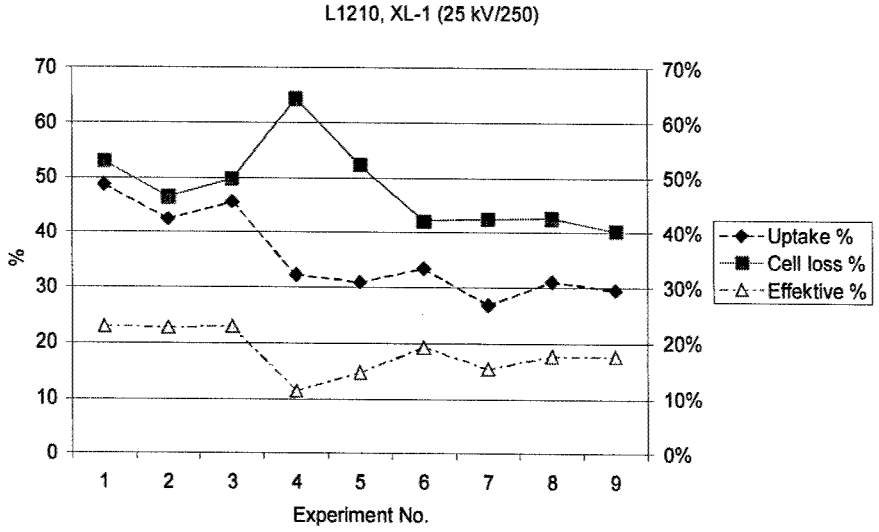

FIGURE 4. Reference experiments with XL-1: The mean FD-uptake is 36% +- 8 when repeating the experiments several times at several days. The number of lost cells is 48%+- 8, yielding an overall transfer efficacy in L1210 cells of 18% +-4.

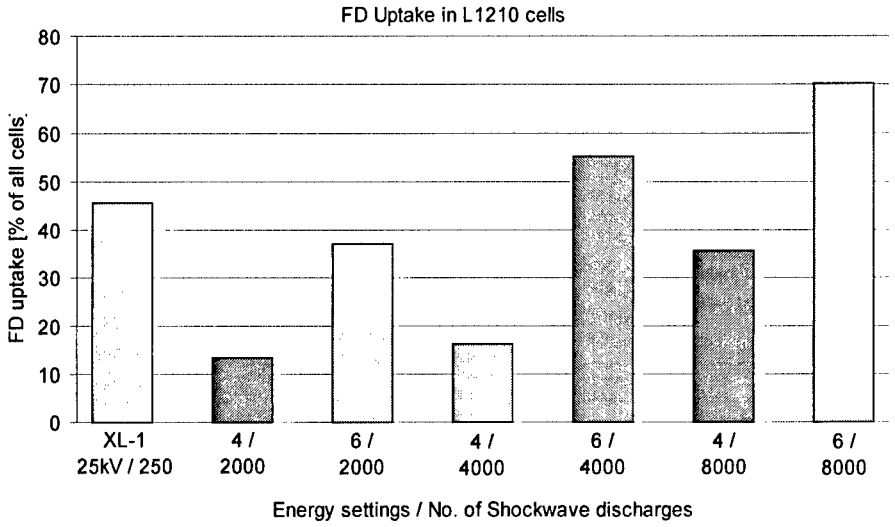

FIGURE 5. Fluorescin-Dextran uptake in Lymphocytes using XL-1 and PR-II sources at 1 Hz pulse repetition frequency. Parameters: pressure pulse intensity and number of pulses.

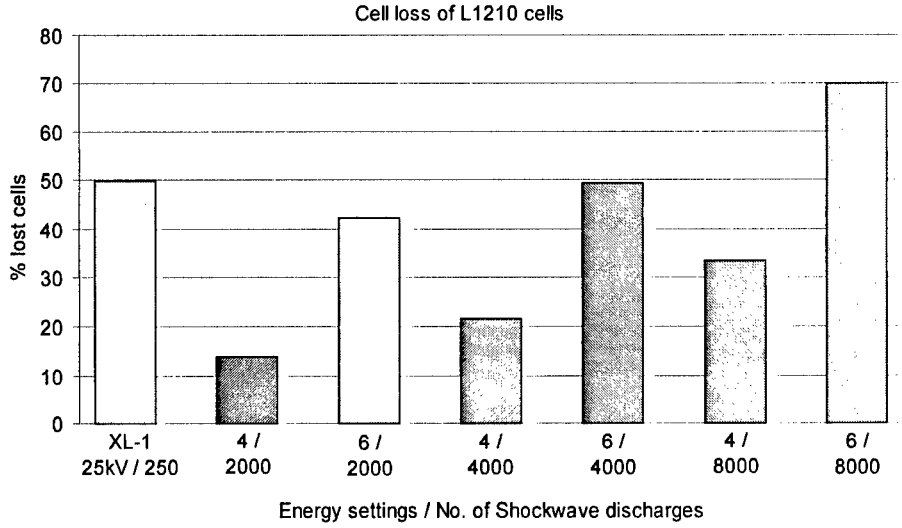

FIGURE 6. Number of lost cells in the experiments as of Figure 5.

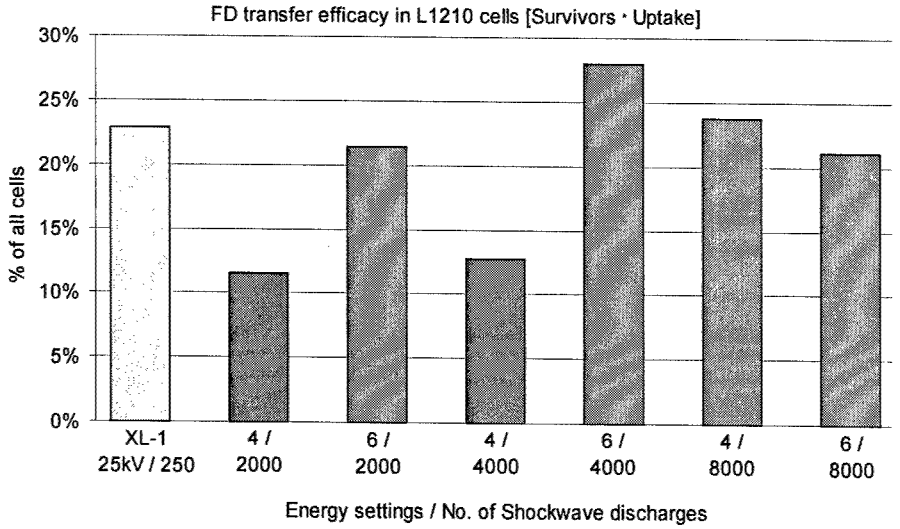

FIGURE 7. Effective number of surviving cells out of the original amount (10^6 cells per Milliliter) which have taken up FD molecules.

DISCUSSION

The first results using the piezoelectric source are promising. Future experiments will involve characterization and optimisation of the acoustic output as well as tests of more cell / molecule systems.

By selection of the appropriate parameters molecules can be transferred into cells with a high efficacy and repeatability by using pressure pulses.

Besides the molecule uptake another important parameter is the amount of lost cells. Depending on the scope of the experiments an optimum between molecule uptake and lost cells can be chosen. It is already known from further experiments using oligonucleotides that the molecules actually penetrate the cell core and are able to control the behavior of the cell [7]. Thus sound poration using pressure pulses can be a tool for the molecule transfer into cells in biotechnology.

The most important advantage of this method could be the *in vivo* use, because it is feasible to penetrate the deepest layers of the body with shock waves and pressure pulses, as proven by lithotripsy. Extracorporeal induced, focused pressure pulses may become a therapeutic option for the targeted activation of biotechnological drugs, which are given to the patient in sub-critical doses.

ACKNOWLEDGMENTS

Thanks to Stefan Endres, Gunther Hartmann, Heckelsmiller, Miren Kerkmann and Katharina Tschoep, Innenstadtklinik, Universität München; and Gerhard Adams,

Universitäts-Klinikum Grosshadern, München. This work was supported in part by a research grant from Bayern Innovativ.

REFERENCES

1. Rooney, "Hemolysis near a ultrasonically pulsating gas bubble," *Science*, **258**, pp. 869-871 (1970).
2. M. Delius, "Schwellintensitäten kavitativer Ultraschallwirkungen," in: Sicherheitsaspekte der Sonographie, Sachverständigenanhörung der Strahlenschutzkommission, 2./3. März 1995, Stuttgart: G.Fischer, 1998.
3. Philipp, Delius, Scheffcyk, Vogel und Lauterborn, "Interaction of lithotripter-generated shock waves with air bubbles," *JASA*, **5**, pp. 2496-2509 (1993).
4. Fowlkes und Crum, "Cavitation threshold measurements for microsecond length pulses of ultrasound," *JASA*, **83**, pp. 2190-2201 (1988).
5. P. Steinbach, "Effekte hochenergetischer Ultraschallstoßwellen auf Tumorzellen *in vitro* und humane Endothelzellen *in situ*," in: Die Stoßwelle: (Chaussy et al., eds.), pp. 104-109, Tübingen: Attempto (1993).
6. Gambihler, Delius und Ellwart, "Permeabilization of the plasma membrane of L1210 mouse leukaemia cells using lithotripter shock waves," *J Membr Biol*, **141** (1994).
7. Tschoep, Hartmann, Jox, Thompson, Eigler, Krug, Erhardt, Adams, Endres, Delius, "Shock waves: a novel method for cytoplasmic delivery of antisense oligonucleotides," *J Mol Med*, **79**, pp. 306-313 (2001).
8. Luderer, Bohris, Bellemann, "Quantitative evaluation of cavitation bubble fields induced by lithotripter shock waves," Biomedizinische Technik (Sonderband), No. 1030 (2002).

Effects Of Diagnostic Ultrasound Parameters On Molecular Uptake And Cell Viability

Annemieke van Wamel[1-2], Ayache Bouakaz[1-2], Jaco Houtgraaf[3], Folkert ten Cate[1], and Nico de Jong[1-2]

[1]*Thoraxcentre, Erasmus MC, Rotterdam, P.O. box 1738, NL-3000DR Rotterdam, The Netherlands*
[2]*ICIN, Utrecht, The Netherlands*
[3]*Cell Biology & Genetics, Erasmus MC Rotterdam, The Netherlands*

Abstract. The success of drug or gene delivery is limited by the inability of those components to cross biological barriers like the cell membrane. Ultrasound (US) has shown to increase cell membrane permeability in a process known as sonoporation. So far most of the recognized investigations used acoustic settings such as CW or HIFU, which are well far from the diagnostic range. Since a few years now, other studies used US waves within the diagnostic range but in combination with contrast-bubbles. The purpose of our study is to determine the effect of US alone on cell uptake using diagnostic parameters, and to correlate the sonoporation mechanism on the different diagnostic conditions. A monolayer of CHO cells, fixed on a membrane, and Texas-red labeled dextran, as a marker, are used. US at 1 MHz is used, and the effects of MI, duty cycle, pulse length and total exposure are explored at 37° C. The molecular uptake increases with MI when exposed for less than 30 seconds. Using MI between 0.2-0.7, efficiency is reached after 2 minutes of exposure. MI of 1.4 for 30 sec gives the highest molecular uptake (33%) but also a high cell lysis (40%). Under stronger diagnostic conditions (MI 1.4 exposure above 2 min), lysis occurs up to 65%. Significant molecular uptake can be induced by diagnostic pulsed ultrasound without using contrast bubbles. Both molecular uptake and cell viability strongly depend on total exposure time and applied MI. Repetition rate and duty cycle also influence molecular uptake and cell viability. Addition of ultrasound microbubbles increases the ultrasound effects.

INTRODUCTION

Sonoporation is a physical method of permeabilization that uses ultrasound and enables the transfer of impermeable molecules into the cell. More insight into the mechanism of ultrasound permeabilization will give a better understanding of how ultrasound can be used to increase the success of drug and gene delivery. Sonoporation can be invoked with different sets of ultrasound parameters, i.e. the strength of applied field, number of pulses, their duration and repetition frequency. Since theoretical understanding of the sonoporation is still incomplete, the optimal sets of ultrasound parameters for desirable applications are also unknown. Because there have been only relatively few studies on the role of pulse amplitude, duty cycle, and total exposure time in cell sonoporation, we examined the effects of these individual ultrasound parameters on sonoporation efficiency. Correlation of ultrasound and sonoporation efficiency allows a better optimization of the process.

Sonoporation is transient membrane permeabilization with cell survival, and can be detected by uptake of large fluorescent molecules that are normally excluded by the cells. In our in vitro experiments we used Texas-labeled 70 kDa Dextran, which is normally not taken up by cultured cells. Cell lysis is the result from irreversible cell membrane damage and is characterized by the leakage of the cell content into the surrounding resulting in an empty dead cell.

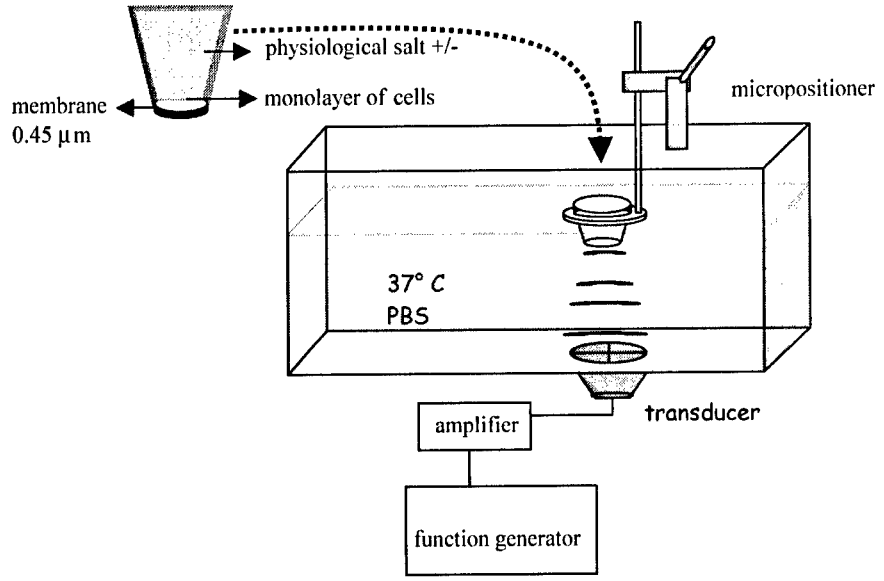

FIGURE 1. *In vitro* set-up.

The experimental acoustic setup is illustrated in Figure 1. A 1-MHz single-element transducer focused at 75 mm, with an aperture of 37 mm, is mounted in a water tank. The cell monolayer was positioned using a micro-positioner at a distance of 75 mm from the transducer and the temperature of the medium was kept constant 37° C. The peak negative acoustic pressure generated at the region of interest extended from 0.2 to 1.4 MPa. These acoustic pressures correspond to mechanical indices between 0.2 and 1. The length of the transmitted pulse ranged from 10 to 15 µs with a duty cycle between 0.1 and 0.75%. The combination of pulse length and duty cycle corresponded to pulse repetition frequencies of the excitation between 0.1 kHz and 0.15 kHz. The duration of the total ultrasound exposures was 10 to 360 seconds. Cells were grown on BD Falcon^{TM} Cell culture Inserts to 90% confluence. Cells (10^5 cell /cm^2) were immersed in PBS containing 5% Texas Red-Dextran with and without microbubbles ($2x10^5$ microbubbles/ml). Cell samples/cultures were exposed to ultrasound at conditions described previously. Using fluorescence microscope, molecular uptake caused by ultrasound was determined by counting the red labeled cells. Cells that were still attached were considered to be viable (Figure 2). Detached cells were considered to be dead. Trypan blue, a marker for cell viability, has been used as exclusion assay in a separate experiment and confirmed that attached cells are viable and dislodged cells are dead.

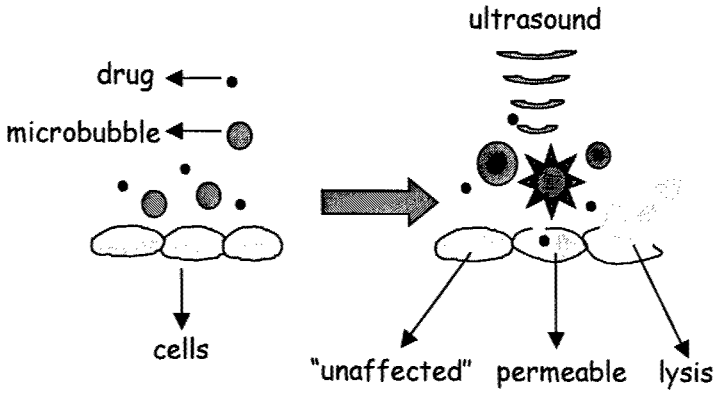

FIGURE 2. Schematic representation of the basic protocol.

RESULTS

The molecular uptake increases with MI when exposed for less than 30 seconds (Figure 3). Using MI between 0.2-0.7, efficiency is reached after 2 minutes of exposure. MI of 1.4 for 30 sec gives the highest molecular uptake (33%) but also a high cell lysis (40%). Under stronger diagnostic conditions (MI 1.4 exposure above 2 min), lysis occurs up to 65%. Significant molecular uptake can be induced by diagnostic pulsed ultrasound without using contrast bubbles. Both molecular uptake and cell viability strongly depend on total exposure time and applied MI. Repetition rate (data not shown) and duty cycle (Figure 4) also influence molecular uptake and cell viability. Molecular uptake as a function of time and ultrasound amplitude (total applied power) onto the cells has a pronounced peak.

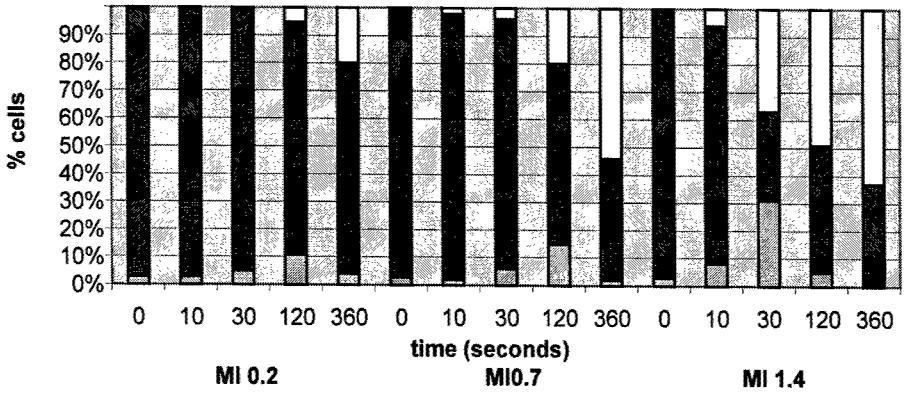

FIGURE 3. The normalized viable cells values for the control (no ultrasound) are expressed as 100% and the values of red stained cells as % of normalized viable cells.

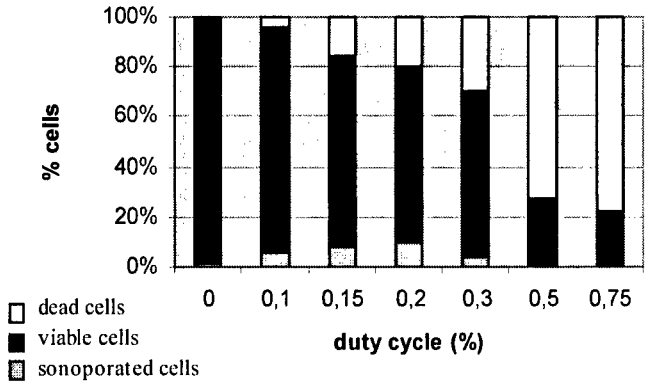

FIGURE 4. Effect of duty cycle on cell viability and molecular uptake.

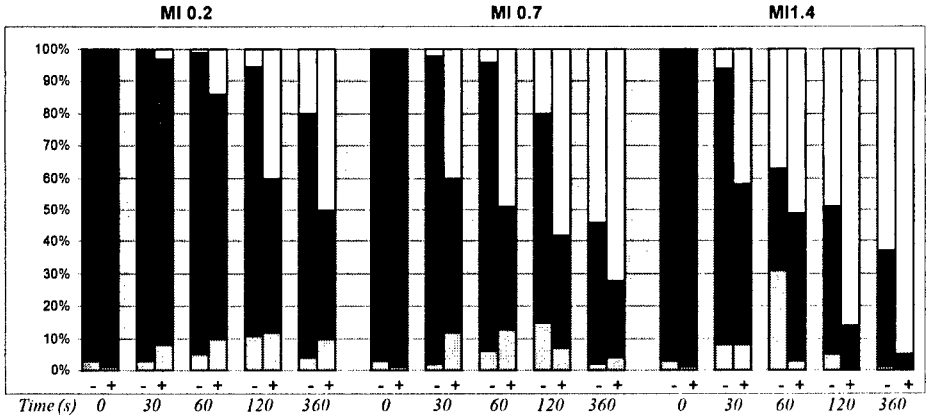

FIGURE 5. The normalized viable cells values for the control (no ultrasound) are expressed as 100% and the values of red stained cells as % of normalized viable cells. ■ viable cells. □ dead cells, ■ sonoporated cells. All shown data are mean of four separate experiments.

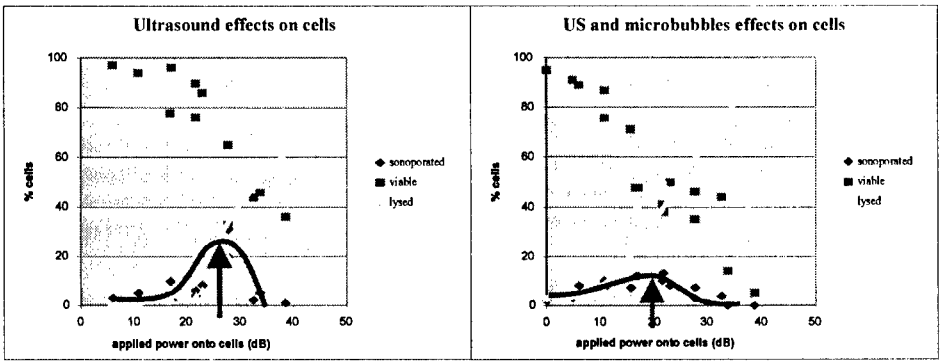

FIGURE 6. The normalized values for the minimal applied power.

Figures 5 and 6. Addition of microbubbles result in a shift of the peak to the left but the peak is lower than without microbubbles. Cell lysis increases as function of time or applied power. Addition of microbubbles results in a shift of the curve to the left.

CONCLUSIONS

Molecular uptake is correlated to time and applied power. When using microbubbles less ultrasound power is needed to lyse cells. For some applications, such as gene therapy, it is important not to lyse any cells whereby the existence of every cell is important. So finding a setting in with cell are not lysed will be important. For other applications, like tumor treatment, it even may be an advantage if a lot of are lysed because finally the aim is to destroy them.

ACKNOWLEDGEMENTS

We gratefully acknowledge the financial support from the Netherlands Technology Foundation STW (Grant RKG 5104).

APPENDIX

ISTU2 Author Attendees

Allen, Mark
Royal Marsden Hospital
Downs Road, Sutton,
Surrey SM2 5PT UK
+44 208 642 6011, x 1238
mark.allen@
rmh.nthames.nhs.uk

Anand, Ajay
Applied Physics Lab, UW
1013 40th St NE
Seattle, WA 98105 USA
206-221-6582
ajaya@apl.washington.edu

Andrew, Marilee
Applied Physics Lab, UW
1013 N.E. 40th St.
Seattle WA 98040 USA
(206) 543-1345
marilee@
apl.washington.edu

Asano, Takehide
Chiba Cancer Center
666-2 Nitona-Cho Chuo-ku
Chiba 260-8717 Japan
81-43-264-5431
Fax 81-43-262-8680
asano@
chiba-cc.pref.chiba.jp

Bai, Jingfeng
Shanghai Jiao Tong Univ.
Rm 0818 of HaoRan Bldg,
1954 HuaShan Rd
Shanghai 200030 China
++86-21-62933209
jfbai@mail.sjtu.edu.cn

Bailey, Michael
Applied Physics Lab, UW
1013 NE 40th St.
Seattle, WA 98105 USA
206-685-8618
bailey@apl.washington.edu

Berriet, Rémi
IMASONIC
15 Rue Alain Savary
Besancon 25000 France
(33) 381 403130
imasonic@imasonic.com

Brayman, Andrew
Applied Physics Lab, UW
1013 NE 40th Street
Seattle, WA 98105 USA
206-543-9825
brayman@apl.washington.edu

Chan, Arthur
Applied Physics Lab, UW
1013 NE 40th Street
Seattle, WA 98105 USA
206-221-6528
ahchan@u.washington.edu

Chapelon, Jean-Yves
INSERM
151, Cours Albert Thomas
Lyon, 69424 Cedex 03 France
33 472 681 934
chapelon@lyon.inserm.fr

Chaussy, Christian
Staedt. Krankenhaus
München-Harlaching
Sanatoriumsplatz 2
Muenchen 81545 Germany
49 89 6210 2790
chau1@aol.com

Chen, Wen-Shiang
Duke University
910 Constitution Dr, # 507
Durham NC 27705 USA
206-685-8225
wschen@duke.edu

Crum, Lawrence
Applied Physics Lab, UW
1013 NE 40th Street
Seattle, WA 98105 USA
206-685-8622
lac@apl.washington.edu

Cunitz, Bryan
Applied Physics Lab, UW
1013 NE 40th Street
Seattle, WA 98105 USA
206-543-1300
bwc@apl.washington.edu

Curra, Francesco
Applied Physics Lab, UW
1013 NE 40th street
Seattle. WA 98105 USA
206 543-9848
fcurra@apl.washington.edu

Damianou , Christakis
Frederick Inst. of Technology
7 Yianni, 11 Despinas Patthi
Limassol 3071 Cyprus
357-99-471977
cdamianou@cytanet.com.cy

de Jong, Nico
Erasmus University
Dr. Molewaterplein 50
Rotterdam 3015 GE
Netherlands
+31 10 4088037
dejong@tch.fgg.eur.nl

Deng, Cheri
Riverside Research Inst.
156 William Street
New York, NY 10038 USA
212 502-1773
cheri@rrinyc.org

Draper, David
Brigham Young University
RB 120-C
Provo, UT 84602 USA
801-422-7866
david_draper@byu.edu

Ebbini, Emad
University of Minnesota
Rm 4-174 EE/CSci Bldg
200 Union St SE
Minneapolis, MN USA
6126251852
emad@ece.umn.edu

Feng, Ruo
Nanjing University
Hankou load 22
Nanjing 210093 China
025-3594964
fengruo@nju.edu.cn

Fink, Mathias
LOA
E.S.P.C.I 10 rue Vauquelin
Paris 75005 France
33 1 40 79 44 52
michael.tanter@espci.fr

Fried, Nathaniel
Johns Hopkins University
Bayview Medical Center
Urology, Bldg A, Rm 347c
Baltimore, MD 21224 USA
410-550-7906
nfried@jhmi.edu

Frizzell, Leon
University of Illinois
405 North Mathews Avenue
Urbana, IL 61801 USA
217-333-0849
frizz@uiuc.edu

Fujimoto, Katsuhiko
Toshiba Corp. Medical Systems Company
1385, Shimo-Ishigami
Otawara-Shi, Tochigi 324-8550 Japan
+81-287-26-6228
katsuhiko.fujimoto@toshiba.co.jp

Furuhata, Hiroshi
Jikei University School of Medicine
25-8 Nishishinbashi 3,Minatoku
Tokyo 105-8461 Japan
81-3-3433-1111
furuhata@kt.rim.or.jp

Greenleaf, James
Mayo Clinic
200 First Street SW
Rochester, MN 55905 USA
507 284-8496
jfg@mayo.edu

He, Shen Xu
Peking University
No.133, Fu Nei Street,
West City District
Beijing 100034 China
8610-66165994
beiyi168@21cn.com

Hepp, Wolfgang
Dornier MedTech Systems
Gmb H, Argelsrieder Feld 7
D-82234 Wessling Germany
0049 8153-888598
whepp@dornier.com

Hwang, Joo Ha
Applied Physics Lab, UW
Box 356424
Seattle, WA 98195 USA
206-221-6528
jooha@u.washington.edu

Jiwei , Jiang (Fank)
Shanghai A&S Technology Development Co., Ltd.
No. 151 Keyuan Road
Zhang Jiang High-Technology Park
Pudong New District,
Shanghai 201203 China
008621-38953611
jiw@aishen-technology.com

Kubota, Jun
Hitachi Medical Corp.
2-1 Shintoyofuta Kashiwa-shi
Chiba-ken 277-0804 Japan
+81-4-7131-4159
kubota@rd.hitachi-medical.co.jp

Kaczkowski, Peter
Applied Physics Lab, UW
1013 NE 40th Street
Seattle, WA 98105 USA
206-543-1283
peter@apl.washington.edu

Kamaev, Pavel P.
Georgia Inst. of Technology
315 Ferst Dr
Atlanta, GA 30332 USA
404-894-4490
pavel.kamaev@che.gatech.edu

Kargl, Steven
Applied Physics Lab, UW
1013 NE 40th street
Seattle. WA 98105 USA
206 685-4677
kargl@apl.washington.edu

Karp, Floyd
EKOS Corporation
22030 20th Ave SE, Ste 101
Bothell, WA 98021 USA
425-482-1108
FKarp@ekoscorp.com

Kawabata, Ken-ichi
Central Research Lab.
Hitachi, Ltd.
1-280 Higashi-Koigakubo
Kokubunji
Tokyo 185-8601 Japan
+81-42-323-1111
kk@crl.hitachi.co.jp

Kennedy, James
The Churchill Hospital
40 Bartelmas Road
Oxford OX4 1XX ENGLAND
(44)1865763100
jekennedy@doctors.org.uk

Kimmel, Eitan
Technicon IIT
1 Ela Ramat-Hasharon
47212 Israel
972-3-5407066
agreita@tx.technion.aYc.il

Lacoste, François
EDAP Technomed
Parc D'Activites La Poudrette
4-6, Rue du Dauphine
Vaaulx en Velin 69120 France
33(0)472153150
Flacoste@compuserve.com

Lafon, Cyril
INSERM
151, Cours Albert Thomas
Lyon 69003 France
(33) 472 68 1930
lafon@lyon.inserm.fr

LeBaron, Olivier
IMASONIC
15 Rue Alain Savary
Besancon 25000 France
(33) 381 403130
olivier.lebaron@imasonic.com

Lizzi, Frederic
Riverside Research Inst.
156 William Street
New York, NY 10038 USA
212 502-1774
lizzi@rrinyc.org

Makin, Inder
Ethicon Endo-Surgery
4545 Creek Road
Cincinnati, OH 45242 USA
513-337-7353
imakin@eesus.jnj.com

Marberger, Michael
University of Vienna
Wdhringer G|rtel 18-20, A-1090
Vienna, Austria
43 1 402 79 22
uroldep@akh-wien.ac.at

Martin, Roy
Applied Physics Lab, UW
1013 NE 40th St
Seattle, WA 98105 USA
206 221 6527
rmartin@apl.washington.edu

Matsumoto, Yoichiro
The University of Tokyo
Hongo, Bunkyo-ku
Tokyo 113-8656 Japan
+81-5841-6286
ymats@mech.t.u-tokyo.ac.jp

McAteer, James
Indiana Univ Sch of Medicine
635 Barnhill Dr., MS 5055
Indianapolis, IN 46202 USA
317-274-7935
mcateer@anatomy.iupui.edu

Melo De Lima, David
INSERM
151, Cours Albert Thomas
Lyon 69003 France
(33) 472 68 1930
melodelima@
lyon151.inserm.fr

Miao, Carol
University of Washington
Box 356320
Seattle, WA 98195 USA
(206) 685-0487
miao@u.washington.edu

Miller, Douglas
University of Michigan
3315 Kresge III, 200 Zina
Pitcher Place
Ann Arbor, MI 48109-0553
USA
734-647-3344
douglm@umich.edu

Mortimer, Bruce
EAI
933 Lewis Drive, Suite C
Winter Park, FL 32789 USA
+27 21 4603096
bmort@ctech.ac.za

Mourad, Pierre
Applied Physics Lab, UW
1013 NE 40th Street
Seattle, WA 98105 USA
206-543-6921
pierre@apl.washington.edu

Muratore, Robert
Riverside Research Inst.
156 William St Fl 9
New York NY 10038 USA
+1 (212) 502-1701
muratore@rrinyc.org

Noble, Misty
Applied Physics Lab, UW
1013 NE 40th street
Seattle. WA 98105 USA
206 221 6526
mnoble@apl.washington.edu

Nogata, Fumio
Gifu University
Gifu-city 501-1193 Japan
+81-58-293-2506
nogata@cc.gifu-u.ac.jp

Paun, Marla
Applied Physics Lab, UW
1013 NE 40th Street
Seattle, Wa. 98105 USA
206-417-1322
mpaun@apl.washington.edu

Porter, Tyrone
Applied Physics Lab, UW
1013 NE 40th St
Seattle, WA 98105 USA
(206) 543-1323
tporter@apl.washington.edu

Prokop, Adrian
Applied Physics Lab, UW
1013 NE 40th ST
Seattle, WA 98105 USA
206-221-6528
adrianp@u.washington.edu

Reed, Justin
Applied Physics Lab, UW
1013 NE 40th Street
Seattle, WA 98105 USA
jphys007@u.washington.edu

Rivens, Ian
Inst. of Cancer Research
Joint Department of Physics
Sutton, Surrey, SM2 5PT UK
+44 (0)20 8661 3708
ian@icr.ac.uk

Roy, Ronald
Boston University
110 Cummington Street
Boston, MA 02215 USA
617-353-4846
ronroy@bu.edu

Saguchi, Takayuki
Jikei Univ. Sch. of Medicine
25-8 Nishishinbashi 3,
Minatoku
Tokyo 105-8461 Japan
81-3-3433-1111
saguchi@jikei.ac.jp

Sanghvi, Narendra
Focus Surgery Inc.
3940 Pendleton Way
Indianapolis, IN 46226 USA
317-541-1580
nsanghvi@focus-surgery.com

Seip, Ralf
Focus Surgery Inc.
3940 Pendleton Way
Indianapolis, IN 46226 USA
317-541-1580
rseip@focus-surgery.com

Sheehan, Florence
University of Washington
Box 356422
1959 NE Pacific St
Seattle, WA 98195 USA
206-543-4535
sheehan@u.washington.edu

Simari, Robert
Mayo Clinic
200 1st St. SW
Rochester, MN 55902 USA
507-284-3727
simari.robert@mayo.edu

Sokka, Shunmugavelu
Brigham & Women's Hosp.
65 Landsdowne St, Ste 252
Cambridge, MA 02139 USA
617-768-8310
sham@mit.edu

Sun, Fucheng
Shanghai Jiao Tong Univ.
1954 Hua Shan Road
Shanghai 200030
P.R.China
0086-21-50802150
fucheng_sun@hotmail.com

Tachibana, Katsuro
Fukuoka University
School of Medicine
7-45-1 Nanakuma Jonan
Fukuoka 814-0180 JAPAN
81-92-801-1011
k-tachi@cis.fukuoka-u.ac.jp

Tachibana, Shunro
Sasaguri Hospitale
1-6-18 Kusagae, Chuo
Fukuoka 810-0045 JAPAN
81-92-741-3279
k-tachi@cis.fukuoka-u.ac.jp

Tanter, Mickael
Laboratoire Ondes et Acoustique
E.S.P.C.I 10 rue Vauquelin
Paris 75005 France
33 1 40 79 51 67
michael.tanter@espci.fr

Tasaki, Kentaro
Chiba Cancer Center
666-2 Nitona, Chuo-ku
Chiba 260-8717 Japan
81-43-264-5431
ktasaki@chiba-cc.pref.chiba.jp

Tavakkoli, Jahan
Focus Surgery Inc.
3940 Pendleton Way
Indianapolis, IN 46226 USA
317-541-1580
jahan@focus-surgery.com

Taylor, Lawrence (Larry)
University of Rochester
P.O. Box 270126
Rochester, NY 14627 USA
585-273-4919
lataylor@ece.rochester.edu

ter Haar, Gail
Inst. of Cancer Research
Royal Marsden Hospital
Sutton, Surrey SM2 5PT UK
+44 208 947 7747
gail@icr.ac.uk

Umemura, Shin-ichiro
Hitachi Ltd.
Kokubunji
Tokyo 185-8601 Japan

Vaezy, Shahram
Applied Physics Lab, UW
1013 NE 40th Street
Seattle, WA 98105 USA
206-543-8533
vaezy@apl.washington.edu

van Wamel, Annemekie
Erasmus University
Dr. Molewaterplein 50
Rotterdam 3015 GE
Netherlands
+31 10 4088031
vanwamel@tch.fgg.eur.nl

Wang, Wei
Beijing 307 Hospital
#2 Beitaiping Road
Dept. of Ultrasound
307 Hospital Address2
Beijing 100039 P.R.China
86-10-66874788
8wangw@ammms.ac.cn

Wang, Zhibiao
Institute of Ultrasound Engineering in Medicine
Chongqing 400016
PR China
c/o mfengwu@yahoo.com

Wu, Feng
Clinical Center for Tumor Therapy of 2nd Affiliated Hospital
Chongqing Univ of Medical Science
Chongqing 400016
P. R. China
+86-23-6373-7940
mfengwu@yahoo.com

Zderic, Vesna
Applied Physics Lab, UW
1013 NE 40th Street
Seattle, WA 98105 USA
206-221-6528
vesna@u.washington.edu

Zhang, Ming
Jiangsu Cancer Hospital
42 Bai Zi Ting Str.
Nanjing,Jiangsu 210009
P.R.China
7714924
mingmin1206.@sina.com

Zheng, Guoqiang
Peking University
School of Oncology
Beijing Cancer Hospital
Beijing, PR China
guoqiang0911@263.net

Zhong, Pei
Duke University
144 Hudson Hall
3000 Science Drive
Durham, NC 27708 USA
919-660-5336
pzhong@duke.edu

AUTHOR INDEX